Advances in Experimental Medicine and Biology 1395

Felix Scholkmann
Joseph LaManna
Ursula Wolf *Editors*

Oxygen Transport to Tissue XLIII

Springer

Advances in Experimental Medicine and Biology

Volume 1395

Advances in Experimental Medicine and Biology provides a platform for scientific contributions in the main disciplines of the biomedicine and the life sciences. This series publishes thematic volumes on contemporary research in the areas of microbiology, immunology, neurosciences, biochemistry, biomedical engineering, genetics, physiology, and cancer research. Covering emerging topics and techniques in basic and clinical science, it brings together clinicians and researchers from various fields.

Advances in Experimental Medicine and Biology has been publishing exceptional works in the field for over 40 years, and is indexed in SCOPUS, Medline (PubMed), EMBASE, BIOSIS, Reaxys, EMBiology, the Chemical Abstracts Service (CAS), and Pathway Studio.

2021 Impact Factor: 3.650 (no longer indexed in SCIE as of 2022)

Felix Scholkmann
Joseph LaManna • Ursula Wolf
Editors

Oxygen Transport to Tissue XLIII

Springer

Editors
Felix Scholkmann
Institute of Complementary and Integrative Medicine
University of Bern
Bern, Switzerland

Biomedical Optics Research Laboratory, Department of Neonatology
University Hospital Zurich, University of Zurich
Zurich, Switzerland

Ursula Wolf
Institute of Complementary and Integrative Medicine
University of Bern
Bern, Switzerland

Joseph LaManna
Department of Physiology & Biophysics
Case Western Reserve University
Cleveland, OH, USA

ISSN 0065-2598 ISSN 2214-8019 (electronic)
Advances in Experimental Medicine and Biology
ISBN 978-3-031-14189-8 ISBN 978-3-031-14190-4 (eBook)
https://doi.org/10.1007/978-3-031-14190-4

This Springer imprint is published by the registered company Springer Nature Switzerland AG
The registered company address is: Gewerbestrasse 11, 6330 Cham, Switzerland

Organization ISOTT 2021

Organizing Committee
Oliver Kress, University of Bern, Switzerland
Tarcisi Cantieni, University of Bern, Switzerland
Felix Scholkmann, University of Bern, Switzerland
Martin Wolf, University of Zurich, Switzerland
Ursula Wolf, University of Bern, Switzerland

ISOTT Officers and Executive Committee
Ursula Wolf (President, Bern, Switzerland)
Oliver Thews (Secretary, Halle, Germany)
Peter E. Keipert (Treasurer, San Diego, CA, USA)
Joseph LaManna (Publication Committee, OH, Cleveland, USA)
Edwin M. Nemoto (Past President, Albuquerque, NM, USA)
Kaoru Sakatani and Kazuto Masamoto (Presidents-Elect, Tokyo, Japan)
Gemma Bale (Executive Committee, Cambridge, UK
Hiroshi Hirata (Executive Committee, Sapporo, Japan)
Sally Pias (Executive Committee, Albuquerque, NM, USA)
Michelle A. Puchowicz (Executive Committee, Memphis, TE, USA)
Anne Riemann (Executive Committee, Halle, Germany)
Guennadi Saiko (Executive Committee, Toronto, Canada)
Felix Scholkmann (Executive Committee, Bern and Zurich, Switzerland)
Harold M. Swartz (Executive Committee, Hanover, USA)

Conference Organization
Paolo Demaria

Impression of the ISOTT2021 Online Conference

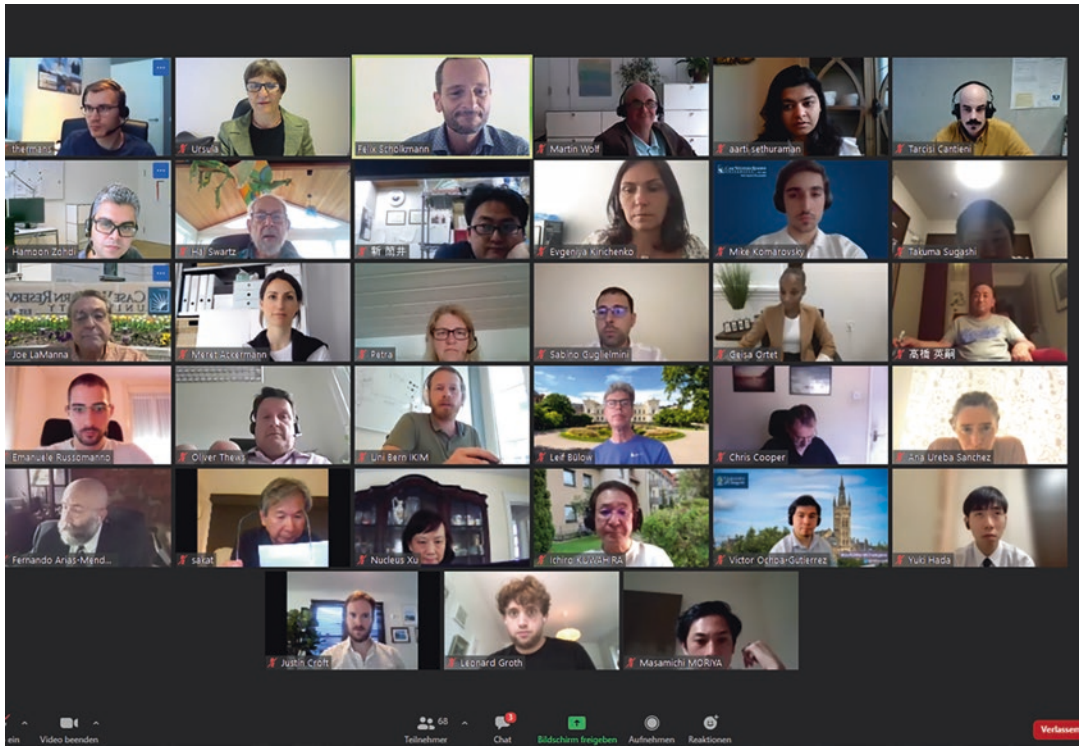

Picture of some participants during the ISOTT 2021 conference

Awards

The Melvin H. Knisely Award

It was established in 1983 to honor Dr. Knisely's accomplishments in the field of the transport of oxygen and other metabolites and anabolites in the human body. Over the years, he has inspired many young investigators, and this award is to honor his enthusiasm for assisting and encouraging young scientists and engineers in various disciplines. The award is to acknowledge outstanding young investigators. Award recipients:

1983: Antal G. Hudetz (Hungary)
1984: Andras Eke (Hungary)
1985: Nathan A. Bush (USA)
1986: Karlfried Groebe (Germany)
1987: Isumi Shibuya (Japan)
1988: Kyung A. Kang (Korea/USA)
1989: Sanja Batra (Canada)
1990: Stephen J. Cringle (Australia)
1991: Paul Okunieff (USA)
1992: Hans Degens (The Netherlands)
1993: David A. Benaron (USA)
1994: Koen van Rossem (Belgium)
1995: Clare E Elwell (UK)
1996: Sergei A. Vinogradov (USA)
1997: Chris Cooper (UK)
1998: Martin Wolf (Switzerland)
1999: Huiping Wu (USA)
2000: Valentina Quaresima (Italy)
2001: Fahmeed Hyder (Bangladesh)
2002: Geofrey De Visscher (Belgium)
2003: Mohammad Nadeem Khan (USA)
2004: Fredrick Palm (Sweden)
2005: Nicholas Lintell (Australia)
2007: Ilias Tachtsidis (UK)
2008: Kazuto Masamoto (Japan)
2009: Rossana Occhipinti (USA)
2010: Sebatiano Cicco (Italy)
2011: Mei Zhang (USA)
2012: Takahiro Igarashi (Japan)

2013: Malou Friederich-Persson (Sweden)
2014: David Highton (UK)
2015: Alexander Caicedo-Dorado (Belgium)
2016: Sally Pias (USA)
2017: Felix Scholkmann (Switzerland)
2018: Anne Riemann (Germany)
2019: Ting Li (China)
2021: An Ghysels (Belgium)

The Dietrich W. Lübbers Award

It was established in honor of Professor Lübbers's long-standing commitment, interest, and contributions to the problems of oxygen transport to tissue and to the society. Award recipients:

1994: Michael Dubina (Russia)
1995: Philip E. James (UK/USA)
1996: Resit Demit (Germany)
1997: Juan Carlos Chavez (Peru)
1998: Nathan A. Davis (UK)
1999: Paola Pichiule (USA)
2000: Ian Balcer (USA)
2001: Theresa M. Busch (USA)
2002: Link K. Korah (USA)
2003: James J. Lee (USA)
2004: Richard Olson (Sweden)
2005: Charlotte Ives (UK)
2006: Bin Hong (China/USA)
2007: Helga Blockx (Belgium)
2008: Joke Vanderhaegen (Belgium)
2009: Matthew Bell (UK)
2010: Alexander Caicedo Dorado (Belgium)
2011: Malou Friedrich (Sweden)
2012: Maria Papademetriou (UK)
2013: Nannan Sun (China)
2014: Felix Scholkmann (Switzerland)
2015: Shun Takagi (Japan)
2016: Gemma Bale (UK)
2017: Ben Jones (UK)
2018: Hamoon Zohdi (Switzerland)
2019: Kazaki Hotta (Japan)
2021: Masamichi Moriya (Japan)

The Britton Chance Award

It was established in honor of Professor Chance's long-standing commitment, interest and contributions to the science and engineering aspects of oxygen transport to tissue and to the society. Award recipients:

2004: Derek Brown (Switzerland)
2005: James Lee (USA)
2006: Hanzhu Jin (China/USA)
2007: Eric Mellon (USA)
2008: Jianting Wang (USA)
2009: Jessica Spires (USA)
2010: Ivo Trajkovic (Switzerland)
2011: Alexander Caicedo Dorado (Belgium)
2012: Felix Scholkmann (Switzerland)
2013: Tharindi Hapuarachchi (UK)
2014: Anne Riemann (Germany)
2015: Wenhao Xie (China)
2016: Linda Ahnen (Switzerland)
2017: Helene Isler (Switzerland)
2018: Jingjing Jiang (Switzerland)
2019: Alexander Kalyanov (Switzerland)
2021: Maheen Siddiqui (UK)

The Duane F. Bruley Travel Awards

They were established in 2003. They were created to provide travel funds for student researchers in all aspects of areas of oxygen transport to tissue. It is hoped that receiving the Duane F. Bruley Travel Award will inspire students to excel in their research and will assist in securing future leadership for ISOTT.

2004: Helga Blocks (Belgium), Jennifer Caddick (UK), Charlotte Ives (UK), Nicholas Lintell (Australia), Leonardo Mottola (Italy), Samin Rezania (USA/Iran), Ilias Tachtsidis (UK), Liang Tang (USA/China), Iyichi Sonoro (Japan), Antonio Franco (Italy)
2005: Robert Bradley (UK), Harald Oey (Australia), Kathy Hsieh (Australia), Jan Shah (Australia)
2006: Ben Gooch (UK), Ulf Jensen (Germany), Smruta Koppaka (USA), Daya Singh (UK), Martin Tisdall (UK), Bin Wong (USA), Kui Xu (USA)
2007: Dominique De Smet (Belgium), Thomas Ingram (UK), Nicola Lai (USA), Andrew Pinder (UK), Joke Vanderhaegen (Belgium)
2008: Sebastiano Chicco (Italy)
2009: Lei Gao (UK), Jianting Wang (USA), Obinna Ndubuizu (USA), Joke Vanderhaegen (Belgium)
2010: Zareen Bashir (UK), Tracy Moroz (UK), Mark Muthalib (Australia), Catalina Meßmer (USA), Takashi Eriguchi (Japan), Yoshihiro Murata (Japan), Jack Honeysett (UK), Martin Biallas (Switzerland)
2011: Catherine Hesford (UK), Luke S. Holdsworth (UK), Andreas Metz (Switzerland), Maria D. Papademetriou (UK), Patrik Persson (Sweden), Felix Scholkmann (Switzerland), Kouichi Yoshihara (Japan)

2012: Allann Al-Armaghany (UK), Malou Friederich-Persson (Sweden), Tharindi Hapuarachchi (UK), Benjamin Jones (UK), Rebecca Re (Italy), Yuta Sekiguchi (Japan), Ebba Sivertsson (Sweden), André Steimers (Germany)

2013: Allann Al-Armaghany (UK), Gemma Bale (UK), Alexander Caicedo-Dorado (Belgium), Luke Dunne (UK)

2014: Geraldine De Preter (Belgium), Benjamin Jones (UK), Stefan Kleiser (Switzerland), Nassimsadat Nasseri (Switzerland), Marie-Aline Neveu (Belgium), Shinsuke Nirengi (Japan), Takuya Osawa (Japan)

2015: Gemma Bale (UK), Chenyang Gao (China), Chae Jeong Lim (Korea), Phong Phan (UK), Guennadi Saiko (Canada), Kuangyu Shi (Germany), Nannan Sun (China)

2016: Isabel De Roever (UK), Yuya Enokida (Japan), Jingjing Jiang (Switzerland), Frédéric Lange (UK), Andreas J Metz (Switzerland), Shun Takagi (Japan)

2017: Luca Giannoni (UK), Jingjing Jiang (Switzerland), Alexander Kalyanov (Switzerland), Zuzana Kovacsova (UK), Nassim Nasseri (Switzerland), Maheen Faisal Siddiqui (UK), Shun Takagi (Japan), Yusuke Tsuruno (Japan), Lina Xu (Germany), Hamoon Zohdi (Switzerland)

2018: Andrei Belten (Canada), Aldo Di Costanzo Mata (Switzerland), Yuki Komuro (Japan), Joshua Russell-Buckland (UK), Dries Hendrikx (Belgium), Shun Takagi (Japan)

2019: Gary Angles (USA), Min Feng (USA), Thea Hüsing (Germany), Bhabuk Koirala (USA), Sho Kojima (Japan), Jonathan Nguyen (USA), Labiblais Rahman (Japan), Mandy Rauschner (Germany), Aarti Sethuraman (USA), Eileen Thiessen (USA)

Preface

Having successfully secured a booking at the famous Conference Center on Monte Verità, Switzerland, and with financial support for the ISOTT 2020 conference confirmed, the COVID-19 pandemic came along and the event had to be cancelled. We postponed the conference to 2021 but our hopes were once again dashed as ongoing uncertainty and travel restrictions made it impossible to hold the ISOTT conference on site 1 year later. Within our community of scientists, and particularly among the younger members, the wish to present work and share findings remained strong, however, and so we decided to take a digital approach. The 2021 ISOTT conference was held online for first time in our history and open to all attendees free of charge. The call for registrations was well received as a high number of scientists from all over the world signed up to take part. Talks were presented and discussed via Zoom, while gather.town hosted poster presentations as well as informal gatherings and discussions.

The highly interdisciplinary scientific program covered all aspects of oxygen transport – from air to the cells, organs, and organisms; to instrumentation and methods to measure oxygen; and to clinical evidence. We focused our attention on contributions from young scientists since they had suffered most as a result of measures during the pandemic. The program included 39 invited speakers, 101 abstracts (39 talks and 62 posters), and 152 registered participants (54 students) from 18 countries. The spirit of ISOTT was alive and palpable despite the novel format: an interested, prestigious, and active audience, well-attended sessions, and lively follow-up discussions at a high scientific level. Alongside the atmosphere of enthusiasm and mutual interest, a key highlight was the constructive and stimulating interaction between experts in the field and students. And so it was that we were able to celebrate the huge success of our ISOTT 2021 online conference. We would like to thank everyone who participated or assisted in carrying out this event.

Ursula Wolf, MD, Professor of Medicine
President ISOTT, 2021

In Memoriam: David Keith Harrison (1951–2021)

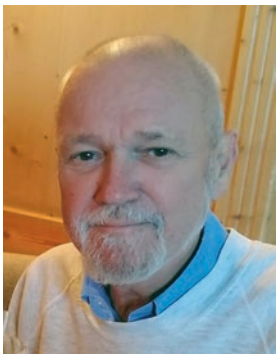

David K. Harrison was born in Cleethorpes, Lincolnshire (UK), on 8 August 1951 – a real "Yellowbelly" as he was proud to say. He attended Clee Humberstone Foundation Grammar School and then, in 1969, went to Dundee to study electrical engineering but switched to physics. He graduated with honors in 1973 and was appointed as an economic forecaster at BP. Later, after turning down a post in the NHS, David was offered a PhD in medical biophysics, based in Ninewells Hospital. After graduation, David took a post with the new principal of the University, Adam Neville, a world-renowned civil engineer, whose textbooks on concrete, especially creep in concrete, needed revision for the new editions – David's first experiences of scientific editing, a sign of the future.

In 1980, David attended a small meeting on oxygen transport hosted by the Max-Planck-Institute for Applied Physiology in Dortmund (Germany). This was a visit which was to have far-reaching consequences and change his life. During the meeting he was approached by Professor Manfred Kessler, who had just moved from Dortmund to Erlangen to build up his research team in the 2nd Institute of Physiology on the University campus in Erlangen.

For David, this was a move with a decisive change in direction. In spring 1981, David was awarded a prestigious "Alexander von Humboldt Stipendium," allowing him to join the Erlangen group. The Harrison family remained for nearly 10 years in Erlangen, and David completed his habilitation (venia legendi, Dr. med. habil.) in January 1990.

Later in 1990, the Harrison family set off back to the UK as David took up a new post at Ninewells Hospital in Dundee. David refined the oxygen methods to be used in clinical measurement that would be applied in the neo-

natal unit, in radiotherapy monitoring, and amputation assessment in diabetics.

Then came another move – as head of medical physics in Durham, then part of the largest medical physics department in Europe. There he continued his research and extended the clinical work to O_2 measurement in bowel stomas and breast reconstruction. Unfortunately, in the following decade, his post became increasingly administrative and time for research extremely limited. As a consequence, David retired early and the Harrisons moved to St. Lorenzen/Tyrol, Italy. The University of Innsbruck/Austria being the nearest academic institution, David joined Professor Erich Gnaiger at Oroboros Instruments and moved field again into high-resolution respirometry and mitochondrial research with their O2k devices.

Over the years, David has published numerous research articles related to oxygen transport in tissue in esteemed journals, above all in the ISOTT Proceedings. David's first ISOTT meeting was held in Nijmegen (1984). The next was the Sapporo meeting (1987). After the meeting in Mainz (1992), he attended most of the following meetings. Unfortunately, he could not attend the Istanbul meeting in 1994 because a few weeks before he was diagnosed with a highly aggressive mediastinal tumor. In his absence, at the meeting, he was nominated President Elect, and 2 years later, David and Eileen Harrison welcomed ISOTT to Dundee for a very Scottish meeting with high tea, haggis, whisky, pipers, a ceilidh, and a boat, the "Discovery," which was to start a tradition that lasted for a long time with river trips at many later meetings.

David's outstanding services for ISOTT include his Editorships on 17 *Oxygen Transport to Tissue* (OTTT) volumes, beginning with the proceedings from his ISOTT meeting in Dundee, 1996 (OTTT XIX). In 2003 a decision was taken that David should act as a scientific editor to ensure continuity, joining Laraine Visser who after the Curacao meeting did the language editing for two decades. When all editorial work went digital, Eileen M. Harrison joined the editorial team acting as technical editor. As scientific editor, David also organized the mandatory review of all manuscripts submitted, always selecting appropriate reviewers to guarantee the high scientific standard of the OTTT volumes, which were co-edited by the president of the respective ISOTT meeting.

In 2019, David realized that, in the future, his health was not going allow him to devote the 6 months per year required for this task and resigned as scientific editor. In fact, he completed the final bits of the Albuquerque book (OTTT XLII) with some difficulty as he had fallen and had a spinal fracture. After the fall he never really recovered as the coronavirus pandemic spread just as he should have started rehabilitation. He deteriorated physically due to several subsequent falls and was referred to palliative care, where he temporarily improved his physical and mental status. Finally, his daughters Natalie and Francesca provided exemplary 24/7 care for him at home until his redemptive death on 29 October 2021.

With David's passing I have lost a long-standing, dear friend, and the ISOTT community has lost a loyal and highly supportive member. During 35 years of ISOTT membership, David presented himself as an innovative

researcher, fair and supportive discussant, and as a friendly, very kind, open-minded, restrained, and extremely sociable person. He will be sorely missed. R.I.P.

On behalf of ISOTT

Dr. med. Peter Vaupel, Professor (emeritus) of Physiology and Pathophysiology

Acknowledgments

Sponsors
As president of the 2021 Conference of the International Society on Oxygen Transport to Tissue, held virtually from July 27 to 30 2021, I would like to gratefully acknowledge the support of our sponsors:
EXCITE ZURICH

EXCITE
ZURICH IMAGING

Contributors
In addition, I would like to thank those who helped make this meeting a success: Oliver Kress, Tarcisi Cantieni, Martin Wolf, and in particular Paolo Demaria.

Reviewers
The editors would like to thank the following experts, who scientifically reviewed the manuscripts:

Reviewer	Institution
Ilias Tachtsidis	University College London, UK
Katsunori Oyama	Nihon University, Japan
Sebastiano Cicco	University of Bari, Italy
Hiroshi Hirata	Hokkaido University, Japan
Chris Cooper	University of Essex, UK
Kui Xu	Case Western Reserve University, Cleveland, USA
H. Nucleus Xu	University of Pennsylvania, Philadelphia, USA
Kaoru Sakatani	University of Tokyo, Japan
Lin Li	University of Pennsylvania, Philadelphia, USA
Denis Bragin	Lovelace Biomedical Research Institute, USA
Yu Okuma	Fukuyama City Hospital, Japan
Oliver Kress	University of Bern, Switzerland
Joseph LaManna	Case Western Reserve University, Cleveland, USA
Akinori Ebihara	Tokai University, Japan
Peter Vaupel	University of Freiburg, Germany
Eiji Takahashi	Saga University, Japan
Ed Nemoto	University of New Mexico, Albuquerque, USA

Reviewer	Institution
Michelle Puchowicz	University of Tennessee Health Science Center, Memphis, USA
Frederick Lange	University College London, UK
Oliver Thews	University of Halle, Germany
Jeff Dunn	University of Calgary, Canada
Hal Swartz	Geisel College of Medicine at Dartmouth, Hanover, USA
Howard Halpern	University of Chicago, USA
Sally Pias	New Mexico Institute of Mining and Technology, USA
Felix Scholkmann	University of Bern & University of Zurich, Switzerland
Martin Wolf	University of Zurich, Switzerland
Ursula Wolf	University of Bern, Switzerland

We also thank Rachel Scholkmann for proofreading all manuscripts.

Contents

Part V Tissue Oxygenation

Part VI Muscle

Part I

Brain

Involvement of Endothelial Nitric Oxide Synthase in Cerebral Microcirculation and Oxygenation in Traumatic Brain Injury

Denis E. Bragin, Olga A. Bragina, Alex O. Trofimov, Paul L. Huang, and Dmitriy N. Atochin

Abstract

Traumatic brain injury (TBI) leads to cerebral microvascular dysfunction and cerebral ischemia. Endothelial nitric oxide synthase (eNOS) is a key regulator of vascular homeostasis. We aimed to assess the role of eNOS in cerebral blood flow (CBF) changes after TBI. Moderate TBI was induced in eNOS knockout (KO) and wild-type (WT) mice (8 per group). Cerebral microvascular tone, microvascular CBF (mCBF) and tissue oxygenation (NADH) were measured by two-photon laser scanning microscopy (2PLSM) before and 1 h, 1 day and 3 days after TBI. Cerebrovascular reactivity (CVR) was evaluated by the hypercapnia test. Laser Doppler cortical flux (cLDF) was simultaneously measured in the perilesional area. One hr after TBI, cLDF was 59.4 ± 8.2% and 60.3 ± 9.1% from the baseline ($p < 0.05$) in WT and eNOS KO, respectively. 2PLSM showed decreased arteriolar diameter, the number of functioning capillaries, mCBF and tissue oxygenation ($p < 0.05$). At 1 day, cLDF increased to 65.2 ± 6.4% in the WT group, while it decreased to 56.1 ± 7.2% in the eNOS KO mice. 2PLSM revealed a further decrease in the number of functioning capillaries, mCBF, and oxygen supply which was slightly milder in WT mice ($p < 0.05$ from the baseline). On the third day after TBI, cLDF increased to 72 ± 5.2% in the WT, while it stayed the same in the eNOS KO group (55.9 ± 6.4%, $p < 0.05$ from the WT). 2PLSM showed reduction in arterioles with vasospasm, increase in the number of functioning capillaries, and improvement in mCBF and tissue oxygen supply in WT, while no significant changes were observed in eNOS KO ($p < 0.05$). CVR was impaired in both groups 1 h after TBI, and improved by the third day in the WT, while staying impaired in eNOS KO. In the subacute TBI period, the significance of eNOS in maintaining cerebral microcirculation and oxygen supply increases with time after the injury.

D. E. Bragin (✉)
Lovelace Biomedical Research Institute, Albuquerque, NM, USA

Department of Neurology, University of New Mexico School of Medicine, Albuquerque, NM, USA

National Research Saratov State University, Saratov, Russia
e-mail: dbragin@lovelacebiomedical.org

O. A. Bragina
Lovelace Biomedical Research Institute, Albuquerque, NM, USA

A. O. Trofimov
Department of Neurology, Privolzhsky Research Medical University, Nizhny Novgorod, Russia

P. L. Huang · D. N. Atochin
Cardiovascular Research Center, Massachusetts General Hospital, Harvard Medical School, Boston, MA, USA

F. Scholkmann et al. (eds.), *Oxygen Transport to Tissue XLIII*, Advances in Experimental Medicine and Biology 1395, https://doi.org/10.1007/978-3-031-14190-4_1

Keywords

eNOS · Cerebral blood flow · CBF · NADH fluorescence · Vasoreactivity

1 Introduction

Post-traumatic cerebral microvascular dysfunction, characterised by vasoconstriction and vascular occlusion, ultimately leads to cerebral ischemia following traumatic brain injury (TBI) [1]. Nitric oxide (NO), produced by vascular endothelial nitric oxide synthase (eNOS), is a central regulator of vascular homeostasis and cerebral blood flow [2]. Several studies showed that eNOS is essential for the maintenance of cerebral blood flow (CBF) after TBI [3–5]. However, the involvement of eNOS and NO in TBI pathophysiology is still under-investigated. The objective of this pilot work was to assess the involvement of eNOS in cerebral microvascular changes after TBI by comparing it in eNOS knockout (KO) and wild-type (WT) mice. Our working hypothesis was that eNOS mediates cerebral microvascular and oxygen supply changes after TBI in a time-dependent manner.

2 Materials and Methods

Animal procedures were approved by the Institutional Animal Care and Use Committee of the Lovelace Biomedical Research Institute under the Animal Protocol #FY20-058. Moderate TBI was induced in 8 C57BL/6 wild type and 8 eNOS knockout mice (eNOS KO) [6] by Benchmark Controlled Cortical Stereotaxic Impactor (Leica Biosystems, Germany) through craniotomy (5 mm diameter, centred at 3.5 mm posterior and left-lateral to bregma) using a 3-mm flat-tip impounder deployed at a velocity of 5 m/s and depth of 2.0 mm from the cortical surface, as in our previous study [7]. Regional CBF (rCBF) was visualised by RFLSI II Laser Speckle Contrast Imaging System (RWD Life Science Co., Shenzhen, China) before and 1 h, 1 day and 3 days after the TBI. Cortical microvascular tone, microvascular CBF (mCBF) and tissue oxygen supply (NADH) were measured by two-photon laser scanning microscopy (2PLSM) before and 1 h, 1 day and 3 days after the TBI.

Two-Photon Laser Scanning Microscopy The number of perfused capillaries, microcirculation, and tissue oxygen supply were visualised in anesthetised mice (2% isoflurane in 70% N_2O and 30% O_2) using Olympus BX 51WI upright microscope and water-immersion XLUMPlan FI 20x/0.95W objective as previously described [7]. Excitation was provided by a Prairie View Ultima multiphoton laser scan unit powered by a Millennia Prime 10 W diode laser source pumping a Tsunami Ti: sapphire laser (Spectra-Physics, Mountain View, CA). Red blood cells (RBC) flow velocity was measured in microvessels, ranging from 3–50 μm diameter up to 500 μm below the surface of the parietal cortex. NADH autofluorescence measurement was used to evaluate mitochondrial activity (metabolic status) and tissue oxygenation [8]. In offline analyses using NIH ImageJ software, three-dimensional anatomy of the vasculature in areas of interest was reconstructed from two-dimensional (planar) scans of the fluorescence intensity obtained at successive focal depths in the cortex (XYZ stack).

Cerebrovascular Reactivity Testing by Hypercapnia Challenge Cerebrovascular reactivity (CVR) was evaluated by measuring changes in arteriolar diameters and NADH (tissue oxygen supply) during hypercapnia test as previously described [7]. Transient hypercapnia was induced by a 60-s increase in CO_2 concentration to 10% in the inhalation mixture through the face mask. Each trial consisted of 3 min of baseline data acquisition, followed by 1 min of the hypercapnia challenge, and 3 min of the post-hypercapnic surveillance period.

Statistical Analyses were done using GraphPad Prism software (La Jolla, CA, USA) by independent Student's t-test or Kolmogorov–Smirnov tests where appropriate. Differences between

groups and time were determined using a two-way repeated measures ANOVA analysis for multiple comparisons and post hoc testing using the Mann-Whitney U test. Variables are expressed as mean ± SEM. The level of significance was set at 0.05.

3 Results

At a baseline, regional CBF, arteriolar diameter and capillary flow velocity were slightly less in eNOS KO but not significantly different than in wild-type mice (Fig 1a, c). However, the number of functional capillaries and tissue oxygen supply (NADH) was similar in both WT and eNOS KO mice (Fig. 1b, d). In contrast, the baseline hypercapnia test showed that in eNOS KO mice, cerebral arterioles dilated by 30 ± 8% during inhalation of 10% CO_2, which was significantly less than in WT mice (45 ± 6%, Fig. 2a). Simultaneous NADH autofluorescence imaging did not show any transient changes in tissue oxygen supply during hypercapnia in WT animals as a result of arteriolar dilatation and increased RBC traffic, reflecting intact mCBF regulation. In eNOS KO mice, hypercapnia caused a slight increase in NADH autofluorescence, corresponding to the impaired CVR (Fig. 2b). However, this NADH change was not statistically different from the WT mice.

One hour after the TBI, rCBF fell to 59.4 ± 8.2% and 60.3 ± 9.1% from the baseline in the ipsilateral hemisphere in WT and eNOS KO mice, respectively (Fig. 1a, $p < 0.05$) without a difference between groups. In the peri-lesion cortex, 2PLSM showed decreased arteriolar diameter, the number of functioning capillaries, mCBF, and tissue oxygen supply without significant difference between the groups (Fig. 1b–d, $p < 0.05$ from the baseline).

At one day after the TBI, rCBF in the ipsilateral hemisphere increased to 65.2 ± 6.4% in the WT group, decreasing further to 56.1 ± 7.2% in

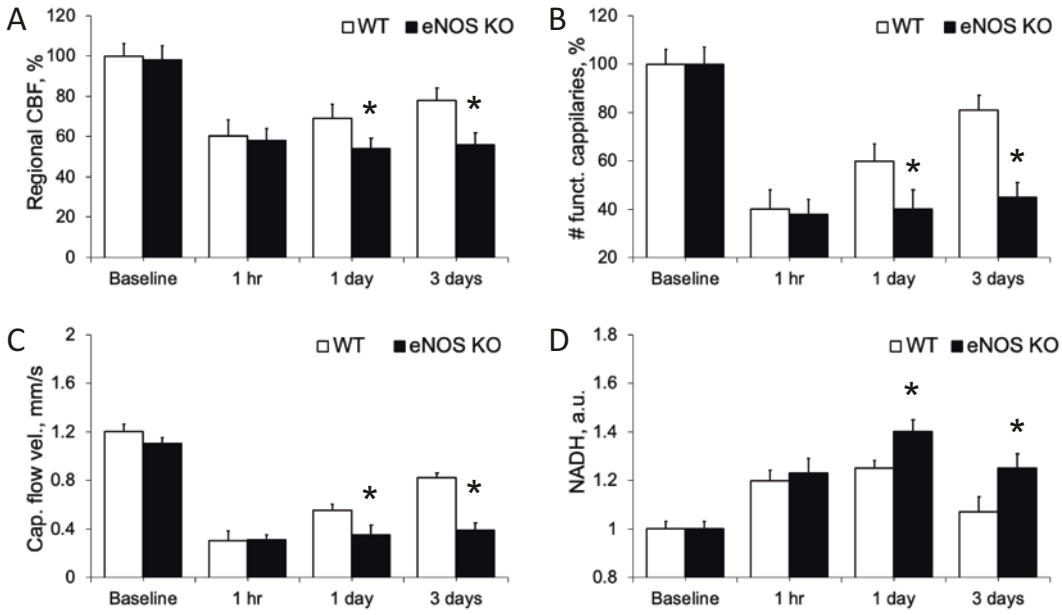

Fig. 1 After traumatic brain injury: (**a**) regional cerebral blood flow in the peri-lesion cortex dropped in eNOS KO mice more significantly than in wild-type (WT); (**b**) the number of functional capillaries in the peri-lesion cortex was less in eNOS KO mice comparing to WT; (**c**) the capillary flow velocity in the peri-lesion cortex was less in eNOS KO mice comparing to WT; and (**d**) tissue oxygen supply (inversely reflected by nicotinamide adenine dinucleotide level, NADH) in the peri-lesion cortex was less in eNOS KO mice comparing to WT. n = 8 per group, *$p < 0.05$, mean ± SEM

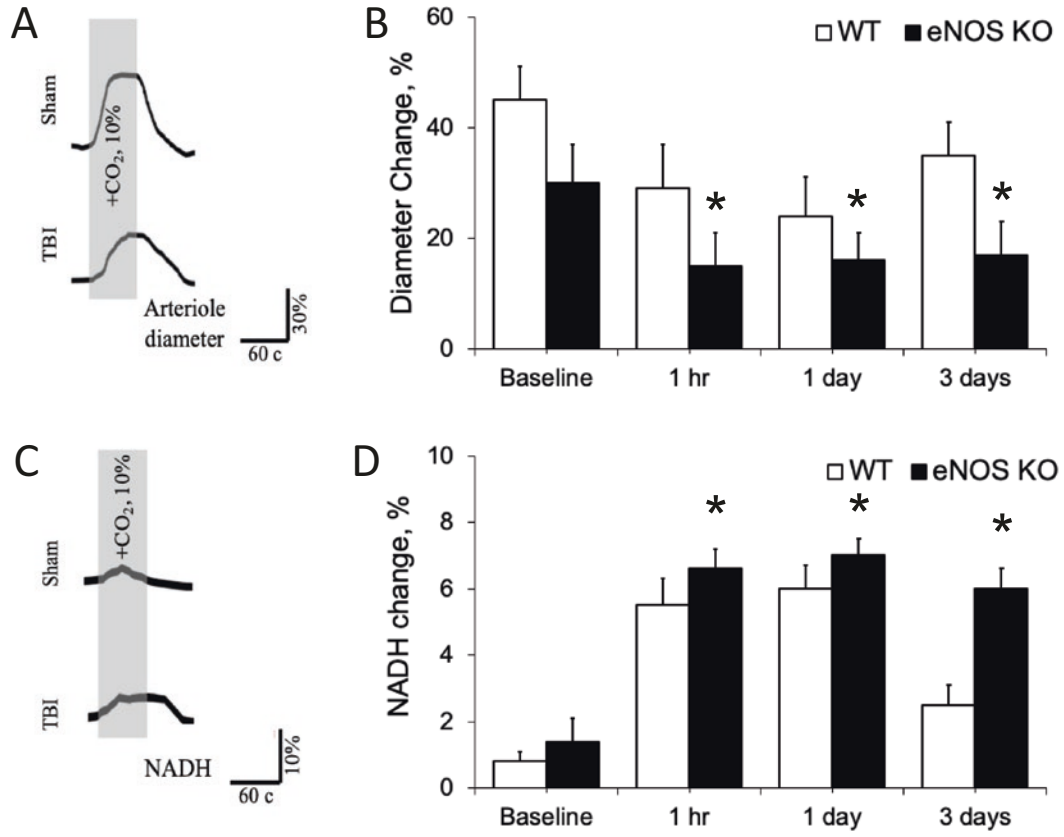

Fig. 2 Nitric oxide-dependent cerebrovascular reactivity in wild-type (WT) and eNOS knockout (KO) mice. (**a** and **b**) Cerebrovascular reactivity is impaired in eNOS KO mice reflected by less change in the arterioles' diameter during hypercapnia test compared to WT; and (**c** and **d**) Nicotinamide adenine dinucleotide (NADH) autofluorescence dynamics during the hypercapnia test. n = 8 per group, *p < 0.05, mean ± SEM

the eNOS KO mice (Fig. 1a, $p < 0.05$). At this time, 2PLSM over the peri-lesion cortex revealed a further decrease in the number of functioning capillaries, mCBF and tissue oxygen supply, which was slightly milder in WT mice than in eNOS KO mice (Fig. 1b–d, $p < 0.01$).

On the third day after TBI, cLDF in the ipsilateral hemisphere further increased to 72 ± 5.2% in the WT group, while it stayed the same in the eNOS KO group (55.9 ± 6.4%, $p < 0.05$ from the WT, Fig. 1a). 2PLSM showed reduction in arterioles with vasospasm, increase in the number of functioning capillaries, and improvement in mCBF and tissue oxygen supply in WT mice, while no significant changes were observed in eNOS KO mice (Fig. 1b–d, $p < 0.05$).

CVR was impaired in both groups one hour after TBI (29.3 ± 7.1% and 15.2 ± 5.4% in WT and eNOS KO mice, respectively), and improved by the third day after TBI in the WT group (35.1 ± 6.2%), while it remained impaired in eNOS KO mice (16.2 ± 5.4%, Fig. 2a, b, $p < 0.05$). Simultaneous NADH autofluorescence imaging revealed that one hour after TBI, tissue oxygen supply during the hypercapnia test transiently decreased by 5.5 ± 0.7% and 6.6 ± 0.6% in WT and eNOS KO mice, respectively, corresponding with impaired CVR. At three days after the TBI, it improved in WT mice (2.5 ± 0.4%) compared to eNOS KO mice (6.1 ± 0.5%, Fig. 2c, d $p < 0.05$).

4 Discussion

The differences in cerebral hemodynamic and metabolism between the eNOS KO and the wild-type mice suggest a critical role of the eNOS in preserving cerebral blood flow metabolism in the contused brain after traumatic injury. The obtained results are in agreement with works performed by Haltky et al., who also demonstrated regional CBF reduction in the acute period of TBI [3]. Lundblad et al. did not find a difference in CBF between WT and eNOS KO mice at 3 h after the TBI, but at 24 h, CBF was lower in eNOS KO than in WT mice in our studies [4]. However, in contrast to our research, they did not find any differences in the number of perfused capillaries [4].

5 Conclusions

The significance of eNOS in maintaining cerebral microcirculation and tissue oxygen supply increases with time in the subacute period of TBI. The impaired vasoreactivity due to limited NO production in eNOS KO mice is responsible for poor outcomes. eNOS knockout mouse model in combination with NOS inhibitors and NO donors might be helpful for work investigating NO-targeted TBI therapies**.**

Acknowledgments Support: Lovelace Biomedical Startup Funds, RF Govermental Grant 075-15-2022-1904 and NIH R01NS112808.

References

1. Salehi A, Zhang JH, Obenaus A (2017) Response of the cerebral vasculature following traumatic brain injury. J Cereb Blood Flow Metab 37(7):2320–2339
2. Zhu J, Song W, Li L et al (2016) Endothelial nitric oxide synthase: a potential therapeutic target for cerebrovascular diseases. Mol Brain 22(9):30
3. Hlatky R, Lui H, Cherian L et al (2003) The role of endothelial nitric oxide synthase in the cerebral hemodynamics after controlled cortical impact injury in mice. J Neurotrauma 20(10):995–1006
4. Schwarzmaier SM, Terpolilli NA, Dienel A et al (2015) Endothelial nitric oxide synthase mediates arteriolar vasodilatation after traumatic brain injury in mice. J Neurotrauma 32(10):731–738
5. Lundblad C, Grände PO, Bentzer P (2009) Hemodynamic and histological effects of traumatic brain injury in eNOS-deficient mice. J Neurotrauma 26(11):1953–1962
6. Atochin DN, Huang PL (2010) Endothelial nitric oxide synthase transgenic models of endothelial dysfunction. Pflugers Arch 460(6):965–974
7. Bragina OA, Lara DA, Nemoto EM et al (2018) Increases in microvascular perfusion and tissue oxygenation via vasodilatation after anodal Transcranial direct current stimulation in the healthy and traumatized mouse brain. Adv Exp Med Biol 1072:27–31
8. Chance B, Cohen P, Jobsis F et al (1962) Intracellular oxidation-reduction states in vivo. Science 137(499–508):8

Imaging Cerebral Energy Metabolism in Healthy Infants

M. F. Siddiqui, S. Brigadoi, L. Collins-Jones, S. Lloyd-Fox, E. J. H. Jones, I. Tachtsidis, M. H. Johnson, and C. E. Elwell

Abstract

Broadband near-infrared spectroscopy (bNIRS) has the potential to provide non-invasive measures of cerebral haemodynamic changes alongside changes in cellular oxygen utilisation through the measurement of mitochondrial enzyme cytochrome-c-oxidase (oxCCO). It therefore provides the opportunity to explore brain function and specialisation, which remains largely unexplored in infancy. We used bNIRS to measure changes in haemodynamics and changes in oxCCO in 4-to-7-month-old infants over the occipital and right temporal and parietal cortices in response to social and non-social visual and auditory stimuli. Changes in concentration of oxygenated-haemoglobin ($\Delta[HbO_2]$), deoxygenated haemoglobin (Δ[HHb]) and change in the oxidation state of oxCCO (Δ[oxCCO]) were calculated using changes in attenuation of light at 120 wavelengths between 780 and900 nm, using the UCLn algorithm. For 4 infants, the attenuation changes in a subset of wavelengths were used to perform image reconstruction, in an age-matched infant model, for channels over the right parietal and temporal cortices, using a multispectral approach which allows direct reconstruction of concentration change data. The volumetric reconstructed images were mapped onto the cortical surface to visualise the reconstructed changes in concentration of HbO_2 and HHb and changes in metabolism for both social and non-social stimuli. Spatially localised activation was observed for Δ[oxCCO] and $\Delta[HbO_2]$ over the temporo-parietal region, in response to the social stimulus. This study provides the first reconstructed images of changes in metabolism in healthy, awake infants.

Keywords

NIRS · Cytochrome oxidase · Cerebral haemodynamics · Oxyhaemoglobin · Deoxyhaemoglobin

M. F. Siddiqui (✉) · E. J. H. Jones
Centre for Brain and Cognitive Development, Department of Psychology, Birkbeck College, University of London, London, UK
e-mail: ucbtfai@ucl.ac.uk

S. Brigadoi
Department of Development and Social Psychology, University of Padova, Padua, Italy

Department of Information Engineering, University of Padova, Padua, Italy

L. Collins-Jones
Department of Medical Physics and Biomedical Engineering, University College London, London, UK

S. Lloyd-Fox · I. Tachtsidis · M. H. Johnson · C. E. Elwell
Department of Psychology, University of Cambridge, Cambridge, UK

F. Scholkmann et al. (eds.), *Oxygen Transport to Tissue XLIII*, Advances in Experimental Medicine and Biology 1395, https://doi.org/10.1007/978-3-031-14190-4_2

1 Introduction

Near-infrared spectroscopy (NIRS) is a non-invasive neuroimaging technique that provides measures of changes in cerebral haemodynamic activity and oxygenation. Due to its feasibility, it has become an established research tool in the field of Psychology to study neurodevelopment and investigate both typical [1] and atypical brain development [2]. NIRS uses near-infrared light to quantify changes in the concentration of oxygenated $\Delta[HbO_2]$ and deoxygenated haemoglobin Δ[HHb]. More recently, broadband NIRS [3–5] systems have been developed to allow for the measurement of changes in metabolic activity alongside haemodynamic activity. This is performed by measuring changes in the oxidation state of mitochondrial enzyme cytochrome-c-oxidase Δ[oxCCO], which is responsible for 95% of energy metabolism. oxCCO is a more direct marker of brain activity. Compared to haemoglobin-based measures, oxCCO can potentially provide a more direct marker of brain activation, and animal studies [6] have found a significant correlation between oxCCO measures and phosphorus magnetic resonance spectroscopy biomarkers of cerebral energy metabolism.

More recently in the field of functional NIRS (fNIRS), technological advancement has allowed the reconstruction of images of $\Delta[HbO_2]$ and Δ[HHb] (in both adults and infants) [7] and Δ[oxCCO] (in adults) [8]. To date, no studies have reconstructed images of changes in haemodynamics and metabolism in infants. These reconstructed images could provide the opportunity to investigate the spatial specificity of cerebral energy metabolism during development and to understand its role in functional cortical specialisation. In this study, we used a broadband NIRS (bNIRS) system to measure changes in the redox state of CCO alongside haemodynamic changes in typically developing infants. We performed image reconstruction for four of the infants in the study, to visualise, for the first time, reconstructed bNIRS measured changes in response to functional activation.

2 Materials and Methods

The study protocol and procedures were approved by the Birkbeck Psychology Research Ethics Committee. Forty-two healthy 4-to-7-month-old infants participated in the study (22 males, 20 females: age 179 ± 16 days old). All parents volunteered and gave written, informed consent to participate.

2.1 Instrumentation

Measurements were performed using a broadband system developed in-house at University College London [3]. The system consisted of four light sources (at the subject-end) which were controlled using a time multiplexed mechanism whereby one pair of light sources was on every 1.4 s. The system also consisted of fourteen detector fibres (at the subject-end). The attenuation signal was obtained from changes in attenuation of light at 120 wavelengths between 780–900 nm. The sources and detectors were positioned on the head using custom-built, 3-D printed arrays (all source/detector separation 2.5 cm, with three additional long-separation channels at 4.3 cm used for image reconstruction) which were positioned over the occipital and the right temporo-parietal regions. A NIRS-MRI co-registration map [9] was used to position the temporo-parietal array such that two channels were located over the superior temporal sulcus – temporo-parietal junction (STS-TPJ) region which has been shown to be activated to social stimuli [10]. Figure 1a shows the placement of the array on a participant and Fig. 1b shows the locations of each of the channels on the head, including the long-distance channels used for image reconstruction.

2.2 Protocol and Measurements

During the study, infants were seated on their parent's lap at an approximate viewing distance of 65 cm. A 35-in screen was used to display the

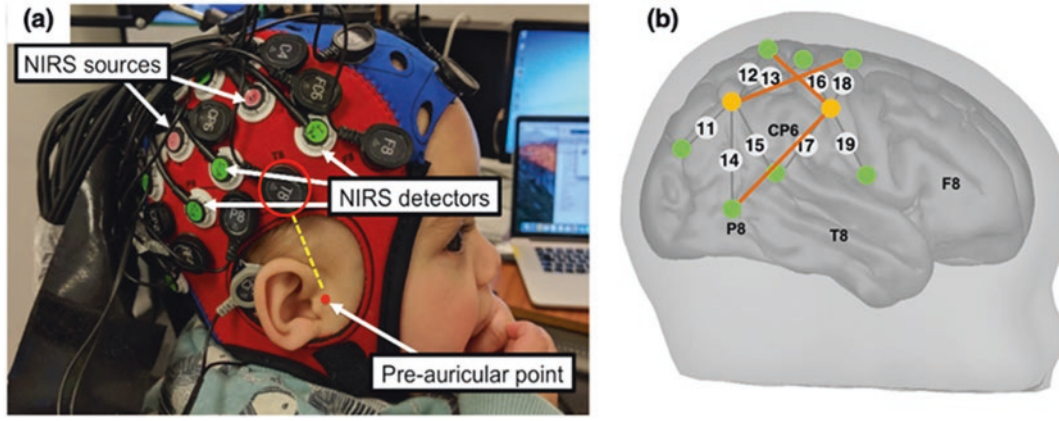

Fig. 1 (**a**) The headgear is shown positioned on an infant's head with NIRS sources and detectors indicated. The black electrodes/fibres are EEG electrodes for concurrent EEG measurements that are not discussed in this paper. (**b**) Locations of the bNIRS channels (grey circles) and locations of the sources (orange circles) and detectors (green circles) over the right hemisphere. The grey lines show each source-detector pair that forms each channel (separation 2.5 cm) and the dark orange lines shows the long-distance channels used for image reconstruction (separation 4.3 cm)

Fig. 2 Order of stimulus presentation

experimental stimuli. These were visual and auditory stimuli comprising a 'social' condition which consisted of dynamic videos of actors performing nursery rhymes such as 'incy-wincy' and a 'non-social' condition which consisted of moving mechanical toys. The baseline condition consisted of still images of transport vehicles. Both the social and non-social stimuli were presented for a varying duration of 8–12 s while the baseline was presented for 8 s. Figure 2 shows the order of stimulus presentation. The study began with a rest period (10 s minimum) to draw the infant's attention towards the screen, during which the infant was shown shapes in the four corners of the screen. Following this, the baseline and experimental conditions were alternated until the infant became bored or fussy. Alerting sounds were occasionally played during the baseline period to draw the infant's attention back to the screen.

2.3 Data Analysis

Data analysis was carried out in MATLAB (Mathworks, USA) and has been described elsewhere [4]. Image reconstruction was performed at the individual subject level. A four-layer volumetric infant head model was built using average MRI data from a cohort of 12-month-old infants [7, 11] using the iso2mesh software [12]. A grey matter (GM) surface mesh was built similarly

and used to display the reconstructed images. Images of HbO_2, HHb and ΔoxCCO were reconstructed from the block-averaged attenuation changes at 13 discrete wavelengths (from 780 to 900 nm at 10 nm intervals) using the multispectral approach [13] as described elsewhere [8]. Toast++ [14] was used to compute wavelength-specific Jacobians on the tetrahedral mesh. Optical properties were assigned to each tissue type and for each wavelength by fitting all published values for these tissue types [15–17]. The inverse problem was solved employing the LSQR method (maximum number of iterations: 50; tolerance: 10^{-5}) to solve the matrix equations resulting from the minimisation and using first-order Tikhonov regularisation, with the parameter covariance matrix containing the diagonal square matrices with the background concentration values of the three chromophores (23.7 for ΔHbO_2, 16 for ΔHHb and 6 for ΔoxCCO) [18, 19] and the noise covariance matrix set as the identity matrix. The regularisation hyper-parameter was set to 10^{-2}. The volumetric reconstructed images were mapped to the GM surface mesh; changes in concentration for HbO_2 and HHb were normalised to the maximum change in HbO_2, while oxCCO was normalised to its maximum change.

3 Results

Figure 3 shows reconstructed images from a single infant at three different time points for both social and non-social conditions. Figure 4 shows reconstructed images from three different infants at time point 14 s post-stimulus onset (the response is expected to have reached a maximum around this time). Figure 5 shows the reconstructed images of the group average (averaging across the four infants shown in Figs. 3 and 4) at three different time points. In general, in response to the social condition, a widespread initial decrease in $\Delta[HbO_2]$ and Δ[oxCCO] was observed over the temporal and parietal brain regions which was followed by a more spatially localised increase in $\Delta[HbO_2]$ and Δ[oxCCO]. Δ[oxCCO] displayed activity which was more localised to the parietal region. Meanwhile Δ[HHb] showed an initial increase in response to the stimulus followed by a

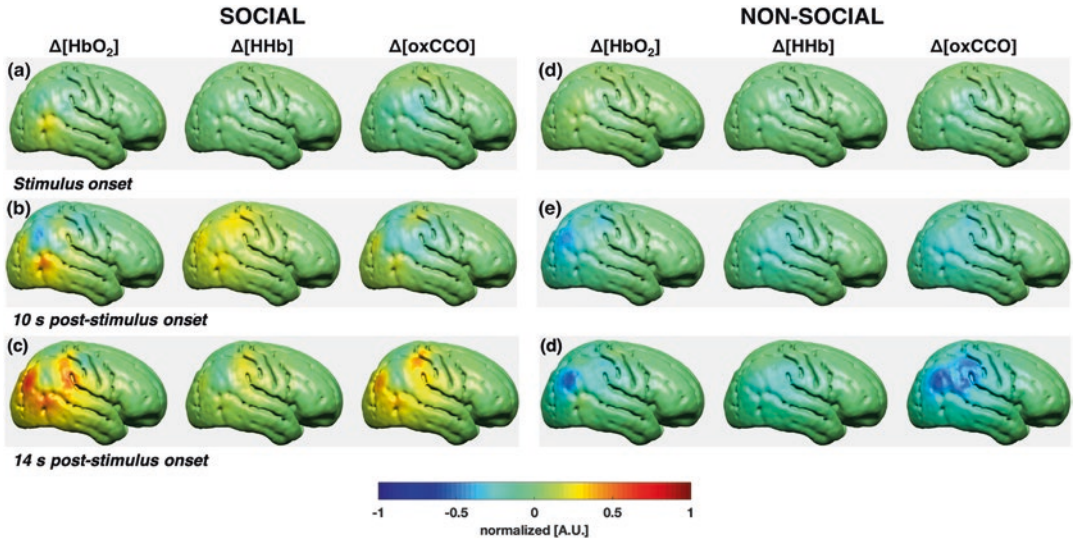

Fig. 3 Reconstructed images from one infant at three different time points; stimulus onset, 10 s post-stimulus onset and 14 s post-stimulus onset for both social ((**a**) – (**c**)) and non-social conditions ((**d**) – (**f**)). The concentration changes of HbO_2 and HHb have been normalised to the maximum of HbO_2 and changes in oxCCO have been normalised to its maximum

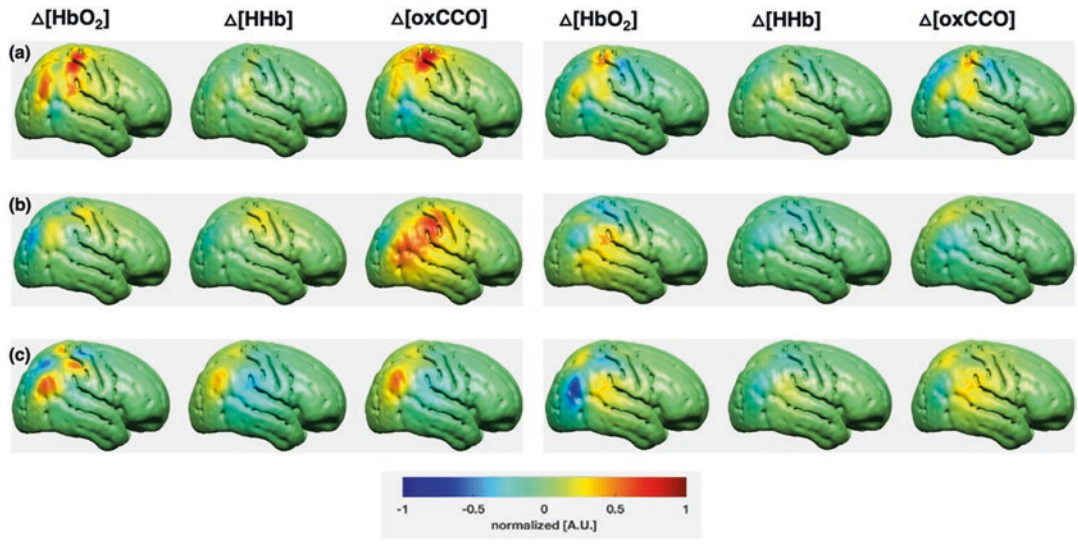

Fig. 4 Reconstructed images from three different infants ((**a**) – (**c**)) at time point 14 s post-stimulus onset for both social and non-social conditions

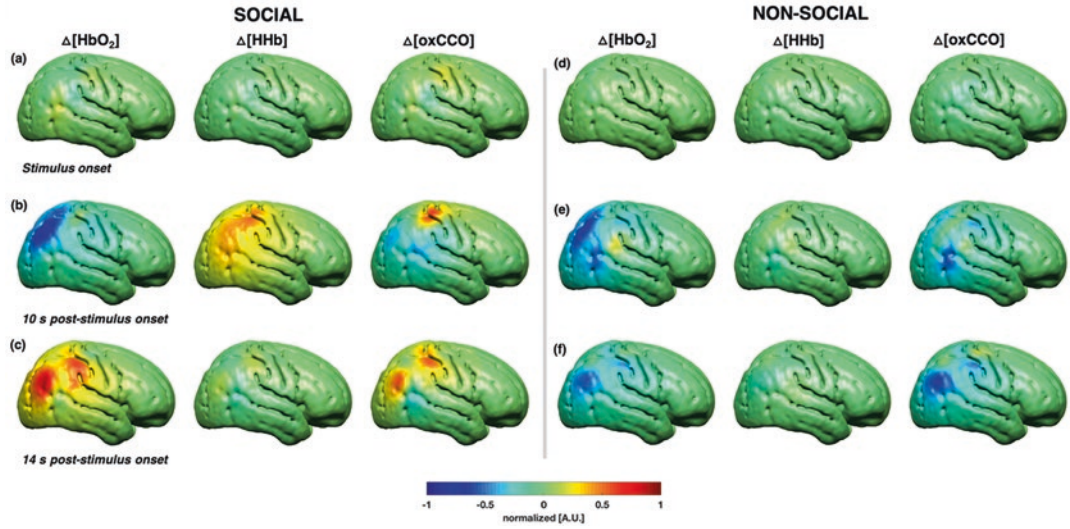

Fig. 5 Group average reconstructed images of the infants shown in Figs. 3 and 4 at three different time points; stimulus onset, 10 s post-stimulus onset and 14 s post-stimulus onset for both social ((**a**) – (**c**)) and non-social conditions ((**d**) – (**f**)). The concentration changes of HbO_2 and HHb have been normalised to the maximum of HbO_2 and changes in oxCCO have been normalised to its maximum

decrease. Moreover, in response to the non-social condition, both $\Delta[HbO_2]$ and Δ[oxCCO] displayed a decrease with Δ[oxCCO] showing a more widespread decrease over the temporal and parietal regions.

4 Conclusions

In this study, we used a bNIRS system to explore the feasibility of reconstructing images of changes in haemodynamic and metabolic activity in awake infants, during functional activation.

Broadband data were acquired in 42 healthy infants during a social/non-social experimental paradigm that is known to elicit strong activation over the temporal and parietal brain regions [20]. Spatially localised activation was observed for $\Delta[HbO_2]$ and Δ[oxCCO] over the temporal and parietal regions during the period of maximum response to the stimulus in the four reconstructed infants. These results are in line with each infant's channel-wise data which show a clear increase in $\Delta[HbO_2]$ and Δ[oxCCO] in channels over the temporo-parietal region in response to the stimulus.

We have demonstrated for the first time in awake, healthy infants the reconstruction of simultaneous changes in the concentration of HbO_2, HHb and oxCCO. Image reconstruction of changes in oxCCO provides the opportunity to investigate cerebral energy metabolism during neurodevelopment and to understand its role in specialisation of brain function. While in the healthy brain, as in the case of the infants in this study, HbO_2 and oxCCO showed similar patterns of activation, the same pattern may not be observed and needs to be studied in clinical populations. This technique is therefore useful to understand not only typical brain development, but atypical brain development in disorders such as autism spectrum disorders (ASD) where studies have shown a link to mitochondrial dysfunction [21].

References

1. Wilcox T, Bortfeld H, Woods R, Wruck E, Boas DA (2008) Hemodynamic response to featural changes in the occipital and inferior temporal cortex in infants: a preliminary methodological exploration: Paper. Dev Sci. https://doi.org/10.1111/j.1467-7687.2008.00681.x
2. Kita Y et al (2011) Self-face recognition in children with autism spectrum disorders: a near-infrared spectroscopy study. Brain Dev 33(6):494–503. https://doi.org/10.1016/j.braindev.2010.11.007
3. Phan P, Highton D, Lai J, Smith M, Elwell C, Tachtsidis I (2016) Multi-channel multi-distance broadband near- infrared spectroscopy system to measure the spatial response of cellular oxygen metabolism and tissue oxygenation. Biomed Opt Express 7(4424). https://doi.org/10.1364/BOE.7.004424
4. Siddiqui MF, Lloyd-Fox S, Kaynezhad P, Tachtsidis I, Johnson MH, Elwell CE (2017) Non-invasive measurement of a metabolic marker of infant brain function. Sci Rep 7(1). https://doi.org/10.1038/s41598-017-01394-z
5. Pinti P, Siddiqui MF, Levy AD, Jones EJH, Tachtsidis I (2021) An analysis framework for the integration of broadband NIRS and EEG to assess neurovascular and neurometabolic coupling. Sci Rep. https://doi.org/10.1038/s41598-021-83420-9
6. Bainbridge A et al (2014) Brain mitochondrial oxidative metabolism during and after cerebral hypoxia-ischemia studied by simultaneous phosphorus magnetic-resonance and broadband near-infrared spectroscopy. NeuroImage 102(P1):173–183. https://doi.org/10.1016/j.neuroimage.2013.08.016
7. Collins-Jones LH et al (2021) Longitudinal infant fNIRS channel-space analyses are robust to variability parameters at the group-level: an image reconstruction investigation. Neuroimage:118068. https://doi.org/10.1016/j.neuroimage.2021.118068
8. Brigadoi S et al (2017) Image reconstruction of oxidized cerebral cytochrome C oxidase changes from broadband near-infrared spectroscopy data. Neurophotonics. https://doi.org/10.1117/1.NPh.4.2.021105
9. Lloyd-Fox S, Richards JE, Blasi A, Murphy DGM, Elwell CE, Johnson MH (2014) Coregistering functional near-infrared spectroscopy with underlying cortical areas in infants. Neurophotonics 1(2):025006. https://doi.org/10.1117/1.NPh.1.2.025006
10. Lloyd-Fox S, Blasi A, Volein A, Everdell N, Elwell CE, Johnson MH (2009) Social perception in infancy: a near infrared spectroscopy study. Child Dev. 80(4):986–999. https://doi.org/10.1111/j.1467-8624.2009.01312.x
11. Duncan A et al (1995) Optical pathlength measurements on adult head, calf and forearm and the head of the newborn infant using phase resolved optical spectroscopy. Phys Med Biol 40(2):295. [Online]. Available: http://stacks.iop.org/0031-9155/40/i=2/a=007
12. Fang Q, Boas DA (2009) Tetrahedral mesh generation from volumetric binary and grayscale images. https://doi.org/10.1109/ISBI.2009.5193259
13. Corlu A et al (2005) Diffuse optical tomography with spectral constraints and wavelength optimization. Appl Opt. https://doi.org/10.1364/AO.44.002082
14. Schweiger M, Arridge S (2014) The Toast++ software suite for forward and inverse modeling in optical tomography. J Biomed Opt. https://doi.org/10.1117/1.jbo.19.4.040801
15. Bevilacqua F, Piguet D, Marquet P, Gross JD, Tromberg BJ, Depeursinge C (1999) In vivo local determination of tissue optical properties: applications to human brain. Appl Opt. https://doi.org/10.1364/ao.38.004939
16. Strangman G, Culver JP, Thompson JH, Boas DA (2002) A quantitative comparison of simultaneous BOLD fMRI and NIRS recordings during functional

brain activation. Neuroimage 17(2):719–731. https://doi.org/10.1016/S1053-8119(02)91227-9
17. Custo A, Wells WM, Barnett AH, Hillman EMC, Boas DA (2006) Effective scattering coefficient of the cerebral spinal fluid in adult head models for diffuse optical imaging. Appl Opt. https://doi.org/10.1364/AO.45.004747
18. Zhao J, Ding HS, Hou XL, Le Zhou C, Chance B (2005) In vivo determination of the optical properties of infant brain using frequency-domain near-infrared spectroscopy. J Biomed Opt. https://doi.org/10.1117/1.1891345
19. Franceschini MA et al (2007) Assessment of infant brain development with frequency-domain near-infrared spectroscopy. Pediatr Res. https://doi.org/10.1203/pdr.0b013e318045be99
20. Lloyd-Fox S, Blasi A, Elwell CE (2010) Illuminating the developing brain: the past, present and future of functional near infrared spectroscopy. Neurosci Biobehav Rev 34(3):269–284. https://doi.org/10.1016/j.neubiorev.2009.07.008
21. Siddiqui MF, Elwell CE, Johnson MH (2016) Mitochondrial dysfunction in autism spectrum disorders. Autism Open-Access 6(5):1000190

Changes in Cerebral Oxygenation and Systemic Physiology During a Verbal Fluency Task: Differences Between Men and Women

Hamoon Zohdi, Felix Scholkmann, and Ursula Wolf

Abstract

Background: Sex differences in behavioural performance of a cognitive task have been repeatedly reported in the literature. Whether such differences are also relevant for evoked cerebral haemodynamic and oxygenation responses as well as systemic physiological changes is a topic of ongoing investigations. Aim: We investigated whether changes in cerebral oxygenation and systemic physiological activity are sex-dependent during a verbal fluency task (VFT). Subjects and methods: VFT performance and changes in cerebral oxygenation and systemic physiology were investigated in 32 healthy right-handed adults (17 females, 15 males, age: 25.5 ± 4.3 years). The total duration of the VFT was 9 min. During this phase, subjects were also exposed to blue light (peak wavelength: 450 nm, illuminance: 120 lux). Before and after the VFT, subjects were in darkness. In this study, we used the systemic physiology augmented functional near-infrared spectroscopy (SPA-fNIRS) approach. Absolute concentration changes of oxyhaemoglobin ($[O_2Hb]$), deoxyhaemoglobin ([HHb]), total haemoglobin ([tHb]), as well as tissue oxygen saturation (StO_2) were measured bilaterally over the prefrontal cortex (PFC) and visual cortex (VC). Systemic physiological parameters were also recorded in parallel (e.g., end-tidal CO_2, heart rate, respiration rate, skin conductance). Results: We found that: (i) Females were better VFT performers in comparison to males. (ii) Changes in $[O_2Hb]$ and [HHb] in the VC were higher for males compared to females during the VFT under blue light exposure. (iii) Lower and higher StO_2 changes were detected for males compared to females in the PFC and VC, respectively. (iv) Sex-dependent changes were also evident for end-tidal CO_2, heart rate, respiration rate, and pulse-respiration quotient. Conclusions: Our study showed that sex differences are not only observed in task performance but also in the magnitudes of changes in cerebral and physiological parameters. The findings of the current study emphasise that sex differences in brain activation and systemic physiological activity need to be considered when interpreting functional neuroimaging data. These findings offer a broad range of implications for educational purposes and facilitate a better understanding of the

H. Zohdi (✉) · U. Wolf
Institute of Complementary and Integrative Medicine, University of Bern, Bern, Switzerland
e-mail: hamoon.zohdi@unibe.ch

F. Scholkmann
Institute of Complementary and Integrative Medicine, University of Bern, Bern, Switzerland

Biomedical Optics Research Laboratory, Department of Neonatology, University Hospital Zurich, University of Zurich, Zurich, Switzerland

F. Scholkmann et al. (eds.), *Oxygen Transport to Tissue XLIII*, Advances in Experimental Medicine and Biology 1395, https://doi.org/10.1007/978-3-031-14190-4_3

effects of sex on behavioural performance as well as human physiology.

Keywords

Sex differences · SPA-fNIRS · Verbal fluency task · Systemic physiology · Cerebral haemodynamics

1 Introduction

Sex dependency of cognitive functions has been well established in behavioural studies, e.g. females were found to perform better in verbal tasks while males better in visual-spatial tasks [1]. Neuroimaging studies, e.g., functional magnetic-resonance imaging (fMRI), showed this sex dependency too [2]. The increasing awareness of the sex dependency of neuroimaging findings motivated us to investigate if such differences also play a role for functional near-infrared spectroscopy (fNIRS) studies.

In previous studies by our group we investigated how cerebral haemodynamics and systemic physiology change during various paradigms involving long-term or short-term coloured light exposures with different colours [3–5]. The aim of our present study was to investigate whether changes in cerebral haemodynamics and systemic physiology are sex-dependent during a cognitive task (verbal fluency task; VFT) performed under blue light exposure.

2 Subjects and Methods

Thirty-two healthy right-handed subjects (17 female, 15 male, age: 25.5 ± 4.3 years) were recruited in the current study. The subjects sat upright in a comfortable chair while performing a VFT. The total duration of the VFT was 9 min. During this phase, subjects were also exposed to blue light (LED headlights, spectral peak: 450 nm, illuminance: 120 lux) continuously. Before (baseline, 8 min) and after (recovery, 15 min) the VFT, subjects were in darkness and were asked to relax. We used the systemic physiology augmented functional near-infrared spectroscopy (SPA-fNIRS) approach, enabling changes in cerebral oxygenation and haemodynamics to be measured simultaneously with systemic physiology. A multichannel frequency-domain near-infrared spectroscopy system (Imagent, ISS Inc., Champaign, IL, USA) was used to measure absolute concentration changes of oxyhaemoglobin ([O_2Hb]), deoxyhaemoglobin ([HHb]), total haemoglobin ([tHb]), as well as tissue oxygen saturation (StO_2) bilaterally over the prefrontal cortex (PFC) and visual cortex (VC). Systemic physiological parameters, i.e., end-tidal CO_2 ($P_{ET}CO_2$), mean arterial pressure (MAP), skin conductance level (SCL), arterial oxygen saturation (SpO_2), heart rate (HR), respiration rate (RR), and pulse-respiration quotient (PRQ) were also recorded. A detailed description of the experimental protocol as well as the SPA-fNIRS measurement setup can be found in our previous studies [6, 7].

Too noisy fNIRS signals were rejected by manual assessment. Movement artefacts were removed and a low pass filter (RLOESS) with a span of 3 min was applied to remove high-frequency noise. Signals from the left and right PFC and VC were averaged to obtain signals for the whole PFC and VC, respectively. All systemic physiological signals, except the SCL, were also denoised by the RLOESS with a span of 3 min. The SCL signals were processed with the Ledalab toolbox [8].

All signals were then normalised to the last minute of the baseline phase. Signals for males and females were block-averaged.

3 Results

VFT Performance Females were better VFT performers in comparison to males ($p < 0.05$; effect size (Cohen's d): $d = 0.8$). They produced 62.2 ± 15.5 (mean ± SD) correct nouns during the VFT, while males were able to articulate 51.1 ± 13.2 correct words.

Cerebral Haemodynamics and Oxygenation The group-averaged long-term changes of [O_2Hb], [HHb], [tHb] and StO_2 at the PFC and VC for both females and males are shown in Fig. 1. The typical patterns of cerebral activation were found during the VFT in the PFC and VC for both groups. However, some haemodynamic changes were different between females and males: (i) evoked changes in [O_2Hb] and [HHb] at the VC were higher for males in comparison with females during the VFT under blue light exposure ($p < 0.001$; $d = 2.7$ and $p < 0.001$; $d = 1.4$, respectively); (ii) lower and higher StO_2 changes were detected for males compared to females in the PFC ($p < 0.01$; $d = 0.8$) and VC ($p < 0.001$; $d = 1.9$), respectively.

Systemic Physiological Parameters Figure 2 presents the group-averaged changes of systemic physiological parameters. No significant difference in evoked changes of MAP, SCL and SpO_2 was found between females and males. Sex-dependent changes were observed however for $P_{ET}CO_2$ ($p < 0.001$; $d = 2.1$), HR ($p < 0.001$; $d = 1.3$), RR ($p < 0.001$; $d = 1.1$) and PRQ ($p < 0.01$; $d = 0.7$).

4 Discussion and Conclusions

We found that females were more successful than males in performing the VFT. This could be due to dissimilarities in the language-related cortex structure and the cerebral organisation of language function as well as different processing strategies to perform VFT tasks [1, 9]. We also observed that cerebral haemodynamic and oxygenation responses in the VC during the VFT under the blue light exposure are sex-dependent, i.e., higher for males. These differences between females and males in the VC may be attributed to the effects of the blue light rather than the VFT as well as dissimilarities in the structure of the VC, visual perception and sex differences in both basic and high-level visual processing [10]. We also hypothesise that the underlying reasons for sex differences in the VC lie in specific areas of the visual pathway, including amygdala, thalamus and in particular area V4, which is very responsive to colour and is also considered as a vital site for colour perception.

A variety of physiological responses can be triggered in the presence of stressors (like performing a VFT tasks), leading to an increase in HR, for example. This phenomenon was observed in both female and male groups during the VFT. A significant stronger increase in HR, especially at the end of the VFT, in males compared to females can be related to their poorer VFT performance. The reason for further increased stress and consequently increased HR in males could be that males put themselves under pressure, since they were not so satisfied with their results. Thus, they were stressed to perform better and strove to provide more nouns within a restricted time. Furthermore, a decrease of RR in females and insignificant changes of RR in males during the VFT can also be attributed to the behavioural performance. It is known that speech production increases the duration of breathing cycles (i.e., a decrease in RR). Since females continuously produced nouns and they were generally much more fluent than males during the VFT, such changes in RR were expected for both groups.

The sex-dependency of the PRQ can also be interpreted based on changes in HR and RR during the VFT for both females and males, as discussed above. A comprehensive review on the PRQ as well as on internal and external factors (e.g., sex) affecting this parameter have been thoroughly discussed in our recent paper [11]. We also found that $P_{ET}CO_2$ changes during the VFT were sex-dependent. It is known that speech tasks causes hyperventilation leading to hypocapnia (i.e., a decrease in $P_{ET}CO_2$). The hypocapnia in females was weaker compared to males. Multiple reasons may account for the sex difference in $P_{ET}CO_2$ during the VFT, including differences in the dynamic cerebral autoregulation, which were found to be more efficient in females [12]. Moreover, the role of sex hormones (e.g., progesterone's effect as a respiratory stimulant) as well as the influence of the menstrual cycles should not be overlooked.

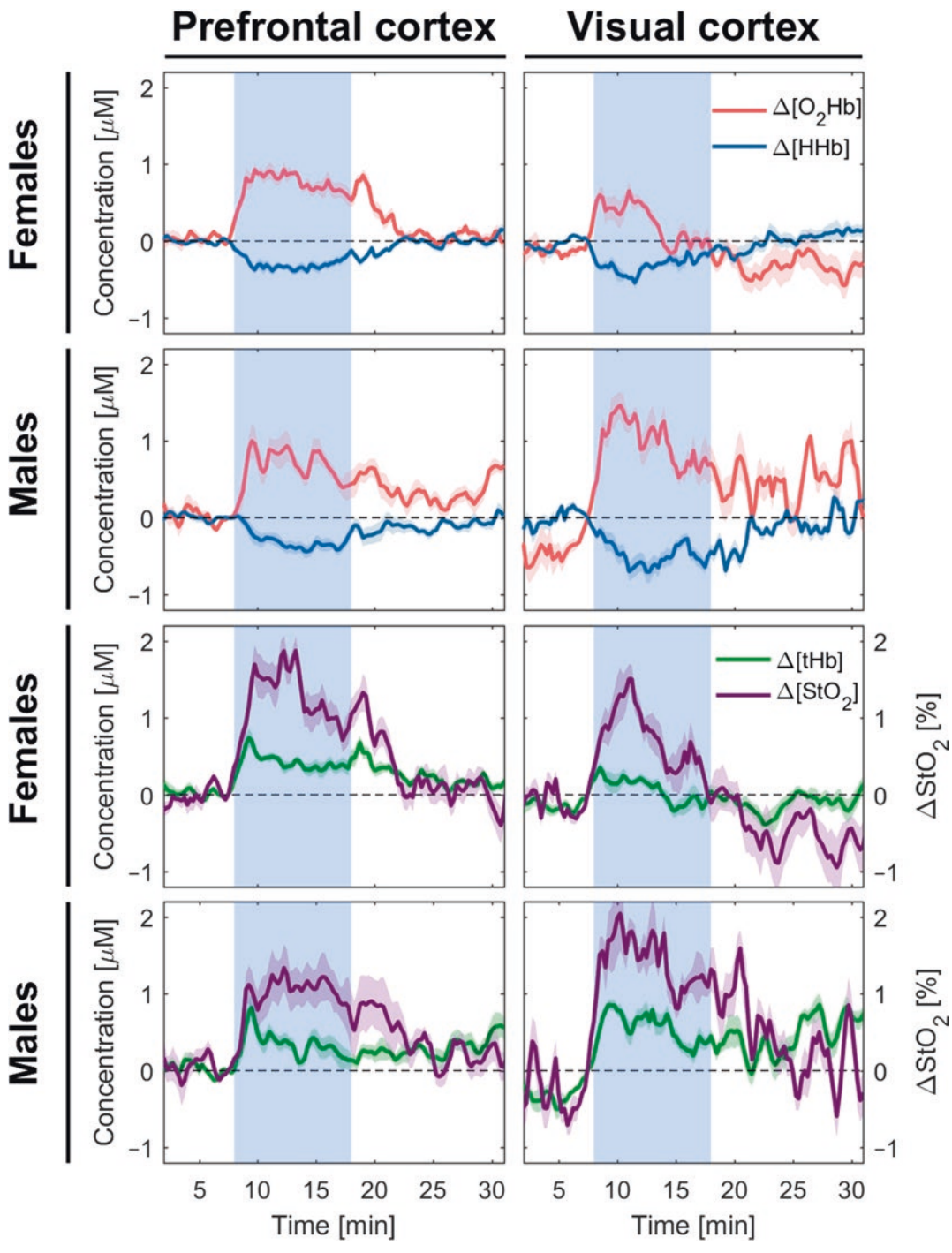

Fig. 1 Group-averaged changes in haemodynamic and oxygenation responses of the PFC and VC. The blue shaded areas represent the VFT periods during which the subjects were also exposed to the blue light. Median ± standard error of median (SEM) are shown

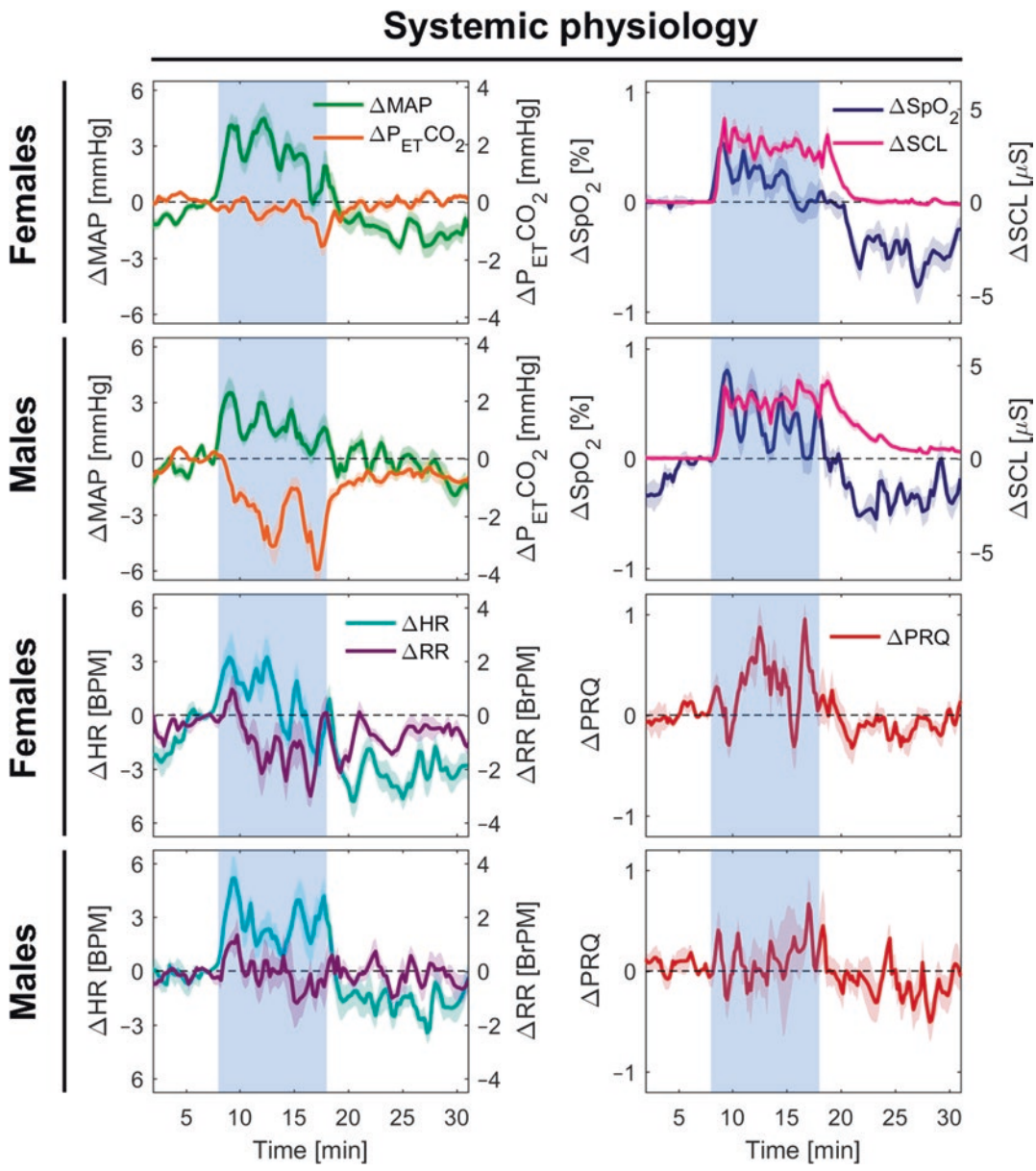

Fig. 2 Group-averaged changes in systemic physiological parameters. The blue shaded areas represent the VFT periods during which the subjects were also exposed to the blue light. Median ± SEM are shown

In conclusion, this is the first VFT study employing the SPA-fNIRS method, constituting a comprehensive approach that simultaneously measures fNIRS parameters alongside with important physiological parameters to measure effects of sex on behavioural performance, cerebral haemodynamics and oxygenation responses and systemic physiological activity. Our study showed that sex differences are observed in task performance and also in the magnitudes of changes in cerebral and physiological parameters. The findings of the current study emphasise that sex differences in brain activation and systemic physiological

activity need to be considered when interpreting fNIRS neuroimaging data in particular and functional neuroimaging data (e.g., fMRI) in general.

Acknowledgements The financial support of the Software AG Foundation, Christophorus Foundation, and Graduate School for Health Sciences at the University of Bern is gratefully acknowledged.

References

1. Weiss EM, Siedentopf C, Hofer A et al (2003) Brain activation pattern during a verbal fluency test in healthy male and female volunteers: a functional magnetic resonance imaging study. Neurosci Lett 352:191–194
2. Spets DS, Slotnick SD (2020) Are there sex differences in brain activity during long-term memory? A systematic review and fMRI activation likelihood estimation meta-analysis. Cogn Neurosci 12(3–4):163–173
3. Zohdi H, Scholkmann F, Wolf U (2020) Long-term blue light exposure changes frontal and occipital cerebral hemodynamics: not all Subjects React the Same. Adv Exp Med Biol 1269:217–222
4. Scholkmann F, Hafner T, Metz AJ et al (2017) Effect of short-term colored-light exposure on cerebral hemodynamics and oxygenation, and systemic physiological activity. Neurophotonics 4:045005
5. Metz AJ, Klein SD, Scholkmann F, Wolf U (2017) Continuous coloured light altered human brain haemodynamics and oxygenation assessed by systemic physiology augmented functional near-infrared spectroscopy. Sci Rep 7:10027
6. Zohdi H, Egli R, Guthruf D et al (2021) Color-dependent changes in humans during a verbal fluency task under colored light exposure assessed by SPA-fNIRS. Sci Rep 11:9654
7. Zohdi H, Scholkmann F, Wolf U (2021) Individual differences in hemodynamic responses measured on the head due to a long-term stimulation involving colored light exposure and a cognitive task: a SPA-fNIRS study. Brain Sci 11:54
8. Benedek M, Kaernbach C (2010) A continuous measure of phasic electrodermal activity. J Neurosci Methods 190:80–91
9. Scheuringer A, Wittig R, Pletzer B (2017) Sex differences in verbal fluency: the role of strategies and instructions. Cogn Process 18:407–417
10. Vanston JE, Strother L (2017) Sex differences in the human visual system. J Neurosci Res 95:617–625
11. Scholkmann F, Wolf U (2019) The pulse-respiration quotient: a powerful but untapped parameter for modern studies about human physiology and pathophysiology. Front Physiol 10:1–18
12. Minhas JS, Panerai RB, Robinson TG (2018) Sex differences in cerebral haemodynamics across the physiological range of PaCO2. Physiol Meas 39:105009

Brain Tissue Conductivity in Focal Cerebral Ischemia

Liang Shu, Ruwen Böhm, Ulrich Katscher, and Ulf Jensen-Kondering

Abstract

Background: Cerebral ischemia leads to oxygen depletion with rapid breakdown of transmembrane transporters and subsequent impaired electrolyte haemostasis. Electric properties tomography (EPT) is a new contrast in MRI which delivers information on tissue electrical conductivity. In the clinical realm it has been mostly used for tumour mapping. Ischemic cerebral stroke is another promising but neglected application. It might deliver additional information on tissue viability and possible response to therapy.

Aim: The aim of this study was to demonstrate tissue conductivity in a rodent model of stroke. Further, we aimed to compare electric conductivity in ischemic and non-ischemic cerebral tissue.

Materials and Methods: Two male Wistar rats were used in this study and were subjected to permanent MCAO. The animals were scanned in a 3 Tesla system (Philips Achieva/Best, the Netherlands) using a dedicated solenoid animal coil (Philips/Hamburg, Germany). In addition to diffusion weighted imaging (DWI), EPT was performed using a steady-state free-precession (SSFP) sequence (repetition time/echo time = 4.5/2.3 ms, measured voxel size = 0.6 × 0.6 × 1.2 mm^3, flip angle = 38°, number of excitations = 4). From the transceive phase ϕ of these SSFP scans, conductivity σ was estimated by the equation $\sigma = \Delta\phi/(2\mu_0\omega)$ with Δ the Laplacian operator, μ_0 the magnetic permeability, and ω the Larmor frequency. Subsequently, a median filter was applied, which was locally restricted to voxels with comparable signal magnitude.

Results: The animals exhibited an infarct as demonstrated on DWI. Conductivity within the infarcted region was 60-70 % of the conductivity of not affected contralateral tissue (0.39 ± 0.07 S/m and 0.31 ± 0.14 S/m vs. 0.64 ± 0.15 S/m and 0.66 ± 0.16 S/m, respectively).

L. Shu
Department of Radiology and Neuroradiology, University Hospital Schleswig-Holstein, Campus Kiel, Kiel, Germany

Department of Neurology, Shanghai Ninth People's Hospital, Shanghai Jiao Tong University School of Medicine, Shanghai, China

R. Böhm
Department of Clinical and Experimental Pharmacology, University Hospital Schleswig-Holstein, Campus Kiel, Kiel, Germany

U. Katscher
Philips Research, Hamburg, Germany

U. Jensen-Kondering (✉)
Department of Radiology and Neuroradiology, University Hospital Schleswig-Holstein, Campus Kiel, Kiel, Germany

Institute of Neuroradiology, University Hospital Schleswig-Holstein, Campus Lübeck, Lübeck, Germany
e-mail: Ulf.Jensen-Kondering@uksh.de

F. Scholkmann et al. (eds.), *Oxygen Transport to Tissue XLIII*, Advances in Experimental Medicine and Biology 1395, https://doi.org/10.1007/978-3-031-14190-4_4

Discussion: Infarcted tissue exhibited decreased conductivity. Further in-vivo experiments with examination of the influence of reperfusion status and temporal evolution of the infarcted areas should be conducted. Depiction of the ischemic penumbra and possibly subclassification of the DWI lesion still seems to be a fruitful target for further studies.

Keywords

Electric properties tomography (EPT) · Stroke · MRI · Imaging

1 Introduction

Despite recent dramatic therapeutic advances [1] cerebral ischemia is the leading cause of acquired disability and one of the most frequent cause of death worldwide [2]. Cerebral imaging remains a fundamental part of the diagnostic work-up for initial diagnosis and follow-up. Magnetic resonance imaging (MRI) provides high resolution images of structural changes and numerous sequences have been developed to provide insight into pathophysiology, e.g., diffusion and perfusion imaging [3], oxygen imaging [4], temperature [5] and pH-mapping [6].

Early ischemic changes on a cellular level includes deranged homeostasis caused by ion and water shift across cell membranes into neuronal cells and the extracellular space due to energy failure by oxygen depletion [7, 8]. In a first phase cytotoxic oedema develops with water influx into cells which does not cause overall tissue swelling since no additional component is added. However, it represents the irreversibly damaged core. The following phase of oedema development is caused by water influx from the intravascular space which in turn causes tissue swelling which is detrimental to brain tissue by increasing the intracranial pressure due to brain confinement by the skull. On standard imaging, only diffusion-weighted imaging is available as a surrogate marker for cytotoxic oedema. [7, 8].

Electric properties tomography (EPT) is a relatively new technique which provides an estimation of absolute tissue electric conductivity [9]. It can be performed using standard MRI systems and standard MRI sequences, so no application of external currents to the patient (via mounted electrodes or the like) are required. Instead, the acquired standard MRI images are post-processed according to Maxwell's equations. EPT has been mainly employed in cancer imaging [10, 11] while only a few studies focused on cerebral ischemia [12–15]. We hypothesised that early ischemic changes will alter tissue conductivity.

2 Material and Methods

2.1 Surgery

Middle cerebral artery thread occlusion (MCAo) was performed in two male Wistar rats. The established MCAo model initially described by Koizumi and co-workers [16] was used. In short, a midline incision is made in the neck and the left common carotid artery is exposed. After proximal and distal clip occlusion the artery is incised and the thread is inserted. The distal clip is released and the thread is advanced until resistance is felt and local cerebral blood in the left middle cerebral artery territory measured by laser flow drops to 30% of baseline. The thread was left in place during the MRI. Time from occlusion to MRI was ~45 min. Throughout all procedures ketamine and medetomidine were used as anaesthetics and metamizole was used as analgesic. After the MRI the animals were euthanized. Institutional approval was obtained and animals were handled according to applicable requirements for animal care.

2.2 Magnetic Resonance Imaging

MRI was performed in a Philips Achieva 3 Tesla scanner (Philips, Best, The Netherlands) using a dedicated solenoid animal coil (Philips Research Laboratories, Hamburg, Germany). We per-

formed a diffusion-weighted scan (DWI: TR/TE = 2399/165 ms, slice thickness = 1.3 mm, gap = 0.2 mm, 64 × 64 matrix, FOV = 50 × 50 mm, flip angle = 90°, *b*-values 0 and 2000 s/mm^2) and EPT (TR/TE = 4.5/2.3 ms, voxel size = 0.6 × 0.6 × 1.2 mm^3, flip angle = 38°) using a steady-state free-precession (SSFP) sequence.

2.3 Electric Properties Reconstruction

Performing EPT as described in, e.g., [9], conductivity σ was estimated from the transceive phase ϕ of the SSFP scans by $\sigma = \Delta\phi/(2\mu_0\omega)$ (Δ: Laplacian operator, μ_0: magnetic permeability, ω: Larmor frequency) Subsequently, a median filter was applied, which was locally restricted to voxels with comparable signal magnitude [9].

2.4 Image Analysis

Side-by-side comparison of DWI and conductivity maps was performed in a quantitative and qualitative manner as described previously [14]. In short, a region of interest was outlined on the DWI images encompassing the infarct and transferred to the conductivity maps. Absolute conductivity values were calculated as described above and compared to the contralateral not affected side. Additionally, the conductivity maps of the affected and not affected side were compared, and altered conductivity was detected in a qualitative manner.

3 Results

Both animals exhibited a lesion that could be well delineated on the DWI images (Fig. 1b, e) in the left middle cerebral artery territory. Conductivity within the infarct was 0.39 ± 0.07 S/m and 0.31 ± 0.14 S/m for animal 1 and 2, respectively. In the contralateral not affected side it was 0.64 ± 0.15 S/m and 0.66 ± 0.16 S/m, respectively. This difference was also clearly visible by qualitative inspection of the conductivity maps (Fig. 1c, f). The corresponding ADC values calculated from the two b-values were 0.27 ± 0.10 × 10^{-3} mm^2/s and 0.19 ± 0.11 × 10^{-3} mm^2/s. In contralateral not infarcted tissue it was 0.68 ± 0.28 × 10^{-3} mm^2/s and 0.59 ± 0.16 × 10^{-3} mm^2/s, respectively, in the two animals.

4 Discussion

We found decreased conductivity after acute focal permanent cerebral ischemia in a rat model of stroke.

When oxygen supply is acutely and critically diminished, many processes take place on a cellular level which might influence tissue conductivity. Energy failure leads to impairment of ion transporters like the Na^+/K^+-ATPase and the Na^+/Ca^{2+}-antiport and ion channels, e.g., for calcium and chloride are opened. As a result, net water influx ensues called cytotoxic oedema [7, 8]. Glutamate sensitive receptors increase the permeability for Na^+, K^+ and Ca^{2+} [7, 8]. At the same time, the extracellular space is first depleted of sodium, then replenished by transcapillary sodium flux [17]. When reperfusion takes place, these processes can be partially reversed but reperfusion injury may occur [17] that causes additional damage to brain cells. In the subacute stage an impaired blood brain barrier causes vasogenic oedema of the extracellular space by passage of large molecules followed by water [18].

Others have described increased conductivity in subacute cerebral ischemia in humans two months [12] and seven days [13] after the insult as well as in transient experimental cerebral ischemia 45 min [14] and 24 h [15] after the insult in rats. In contrast to the present study, blood flow was re-established [14, 15] at the time of image acquisition or is expected to occur when spontaneous recanalisation takes place [12, 13]. Further, vasogenic oedema is expected to occur in the subacute stage of the insult. In the present study in the face of persistent vessel occlusion and thus critically diminished blood flow and the acute stage of the insult, vasogenic oedema is not

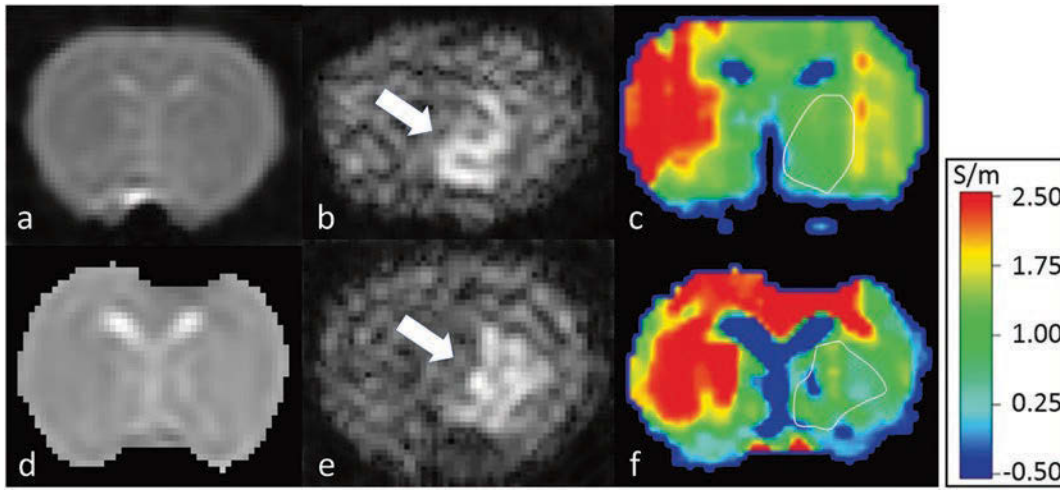

Fig. 1 Representative image montage of the two animals (**a**–**c**: animal #1, **d**–**f**: animal #2) with permanent MCAo. Structural SSFP magnitude image (**a** and **d**), diffusion weighted images (DWI, **b** and **e**) with an infarct (arrows) and conductivity maps (**c** and **f**) demonstrating decreased conductivity (0.39 ± 0.07 vs. 0.64 ± 0.15 S/m in **c** and 0.31 ± 0.14 vs. 0.66 ± 0.16 S/m in **f**) within the DWI lesion that also can be well appreciated when comparing the affected side with the non-affected side). Note the colour scale for image **c** and **f** (in S/m)

expected. Concurring with that notion, ADC values were markedly diminished, indicating restricted water molecule movement, cell swelling and irreversible tissue damage.

It is intriguing to speculate that the effects of cytotoxic and vasogenic oedema and the related sodium concentration determines tissue conductivity. However, the exact mechanism of conductivity changes cannot be elucidated here since we did not perform histological work-up or electrophysiological experiments. Further, we did not perform additional imaging to depict the ischemic penumbra. Thus, only information on the final infarct depicted by DWI potentially encompassing penumbra already recruited into the core is available. More experiments are needed to confirm these first preliminary experiments.

We hope that EPT might offer an additional contrast parameter in addition to existing conventional and functional sequences. Potentially, it can be used as a surrogate imaging marker of cytotoxic oedema. EPT can be obtained without the need for special coils, scanners or any other dedicated hardware and can be calculated by using the phase information of routinely acquired standard sequences [9] which makes it an attractive candidate technique for stroke imaging. Studies on the temporal behaviour of conductivity after focal cerebral ischemia and reperfusion should be conducted. Further, different compartments of ischemia (core, penumbra, oligemia) and their conductivity should be studied.

Acknowledgement This work was in part supported by a grant by the Medical Faculty of the Christian-Albrecht University of Kiel.

References

1. Saver JL, Goyal M, Bonafe A et al (2015) Stent-retriever thrombectomy after intravenous t-PA vs. t-PA alone in stroke. N Engl J Med 372:2285–2295
2. Johnston SC, Mendis S, Mathers CD (2009) Global variation in stroke burden and mortality: estimates from monitoring, surveillance, and modelling. Lancet Neurol 8:345–354
3. Neumann-Haefelin T, Wittsack HJ, Wenserski F et al (1999) Diffusion- and perfusion-weighted MRI. The DWI/PWI mismatch region in acute stroke. Stroke 30:1591–1597
4. Jensen-Kondering U, Manavaki R, Ejaz S et al (2017) Brain hypoxia mapping in acute stroke: Back-to-back T2' MR versus ^{18}F-fluoromisonidazole PET in rodents. Int J Stroke 12:752–760
5. Dehkharghani S, Fleischer CC, Qiu D et al (2017) Cerebral temperature dysregulation: MR thermo-

graphic monitoring in a nonhuman primate study of acute ischemic stroke. AJNR Am J Neuroradiol 38:712–720
6. Harston GW, Tee YK, Blockley N et al (2015) Identifying the ischaemic penumbra using pH-weighted magnetic resonance imaging. Brain 138:36–42
7. Brott T, Bogousslavsky J (2000) Treatment of acute ischemic stroke. N Engl J Med 343:710–722
8. Dirnagl U, Iadecola C, Moskowitz MA (1999) Pathobiology of ischaemic stroke: an integrated view. Trends Neurosci 22:391–397
9. Katscher U, van den Berg CAT (2017) Electric properties tomography: biochemical, physical and technical background, evaluation and clinical applications. NMR Biomed 30
10. Tha KK, Katscher U, Yamaguchi S et al (2018) Noninvasive electrical conductivity measurement by MRI: a test of its validity and the electrical conductivity characteristics of glioma. Eur Radiol 28:348–355
11. Kim SY, Shin J, Kim DH et al (2016) Correlation between conductivity and prognostic factors in invasive breast cancer using magnetic resonance electric properties tomography (MREPT). Eur Radiol 26:2317–2326
12. van Lier A, Kolk A, Brundel M et al (2012) Electrical conductivity in ischemic stroke at 7.0 Tesla: a case study. In: Proceedings of the 20th scientific meeting of the International Society of Magnetic Resonance in Medicine:3484
13. Gurler N, Oran OF, Keklikoglu HD et al (2016) Application of generalized phase based electrical conductivity imaging in the subacute stage of hemorrhagic and ischemic strokes. In: Proceedings of the 24th scientific meeting of the International Society of Magnetic Resonance in Medicine:2994
14. Jensen-Kondering U, Shu L, Böhm R et al (2020) In-vivo pilot study at 3 Tesla: Feasibility of electric properties tomography in a rat model of stroke. Phys Med 9:100024
15. Amouzandeh G, Mentink-Vigier F, Helsper S et al (2020) Magnetic resonance electrical property mapping at 21.1 T: a study of conductivity and permittivity in phantoms, ex vivo tissue and in vivo ischemia. Phys Med Biol 65:055007
16. Koizumi J, Yoshida Y, Nakazawa T et al (1986) Experimental studies of ischemic brain edema. 1. A new experimental model of cerebral embolism in rats in which recirculation can be introduced in the ischemic area. Jpn J Stroke 8:1–8
17. Pan J, Konstas AA, Bateman B (2007) Reperfusion injury following cerebral ischemia: pathophysiology, MR imaging, and potential therapies. Neuroradiology 49:93–102
18. Simard JM, Kent TA, Chen M et al (2007) Brain oedema in focal ischaemia: molecular pathophysiology and theoretical implications. Lancet Neurol 6:258–268

Physical Stress Attenuates Cognitive Inhibition: An fNIRS Examination

Lei Ma, Kui Xu, Jinhong Ding, Jianren Gao, and Xianliang Wang

Abstract

This study aimed to assess the haemodynamics in the prefrontal cortex (PFC) and salivary α-amylase (sAA) response during acute physical stress. Acute stress was induced using the cold pressor task (CPT). The haemodynamics in the prefrontal cortex was measured using functional near-infrared spectroscopy (fNIRS). The Stroop test was performed and the sAA levels were measured before and after the task. The accuracy rate (%) of the Stroop test decreased significantly in the stress group ($t = 2.80$, $p = 0.008$) but not the control group ($t = -1.05$, $p = 0.298$). The results showed that oxyHb activation in the mid-left and mid-right regions of PFC after the CPT. The sAA levels significantly increased during and after the CPT in the stress group (U/ml, 2527.58 ± 437.54, mean ± SD, n = 26) but not the control group (U/ml, 1506.92 ± 291.05, n = 23). Our data showed that the acute stress exposure attenuated cognitive inhibition, which may be due to changes of scalp blood flow and/or cerebral haemodynamics near the mid-left PFC and mid-right PFC following acute stress.

Keywords

Cerebral haemodynamics · salivary α-amylase response · cold pressor task · cognitive regulation · Stroop test

1 Introduction

Cognitive regulation has been widely shown in the laboratory to be an effective way to alter decision-making responses [1]. Executive functions are cognitive control mechanisms that allow goal-oriented, flexible and effective action and thinking [2, 3]. Cognitive regulation is generally a complex, goal-directed process that relies on many higher cognitive functions, such as cognitive inhibition, cognitive flexibility [4]. The prefrontal cortex (PFC) is a key brain region that is involved in these functions [5, 6]. The successful cognitive regulation depends on complete execu-

L. Ma
School of Information Science and Technology, Nantong University,
Nantong, Jiangsu Province, China

K. Xu
Department of Physiology & Biophysics, Case Western Reserve University, Cleveland, OH, USA

J. Ding
School of Education Science, Nantong University,
Nantong, Jiangsu Province, China

J. Gao
College of Arts and Sciences, Case Western Reserve University, Cleveland, OH, USA

X. Wang (✉)
School of Physical Education, Shandong University,
Jinan, Shandong Province, China
e-mail: wangxianliang@sdu.edu.cn

F. Scholkmann et al. (eds.), *Oxygen Transport to Tissue XLIII*, Advances in Experimental Medicine and Biology 1395, https://doi.org/10.1007/978-3-031-14190-4_5

tive functioning and engagement of the PFC [7]. Stress is defined as the non-specific response of the body/mind to any demand of change [8]. There is growing evidence that stress can decrease attention and cognitive inhibition [9]. Functional Near-Infrared Spectroscopy (fNIRS) is a promising neuroimaging technique to measure the cerebral haemodynamics associated with neural activity related to cognitive behaviour [10]. In this study we used the cold pressor task (CPT) to induce acute stress. The haemodynamics in the PFC was measured using fNIRS, and the levels of salivary α-amylase (sAA) of participants were analysed before and after the stress. The cognitive function was assessed using the Stroop test. The importance of linking stress and cognitive inhibition to cognitive health was discussed.

2 Methods

2.1 Participants

Forty-nine healthy male participants were recruited from Nantong University in Jiangsu province (age: 20–25 years, 21.30 ± 1.85, mean ± SD). We randomly assigned the participants to the stress group (n = 26) and control group (n = 23). Individuals were recruited until we reached the maximum number of participants approved by the institutional review board for this project.

2.2 Cold Pressor Task (CPT) and Stroop Test

The CPT was used to induce acute stress as described previously [11]. All participants who underwent CPT in the stress group were asked to place their non-dominant hands in ice-cold (1–3 °C) water for 3 min, while participants who underwent sham CPT in the control group were asked to place their non-dominant hands in room-temperature (~22 °C) water for 3 min.

Participants' cognitive inhibition was assessed using a computerised version of the Stroop test [12]. The Stroop colour and word test was used to assess the ability to inhibit cognitive interference that occurs when the processing of a specific stimulus feature impedes the simultaneous processing of a second stimulus attribute. Participants had to select the correct answers within a limited time period. The entire test lasted about 300s. The reaction time and accuracy rate were recorded.

2.3 Procedural Flow

The scheme of the experimental protocol is shown in Fig. 1. The participants needed to wear an fNIRS cap for the entire experiment. After completion of the baseline Stroop test, the participant underwent the CPT or sham CPT and then completed the post-task Stroop test. Saliva samples were collected before and after each Stroop test and the sAA levels were measured. We used 22 channel LIGHTNIRS system (Shimadzu Corporation) to indicate the brain oxyHb concentrations using the 2 × 8 Prefrontal Cortex map. All the raw optical intensity values data were preprocessed and converted into haemodynamics response [4].

2.4 Statistical Analysis

Data are expressed as mean ± SD. Statistical analyses were performed using SPSS V19.0 for Windows. For sAA analysis, a 2 × 4 mixed repeated ANOVA with condition (stress vs. control) as a between-subjects variable and time as a within-subjects variable was calculated. To compare the Stroop response of different groups (stress vs. control) before and after stress stimulus, a 2 × 2 mixed ANOVA was used. For the fNIRS results, the comparison between any two groups was analysed one-sided t-test. Significance was considered at the level of $p < 0.05$.

3 Results

3.1 sAA Characteristics

As seen in Fig. 2, the sAA analysis revealed a significant between-subjects interaction effect [F

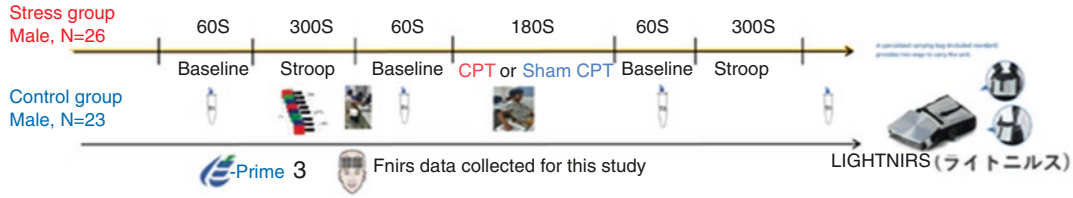

Fig. 1 Scheme of the experimental protocol

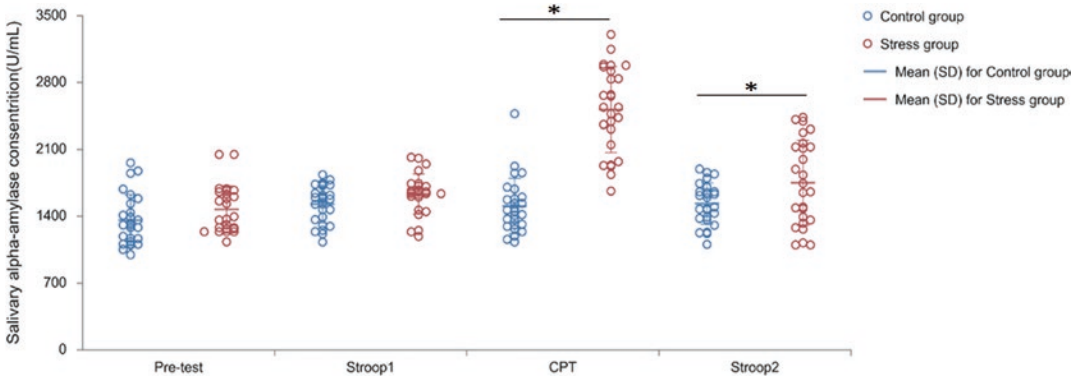

Fig. 2 The mean sAA levels at the pretest and after Stroop test 1, CPT (or sham CPT), and Stroop test 2. CPT: cold pressor task. * indicates significance ($p < 0.05$) between the stress group and the control group

(2, 49) = 48.576, $p < 0.001$] and a significant within-subjects interaction effect [F (1, 50) = 43.662, $p < 0.001$]. There was also a significant main effect between-subjects [F (1, 50) = 35.949 $p < 0.001$]. The sAA levels were significantly increased during CPT and after CPT in the stress group (U/ml, 2527.58 ± 437.54, mean ± SD) but not in the control group (U/ml, 1506.92 ± 291.05), indicating that an acute stress was successfully induced by the CPT.

3.2 Stroop Test Results

The Stroop response of different groups (stress vs. control) before and after the stress is shown in Table 1. The participants in the control group improved in their performance after the stress stimulus, regardless of time [F (1, 51) = 6.743, $p = 0.012$]. The accuracy rate (%) of participants decreased significantly in the stress group [$t = 2.80$, $p = 0.008$] but not in the control group [$t = -1.05$, $p = 0.298$]. However, no significant interaction between condition and time of measurement was found [F (1, 51) = 12.18, $p = 0.26$].

3.3 fNIRS Results

Figure 3 shows the averaged β values of the oxyHb (Fig. 3a) and deoxyHb (Fig. 3c) concentrations after CPT. Figure 3b, d demonstrate the regions of significant differences (t-test, $p < 0.05$) in averaged β values of the oxyHb (Fig. 3a) and deoxyHb (Fig. 3c) concentrations of participants in the stress group before and after CPT. Figure 3b indicates oxyHb activation in the mid-left PFC and mid- right PFC after the CPT. Figure 3b shows that the β values of deoxyHb in the mid-left, mid-right and right regions of PFC significantly changed after CPT.

As shown in Table 2, the levels of oxyHb in the mid-left and mid-right PFC regions were significantly different than the baseline levels [$t = 2.53$, $p = 0.02$] and the levels of the recovery phase. The oxyHb levels in mid-right PFC were

Table 1 Executive functions on the Stroop test

Group		Accuracy rate (%)	Reaction time (ms)
Stress (n = 26)	Before CPT	91.15 ± 15.86	1155 ± 228
	After CPT	84.90 ± 12.16*	1310 ± 213*
Control (n = 23)	Before sham CPT	90.84 ± 14.54	1244 ± 206
	After sham CPT	94.09 ± 12.18*	1056 ± 195*

Note: data are mean ± SD; *CPT* cold pressor task, ∗ indicates significance vs. the values before the task ($p < 0.05$, ANOVA)

perfusion, suggesting that the CPT stimulus significantly influenced the cognitive process in the mid-left and mid-right regions of PFC but not the left and right regions of PFC.

4 Discussion

Our results showed acute stress attenuated cognitive inhibition. The regulatory hormonal rhythms may be associated with the changes in oxyHb in PFC [13]. We explored the relationship between brain haemodynamics and sAA

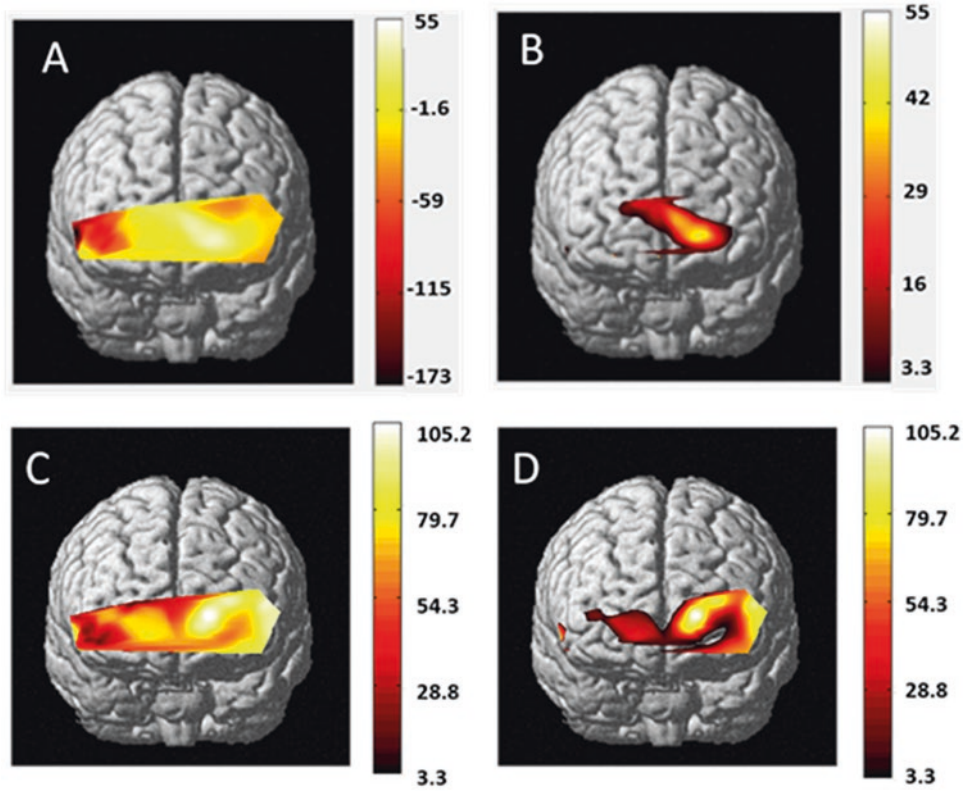

Fig. 3 Averaged β values (t-tests) of the oxyHb and deoxyHb concentrations after cold pressor task (CPT). (**a**) averaged β values of the oxyHb: (**d**) indicates the regions of significant differences (t-test, $p < 0.05$) in averaged β values of the oxyHb (**a**); (**c**) averaged β values of the deoxyHb; 3D: indicates the regions of significant differences (t-test, $p < 0.05$) in averaged β values of the deoxyHb (**c**)

−0.006 ± 0.02 (mean ± SD) and 0.020 ± 0.04 for the duration CPT and the recovery phase, respectively, and they were significantly lower compared to baseline (0.06 ± 0.19). This could be interpreted as corresponding changes in cortical responses associated with acute stress. Participants who had higher levels of oxyHb in the mid-left and mid-right regions of PFC following cold exposure seemed to have a lower score of reaction time post-stress on Stroop test

Table 2 Measurement of oxyHb using fNIRS before, during and after the stress

Regions of PFC	Baseline	During CPT or sham CPT	Post-task recovery
Stress Group (n = 23)			
Left	0.060 ± 0.14	−0.007 ± 0.12	0.070 ± 0.12
Mid-left	0.040 ± 0.16	−0.008 ± 0.04*	0.060 ± 0.06*
Mid-right	0.060 ± 0.19	−0.006 ± 0.02*	0.020 ± 0.04*
Right	0.070 ± 0.17	−0.010 ± 0.15	0.080 ± 0.12
Control group (n = 24)			
Left	−0.007 ± 0.42	−0.006 ± 0.35	−0.050 ± 0.21
Mid-left	−0.090 ± 0.03	−0.030 ± 0.05	−0.080 ± 0.04
Mid-right	−0.320 ± 1.35	0.005 ± 1.16	0.190 ± 1.02
Right	−0.072 ± 0.16	−0.007 ± 0.15	0.060 ± 1.35

Note: *fNIRS* functional Near-Infrared Spectroscopy, *CPT* cold pressor task; data are mean ± SD; * indicates significance ($p < 0.05$, t-test) vs. baseline values

but the accuracy rate did not change significantly. Changes of blood pressure and heart rates would be expected after CPT, which may give spurious results due to changes in skin blood flow [14]. The changes in oxyHb we observed could be simply a change in scalp blood flow and/or changes in cerebral haemodynamics induced entirely by causes other than neurovascular-coupling. One of the important causes may be the CPT-induced strong increase in sympathetic nervous system activity, leading to an increase in blood pressure and vasoconstriction, resulting in a change in oxyHb [15]. Our results showed that the oxyHb levels were increased in the mid-left PFC and middle right PFC after acute stress, which may not directly reflect the changes in cognitive inhibition. Further study is required to control the possible interference in fNIRS measurement and identify other possible solutions.

References

1. Testa R, Bennett P, Ponsford J (2012) Factor analysis of nineteen executive function tests in a healthy adult population. Arch Clin Neuropsychol 27(2):213–224
2. Diamond A (2013) Executive functions. Annu Rev Psychol 64:135–168
3. Raio CM, Orederu TA, Palazzolo L et al (2013) Cognitive emotion regulation fails the stress test. Proc Natl Acad Sci U S A. 110(37):15139–15144
4. Kalia V, Vishwanath K, Knauft K et al (2018) Acute stress attenuates cognitive flexibility in males only: an fNIRS Examination. Front Psychol 9:2084
5. Buck R (1985) Prime theory: an integrated view of motivation and emotion. Psychol Rev 92(3):389–413
6. Arnsten AF (1997) Catecholamine regulation of the prefrontal cortex. J Psychopharmacol 11(2):151–162
7. Putman P, Verkuil B, Arias-Garcia E et al (2014) EEG theta/beta ratio as a potential biomarker for attentional control and resilience against deleterious effects of stress on attention. Cogn Affec Behav Neurosci 14(2):782–791
8. Arnsten AF (2009) Stress signaling pathways that impair prefrontal cortex structure and function. Nat Rev Neurosci 10(6):410–422
9. Anderson ND, Lau MA, Segal ZV et al (2007) Mindfulness-based stress reduction and attentional control. Clin Psychol Psychother 14(6):449–463
10. Al-Shargie F, Kiguchi M, Badruddin N et al (2016) Mental stress assessment using simultaneous measurement of EEG and fNIRS. Biomed Opt Express 7(10):3882–3898
11. Schoofs D, Wolf OT, Smeets T (2009) Cold pressor stress impairs performance on working memory tasks requiring executive functions in healthy young men. Behav Neurosci 123(5):1066
12. Scarpina F, Tagini S (2017) The stroop color and word test. Front Psychol. 8:557
13. Cerqueira JJ, Almeida OF, Sousa N (2008) The stressed prefrontal cortex. Left? Right! Brain Behav Immun 22(5):630–638
14. Gullifer JW, Chai XJ, Whitford V et al (2018) Bilingual experience and resting-state brain connectivity: Impacts of L2 age of acquisition and social diversity of language use on control networks. Neuropsychologia 117:123–134
15. Tachtsidis I, Scholkmann F (2016) False positives and false negatives in functional near-infrared spectroscopy: issues, challenges, and the way forward. Neurophotonics 3(3):031405

Changes in Prefrontal Cortical Oxygenation During Tilt Table Orthostatic Hypotension in Subarachnoid Haemorrhage Patients

Masamichi Moriya

Abstract

Cerebral vasospasm and delayed cerebral ischaemia in patients with subarachnoid haemorrhage (SAH) are more likely to occur within the first two weeks of bleeding. Thus, conventional management involves absolute rest for two weeks. Recently, studies have reported on the possibility of early mobilisation after SAH; however, its safety has not been sufficiently evaluated. The present study investigates the relationship between cerebral cortex oxygenation and orthostatic hypotension in SAH patients using near-infrared spectroscopy (NIRS). Four SAH patients were laid supine for 5 min before performing a head-up tilt (HUT) to 30°, 45°, and 60° every 5 min using a tilt table bed. Arterial blood pressure was measured before and immediately after HUT. We evaluated O_2Hb levels of the left and right prefrontal cortex (PFC) in 11 of 12 times that could be performed without stopping due to orthostatic hypotension. We analysed O_2Hb levels at up to 60 s at 10-s intervals after HUT 60 s before mobilisation. We found that O_2Hb levels decreased after the first (30°) HUT, but increased after HUT at 45° and 60°. Over a 60-s period, no statistically significant difference was observed. Arterial blood pressure fell by 6% on average across all the 12 tests. These results reveal that HUT orthostatic arterial hypotension caused an instantaneous decrease in oxygenation, but it returned to the baseline shortly thereafter. It is important to monitor the degree of orthostatic hypotension in patients after SAH. Gradual mobilisation may minimise the decrease in arterial blood pressure and maintain oxygenation of the cerebral cortex.

Keywords

NIRS · Oxyhaemoglobin · Orthostatic hypotension · Head up tilt (HUT)

1 Introduction

Rehabilitation in the acute phase of subarachnoid haemorrhage (SAH), which is performed in parallel with emergency medical care, has attracted international attention in the recent years. The guidelines of the American Society of Clinical Care Medicine (SCCM) [1] and the expert consensus of early rehabilitation by the Japanese Society of Intensive Care Medicine [2] recommend the procedure of rehabilitation from the hyperacute stage. However, several guidelines have previously recommended the mobilisation

M. Moriya (✉)
Department of Physical Therapy, Faculty of Health Care and Medical Sports, Teikyo Heisei University, Tokyo, Japan
e-mail: m.moriya@edu.k.u-tokyo.ac.jp

F. Scholkmann et al. (eds.), *Oxygen Transport to Tissue XLIII*, Advances in Experimental Medicine and Biology 1395, https://doi.org/10.1007/978-3-031-14190-4_6

of patients with SAH, with careful intervention [3, 4].

Cerebral vasospasm and delayed cerebral ischaemia are more likely to occur in patients after SAH, usually within the first two weeks of bleeding. Since cerebral vasospasm is a reversible narrowing of the cerebral artery lumen that occurs near the ruptured cerebral aneurysm, aggressive physical therapy was contraindicated considering the possible risk of changes in cerebral circulation upon being mobilised. Several recent studies of early mobilisation in SAH patients have been reported [5, 6] and our study also reported consistent results [7]. However, the safety on mobilisation has not been sufficiently verified. The present study investigates the relationship between cerebral cortex oxygenation and orthostatic hypotension in SAH patients using near-infrared spectroscopy (NIRS).

2 Methods

2.1 Subjects

A total of four patients with aneurysmal SAH were enrolled (Table 1). The inclusion criteria were as follows: (1) systolic blood pressure (SBP) 120–220 mmHg; (2) heart rate (HR) 40–100 bpm; (3) oxygen saturation >92%; (4) temperature < 38.5 °C. The exclusion criteria were as follows: (1) mean blood pressures < 70 or > 120 mmHg; (2) HR < 40 or >130 bpm; (3) respiratory rate < 5 or > 40 bpm; (4) oxygen saturation < 88%; (5) if intracranial pressure (ICP) is monitored, ICP > 15 mmHg; (6) sudden changes in neurologic symptoms or level of consciousness. These criteria reflect the expert consensus of the Japan Intensive Care Medical Society [2].

Table 1 Clinical profiles of the subjects

ID.No	Age	Sex	GCS	Location (surgery)
1	73	F	8	Rt PICA (Clip)
2	71	F	9	Lt IC-PC (Clip)
3	88	F	11	A-com (Clip)
4	64	M	6	M1-M2 (Coil)

PICA Posterior inferior cerebellar artery, *IC-PC* Internal carotid artery-posterior communicating artery, *A-com* Anterior communicating artery, *M1-M2* Sphenoidal-insular

2.2 Study Design

Each trial consisted of the following steps: First, each subject was positioned on the tilt table in the supine position for 10 min. Next, the standing load was increased to 30°, 45° and 60° every 5 min. Finally, the table was returned to 0° and maintained in this position for 10 min. To avoid the influence of environmental stress, the study was performed in a rehabilitation room with air conditioning throughout the trials.

We used 2-channel NIRS (Pocket NIRS Duo, Dyna Sense, Hamamatsu, Japan) for the measurement of cerebral blood oxygenation (O_2Hb) in the bilateral prefrontal cortex (PFC). The NIRS probes were set symmetrically on the forehead with a flexible fixation pad, so that the midpoint between the emission and detection probes was 3 cm above the centres of the upper edges of the bilateral orbital sockets. Distance between the emitter and detector probe was set at 3 cm. This positioning is similar to positions Fp1 (left) and Fp2 (right) of the international electroencephalographic 10–20 system.

Using the NIRS equipment, we measured the bilateral PFC activity at rest (10 min) and during a gradual increase in the standing load (30°, 45°, 60°) using the tilt table. In addition, we measured blood pressure using a non-invasive brachial sphygmomanometer (HEM-7120, OMRON HEALTHCARE, Japan. The cuff was wrapped around the upper arm without being removed from the beginning to the end of the experiment. The measurement was performed manually by the examiner immediately after mobilisation of the patient.

2.3 Data Analysis

We analysed the changes in NIRS parameters by subtracting the mean before mobilisation values from the mean after mobilisation values. The time course of the rate of change in O_2Hb was

analysed by a Friedman's test followed by Dunnett's multiple comparisons test. Statistical analysis was performed using Prism 8 software (GraphPad Software Inc., La Jolla, CA, USA). For all statistical analyses, differences with a $p < 0.05$ were deemed statistically significant.

3 Results

The results showed that the O_2Hb levels decreased after the first head-up tilt (HUT) at 30°, but increased after the subsequent HUTs at 45° and 60°. However, not all cases revealed the raised O_2Hb levels. Over a 60-s period, no statistically significant difference was observed. In the second and subsequent HUTs (i.e., at 45° and 60°), O_2Hb levels decreased only after 10 s, but returned to a value higher than the baseline after 20 s (Fig. 1).

In addition, lowered blood pressure was observed in all the cases except one (Table 2). The rate of change was highest at 45° after mobilisation (Fig. 2). HR was observed to increase in all cases on mobilisation.

4 Discussion

Here, we show that in SAH patients, O_2Hb temporarily decreases after mobilisation, but rapidly returns to the baseline. The reason for the decrease in blood pressure and the increase in HR due to mobilisation could possibly be the physiological response to orthostatic hypotension. It has previously been reported that the mobilisation from supine to sitting results in an increase in HR, but no significant haemodynamic changes were observed [8]. In this study, the mobilisation using the tilt table resulted in a similar physiolog-

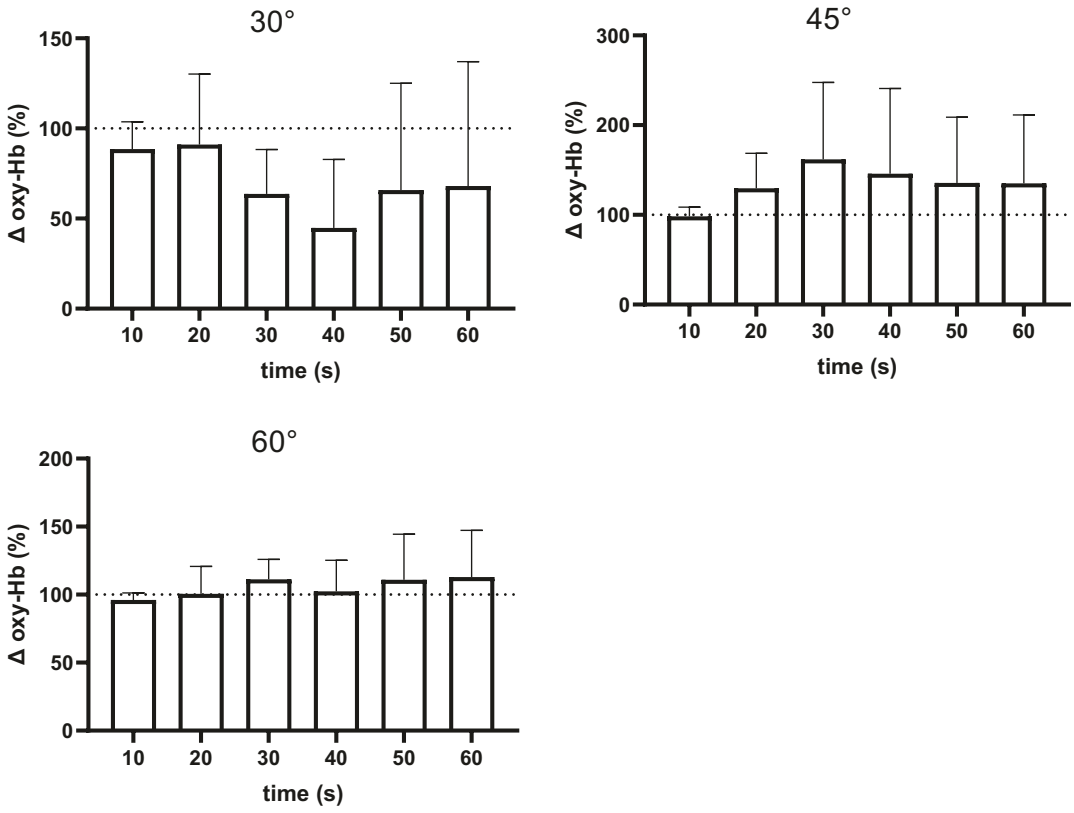

Fig. 1 Time course of rate of changes in O_2Hb at each angle

Table 2 Systolic blood pressure and heart rate change due to mobilisation

	0°	30°	45°	60°	
case1	178 (82)	186	187	188 (82)	SBP (HR)
case2	159 (93)	143	135	138 (95)	mmHg (bpm)
case3	131 (81)	133	112	114 (100)	
case4	108 (101)	99	96	104 (117)	

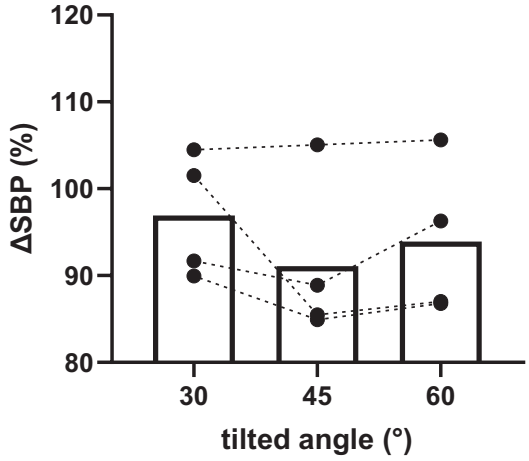

Fig. 2 Rate of change in blood pressure due to mobilisation

ical response. In other words, cerebral oxygenation is often maintained even when blood pressure is low.

Since Schwickert's research report [9], awareness of early mobilisation has increased, and the number of facilities promoting that patients leave the bed as soon as possible has rapidly increased, provided that the criteria for discontinuation are met during acute rehabilitation. However, regarding SAH, the safety of expedited mobilisation is questioned, and no consensus has been obtained as yet. At the same time, several studies have reported the possibility of spasm reduction effect due to mobilisation [5, 10]. The subjects of this study did not develop spasms. We recommend clinics to proceed with immediate mobilisation in a step-by-step manner after fully checking the cerebral circulation index.

A limitation of this study is that only four subjects were evaluated, thus limiting the interpretation of the results substantially.

Acknowledgments We would like to thank Editage (www.editage.com) for English language editing. This research was supported by the Promotion and Mutual Aid Corporation for Private Schools of Japan.

References

1. Barr J, Fraser GL, Puntillo K et al (2013) Clinical practice guidelines for the management of pain, agitation, and delirium in adult patients in the intensive care unit. Crit Care Med 41:263–306
2. Ad Hoc Committee for Early Rehabilitation, The Japanese Society of Intensive Care Medicine. The Japanese Society of Intensive Care Medicine (2017) Evidence based expert consensus for early rehabilitation in the intensive care unit. J Jpn Soc Intensive Care Med 24:255–3036
3. Steiner T, Juvela S, Unterberg A et al (2013) European Stroke Organization guidelines for the management of intracranial aneurysms and subarachnoid haemorrhage. Cerebrovasc Dis. 35:93–112
4. Bederson JB, Connolly ES Jr, Batjer HH et al (2009) Guidelines for the management of aneurysmal subarachnoid hemorrhage : a statement for healthcare professionals from a special writing group of the Stroke Council, American Heart Association. Stroke 40(3):994–1025
5. Karic T, Røe C, Nordenmark TH et al (2016) Impact of early mobilization and rehabilitation on global functional outcome one year after aneurysmal subarachnoid hemorrhage. J Rehabil Med. 48(8):676–682
6. Olkowski BF, Devine MA, Slotnick LE et al (2013) Safety and feasibility of an early mobilization program for patients with aneurysmal subarachnoid hemorrhage. Phys Ther 93:208–215
7. Moriya M, Sumi K, Miyazaki S et al (2016) Study of factors affecting the outcome and effect of early mobilization of SAH patients. J Stroke. 38(3):161–167
8. Merino C, Heap P, Vergara V et al (2014) Changes in cerebral blood flow velocity in supine and sitting position in patients with aneurysmal subarachnoid hemorrhage. Rev Med Chil. 142(12):1502–1509
9. Schwickert WD, Pohlman MC, Pohlman AS et al (2009) Early physical and occupational therapy in mechanically ventilated, critically ill patients: a randomized controlled trial. Lancet 373:1874–1882
10. Riordan MA, Kyle M, Dedeo C et al (2015) Mild exercise reduces cerebral vasospasm after aneurysm subarachnoid hemorrhage: a retrospective clinical study and correlation with laboratory investigation. Acta Neurochir Suppl 120:55–61

Effects of Different Optical Properties of Head Tissues on Near-Infrared Spectroscopy Using Monte Carlo Simulations

E. Russomanno, A. Kalyanov, J. Jiang, M. Ackermann, and M. Wolf

Abstract

In near-infrared spectroscopy (NIRS), it is crucial to have an accurate and realistic model of photon transport in the adult head for obtaining accurate brain oxygenation values. There are several studies on the influence of thickness, the morphology of extracerebral layers, and source-detector distance on the sensitivity of NIRS to the brain. However, the optical properties of the different layers vary between different publications. How is the performance of NIRS affected when the real optical properties differ from the assumed ones?

We aim to investigate the influence of variation in scattering and absorption in a five-layered head model (scalp, skull, CSF, grey and white matter). We performed Monte Carlo simulations focusing on a five-layered slab mesh. The range of optical properties is based on a review of the published literature. We assessed the effect on light propagation by measuring the difference in the mean partial path lengths, attenuation, and the number of the detected photons between the different optical properties performing Monte Carlo simulations. For changes in the reduced scattering, we found that the upper layers tend to have a negative impact. In contrast, changes in lower layers tend to impact the brain's influence metrics positively. Furthermore, for small source-detector distances, the relative percentage difference between lower and higher values is greater than larger distances. *Conclusions*: We conclude that the assumption of different optical properties has a substantial effect on the sensitivity to the brain. This means that it is important to determine the correct optical properties for NIRS measurements in vitro and in vivo.

Keywords

NIRS · Inhomogeneous head model · Cerebral oxygenation · Light scattering

1 Introduction

One of the techniques capable of non-invasively measuring tissue oxygenation and their optical properties using diffuse light is near-infrared spectroscopy (NIRS). NIRS is widely applied to

E. Russomanno (✉) · M. Wolf
Biomedical Optics Research Laboratory, Department of Neonatology, University Hospital Zurich, University of Zurich, Zurich, Switzerland

D-ITET, ETH Zurich, Zurich, Switzerland
e-mail: emanuele.russomanno@usz.ch

A. Kalyanov · J. Jiang · M. Ackermann
Biomedical Optics Research Laboratory, Department of Neonatology, University Hospital Zurich, University of Zurich, Zurich, Switzerland

F. Scholkmann et al. (eds.), *Oxygen Transport to Tissue XLIII*, Advances in Experimental Medicine and Biology 1395, https://doi.org/10.1007/978-3-031-14190-4_7

the head of humans to determine the oxygenation of the brain because oxygenation is an important parameter, particularly for the brain. However, it is known that this measurement is substantially influenced by extracerebral tissue [1–4]. To measure the oxygenation correctly in the adult head, the measured data should be fitted with an inhomogeneous model representing the multi-layered structure of the involved tissues. Currently often homogeneous models are employed that lead to loss in precision. One effort when building a realistic model is the difficulty of retrieving accurate optical properties of the different layers of an adult head, since many published works use and report different values, leaving no common agreement on this matter.

This study aims to investigate the impact of this uncertainty in the optical properties. How is the performance of NIRS affected when the real optical properties differ from the assumed ones?

2 Material and Methods

For this investigation, the simulations were performed using the state-of-the-art mesh-based Monte Carlo (MC) toolkit, the MMC [6], which provides an accurate solution to the radiative transfer equation. MC gives us also the ability to retrieve information about path of the simulated photons through the layers of the model. One light source, pencil beam type, and eight detectors of 1.2 mm radius, distanced from each other by 5 mm, were placed on the surface of the model. The experiments were executed in reflection mode with 1×10^8 simulated photons emitted into the mesh. We modelled a slab with a dimension of $100 \times 100 \times 100\text{mm}^3$, max volume size of 1 mm^3, 1.894.993 elements and five layers to represent the adult head, using the TetGen toolkit [7]. We chose a slab rather than an MRI-based head model to reduce the computational time and to avoid the position dependency, which is often present in a full head model. The thickness of the various layers was chosen to simulate an adult male, with a cranial thickness above average. The value for the skull is based on the study from DeBoer et al. [8] and the different thicknesses of this slab mesh are shown in Table 1.

Due to the already stated variability between the reported optical properties of the different layers, we composed a reasonable range of optical properties that were taken from a review of the published literature. Table 2 shows the respective range of reduced scattering ($\mu_s`$) and absorption (μ_a) coefficients.

We used the following metrics for the further analysis: mean partial path length (PPL), attenuation or final weight, photon arrival time and photon count. The PPL is the average path length that photons have travelled in every single layer. The attenuation is the final detected photon weight based on the partial path data and optical properties [9].

One of the objectives is to assess the influence that the variation of optical properties in a specific layer has on the measured brain data. For this reason, we first picked a specific layer and then changed the optical properties for that layer in every new simulation, while keeping the optical properties of the other layers at a fixed value. This was executed by first varying the $\mu_s`$ and then the μ_a parameter in their range (Fig. 1).

We considered the photons that have travelled at least 5 mm deep inside the brain volume as brain data. The brain percentage attenuation and brain percentage partial path length used in the next plots are computed as shown in Eqs. 1 and 2.

$$Att.Brain\% = \frac{100 * \sum Att.\ \ Brain\ Photons}{\sum Att.\ \ Photons} \quad (1)$$

$$PPL\,Brain\% = \frac{100 * \sum PPL\ \ \ Brain\ Layers}{\sum PPL\,Head\ Layers} \quad (2)$$

Table 1 Thickness of head model layers

Scalp	Skull	CSF	Grey matter	White matter
3 mm	9 mm	3 mm	5 mm	80 mm

Table 2 Range of optical properties for a specific layer with the fixed value outside brackets

	Scalp	Skull	CSF	Grey matter	White matter
$\mu_s` \ cm^{-1}$	10 [8:12]	11 [8:12]	5 [3:8]	12 [6:14]	12 [6:14]
$\mu_a \ cm^{-1}$	0.1 [0.05:0.15]	0.1 [0.05:0.15]	0.04 [0.02:0.06]	0.15 [0.1:0.2]	0.15 [0.1:0.2]

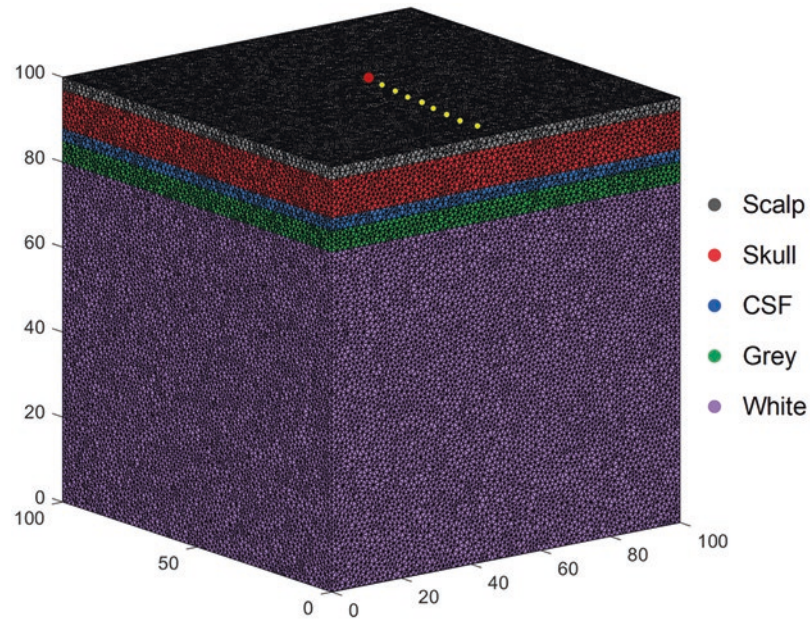

Fig. 1 Mesh slab representing an adult head used for the Monte Carlo simulations

3 Results and Discussion

Figure 2 shows the results obtained by the simulations in slab head model. Every simulation took on average ≤60s and total number of simulations performed is 34 for the $\mu_s`$ variation and 49 for the μ_a changes. Every coloured dot in the plots corresponds to the result of a simulation while varying the optical properties only of the specific layer, written in the legend. It is clearly visible that an increase of the source-detector distance will increase the percentage of information that is related to the brain, but the absolute number of photons that reached the brain is still higher at the small source-detector distance. This observable in Fig. 3.

On the other hand, an increase of the $\mu_s`$ in the brain layers will increase the number of photons that travel into the brain and so giving us photons that are more influenced by the brain, i.e., higher sensitivity to the brain tissue. The smaller the source-detector distance (SDD), the higher the relative variation in brain sensitivity when varying from the lower to the higher $\mu_s`$ values, as visible in the skull layer. For this superficial layer, in the case of the closest SDD, we have a decrease in brain information between lower and higher $\mu_s`$ values by half, while for large SDDs, there is a decrease of only 10%. Figures 2c, d show the same metrics while varying the absorption value. In Fig. 2d we see that with an increase of SDD the influence of the upper layers changes. For the longer SDD, increasing the μ_a increases the brain influence. Meanwhile increasing the μ_a in the lower layers causes a reduction of it. This is consistent across the various distances. As a preliminary finding, we also detected an increase in photon arrival time when increasing the $\mu_s`$ in a specific layer. This will be further investigated in future work. This could be useful for time-domain NIRS devices, since we can identify a time bin with most of the photons related to a specific layer of tissue, and therefore better estimate the influence of this particular layer.

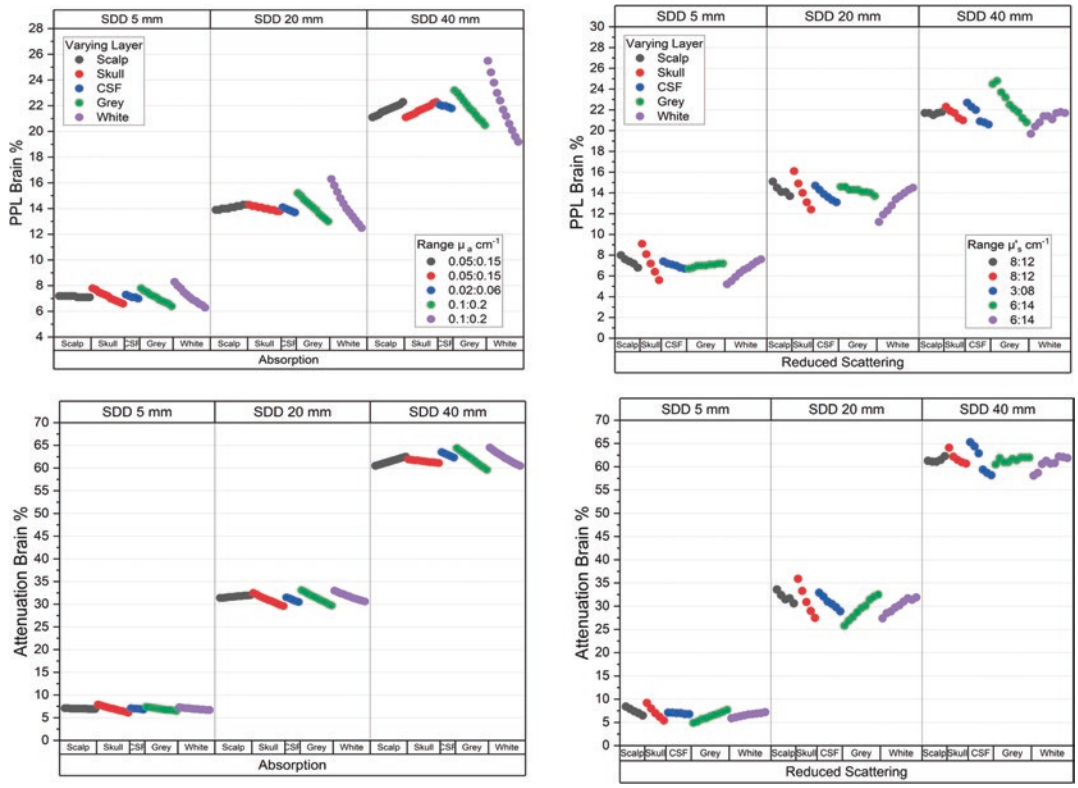

Fig. 2 Scatter plots of the PPL (top) and Attenuation (bottom) relative to the brain photons by varying the scattering (right) and the absorption (left) of a specific layer. From left to right, in every sub-groups of coloured dots, the $\mu_s`$ or μ_a starts with the lowest value in the range and is then increased. *SDD* source detector distance; *PPL* partial path length

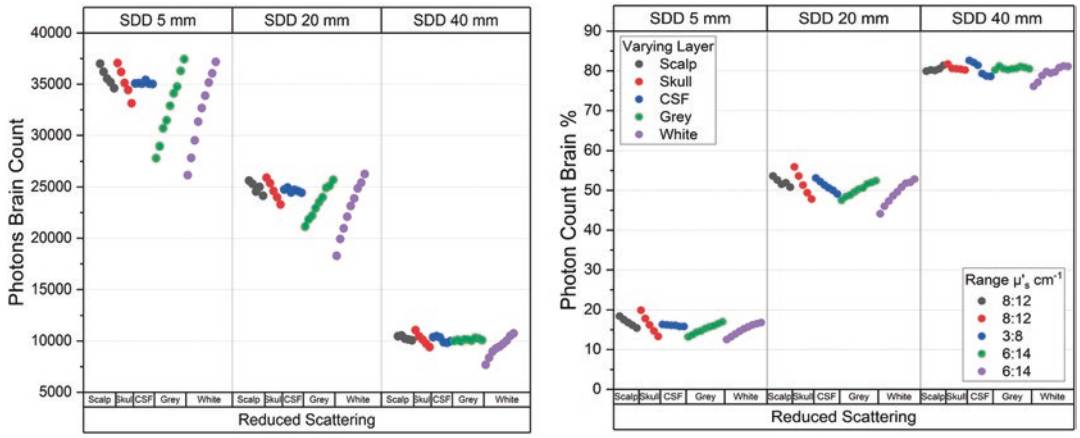

Fig. 3 Scatter plots of the raw count of the brain photons (left) and the percentage of photon that have travelled through the brain (right) by varying the $\mu_s`$ of a specific layer

Many other studies have investigated how brain sensitivity is affected by changes in source detector separation, the thickness of superficial tissue layers and variation of the scattering of a particular layer such as the cerebrospinal fluid (CSF) layer. These groups also used Monte Carlo simulations applied to simple geometries as well as MRI-based head models [5].

In our study, we have presented a preliminary study to assess the effect of a range of $\mu_s`$ and μ_a values on the light propagation in the brain by simulating these changes in every tissue layer of an adult head slab model. Our results suggest that it is important to determine the correct optical properties of the superficial layers for precise NIRS measurements in vitro and in vivo. Switching from the extreme values on our selected range caused the brain's influence on the data to be increased or reduced in the worst case even by half. Increasing the evaluated range or the gap between the assumed and the real value will increase this discrepancy. The variation in the optical properties for upper and lower layers tend to, respectively, influence the sensitivity negatively and positively. For small source-detector distances, the relative percentage difference between lower and higher values appears to be greater than for the larger distances.

In the next step, we will further evaluate this influence on a real phantom experiment with our in-house TD-NIRS device, changes in photon arrival time and the computation of the absolute blood saturation level.

4 Conclusions

We conclude that different optical properties have a substantial effect on the efficiency of a NIRS device to measure brain data. It is impossible to determine the true combination of optical properties just from the literature. For a future NIRS device, it is important to obtain a correct $\mu_s`$ value of the tissue. This is only possible with time-domain or frequency domain devices.

Acknowledgments We gratefully acknowledge funding by the Swiss National Science Foundation (159490 and 197079), the Innovationspool of the University Hospital Zurich. MW declares that he is president of the board and co-founder of OxyPrem AG as conflict of interest.

References

1. Okada E (2000) The effect of superficial tissue of the head on spatial sensitivity profiles for near infrared spectroscopy and imaging. Opt Rev 7:375–382
2. Okada E, Delpy DT (2000) Investigation of the effect of discrete scatterers in CSF layer on optical path length in the brain. Photon Migration, Diffuse Spectroscopy and Optical Coherence Tomography: Imaging and Functional Assessment 4160:196–203
3. Okada E, Delpy DT (2003) Near-infrared light propagation in an adult head model. II. Effect of superficial tissue thickness on the sensitivity of the near-infrared spectroscopy signal. Appl Opt 42:2915–2922
4. Ostojic D, Jiang J, Isler H et al (2020) Impact of skull thickness on cerebral NIRS 1 oximetry in neonates: an in silico study. Adv Exp Med Biol 1232:33–38
5. Strangman G, Li Z, Zhang Q (2013) Depth sensitivity and source-detector separations for near infrared spectroscopy based on the Colin27 brain template. PLoS One 8:e66319
6. Fang Q (2010) Mesh-based Monte Carlo method using fast ray-tracing in Plücker coordinates. Biomed Opt Express 1:165
7. Si H (2015) TetGen, a Delaunay-based quality tetrahedral mesh generator. ACM Trans Math Softw 41:1–36
8. De Boer H, Van der Merwe A, Soerdjbalie-Maikoe V (2016) Human cranial vault thickness in a contemporary sample of 1097 autopsy cases: relation to body weight, stature, age, sex and ancestry. Int J Legal Med 130:1371–1377
9. Fang Q, Yan S (2019) Graphics processing unit-accelerated mesh-based Monte Carlo photon transport simulations. J Biomed Opt 24:1

Frontal Cerebral Oxygenation in Humans at Rest: A Mirror Symmetry in the Correlation with Cardiorespiratory Activity

Felix Scholkmann, Hamoon Zohdi, Martin Wolf, and Ursula Wolf

Abstract

Background: Although several studies published reference values for frontal cerebral tissue oxygen saturation (StO_2) measured with near-infrared spectroscopy (NIRS) based cerebral oximetry, a detailed investigation, whether and which factors from systemic physiology are related to the individual StO_2 values, is missing. Aim: We investigated how the state of the cardiorespiratory system is linked to StO_2 values at rest. Subjects and methods: Absolute StO_2 values (median over a 5 min resting-phase while sitting) were obtained from 126 healthy subjects (age: 24.0 ± 0.2 years, 45 males, 81 females) over the left and right prefrontal cortex (PFC) by employing frequency-domain NIRS as part of a systemic physiology augmented functional near-infrared spectroscopy (SPA-fNIRS) study. In addition, heart rate (HR) and respiration rate (RR) were measured, and the pulse respiration quotient (PRQ) was determined (PRQ = HR/RR). General additive models (GAM) were used to analyse the data. Results: The GAM analysis revealed a specific relationship between the overall PFC StO_2 values (mean over right and left PFC) and the variables HR and RR: HR was positively correlated with mean StO_2, while RR showed no correlation. In the mirror case, RR was negatively linearly correlated with the frontal cerebral oxygenation asymmetry (FCOA), which was not correlated with HR. The right PFC StO_2 was not linked to the RR, whereas the left PFC StO_2 was. Positive correlations of the PRQ with the mean PFC StO_2 as well as the FCOA were also found. GAM modelling revealed that the individual FCOA values are explained to a large extent (deviance explained: 88.8%) by the individual mean PFC StO_2 and PRQ. We conclude that (i) the state of the cardiorespiratory system is significantly correlated with StO_2 values and (ii) there is a mirror symmetry with regard to the impact of cardiorespiratory parameters on the mean PFC StO_2 and FCOA.

F. Scholkmann (✉)
Institute of Complementary and Integrative Medicine, University of Bern, Bern, Switzerland

Biomedical Optics Research Laboratory, Department of Neonatology, University Hospital Zurich, University of Zurich, Zurich, Switzerland
e-mail: Felix.Scholkmann@unibe.ch

H. Zohdi · U. Wolf
Institute of Complementary and Integrative Medicine, University of Bern, Bern, Switzerland

M. Wolf
Biomedical Optics Research Laboratory, Department of Neonatology, University Hospital Zurich, University of Zurich, Zurich, Switzerland

F. Scholkmann et al. (eds.), *Oxygen Transport to Tissue XLIII*, Advances in Experimental Medicine and Biology 1395, https://doi.org/10.1007/978-3-031-14190-4_8

Keywords

Frontal cerebral tissue oxygen saturation · NIRS · SPA-fNIRS · Cardiorespiratory activity

1 Introduction

What are typical values of frontal cerebral oxygen saturation (StO_2) at rest for healthy adults measured by cerebral oximetry, i.e., near-infrared spectroscopy (NIRS)? Although several studies have published such StO_2 reference values (e.g., [1–7]), there has not yet been a detailed investigation of whether and which systemic physiology factors are related to these StO_2 values measured on the forehead. Knowing these factors and how they impact the measurements is important since they confound the definition of reference ranges.

Previous work from our group already showed that frontal cerebral StO_2 from healthy young adults at rest was dependent on several factors, including heart rate (HR), respiration rate (RR), partial pressure of end-tidal CO_2 ($P_{ET}CO_2$), sex, room temperature and time of measurement (i.e., season and time of day) [8].

The aim of this study was to investigate how frontal cerebral StO_2 in healthy young adults depends on their cardiorespiratory state at the time of measurement.

2 Subjects and Methods

Participants and Measurements Data from a previously published systemic physiology augmented functional near-infrared spectroscopy (SPA-fNIRS) study conducted by us [8–10] was employed. For the present analysis, data analysed were from 126 healthy subjects (age: 24.0 ± 0.2 years, age range: 20–28 years, 45 males, 81 females) were measured four times on different days, resulting in 504 single measurements. Absolute StO_2 values during resting state in sitting position were obtained over the left and right prefrontal cortex (R-PFC, L-PFC) by employing a frequency-domain (FD) NIRS device (Imagent, ISS Inc., Champaign, Illinois, USA). HR was measured with the wrist-worn SOMNOtouch™ non-invasive blood pressure device (SOMNOmedics GmbH, Randersacker, Germany) and RR with a NONIN LifeSense patient monitor (NONIN Medical, Plymouth, Minnesota, USA).

Data Analysis Data was low-pass filtered with a robust second-order moving average (window lengths: 2 min (StO_2), 3 min (HR) and 2 min (RR)) to remove high-frequency fluctuations not of interest for the present analysis. Median values were calculated based on 5 min long time-series of StO_2 (mean of R-PFC and L-PFC), ΔStO_2 (R-PFC–L-PFC; representing the frontal cerebral oxygenation asymmetry, FCOA), StO_2 at the right PFC and left PFC, HR and RR. Furthermore, the pulse respiration quotient (PRQ) was determined (PRQ = HR/RR) [11]. Blood pressure data was not used in the analysis since we wanted to investigate the relationship between respiration and heart rate on StO_2 in particular.

Outliers in the data (three standard deviations away from the mean) due to unstable measurements were removed before the final statistical analysis. General additive models (GAM), an extension of generalised linear models, were used to analyse the data. The following GAMs were employed: (i) $g(X) = \beta_0 + f(\text{HR}) + f(\text{RR}) + \text{Subject} + \varepsilon$, (ii) $g(X) = \beta_0 + f(\text{PRQ}) + \text{Subject} + \varepsilon$, and (iii) $g(Y) = \beta_0 + f_{ts}(\text{PRQ}\ \Delta StO_2) + \text{Subject} + \varepsilon$, with $X = \{StO_2, \text{R-}StO_2, \text{L-}StO_2, \Delta StO_2\}$, $Y = StO_2$, β_0 the intercept, f a regression spline function, f_{ts} a tensor product smooth function, g a smooth monotonic link function, ε the residual and 'Subject' a categorical variable with the individual subject identification number (modelled as a random effect). The models were fitted by penalised likelihood maximisation.

Signal processing was performed by Matlab (R2017a, MathWorks, Inc., Massachusetts, USA) and statistical analysis in R (version 3.5.1) [12] using the *ggplot2* [13] and *mgcv* [14] packages.

3 Results

Distribution of the Parameter Values: Normal and Log-Normal All parameter values were normally distributed (Shapiro-Wilk test; StO_2: 72.7 ± 0.5%, R-StO_2: 73.8 ± 0.6%, L-StO_2: 71.7 ± 0.6%, ΔStO_2: 2.4 ± 0.5%, HR: 1.106 ± 0.016 Hz, RR: 0.2660 ± 0.004 Hz), except the PRQ ones that followed a log-normal distribution (PRQ, median: 4.1, 95% CI: 2.8–6.2) (Fig. 1).

Frontal Cerebral Oxygenation and Cardiorespiratory Activity: A Mirror-Symmetry in Their Correlation The GAM analysis revealed a specific relationship between the overall PFC StO_2 values and the variables HR and RR: HR was positively correlated with mean StO_2 (p = 0.0000116) while RR showed no correlation (p = 0.448) (GAM adjusted R^2: 0.814, deviance explained: 87.2%) (Fig. 2a, b). In the mirror case, ΔStO_2 was negatively correlated with RR (p = 0.0149) but not with HR (p = 0.7040) (GAM adjusted R^2: 0.539, deviance explained: 68.5%) (Fig. 2c, d). Further analysis revealed a link between L-PFC StO_2 and HR (p = 0.000503) as well as RR (p = 0.007722) (GAM adjusted R^2: 0.775, deviance explained: 84.4%) (Fig. 2e, f), while the R-PFC was shown to be related to HR (p = 0.00265) but not the RR (p = 0.54568) (GAM adjusted R^2: 0.747, deviance explained: 82.6%) (Fig. 2g, h).

Frontal Cerebral Oxygenation and Cardiorespiratory Activity: The Significance of the PRQ Positive correlations of the PRQ with the mean PFC StO_2 as well as ΔStO_2 were found. Modelling the interaction of these three parameters proved a statistically significant high correlation (p = 0.000095) and an excellent model fit (GAM adjusted R^2: 0.829, deviance explained: 88.8%) (Fig. 3e–g). This shows that individual FCOA values can be explained to a large extend by the individual mean PFC StO_2 and individual PRQ. Furthermore, PRQ was found to be tendentially positively correlated with StO_2 (p = 0.0595) and ΔStO_2 (p = 0.0942), significantly positively correlated with R-StO_2 (p = 0.0086) but interestingly not with L-StO_2 (p = 0.577) (Fig. 3a–d).

Figure 4 demonstrates the importance of controlling for intersubject variability when analysing the relationship between StO_2, ΔStO_2 and PRQ: considering the intersubject variability to explain the intertrial variability of StO_2 results in

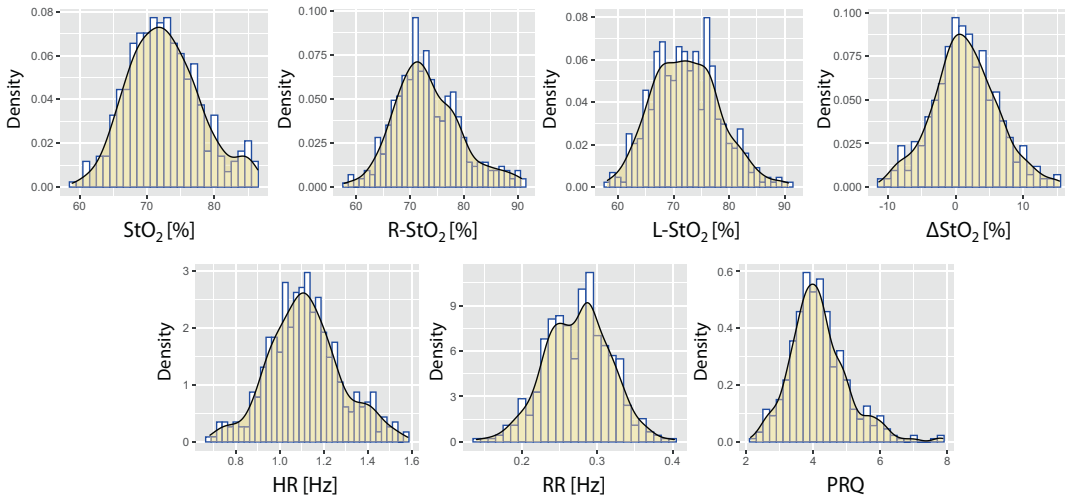

Fig. 1 Distribution of physiological parameters from 504 single measurements obtained during the resting state in 126 healthy subjects. Shown are the histogram and the empirical distribution function for each distribution

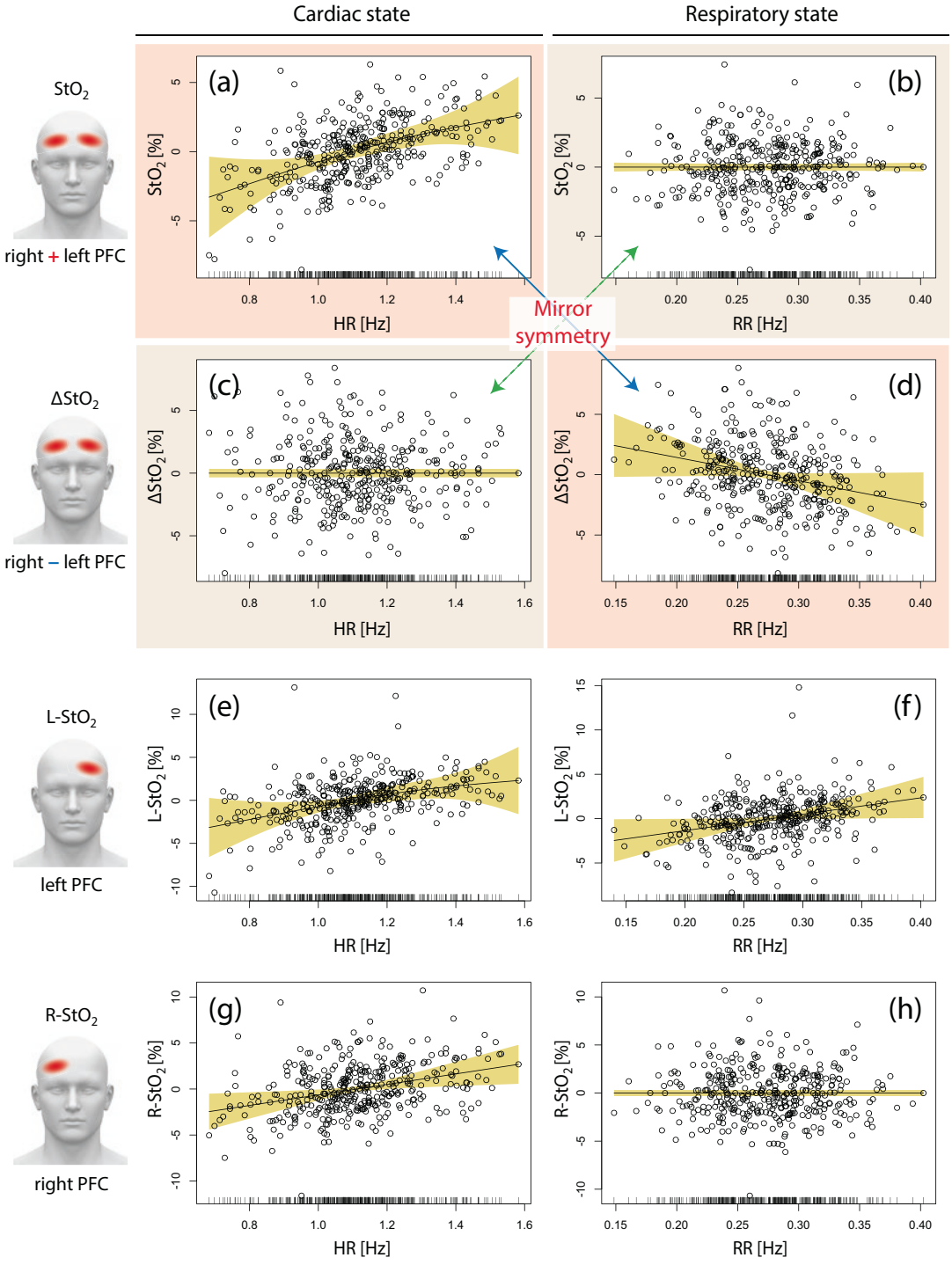

Fig. 2 Results of four GAM models linking frontal cerebral oxygenation. Cerebral oxygenation with cardiorespiratory activity at rest. (**a**, **b**) $g(StO_2) = \beta_0 + f(HR) + f(RR) + Subject + \varepsilon$, (**c**, **d**) $g(\Delta StO_2) = \beta_0 + f(HR) + f(RR) + Subject + \varepsilon$, (**e**, **f**) $g(L\text{-}StO_2) = \beta_0 + f(HR) + f(RR) + Subject + \varepsilon$, and (**g**, **h**) $g(R\text{-}StO_2) = \beta_0 + f(HR) + f(RR) + Subject + \varepsilon$

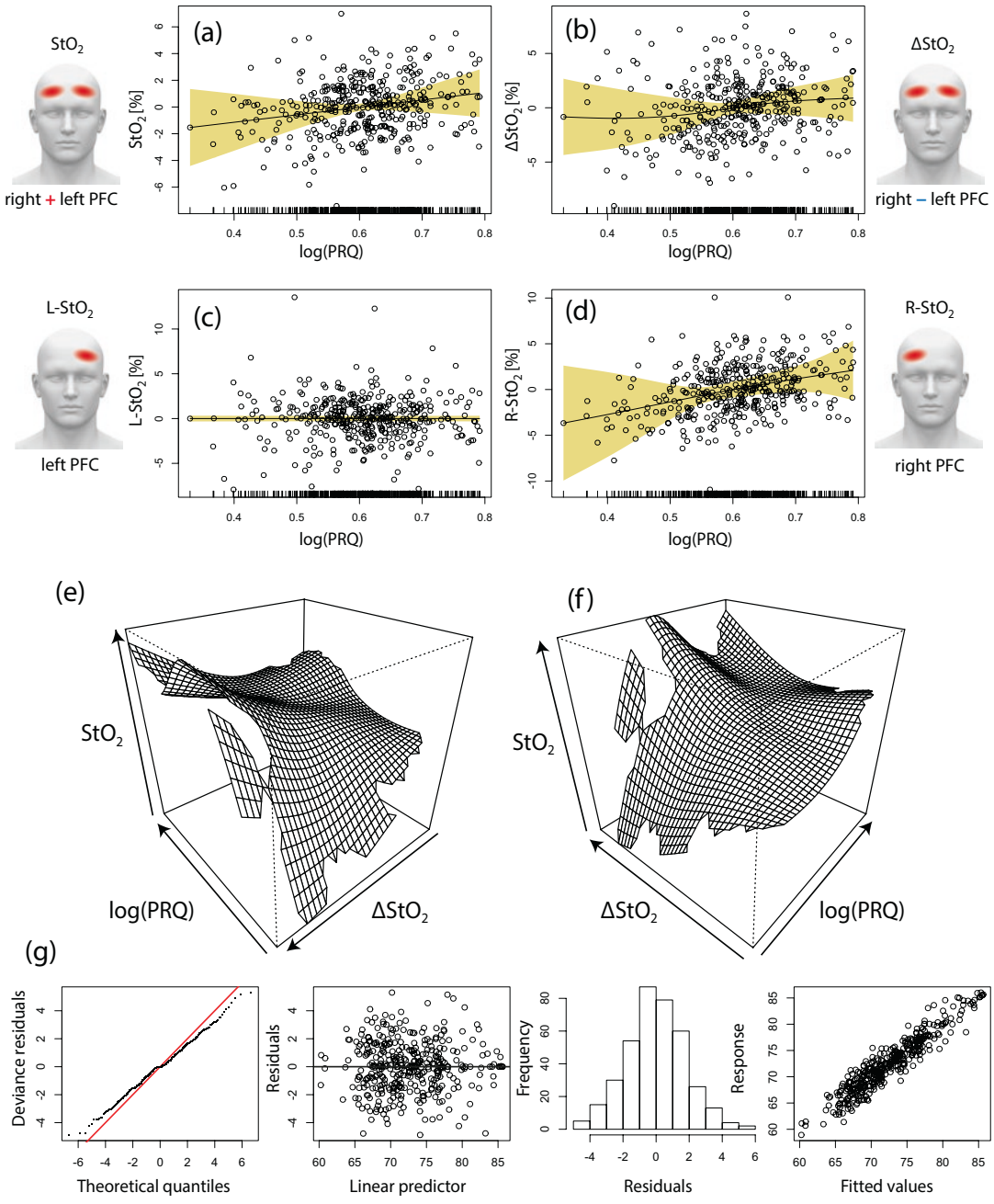

Fig. 3 Results of four GAM models linking frontal cerebral oxygenation with cardiorespiratory activity (quantified with the PRQ) at rest. (**a**) $g(StO_2) = \beta_0 + f(PRQ) + Subject + \varepsilon$, (**b**) $g(\Delta StO_2) = \beta_0 + f(PRQ) + Subject + \varepsilon$, (**c**) $g(L\text{-}StO_2) = \beta_0 + f(PRQ) + Subject + \varepsilon$, (**d**) $g(R\text{-}StO_2) = \beta_0 + f(PRQ) + Subject + \varepsilon$, and (**e**–**g**) $g(StO_2) = \beta_0 + f_{ts}(PRQ, \Delta StO_2) + Subject + \varepsilon$. (**g**) shows the goodness-of-fit characteristics of the model

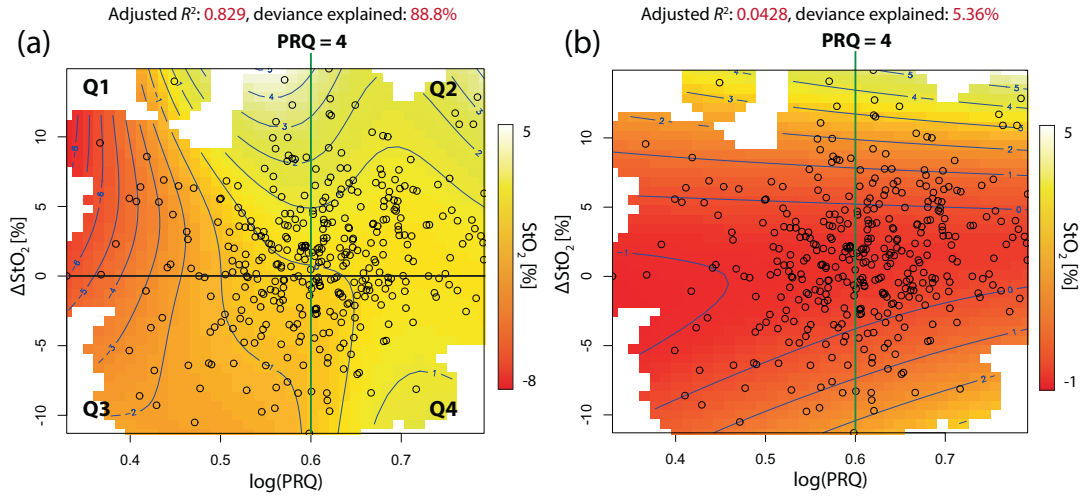

Fig. 4 GAM modelling of the relationship between StO_2, ΔStO_2 and PRQ while (**a**) considering the intersubject variability as a random effect and (**b**) combining the intersubject and intertrial variability. Only approach (**a**) is able to explain a large amount of variability of the data. The green line refers to the PRQ normally observed in healthy humans at rest. Q1–4: quadrants 1–4

a superior fit compared to the case when intersubject and intertrial variabilities are not differentiated when analysing the data via the GAM approach. Figure 4a also highlights the complexity of the relationship between StO_2, ΔStO_2 and PRQ; the condition 'PRQ > 4' is correlated with an increase of StO_2 the higher the FCOA is (regions Q1 and Q4), while PRQ < 4 is related to a decrease in StO_2 especially when a positive FCOA is predominant (region Q1).

4 Discussion, Conclusion and Outlook

Our study showed that (i) the state of the cardiorespiratory system is significantly correlated with absolute StO_2 values (mean StO_2 over the PFC, and FCOA), and (ii) there is a mirror symmetry with regard to the impact of cardiorespiratory parameters (HR and RR) on the mean PFC StO_2 and FCOA.

Our finding that the cardiorespiratory system impacts resting-state StO_2 values was also partially observed by other studies. For example, Eyeington et al. [2] found their frontal cerebral resting-state StO_2 values to correlate positively with mean arterial pressure and cardiac index (CI). Since CI is positively correlated with HR [15], the findings of this study agree with our findings of a positive correlation between frontal StO_2 and HR during rest. However, we are not aware of a study, despite our previously published report about our measurements [8], that investigated the effect of the resting-state HR and RR in parallel on resting-state cerebral frontal StO_2 values (mean and FOCA). Our results are therefore novel and provide additional insights into possible confounding factors for the determination of StO_2 reference ranges for healthy adults. Our study is also the first to show the significance of the PRQ with regard to explaining the inter-trial variability of StO_2. The PRQ is a unique parameter capturing the coupling state between the cardiac and respiratory systems [11] with a 4:1 (PRQ = 4) attractor state in the resting-state [16].

The mirror symmetry found (i.e., cardiac activity is linked to StO_2 and respiration to ΔStO_2) is intriguing and has not been reported so far to the best of our knowledge. It might be the case that the link between respiration and FCOA is mediated by the autonomic nervous system or the emotional state of the person, since frontal

neuronal asymmetry is linked to mood [17] and the mood and emotional state are also related to respiratory activity [18].

In conclusion, our study provides the following novel insights with regard to resting-state frontal cerebral StO_2 reference values for healthy adults: (i) StO_2 and ΔStO_2 depend on cardiorespiratory activity (HR, RR, PRQ), (ii) the GAM approach has been proven to be suitable to determine the non-linear relationships between cardiorespiratory activity and StO_2/ΔStO_2, (iii) cerebral oxygenation shows a mirror symmetry with respect to its correlation with cardiorespiratory activity. In short, when interpreting absolute frontal StO_2 values, the cardiorespiratory state of the subject needs to be considered.

Acknowledgments We gratefully acknowledge funding by the Software AG Foundation. MW declares that he is president of the board and co-founder of OxyPrem AG.

References

1. Chan MJ et al (2017) Near-infrared spectroscopy in adult cardiac surgery patients: a systematic review and meta-analysis. J Cardiothorac Vasc Anesth 31(4):1155–1165
2. Eyeington CT et al (2019) Modern technology-derived normative values for cerebral tissue oxygen saturation in adults. Anaesth Intensive Care 47(1):69–75
3. Tisdall MM et al (2009) The effect on cerebral tissue oxygenation index of changes in the concentrations of inspired oxygen and end-tidal carbon dioxide in healthy adult volunteers. Anesth Analg 109(3):906–913
4. Newman L et al (2020) Age and sex differences in frontal lobe cerebral oxygenation in older adults-normative values using novel, scalable technology: findings from the Irish longitudinal study on ageing (TILDA). Arch Gerontol Geriatr 87:103988
5. Gatto R et al (2006) Frequency domain near-infrared spectroscopy technique in the assessment of brain oxygenation: a validation study in live subjects and cadavers. J Neurosci Methods 157(2):274–277
6. Olopade CO et al (2007) Noninvasive determination of brain tissue oxygenation during sleep in obstructive sleep apnea: a near-infrared spectroscopic approach. Sleep 30(12):1747–1755
7. Choi J et al (2004) Noninvasive determination of the optical properties of adult brain: near-infrared spectroscopy approach. J Biomed Opt 9(1):221–229
8. Zohdi H, Scholkmann F, Wolf U (2020) Frontal cerebral oxygenation asymmetry: intersubject variability and dependence on systemic physiology, season, and time of day. Neurophotonics 7(2):025006
9. Zohdi H et al (2021) Color-dependent changes in humans during a verbal fluency task under colored light exposure assessed by SPA-fNIRS. Sci Rep 11(1):9654
10. Zohdi H, Scholkmann F, Wolf U (2021) Individual differences in hemodynamic responses measured on the head due to a long-term stimulation involving colored light exposure and a cognitive task: a SPA-fNIRS study. Brain Sci 11(1)
11. Scholkmann F, Wolf U (2019) The pulse-respiration quotient: a powerful but untapped parameter for modern studies about human physiology and pathophysiology. Front Physiol 10:371
12. Team RC (2014) R: a language and environment for statistical computing. R Foundation for Statistical Computing, Vienna, Austria
13. Wickham H (2016) ggplot2: elegant graphics for data analysis. Springer, New York
14. Wood SN (2017) Generalized additive models. Boca Raton, Chapman and Hall/CRC
15. Claessen G et al (2019) Heart rate reserve in fontan patients: chronotropic incompetence or hemodynamic limitation? J Am Heart Assoc 8(9):e012008
16. Scholkmann F, Zohdi H, Wolf U (2019) The resting-state pulse-respiration quotient of humans: Lognormally distributed and centered around a value of four. Physiol Res 68(6):1027–1032
17. Palmiero M, Piccardi L (2017) Frontal EEG asymmetry of mood: a mini-review. Front Behav Neurosci 11:224
18. Boiten FA, Frijda NH, Wientjes CJE (1994) Emotions and respiratory patterns: review and critical analysis. Int J Psychophysiol 17(2):103–128

Photomodulation of Lymphatic Delivery of Bevacizumab to the Brain: The Role of Singlet Oxygen

Oxana Semyachkina-Glushkovskaya, Sergey Diduk, Eroshova Anna, Dosadina Elina, Kruglov Artem, Alexander Khorovodov, Alexander Shirokov, Ivan Fedosov, Alexander Dubrovsky, Inna Blokhina, Andrey Terskov, Georgy Karandin, Arina Evsukova, Anna Tsven, Valeria Telnova, Ilana Afranovich, Sergey Sokolovski, Edik Rafailov, and Jürgen Kurths

O. Semyachkina-Glushkovskaya (✉)
Humboldt University, Berlin, Germany

Saratov State University, Saratov, Russia

S. Diduk · E. Anna · D. Elina · K. Artem
Pushchino State Institut of Natural Science, Moscow, Russia

A. Khorovodov · I. Fedosov · A. Dubrovsky · I. Blokhina · A. Terskov · G. Karandin · A. Evsukova · A. Tsven · V. Telnova · I. Afranovich
Saratov State University, Saratov, Russia

A. Shirokov
Saratov State University, Saratov, Russia

Institute of Biochemistry and Physiology of Plants and Microorganisms, Russian Academy of Sciences, Saratov, Russia

Saratov State Medical University, Saratov, Russia

S. Sokolovski · E. Rafailov
Physics Department, Humboldt University, Berlin, Germany

J. Kurths
Humboldt University, Berlin, Germany

Physics Department, Humboldt University, Berlin, Germany

Potsdam Institute for Climate Impact Research, Potsdam, Germany

Abstract

The blood-brain barrier (BBB) poses a significant challenge for drug delivery to the brain. Therefore, the development of safe methods for an effective delivery of medications to the brain can be a revolutionary step in overcoming this limitation. Using a quantum-dot-based 1267 nm laser (photosensitiser-free generation of singlet oxygen), we clearly show the photostimulation of lymphatic delivery of bevacizumab (BMZ) to the brain tissues and the meninges. These pilot findings open promising perspectives for photomodulation of a lymphatic brain drug delivery bypassing the BBB, and potentially enabling a breakthrough strategy in therapy of glioma using BMZ and other chemotherapy drugs.

Keywords

Blood-brain barrier · Photostimulation · Glymphatics · Meningeal lymphatic vessels · Lymphatics

F. Scholkmann et al. (eds.), *Oxygen Transport to Tissue XLIII*, Advances in Experimental Medicine and Biology 1395, https://doi.org/10.1007/978-3-031-14190-4_9

1 Introduction

The blood-brain barrier (BBB) has been a great hurdle for brain drug delivery and excludes the vast majority of cancer therapeutics from the brain. However, the importance of the BBB in limiting drug delivery and efficacy is controversial in high-grade brain tumours, such as glioblastoma (GBM). Most clinical data clearly demonstrate that GBM patients have an intact BBB around the tumour, and a cure will only be possible if these tumour regions are extensively treated [1]. Therefore, there is growing demand to develop safe methods to bypass the BBB and blood-tumour barriers for effective therapy of GBM [1].

The bevacizumab (BMZ) is a monoclonal antibody that prevents activation of the vascular endothelial growth factor demonstrating antiangiogenic effects. GBM development depends on its angiogenesis, which provides high potential for antiangiogenic cancer therapy. However, BMZ is effective in controlling oedema in some GBM patients, but clinical trials have not demonstrated a convincing impact on patient survival [2]. There is the hypothesis that a newly formed GBM by recruiting the normal cerebral vessels within an intact BBB limits effectiveness of the therapeutic dose of high molecular weight BMZ. The modulation of BMZ delivery into the brain can significantly improve the therapeutic effects of antiangiogenic therapy of GBM.

In our previous work we reported photostimulation (PS) of the meningeal lymphatic vessels (MLVs) [3–6] using a quantum-dot 1267 nm laser, which can directly generate a singlet oxygen ($^1O_2$) from the triplet oxygen state without photosensitisers [7]. We discovered that PS stimulates the clearance of macromolecules from the brain via MLVs as well as PS causes an increase in the permeability of the lymphatic endothelium to macrophages [3–5]. In our pilot experiments on rats, we demonstrated laser-suppression of glioma growth that was associated with the activation of the lymphatic drainage system [5]. These findings open new strategies for therapy of glioma by modulation of the lymphatic functions via PS.

In this work, we aim to study a lymphatic delivery of BMZ to the murine brain bypassing the BBB. We also sought to examine modulation of lymphatic transport of fluorescent BMZ by PS.

2 Methods

Male BALB/c mice (20–25 g) were used in all experiments. All procedures were performed in accordance with the Guide for the Care and Use of Laboratory Animals. The experimental protocols were approved by the Local Bioethics Commission of the Saratov State University (Protocol No. 7). The experiments were performed in the following groups: (1) BMZ injection (10 μl) in the right deep cervical lymph node (dcLN) without PS and (2) with PS, n = 7 in each group.

A fibre Bragg grating wavelength locked high-power laser diode (LD-1267-FBG-350, Innolume, Dortmund, Germany) emitting at 1267 nm was used as a source of irradiation using algorithm: 17 min PS + 5 min pause +17 min PS + 5 min pause +17 min PS of 100 mW laser power intensity with the total dose applied of 1611 J/см^2 (on the surface of skull) and 470 J/см2 (on the surface of the brain, [11]) under 1% isoflurane at 1 L/ min N_2O/O_2–70/30 ratio.

The BMZ was labelled with the FluoReporter FITC Protein Labeling Kit (Invitrogen). The molecular weight of FITC-BMZ was 149 kDa.

For the quantitative analysis of intensity signal from BMZ, ImageJ was used for image data processing and analysis. The areas of specific signals from fluorescence were calculated using the plugin ‘Analyze Particles’ in the ‘Analyze’ tab. In all cases, 10 regions of interest were analysed.

For confocal imaging of BMZ distribution, we used the protocol for immunohistochemistry (IHC) with the markers for lymphatic vessel endothelial hyaluronan receptor 1 (Lyve-1), for the pericytes in the blood vessels, such as the neuron-glial antigen 2 (NG2), for the blood endothelium with cell adhesion molecule 1 (CD31), and for astrocytes by glial fibrillary acidic protein (GFAP). The brain tissues and the meninges were collected

and fixed for 48 h in a 4% saline solution-buffered formalin, then sections of the brain with a thickness of 40–50 microns were cut on a vibratome (Leica, Germany). Sections were processed according to the standard IHC protocol with the corresponding primary and secondary antibodies. The sections of the mouse brain and the meninges were imaged using a Leica SP8 confocal laser scanning microscope (Leica, Germany).

3 Results

3.1 Lymphatic Delivery of BMZ into the Meninges

In the first step, we studied the lymphatic pathway of BMZ spreading after injection into the dcLN (Fig. 1a). The cribriform plate is a centre of lymphatic pathway of metabolic clearance and is a connective bridge between the cerebral spinal fluid (CSF) and the cervical lymphatic system [8]. The cribriform plate is a fenestrated bony plate of the ethmoid bone that separates the cranial and nasal cavities. Once through the plate, CSF is absorbed by the lymphatic vessels (LVs) in the nasal mucosa and drained into the cervical lymph nodes [8]. There is evidence that the cribriform plate is also a lymphatic window into the brain [8]. Taking into account these facts, we analysed BMZ distribution through the cribriform plate 3 h after injection into the dcLN. Figure 1b, c demonstrate wide spreading of BMZ along the cribriform plate as well as through the meninges. We observed that BMZ was distributed via the lymphatic vessels and the perivascular spaces (PVSs) along the meningeal arteries and veins (Fig. 1d–f). However, we did not find the presence of BMZ in the brain parenchyma.

3.2 Photostimulation of Lymphatic Delivery of BMZ into the Brain Parenchyma

In our previous works, we discovered that PS enhances the lymphatic contractility and drainage due to an increase in the permeability of lymphatic endothelium and the changes in expression of tight junctions [3–6]. Here we tested our hypothesis that PS increases the movement of BMZ in the lymphatic system, including retrograde travelling. With this aim, PS was applied immediately after BMZ injection into dcLN and it was used during one hour. The brain slices were analysed 3 h after BMZ injection + PS (Fig. 1g). Figure 1 h and j clearly demonstrate the presence of BMZ among astrocytic end feet suggesting that PS contributes lymphatic delivery of BMZ into the brain parenchyma. Indeed, PS was accompanied by the high intensity of the fluorescent signal from BMZ compared with the group without PS (Fig. 1i).

4 Discussion

Our results clearly demonstrate that dcLNs are an anatomical structure for unique communication between the meninges, the brain tissues and the peripheral lymphatic network. Indeed, injection of BMZ into the dcLN was accompanied by its delivery to the meninges (without PS) and into the brain parenchyma (with PS). Our findings are consistent with other experimental evidence suggesting that dcLNs are a unique passage, which connects the brain fluid system and the peripheral lymphatics [9].

We revealed that BMZ travelled from dcLN to the brain meninges and parenchyma via the lymphatic backroad. The retrograde movement of tracers into the brain parenchyma was also discussed in other works as physiological properties of the lymphatic/glymphatic mechanisms of exchanges of molecules between the PVS and the brain parenchyma [8].

In our research, we demonstrate that PS enhances the lymphatic delivery of BMZ to the brain parenchyma. The infra-red light of 800–1100 nm is widely used for the PS therapy of various brain diseases [8]. However, the infrared PS has a significant drawback in its limited penetration into the brain due to high scattering and heating effect. The light wavelength of 1300 nm has less scattering and can penetrate

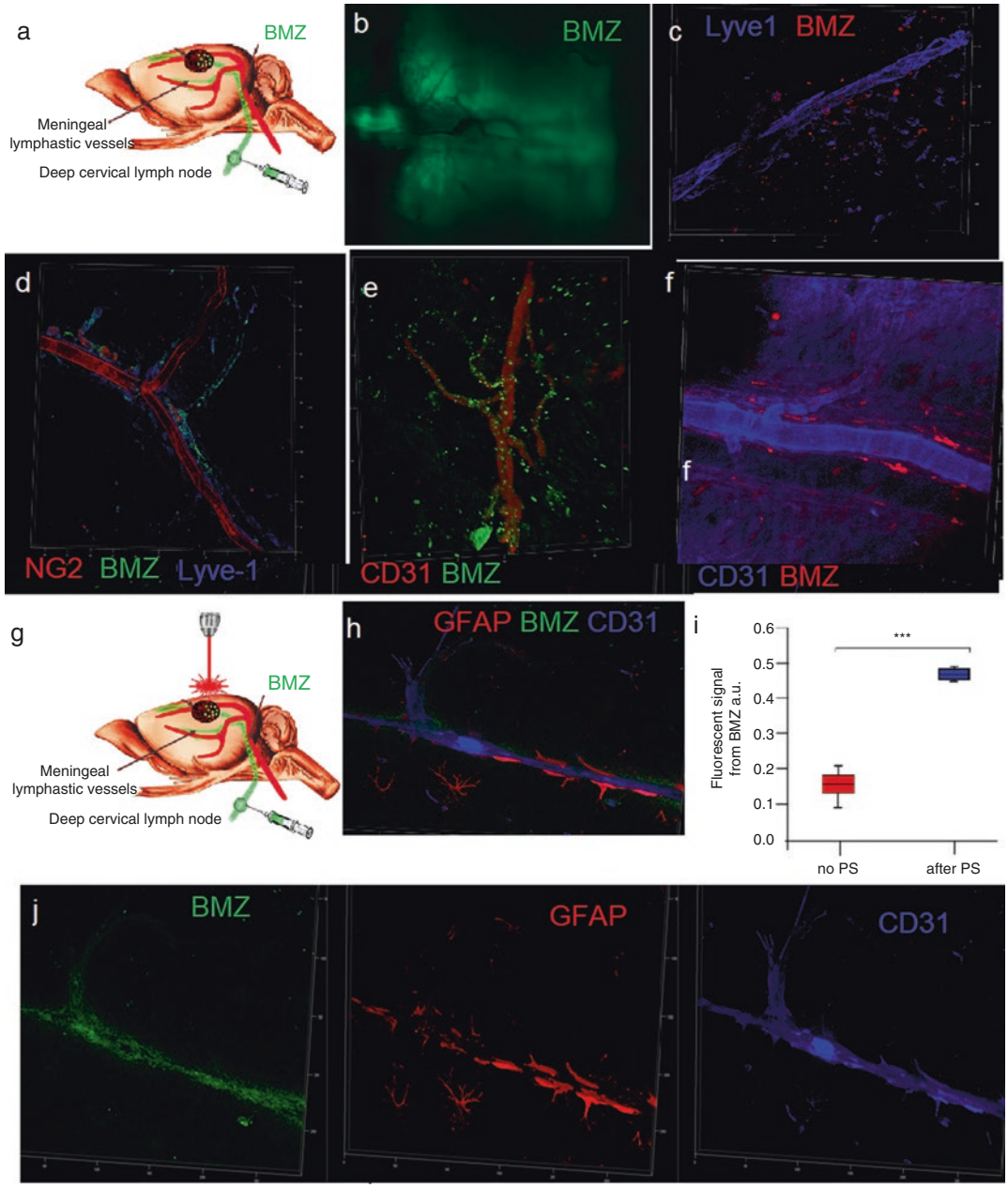

Fig. 1 The lymphatic delivery of BMZ in the brain tissues and in the meninges with and without PS: (**a**) – Schematic illustration of BMZ injection into dcLN with the aim to study of its distribution in the meninges and in the brain tissues; (**b**) and (**c**) – Representative images of BMZ spreading through the cribriform plate (**b**) and in the meninges (**c**); (**d**–**f**) – Representative images of lymphatic and perivascular pathway of BMZ diffusion in the meninges. BMZ is distributed via the Lyve-1+ lymphatic vessels (**d**), over PVSs along the meningeal arteries (**e**) and the meningeal veins (**f**); (**g**) – Schematic illustration of PS effects on lymphatic delivery of BMZ into the brain; (**h**) and (**j**) – Representative image of BMZ distribution in the brain parenchyma after PS, (**j**) – Quantification of fluorescent signal from BMZ in the brain with and without PS (mean ± s.m.e.; n = 10 fields analysed from 7 independent mice in each group; *** – $p < 0.001$ between groups, Mann-Whitney test)

deeper into the brain [10]. This wavelength, highly absorbed by oxygen, is capable of turning triplet oxygen to reactive singlet form [7]. In our recent work, we discovered that PS dilates MLVs, which is associated with PS-mediated stimulation of lymphatic transport of red blood cells from the brain [6]. In this work, we demonstrate that PS activates the nitric oxide (NO) synthesis in lymphatic endothelium isolated cells and the lymphatic vessels contractility might be the possible mechanisms responsible for singlet oxygen stimulation of lymphatic transport of macromolecules into and from the brain tissues.

5 Conclusions

In summary, using a quantum-dot-based 1267 nm laser (photosensitiser-free generation of singlet oxygen), we clearly show the photostimulation of lymphatic delivery of BMZ to the brain parenchyma and the meninges. These pilot findings open promising perspectives for photomodulation of a lymphatic brain drug delivery bypassing the BBB, and potentially enabling a breakthrough strategy in therapy of glioma using BMZ and other chemotherapy drugs.

Acknowledgments S-G O., I.V., A.K, I.B., A.T., A.E., G.K., A.D., V.A., I.A., V.T., A.T., T.P., JK were supported by RF Governmental Grant № 075-15-2022-1094, Grant from RSF № 20-15-00090; 21-75-10088, Grant from RFBR 19-515-55016; China a, 20-015-00308-a.

References

1. Sarkaria J, Hu L, Parney I et al (2018) Is the blood-brain barrier really disrupted in all glioblastomas? A critical assessment of existing clinical data. Neuro-Oncology 20:184–191
2. Gerstner E, Emblem K, Chang K et al (2020) Bevacizumab reduces permeability and concurrent temozolomide delivery in a subset of patients with recurrent glioblastoma. Clin Cancer Res 26:206–212
3. Semyachkina-glushkovskaya O, Abdurashitov A, Dubrovsky A et al (2020) Photobiomodulation of lymphatic drainage and clearance: perspective strategy for augmentation of meningeal lymphatic functions. Biomed Opt Express 11:725–734
4. Semyachkina-Glushkovskaya O, Abdurashitov A, Klimova M et al (2020) Photostimulation of cerebral and peripheral lymphatic functions. Transl Biophotonics 597:e201900036
5. Semyachkina-Glushkovskaya O, Sokolovski S, Noghero A et al (2021) Non-invasive photosensitiser-free laser treatment of glioblastoma in rat brain. Nat Commun 2021 (under review)
6. Li D, Liu S, Yu T et al (2021) Photostimulation of lymphatic clearance of red blood cells from the mouse brain after intraventricular hemorrhage. Nat Commun (2021) (under review). https://doi.org/10.1101/2020.11.16.384149
7. Sokolovski S, Zolotovskaya A, Goltsov A et al (2013) Infrared laser pulse triggers increased singlet oxygen production in tumour cells. Sci Rep 3(1):3484
8. Semyachkina-Glushkovskaya O, Postnov D, Lavrova E et al (2021) Biophotonic strategies of measurement and stimulation of the cranial and the extracranial lymphatic drainage function. IEEE J Sel Top Quantum Electron 27(4):1–13
9. Louveau A, Smirnov I, Keyes T et al (2015) Structural and functional features of central nervous system lymphatic vessels. Nature 523:337–341
10. Wang T, Ouzonov D, Wy S et al (2018) Three-photon imaging of mouse brain structure and function through the intact skull. Nat Methods 15(10):789–792

NIRS-Based Study of Local Cerebral Oxygenation During Transcranial Direct Current Stimulation in Patients with Mild Traumatic Brain Injury

Alex O. Trofimov, Darya I. Agarkova, Dmitry Sergeev, Anton Dubrovin, Kseniia A. Trofimova, Oxana Novosadova, Dmitry Martynov, Kyril Lidji-Goryaev, and Denis E. Bragin

Abstract

The purpose of our study was to assess the dynamics of local cerebral oxygenation (LCO) by near-infrared spectroscopy (NIRS) during transcranial direct current stimulation (tDCS) in the acute stage of mild traumatic brain injury (mTBI). Fifty-seven mTBI patients (18 women and 39 men, 35 ± 11.7 years old, GCS 13.7 ± 0.7) were treated by tDCS at 3–5 days after head injury. Stimulation parameters were: 1 mA, 9 V, duration-20 min. A cerebral oximeter was used to assess LCO-values in the frontotemporal lobes. Anodal and cathodal LCO values were compared before tDCS and every 2 min until the tDCS end. Significance was preset to $p < 0.05$. *Results*: A significant decrease in LCO values on the anodal side was observed at the 8th to 12th minutes of stimulation, compared to the cathodal side (at 8th minute – $p = 0.011$; at 12th minute – $p < 0.00000001$) and compared to LCO values before tDCS ($p < 0.00001$). The LCO on the cathodal side was not significantly different during the whole tDCS. At the end of the procedure, the interhemispheric LCO differences were not statistically significant ($p = 0.757$). *Conclusions*: Transcranial DCS in 3–5 days of mTBI leads to a significant decrease in the LCO value on the anodal side between 8 and 12 min and subsequent recovery to baseline values by the end of the procedure.

A. O. Trofimov (✉)
Department of Neurological Diseases, Privolzhsky Research Medical University, Nizhny Novgorod, Russia

Department of Polytrauma, Regional Hospital named after Semashko, Nizhny Novgorod, Russia

D. I. Agarkova · D. Sergeev · A. Dubrovin
Department of Polytrauma, Regional Hospital named after Semashko, Nizhny Novgorod, Russia

K. A. Trofimova · O. Novosadova · K. Lidji-Goryaev
Department of Neurological Diseases, Privolzhsky Research Medical University, Nizhny Novgorod, Russia

D. Martynov
State Technical University named after R.E. Alekseev, Nizhny Novgorod, Russia

D. E. Bragin
Lovelace Biomedical Research Institute, Albuquerque, NM, USA

Department of Neurology, University of New Mexico School of Medicine, Albuquerque, USA

National Research Saratov State University, Saratov, Russia

F. Scholkmann et al. (eds.), *Oxygen Transport to Tissue XLIII*, Advances in Experimental Medicine and Biology 1395, https://doi.org/10.1007/978-3-031-14190-4_10

Keywords

Local cerebral oxygenation · Transcranial direct current stimulation · Mild traumatic brain injury · Neurovascular coupling

1 Introduction

Traumatic brain injury (TBI) is a worldwide problem. Although 75–90% of TBIs (Glasgow Coma Scale (GCS) score of 13–15) are generally mild, there are about 50 million TBI cases worldwide each year, resulting in significant morbidity and a global economic cost of about 400 billion dollars per year [1, 2]. To date, no drug has been approved by the Food and Drug Administration (FDA) for the treatment of the cognitive effects of mild TBI (mTBI), making the issue of patient rehabilitation highly relevant.

Therefore, the emerging non-invasive brain stimulation techniques in rehabilitation post-TBI have attracted significant attention. Transcranial direct current stimulation (tDCS) is one of the non-invasive brain stimulation techniques that can increase or decrease cortical excitability according to polarity and can be used to promote long-term functional recovery.

Recent clinical studies showed the effectiveness of tDCS for craniocerebral trauma rehabilitation, as well as for early post-traumatic consequences, such as post-traumatic encephalopathy [3–5]. However, the LCO dynamics in the early period of mTBI remains poorly understood, determining the relevance of our study. We hypothesised that anodal tDCS might induce LCO decrease at mTBI acute stage. The objective of our study was to assess the dynamics of LCO values at the anodal and cathodal sides, measured by near-infrared spectroscopy (NIRS), during tDCS at 3–5 days after mTBI.

2 Methods

2.1 Study Design

This is a non-randomised single-centre study involving 57 patients with diffuse, blunt, mild TBI (at 3–5 days after head injury). All patients were treated at Nizhny Novgorod Regional Trauma Centre Level I of Clinical Hospital named after N.A. Semashko between January 2018 and April 2021.

2.2 Population

The study involved 18 women and 39 men with a mean age of 35 ± 11.7 years, and severity at admission according to the Glasgow Coma Scale of 13.7 ± 0.7. Clinical criteria for detecting mild TBI include at least one of the following: confusion and disorientation, loss of consciousness up to 30 min and/amnesia up to 24 h after the head injury, a GCS score of 13–15, and transient focal neurological symptoms [6].

None of the patients had any parenchymal brain lesions on computed tomography. Twenty-two patients had a non-severe concomitant injury (Injury Severity Score of less than 9). Thirty-five patients had non-concomitant (isolated) mTBI [6]. All patients were right-handed and not taking neurotrophic treatment.

The patients received a verbal explanation of the research goals and risks. The patients and their families provided signed informed consent. The study was approved by the local Ethics Committee according to the standard set by the Declaration of Helsinki.

2.3 Transcranial Direct Current Stimulation

Transcranial DCS was delivered by a custom-made stimulator (Nizhny Novgorod State Technical University) with a pair of gel-soaked

surface sponge electrodes (Ambu, USA) (S = 5 cm^2). The tDCS parameters were: 1 mA, 9 V, current density ~0.45 mA/cm^2. The procedure duration was 20 min. The anodal and cathodal electrodes were placed over the left and right supraorbital region (M1-Fp), respectively.

2.4 Local Cerebral Oxygenation

Local cerebral oxygenation was assessed in the left and right frontotemporal lobes using cerebral oximeter Fore-Sight 2030 (CAS Medical Systems Inc., Branford, USA). Received LCO data were collected using a Centaurus-LCO intensive care monitor (Ver. 3.0., Privolzhsky Research Medical University, Russia), which provided 20 sec-by-20 sec average values. Manual corrections of movement artifacts were performed on the whole obtained data. Anodal and cathodal LCO-values were compared before tDCS, then every 2 min until the end of the procedure.

2.5 Statistical Analysis and Endpoints

The endpoint of our study was the determination of NIRS-derived LCO-values in the frontotemporal regions in patients 3–5 days after mTBI during tDCS procedures. Continuous variables are expressed as median [interquartile range]. Data were evaluated for normality distribution using the Smirnov-Kolmogorov test. The differences in LCO values were assessed using a non-parametric Wilcoxon rank-sum test. The level of significance was set at 0.05. All analyses were performed using the software package Statistica 7.0 (Statsoft Inc., USA).

3 Results

Basic statistics and comparisons for recorded parameters (tDCS time, LCO-values) are shown in Table 1. Of 57 patients, after the tDCS procedure, 52 noted a decrease in headaches, 48 a decrease in dizziness, 42 a normalisation of circadian rhythms, and 12 a decrease in tinnitus.

Before tDCS, LCO-values were 66.1% [59.1; 73.1] on the cathodal side and 64.9% [60.7; 68.7] on the anodal side. There were no significant differences between the cathodal and right sides (Z = 0.719; p = 0.472). During the 8th–12th minutes of the stimulation, a significant decrease in LCO values on the anodal side was observed compared to the cathodal side (at 8th minute Z = 2.531; p = 0.011; at 10th minute Z = 4.962; p = 0.000001; at 12th minute Z = 5.478; p < 0.00000001), and compared to LCO values before tDCS procedure (p < 0.00001). The average duration of the 'decline gap' was one-third of the procedure time (about 7 min). The LCO levels on the cathodal side were not significantly different during all tDCS procedures. At the end of the proce-

Table 1 Comparison of the obtained values of the studied parameters

tDCS time (minute)	Cathodal side LCO (%)	Anodal side LCO (%)	Z	p-values
0	66.1[59.1;73.1]	64.9[60.7;68.7]	0.719	0.472
2	65.7[59.3;73.2]	63.4[59.9;67.9]	1.315	0.189
4	63.3[58.9;72.9]	63.7[59.5;67.5]	1.855	0.064
6	65.1[61.9;69.9]	63.1[58.8;66.8]	1.593	0.111
8	65.6[61.4;70.4]	61.2[57.4;65.4]	2.531	0.011*
10	66.7[62.6;70.6]	61.8[58.6;66.6]	4.962	0.000001*
12	66.3[61.7;69.4]	59.2[56.2;64.2]	5.478	p < 0.000001*
14	65.1[61.9;69.9]	63.5[60.3;68.3]	1.871	0.061
16	65.9[62.7;70.7]	64.1[61.2;69.2]	0.624	0.533
18	65.8[62.3;69.3]	64.7[61.5;69.5]	0.123	0.902
20	66.1[62.6;68.6]	64.9[61.7;69.7]	0.310	0.757

LCO local cerebral oxygenation, *tDCS* transcranial direct current stimulation, data are presented as median [interquartile range], * – p < 0.05

dure, the interhemispheric LCO differences were not significantly different (Z = 0.310; p = 0.757). In no patient was stimulation accompanied by a worsening of the clinical condition.

4 Discussion

Transcranial DCS of low amperage and voltage is a relatively new, promising technology for brain cortex modulation [1]. Preclinical and clinical studies demonstrated that tDCS is a safe and efficient stimulation modality with a neuroprotective effect on central nervous system diseases [7–9].

Our previous study using perfusion computed tomography revealed an increase in volumetric cerebral blood flow after tDCS suggesting increased oxygen saturation in patients with post-traumatic encephalopathy at 21 days after moderate TBI (GCS 12) [10]. In the current study, we measured LCO in the frontal cortex before, during and after tDCS at 3–5 days after mTBI. We have obtained a statistically significant decrease in LCO value at the anodal side between 8 and 12 min of the stimulation and its recovery by the end of tDCS to the initial LCO values. On the cathodal side, LCO values during and after the procedure did not significantly differ from the values obtained before tDCS. Although our data seems to contradict earlier results [8, 10], this contradiction is not apparent for several reasons.

First, in our study, patients did not have parenchymal brain lesions noted on CT, i.e., they had mild TBI. In contrast, our previous work and preclinical studies were done on moderate-to-severe TBI with parenchymal lesions.

Second, the current study was done 3–5 days after the injury, while our previous study was at 21 days after TBI [8], and animal studies were done 1–3 weeks after the controlled cortical injury [10].

Third, one of the reasons for the time-dependent effect of tDCS in animal studies was damage of the blood-brain barrier permeability, which, obviously, was not observed in patients with mTBI.

A similar decrease in local brain oxygenation during tDCS has been described by Polanıa et al. [11], who showed that direct current changes the connectivity between different parts of the brain, making it possible to redistribute cerebral cortex blood flow, directing it to the stimulation area. However, these processes have a certain hysteresis, and the redistribution does not occur instantly but with a certain time delay, which was noted in our study.

Del Felice et al. suggest that dynamic internal brain networks have a low entropy, which determines their ability to return to the equilibrium state of physiological parameters independently. The maintenance of oxygen saturation is probably one of such systems [12]. As demonstrated in our work, the mechanism of neurovascular coupling is responsible for restoring LSO in the frontal lobes at the end of the stimulation. A decrease in LCO during the procedure may indicate a functional impairment of neurovascular coupling even with mild TBI, consistent with previous studies [13].

Our study had some limitations. We measured LCO values only in the frontal lobes and thus cannot consider the distribution of LCO values in other cortical areas before, during and after tDCS. We were not able to eliminate completely an error associated with a slight spatial displacement of the tDCS electrodes and NIRS probes. All these issues require further study. We believe that our study results provide conditions for a differentiated approach for the treatment of mTBI patients.

5 Conclusion

Transcranial DCS at 3–5 days after mild TBI leads to a significant decrease in the LCO value on the anodal side between 8 and 12 min and subsequent recovery to baseline values by the end of the procedure.

Acknowledgments RSF 22-45-04406 and 22-15-20002. DB was supported by NIH R01 NS112808.

References

1. Janak J, Pugh M, Langlois Orman J (2015) Epidemiology of TBI. In: Cifu DX, Eapen BC (eds) Traumatic brain injury rehabilitation medicine. Elsevier, Philadelphia, pp 6–352
2. Maas A, Menon D, Adelson P et al (2017) Traumatic brain injury: integrated approaches to improve prevention, clinical care, and research. Lancet Neurol 16(12):987–1048
3. Boissonnault È, Higgins J, LaGarde G et al (2021) Brain stimulation in attention deficits after traumatic brain injury: a literature review and feasibility study. Pilot Feasibility Stud 7(1):115
4. de Amorim R, Brunoni A, de Oliveira M et al (2017) Transcranial direct current stimulation for post-concussion syndrome: study protocol for a randomized crossover trial. Front Neurol 8:164
5. Dhaliwa S, Meek B, Modirrousta M (2015) Non-invasive brain stimulation for the treatment of symptoms following traumatic brain injury. Front Psych 6:119
6. Stuart B, Mandleco B, Wilshaw R et al (2012) Mild traumatic brain injury: are ED providers identifying which patients are at risk? J Emerg Nurs 38(5):435–442
7. Bikson M, Esmaeilpour Z, Adair D et al (2019) Transcranial electrical stimulation nomenclature. Brain Stimul 12(6):1349–1366
8. Trofimov AO, Kalentiev G, Karelsky M et al (2018) Cerebral hemodynamics after transcranial direct current stimulation (tDCS) in patients with consequences of traumatic brain injury. Adv Exp Med Biol 1072:59–62
9. Zhang K et al (2020) Cathodal tDCS exerts neuroprotective effect in rat brain after acute ischemic stroke. BMC Neurosci 21(1):21
10. Bragina O, Lara A, Nemoto E (2018) Increases in microvascular perfusion and tissue oxygenation via vasodilatation after anodal transcranial direct current stimulation in the healthy and traumatized mouse brain. Adv Exp Med Biol 1072:27–31
11. Polanıa R, Paulus W, Antal A et al (2011) Introducing graph theory to track for neuroplastic alterations in the resting human brain: a transcranial direct current stimulation study. NeuroImage 54(3):2287–2296
12. Del Felice A, Magalini A, Masiero S (2015) Slow-oscillatory transcranial direct current stimulation modulates memory in temporal lobe epilepsy by altering sleep spindle generators: a possible rehabilitation tool. Brain Stimul 8(3):567–573
13. Zhao M, Ma H et al (2014) Neurovascular coupling methods, vol 335. Springer, New York, Heidelberg, Dordrecht, London

Postnatal Exposure to Brief Hypoxia Alters Brain VEGF Expression and Capillary Density in Adult Mice

Michael B. Komarovsky, Constantinos P. Tsipis, Khalil A. Almotah, Walter F. Boron, Kui Xu, and Joseph LaManna

Abstract

Perinatal hypoxia leads to changes in cerebral angiogenesis and persistent structural and functional changes in the adult brain. It may also result in greater vulnerability to subsequent challenges. We investigated the effect of postnatal day 2 (P2) hypoxic preconditioning on adult brain capillary density and brain vascular endothelial growth factor (VEGF) expression in mice. P2 mice were exposed to hypoxia (5% O_2) in a normobaric chamber for 2 h then returned to normoxia while their littermates remained in normoxia (P2 control). After 2–6 months, they were euthanised and their brains were removed for capillary density determination. Another set of animals (P2 hypoxic mice and P2 controls) were euthanised at 2, 10, 23, and 60 days after birth and brain VEGF expression was assessed by western blot. Adult brain capillary density was significantly increased in the P2 hypoxic mice when compared to the P2 control mice. Additionally, VEGF expression appeared to be elevated in the P2-hypoxia mice when compared to the P2-control mice at all time points, and VEGF levels in P2-hypoxia mice declined with age similarly to P2-control mice. These data demonstrate that transient early-postnatal hypoxic stress leads to an increase in capillary density that persists in the adult, possibly due to increased VEGF expression. These results might be explained by epigenetic factors in the VEGF gene.

Keywords

Perinatal hypoxia · Hypoxic preconditioning · Postnatal hypoxic stress · Epigenetics

1 Introduction

Prolonged exposure to hypoxia in the adult rodent produces substantial cerebral angiogenesis resulting in increased capillary density [1]. Perinatal stress, including transient hypoxia, leads to persistent structural and functional changes in the adult rat brain [2, 3] including cerebral angiogenesis [4, 5]. Hypoxia associated cerebral angiogenesis primarily occurs through hypoxia inducible factor accumulation and consequent promotion of vascular endothelial growth factor (VEGF) expression [6]. In these experiments, we studied the effect of postnatal transient hypoxia on VEGF expression and the development of brain capillaries in mice. Whether or not perinatal hypoxia results in greater vulnerability to sub-

M. B. Komarovsky · C. P. Tsipis · K. A. Almotah · W. F. Boron · K. Xu · J. LaManna (✉)
Department of Physiology & Biophysics, Case Western Reserve University, Cleveland, OH, USA
e-mail: joseph.lamanna@case.edu

F. Scholkmann et al. (eds.), *Oxygen Transport to Tissue XLIII*, Advances in Experimental Medicine and Biology 1395, https://doi.org/10.1007/978-3-031-14190-4_11

sequent challenges in adulthood remains unknown [7].

2 Methods

The experimental protocol employed by this study was approved by our Institutional Animal Care and Use Committee (IACUC). Mice (C57/B6 background) used in this study were bred in our laboratory for more than 15 generations. All mice were housed and maintained at the Animal Resource Center on a 12:12-h light/dark diurnal cycle with unrestricted access to food and water.

2.1 P2 Hypoxic Exposure

Mice at postnatal day two, with their dam, were exposed to hypoxia (5% O_2 in N_2) for 2 h in a chamber where the inflow of gases (Oxycycler model A44XO, Biospherix, Redfield, NY) was automatically controlled. Mice were then returned to a normoxic environment. Littermates were maintained normoxic in the same room and used as P2 controls. Ambient temperature and humidity of gases was monitored and maintained at 22–24 °C and 40–50%, respectively.

2.2 Determination of Cerebral Capillary Density

Brain microvascular density was determined by immunohistochemical staining for the capillary glucose transporter-1 (GLUT-1) and by counting the number of GLUT-1 positive capillaries per unit area (N/mm^2), as described previously [8–10]. Mice were deeply anaesthetised with isoflurane, a blood sample was taken for haematocrit measurement, and mice were perfused transcardially with PBS (pH 7.4) and 4% paraformaldehyde. Brains were removed and immersed in 4% paraformaldehyde overnight at four degrees Celsius. The brain samples were dehydrated through graded alcohol and embedded in paraffin. Coronal serial sections (five μm) of frontal cortex (levels of Bregma 0.98 mm to 0.38 mm) [11] were made on a microtome. Sections were deparaffinised, rehydrated, and subjected to antigen retrieval at 90 °C for 10 min in 0.1 mol/L sodium citrate buffer and incubated with 3% hydrogen peroxide. Slides were blocked with 10% normal horse serum for 1 h and then incubated with primary antibodies (anti-Glut-1, Santa Cruz, CA) at four degrees Celsius overnight. After three serial washes with 0.1 mol/L PBS-tween solution, the secondary antibody (1:200, Vector Labs, Burlingame, CA) was applied. The slides were washed again and incubated in Vectastain ABC Elite reagent (Vector Labs, Burlingame, CA) for 30 min and then developed using diaminobenzidine. After dehydration and coverslipping, images were taken with a SPOT digital camera in conjunction with a Nikon E600 Eclipse microscope. Images spanning the entire depth of the parietal cortex were resolved at 200X optical resolution. Adobe Photoshop CS5 and ImageJ were used to count positively stained microvessels, less than 20 μm in diameter, to determine the capillary density (number per mm^2 of brain tissue). For each brain, at least our different GLUT-1-stained sections were averaged for quantification. Each quantified section was separated by at least 50 μm from each other.

2.3 Determination of VEGF Expression

Tissue lysate preparation and western blot analyses were done as described previously (Benderro and Lamanna, 2011). Briefly, proteins from the whole cell lysates were separated by using SDS gel electrophoresis and transferred to nitrocellulose membranes (Bio-Rad, Hercules, CA). The membranes were blocked in 5% skimmed milk in tris-buffered saline with 0.1% tween (TBS-T), and incubated in the same blocking solution with the primary antibodies. The specific primary antibodies of interest were: VEGF-A (1:1000; Santa Cruz Biotechnology, Santa Cruz, CA) and β-actin (1:2000; Santa Cruz, CA). The membranes were washed three times with TBS-T, followed by incubation with the appropriate horseradish peroxidase-conjugated secondary antibodies

(Millipore Co., Billerica, MA). After a series of three washes with TBS-T, immunoreactive protein bands were visualised using an enhanced chemiluminescence detection system (SuperSignal ECL Kit, Thermo Scientific, IL) and subsequent exposure of the membrane to Hyperfilm (Thermo Scientific, IL).

2.4 Statistical Analysis

Data are expressed as mean ± SD. Statistical analyses were performed using SPSS V19.0 for Windows. The comparison between any two groups was analyzed with one-sided t-test, and significance was considered at the level of $p < 0.05$.

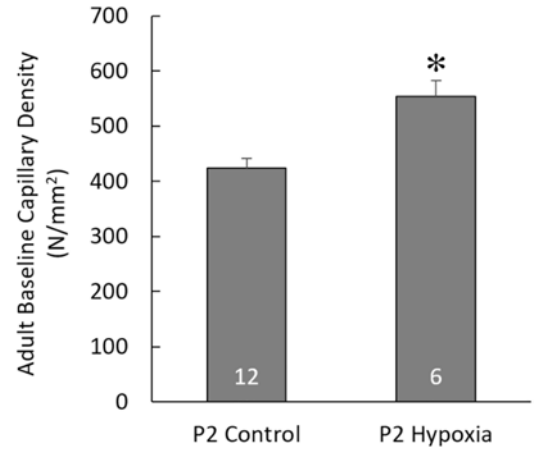

Fig. 1 Adult baseline capillary density (mean ± SD) in controls and mice with hypoxic P2 preconditioning. Number of animals indicated on each bar. *Significance ($p < 0.05$) vs. control group

3 Results

In adult mice that were preconditioned with hypoxia at P2, cortical capillary density was determined and compared to controls. Capillary density was significantly increased in the P2-hypoxia preconditioned mice (554 ± 29, n = 6), when compared to P2-control mice (424 ± 17, n = 12) (Fig. 1).

VEGF levels in P2-hypoxia mice declined with age similarly to P2-control mice. In mice that were preconditioned with hypoxia at P2, VEGF expression was determined at 2, 10, 23, and 60 days after birth and compared to control littermates. VEGF expression was elevated in the P2-hypoxia mice when compared to the P2-control mice at all time points (Fig.2).

4 Discussion

In this study, we have shown that brief postnatal (P2) exposure to hypoxia resulted in a significant increase in baseline capillary density. This observation is consistent with previous studies which have shown that hypoxic insults in the perinatal period can have long-lasting effects on the central nervous system [12, 13] including effects on the cerebral vasculature [14]. Additionally, we observed an increase in VEGF expression in hypoxia preconditioned mice when compared to their control littermates at all time points. Previous studies also reported that the exosomes of cells in hypoxic environments have higher levels of VEGF than cells in normoxic environments [15–17]. These results suggest that the increase in adult baseline capillary density following transient hypoxic preconditioning in the early postnatal period could be caused by an increase in VEGF expression and subsequent exocytosis. These findings may be explained by preliminary results which demonstrate epigenetic changes in methylation of vascular endothelial growth factor genes (*Vegf-A* and *Vegf-B*) in P23 rodents after 2 h of hypoxic exposure at P10 (D. Zhou and G.G. Hadaad, personal communication) as well as a previous study which demonstrated that nuclear microRNA-466c regulates *Vegf-A* expression in response to hypoxia [18].

Additionally, we show that VEGF expression decreases postnatally as expected, with the most dramatic decrease occurring between 2 and 10 days after birth. This result is consistent with the fact that the majority of angiogenesis occurs during the first few days after birth, after which vascular pruning occurs [19]. Therefore, it is possible that rather than stimulating angiogenesis, hypoxic preconditioning is diminishing vascular pruning.

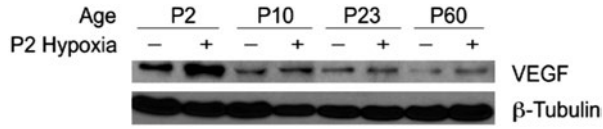

Fig. 2 VEGF expression via western blot normalised against β-Tubulin in controls and mice with hypoxic P2 preconditioning at 2, 10, 23, and 60 days after birth

In conclusion, exposure to brief hypoxia in the early postnatal period increases adult baseline capillary density, possibly explained by a methylation-mediated increase in VEGF expression, that persists into the adult.

References

1. LaManna JC, Vendel LM, Farrell RM (1992) Brain adaptation to chronic hypobaric hypoxia in rats. J Appl Physiol (1985) 72:2238–2243
2. Akers KG, Nakazawa M, Romeo RD et al (2006) Early life modulators and predictors of adult synaptic plasticity. Eur J Neurosci 24:547–554
3. Gustavsson M, Mallard C, Vannucci SJ et al (2007) Vascular response to hypoxic preconditioning in the immature brain. J Cereb Blood Flow Metab 27:928–938
4. Kanaan A, Farahani R, Douglas RM et al (2006) Effect of chronic continuous or intermittent hypoxia and reoxygenation on cerebral capillary density and myelination. Am J Physiol Regul Integr Comp Physiol 290:1105–1114
5. Otellin VA, Khozhai LI, Sishko TT et al (2017) Long-term effects of exposure to perinatal hypoxia on microvascular endothelium of neocortex in rats. J Evol Biochem Physiol 53:49–54
6. LaManna JC, Chavez JC, Pichiule P (2004) Structural and functional adaptation to hypoxia in the rat brain. J Exp Biol 207:3163–3169
7. Tarry-Adkins JL, Ozanne SE (2011) Mechanisms of early life programming: current knowledge and future directions. Am J Clin Nutr 94:1765–1771
8. Xu K, Sun X, Benderro GF et al (2017) Gender differences in hypoxic acclimatization in cyclooxygenase-2-deficient mice. Physiol Rep 5:1–10
9. Tsipis CP, Sun X, Xu K et al (2014) Hypoxia-induced angiogenesis and capillary density determination. Methods Mol Biol 1135:69–80
10. Harik SI, Kalaria RN, Andersson L et al (1990) Immunocytochemical localization of the erythroid glucose transporter: abundance in tissues with barrier functions. J Neurosci 10:3862–3872
11. Paxinos G, Franklin KBJ (Published 2004) The mouse brain in stereotaxic coordinates. Amsterdam, Boston
12. MacFarlane PM, Mayer CA, Litvin DG (2016) Microglia modulate brainstem serotonergic expression following neonatal sustained hypoxia exposure: implications for sudden infant death syndrome. J Physiol 594:3079–3094
13. Decker MJ, Jones KA, Keating GL et al (2018) Postnatal hypoxia evokes persistent changes within the male rat's dopaminergic system. Sleep Breath 22:547–554
14. Dupre N, Arabo A, Orset C et al (2020) Neonatal cerebral hypoxia-ischemia in mice triggers age-dependent vascular effects and disabilities in adults; implication of tissue plasminogen activator (tpa). Exp Neurol 323:1–13
15. Kore RA, Edmondson JL, Jenkins SV et al (2018) Hypoxia-derived exosomes induce putative altered pathways in biosynthesis and ion regulatory channels in glioblastoma cells. Biochem Biophys Rep 14:104–113
16. Han Y, Ren J, Bai Y et al (2019) Exosomes from hypoxia-treated human adipose-derived mesenchymal stem cells enhance angiogenesis through vegf/vegf-r. Int J Biochem Cell Biol 109:59–68
17. Park JE, Tan HS, Datta A et al (2010) Hypoxic tumor cell modulates its microenvironment to enhance angiogenic and metastatic potential by secretion of proteins and exosomes. Mol Cell Proteomics 9:1085–1099
18. Laitinen P, Vaananen MA, Kolari IL et al (2022) Nuclear microrna-466c regulates vegfa expression in response to hypoxia. PLoS One 17:e0265948
19. Coelho-Santos V, Shih AY (2020) Postnatal development of cerebrovascular structure and the neurogliovascular unit. Wiley Interdiscip Rev Dev Biol 9:e363

Impaired Cognitive Performance in Mice Exposed to Prolonged Hyperoxia

Geisa Ortet, Lei Ma, J. Sebastian Garcia-Medina, Joseph LaManna, and Kui Xu

Abstract

Supplementation of oxygen at concentrations significantly above environmental level for prolonged periods may lead to hyperoxia and tissue toxicity. The mammalian brain undergoes structural and functional changes during adaptation to hypoxia and hyperoxia. In this study we investigated the effect of prolonged hyperoxic exposure on cognitive and motor performance in mice. Two-month-old male mice were placed in either hyperoxic (50% O_2) or normoxic conditions for 3 weeks. Cognitive function was measured using the Y-maze test. High alteration rate between the three arms of the maze is indicative of sustained memory and cognitive function. Motor function was measured using the grip strength and rotarod tests. In the rotarod test high speed and long latency are indicative of coordination and resistance. After 3 weeks of exposure, hematocrit levels were significantly decreased in the hyperoxia group compared to normoxic control littermates (%, mean ± SD, 37.8 ± 1.3, n = 15 vs. 49.9 ± 5.1, n = 15, $p < 0.05$). In the Y-maze test, chronic hyperoxic exposure resulted in a statistically significant decrease in alteration rate compared to normoxic control (%, mean ± SD, 53.4 ± 9.9, n = 30 vs. 61.2 ± 9.5, n = 15, $p < 0.05$). The rotarod and grip strength tests did not show statistically significant changes between the two groups. Our data suggest that chronic hyperoxia may lead to decreased cognitive performance in adult mice, which may be secondary to structural and functional changes in the brain.

Keywords

Oxygen supplementation · Spontaneous alternating performance · Cognitive function · Oxidative damage

1 Introduction

Supplemental oxygenation is a pivotal component of clinical medicine. Optimal organ function as well as recovery after injury requires adequate oxygen delivery to tissues. Oxygen is one of the primary components of cellular respiration. In aerobic respiration, oxygen is reduced to water and energy released from this redox reaction is used to generate ATP, the pri-

G. Ortet · J. S. Garcia-Medina · J. LaManna
K. Xu (✉)
Department of Physiology & Biophysics, Case Western Reserve University, Cleveland, OH, USA
e-mail: Kxx@case.edu

L. Ma
School of Electronic Information Science and Technology, Nantong University, Nantong, Jiangsu Province, China

F. Scholkmann et al. (eds.), *Oxygen Transport to Tissue XLIII*, Advances in Experimental Medicine and Biology 1395, https://doi.org/10.1007/978-3-031-14190-4_12

mary energy source of all cells. Oxygen therapy is administered to patients in the hospital for supplemental oxygenation in both acute and chronic settings. It can be a lifesaving or temporising measure in the management of acute respiratory failure secondary to pulmonary embolism, stokes or many other aetiologies. It is also used in chronic settings for long-term management of patients with chronic conditions such as cystic fibrosis and obstructive sleep apnoea (OSA). However, there are adverse effects associated with prolonged hyperoxia.

Hyperoxia is known to lead to formation reactive oxygen species (ROS). These ROS can cause oxidative damage to nucleic acids and proteins, leading to cellular injury and inflammation. Prolonged O_2 therapy used in the management of premature newborns with respiratory distress syndrome in the setting of insufficient surfactant production can result in lung tissue injury seen in bronchopulmonary dysplasia (BPD) [1]. These adverse effects extend beyond the lung tissue and can also cause injury to brain tissue. The mammalian brain undergoes structural and functional changes during adaptation to both hypoxia and hyperoxia. Hypoxia in newborn mice has been demonstrated to stimulate an increase in cerebral capillary density and reduce myelination in the corpus callosum [2]. Chronic hyperoxic exposure in neonates has also been shown to be associated with non-cystic periventricular white matter injury (PWMI) [3].

In this study, we investigated the effect of prolonged hyperoxia on cognitive and motor performance of adult mice.

2 Methods

Male two-month-old C56BL/6 J mice used in this study were purchased from Jackson Laboratories (Bar Harbor, ME, USA) and maintained at the Case Western reserve university Animal Care Facility. The experimental protocol was approved by Institutional Animal Care and Use Committee.

2.1 Exposure to Chronic Hyperoxia

Mice were divided in two groups: the hyperoxia group and the normoxic littermate control group. The hyperoxic mice were exposed to 50% O_2 balanced with N_2 for 3 weeks in a chamber (Oxycycler model A44XO, Biospherix, Redfield, NY) where the inflow of gases was automatically controlled. The normoxic control mice were housed in the same room adjacent to the chamber to match ambient conditions for the same length of time. Body weights were monitored throughout the 3 weeks of exposure. Blood samples for measurement of hematocrit were obtained under anesthesia, just prior to the animals being sacrificed at the end of the study.

2.2 Measurement of Cognitive and Motor Functions

A 3-arm Y-maze was used as measure of cognitive function. The test is based on the innate tendency of rodents to explore a new environment. Mice were placed in the centre of the maze and allowed to freely explore the three arms for 6 min during which the sequencing and total number of arm entries were recorded. Spatial working memory function was measured by scoring spontaneous alternation performance (SAP). A score of 1 SAP is given to each triplet of successive different arm visits (1 SAP = x-y-z, where $x \neq y \neq z$). SAP rate (%) is calculated as total number of SAP divided by (total number entries – 2) x 100. High SAP rate is associated with sustained spatial working memory, hence sustained cognitive performance.

Motor function was evaluated using the rotarod and grip strength tests. Rotarod apparatus unit (Panlab/Harvard Apparatus, Barcelona, Spain) was used, which allows for assessment of motor coordination or fatigue in rodents. Mice were placed on a Rotarod, which has a rotating bar that increases 1 RPM every 3 s, maxing at 40 RPM. A lever plate at the bottom allows for mechanical detection of fall and recording of

maximum speed and latency. Longer latency and higher speed as measures of motor coordination and resistance. Mice were allowed one round to familiarise themselves with the instrument prior to recording results. A grip strength meter (Harvard Apparatus) was used to evaluate neuromuscular function. The mice were allowed to grasp the metal grid or triangular pull bar (using either forepaws or all paws) and are then pulled backwards in the horizontal plane. The maximum force (grams) displayed by an animal just before losing grip was recorded.

2.3 Statistical Analysis

Data are expressed as mean ± SD. Statistical analysis was performed using SPSS V19.0 for Windows. Between group comparisons were conducted using the two-sample t-test. Differences were considered significant at $p < 0.05$.

3 Results

3.1 Physiologic Variables

There was a 100% survival rate in both control and hyperoxic exposure groups. Prior to exposure both groups had a mean body weight of 31.0 g. At the end of the 3-week exposure the body weight in the hyperoxia group and normoxic control group was 31.2 g and 32.0 g, respectively. There was no significant difference between the two groups. Hematocrit was significantly lower in hyperoxic mice at the end of the 3-week exposure when compared to the normoxic littermate (%, mean ± SD, 37.8 ± 1.3, n = 15 vs. 49.9 ± 5.1, n = 15, $p < 0.05$).

3.2 Y-Maze Test

The hyperoxia group showed a statistically significant decrease in SAP rate compared to the control group (%, mean ± SD, 53.4 ± 9.9, n = 30 vs. 61.2 ± 9.5, n = 15, $p < 0.05$), as seen in Fig. 1. Additionally, there was a statistically significant increase in the total number of arm entries seen in the hyperoxia group compared to the normoxic control group (mean ± SD, 53.4 ± 9.9, n = 30 vs. 61.2 ± 9.5, n = 15, $p < 0.05$).

3.3 Rotarod and Grip Strength Tests

In the rotarod test, no significant difference in either latency or speed was observed between the hyperoxia and the control groups. In the grip strength test, no significant difference in strength was observed in either forepaws or all paws between the two groups (Fig. 2).

4 Discussion

The primary finding in this study was that exposure to chronic hyperoxia leads to impaired cognitive performance as seen in the Y-maze test. It additionally showed an increased activity level in the hyperoxia group (Fig. 1a). However, this increase in activity may be non-purposeful. The motor function tests (rotarod and grip strength) did not show significant difference between the hyperoxia and control groups. Our results also demonstrated a decrease in hematocrit following chronic hyperoxia. This is in line with previous studies [4] and is the expected physiological response to elevated oxygen content in blood. This adaptive response ensures optimal oxygen delivery to tissues.

It has been demonstrated that exposure of newborn mice to chronic hyperoxia leads to deficits in spatial and recognition memory [5]. Our studies demonstrated similar findings in adult mice. The nature of the association between hyperoxia and cognitive impairment is unclear. In addition to decrease capillary density, white matter damage has also been shown to be associated with prolonged exposure to hyperoxia. Neonatal exposure to hyperoxia has been shown to cause myelination abnormalities primarily associated with the nodes of Ranvier, leading to impairment of action potential conduction [6].

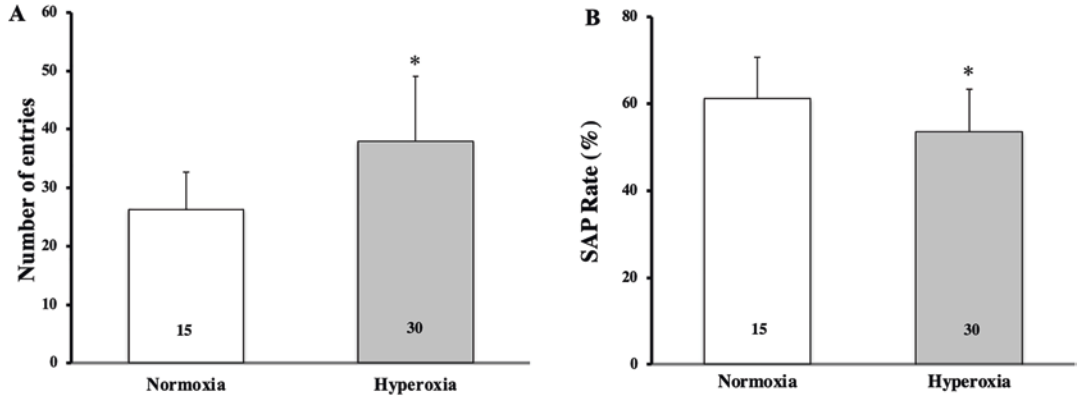

Fig. 1 The Y-maze test in the hyperoxic mice and normoxic controls. (**a**) The number of entries (mean ± SD). (**b**) The SAP rate (%, mean ± SD). Number of animals of each group is indicated on the bar. * = statistical significance compared to the normoxic control group ($p < 0.05$)

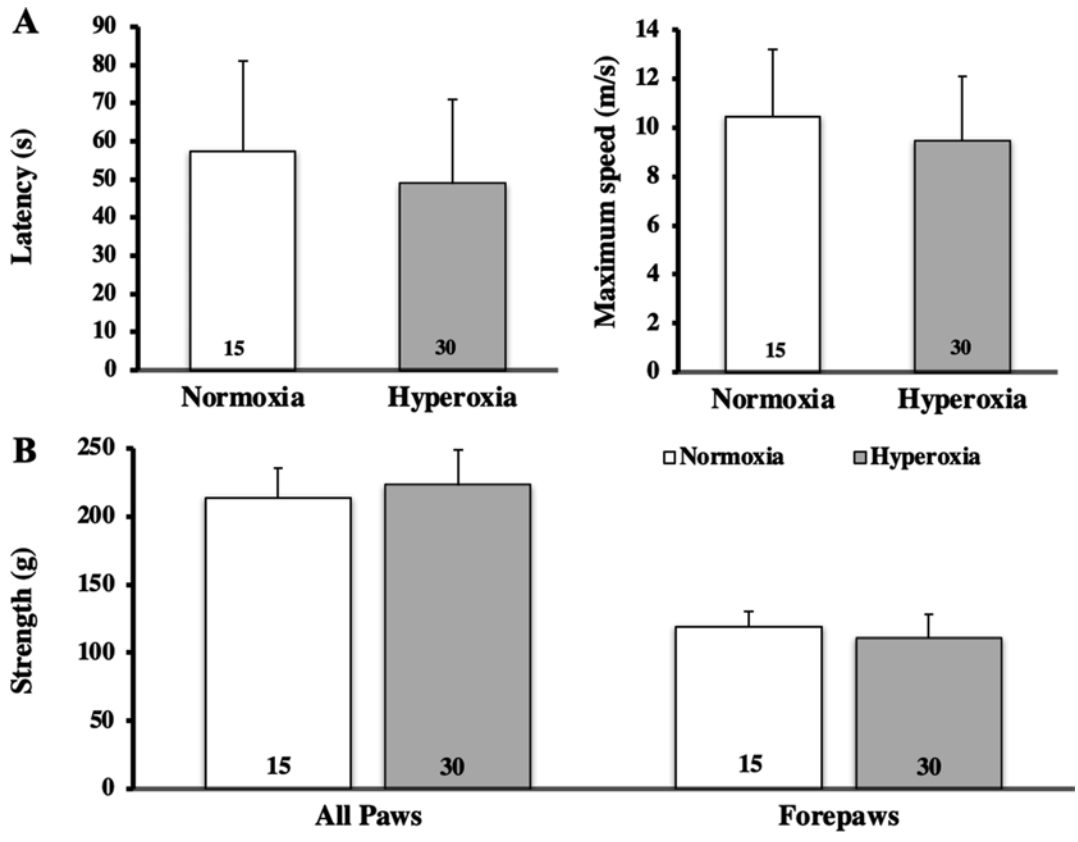

Fig. 2 Measurement of motor function in the normoxic controls and hyperoxic mice. (**a**) Measurement of latency (s) and maximum speed (m/s) in the Rotarod tests. (**b**): Muscle strength (g) of all paws and forepaws. Data are mean ± SD. There were no significant differences in any of the comparisons between the hyperoxia group and control group

Neonatal hyperoxia during the first week of life has also been shown to reduce brain myelination and to be associated with deficits in social interaction and motor coordination in adolescent mice [7]. These findings suggest that the impaired cognitive performance observed in this study may be associated with the underlying white matter changes. The association between neonatal hyperoxia and impairment in cognitive function seen in these animal studies have also been demonstrated in the clinical setting. In very preterm neonates, exposure to prolonged mechanical ventilation has been shown to be associated with impaired brainstem development, abnormal white matter maturation and lower motor scores at preschool age [8].

In conclusion, our main finding was that chronic hyperoxia resulted in impaired cognitive function in adult mice. In future studies we will further explore the roles of capillary density and white matter injury in the mechanism of cognitive impairment seen in chronic hyperoxia.

References

1. Popova AP (2013) Mechanisms of bronchopulmonary dysplasia. J Cell Commun Signal 7(2):119–127
2. Kanaan A, Farahani R, Douglas RM et al (2006) Effect of chronic continuous or intermittent hypoxia and reoxygenation on cerebral capillary density and myelination. Am J Physiol Regul Integr Comp Physiol 290:1105–1114
3. Schmitz T, Ritter J, Mueller S et al (2011) Cellular changes underlying hyperoxia-induced delay of white matter development. J Neurosci 31(11):4327–4344
4. Benderro GF, Sun X, Kuang Y et al (2012) Decreased VEGF expression and microvascular density, but increased HIF-1 and 2α accumulation and EPO expression in chronic moderate hyperoxia in the mouse brain. Brain Res 1471:46–55
5. Ramani M, van Groen T, Kadish I et al (2013) Neurodevelopmental impairment following neonatal hyperoxia in the mouse. Neurobiol Dis 50:69–75
6. Ritter J, Schmitz T, Chew LJ et al (2013) Neonatal hyperoxia exposure disrupts axon-oligodendrocyte integrity in the subcortical white matter. J Neurosci 33(21):8990–9002
7. Lo YC, Chen KY, Chou HC et al (2021) Neonatal hyperoxia induces gut dysbiosis and behavioral changes in adolescent mice. J Chin Med Assoc 84(3):290–298
8. Martin RJ, Harijith AK (2021) The twofold NICU challenge: avoiding hypoxia and hyperoxia. Pediatr Res 90:4–5

Chronic Ketosis Modulates HIF1α-Mediated Inflammatory Response in Rat Brain

Aarti Sethuraman, Prahlad Rao, Atul Pranay, Kui Xu, Joseph LaManna, and Michelle A. Puchowicz

Abstract

Hypoxia inducible factor alpha (HIF1α) is associated with neuroprotection conferred by diet-induced ketosis but the underlying mechanism remains unclear. In this study we use a ketogenic diet in rodents to induce a metabolic state of chronic ketosis, as measured by elevated blood ketone bodies. Chronic ketosis correlates with neuroprotection in both aged and following focal cerebral ischaemia and reperfusion (via middle cerebral artery occlusion, MCAO) in mouse and rat models. Ketone bodies are known to be used efficiently by the brain and metabolism of ketone bodies is associated with increased cytosolic succinate levels that inhibits prolyl hydroxylases allowing HIF1α to accumulate. Ketosis also regulates inflammatory pathways, and HIF1α is reported to be essential for gene expression of interleukin10 (IL10). Therefore we hypothesised that ketosis-stabilised HIF1α modulates the expression of inflammatory cytokines orchestrating neuroprotection. To test changes in cytokine levels in rodent brain, eight-week-old rats were fed either the standard chow diet (SD) or the ketogenic (KG) diet for 4 weeks before ischaemia experiments (MCAO) were performed and the brain tissues were collected. Consistent with our hypothesis, immunoblotting analysis shows IL10 levels were significantly higher in KG diet rat brain compared to SD, whereas the TNFα and IL6 levels were significantly lower in the brains of KG diet fed group.

Keywords

Ketogenic diet · Succinate · Neuroprotection · Beta-hydroxybutyrate · Acetoacetate · IL10

1 Introduction

The mechanism through which diet-induced ketosis confers neuroprotection remains unclear despite its clinical applications for over seven decades [1]. Studies have implicated ketosis in modulating metabolic profiles and inflammatory pathways [1–3]. The ketogenic diet (KG) is a high-fat, very low-carbohydrate diet which results in hepatic production of ketone bodies due

A. Sethuraman · P. Rao · A. Pranay
Department of Pediatrics, University of Tennessee Health Science Center, Memphis, TN, USA

K. Xu · J. LaManna
Department of Physiology & Biophysics, Case Western Reserve University, Cleveland, OH, USA

M. A. Puchowicz (✉)
Department of Pediatrics, University of Tennessee Health Science Center, Memphis, TN, USA

Department of Nutrition, Case Western Reserve University, Cleveland, OH, USA
e-mail: mpuchowi@uthsc.edu

F. Scholkmann et al. (eds.), *Oxygen Transport to Tissue XLIII*, Advances in Experimental Medicine and Biology 1395, https://doi.org/10.1007/978-3-031-14190-4_13

to elevated beta-oxidation of fats by the liver. Ketosis results in elevated blood ketone bodies (beta-hydroxybutyrate and acetoacetate; BHB, AcAc) which are alternate energy substrates to glucose and are known to be well utilised by brain, especially during glucose sparing conditions [3]. Ketones are beneficial substrates during metabolic derangements of glucose metabolism such as with ischaemia reperfusion injury induced oxidative stress. The KG diet is a well-established non-pharmacological approach to treat drug-resistant epilepsy in children and has shown promise in treating other neurological conditions such as Alzheimer's disease and stroke [4, 5].

We have consistently reported that ketosis induced by KG diet or by local intraventricular infusions of BHB correlates with neuroprotection following focal cerebral ischaemia and reperfusion (via middle cerebral artery occlusion, MCAO) in rats, (Fig. 1 (modified [2])) and mice (data not shown), respectively [1, 2]. The metabolic adaptation to chronic ketosis, as well as the mechanistic actions of ketosis in brain (globally and cellular) are multifactorial but not well understood. Prolyl dehydrogenases (PHDs) mediated oxygen sensing and regulation of hypoxia inducible factors have been well studied, but normoxic regulation of this pathway warrants further study. This study focused on investigating the potential mechanisms associated with normoxic accumulation of hypoxia inducible factor-1 alpha (HIF1α) in diet-induced ketotic rats [1]. Specifically, we investigated the role of KG diet on inflammatory responses as associated with HIF1α stabilisation in preconditioned ketotic rat brain. We targeted markers of pro- vs anti-inflammatory cytokines (TNFα and IL6 vs IL10) in cortical brain of ketotic rat to determine potential neuroprotective mechanisms mediated by HIF1α.

2 Methods

Animals: Experimental protocols were approved by the Institutional Animal Care and Use Committee (IACUC) at Case Western Reserve University (CWRU). Male Wistar rats (8 weeks old) were fed either KG (high fat, carbohydrate restricted; n = 4) or standard lab-chow (STD; n = 4) diets for 4 weeks before tissue collections (brain and blood), as previously described [1]. Rats were maintained on a 12:12 light-dark cycle with their diets and water available ad libitum. **Diet protocols:** Ketogenic (KG; 89.5 fat %, 10.4 protein %, 0.1 CHO %, n6:n3 ratio 43.2; research diets, New Brunswick, NJ diet) and standard (STD; 27.5 fat %, 20.0 protein%, 52.6, provided

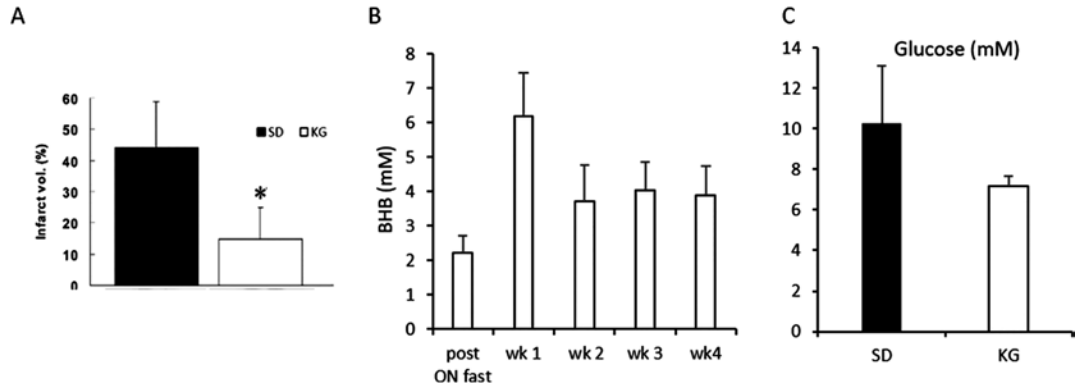

Fig. 1 (**a**) Infarct volumes in rat brains following MCAO were significantly lower in KG vs SD diet fed rats (modified from [2]). (**b**) Blood ketones (BHB) in rats fed with the ketogenic diet was measured with Precision Xtra® hand held keto-monitor. The blood ketone levels in KG fed rats spiked the first week and stabilised in the following weeks. (**c**) Absolute glucose levels measured in blood plasma using GC-MS analysis show that, glucose levels were elevated in the SD as compared to the KG diet fed rats. The values presented are the mean ± S.E.M (n = 4). * Denotes statistical significance ($p < 0.05$)

by the CWRU animal facility). Weekly BHB concentrations were analysed using a keto-meter (Precision Xtra, Abbott, Alameda California) from a small blood sample taken from the tail. **Metabolic panels (GCMS-based analysis):** Gas chromatography mass spectrometry (GC-MS): Absolute glucose concentration (mM) was measured from blood plasma collected. The metabolite derivatives were assayed on an Agilent 5973 N-MSD equipped with an Agilent 6890 GC system coupled to a DB-17MS capillary column (30 m × 0.25 mm × 0.25 μm) and operated in electron impact ionisation mode [3]. **Western blot analysis:** Nuclear protein extracts prepared from cortical brain were immunoblotted using anti-HIF1α and anti-HIF2α antibodies and normalised to TBP; while the cytosolic protein extract was immunoblotted with anti-IL10, anti-IL6 and anti-TNFα and normalised to GAPDH, as previously described [6, 7]. Proteins were detected by chemiluminescence, and densitometric quantification was performed using ImageJ software. **Statistical analysis:** All values were presented as mean ± SEM. Statistical analyses were performed using GraphPad Prism 7 ®. The comparison between any two groups was analysed with a t-test for paired sample, two-tailed. Significance was considered at the level of $p < 0.05$.

3 Results

Blood metabolites in KG and SD diet-fed rats: Blood ketone levels in KG-fed rats spiked in first week of diet to 6.2 mM and stabilised throughout the remaining weeks to an average of 3.9 mM (Fig. 1b). Absolute concentrations of plasma glucose were determined using GC-MS, Fig. 1c. Plasma glucose concentrations trended lower (but not statistically significant) in KG compared to SD diet group. **Diet-induced ketosis on HIF1α-mediated inflammatory response:** Immunoblotting results (Fig. 2) show significantly higher protein levels of HIF1α in cortical brain of KG rats compared to SD group while HIF2α levels remained unchanged between groups. Consistent with our hypothesis, IL10 levels were significantly higher in KG rat cortical brain compared to SD; while the TNFα and IL6 levels were significantly lower in KG group (Fig. 2b).

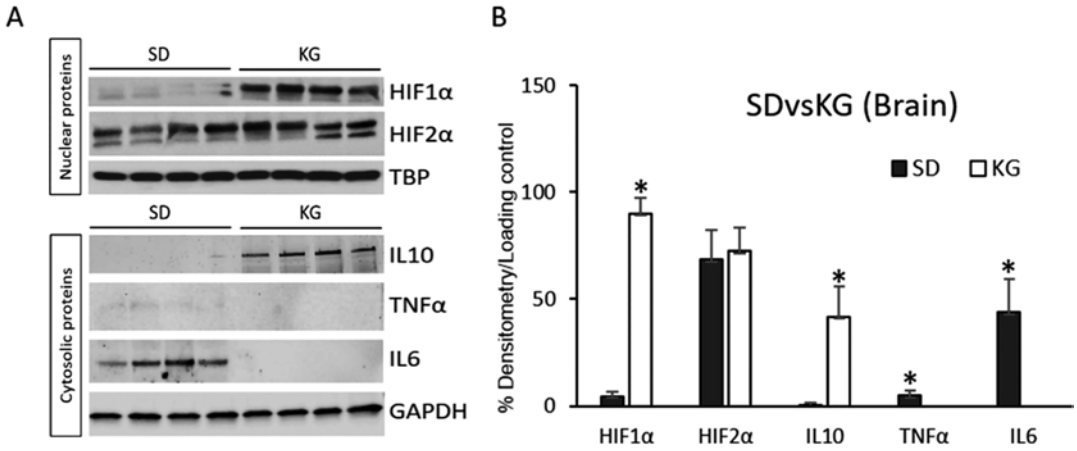

Fig. 2 (**a**) Western blot analysis of HIF1α, HIF2α and cytokines IL10, TNFα and IL6. HIF1α and HIF2α protein levels were normalised to TATA-box binding protein (TBP) loading control, while IL10, TNFα and IL6 were normalised to GAPDH (**b**) HIF2α protein levels remain unchanged, but HIF1α was significantly higher in KG rat brain. Expression of anti-inflammatory cytokine IL10 was significantly higher in KG brain while no expression of pro-inflammatory cytokines IL6 and TNFα were observed. The values presented are the mean ± S.E.M. (n = 4). * Denotes statistical significance ($p < 0.05$)

4 Discussion

In this study we show that normoxic stabilisation of HIF1α in cortical ketotic rat brain is associated with modification of inflammatory cytokines which could confer neuroprotection following ischaemic injury.

Diet-induced stabilisation of HIF1α in rodent brain under normoxic ketotic conditions has been previously shown by Puchowicz, et al. [1–3]. HIF1α can transcriptionally regulate IL10 levels by direct binding to hypoxia responsive elements (HRE's) on the IL10 promoter [8]. Further, overexpression of IL10 in mice has been associated with a resistance to ischaemic injury (MCAO) [9]. Our study brings together ketosis-mediated stabilisation of HIF1α and a potential neuroprotective phenotype in rats via IL10-mediated regulation of inflammatory cytokines. The inverse relationship we observe with HIF1α and IL6 levels has also been observed in a study by Schaefer et al. They reported HIF1α protein levels were higher under sustained hypoxia with a significant reduction in both mRNA and protein levels of IL6 [10].

IL10 meditated inflammatory pathways have been extensively studied for its implications in the design of targeted approaches aiming at controlling deleterious inflammation in the brain [11]. Our study connects to IL10-mediated immune regulation through downregulation of pro-inflammatory cytokines. One potential mechanism for this downregulation is via attenuation of the NLRP3 inflammasome as reported by Kanneganti et al. [12], thereby suspending activation of downstream pro-inflammatory cytokines like IL6 and TNFα. Secondly, IL10 receptor activation has been shown to specifically activate the JAK1-STAT3-mediated downregulation of pro-inflammatory cytokines [13]. Further,

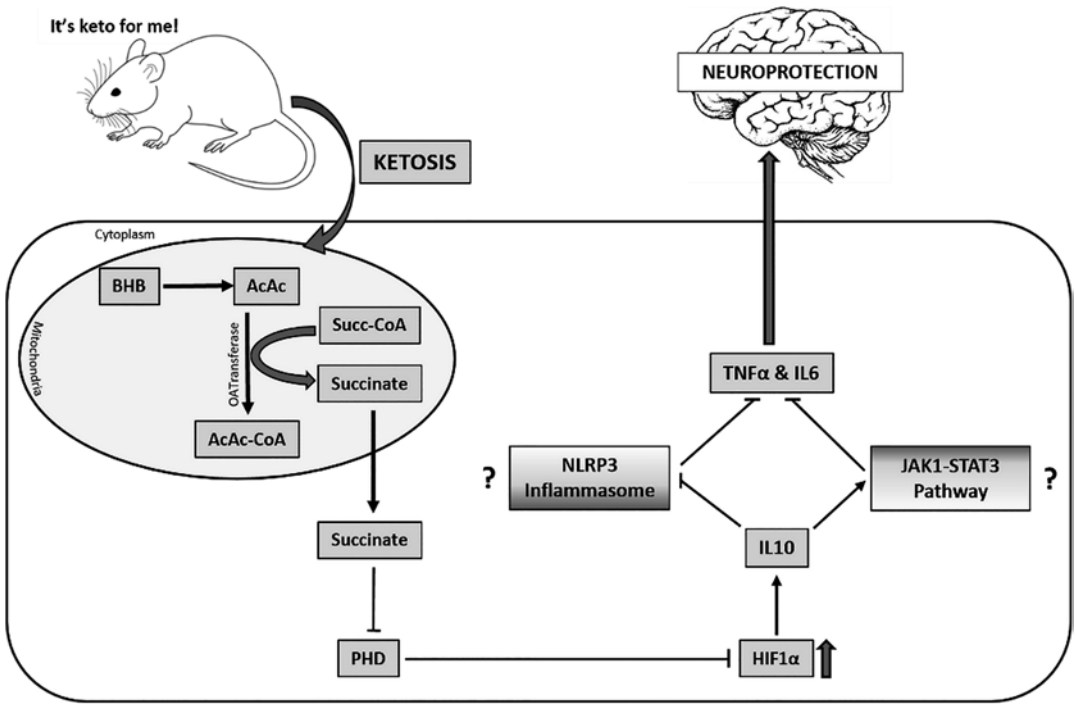

Fig. 3 Schematic model of our conclusion and future direction. Utilisation of ketone bodies generated by metabolism of ketogenic diet as energy source causes accumulation of succinate on a cellular level in rat brains, which in turn inhibits prolyl hydroxylases resulting in accumulation of HIF1α. IL10, in turn, causes a downregulation of pro-inflammatory cytokines- TNFα and IL6, leading to a neuroprotective phenotype. Further studies are needed to delineate the pathways involved in this downregulation. (Abbreviations used: *AcAc* Acetoacetate, *BHB* β-hydroxybutyrate, *CoA* CoenzymeA, *PHD* Prolyl Dehydrogenase, and *Succ-CoA* Succinyl-CoA)

IL10-JAK1-STAT3 pathway has been described as the negative regulator of inflammation that controls both the degree and duration of inflammation [14].

Figure 3 is a scheme of our model system, it depicts the mechanism for HIF1α stabilisation by KG diet is through cellular metabolic redox signalling within the mitochondria. Specifically, succinate is an intermediate of ketone body catabolism which is generated at the level of citric acid cycle following activation of AcAc to AcAc-CoA as coupled to the conversion of succinyl-CoA to succinate via CoA transferase (OAT). To maintain metabolic redox, succinate is transported out of the mitochondria into cytosol where it acts to inhibit prolyl hydroxylases (PHD), and thus resulting in HIF1α accumulation. Lastly, molecular pathway involved in HIF1α-mediated down regulation of pro-inflammatory cytokines (IL6 and TNFα) is via IL10-mediated attenuation of NLRP3 inflammasome or via IL10/JAK1/STAT3-mediated transcriptional attenuation. Thus, neuroprotection by ketosis involves modulation of inflammatory response in rat brain. Our study highlights the potential role of interleukins in neurodegenerative disease. Future studies should include further exploring the potential beneficial effects of ketogenic diets for the treatment of neurological disorders such as autism (autism spectrum disorder) and multiple sclerosis [15, 16].

Acknowledgments This study was supported by NIH grant R01 NS 38632; Mouse Metabolic Phenotyping Consortium (*P&F 20497-21, MMPC*).

References

1. Puchowicz MA, Zechel JL, Valerio J et al (2008) Neuroprotection in diet-induced ketotic rat brain after focal ischemia. J Cereb Blood Flow Metab 28(12):1907–1916
2. Xu K, Ye L, Sharma K et al (2017) Diet-induced ketosis protects against focal cerebral ischemia in mouse. Adv Exp Med Biol 977:205–213
3. Zhang Y, Xu K, Kerwin T et al (2018) Impact of aging on metabolic changes in the Ketotic rat brain: glucose, oxidative and 4-HNE metabolism. Adv Exp Med Biol 1072:21–25
4. Gasior M, Rogawski MA, Hartman AL (2006) Neuroprotective and disease-modifying effects of the ketogenic diet. Behav Pharmacol 17(5–6):431–439
5. Gibson CL, Murphy AN, Murphy SP (2012) Stroke outcome in the ketogenic state—a systematic review of the animal data. J Neurochem 123(Suppl 2):52–57
6. Sethuraman A, Brown M, Seagroves TN et al (2016) SMARCE1 regulates metastatic potential of breast cancer cells through the HIF1A/PTK2 pathway. Breast Cancer Res 18(1):81
7. Sethuraman A, Brown M, Krutilina R et al (2018) BHLHE40 confers a pro-survival and pro-metastatic phenotype to breast cancer cells by modulating HBEGF secretion. Breast Cancer Res 20(1):117
8. Cai Z, Luo W, Zhan H et al (2013) Hypoxia-inducible factor 1 is required for remote ischemic preconditioning of the heart. Proc Natl Acad Sci U S A 110(43):17462–17467
9. Garcia JM, Stillings SA, Leclerc JL et al (2017) Role of Interleukin-10 in acute brain injuries. Front Neurol 8:244
10. Schaefer E, Wu W, Mark C et al (2017) Intermittent hypoxia is a proinflammatory stimulus resulting in IL-6 expression and M1 macrophage polarization. Hepatol Commun 1(4):326–337
11. Lobo-Silva D, Carriche GM, Castro AG et al (2016) Balancing the immune response in the brain: IL-10 and its regulation. J Neuroinflammation 13(1):297
12. Gurung P, Li B, Subbarao Malireddi RK et al (2015) Chronic TLR stimulation controls NLRP3 Inflammasome activation through IL-10 mediated regulation of NLRP3 expression and Caspase-8 activation. Sci Rep 5:14488
13. Verma R, Balakrishnan L, Sharma K et al (2016) A network map of Interleukin-10 signaling pathway. J Cell Commun Signal 10(1):61–67
14. Hutchins AP, Diez D, Miranda-Saavedra D (2013) The IL-10/STAT3-mediated anti-inflammatory response: recent developments and future challenges. Brief Funct Genomics 12(6):489–498
15. Ruskin DN, Svedova J, Cote JL et al (2013) Ketogenic diet improves core symptoms of autism in BTBR mice. PLoS One 8(6):e65021. https://doi.org/10.1371/journal.pone.0065021
16. Özenci V, Kouwenhoven M, Huang YM et al (1999) Multiple sclerosis: levels of Interleukin-10-secreting blood mononuclear cells are low in untreated patients but augmented during interferon-β-1b treatment. Scand J Immunol 49:554–561

Motor Imagery and Frontal Head Oxygenation: An fNIRS Study

Wataru Tsuchiya, Kunihiko Nagao, and Masamichi Moriya

Abstract

Motor imagery (MI) is a manifestation of mental movements, but it cannot be identified visually. Therefore, to a large extent, MI assessment has not yet been established. The present study aimed to investigate whether frontal oxy-Hb changes and cardiac autonomic nervous system activity during MI are associated with the psychometric scale assessment of MI and clarify the utility of each index in MI assessment. Thirty-one healthy men and women were included in this study, and Pocket NIRS Duo was used to assess frontal oxygenated hemoglobin levels during walking MI. Simultaneously, heart rate and sympathetic index (low and high frequency (LF/HF) during MI were evaluated using Chiryou Meijin, a heart rate frequency analyser. In addition, a psychometric scale evaluation was carried out in MC and VAS, and its correlation with oxy-Hb levels, heart rate (HR), and LF/HF was investigated. HRs and LF/HF during MI were significantly increased compared with those at rest. However, oxy-Hb levels during MI were not increased. There was a significant correlation between right oxy-Hb levels and mental chronometry (MC) during MI ($r = -0.3$, $p < 0.05$). HR and LF/HF were not correlated with MC. VAS was not correlated with oxy-Hb levels, HR, or LF/HF. The results of this study confirm an association between MI performance and frontal oxy-Hb changes and that brain activity is not necessarily elevated during MI. HR were significantly increased but did not show any association with MC.

Keyword

Sympathetic index · Prefrontal cortex activity · Oxyhaemoglobin · Timed up and go (TUG) test

1 Introduction

Motor imagery (MI) has been used in a variety of settings, including rehabilitation and sports. Recently, MI training has been positioned as a treatment with a high level of evidence in a systematic review [1], and MI-based training is

W. Tsuchiya
Graduate School of Health Sciences Research, Major of Physical Therapy, Teikyo Heisei University, Tokyo, Japan

Department of Rehabilitation, Nihon University Itabashi Hospital, Tokyo, Japan

K. Nagao · M. Moriya (✉)
Faculty of Health Care and Medical Sports Department of Physical Therapy, Teikyo Heisei University, Chiba, Japan
e-mail: m.moriya@edu.k.u-tokyo.ac.jp

F. Scholkmann et al. (eds.), *Oxygen Transport to Tissue XLIII*, Advances in Experimental Medicine and Biology 1395, https://doi.org/10.1007/978-3-031-14190-4_14

becoming established. However, MI is considered to be a conscious activation of brain activity similar to the preparation and execution of exercise [2, 3], and cannot be visually confirmed. According to previous studies, brain activity during MI includes regions corresponding to motor-related areas such as primary motor cortex, supplementary motor cortex, and premotor cortex [4]. In the case of third-person MI, activity in the visual cortex and other areas has also been observed [5]. In addition, the pre-frontal cortex (PFC) has been found to be activated during MI, and it has been reported that the PFC activity changes depending on the difficulty of MI [6, 7]. Thus, it has been suggested that PFC activity reflects MI activity, and it was hypothesised that MI could be evaluated by PFC activity. In addition, cardiac autonomic nervous system indicators such as heart rate (HR) and low frequency and high frequency (LF/HF) have been reported to increase during MI [8, 9]. In this study, we investigate whether frontal oxy-Hb changes and cardiac autonomic nervous system activity during MI are associated with the psychometric scale assessment of MI and clarify the utility of each index in MI assessment.

2 Methods

2.1 Subjects and Protocol and Imagery Task

Thirty-one healthy male and female subjects (23 males and 8 females, mean age 25.8 ± 8.1 years) were included in the study.

The protocol for this study consisted of three tasks, starting with an imagery task, followed by a real motion task, and finally an imagery task. The resting time before the imagery task was 5 min, and the resting time before the real exercise task was 2 min (Fig. 1a). The imagery task used in this study was the "timed up and go" test (TUG), which is used in gait function assessment. The TUG is a gait function evaluation that measures the time it takes to start from sit-to-stand, forward gait, mid-turn, return gait, and turn-stand-to-sit. We adopted imaged-TUG (hereinafter referred to as iTUG), in which TUG is performed only by imagery without physical movement, referring to previous studies [10, 11] (Fig.1b). The TUG and iTUG tasks in this study consisted of three consecutive circumambulations of a forward marker. After a resting period, the examiner asked the participants to perform the imaginary TUG and the actual TUG at their own timing with the verbal instruction "Please perform the imaginary TUG at your own timing" and "Please perform the actual TUG at your own timing". The students were asked to perform each task at their own timing. The time required for the TUG and iTUG tasks in this study is measured by the subjects themselves. After the above verbal instruction, the subject presses the stopwatch at the moment when his back leaves the chair, and stops the stopwatch when his or her back touches the chair again to measure the time. This study was conducted with the eyes open.

2.2 Motor Imagery Rating Scale

In this study, (1) mental chronometry (MC) [12] and (2) visual analogue scale (VAS) [13] will be used as psychometric scales. (1) MC is an evaluation method that calculates the time difference between the real motion and its imagery task. The smaller the time difference, the better the imagery. In this study, we use the difference between the time required for the TUG and iTUG tasks (calculated by the formula MC = TUG-iTUG). (2) In the VAS, the left end of the 100 mm line is marked "not at all clear" and the right end is marked "perfectly clear", and a check mark is placed at the place that is subjectively close to the clarity of the image you have made. For objective evaluation, (3) frontal oxy-Hb changes (oxy-Hb) concentration during MI was measured using a pocket NIRS duo (Dynasense, Hamamatsu, Japan), and (4) cardiac autonomic nerve activity during MI was measured using a heart rate frequency analyser. (3) Evaluation using Pocket NIRS Duo was based on the oxy-Hb value 5 s before the start of the MI task, and the rate of change of the oxy-Hb value in the image was calculated and used (percentage change in oxy-

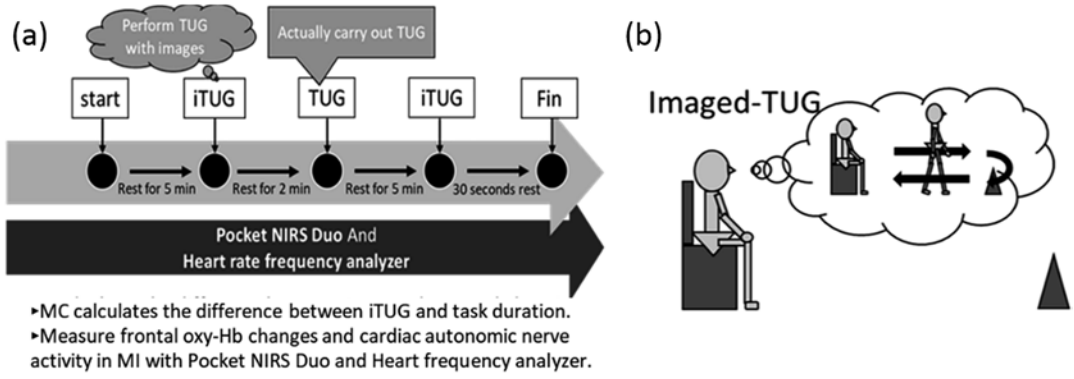

Fig. 1 (**a**) Experimental protocol. (**b**) Imaged TUG

Hb = (oxy-Hb during MI – oxy-Hb at rest)/oxy-Hb at rest x 100). The evaluation using the heart rate frequency analyzer was also performed by measuring the rate of change of HR and LF/HF during MI, using the 5 seconds before the start of MI as a reference. For statistical analysis, we conducted correlation analysis of (1) and (2) using psychometric scales and (3) and (4) using objective evaluations, respectively, to investigate whether each objective evaluation index was related to the psychometric scales.

3 Result

In this study, measurements were performed on 31 healthy male and female subjects. First, a representative example of the waveforms of changes in oxy-Hb, deoxy-Hb, and total-Hb during MI is shown (Fig. 2a). As shown by the representative example waveforms, changes in oxy-Hb concentration reflecting neural activity were observed in all subjects, with an overall decreasing trend (Fig. 2b). On the other hand, there was a significant correlation between right frontal oxy-Hb and MC during MI ($r = -0.3$, $p < 0.05$) (Fig. 2c). However, there was no correlation between left frontal oxy-Hb and MC during MI. There was also no correlation between left and right frontal oxy-Hb and VAS during MI.HR during MI was significantly increased to 74.6 ± 11.8 compared to the resting mean of 72.5 ± 11.1 bpm ($p < 0.05$), and LF/HF showed an increasing trend of 127.3 ± 78.4% during MI compared to 100% at rest (Fig. 2d). LF/HF was not correlated with MC or VAS. Analysis of frontal oxy-Hb changes and cardiac autonomic activity showed no correlation between left and right frontal oxy-Hb and deoxy-Hb changes and LF/HF.

4 Discussion

The present study investigated the relationship between frontal oxy-Hb changes and cardiac autonomic activity during MI and psychometric measures in MI. All subjects showed changes in oxy-Hb concentration reflecting neural activity, and there was a significant negative correlation between right frontal oxy-Hb changes and MC ($p < 0.05$). It has been reported that PFC activity decreases when the difficulty level of the MI task is high [7]. The MI task in this study comprised three consecutive rounds of TUGs consisting of various movements such as standing, walking, changing direction, sitting, etc. Since TUGs are whole-body movements and consist of various movements, we considered that the localisation of attention and perception was difficult. As a result, we thought that the difficulty of the MI task was increased and the frontal oxy-Hb changes was decreased. It has also been reported that the form of PFC activity during MI varies depending on the difficulty of the MI task and the age of the participants. In young healthy subjects, PFC activity increases when the difficulty of the MI task is high and the MC deviation is large [6], while in contrast, PFC activity decreases in

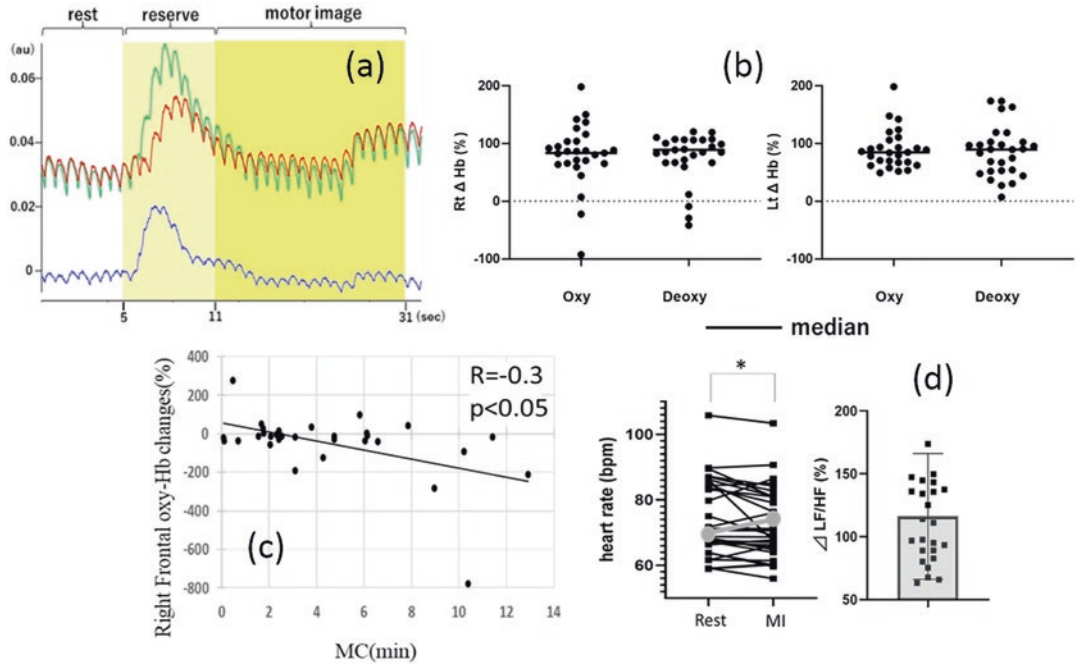

Fig. 2 (**a**) Waveforms of change in oxy-Hb and deoxy-Hb. (**b**) Rate of change in oxy-Hb and deoxy-Hb. (**c**) Scatterplot of oxy-Hb and MC. (**d**) Changes in HR and LF/HF during MI

elderly healthy subjects [7]. The right frontal oxy-Hb changes and MC in this study show a negative correlation. In other words, the greater the MC deviation, the more likely it is that the right frontal oxy-Hb changes is decreasing. The subjects of this study were young healthy people, and the results were different from those of previous studies. This may be due to the difference in difficulty and conditions between the MI task in the previous study and the MI task employed in this study. As mentioned above, this study is an MI task that combines various actions, making it difficult to localise attention and perception. Thus, even in young healthy subjects, frontal oxy-Hb changes did not necessarily increase with MC deviation, suggesting that it may be influenced by the difficulty, conditions, and content of the MI task. It was therefore suggested that frontal oxy-Hb changes may be reduced in MI tasks in which attention and perception are difficult to localise, even in young healthy subjects. In addition, in MI, only the right frontal oxy-Hb was correlated with MC. This is thought to be related to the MI task with open eyes in this study. Previous studies have reported that right PFC acts on spatial working memory and is activated during sustained intentional attention to space [14]. Therefore, we considered that the correlation was observed only in the right frontal.

Next, HR during MI in this study showed a significant increase ($p < 0.05$). Previous studies have reported an increase in cardiac autonomic activity during MI [9]. However, there was no correlation with MC or VAS, suggesting that there may be different mechanisms between frontal oxy-Hb changes and cardiac autonomic activity.

5 Conclusion

It was confirmed that MI ability and frontal oxy-Hb changes are related and do not necessarily increase during MI. In addition, HR and LF/HF increased, but there was no association with MI ability. Therefore, it was suggested that the evaluation of cardiac autonomic nerve activity alone may not be enough to evaluate MI, but that fron-

tal oxy-Hb changes may be useful in MI evaluation.

6 Limitations of the Study

The NIRS used in this study is applied to the skin. Therefore, it is possible that artefacts such as skin blood flow may affect the results. In addition, the analysis method ignores head structure, skull, cerebrospinal fluid, white matter and grey matter, so the results are easily influenced by factors other than cerebral blood flow. Therefore, the present study is limited in that it is only a frontal oxy-Hb study, and cannot be determined as a cerebral blood flow study.

References

1. Langhorne P, Coupar F, Pollock A (2009) Motor recovery after stroke : a systematic review. Lancet Neurol 8:741–754
2. Abbruzzese G, Assini A, Buccolierri A et al (1999) Change of interacortical inhibition during motor imagery in human subjects. Neursci Lett 263:113–116
3. Stinear CM, Byblow WD (2004) Modulation of corticospinal excitability and intracortical during motor imagery is task-dependent. Exp Brain Res 157:351–358
4. Bonda E, Petrides M, Frey S et al (1995) Neural correlates of mental transformations of the body-in-space. Proc Natl Acad Sci U S A 92:11180–11184
5. Solodkin A, Hlustiket CEE et al (2004) Fine modulation in netwaork activation during motor execution and motor imagery. Cereb Cortex 14:1246–1255
6. Kotegawa K, Yasumura A, Teramoto W (2020) Activity in the prefrontal cortex during motor imagery of precision gait: an fNIRS study. Exp Brain Res 238:221–228
7. Kotegawa K, Yasumura A, Teramoto W (2021) Changes in prefrontal cortical activation during motor imagery of precision gait with age and task difficulty. Behav Brain Res 399:113046
8. Peixoto Pinto T, Mello Russo Ramos M, Lemos T et al (2017) Is heart rate variability affected by distinct motor imagery strategies? Comparative Study 177:189–195
9. Bunno Y, Suzuki T, Iwatsuki H (2015) Motor imagery muscle contraction strength influences spinal motor neuron excitability and cardiac sympathetic nerve activity. J Phys Ther Sci 27:3793–3798
10. Beauchet O, Annweiler C, Assal F et al (2010) Imagined timed up & go test: a new tool to assess higher-level gait and balance disorders in older adults? J Neurol Sci 294:102–106
11. Moriya M, Sakatani K (2017) Effects of motor imagery on cognitive function and prefrontal cortex activity in Normal adults evaluated by NIRS. Adv Exp Med Biol 977:227–231
12. Decety J, Jeannerod M, Prablanc C (1989) The timing of mentally represented actions. Behav Brain Res 34:35–42
13. Lotze M, Scheler G, Tan H-RM et al (2003) The musician's brain : functional imaging of amateurs and professionals during performance and imagery. NeuroImage 20:1817–1829
14. Cona G, Scarpazza C (2018) Where is the "where" in the brain? A meta-analysis of neuroimaging studies cognition. Hum Brain Mapp 40:1867–1886

Part II

Clinical Application

Non-invasive Detection of Persistent Cortical Hypoxia in Multiple Sclerosis Using Frequency Domain Near-Infrared Spectroscopy (fdNIRS)

Damilola D. Adingupu, T. Evans, A. Soroush, S. Jarvis, L. Brown, and J. F. Dunn

Abstract

There may be a relationship between hypoxia and inflammation, which is important in the outcomes of a wide array of human diseases. Multiple sclerosis (MS) is one such disease. There is evidence that hypoxia may influence inflammation in MS. We showed previously that about 40% of participants with MS had hypoxia in the cortical grey matter using frequency-domain near-infrared spectroscopy (fdNIRS). In this study, we aimed to determine if hypoxia in MS persists chronically (for a year or more) by measuring at baseline and ≥12 months later. We found that hypoxia persists for at least a year in 80% of participants with MS. As more individuals remained hypoxic than returned to normoxia, the development of hypoxia may relate to disease progression.

Keywords

Inflammation · Neurodegenerative disease · Demyelination · White matter disease

D. D. Adingupu (✉)
Department of Radiology, University of Calgary, Calgary, Canada
e-mail: deborah.adingupu@ucalgary.ca

T. Evans · A. Soroush · J. F. Dunn
Department of Radiology, University of Calgary, Calgary, Canada

Hotchkiss Brain Institute (HBI), University of Calgary, Calgary, Canada

Department of Clinical Neurosciences, University of Calgary, Calgary, Canada

S. Jarvis
Hotchkiss Brain Institute (HBI), University of Calgary, Calgary, Canada

Alberta Neurologic Centre, Calgary, Canada

L. Brown
Department of Clinical Neurosciences, University of Calgary, Calgary, Canada

1 Introduction

Continuous delivery of oxygen is required for the brain to maintain cellular homeostasis and energy metabolism. In conditions where there are insufficient delivery and/or uptake of oxygen by cells, hypoxia is the result. In normal physiology, there are adaptation processes that takes place in the face of moderate acute, intermittent hypoxia. These include increased capillary surface area which will enhance oxygen delivery, decreased energy demand and changes in metabolic responses, all working together to stabilise oxygen to the tissue [1]. In neurodegenerative dis-

F. Scholkmann et al. (eds.), *Oxygen Transport to Tissue XLIII*, Advances in Experimental Medicine and Biology 1395, https://doi.org/10.1007/978-3-031-14190-4_15

eases, chronic hypoxia may be present which does not benefit from the same physiological adaptations as moderate acute hypoxia [2]. Furthermore, inflammation is also a potent modulator of the adaptive response to hypoxia [2], therefore in conditions where inflammation is present, all the above-mentioned adaptive benefits is not present.

In neurodegenerative diseases, the relationship between hypoxia and inflammation may be an important outcome measure. One such disease is multiple sclerosis (MS), which is characterised by inflammation, demyelination and axonal damage within the central nervous system (CNS) [3]. There is evidence from human studies that in multiple sclerosis hypoxia is present [4–6], and this hypoxia may influence inflammation [7]. In the experimental autoimmune encephalomyelitis (EAE) animal model of MS, hypoxia has been studied and has been associated with white and grey matter autoimmune demyelination [8, 9]. Hypoxia in the context of human disease MS is defined as a significant reduction in the CNS tissue oxygenation compared to that of healthy controls.

Using frequency-domain near-infrared spectroscopy (fdNIRS), we showed previously that about 40% of participants with MS had hypoxia in the cortical grey matter [4]. fdNIRS uses intensity-modulated light to measure the attenuation and phase shift of NIR light when it returns to the detector after passing through prefrontal cortical tissue [10, 11]. For the calculation of absolute haemoglobin (Hb) concentrations, fdNIRS uses multiple light sources that are situated at varying distances from a single detector. Changes in attenuation and phase as a function of source-detector distance allow for the quantification of absorption and scattering coefficients [12]. These coefficients can then be used to calculate absolute oxyhaemoglobin (HbO) and Hb concentrations, when multiple wavelengths of NIR light are used to distinguish tissue elements from one another [13, 14]. The ratio of HbO to total haemoglobin (tHb) provides a measure of the absolute cortical microvasculature haemoglobin saturation (S_tO_2), which is a value that is used as an indicator of the brain oxygenation status [4]. Although there are significant partial volume effects, in that light has to pass through non-brain tissue, we control for that by showing that arterial saturation does not change. Given the relationship between hypoxia and inflammation, it is possible that fdNIRS-measures of hypoxia reflect ongoing inflammation in the brain.

We believe that fdNIRS has the potential to become a method for use in the detection of grey matter hypoxia in individuals with MS. In this project, we aim to determine if hypoxia in MS is acute or if it persists chronically (for a year or more) using fdNIRS to measure cortical oxygenation at baseline and ≥12 months.

2 Methods

Participants with confirmed diagnosis of multiple sclerosis (relapsing-remitting MS (RRMS), secondary progressive MS (SPMS) and primary progressive MS (PPMS)) were recruited. The inclusion criteria were (i) age 18–65 years; (ii) men and women; (iii) clinical diagnosis of MS and (iv) non-smoker (nicotine or marijuana). Thirty-nine participants with MS (RRMS = 35, SPMS = 4) were enrolled into the study and measured at baseline and at ≥12 months. Healthy controls aged 18–65 years (n = 55) who are non-smokers (nicotine or marijuana), with no recent systemic infection, and no history of cardiovascular/vascular disease were recruited. All individuals provided written informed consent prior to commencement of their participation. This study complied with the Declaration of Helsinki. Ethics approval was obtained from the Conjoint Health and Research Board at the University of Calgary.

Age, sex, S_tO_2, arterial saturation of oxygen (S_aO_2), and heart rate (HR) were recorded. S_aO_2 and HR were measured using a pulse oximeter. Physical disability of participants with MS was assessed using the patient-determined disease steps (PDDS). The 9-hole peg test (9-HPT) was measured to evaluate dexterity. The Beck's depression inventory-II (BDI-II) was used to assess depression, and for fatigue the modified fatigue impact scale (MFIS) was completed. The

paced auditory serial addition test (PASAT) was administered to test auditory processing speed and working memory. All measurements were administered by trained researchers. S_tO_2 was evaluated using fdNIRS (Fig. 1).

At baseline, comparison of S_tO_2, age, sex, S_aO_2 and HR was made between groups using independent samples t-test. Hypoxic values were defined as S_tO_2 values that are 2 standard deviations below the healthy control group mean. Baseline S_tO_2 values were compared with 1-year follow-up (1YrFU) values for the participants with MS using a paired t-test.

3 Results

Table 1 summarises the baseline data for the comparison of healthy controls to participants with MS. Participants with MS were older, with a lower S_tO_2, and higher HR compared with healthy controls. S_tO_2 data was further grouped into normoxic ($S_tO_2 \geq 55.1\%$) and hypoxic groups ($S_tO_2 < 55.1\%$). At baseline, of the 39 participants with MS, 24 were characterised as normoxic and 15 as hypoxic.

Table 2 summarises oxygen saturation parameters, measures of dexterity, depression and physical disability measured at baseline and at one-year follow-up (1YrFU) in participants with MS. There was no statistically significant difference in S_tO_2, S_aO_2, and HR measured at baseline and at 1YrFU. There was a trend for longer completion time for 9-HPT at 1YrFU compared with baseline.

In a separate analysis, data for participants with MS were separated into hypoxic and normoxic groups as determined at baseline. This was to elucidate if participants remained in their S_tO_2 groups at 1YrFU (Fig. 2). The median S_tO_2 in normoxic and hypoxic groups for the baseline vs. 1YrFU was 61.9% vs. 57.6% and 52.48% vs. 51.2%, respectively. In the hypoxic group at baseline, 12 of 15 remained hypoxic at 1 YrFU and in the MS participants grouped as normoxic at baseline, 5 of 24 became hypoxic by 1 year.

4 Conclusion

We confirm the previous observation that approximately 40% of participants with MS have significant hypoxia in the brain [4]. Furthermore, we show that hypoxia is chronic and persists for at least a year in 80% of participants with MS. It is however clear from our data that some individu-

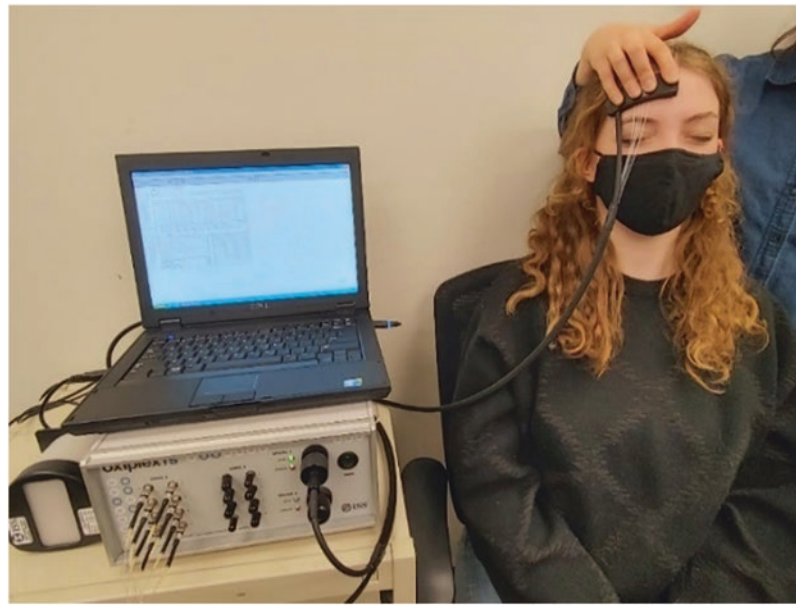

Fig. 1 Frequency-domain near-infrared spectroscopy (ISS OxiplexTS, model 96,208, ISS Inc., Champaign, IL) used in the measurement of frontal cortical microvascular oxygenation (S_tO_2)

Table 1 Demographic and oxygen saturation parameters measured in healthy controls and participants with MS (mean ± SD)

	Healthy controls (n = 55)	Participants with MS (n = 39)	*p* value
Age (year)	47.7 ± 13.3	52.8 ± 7.8	0.022
Sex	Male, n = 17 Female, n = 38	Male, n = 7 Female, n = 32	Ns
S_tO_2 (%)	62.3 ± 3.6	57.2 ± 7.4	<0.001
S_aO_2 (%)	96.9 ± 1.6	96.4 ± 1.7	Ns
HR (BPM)	69.2 ± 6.5	75.6 ± 11.7	0.003

Table 2 Repeated measure in individuals with MS at baseline and one-year follow-up. Data presented as mean ± SD

	Baseline	1 YrFU	*p* value
S_tO_2 (%)	57.2 ± 7.4	55.9 ± 6.7	0.250
S_aO_2 (%)	96.4 ± 1.7	96.5 ± 2.0	0.862
HR (BPM)	75.6 ± 11.7	75.5 ± 10.0	0.893
PDDS	1.8 ± 2.0	1.8 ± 2.0	0.720
BDI	9.7 ± 7.6	9.0 ± 7.5	0.534
MFIS	34.5 ± 16.9	33.2 ± 18.5	0.603
9-HPT Dom hand Z score (seconds)	25.9 ± 24.6	28.9 ± 34.6	0.078
9-HPT Non-Dom hand Z score (seconds)	32.4 ± 52.6	34.4 ± 54.5	0.066
PASAT Z score	0.014 ± 0.168	0.168 ± 0.175	0.201

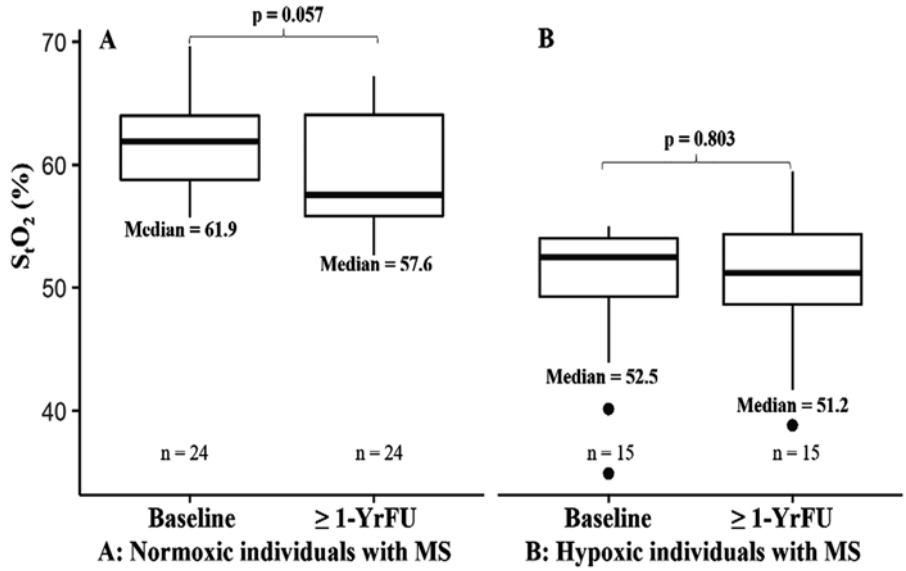

Fig. 2 Box plot showing S_tO_2 for participants with MS at baseline and at one-year follow-up, grouped into normoxic (**a**) or hypoxic (**b**) at baseline

als can either return to normoxia or become hypoxic. We found that more individuals became hypoxic than returned to normoxia. This suggests that the development of hypoxia may relate to disease progression. Our data does not indicate a decline in cognitive function, as measured by PASAT, however the result for 9-HPT shows a trend towards decline in upper-extremity function. It has been shown that individuals with early RRMS with moderately preserved clinical and cognitive functions have reduced cerebral blood volume [15]. Furthermore, it has also been shown that MS patients exhibit reductions in cerebral blood flow and that there was a negative correlation between expanded disability status scale score and blood flow in the frontal cortex [16]. Taken together, reduced cerebral blood volume and blood flow could lead to tissue hypoxia.

We propose that chronic hypoxia may exacerbate inflammatory response, which can in turn further result in hypoxia (a hypoxia-inflammation cycle) [7]. These data indicate that fdNIRS measures of hypoxia in the brain of participants with MS could provide novel indices of disease progression and inflammatory response.

Acknowledgments This study was funded by the National Multiple Sclerosis Society, grant number: RG-1806-31457.

References

1. Puchowicz MA, Koppaka SS, LaManna JC (2008) Brain metabolic adaptations to hypoxia. Springer, New York, pp 15–30
2. Burtscher J, Mallet RT, Burtscher M, Millet GP (2021) Hypoxia and brain aging: neurodegeneration or neuroprotection? Ageing Res Rev 68:101343. https://doi.org/10.1016/j.arr.2021.101343
3. Brück W (2005) The pathology of multiple sclerosis is the result of focal inflammatory demyelination with axonal damage. (in eng), J Neurol 252(Suppl 5):v3–v9. https://doi.org/10.1007/s00415-005-5002-7
4. Yang R, Dunn JF (2015) Reduced cortical microvascular oxygenation in multiple sclerosis: a blinded, case-controlled study using a novel quantitative near-infrared spectroscopy method. Sci Rep 5(1):16477. https://doi.org/10.1038/srep16477
5. Lassmann H (2003) Hypoxia-like tissue injury as a component of multiple sclerosis lesions. J Neurol Sci 206(2):187–191. https://doi.org/10.1016/s0022-510x(02)00421-5
6. Lucchinetti C, Bruck W, Parisi J, Scheithauer B, Rodriguez M, Lassmann H (2000) Heterogeneity of multiple sclerosis lesions: implications for the pathogenesis of demyelination. Ann Neurol 47(6):707–717. https://doi.org/10.1002/1531-8249(200006)47:6<707::aid-ana3>3.0.co;2-q
7. Yang R, Dunn JF (2019) Multiple sclerosis disease progression: contributions from a hypoxia-inflammation cycle. (in eng), Mult Scler 25(13):1715–1718. https://doi.org/10.1177/1352458518791683
8. Johnson TW, Wu Y, Nathoo N, Rogers JA, Wee Yong V, Dunn JF (2016) Gray matter hypoxia in the brain of the experimental autoimmune encephalomyelitis model of multiple sclerosis. PLoS One 11(12):e0167196. https://doi.org/10.1371/journal.pone.0167196
9. Davies AL et al (Dec 2013) Neurological deficits caused by tissue hypoxia in neuroinflammatory disease. Ann Neurol 74(6):815–825. https://doi.org/10.1002/ana.24006
10. Ferrari M, Quaresima V (2012) A brief review on the history of human functional near-infrared spectroscopy (fNIRS) development and fields of application. (in eng), Neuroimage 63(2):921–935. https://doi.org/10.1016/j.neuroimage.2012.03.049
11. Kurth CD, Thayer WS (1999) A multiwavelength frequency-domain near-infrared cerebral oximeter. (in eng), Phys Med Biol 44(3):727–740. https://doi.org/10.1088/0031-9155/44/3/015
12. Gratton E, Toronov V, Wolf U, Wolf M, Webb A (2005) Measurement of brain activity by near-infrared light. J Biomed Opt 10(1):11008. https://doi.org/10.1117/1.1854673
13. Zhao J, Ding HS, Hou XL, Zhou CL, Chance B (2005) In vivo determination of the optical properties of infant brain using frequency-domain near-infrared spectroscopy. J Biomed Opt 10(2):024028. https://doi.org/10.1117/1.1891345
14. Toronov V et al (2001) Study of local cerebral hemodynamics by frequency-domain near-infrared spectroscopy and correlation with simultaneously acquired functional magnetic resonance imaging. Opt Express 9(8):417–427. https://doi.org/10.1364/oe.9.000417
15. Lagana MM, Pelizzari L, Baglio F (2020) Relationship between MRI perfusion and clinical severity in multiple sclerosis. (in eng), Neural Regen Res 15(4):646–652. https://doi.org/10.4103/1673-5374.266906
16. de la Pena MJ et al (2019) Early perfusion changes in multiple sclerosis patients as assessed by MRI using arterial spin labeling. Acta Radiol Open 8(12):2058460119894214. https://doi.org/10.1177/2058460119894214

Evaluation of Intraoperative End-Tidal Carbon Dioxide Change Relates to Length Hospitalisation in Peridiaphragmatic Surgery: A Pilot Study

Christel Cariddi, L. Andresciani, C. Calabrò, M. Laforgia, M. Ronchi, S. De Summa, R. Boccuzzi, A. De Rosa, E. Rizzo, G. Losito, G. Bradascio, G. Napoli, M. Simone, G. Carravetta, and G. Mastrandrea

Abstract

Intraoperative evaluation is deeply changed using many new tools, both invasive and non-invasive. Peripheral oxygen saturation percentage (SpO_2) is the more reliable method for a non-invasive monitoring of patient's blood oxygen concentration. Capnography (using end-tidal CO_2 ($EtCO_{2)}$) evaluation is an immediate and continuous non-invasive monitoring of carbon dioxide (CO_2) in the breathing that provides important information on circulatory status and ventilation.

Aim of this study is to perform a preliminary analysis of oxygen change during surgery exploring its possible influence on post-operative evolution.

Methods and results: Intraoperative evaluation of SpO_2 and $EtCO_2$ was performed. Change in each parameter was categorised as 1 point for each five-point variation from baseline value (ΔSpO_2 as 1 point for each 5%, $\Delta EtCO_2$ as 1 point for each 5 mmHg). For each patient, the length of stay (LOS) in the intensive care unit (ICU), total hospitalisation, duration of intervention, surgical risk and complications were recorded.

Results: We analysed 93 consecutive patients (43 males and 40 females, aged 66.35 ± 9.79 years) that underwent peridiaphragmatic surgery. Forty patients (48.19%) presented complications after surgery. There was no statistically significant difference in age, duration of intervention and length of stay in ICU between complicated and non-complicated patients. As expected, patients with complications present an increased hospitalisation time compared to uncomplicated cases (14.69 ± 11.41 days vs 10.70 ± 6.28 days; $p < 0.05$). $\Delta EtCO_2$ was significantly increased ($p < 0.05$) in complicated compared to non-complicated. No differences were found in ΔSpO_2 between the two groups. Considering the whole population, $\Delta EtCO_2$ presents a sig-

C. Cariddi (✉) · L. Andresciani
Dipartimento dell'Emergenza e Trapianti d'Organo (DETO), Sezione di Anestesiologia e Rianimazione, Ospedale Policlinico, University of Bari Aldo Moro, Bari, Italy

C. Calabrò · M. Laforgia · M. Ronchi · S. De Summa · R. Boccuzzi · A. De Rosa · E. Rizzo · G. Losito · G. Bradascio · G. Napoli · M. Simone · G. Carravetta · G. Mastrandrea
IRCCS Istituto Tumori Giovanni Paolo II – Viale O. Flacco, Bari, Italy

F. Scholkmann et al. (eds.), *Oxygen Transport to Tissue XLIII*, Advances in Experimental Medicine and Biology 1395, https://doi.org/10.1007/978-3-031-14190-4_16

nificant direct correlation to surgical risk, hospitalisation and duration of intervention.

Conclusion: $\Delta EtCO_2$ may be related to possible complications after surgery and hospitalisation. An important comparison between SpO_2 and $EtCO_2$ and strict monitoring with an intraoperative arterial blood gas (ABG) sample during the main steps of surgery could bring some essential information to understand oxygen changes in intra- and post-operative evolution. However, a further validation analysis is needed before the approach can be used extensively in daily clinical settings.

Keywords

Capnography · Tumor surgery · Hypoxemia · Hypoxia · Peripheral oxygen saturation percentage (SpO2)

1 Introduction

Hypoxia in the tumour microenvironment is typically characterised by impaired oxygen delivery and consumption. The restriction of oxygen diffusion in avascular primary tumours along with the higher oxygen consumption due to hyperproliferation of cancer cells, induces the rise of hypoxia. [1] Cellular responses to hypoxia are essential for tumour progression in many aspects, such as cancer cell survival, proliferation, epithelial-to-mesenchymal transition (EMT), invasion, angiogenesis, drug resistance and metastasis. While the association between tumour hypoxia and poor prognosis in primary carcinomas is well known, understanding hypoxia-promoting factors is important to ensure better treatment for cancer patients.

A simple way to evaluate oxygen blood level is arterial oxyhaemoglobin saturation (SaO_2): it is either measured directly on arterial blood or estimated from pulse oximetry (SpO_2). Several patients undergo surgery in order to remove or reduce tumour mass. During surgical intervention, many factors could worsen tissue hypoxia such as circulatory and respiratory variations. SpO_2 is the more reliable method for a non-invasive monitoring of a patient's blood oxygen concentration in the intraoperative setting.

Increases in arterial blood pO_2 and pCO_2 could determine a systemic blood vessel vasoconstriction and vasodilation, respectively, but also dynamic vascular changes in tumour mass [4], linked with cancer dissemination and metastasis.

Another kind of intraoperative evaluation is capnometry (using end-tidal CO_2 ($EtCO_2$)), an immediate and continuous non-invasive monitoring of carbon dioxide (CO_2) of respiratory gases that provides important information on circulatory status and ventilation.

The aim of this study is to perform a preliminary analysis of oxygen changes during surgery and explore the possible influence of these on post-operative evolution.

2 Materials and Methods

Intraoperative evaluation of SpO_2 and $EtCO_2$ was performed in 83 patients that underwent cancer surgery. Changes in each parameter were evaluated from baseline value (ΔSpO_2, $\Delta EtCO_2$).

To obtain an easy step grade evaluation, the delta-change for these two parameters was categorised as 1 point for each five-point variation from baseline value (ΔSpO_2 as 1 point for each 5%, $\Delta EtCO_2$ as 1 point for each 5 mmHg).

For each patient, the length of stay (LOS) in an intensive care unit (ICU), total hospitalisation, duration of intervention, perioperative risk based on physical status examination assessed by ASA (American Society of Anaesthesiologists) score [6], and complications were recorded.

Statistical analysis was performed with GraphPad Prism® 6 considering a p-value <0.05 as significant. Data are presented as mean and standard deviation. After a normality distribution test, values were classified as parametric or not. Parametric values were analysed using Student's t-test comparison and Pearson correlation. Non-parametrics were compared using Mann-Whitney and Spearman correlation. Distribution was evaluated using Chi-squared test.

3 Results

We analysed 83 consecutive patients (43 males and 40 females, aged 66.35 ± 9.79 years) that underwent to peridiaphragmatic surgery. Forty patients (48.19%) presented complications after surgery (24 males and 16 females, aged 68.75 ± 8.03 years). The remaining 43 patients (51.78%, 19 males and 24 females, aged 65.10 ± 8.79 years) did not present any complication after surgery. There was no difference in age and sex distribution between the two groups (Table 1).

There was no statistically significant difference in duration of intervention and length of stay in ICU between complicated and non-complicated patients (Table 1).

As predictable, patients with complications presented an increased hospitalisation time compared to no complicated (14.69 ± 11.41 days vs 10.70 ± 6.28 days; $p < 0.05$) (Table 1). $\Delta EtCO_2$ was significantly increased ($p < 0.05$) in complicated compared to non-complicated (Table 1). No differences were found in ΔSpO_2 between the two groups.

Considering the whole population, $\Delta EtCO_2$ presents a significant direct correlation to hospitalisation and duration of intervention (Table 2). Moreover, $\Delta EtCO_2$ results increased according to the increase in perioperative risk (ANOVA $p = 0.03$ for trend; Fig. 1).

4 Discussion

Several factors during surgery could impair oxygen blood level, especially in cancer patients, such as variations in mean arterial blood pressure, cardiac frequency, haemorrhages and types of surgery that could acutely overlap a preoperative hypoxic condition in oncological patients. Vaupel et al. added another relevant pathogenetic factor for the development of tumour hypoxia, i.e., *hypoxemic hypoxia*, which may be either chronic (e.g., in tumour-associated or therapy-induced anaemia) or acute (e.g., during plasma flow only in the tumour microvasculature) [2]. The relationship between hypoxia and tumour growth and metastasis is also observed in patients with obstructive sleep apnoea (OSA): in this disease, systemic intermittent hypoxia can alter tumour cell behaviour and the tumour microenvironment independent of the other effects of OSA [3]. Most of our knowledge of physiological "intermittent hypoxia" experienced during OSA is based on measurements of arterial oxyhaemoglobin saturation. In the intraoperative setting, SpO_2 and arterial blood gas analysis help clinicians understand oxygen level impairment. Given that hypoxia detection in cancer assumes a prognostic significance in the pre-therapeutic approach, as demonstrated in 15 tumour entities (accessible SCCHNs, breast cancers, cervix cancers, soft tissue sarcomas and primary brain tumours) [2], intraoperative blood oxygen evaluation is important to ensure a stable and continu-

Table 1 Clinical and laboratory findings

	Complicated	Uncomplicated	p
Age (years)	68.75 ± 8.03	65.10 ± 8.79	Ns
Sex (M/F)	24/16	29/24	Ns*
Duration of intervention (h)	4.71 ± 2.02	3.99 ± 1.86	Ns #
Length of ICU stay (days)	2.32 ± 1.93	1.72 ± 1.36	Ns #
Hospitalisation (days)	14.69 ± 11.41	10.70 ± 6.28	<0.05 #
$\Delta EtCO_2$ (mmHg)	3.95 ± 6.07	1.98 ± 3.91	<0.05
$\Delta EtCO_2$ score	0.50 ± 1.20	0.12 ± 0.77	<0.05
ΔSpO_2 (%)	7.00 ± 8.13	5.50 ± 6.10	Ns
ΔSpO_2 score	1.07 ± 1.54	0.73 ± 1.22	Ns
Surgical risk	2.25 ± 0.44	2.26 ± 0.44	Ns #

Values are show as mean ± SD or median for non-parameters variables. *P* values are from t-test and Mann-Whitney indicated with #. Distribution was evaluated by Chi-squared test indicated as *; *Ns* non significant

Table 2 Spearman correlation between ΔEtCO2 score and clinical management in all population studied

	R	P
Duration of intervention	0.17	0.03
Hospitalisation	0.22	0.005

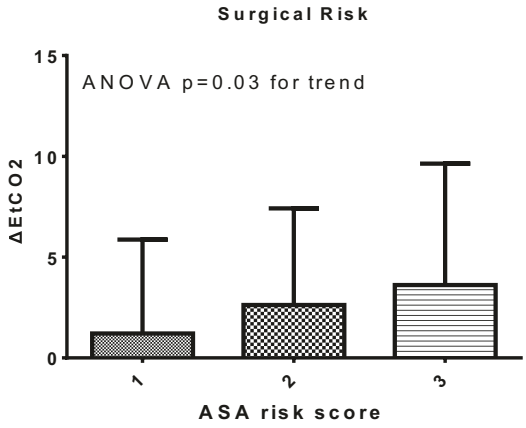

Fig. 1 ΔEtCO2 (mean ± SD) evaluation according to the different increase in perioperative risk (ASA Score)

ous oxygen level for a better postoperative outcome. Therefore, during cancer surgery, it is necessary to determine and monitor both ventilation and circulation.

Monitoring respiratory status using $EtCO_2$, which reliably reflects arterial $PaCO_2$ in intubated patients under general anaesthesia, is a cornerstone of intraoperative patient assessment. Peridiaphragmatic surgery requires management of the high-risk surgical patient throughout the perioperative period using a set of parameters, protocols and user interfaces that facilitate assessment and optimisation of anaesthesia, fluids and drugs. $EtCO_2$ has a variety of uses and has been well documented to be reduced in volume-related hypotensive states where the cardiac output is reduced, meaning that $EtCO_2$ should be able to reflect any systemic hypoperfusion non-invasively and almost immediately [5]. In this view, dynamic vascular changes and related hypoperfusion of different tissues during cancer surgery should influence post-operative complications and tumour cell behaviour.

$\Delta EtCO_2$ may be related to possible complications after surgery and hospitalisation. An important comparison between SpO_2, $EtCO_2$ and strict monitoring using an intraoperative arterial blood gas (ABG) sample during the main steps of surgery could bring some essential information to understand oxygen changes in intra- and post-operative evolution. However, a further validation analysis is needed before the approach can be used extensively in daily clinical settings.

References

1. Brown JM, Giaccia AJ (1998) The unique physiology of solid tumors: opportunities (and problems) for cancer therapy. Cancer Res 58:1408–1416
2. Vaupel P, Flood AB, Swartz HM. Oxygenation status of malignant tumors vs. normal tissues: critical evaluation and updated data source based on direct measurements with po2 microsensors. Appl Magn Reson. Published Online First: 2021. https://doi.org/10.1007/s00723-021-01383-6
3. Hunyor I, Cook KM (2018) Models of intermittent hypoxia and obstructive sleep apnea: molecular pathways and their contribution to cancer. Am J Physiol – Regul Integr Comp Physiol 315:R669–R687. https://doi.org/10.1152/ajpregu.00036.2018
4. Jiang S, Pogue BW, Michaelsen KE et al (2013) Pilot study assessment of dynamic vascular changes in breast cancer with near-infrared tomography from prospectively targeted manipulations of inspired end-tidal partial pressure of oxygen and carbon dioxide. J Biomed Opt 18:076011. https://doi.org/10.1117/1.jbo.18.7.076011
5. Kheng CP, Rahman NH (2012) The use of end-tidal carbon dioxide monitoring in patients with hypotension in the emergency department. Int J Emerg Med 5:1–7. https://doi.org/10.1186/1865-1380-5-31
6. Hocevar LA, Fitzgerald BM (2021) American society of anesthesiologists staging. [Updated 2021 May 9]. In: StatPearls [Internet]. Treasure Island (FL): StatPearls Publishing. Available from: https://www.ncbi.nlm.nih.gov/books/NBK549785/

Pulmonary Embolism in COVID-19 Patients Is Not Related to a Deterioration of Tissue Oxygenation

Sebastiano Cicco, F. Albanese, R. Didonna, A. Magistro, A. Vacca, C. Cariddi, G. Lauletta, F. Pappagallo, A. G. Solimando, and R. Ria

Abstract

Background: COVID-19 induces robust systemic inflammation. One of the main complications is the increased coagulation due to endotheliitis. There is an increased incidence of pulmonary embolism (PE) in COVID-19 patients. However, clinical characteristics for a strict analysis are yet to be determined. Aim**:** We evaluated oxygenation and characteristics in patients with COVID-19 PE (CPE). Material and methods: We evaluated 215 COVID-19 patients from 1 January to 30 April 2021. We found 18 patients affected by PE (CPE, 50.0% males, aged 67.00 ± 10.86 years). As controls, we used data from patients affected by PE evaluated in our ward between 1 January 2015 and 31 December 2019 (64 patients, 53.1% males, aged 70.88 ± 16.44 years). All patients underwent a complete physical examination, pulmonary computerised tomography, laboratory tests, D-dimers and blood gas analysis at the time of diagnosis. Results: There were no differences in laboratory tests nor in D-dimers between the two groups. In the CPE group we found a significantly increased pO_2 (92.83 ± 42.52 vs. 76.11 ± 32.58 mmHg; $p < 0.05$), difference of oxygen between alveoli and arteries (A-aDO_2; 169.3 ± 171.9 vs. 52.97 ± 39.65 mmHg; $p < 0.05$), and oxygen saturation % (97.06 ± 2.59 vs. 93.77 ± 5.53%; $p < 0.05$) compared to controls. No difference was found in pCO_2 and the ratio between pO_2 and percentage of inspired oxygen (P/F). Finally, a significantly decreased urate (3.67 ± 1.49 vs. 5.60 ± 2.10; $p < 0.05$) was found in CPE compared to controls. In CPE, platelets count presents an inverse correlation to P/F ($r = -0.389$, $p = 0.02$) but a direct correlation to A-aDO_2 ($r = 0.699$, $p = 0.001$). No similar findings were present in controls. Discussion: COVID-19 PE appears to have a different clinical setting. Reduced oxygenation described in PE may not to be considered as a sign of disease. The increased A-aDO_2 may indicate that COVID-19 PE involved smaller vessels compared to classical PE. A possible diffuse capillary thrombosis could explain these results.

S. Cicco (✉) F. Albanese · R. Didonna · A. Magistro · G. Lauletta · F. Pappagallo · A. G. Solimando · R. Ria
COVID Section, Unit of Internal Medicine "Guido Baccelli", Department of Biomedical Sciences and Human Oncology, University of Bari, University Hospital Policlinico di Bari, Bari, Italy

A. Vacca
Division of Internal Medicine, Department of Medicine, Building 8, University of Udine, Udine (UD), Italy

C. Cariddi
Dipartimento dell'Emergenza e Trapianti d'Organo (DETO), Sezione di Anestesiologia e Rianimazione, Ospedale Policlinico, University of Bari Aldo Moro, Bari, Italy

F. Scholkmann et al. (eds.), *Oxygen Transport to Tissue XLIII*, Advances in Experimental Medicine and Biology 1395, https://doi.org/10.1007/978-3-031-14190-4_17

Keywords

Severe acute respiratory syndrome coronavirus 2 (SARS-CoV2) · Systemic inflammation · Endotheliitis · Platelet counts

1 Introduction

In 2020, health care systems worldwide faced the challenge of the pandemic triggered by the new severe acute respiratory syndrome coronavirus 2 (SARS-CoV-2). The novel disease caused by the virus was called Coronavirus Disease 2019 (COVID-19). Infection induces robust systemic inflammation [1]. The reduced pulmonary capacity could be a consequence of many different conditions. Cardiovascular involvement is one of the leading factors in clinical deterioration [2–4]. The increase in thrombosis is one of the main complications in COVID-19 as a result of systemic inflammation and endotheliitis [1, 2]. The immune cell activation may induce a release of multiple cytokines and mediators that may induce a possible local thrombosis [1, 5]. There is an increased incidence of pulmonary embolism (PE) in COVID-19 patients [6]. Data on the difference between COVID-19 PE and non-COVID-19 patients are needed. Clinical characteristics for a strict analysis are far to be determined between the two populations. The aim of this study was to evaluate oxygenation and characteristics in COVID-19 PE compared to PE not affected by SARS-CoV-2 infection.

2 Materials and Methods

We evaluated 215 COVID-19 patients admitted to the Internal Medicine department from 1 January to 30 April 2021. We found 18 patients (8.37%) were affected by PE (CPE, 50.0% males, aged 67.00 ± 10.86 years). All of those were dyspneic and received oxygen treatment and antibiotic therapy with Azithromycin after admission. As controls, we used data from patients affected by PE evaluated in our ward between 1 January 2015 and 31 December 2019 (64 patients, 53.1% males, aged 70.88 ± 16.44 years). Both patients from CPE and controls underwent a complete physical examination, chest imaging, laboratory tests, D-dimers and blood gas analysis (BGA) at the time of diagnosis. All patients were evaluated also according to PaO_2/FiO_2 (P/F) ratio. All patients were screened for a deep vein thrombosis (DVT) at admission in our ward using compressive ultrasound. To have a comprehensive and comparable clinical evaluation we calculated the National Early Warning Score (NEWS) including heart rate, respiratory rate, body temperature, systolic blood pressure, Glasgow coma scale, oxygen saturation percentage, and oxygen given.

SARS-CoV-2 infection was diagnosed after a positive nasal-throat swab test.

Both CPE and controls had a good haemodynamic status, thus low molecular weight heparin was given, as indicated in the 2019 European Society of Cardiology (ESC) guidelines for PE [7]. As standard treatment we used enoxaparin 100 U/kg twice a day for PLT count more than 50,000 cells/mm^3 and glomerular filtration rate > 30 ml/min.

Statistical analysis was performed with GraphPad Prism® 6 considering a p-value <0.05 as significant. After a normality distribution test, value were classified as parametric or not. Parametric values were presented as mean and standard deviation and they were analysed using Student t-test comparison and Pearson correlation. Non-parametric values were compared using Mann-Whitney and Spearman correlation and were presented as median and interquartile range.

3 Results

No DVT was found in CPE patients while it was described in 30 (47.62%) controls. In the CPE group, 5 (27.78%) were hypertensives, 3 (16.67%) diabetes, and 2 (11.11%) presented with an active tumour.

There was no difference in the NEWS score (median 2 [2, 3] vs. 2 [2–4]; p = ns). No differences were found in laboratory tests nor in D-dimers between the two groups (Table 1).

Table 1 Laboratory findings

	CPE	Controls	P value
Hb (gr/dl)	12.40 ± 1.55	11.72 ± 2.04	Ns
WBC (×10^3 cells/ml)	9.74 ± 3.29	9.14 ± 4.90	Ns
PLT (cells/ml)	249.6 ± 85.9	242.1 ± 138.0	Ns
N%	79.99 ± 11.92	73.31 ± 13.82	Ns
L%	13.96 ± 8.85	18.08 ± 9.77	Ns
NLR	8.82 ± 6.22	7.09 ± 7.78	Ns
PLT	250.5 ± 131.3	219.5 ± 148.1	Ns
D-dimer	6663 ± 9459	6445 ± 11,354	Ns
C-reactive protein	91.15 ± 69.39	68.99 ± 73.77	Ns
Uric acid (mg/dl)	3.67 ± 1.49	5.59 ± 2.10	**<0.05**

Values are show as mean ± SD or median for non-parameters variables. P values are from t test

In the CPE group we found a significantly increased pO_2 (92.83 ± 42.52 vs. 76.11 ± 32.58 mmHg; $p < 0.05$), a difference in oxygen between alveoli and arteries (A-aDO_2; 169.3 ± 171.9 vs. 52.97 ± 39.65 mmHg; $p < 0.05$), and oxygen saturation percentage at BGA (97.06 ± 2.59 vs. 93.77 ± 5.53%; $p < 0.05$) compared to controls. There was no difference in pCO_2 and the ratio between pO_2 and percentage of inspired oxygen (P/F) (Table 2). Finally a significantly decreased urate (3.67 ± 1.49 vs. 5.60 ± 2.10; $p < 0.05$) was found in CPE compared to controls.

In CPE, platelets count presents an inverse correlation to P/F ($r = -0.389$, $p = 0.02$) but a direct correlation to A-aDO_2 ($r = 0.699$, $p = 0.001$) (Fig. 1a). No similar findings were present in controls (Fig. 1b).

4 Discussion

Pulmonary embolism can be a real life-threating condition [7]. In SARS-CoV-2 infection endotheliitis may induce an activation of thrombosis [8]. Vascular endothelium is one of the main targets of the virus [2] due its entry properties via angiotensin converting enzyme 2 (ACE2). This activation is mostly a consequence of immune cell infiltration and cytokine release [1]. The consequent inflammation induces the activation of the coagulative cascade [8]. In recent large study, it has been demonstrated that PE in COVID-19 disease is mostly described in smaller vessel compared to non-COVID-19 PE [9].

The increase in pO_2 of our CPE should be a consequence of the patients evaluated. In fact, due to the health organization in Apulia, more severe patients were hospitalized in intensive care units. Our patients presented a less severe phenotype and both CPE patients and controls underwent oxygen treatment. However, P/F was not different between the two groups despite presenting a statistical tendency toward significance.

In our patients we found that the increase in PLT value correlates to two respiratory parameters evaluated in CPE. The increase in PLT is mostly a consequence of the systemic inflammatory state. The cytokine release induces an acute increase in PLT. The direct correlation to the increase in alveolar-capillary interface and the inverse correlation to P/F ratio may be all part of the same inflammatory mechanism. Therefore, the key role of inflammation is still the masterpiece of this disease. This is supported by the increased CRP value in CPE, despite the value results not being significantly different to controls, perhaps due to the large deviation we found.

The main limitation of this study is that a single centre collected data.

In conclusion, COVID-19 PE appears to have a different clinical setting. Reduced oxygenation described in PE may not to be considered as a sign of disease. The increased A-aDO_2 may indicate that COVID PE involved smaller vessels

Table 2 Blood gas analysis results between the two groups

	CPE	Controls	p
pO_2 (mmHg)	92.83 ± 42.52	76.11 ± 32.58	<0.05
pCO_2 (mmHg)	37.44 ± 11.23	35.33 ± 7.38	Ns
SO_2 (%)	97.06 ± 2.59	93.77 ± 5.53	<0.05
A-aDO_2 (mmHg)	169.3 ± 171.9	52.97 ± 39.65	<0.05
P/F	268.5 ± 151.8	331.0 ± 128.2	0.10

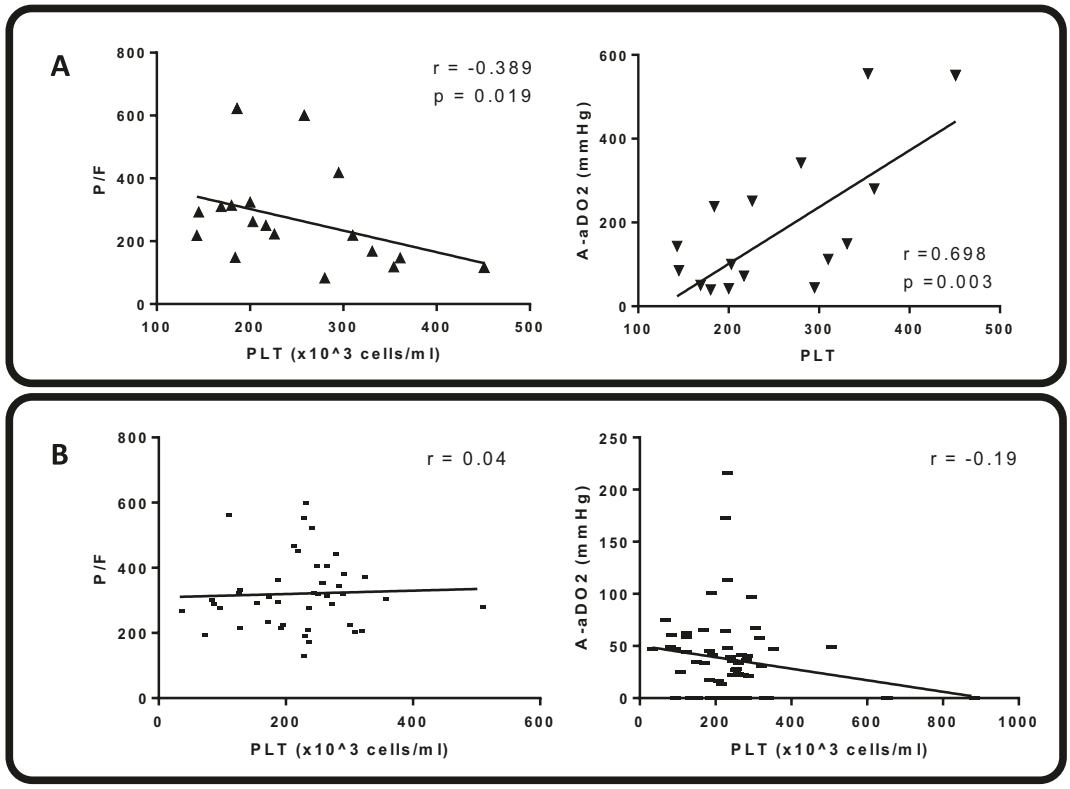

Fig. 1 Correlation between platelet count (PLT) value and P/F and alveolar-artery oxygen difference in patients affected by COVID-19 (panel A) and non-COVID-19 (panel B) pulmonary embolism

compared to classical PE. A possible diffuse capillary thrombosis could explain these results.

References

1. Cicco S, Cicco G, Racanelli V et al (2020) Neutrophil Extracellular Traps (NETs) and Damage-Associated Molecular Patterns (DAMPs): two potential targets for COVID-19 treatment. Mediat Inflamm 2020:1–25. https://doi.org/10.1155/2020/7527953
2. Cicco S, Vacca A, Cariddi C et al (2021) Imaging evaluation of pulmonary and non-ischaemic cardiovascular manifestations of COVID-19. Diagnostics 11:1271. https://doi.org/10.3390/diagnostics11071271
3. Mozzini C, Cicco S, Setti A et al (2021) Spotlight on cardiovascular scoring systems in Covid-19: severity correlations in real-world setting. Curr Probl Cardiol 46:100819. https://doi.org/10.1016/j.cpcardiol.2021.100819
4. Cicco S, Vacca A, Cittadini A et al (2020) Long-term follow-up may be useful in coronavirus disease 2019 survivors to prevent chronic complications. Infect Chemother 52:407. https://doi.org/10.3947/ic.2020.52.3.407
5. Mozzini C, Girelli D (2020) The role of neutrophil extracellular traps in Covid-19: only an hypothesis or a potential new field of research? Thromb Res 191:26–27. https://doi.org/10.1016/j.thromres.2020.04.031
6. Grillet F, Behr J, Calame P et al (2020) Acute pulmonary embolism associated with COVID-19 pneumonia detected with pulmonary CT angiography.

Radiology 296:E186–E188. https://doi.org/10.1148/radiol.2020201544

7. Konstantinides SV, Meyer G, Becattini C et al (2019) ESC guidelines for the diagnosis and management of acute pulmonary embolism developed in collaboration with the European Respiratory Society (ERS). Eur Heart J 2019:1–61. https://doi.org/10.1093/eurheartj/ehz405
8. Bonaventura A, Vecchié A, Dagna L et al Endothelial dysfunction and immunothrombosis as key pathogenic mechanisms in COVID-19. Nat Rev Immunol. Published Online First: 6 Apr 2021. https://doi.org/10.1038/s41577-021-00536-9
9. Miró Ò, Jiménez S et al (2021) Pulmonary embolism in patients with COVID-19: incidence, risk factors, clinical characteristics, and outcome. Eur Heart J 42:3127–3142. https://doi.org/10.1093/eurheartj/ehab314

Cardiovascular Risk Score and Pulmonary Gas Exchange in COVID-19 Patients Show No Correlation

Sebastiano Cicco, C. Mozzini, R. Carella, G. De Fazio, A. Vacca, C. Cariddi, A. Setti, F. Pappagallo, A. G. Solimando, and R. Ria

Abstract

Background: COVID-19 induces robust systemic inflammation. Patients with cardiovascular disease (CVD) are at an increased risk of death. However, much effort is being spent to identify possible predictors of negative outcomes in order to have a more specific clinical setting. CVD scores are a useful tool in evaluating risk of cardiovascular events. Aim: We evaluated oxygenation and characteristics in COVID-19 patients according to cardiovascular risk stratification performed using the Framingham risk score (FRS) for cardiovascular disease. Materials and methods: We evaluated 155 COVID-19 patients (110 males and 45 females, aged 67.43 ± 14.72 years). All patients underwent a complete physical examination, chest imaging, laboratory tests and blood gas analysis at the time of diagnosis. Seventeen patients died (10 males and 7 females, aged 74.71 ± 7.23 years) while the remaining 138 patients (100 males and 38 females, aged 66.07 ± 15.16 years) were alive at discharge. Results: Deceased patients have an increased FRS compared to those that survived (27.37 ± 5.03 vs. 21.33 ± 9.49, $p < 0.05$). Compared to survivors, the deceased group presents with a significant increase in white blood cells ($p < 0.05$) and D-dimers ($p < 0.05$). There was no difference in pCO_2, SO_2, and in alveolar arteriolar oxygen difference ($A\text{-}aDO_2$). On the contrary, in deceased patients there was an increased pO_2 ($p < 0.05$) and a decreased ratio between oxygen inspired and pO_2 (P/F; $p < 0.05$). FRS shows a negative correlation to P/F ($r = 0.42$, $p < 0.05$) in the

S. Cicco (✉)
COVID Section, Unit of Internal Medicine "Guido Baccelli", Department of Biomedical Sciences and Human Oncology, University of Bari, Bari, Italy

Unit of Internal Medicine "Guido Baccelli", Department of Biomedical Sciences and Human Oncology, University of Bari, University Hospital Policlinico di Bari, Bari, Italy

C. Mozzini
Department of Medicine, Section of Internal Medicine, Carlo Poma Hospital, Mantova, Italy

R. Carella · G. De Fazio · F. Pappagallo · A. G. Solimando · R. Ria
COVID Section, Unit of Internal Medicine "Guido Baccelli", Department of Biomedical Sciences and Human Oncology, University of Bari, Bari, Italy

A. Vacca
Division of Internal Medicine, Department of Medicine, Building 8, University of Udine, Udine (UD), Italy

C. Cariddi
Dipartimento dell'Emergenza e Trapianti d'Organo (DETO), Sezione di Anestesiologia e Rianimazione, Ospedale Policlinico, University of Bari Aldo Moro, Bari, Italy

A. Setti
Department of Medicine, Section of Internal Medicine, University of Verona, Verona, Italy

F. Scholkmann et al. (eds.), *Oxygen Transport to Tissue XLIII*, Advances in Experimental Medicine and Biology 1395, https://doi.org/10.1007/978-3-031-14190-4_18

deceased while no correlation was found in the survivors. No other correlation has been found with blood gas parameters or in the inflammation parameters evaluated in the two groups. Discussion: CVD may be considered as a major risk factor for death in COVID-19 patients. The increased risk relates to a reduced lung capacity but it is not related to blood gas values. Similarly, CV risk score results are independent from the inflammatory status of the patients.

Keywords

Severe acute respiratory syndrome coronavirus 2 (SARS-CoV2) · Systemic inflammation · Framingham risk score · Cardiovascular disease · Endothelial damage

1 Introduction

In 2020, health care systems worldwide faced the challenge of the pandemic triggered by the new severe acute respiratory syndrome coronavirus 2 (SARS-CoV-2). The novel disease caused by the virus was called Coronavirus Disease 2019 (COVID-19). Infection induces robust systemic inflammation [1, 2]. The reduced pulmonary capacity is a consequence of many different conditions. Cardiovascular involvement is one of the leading factors for clinical deterioration and cardiovascular disease (CVD) patients are at an increased death risk [3–5]. This complication in COVID is mostly induced by systemic inflammation and endotheliitis [1, 3]. Much effort is being spent to identify possible predictors of negative outcomes in order to have a more specific clinical setting. CVD scores are a useful tool in evaluating the risk of cardiovascular events [6]. First reports showed clinical derioration according to the increase in CVD risk score [4]. A first report on the use of the Framingham risk score (FRS) in COVID patients confirmed that highest scores were more at risk of a fatal CV event [7].

The aim of this study was to evaluate oxygenation and characteristics in COVID-19 patients according to cardiovascular risk stratification performed using FRS for cardiovascular disease comparing patients who died and who were alive at discharge.

2 Materials and Methods

Out of 530 COVID-19 patients, we evaluated 155 (110 males and 45 females, aged 67.43 ± 14.72 years) admitted to the Internal Medicine department from 1 January to 30 April 2021.

All of them were dyspneic, received oxygen treatment and antibiotic therapy with Azithromycin after admission. All patients underwent a complete physical examination, chest imaging, laboratory tests, D-dimers and blood gas analysis (BGA) at the time of diagnosis. Patients with suspected pulmonary embolism were evaluated by a chest angiographic study using computerised tomography and were excluded from this study. Similarly, we excluded patients with known history of ischemic CVD or stroke. All patients were evaluated also according to PaO_2/FiO_2 (P/F) ratio. FRS was evaluated at admission.

SARS-CoV-2 infection was diagnosed after a positive nasal-throat swab test.

As standard treatment we used Dexametasone 20 mg/day iv and enoxaparin 4000 UI once a day for PLT counts of more than 50,000 cells/mm^3 and glomerular filtration rate > 30 ml/min in primary prevention.

Seventeen patients died (10 males and 7 females, aged 74.71 ± 7.23 years) while the remaining 138 patients (100 males and 38 females, aged 66.07 ± 15.16 years) were alive at discharge.

Statistical analysis was performed with GraphPad Prism® 6 considering a p-value <0.05 as significant. After a normality distribution test, values were classified as parametric or not. Parametric values were presented as mean and standard deviation and were analysed using Student t-test comparison and Pearson correlation. Non-parametric values were compared using Mann-Whitney and Spearman correlation and were presented as median and interquartile range.

3 Results

Deceased patients had increased FRS compared to survivors (27.37 ± 5.03 vs. 21.33 ± 9.49, $p < 0.05$) (Fig. 1). No differences were found in Hb, NLR, and C-reactive protein (CRP) (Table 1).

Compared to survivors, the deceased group presents with a significant increase in white blood cells ($p < 0.05$) and D-dimers ($p < 0.05$) (Table 1). There was no difference in pCO_2, SO_2, and in alveolar arteriolar oxygen difference ($A\text{-}aDO_2$). On the contrary, in deceased patients there is an increased pO_2 ($p < 0.05$) and a decreased ratio between inspired oxygen and pO_2 (P/F; $p < 0.05$) (Table 1).

FRS presents a negative correlation to P/F (r-0.42, $p < 0.05$) in dead patients while no correlation was found in survivors (Fig. 2). No other correlations have been found with blood gas parameters or in the inflammation parameters evaluated in the two groups.

4 Discussion

CVD is the main comorbidity in COVID patients [8]. Moreover, CVD represents one of the leading causes of death [9] and patients with CV involvement are more prone to a fatal outcome [10]. In this view, the identification of a simple tool to stratify patients according to CVD may be useful as an early evaluation of patients that may have a fatal outcome.

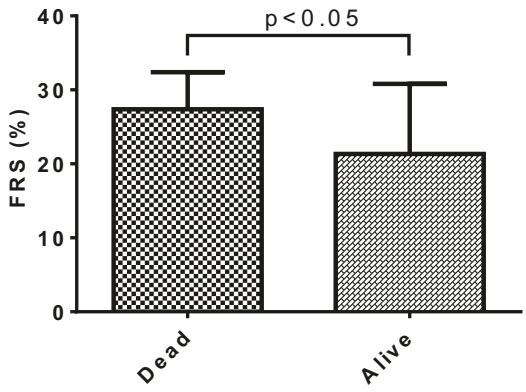

Fig. 1 Differences in Framingham Risk Score values in the two groups. Analysis: Student t-test

Endothelial damage is a cornerstone of CVD. In fact, there is a direct correlation between endothelial dysfunction and cardiovascular damage as well as between endothelial damage and CVD risk evaluated with FRS [11]. Moreover, tissue oxygenation is particularly challenging in COVID-19 and may induce cardiovascular damage, both acute [12] and chronic [3].

The endothelium is involved in disease in SARS-CoV-2 infection [3]. In COVID-19 patients diffuse vascular damage occurs in parallel to lung disease [13]. It has been also demonstrated that there is an endothelial senescence in these patients [14] as a consequence of reactive oxygen species and inflammation [1, 15, 16]. Therefore, a possible use of FRS in predicting clinical deterioration may be related to the change in blood gases.

The increase in cardiovascular involvement by SARS-CoV-2 virus is related to inflammation evaluated by CRP in first Chinese reports [10]. However, we found that there was no difference between deceased and survivors' CRP and no correlation to FRS. On the contrary, NLR results dramatically increased in those who died compared to those who survived, indicating huge inflammation. This inflammatory burst also explains the increase in D-dimers without a pulmonary embolism.

We also found an inverse correlation between FRS and P/F. This is an impressive result. To date, no previous research described this correlation. We can speculate about a possible role of CVD inducing a reduction of lung capacity. In fact, in the deceased group there was an increase in FRS as well as a reduced P/F. However, the correlation between the two parameters stressed how the lung-cardiovascular connection may result as a cornerstone in understanding the SARS-CoV-2 effects on the host.

We found an increase in pO_2 at admission in patients who died. This is related most to oxygen treatment performed. Despite these were not intensive care patients, severe COVID need high flow oxygen. Therefore, P/F is an accurate evaluation of lung function more than pO_2. Moreover, the normal arterial pO_2 value may not be sufficient to reduce the tissue hypoxia. The lack in

Table 1 Clinical and laboratory findings

	Dead	Alive	p value
WBC (cells/ml)	10.7 ± 3.9	7.32 ± 4.9	<0.05
Hb (gr/dl)	12.6 ± 2.3	12.9 ± 2.5	Ns
NLR	18.9 ± 17.8	8.2 ± 7.6	<0.0001
D-dimers (mg/dl)	6122 ± 14,312	2547 ± 7528	<0.05
CRP (mg/dl)	137.1 ± 115.2	162.0 ± 185.8	Ns
pCO_2 (mmHg)	35.2 ± 5.3	35.2 ± 4.7	Ns
pO_2 (mmHg)	114.3 ± 89.5	87.5 ± 35.1	<0.05
SaO_2 (%)	95.8 ± 2.2	96.9 ± 2.9	Ns
A-aDO_2 (mmHg)	118.0 ± 117.2	182.3 ± 142.9	Ns
P/F	153.6 ± 94.0	248.4 ± 112.2	<0.05

Values are show as mean ± SD. P values are from t test

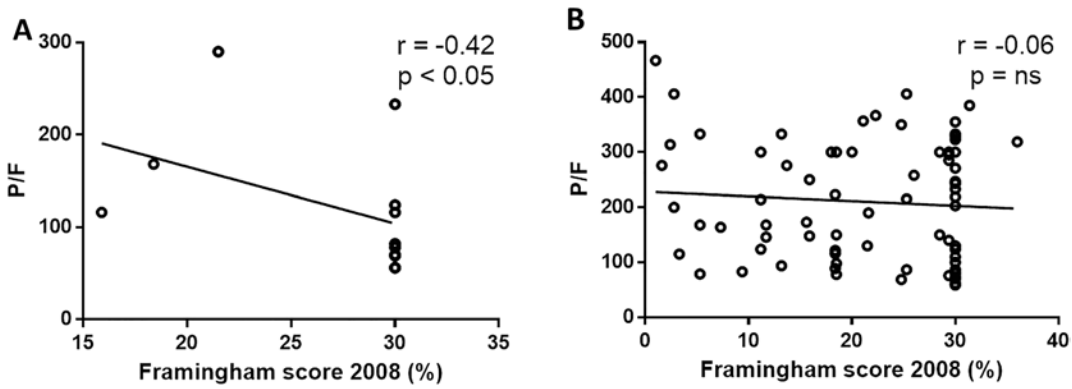

Fig. 2 Correlation between Framingham Risk Score 2008 and P/F values in deceased (panel A) and surviving (panel B) patients

correlation between FRS and admission evaluation of pO_2 or A-aDO_2 may indicates that not only hypoxic burden may influence the CVD worsening in COVID-19.

Further studies are needed to understand how to reduce the ischemia/hypoxic burden effect on cardiovascular system. COVID-19 has served as a great teacher in helping us to understand this regulation.

In conclusion, CVD may be considered as a major risk factor for death in COVID-19 patients. The increased risk relates to a reduced lung capacity but it is not related to alterations in blood gas values. Similarly, CV risk score results are independent of the inflammatory status of the patients.

References

1. Cicco S, Cicco G, Racanelli V, Vacca A (2020) Neutrophil Extracellular Traps (Nets) and Damage-Associated Molecular Patterns (DAMPs): two potential targets for COVID-19 treatment. Mediat Inflamm 2020:1–25. https://doi.org/10.1155/2020/7527953
2. Mozzini C, Girelli D (2020) The role of neutrophil extracellular traps in Covid-19: only an hypothesis or a potential new field of research? Thromb Res 191:26–27. https://doi.org/10.1016/j.thromres.2020.04.031
3. Cicco S, Vacca A, Cariddi C, Carella R, Altamura G, Solimando AG, Lauletta G, Pappagallo F, Cirulli A, Stragapede A et al (2021) Imaging evaluation of pulmonary and non-ischaemic cardiovascular manifestations of COVID-19. Diagnostics 11:1271. https://doi.org/10.3390/diagnostics11071271
4. Mozzini C, Cicco S, Setti A, Racanelli V, Vacca A, Calciano L, Pesce G, Girelli D (2021) Spotlight on cardiovascular scoring systems in Covid-19: severity correlations in real-world setting. Curr

Probl Cardiol 46:100819. https://doi.org/10.1016/j.cpcardiol.2021.100819
5. Cicco S, Vacca A, Cittadini A, Marra AM (2020) Long-term follow-up may be useful in coronavirus disease 2019 survivors to prevent chronic complications. Infect Chemother 52:407. https://doi.org/10.3947/ic.2020.52.3.407
6. D'Agostino RB, Vasan RS, Pencina MJ, Wolf PA, Cobain M, Massaro JM, Kannel WB (2008) General cardiovascular risk profile for use in primary care: the Framingham heart study. Circulation 117:743–753. https://doi.org/10.1161/CIRCULATIONAHA.107.699579
7. Batty GD, Hamer M (2020) Vascular risk factors, framinghamrisk score, and covid-19: community-based cohort study. Cardiovasc Res 116:1664–1665. https://doi.org/10.1093/cvr/cvaa178
8. Shi S, Shi S, Shi S, Qin M, Cai Y, Liu T, Liu T, Liu T, Shen B, Shen B et al (2020) Characteristics and clinical significance of myocardial injury in patients with severe coronavirus disease 2019. Eur Heart J 41:2070–2079. https://doi.org/10.1093/eurheartj/ehaa408
9. Meintrup D, Borgmann S, Seidl K, Stecher M, Jakob CEM, Pilgram L, Spinner CD, Rieg S, Isberner N, Hower M et al (2021) Specific risk factors for fatal outcome in critically ill COVID-19 patients: results from a European multicenter study. J Clin Med 10:3855. https://doi.org/10.3390/jcm10173855
10. Guo T, Fan Y, Chen M, Wu X, Zhang L, He T, Wang H, Wan J, Wang X, Lu Z (2020) Cardiovascular implications of fatal outcomes of patients with coronavirus disease 2019 (COVID-19). JAMA Cardiol 5:811–818. https://doi.org/10.1001/jamacardio.2020.1017
11. Campuzano R, Moya JL, García-Lledó A, Tomas JP, Ruiz S, Megías A, Balaguer J, Asín E (2006) Endothelial dysfunction, intima-media thickness and coronary reserve in relation to risk factors and Framingham score in patients without clinical atherosclerosis. J Hypertens 24:1581–1588. https://doi.org/10.1097/01.hjh.0000239294.17636.27
12. Esposito L, Cancro FP, Silverio A, Di Maio M, Iannece P, Damato A, Alfano C, De Luca G, Vecchione C, Galasso G (2021) COVID-19 and acute coronary syndromes: from pathophysiology to clinical perspectives. Oxidative Med Cell Longev 2021:1–13. https://doi.org/10.1155/2021/4936571
13. Dupont A, Rauch A, Staessens S, Moussa M, Rosa M, Corseaux D, Jeanpierre E, Goutay J, Caplan M, Varlet P et al (2021) Vascular endothelial damage in the pathogenesis of organ injury in severe COVID-19. Arterioscler Thromb Vasc Biol 41:1760–1773. https://doi.org/10.1161/ATVBAHA.120.315595
14. Meyer K, Patra T, Vijayamahantesh, Ray R (2021) SARS-CoV-2 spike protein induces paracrine senescence and leukocyte adhesion in endothelial cells. J Virol 95. https://doi.org/10.1128/jvi.00794-21
15. Levy JH, Iba T, Gardiner EE (2021) Endothelial injury in COVID-19 and acute infections: putting the pieces of the puzzle together. Arterioscler Thromb Vasc Biol 41:1774–1776. https://doi.org/10.1161/ATVBAHA.121.316101
16. Fodor A, Tiperciuc B, Login C, Orasan OH, Lazar AL, Buchman C, Hanghicel P, Sitar-Taut A, Suharoschi R, Vulturar R et al (2021) Endothelial dysfunction, inflammation, and oxidative stress in COVID-19—mechanisms and therapeutic targets. Oxidative Med Cell Longev 2021:1–15. https://doi.org/10.1155/2021/8671713

Heme Oxygenase-1/High Mobility Group Box 1 Pathway May Have a Possible Role in COVID-19 ARDS (Acute Respiratory Distress Syndrome): A Pilot Histological Study

G. Cicco, S. Sablone, G. Cazzato, S. Cicco, G. Ingravallo, F. Introna, and A. Cossarizza

Abstract

COVID-19 is a pandemic disease caused by the severe acute respiratory syndrome coronavirus 2 (SARS-CoV-2). The persistent and excessive inflammatory response can build up a clinical picture that is difficult to manage and potentially fatal. Potent activators of inflammatory phenomena are damage-associated molecular patterns (DAMPs) and, in particular, the high-mobility group box 1 (HMGB1). HMGB1 is an intranuclear protein that is either passively released during hypoxia-related necrosis or actively released by macrophages. Heme oxygenase (HO-1) has an anti-inflammatory effect by inhibiting HMGB1, which could be a therapeutic target to reduce COVID-19 inflammation. In our study, we evaluated CD3, CD4, CD8, HMGB1 and HO-1 in the COVID-19 lung and correlated it to clinical data.

Keywords

Severe acute respiratory syndrome coronavirus 2 (SARS-CoV2) · Damage-associated molecular patterns (DAMPs) · Respiratory failure · Inflammation · Cytokine storm

1 Introduction

COVID-19 is a pandemic challenge caused by the severe acute respiratory syndrome coronavirus 2 (SARS-CoV-2) [1] that is currently imposing heavy stress on many health systems worldwide. SARS-CoV-2 belongs to the coronavirus family that includes the Severe Acute Respiratory Syndrome Coronavirus type 1

G. Cicco (✉)
School of Clinical Pathology and Clinical Biochemistry, Department of Medical and Surgical Sciences for Children and Adults, University of Modena and Reggio Emilia, Modena, Italy

Section of Pathology, University of Bari 'Aldo Moro', Bari, Italy

S. Sablone · F. Introna
Section of Legal Medicine, University of Bari 'Aldo Moro', Bari, Italy

G. Cazzato · G. Ingravallo
Section of Pathology, University of Bari 'Aldo Moro', Bari, Italy

S. Cicco
COVID Section, Unit of Internal Medicine "Guido Baccelli", Department of Biomedical Sciences and Human Oncology, University of Bari, Bari, Italy

A. Cossarizza
School of Clinical Pathology and Clinical Biochemistry, Department of Medical and Surgical Sciences for Children and Adults, University of Modena and Reggio Emilia, Modena, Italy

F. Scholkmann et al. (eds.), *Oxygen Transport to Tissue XLIII*, Advances in Experimental Medicine and Biology 1395, https://doi.org/10.1007/978-3-031-14190-4_19

(SARS-CoV) and Middle East Respiratory Syndrome (MERS-CoV) viruses. Coronaviruses have a preferential tropism for lung cells [2]. SARS-CoV-2 is known to use the same receptor as SARS-CoV to enter the host cell, namely, angiotensin-converting enzyme II (ACE2) [2]. Acute SARS-CoV-2 patients present with a wide range of clinical manifestations, ranging from asymptomatic or mildly symptomatic (common cold) up to severe, often fatal disease. The latter form usually presents with bilateral interstitial pneumonia and moderate to severe oxygen desaturation and hypoxia. Many patients develop respiratory failure (RF) and acute respiratory distress syndrome (ARDS) [3], requiring prompt admission to the intensive care unit (ICU). Unlike the usual ARDS, these patients show a normal or slightly increased lung compliance and mostly need high-flow oxygen or continuous positive airway pressure (CPAP) ventilation [4]. The ventilation outcome of SARS-CoV-2 pneumonia is similar to the one described in the respiratory failure in interstitial lung disease [5]. Damaged tissues and neutrophils themselves both produce cytokines that enhance neutrophil activity. In fact, cytokines are produced after SARS-CoV-2 infection. Their action will play a role in the chemotactic recruitment of neutrophils, enhancing formation of reactive oxygen species and neutrophil extracellular traps (NET). The induction of NETosis is also due to other molecules secreted by damaged tissues such as damage-associated molecular patterns (DAMPs) [6].

These endogenous self-antigens, such as HMGB1 and heat shock proteins (HSPs), activate signalling of mitogen-activated protein kinases (MAPKs) and nuclear factor of kappa light polypeptide gene enhancer in B-cells (NF-κB), which trigger the inflammatory response [7, 8]. HMGB1 is a chromatin-associated protein formed by two domains connected by a nine-amino acid loop and a highly disordered negatively charged C-terminal tail [9, 10]. It performs different functions depending on its cellular localisation. As a nuclear protein, it is involved in DNA repair, transcription, and genome stability [11, 12], while during cellular death or inflammation, it is released into the extracellular space where it is classified as an alarmin [13, 14]. It induces the release of inflammatory cytokines such as tumour necrosis factor (TNF), interleukin- (IL-) 1β, and IL-12 that aggravate acute tissue damage. In acute lung diseases, HMGB1 acts as an activator of innate immunity, leading to the production of IL-1β, IL-6, and TNF-α. Heme oxygenase-1 (HO-1) is an inducible microsomial enzyme that catalyses the degradation of heme. This produces biliverdin, ferrous iron, and carbon monoxide [15, 16]; scientific evidence highlighted an inverse relation between HO-1 and HMGB1 level [17]. The expression of heme oxygenase seems to have a defence activity against pulmonary viruses [18, 19]. Additionally, the COVID-19-related heme reduction may contribute to even lower HO-1. Low-grade inflammation associated with these risk factors contributes to triggering a cytokine storm that spreads to multi-organ failure and near death. The high mortality of those treated with ventilator assistance may partially be explained by ventilator-induced inflammation [20].

2 Methods

A retrospective study was made on 13 consecutive cases. Seven cases of lung tissue from autopsies of deceased COVID-19 patients (group 1) were compared with 6 consecutive cases of lung specimen from patients died from pulmonary emphysema (group 2). In the first group, clinical parameters were collected at the time of demise: Age, Sex, SpO_2, D-Dimers, complete blood cell count, LDH and NLR (Ratio between peripheral neutrophil count and lymphocytes) (Table figure 1). Excisional biopsy samples were obtained for histological examination, fixed in neutral 10% buffered formalin, dehydrated, and included in paraffin. From the paraffinated blocks, 5 μm slices were taken, deparaffinated, rehydrated and routinely stained with hematoxylin-eosin. Immunohistochemistry was then performed using antibodies for the following markers: **anti-CD3** mouse monoclonal Ab (mAb), code NCL-L-CD3- 565, (Novocastra Laboratories Ltd. Leica Biosystems, Buffalo Grove, IL, USA),

diluted 1:200 **anti-CD4**: mouse monoclonal Ab (mAb), code M7310, (DAKO, Carpinteria, CA, USA), diluted 1:50; **anti-CD8**: mouse monoclonal Ab (mAb), code NCLCD8-295, (Novacastra Laboratories Ltd.), diluted 1:50, **anti-HMGB1**: Rabbit polyclonal Ab, Ab18256, (Abcam), diluted 1:1000, **Anti-Heme oxygenase-1** (HO-1): Rabbit Polyclonal Ab, GeneTex, GTX101147, diluted 1:500. The blocks had been pretreated using the PT-LINK (DAKO) device, with EDTA [EnVision Flex, target retrieval solution, High Ph (50×), DAKO] for antibodies for CD3,CD4, CD8, and Citrate [EnVision Flex, target retrieval solution, Low Ph (50×), DAKO] for the HMGB1, OH1 antibodies. The immunohistochemical reactions were read, investigating the cell density for the CD3,CD4 and CD8 markers by counting positive cells in 10 fields (HPF) for each clinical case. A Reichert Polyvar 2 microscope was employed with a JTV digital telecamera and Trinitron monitor, Sony. Each field was examined at 400× magnification; the size of each field was 140 μm in length by 110 μm in width, the total amplitude of the field being 15,400 μm^2. Assessment of the expression of HMGB1 and HO-1 was done by highlighting the chromogen signal on the plasma membrane, in the nucleus, cytoplasm or extracellular medium of the samples analysed. For HMGB1, HO-1, a score given by the sum of the score for the different degrees of staining intensity (grade 0 = no staining; grade 1 = weak staining; grade 2 = moderate staining; grade 3 = intense staining) plus the score for the percentage of extension of the mass (score 0: <1%; score 1: 1–25%; score 2: 26–50%; score 3: 51–74%; score 4: ≥75%). The final score (sum of the 2 previous scores) was considered high if >3, and low if ≤3. The peritumoral cellular infiltrate was assessed in the same way.

Statistical analysis was carried out using the Prism 6 program, GraphPad software, La Jolla (USA). The mean and standard deviation values for the 10 fields were taken for each patient. The distribution of dichotomous values was analysed using Chi-squared test. The Kolmogorov-Smirnov test was applied to assess normal distribution. Nonparametric statistics were used for non-normally distributed data (the Mann-Whitney test for comparisons and Spearman distribution for correlation). Parametric statistics were used for normally distributed data: unpaired t test was used for comparison between groups and Pearson distribution for correlation. P-values are shown only for statistically significant comparisons. Survival comparison was made with the log-rank method (presented as Kaplan–Meier curves). P-values <0.05 were considered significant.

3 Results

Clinical characteristics of Group 1-2 were reported in Table in figure 1

CD3+ lymphocyte expression values were significantly increased in Group 1 (First Group 2.57 ± 0.79 cells/mm^2 vs. Second Group1.71 ± 0.49 cells/mm^2; P = 0.03). This result is mostly related to the significantly increased **CD8+** lymphocyte expression in Group 1 (First Group 2.86 ± 0.69 cells/mm^2 vs. Second Group 1.83 ± 0.75 cells/mm^2; P = 0.04), but not in **CD4+** (First Group 2.71 ± 0.95 cells/mm^2 vs. Second Group 2.80 ± 0.45 cells/mm^2; P = ns).

In group 1 we found a significant decrease of **HO-1** (First Group 2.71 ± 0.76 signals/mm^2 vs. Second Group 4.80 ± 0.45 signals/mm^2; P = 0.0025) (Fig. 1-2A) and an increased expression of **HMGB1** (First Group 4.83 ± 0.75 signals/mm^2 vs. Second Group 2.80 ± 0.45 signals/mm^2; P = 0.0022) (Fig. 1-2B). In Group 1 we found that HMGB1 showed an inverse correlation with HO-1 (r = −0.433; p = 0.0075). Furthermore, in group 1 there was a direct correlation between HMGB1 and SpO_2 (r = 0.689; P = 0.018) while there was an inverse correlation between HMGB1 and NLR (r = −0.775, P = 0.0001). Moreover, HO-1 presented an inverse correlation with age (r = −0.759; P = 0.0022) but not to SpO_2 and NLR. Finally, HO-1 but not HMGB1 showed a weak inverse correlation (r = −0.289; p = 0.049) to CD3+ T lymphocyte count in group 1. No correlation was found in Group 2.

Correlation between HMGB1 and HO1 into the two studied groups								
	Group 1				Group 2			
	HMGB1		HO1		HMGB1		HO1	
	r	P	r	p	R	p	r	p
HO1	-0.43	0.007	-	-	-0.25	Ns	-	-
HMGB1	-	-	-0.43	0.007	-	-	-0.25	Ns
CD3+	-0.22	Ns	-0.29	0.030	0.25	Ns	0.004	Ns
Age	-0.235	Ns	-0.76	0.0007	0.01	Ns	0.70	Ns
SpO2	0.69	0.019	-0.09	Ns	0.26	Ns	0.25	Ns
NLR	-0.785	<0.001	-0.34	Ns	0.23	Ns	0.26	Ns

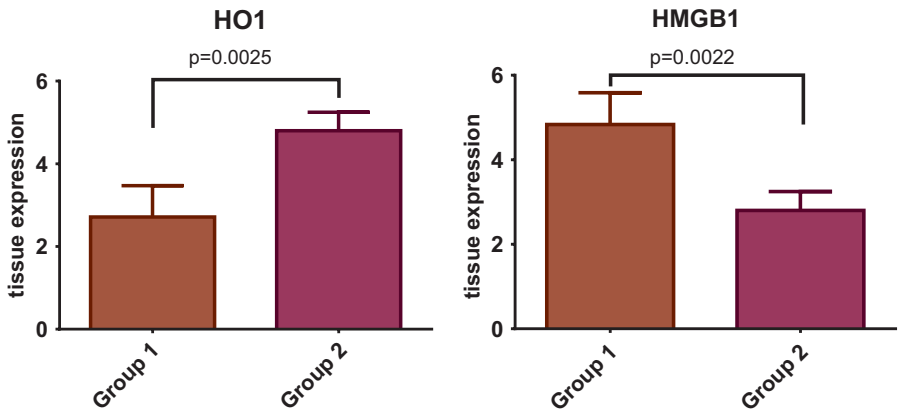

Fig. 1 Correlation between HMGB1 and HO1 in the two studied groups

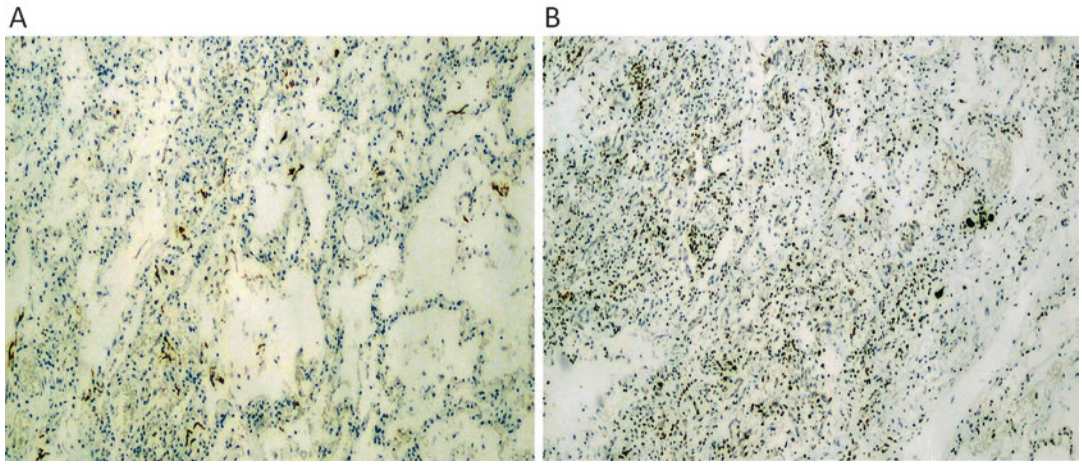

Fig. 2 Immunohistochemistry of excisional biopsy samples

4 Discussion

HO-1 is an inducible microsomial enzyme that catalyses the degradation of heme. This produces biliverdin, ferrous iron, and carbon monoxide [15, 16].

The reduction of HO-1 in COVID-19 patients is associated with a worse clinical trend. Our data with a low infiltration of HO-1 therefore find confirmation in the bibliography [21–23]. Our data shows an inverse correlation between HO-1 and HMGB1 in the lung infiltration. HMGB1 is an intranuclear protein that is either passively released during hypoxia-related necrosis or actively released by macrophages in inflammation [6, 7].

It has been described that HMGB1 occurs through an AMP-Kinase and Heme Oxygenase 1 dependent pathway [17, 24]. In the bibliography this pathway has also been described in the lung, both in vitro [25] and in vivo [26, 27]. Our studies therefore showed that there is a greater infiltration of HMGB1 in the COVID-19 lung, and this would correlate to a worst clinical outcome.

In a recent study, the peak serum level of HMGB1 seems to anticipate the serum peak of interleukin 6 (IL-6) by 5 h in patients affected CAR-T-related toxicities (CARTOX), in a situation like the cytokine storm of COVID-19 [28]. Our results about neutrophil-to-lymphocyte ratio (NLR) shows an increase of its value according to the bibliography [29], but presents an indirect correlation with HMGB1. This data could have an explanation with the migration of neutrophils to the lung which induces a large NET infiltration. The SpO_2 and HMGB1 in our study have a direct correlation and this data could be explained by the use of mechanical ventilation in all of these patients, which induces slight damage of the bronchial epithelium of lung, leading to an increase in HMGB1.

The low level of HO-1, that it has a direct correlation between the low number of T reg lymphocytes (Foxp3) and CD163 Macrophages. This evidence could explain the inflammatory environment in ARDS COVID-19. The high expression of extracellular HMGB1 then binds TLR4 on macrophages surfaces which would cause the shedding of macrophages CD163 into sCD163 [30] which is increased in serum COVID-19 patients [31].

COVID-19 results to be far worse in elderly patients. The inverse correlation between HO-1 and patients' age which could be a possible explanation.

These results were obtained from a small sample size, and may require further investigations to be confirmed.

5 Conclusion

The low HO-1 infiltrate and high HMGB1 infiltrate in the COVID-19 patient's lung can therefore correlate the clinical features to the biological mechanism that is established, thus opening up new therapeutic strategies that reduce inflammation and the cytokine storm in COVID-19. The pathway HO-1/HMGB1 also opens up avenues of investigation on the connection between oxygen, mitochondria and inflammation that will be investigated in the future.

References

1. Adhikari SP, Meng S, Wu YJ et al (2020) Epidemiology, causes, clinical manifestation and diagnosis, prevention and control of coronavirus disease (COVID-19) during the early outbreak period: a scoping review. Infect Dis Poverty 9(1):29
2. Wölfel R, Corman VM, Guggemos W et al (2020) Virological assessment of hospitalized patients with COVID-2019. Nature 581(7809):465–469
3. Zhou F, Yu T, Du R et al (2020) Clinical course and risk factors for mortality of adult inpatients with COVID-19 in Wuhan, China: a retrospective cohort study. Lancet 395(10229):1054–1062
4. Gattinoni L, Chiumello D, Caironi P et al (2020) COVID-19 pneumonia: different respiratory treatments for different phenotypes? Intensive Care Med 46(6):1099–1102
5. Aliberti S, Messinesi G, Gamberini S et al (2014) Non-invasive mechanical ventilation in patients with diffuse interstitial lung diseases. BMC Pulm Med 14(1):1–8
6. Cicco S, Cicco G, Vacca A et al (2020) Neutrophil Extracellular Traps (NETs) and Damage-Associated Molecular Patterns (DAMPs): two potential targets for COVID-19 treatment. Mediat Inflamm 2020:1–25. https://doi.org/10.1155/2020/7527953

7. Tang D, Kang R, Lotze MT et al (2012) PAMPs and DAMPs: signal 0s that spur autophagy and immunity. Immunol Rev 249(1):158–175
8. Liu X, Cao H, Li J et al (2017) Autophagy induced by DAMPs facilitates the inflammation response in lungs undergoing ischemia-reperfusion injury through promoting TRAF6 ubiquitination. Cell Death Differ 24(4):683–693
9. Kang R, Zhang Q, Zeh HJ, Tang D et al (2013) HMGB1 in cancer: good, bad, or both? Clin Cancer Res 19(15):4046–4057
10. Venereau E, De Leo F, Bianchi ME et al (2016) HMGB1 as biomarker and drug target. Pharmacol Res 111:534–544
11. Liu W, Yan ST et al (2015) Hypoxia induced HMGB1 and mitochondrial DNA interactions mediate tumor growth in hepatocellular carcinoma through Toll-like receptor 9. J Hepatol 63(1):114–121
12. Zappavigna V, Falciola L, Bianchi ME et al (1996) HMGB1 interacts with HOX proteins and enhances their DNA binding and transcriptional activation. EMBO J 15(18):4981–4991
13. Andersson U, Yang H, Harris H (2018) High-mobility group box 1 protein (HMGB1) operates as an alarmin outside as well as inside cells. Semin Immunol 38:40–48
14. Yanai H, Ban T, Wang Z et al (2009) HMGB proteins function as universal sentinels for nucleic-acid-mediated innate immune responses. Nature 462(7269):99–103
15. Kikuchi G, Yoshida T, Noguchi M (2005) Heme oxygenase and heme degradation. Biochem Biophys Res Commun 338(1):558–567
16. Ryter SW, Alam J, Choi AM (2006) Heme oxygenase-1/carbon monoxide: from basic science to therapeutic applications. Physiol Rev 86(2):583–650. https://doi.org/10.1152/physrev.00011.2005. PMID 16601269
17. Park EJ, Kim YM, Chang KC (2017) Hemin reduces HMGB1 release by UVB in an AMPK/HO-1-dependent pathway in human keratinocytes HaCaT cells. Arch Med Res 48:423–431
18. Kalergis González M, Riedel CA, Bueno SM (2017) Pathogenesis during infection respiratory syncytial virus replication and heme oxygenase-1 modulates human. J Immunol 199:212–223. https://doi.org/10.4049/jimmunol.1601414
19. Espinoza JA, González PA, Kalergis AM (2017) Modulation of an-tiviral immunity by heme oxygenase-1. Am J Pathol 187:487–493
20. Hooper PL (2020) COVID-19 and heme oxygenase: novel insight into the disease and potential therapies. Cell Stress Chaperones 25:707–710
21. Singh D, Wasan H, Reet KH (2020) Heme oxygenase-1 modulation: a potential therapeutic target for COVID-19 and associated complications. Free Radic Biol Med 161:263–271
22. Wagener FADTG, Pickkers P, Peterson SJ et al (2020) Targeting the heme-heme oxygenase system to prevent severe complications following COVID-19 infections. Antioxidants 9(6):540. https://doi.org/10.3390/antiox9060540
23. Rossi M, Piagnerelli M, Van Meerhaeghe A et al (2020) Heme oxygenase-1 (HO-1) cytoprotective pathway: a potential treatment strategy against coronavirus disease 2019 (COVID-19)-induced cytokine storm syndrome. Med Hypotheses 144:110242. https://doi.org/10.1016/j.mehy.2020.110242. Epub 3 Sep 2020
24. Elfeky M, Kaede R, Okamatsu-Ogura Y et al Adiponectin inhibits LPS-induced HMGB1 release through an AMP kinase and heme oxygenase-1-dependent pathway in RAW 264 macrophage cells. Mediators Inflamm 2016, Article ID 5701959, 9 pages. https://doi.org/10.1155/2016/5701959
25. Luo M, Hong XQ, Zhu H et al (2020) The HO-1 signal prevents HMGB1-mediated activation of NLRP3 inflammasomes in lipopolysaccharide-induced acute lung injury in vitro. J Surg Res 247:335–343. https://doi.org/10.1016/j.jss.2019.10.011. Epub 22 Nov 2019
26. Yu Y, Yang Y, Yang M et al (2019) Hydrogen gas reduces HMGB1 release in lung tissues of septic mice in an Nrf2/HO-1-dependent pathway. Int Immunopharmacol 69:11–18. https://doi.org/10.1016/j.intimp.2019.01.022. Epub 18 Jan 2019
27. Gong Q, Yin H, Fang M et al (2008) Heme oxygenase-1 upregulation significantly inhibits TNF-alpha and Hmgb1 releasing and attenuates lipopolysaccharide-induced acute lung injury in mice. Int Immunopharmacol 8(6):792–798. https://doi.org/10.1016/j.intimp.2008.01.026. Epub 7 Mar 2008
28. Deng T, Tang C, Zhang G et al (2021) DAMPs released by pyroptotic cells as major contributors and therapeutic targets for CAR-T-related toxicities. Cell Death Dis 12:129. https://doi.org/10.1038/s41419-021-03428-x
29. Yang A-P, Liu J-P, Tao W-Q et al (2020) The diagnostic and predictive role of NLR, d-NLR and PLR in COVID-19 patients. Int Immunopharmacol 84:106504. https://doi.org/10.1016/j.intimp.2020.106504. Epub 13 Apr 2020
30. Karakike E, Giamarellos-Bourboulis EJ Macrophage activation-like syndrome: a distinct entity leading to early death in sepsis. Front Immunol. https://doi.org/10.3389/fimmu.2019.00055
31. Gómez-Rial J, Currás-Tuala MJ, Rivero-Calle I (2020) Increased serum levels of sCD14 and sCD163 indicate a preponderant role for monocytes in COVID-19 immunopathology. Front Immunol 11:560381. https://doi.org/10.3389/fimmu.2020.560381. eCollection 2020

Silent Hypoxemia in COVID-19 Pneumonia

Akinori Ebihara, Asako Kitahara,
Tokuzen Iwamoto, and Ichiro Kuwahira

Abstract

In patients suffering from Coronavirus Disease 2019 (COVID-19), dyspnoea is less likely to occur despite hypoxemia. Even if the patient develops severe hypoxemia, it cannot be detected from subjective symptoms. In other words, it becomes more serious without the person or the surroundings noticing it. Initially less talked about, hypoxemia without dyspnoea (silent hypoxemia or happy hypoxia: hypoxemia that does not coincide with dyspnoea) is now experienced in many institutions. Dyspnoea is defined as "the unpleasant sensation that accompanies breathing." Dyspnoea occurs when afferent information is transmitted to the sensory area. Receptors involved in the development of dyspnoea include central and peripheral chemoreceptors, chest wall receptors, lung receptors, upper respiratory tract receptors and corollary discharge receptors. In the present study, we considered mechanisms mediating the silent hypoxemia through three cases experienced at our hospital as a dedicated coronavirus treatment hospital. We have treated about 600 people infected with COVID-19, of which about 10% were severe cases. In the present study, the patients' condition was retrospectively extracted and analysed. We investigated three typical cases of COVID-19 pneumonia admitted to our hospital (men and women between the ages of 58 and 86 with hypoxemia and tachypnoea). Silent hypoxemia is not entirely without dyspnoea, but hypoxemia does not cause dyspnoea commensurate with its severity. The virus may have specific effects on the respiratory control system. In our cases, respiratory rate significantly increased with hypoxemia, and hyperventilation occurred. Therefore, information about hypoxemia is transmitted from the carotid body. Since hyperventilation occurs, it is suggested that information is transmitted to effectors such as respiratory muscles. The fact that these patients did not feel the unpleasant sensation indicates that information is not accurately transmitted to the sensory area of the cerebral cortex. These cases suggest that there may be a problem somewhere in the path from the respiratory centre to the sensory area.

Keywords

Severe acute respiratory syndrome coronavirus 2 (SARS-CoV2) · Hypoxia · Dyspnoea · Happy hypoxia

A. Ebihara (✉) · A. Kitahara · T. Iwamoto · I. Kuwahira
Department of Pulmonary Medicine, Tokai University, Tokyo Hospital, Tokyo, Japan
e-mail: akinoriebihara@tok.u-tokai.ac.jp

F. Scholkmann et al. (eds.), *Oxygen Transport to Tissue XLIII*, Advances in Experimental Medicine and Biology 1395, https://doi.org/10.1007/978-3-031-14190-4_20

1 Introduction

Currently, many people are infected due to the pandemic of the novel coronavirus infection which can lead to Coronavirus Disease 2019 (COVID-19). In Japan as well, the number is steadily increasing, and the number of home care recipients has exceeded 17,000 (as of 2021.8.11). Under such circumstances, there are many cases in which the symptoms are poor and there is a delay before aggravation is noticed. In COVID-19, dyspnoea is less likely to occur despite hypoxemia. Even if the patient develops severe hypoxemia, it cannot be detected from subjective symptoms. In other words, it becomes more serious without the person or the surroundings noticing it. Initially less talked about hypoxemia without dyspnoea (silent hypoxemia or happy hypoxia: hypoxemia that does not coincide with dyspnoea) is now experienced in many institutions. If we cannot understand the concept of silent hypoxemia, patients in home care may not receive hospital care unless they become seriously ill.

Dyspnoea is defined as "the unpleasant sensation that accompanies breathing." Dyspnoea occurs when afferent information is transmitted to the sensory area. Receptors involved in the development of dyspnoea include central and peripheral chemoreceptors, chest wall receptors, lung receptors, upper respiratory tract receptors, and corollary discharge receptors [1–8]. In the present study, we considered mechanisms mediating the silent hypoxemia by reviewing the cases experienced at our hospital as a dedicated coronavirus treatment hospital.

2 Methods

We have treated about 600 people infected with COVID-19, of which about 10% were severe cases. Because patients with severe pneumonia were not in a good condition, informed consent and the following data were obtained from only three patients (men and women between the ages of 58 and 86 with hypoxemia and tachypnoea). We do not believe that these three cases reflect all COVID-19 patients, possible causes of silent hypoxemia could be retrospectively analysed. Clinical symptoms, vital signs, arterial blood gas data and the modified Borg scale values for dyspnoea (range 0–10) were analysed. As shown in Table 1, this is a measure to assess the difficulty of breathing. It starts at number 0, where the patient's dyspnoea does not cause any difficulty, and progresses to number 10, where the patient's dyspnoea is maximum [9]. The institutional review board approved this study.

Table 1 Modified Borg scale [9]

modified Borg scale	
0	Nothing at all
0.5	Very very slight
1	Very slight
2	Slight
3	Moderate
4	Somewhat severe
5	Severe
6	
7	Very severe
8	
9	Vere very severe (almost maximal)
10	Maximal

3 Results

Case 1 (Fig. 1).

A 58-year-old man had a BMI of 28.2 (mildly obese). The underlying disease was dyslipidaemia. He had a temperature of 39.1 °C. At the time of admission, his SpO_2 was 93% (room air) and the modified Borg scale was 2 (slight). As shown in Fig. 1, his chest CT images showed ground glass opacities in the bilateral lung fields. Arterial blood gas data on the third day of hospitalisation showed mild hypoxemia and A-aDO_2 was increased.

Case 1

58 Y/O Male

SpO_2 on admission: 93% (Room air)
Respiratory rate 30/min
modified Borg scale:2
Slight

Taste disorder +

BGA (Room air)
(3 days after hospitalization)

pH 7.472
$PaCO_2$ 38.4 mmHg
PaO_2 72.6 mmHg
HCO_3^- 27.4 mmol/L
BE 3.7 mmol/L
A-aDO_2 29.1 mmHg

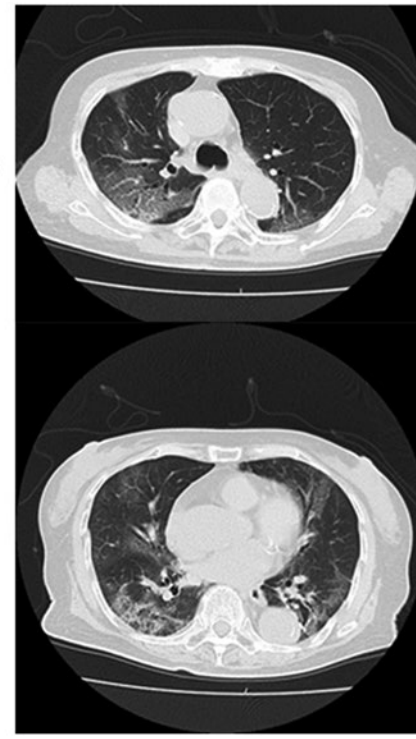

Fig. 1 Chest CT 3 days after hospitalization in case 1

Case 2 (Fig. 2).

A 58-year-old man had a BMI of 30.1 (obese). Underlying diseases included diabetes and hypertension. Body temperature was 38.7 °C. Although his SpO_2 was 87% (room air) at the time of admission, which indicates his PaO_2 was less than 60 mmHg, the modified Borg scale was only 4 (somewhat severe). As shown in Fig. 2, his chest CT images showed diffuse pneumonic shadows in the bilateral lung fields, indicating moderate to severe COVID-19 pneumonia. Arterial blood gas data on the second day of hospitalisation showed acute respiratory alkalosis. His PaO_2 was 72.0 mmHg under high flow of oxygen 7 L/min. His respiratory rate increased to 34/min and hyperventilation was observed, but the modified Borg scale remained unchanged and no strong dyspnoea was observed.

Case 3 (Fig. 3).

An 86-year-old female had a BMI of 23.5. The underlying diseases were diabetes, hypertension and angina. She had a temperature of 37.8 °C. Although her SpO_2 was 88% (room air) at the time of admission, which indicates her PaO_2 was less than 60 mmHg, the modified Borg scale was 4 (somewhat severe). As shown in Fig. 3, her chest CT images showed diffuse pneumonic shadows in the bilateral lung fields, indicating moderate to severe COVID-19 pneumonia. Arterial blood gas data on the second day of hospitalisation showed that her PaO_2 was kept at 68.3 mmHg under high flow of oxygen 5 L/min. Her respiratory rate increased to 36/min and hyperventilation was observed, but the modified Borg scale remained unchanged and no strong dyspnoea was observed.

Despite hypoxemia, increased respiratory rate and hyperventilation in these cases, the modified Borg scale values were only 2–4. In particular, two cases (cases 2 and 3) developed severe respiratory failure, but the modified Borg scale values indicated "somewhat severe".

Case 2

58Y/O Male

SpO_2 on admission: 87% (Room air)
Respiratory rate 34/min
modified Borg scale:4
Somewhat severe

No taste disorder

BGA (O_2 7L/min)
(2 days after hospitalization)

pH 7.501
$PaCO_2$ 35.1 mmHg
PaO_2 72.0 mmHg
HCO_3^- 26.8 mmol/L
BE 3.9 mmol/L

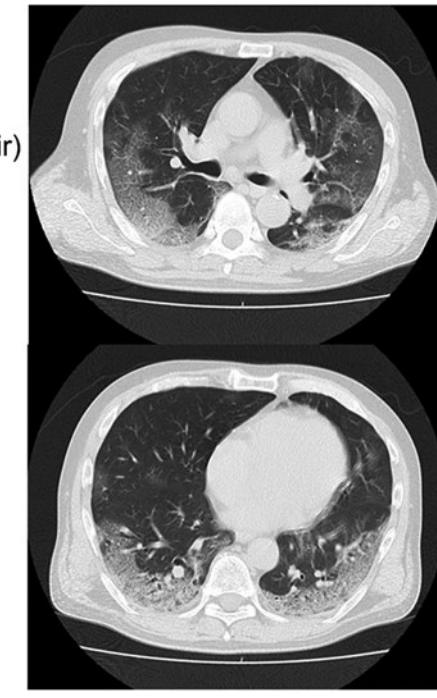

Fig. 2 Chest CT 2 days after hospitalization in case 2

Case 3

86 Y/O Female

SpO_2 on admission: 88% (Room air)
Respiratory rate 36/min
modified Borg scale:4
Somewhat severe

No taste disorder

BGA (O_2 5L/min)
(2 days after hospitalization)

pH 7.445
$PaCO_2$ 35.5mmHg
PaO_2 68.3 mmHg
HCO_3^- 23.8 mmol/L
BE 0.3 mmol/L

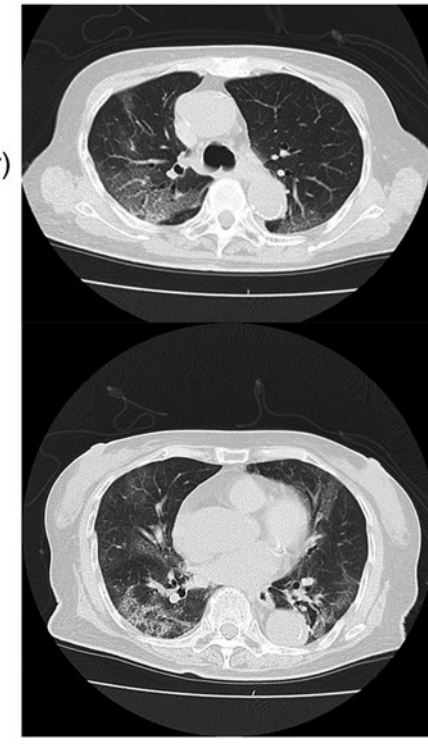

Fig. 3 Chest CT 2 days after hospitalization in case 3

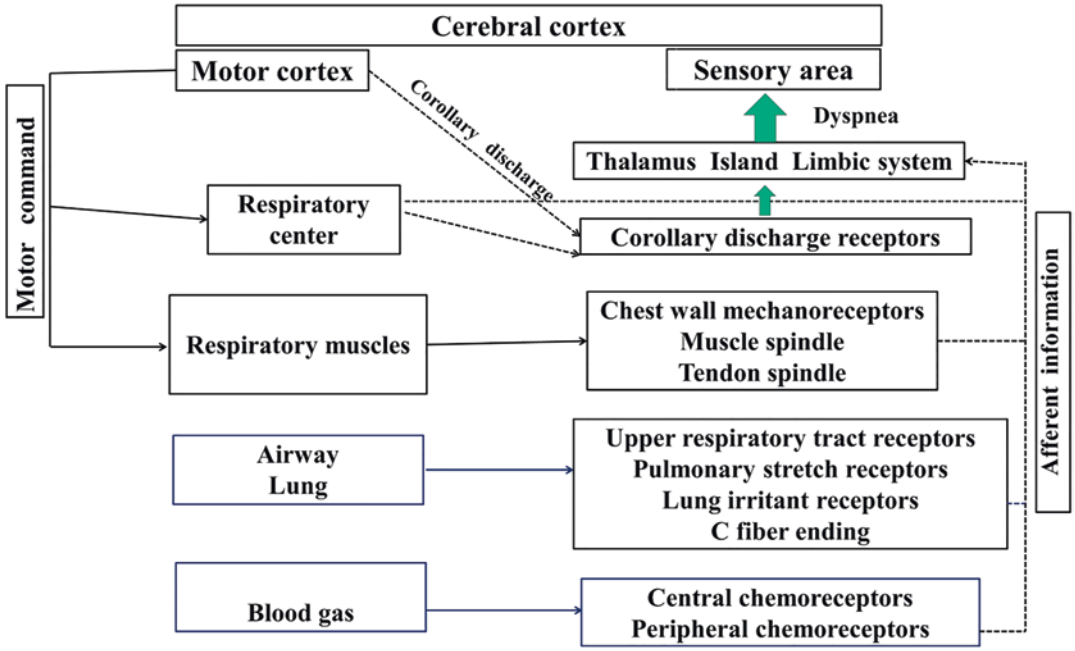

Fig. 4 Dysnonea and respiratory control system. (Modified from Ref. [10])

4 Discussion

In the present study, only three cases were reviewed. Although these cases do not reflect clinical features of all COVID-19 patients, we think possible causes of silent hypoxemia could be analysed by reviewing these cases.

Severe acute respiratory syndrome coronavirus 2 (SARS-CoV-2) mainly invades alveolar type-2 epithelial cells and spreads throughout the body through systemic circulation, neurotransmission and attachment to ACE2-expressing cells. The virus can spread directly to the central nervous system by the olfactory epithelium.

Silent hypoxemia would be defined as follows: Despite the intensity of hypoxemia, the intensity of dyspnoea is inappropriate to the degree of arterial hypoxemia. The clinical presentation of silent hypoxemia in patients with COVID-19 might be (1) impairment of peripheral oxygen-sensing and/or (2) impairment of central processing of hypoxia-stimulated afferent inputs within higher-order somatosensory brain regions that manifest perceptions of dyspnea [10]. The virus could bind to the ACE2 receptors on the glomus cells of the carotid body, resulting in damage of the mitochondrial electron transport chain in O_2-sensing cells. This damage would reduce afferent information to the brain despite hypoxemia and may reduce dyspnoea sensation [11]. However, as shown in the results and Fig. 4, the fact that these patients developed tachypnoea and hyperventilation in the present study suggests that some afferent information, even if reduced, is processed centrally enough to produce an efferent ventilatory response. In addition to this, although it is possible that olfactory abnormalities may affect dyspnoea, olfactory dysfunction was not present in any cases throughout the course in the present study. From these data, it would be suggested that the virus may interfere with central processing of sensory afferent neural inputs in patients with silent hypoxemia. Since correlations between neurological symptoms and the brain pathology findings in COVID-19 patients remain largely unknown [12], future prospective studies with control and COVID-19 groups will be necessary to determine the mechanisms of silent hypoxemia.

Acknowledgments We would like to thank all the staff who treated the patients infected with the novel coronavirus.

References

1. Martin JT, Franco L, Amal J (2020) Why COVID-19 silent hypoxemia is baffling to physicians. Am J Respir Crit Care Med 202:356–360
2. Fung ML (2015) Expressions of angiotensin and cytokine receptors in the paracrine signaling of the carotid body in hypoxia and sleep apnea. Respir Physiol Neurobiol 209:6–12
3. Sedaghat AR, Gengler I, Speth MM (2020) Olfactory dysfunction: a highly prevalent symptom of COVID-19 with public health significance. Otolaryngol Head Neck Surg 5:194599820926464
4. Netland J, Meyerholz DK, Moore S et al (2008) Severe acute respiratory syndrome coronavirus infection causes neuronal death in the absence of encephalitis in mice transgenic for human ACE2. J Virol 82:7264–7275
5. Couzin-Frankel J (2020) The mystery of the pandemic's 'happy hypoxia'. Science 368:455–456
6. Wichmann D, Sperhake J-P, Lütgehetmann M et al (2020) Autopsy findings and venous thromboembolism in patients with COVID-19. Ann Intern Med 173:268–277
7. Sanchez O, Caumont-Prim A, Riant E et al (2017) Pathophysiology of dyspnoea in acute pulmonary embolism: a cross-sectional evaluation. Respirology 22:771–777
8. Nakano T, Iwazaki M, Sasao G et al (2015) Hypobaric hypoxia is not a direct dyspnogenic factor in healthy individuals at rest. Respir Physiol Neurobiol 218:8–31
9. Borg AG (1982) Psychophysical bases of perceived exertion. Med Sci Sports Exerc 14:377–381
10. Nishino T (2010) Respiratory center and respiratory sensation. J Jpn Soc Clin Aneseth 20:12
11. Jacquie B, Anthony VI, Richard JA et al (2021) Syncope and silent hypoxemia in COVID-19: implications for the autonomic field. Auton Neurosci 235:102842
12. Cosentino G, Todisco M, Hota N et al (2021) Neuropathological findings from COVID-19 patients with neurological symptoms argue against a direct brain invasion of SARS-CoV-2: a critical systematic review. Eur J Neurol 28(11):3856–3865. https://doi.org/10.1111/ene.15045

Low Flow and Microvascular Shunts: A Final Common Pathway to Cerebrovascular Disease: A Working Hypothesis

Edwin M. Nemoto and Denis Bragin

Abstract

Low flow and microvascular shunts (MVS) is the final common pathway in cerebrovascular disease. Low flow in brain capillaries (diam. 3–8 μm) decreases endothelial wall shear rate sensed by the glycocalyx regulating endothelial function: water permeability; nitric oxide synthesis via nitric oxide synthase; leucocyte adhesion to the endothelial wall and penetration into the tissue; activation of cytokines and chemokines initiating inflammation in tissue. Tissue edema combined with pericyte and astrocyte capillary constriction increases capillary resistance. Increased capillary resistance diverts flow through MVS (diam. 10–25 μm) that are non-nutritive, without gas exchange, waste or metabolite clearance and cerebral blood flow (CBF) regulation. MVS predominate in subcortical and periventricular white matter. The shift in flow from capillaries to MVS is a pathological, maladaptive process. Low perfusion in the injured tissue exacerbates brain edema. Low blood flow and MVS alone can lead to all of the processes involved in tissue injury including inflammation and microglial activation.

Keywords

Cerebral blood flow · Cerebral capillary flow autoregulation · Intracranial pressure · Capillary shear rate

1 Introduction

We recently showed the transition from brain capillary (CAP) to MVS flow with increased intracranial pressure (ICP), it's role in the loss of cerebral blood flow (CBF) autoregulation and the circulatory isolation of injured brain tissue by perfusion through microvascular shunts (MVS) [5]. Our investigations into MVS were initiated by the study by Miller et al. in 1972 [1] reporting an unexplained decrease in the critical cerebral perfusion pressure (CPP) threshold of CBF autoregulation from 50 to 30 mmHg when CPP was decreased by increasing ICP instead of decreasing arterial pressure as conventionally done in studies [2, 3]. We hypothesized that the decrease in critical CPP when ICP rather than mean arterial pressure (MAP) was used to decrease CPP, was due to MVS flow resulting in a falsely elevated CBF and apparently maintained CBF at a lower critical CPP of 30 mmHg. We then showed brain MVS in our studies using two photon laser scanning microscopy (2PLSM) [4, 5].

E. M. Nemoto (✉) · D. Bragin
Department of Neurosurgery, University of New Mexico, Albuquerque, NM, USA
e-mail: enemoto@salud.unm.edu

F. Scholkmann et al. (eds.), *Oxygen Transport to Tissue XLIII*, Advances in Experimental Medicine and Biology 1395, https://doi.org/10.1007/978-3-031-14190-4_21

2 Evidence on Microvascular Shunts

Shunt Flow in Traumatic Brain Injury A dramatic example of non-nutritive shunt flow after traumatic brain injury was observed in a 7-year-old female who suffered severe left hemispheric infarction and at 7 days after injury was placed under barbiturate coma for treatment of intracranial hypertension (Fig. 1). CBF measured by stable xenon-CT showed that the infarcted left hemisphere was extremely hyperemic whereas the right hemisphere was hypoperfused due to barbiturate suppression of metabolism and depressed CBF. This remarkable demonstration of MVS triggered our search to prove the occurrence of brain MVS.

MVS in Human Cerebrum Histological sections of human cerebrum suggest bridges of vessels without intervening capillary beds in the microvasculature [6]. These MVS 10–25 μm diameter are larger than capillaries which were measured at about 3–8 μm in outer diameter and arterio-venous and veno-venous anastomoses in the range of 25 μm.

Cerebral Capillary Flow Autoregulation Hudetz et al. [7] reported two populations of microvessel flow velocities; one above and one below one mm/sec. High flow velocity microvessels showed no autoregulation whereas low flow velocity vessels showed constant flow velocity until the lower limit of autoregulation was reached.

Microvascular Shunts with Increased ICP Our first definitive evidence of MVS in the healthy rat brain was by increasing ICP with a reservoir of mock CSF with a catheter into the cisterna magna using two photon laser scanning microscopy (2PLSM) [4, 5]. Increased ICP showed increased flow velocity in vessel diameters >10 μm which was not observed when CPP was decreased by decreasing mean arterial pressure (MAP) (Fig. 2).

Consistent with the effect of MVS as non-nutritive and without clearance of metabolic waste products or gas exchange, tissue hypoxia develops as indicated by the increase in NADH, i.e. a reflection of tissue hypoxia or low oxygen, with increasing ICP which was partially mitigated by increasing CPP. The effect of increasing ICP which also increased brain edema (water

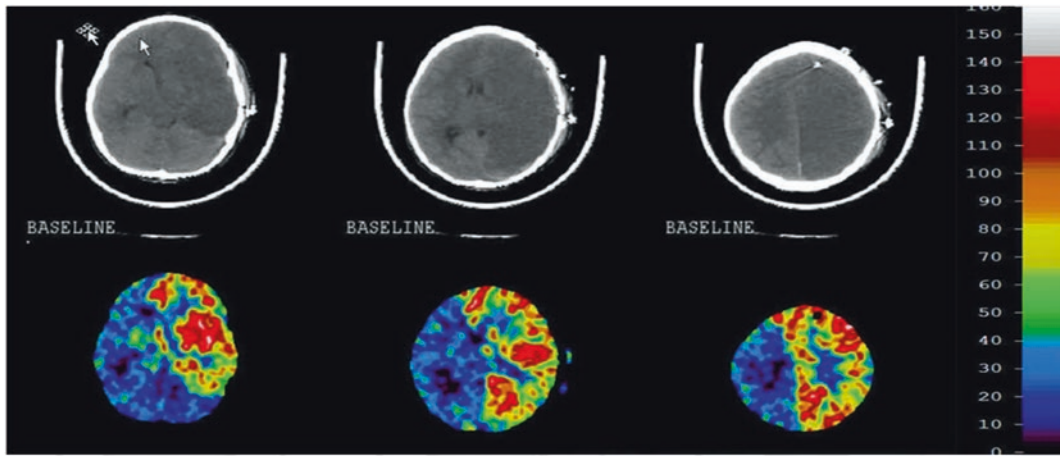

Fig. 1 CT scan (top) and stable xenon CBF maps (bottom) a 7 year old female 7 days after severe brain trauma under barbiturate coma for high ICP. The left hemisphere is completely infarcted and the right hemisphere normal. CBF in the normal hemisphere is depressed by barbiturate indicating flow-metabolism coupling. The left hemisphere shows marked hyperemia and "nonnutritive flow" loss off CBF autoregulation

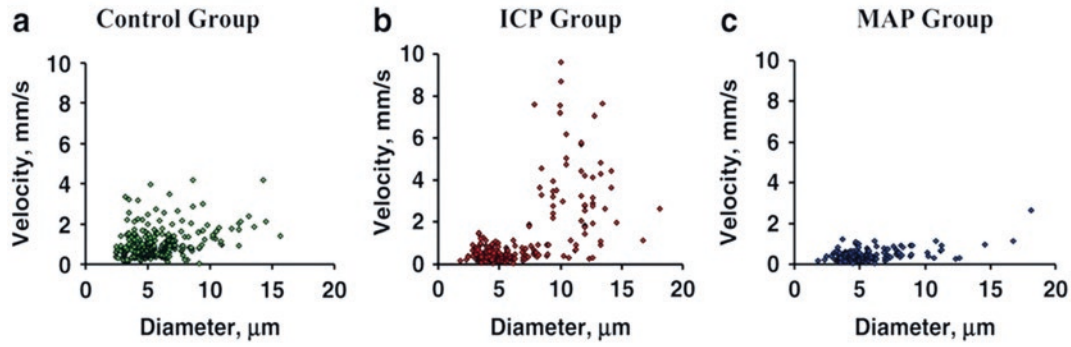

Fig. 2 (**a**) normal CPP (70 mmHg) and by (**b**) decreased CPP to 30 mmHg by increasing ICP. (**c**) Decreased MAP to reduce the CPP to 30 mmHg [5]. (Reproduced with the permission of the Editor of J Neurotrauma [4])

content) was partly mitigated by increasing CPP. Increasing ICP caused a progressive decrease in CAP/MVS ratio and shunting with increasing hypoxia and Doppler flux.

3 Low Blood Flow and Shear Rate on Endothelial Function

There are multiple shear stress related controls for blood vessels in the circulation in large arteries, small arteries to arterioles, capillaries, venules and veins [8]. For each of these vessels of different calibers, there are processes related to: blood vessel growth, angiogenesis, re thrombolysis and inflammatory processes such as sepsis all controlled by shear stresses in the blood vessels [9, 11].

The shear rate on the endothelium of capillaries is highest as it is inversely proportional to the third power of the vessel diameter [8, 11]. Endothelial shear rate plays an important role in endothelial function through the glycocalyx, a carbohydrate-rich layer 0.2–0.5 µm thick gel-like layer lining the luminal membrane of the endothelium (8, 10, 12). It connects to the endothelium by core molecules containing proteoglycans and glycoproteins [12] triggered by the shear rate and torque applied to endothelial cells (Fig. 3). It consists of proteoglycans 50–90% of which is heparin sulfate and glycoproteins anchored to the endothelium by glycosaminoglycans. It maintains the colloid osmotic gradient of the vascular barrier; regulates vascular exchange of water and solutes and leucocyte adhesion; provides binding sites for several molecules antithrombin III, lipoprotein lipase vascular endothelial growth factor; and acts as a shear stress sensor and regulator [12]. The glycocalyx controls capillary endothelial function as the interface between the tissue and the circulation.

4 Low Blood Flow and MVS in the Final Common Pathway in Cerebrovascular Disease

The role of low blood flow in cerebrovascular disease is increasingly recognized in the pathogenesis of all cerebrovascular diseases including vascular dementia, Alzheimer's Disease [13]. MVS occur primarily in the deep cortical white matter and in the periventricular white matter where white matter hyperintensities (WMH) are most frequently observed. The role of MVS in the pathophysiology of cerebrovascular disease may be a means of isolating injured tissue from further perfusion shunting blood around dead and edematous tissue inducing further edema in injured tissue. MVS do not conduct nutrient nor gas exchange with tissue which would reduce further brain edema development in injured tissue.

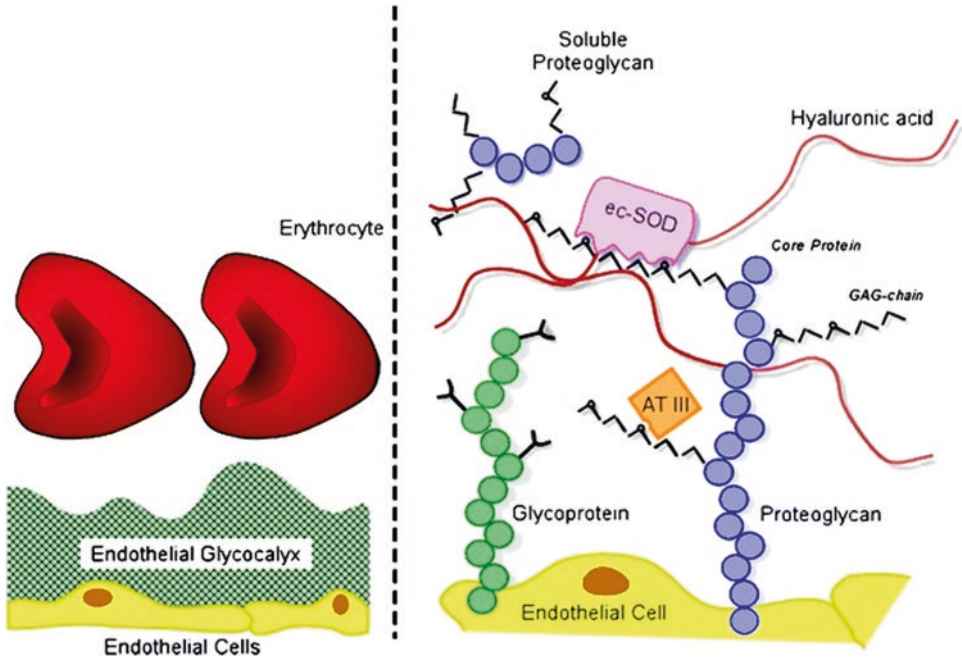

Fig. 3 Schematic representation of the endothelial glycocalyx, showing its main components. Left: The endothelial glycocalyx observed in vivo as a red blood cell exclusion zone, located on the luminal side of the vascular endothelium. It consists of membrane bound and soluble molecules. Right: Components of the endothelial glycocalyx [10]. (Reproduced Springer Verlag)

Acknowledgements Supported by NIH and American Heart Association grants to Drs Nemoto and Bragin. NIH-NIGMS Sub-award from P20 GM109089-01A1, NIH-NINDS 1R21NS091600-01A1, NIH-NINDS RO1-NS051639-05, NIH-NINDS R03 NS061216-01A1.

References

1. Miller JD, Stanek A, Langfitt TW (1972) Concepts of cerebral perfusion pressure and vascular compression during intracranial hypertension. Prog Brain Res 35:411–432
2. Artru AA, Katz RA, Colley PS (1989) Autoregulation of cerebral blood flow during normocapnia and hypocapnia in dogs. Anesthesiology 70:288–292
3. Rapela CE, Green HD (1964) Autoregulation of canine cerebral blood flow. Circ Res 15(SUPPL):205–212
4. Bragin DE, Bush RC, Müller WS, Nemoto EM (2011) High intracranial pressure effects on cerebral cortical microvascular flow in rats. J Neurotrauma 28:775–785
5. Bragin DE, Bush RC, Nemoto EM (2013) Effect of cerebral perfusion pressure on cerebral cortical microvascular shunting at high intracranial pressure in rats. Stroke 44:177–181
6. Ravens JR (1974) Anastomoses in the vascular bed of the human cerebrum. In: Cervos-Navaro J (ed) Pathology of cerebral microcirculation. Walter de Bruter, Berlin, pp 16–38
7. Hudetz AG, Feher G, Kampine JP (1996) Heterogeneous autoregulation of cerebrocortical capillary flow: evidence for functional thoroughfare channels? Microvasc Res 51(1):131–136
8. Resnick N, Yahav H, Shay-Salit A, Shushy M, Schubert S, Zilberman LC, Wofovitz E (2003) Fluid shear stress and the vascular endothelium: for better and for worse. Prog Biophys Mol Biol 81(3):177–199
9. Ince C, Mayeux PR, Nguyen T, Gomez H, Kellum JA, Ospinatascon GA, Hernandez G, Murray P, DeBacker D, ADQI XIV Workgroup (2016) The endothelium in sepsis. Shock 45:259–270
10. Reitsma S, Slaaf DW, Vink H, van Zandvoort MA, oude Egbrink MGA (2007) The endothelial glycocalyx: composition, functions, and visualization. Pflugers Arch 454:345–359
11. Papaioannou TG, Stefanadis C (2005) Vascular wall shear stress: basic principles and methods. Hell J Cardiol 46:9–15
12. Schött U, Solomon C, Fries D, Bentzer P (2016) The endothelial glycocalyx and its disruption, protection and regeneration: a narrative review. Scand J Trauma Resusc Emerg Med 12(24):48
13. de la Torre JC (2016) Cerebral perfusion enhancing interventions: a new strategy for the prevention of Alzheimer Dementia. Brain Pathol 26:618–631

A Case of Intracranial Vertebral Artery Stenosis Treated with Percutaneous Transluminal Angioplasty and Stenting Guided by Brain Oximetry

Yu Okuma, Nobuyuki Hirotsune, Umair Ahmed, Santiago J. Miyara, Shigeru Daido, and Yukihide Kagawa

Abstract

Surgical treatment should be considered for patients with severe vertebrobasilar artery (VBA) stenosis or progressive symptoms, but there is currently no clear treatment algorithm. We report a case of symptomatic intracranial vertebral artery stenosis with repeated cerebral infarction treated by percutaneous transluminal angioplasty (PTA) and stenting and monitoring of oxygen saturation by a brain oximeter. The patient was a 76-year-old man referred to our hospital due to infarction in the right cerebellum. Angiography showed 60% stenosis in the right vertebral artery and 90% stenosis in the left vertebral artery with progressive stenosis in the left. The patient was treated with intravenous and oral triple antiplatelet therapy but had dizziness again with new cerebral infarctions in the left cerebellum and right pontine. We shaved the patient's hair up to the superior nuchal line and placed left and right oximeter probes on each cerebellar hemisphere (2 cm lateral and 2 cm caudal from the external occipital protuberance). Under evaluation of blood flow in the posterior circulation with INVOS Cerebral/Somatic Oximeter, PTA and stent placement were performed for left vertebral artery stenosis. Postoperatively, the dizziness disappeared, and the patient was discharged on his own with good outcome. He has not had a recurrent stroke in over 6 years. Although medical treatment is generally considered the first choice for VBA stenosis, recurrent cerebral infarction occurs at a high rate in symptomatic lesions, and the prognosis is poor. In addition, the perioperative complication rate is not low, and there is no established method for evaluating perfusion of posterior circulation. The brain

Y. Okuma (✉)
Department of Neurological Surgery, Sonoda Daiichi Hospital, Tokyo, Japan

Department of Neurological Surgery, Hiroshima City Hiroshima Citizens Hospital, Hiroshima, Japan

Department of Neurological Surgery, Fukuyama City Hospital, Fukuyama, Japan

N. Hirotsune
Department of Neurological Surgery, Hiroshima City Hiroshima Citizens Hospital, Hiroshima, Japan

U. Ahmed · S. J. Miyara
Feinstein Institute for Medical Research, Northwell Health System, Manhasset, NY, USA

S. Daido
Department of Neurological Surgery, Fukuyama City Hospital, Fukuyama, Japan

Y. Kagawa
Department of Neurological Surgery, Sonoda Daiichi Hospital, Tokyo, Japan

F. Scholkmann et al. (eds.), *Oxygen Transport to Tissue XLIII*, Advances in Experimental Medicine and Biology 1395, https://doi.org/10.1007/978-3-031-14190-4_22

oximeter is already known to be useful in carotid artery (CA) revascularisation. In this report, we were able to perform a minimally invasive evaluation of blood flow in the posterior circulation using the brain oximeter which might be useful for surgical revascularisation not only in CA but also in VBA.

Keywords

Cerebral infarction · Surgical treatment · Cerebral hyperperfusion syndrome · Regional cerebral oxygen saturation

1 Introduction

In the treatment of vertebrobasilar artery (VBA) stenosis, a high perioperative complication rate is reported for surgical revascularisation, and drug treatment has often been chosen according to guidelines. However, the recurrence rate of cerebral infarction is high in patients with symptomatic VBA stenotic lesions even with adequate medical therapy [1]. Balloon angioplasty and stenting have been reported to be effective, but the results have not been enough to revise the guidelines yet [2, 3]. In recent years, our institute reported that using brain oximeter monitoring might make the carotid artery (CA) revascularisation safer [4]. In this article, we report the result of a case of intracranial vertebral artery stenosis treated with percutaneous transluminal angioplasty and stenting with a brain oximeter.

2 Methods

2.1 Case Presentation

The patient was a 76-year-old man. Dizziness and dysarthria suddenly appeared without any trigger and the patient was transferred to our hospital due to infarction in the right cerebellum from a community hospital. Angiography showed 60% stenosis in the right vertebral artery and 90% stenosis in the left vertebral artery with progressive stenosis in the left. He was treated with intravenous antiplatelet therapy by 160 mg/day of ozagrel sodium and oral dual antiplatelet therapy by 100 mg/day of aspirin and 75 mg/day clopidogrel. The patient was also treated with rosuvastatin, ethyl icosapentate and edaravone, which was a free radical scavenger. But 12 days after treatment started, the patient experienced dizziness again and magnetic resonance imaging (MRI) showed new cerebral infarctions in the left cerebellum and right pontine (Fig. 1). The posterior traffic arteries were hypoplastic bilaterally, and collateral blood flow to the vertebrobasilar artery region was poor. Antiplatelet therapy was added with cilostazol 200 mg/day, but this repeated infarctional mechanism was considered due to atherosclerotic progressive occlusion of the left vertebral artery which was intractable to drugs. Surgical treatment was unavoidable to prevent progressive infarctions of the posterior circulation. In order to make it as safe as possible, we planned to monitor the blood flow in the posterior circulation with INVOS Cerebral/Somatic Oximeter.

2.2 Surgical Treatment Using the Brain Oximeter

We shaved the patient's hair up to the superior nuchal line the day before surgery. We placed the left and right probe, on 2 cm lateral and 2 cm caudal from the external occipital protuberance and checked whether it could monitor both cerebellar hemispheres (Fig. 1). Under local anaesthesia, a 6-F guiding catheter was placed from the right femoral artery to the left vertebral artery (VA) enough not to wedge the left VA. A 0.014-inch microwire was inserted distally to the narrowest section of VA and up to the union of basilar artery followed by a micro balloon 2.5 × 20 mm for percutaneous transluminal angioplasty (PTA) delivered to the narrowest section. During the PTA balloon inflation, the regional cerebral oxygen saturation (rSO2) by the left probe decreased down to an undetectable low value, and the patient had dizziness symptoms. Immediately after PTA, good dilatation of

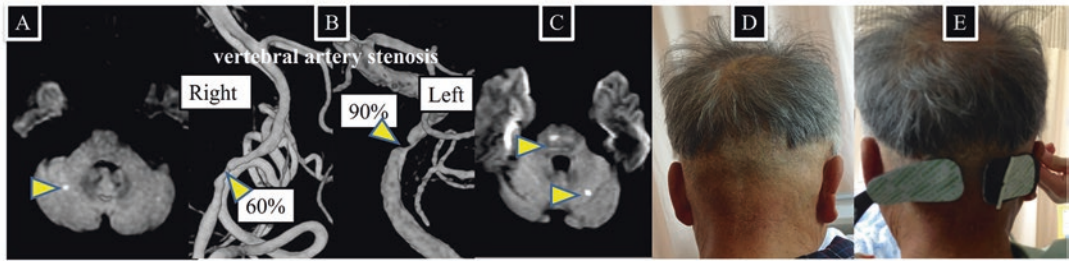

Fig. 1 Magnetic resonance imaging of first onset (**A**) showing an infarction in the right cerebellum. Three-dimensional digital subtraction angiography of first onset (**B**) showing 60% stenosis in the right vertebral artery and 90% stenosis in the left vertebral artery. Magnetic resonance imaging 12 days after treatment started (**C**) showing new cerebral infarctions in the left cerebellum and right pontine. Shaving the patient's hair up to the superior nuchal line (**D**) and placing the left and right probe (**E**)

the stenosis was observed and the blood flow delay disappeared, but the trend of recoiling was observed at 5 min after PTA. The 2.5 × 12 mm bare metal stent was placed, and post-stent dilated with an attached micro balloon. At the same time as the post-stent balloon was inflated, the rSO2 by the left probe decreased down to an undetectable low value again and the patient had similar dizziness symptoms but both rSO2 and symptoms recovered immediately after the balloon was deflated. The stenosis was successfully dilated, and the blood flow delay disappeared absolutely (Fig. 2).

3 Result

No new neurological symptoms appeared after surgery, and the patient's dizziness disappeared postoperatively. After confirming rSO2 was stable overnight, INVOS Cerebral/Somatic Oximeter monitoring was finished before the MRI examination. Head MRI on postoperative day 1 showed that there was no new infarction, fortunately. The patient's antiplatelet therapy was reduced and maintained with aspirin 100 mg/day and cilostazol 200 mg/day. He was discharged on his own with a good outcome. Follow-up MRI showed that the patient had no recurrent stroke and following computed tomography angiography showed the well-dilated stenting was maintained in over 6 years (Fig. 2).

4 Discussion

Intracranial artery stenosis including BBA stenosis is one of the most common mechanisms of cerebral infarction and is more common in Asians. Symptomatic intracranial artery stenosis is associated with a high probability of cerebral infarction in the same region that is intractable to drugs. The Warfarin-Aspirin Symptomatic Intracranial Disease (WASID) study reported a recurrence of cerebral infarction of 23% over 1 year in lesions with greater than 70% intracranial artery stenosis [2]. Since the limitations of drugs for intracranial artery stenosis were indicated, various clinical trials were conducted to evaluate the efficacy of surgical treatments including angioplasty and/or stenting. However, the Stenting and Aggressive Medical Management for Preventing Recurrent Stroke in Intracranial Stenosis (SAMMPRIS) [3] and Vitesse Intracranial Stent Study for Ischemic Stroke Therapy (VISSIT) trials [5] suggested that drug treatment was the better option for symptomatic stenosis. The results of the SAMMPRIS and VISSIT trials determined the Japanese guideline that drug treatment is the first choice for symptomatic stenosis. So we focused on drug treatment in this case initially.

If the patient is intractable to drugs, our institute first examines whether there is insufficient haemodynamic status. In this case, we did not find sufficient collateral circulation, so we considered surgical treatment. Surgical treatment

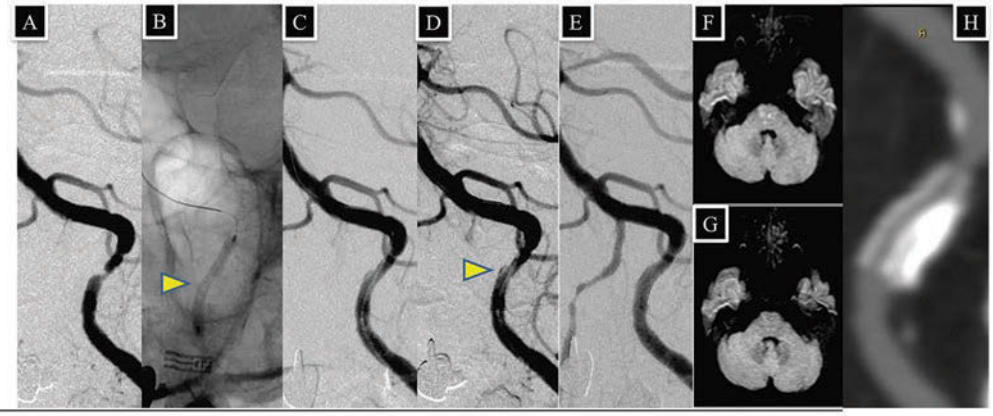

	Before_PTA	PTA	After_PTA	Stent_deploy	Stent_placed	POD1
Con	81	62	72	61	74	80
Ips	78	≦30	74	≦30	75	77

Fig. 2 Anteroposterior view of digital subtraction angiography (DSA) and the regional cerebral oxygen saturation before surgery(**A**), at percutaneous transluminal angioplasty (PTA) balloon inflated (**B**), immediately after PTA (**C**), at 5 min after PTA (**D**), after bare-metal stent placed (**E**). Postoperative magnetic resonance imaging (MRI) (**F**) showing no additional infarction. MRI (**G**) and computed tomography angiography (**H**) 6 years after surgery showing no recurrent stroke and well-dilated stenting continuously. *POD1* postoperative day 1, *Con* contralateral side, *Ips* Ipsilateral side

includes direct bypass surgery and endovascular surgery. Recently, some reports including the China Angioplasty and Stenting for Symptomatic Intra-cranial Severe Stenosis (CASSISS) trial showed the acceptable results of endovascular surgery [6], so we performed angioplasty and stenting.

Recently, in order to have the new surgical option preventing immediate cerebral hyperperfusion syndrome, we devised the outlet gate technique for CA revascularisation, in which the embolic balloon was deflated step by step in accordance with the ratio of ipsilateral rSO2 to contralateral rSO2, measured by a brain oximeter [2]. We applied this concept to the BBA revascularisation. Referring to the neuronavigational simulation by MRI and CT, and the midline suboccipital approach for cerebellar regional neurosurgery [7], we determined the cutline of hair and placement of the probe.

MRI, CT perfusion, and single-photon emission computed tomography are considered as gold standard diagnostic tests to assess the haemodynamic status, but these tests are not able to perform dynamically during surgery [2, 8]. Transcranial doppler is well known as a useful screening method in patients with insufficient haemodynamic status but is easily affected by motion artefacts and moreover requires expert skill [9, 10].

This report had several limitations. First, the criteria for using the evaluation of regional cerebral oxygen saturation remain unclear. Further study is necessary to establish appropriate criteria for using BBA stenosis. Second, there was not a healthy control group. Third, INVOS Cerebral/Somatic Oximeter is versatile but intrinsically not good at showing rSO2 values, especially below 15%, and the principle of analysis is not disclosed (Table 1) [11]. Further cases are needed to confirm the efficiency of the brain oximeter for BBA stenosis, to verify its potential for preventing perioperative complications, and to overcome these limitations.

Table 1 List of near-infrared spectroscopy available in Japan

Product name	INVOS	NIRO	O3 regional oximetry	TOS/HAND ai TOS	ForeSight	SenSmart
Principles of analysis	Not disclosed	Spatially Resolved Spectroscopy	Modified Beer–Lambert	Modified Beer–Lambert	Modified Beer–Lambert	Modified Beer–Lambert
Wavelength (nm)	730, 810	735, 810, 850	Not disclosed	770, 805, 870	690, 730, 770, 810, 870	730, 760, 810, 880
Applicable scope	Adults and infants	Adults and infants	Body weight ≥ 40 kg	Adults and infants	Adults and infants	Body weight ≥ 40 kg
Unique characteristics		Able to detect Oxy-Hb, and Deoxy-Hb concentrations approximatively	Able to integrate seamlessly (EEG etc.)	Able to withstand sunlight and a long period		Able to measure the transcutaneous oxygen saturation

Oxy-Hb oxyhemoglobin, *Deoxy-Hb* deoxyhemoglobin

5 Conclusion

Using the brain oximeter, which performs a minimally invasive evaluation of regional cerebral oxygen saturation, might be useful for surgical revascularisation not only in CA but also in BBA.

References

1. Gulli G, Marquardt L, Rothwell PM et al (2013) Stroke risk after posterior circulation stroke/transient ischemic attack and its relationship to site of vertebrobasilar stenosis: pooled data analysis from prospective studies. Stroke 44:598–604
2. Chimowitz MI, Lynn MJ, Howlett-Smith H et al (2005) Comparison of warfarin and aspirin for symptomatic intracranial arterial stenosis. N Engl J Med 352:1305–1316
3. Derdeyn CP, Chimowitz MI, Lynn MJ et al (2014) Aggressive medical treatment with or without stenting in high-risk patients with intracranial artery stenosis (SAMMPRIS): the final results of a randomised trial. Lancet 383:333–341
4. Okuma Y, Hirotsune N, Shinozaki K et al (2021) Near-infrared spectroscopy might help prevent onset of cerebral hyperperfusion syndrome. Adv Exp Med Biol 1269:63–67
5. Zaidat OO, Fitzsimmons BF, Woodward BK et al (2015) Effect of a balloon-expandable intracranial stent vs medical therapy on risk of stroke in patients with symptomatic intracranial stenosis: the VISSIT randomized clinical trial. JAMA 313:1240–1248
6. Gao P, Zhao Z, Wang D et al (2015) China Angioplasty and Stenting for Symptomatic Intracranial Severe Stenosis (CASSISS): a new, prospective, multicenter, randomized controlled trial in China. Interv Neuroradiol 21:196–204
7. Matsushima K, Yagmurlu K, Kohno M et al (2016) Anatomy and approaches along the cerebellar-brainstem fissures. J Neurosurg 124:248–263
8. Okuma Y, Harada K, Kegoya Y et al (2019) Assessment of the cerebral blood flow using single photon emission computed tomography and digital subtraction angiography in patients with internal carotid artery occlusion. Neurosurg Emerg 24:144–149
9. Cagnie B, Barbaix E, Vinck E et al (2006) Atherosclerosis in the vertebral artery: an intrinsic risk factor in the use of spinal manipulation? Surg Radiol Anat 28:129–134
10. Shu L, Riedel C, Meyne J et al (2017) Successful recanalization in acute basilar artery occlusion treated with endovascular therapy is independent of thrombus length. J NeuroInterventional Surg 9:1047
11. Okuma Y, Becker LB, Yagi T et al (2021) Evaluation of the quality of chest compression with oxyhemoglobin level by near-infrared spectroscopy in a rat asphyxia cardiac arrest model. Adv Exp Med Biol 1269:265–269

Assessment of Optimal Arterial Pressure with Near-Infrared Spectroscopy in Traumatic Brain Injury Patients

Andrey Oshorov, I. Savin, E. Alexandrova, and D. Bragin

Abstract

In patients with severe traumatic brain injury (TBI), simultaneous measurement of intracranial and arterial blood pressure (ICP and ABP, respectively) allows monitoring of cerebral perfusion pressure (CPP) and the assessment of cerebral autoregulation (CA). CPP, a difference between ICP and ABP, is the pressure gradient that drives oxygen delivery to cerebral tissue. CA is the ability of cerebral vasculature to maintain stable blood flow despite changes in CPP and thus, is an important homeostatic mechanism. Pressure reactivity index (PRx), a moving Pearson's correlation between slow waves in ICP and ABP, has been most frequently cited in literature over the past two decades as a tool for CA evaluation. However, in some clinical situations, ICP monitoring may be unavailable or contraindicated. In such cases, simultaneous mean arterial pressure (MAP) monitoring and near-infrared spectroscopy (NIRS) can be used for CA assessment by cerebral oximetry index (COx), allowing calculation of the optimal blood pressure (MAPOPT). The purpose of this study was to compare regional oxygen saturation (rSO2)-based CA (COx) with ICP/ABP-based CA (PRx) in TBI patients and to compare MAPOPT derived from both technologies. Three TBI patients were monitored at the bedside to measure CA using both PRx and COx. Patients were monitored daily for up to 3 days from TBI. Averaged PRx and COx-, and PRx and COx-based MAPOPT were compared using Pearson's correlation. Bias analysis was performed between these same CA metrics. Correlation between averaged values of COx and PRx was $R = 0.35$, $p = 0.15$. Correlation between optimal MAP calculated for COx and PRx was $R = 0.49$, $p < 0.038$. Bland–Altman analysis showed moderate agreement with a bias of 0.16 ± 0.23 for COx versus PRx and good agreement with a bias of 0.39 ± 7.89 for optimal MAP determined by COx versus PRx. Non-invasive measurement of CA by NIRS (COx) is not correlated with invasive ICP/ABP-based CA (PRx). However, the determination of MAPOPT using COx is correlated with MAPOPT derived from PRx. Obtained results demonstrate that COx is not an acceptable substitute for PRx in TBI patients. However, in some TBI cases, NIRS may be useful in determining MAP determination.

A. Oshorov (✉) · I. Savin · E. Alexandrova
Department of Neurosurgical Intensive Care, Burdenko Neurosurgery Institute, Moscow, Russia
e-mail: agvan2@gmail.com

D. Bragin
Lovelace Biomedical Research Institute, Albuquerque, NM, USA

Department of Neurology, University of New Mexico School of Medicine, Albuquerque, NM, USA

F. Scholkmann et al. (eds.), *Oxygen Transport to Tissue XLIII*, Advances in Experimental Medicine and Biology 1395, https://doi.org/10.1007/978-3-031-14190-4_23

Keywords

TBI · NIRS · Intracranial pressure (ICP) · Cerebral perfusion pressure (CPP) · Cerebral oximetry index · Pressure reactivity index (PRx)

1 Introduction

In patients with severe traumatic brain injury (TBI), simultaneous measurement of intracranial and arterial blood pressure (ICP and ABP, respectively) allows monitoring cerebral perfusion pressure (CPP) and the assessment of cerebral autoregulation (CA) [1]. CPP, a difference between ICP and ABP, is the net pressure gradient that drives oxygen delivery to cerebral tissue [2]. Cerebral autoregulation (CA) is a crucial mechanism for maintaining stable cerebral blood flow (CBF) [3]. Compromised cerebral autoregulation is the main reason for hypo- or hyper- perfusion and a key element of secondary brain damage in patients with traumatic brain injury (TBI) [1–3]. Currently, clinicians have access to various methods for assessing the status of autoregulation [4]. The current consensus (expert opinion) is that none of the existing techniques can be considered a standard for autoregulation assessment [5]. Nevertheless, the most straightforward and accessible method of surrogate evaluation of cerebral autoregulation in patients with acute cerebral injury remains the pressure reactivity index (PRx) [5, 6]. PRx is calculated as a moving correlation coefficient between intracranial pressure (ICP) and arterial blood pressure (ABP) signals [7]. However, in some clinical situations, ICP monitoring may be unavailable or contraindicated. In such cases, simultaneous ABP monitoring and near-infrared spectroscopy (NIRS) can be used for CA assessment by cerebral oximetry index (COx), allowing calculation of the optimal blood pressure (MAPOPT) [8, 9]. The purpose of this study was to compare the regional oxygen saturation (rSO2)-based CA (COx) with ICP/ABP-based CA (PRx) in TBI patients and to compare the MAPOPT derived from both technologies.

2 Methods

In this work, we present retrospective data of multimodal neuromonitoring of 3 patients with severe TBI (Tables 1 and 2). The study conformed to the Declaration of Helsinki standards and was approved by the Burdenko Institute Ethics Committee. At the time of hospitalisation, two out of three patients were in a coma, Glasgow Coma Scale (GCS) 7, one patient was confused (GCS 12), but then worsened to coma. All patients required mechanical ventilation and had direct arterial blood pressure (ABP) monitoring using a catheter in the radial artery. All patients were treated according to international guidelines [10]. Codman ICP probes (Codman & Shurtleff Inc., Raynham, MA) were installed at the Kocher point to a depth of 2 cm and connected to 'ICP Express Codman' and bedside 'Philips IntelliVue MP60' (Philips Medical Systems, Best, The Netherlands) monitors.

The patients were connected to 'NIRS INVOS 5100 (Covidien, Boulder, CO)' using self-adhesive sensors attached to each side of the forehead. COx coefficient was carried out in a time window of 6 h, with a successive repetition of 6 times (Table 3). After excluding artifacts, we compared six 6-h epochs (36 h in total) of ABP, ICP, rSO2 simultaneous recordings for each patient. All raw and calculated signals were analysed using ICM+ software (Cambridge, UK) [11]. The COx was calculated as a moving correlation between the slow waves of rSO2 and MAP [8]. The PRx was calculated as a coefficient between slow waves of ICP and MAP [7]. The COx and PRx measurements from the monitoring onset were binned into 5-mmHg increments of MAP for analysis. Optimal MAP for each

Table 1 Clinical characteristics of the patients

Pts no.	Age(years)	Sex	CT Marshall	GCS	GOS
1	16	M	DI II	7	4
2	27	M	DI I	7	5
3	28	M	DI II	12[a]	1

CT Marshall classification of TBI pts. based on computerised tomography, *DI* diffuse injury

[a]Patient № 3 was GCS 12 at the time of hospitalisation, but later deteriorated to GCS 6

Table 2 Physiologic variables (mean ± SD) for all periods of monitoring

Pts no.	MAP(mmHg)	ICP(mmHg)	COx-R	COx-L	PRx
1	92 ± 8	14 + 3	0.02 + 0.32	0.04 + 0.32	−0.32 + 0.33
2	89 ± 7	9.8 + 3	0.08 + 0.25	0.09 + 0.25	0.11 + 0.29
3	86 ± 8	9.5 + 5	0.02 + 0.24	0.03 + 0.28	0.27 + 0.35

MAP mean arterial pressure, *ICP* mean intracranial pressure, *COx-R, and COx-L* cerebral oximetry index on the right and left side, *PRx* pressure reactivity index

Table 3 Data from six sequential 6-h periods of monitoring

Pts no.	6 h-period	COx	PRx	MAP_{opt}_COx	MAP_{opt}_PR
1	1	−0.19	−0.52	94	102
	2	−0.03	−0.55	107	100
	3	−0.07	−0.6	91	90
	4	−0.07	−0.57	103	97
	5	0.07	−0.32	98	77
	6	0.05	−0.28	92	86
2	1	0.07	0.03	84	91
	2	0.02	0.01	88	90
	3	0.14	0.06	99	86
	4	0.05	−0.07	82	86
	5	0.1	0.01	82	85
	6	0.08	0.09	87	88
3	1	−0.12	0.02	102	102
	2	−0.38	−0.24	90	98
	3	−0.07	−0.23	89	89
	4	−0.05	−0.24	71	83
	5	−0.12	−0.13	90	93
	6	−0.09	0.12	92	91

Cox averaged cerebral oximetry index, *PRx* averaged pressure reactivity index, *MAP_{opt}_COx and MAP_{opt}_PRx* optimal blood pressure estimated by COx and PRx

patient was defined as the MAP with the best autoregulation [7, 8]. Statistical analyses were performed using Statistica10.0 (StatSoft, USA). The Blunt-Altman method was used to compare PRx and COx. Correlations between COx and PRx values were determined using Pearson's correlation coefficient. All data are presented as mean ± standard deviation.

3 Results

All patients were male, 23.6 +/− 6.6 years old (Table 1). According to the Marshall CT classification, two patients had diffuse brain injury DI II, and one patient1 had DI I [18]. Data for all periods of monitoring are presented in Table 2. MAP was 89 +/− 7.6 mmHg, ICP was 12 +/− 7.7 mmHg, CPP was 78 +/− 8.9 mmHg, rSO2-R was 74+/− 4.3%, rSO-L was 68.3 +/− 3.8%. Correlation between the averaged values of COx and PRx was not significant $R = 0.35$, $p = 0.15$ (Fig. 1a). Correlation between optimal MAP calculated for COx and PRx was $R = 0.49$, $p < 0.038$ (Fig. 1c). Bland–Altman analysis showed moderate agreement with a bias of 0.16 ± 0.23 for COx versus PRx (Fig. 1b). There was a good agreement with a bias of 0.39 ± 7.89 for optimal MAP determined by COx versus optimal MAP determined by PRx (Fig. 1d).

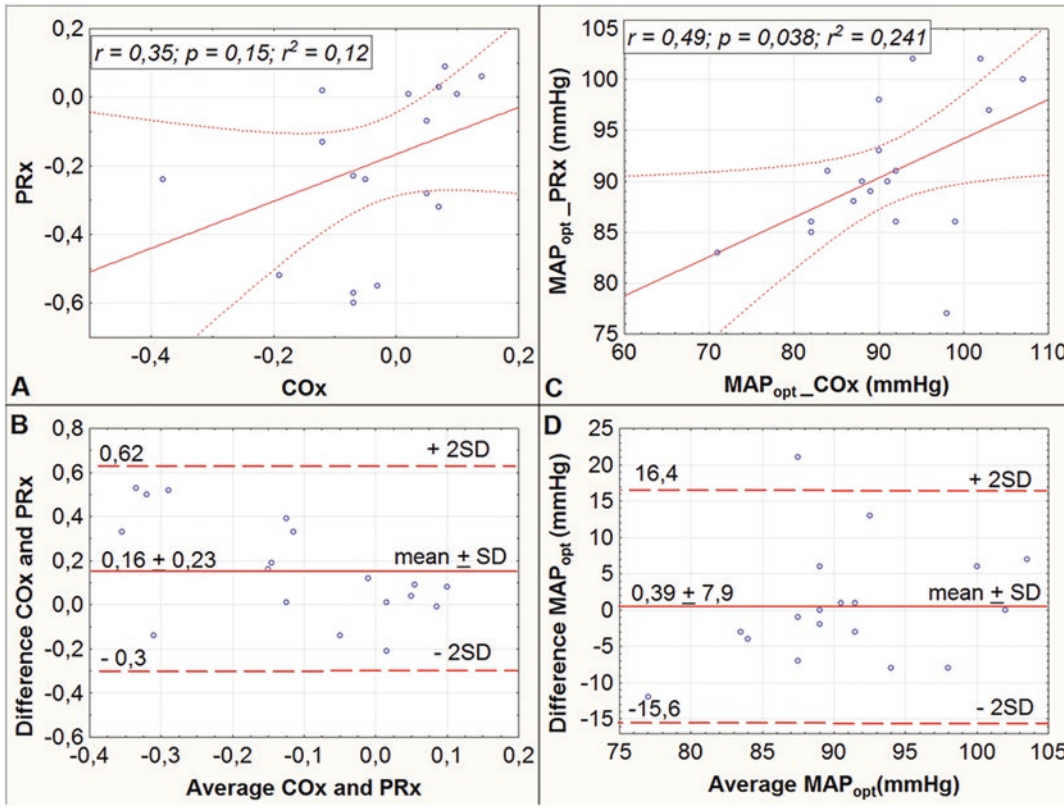

Fig. 1 (**a**, **b**) – correlation and Bland-Altman plot COx and PRx; (**c**, **d**) – correlation and Bland-Altman plot MAPopt_PRx and MAPopt_ORx

4 Discussion

In the presented clinical observations, we compared invasive (PRx) and non-invasive (Cox) methods for autoregulation evaluation. We specifically selected similar patients with severe TBI and diffuse brain injury (DI I and DI II) [12] with unclear or questionable indications of ICP monitoring [13]. Nevertheless, in the absence of indications for invasive ICP monitoring, blood pressure control remains an essential option in the management of such patients; thus, the presence of target optimal blood pressure is probably beneficial. A number of studies have shown that high deviation from optimal blood pressure is associated with worse outcomes in patients with traumatic brain injury [14, 15]. At the same time, in patients after cardiac arrest, maintaining perfusion close to optimal blood pressure improved brain oxygenation [16]. We await the final results of the COGiTATE Study [17] and hope that the protocol for optimising ABP/CPP will take an important place in the management of patients with acute brain damage. We hope that wavelet analysis and controlled generation of slow waves will improve the quality of autoregulation monitoring by reducing signal noise and expanding the possibilities of non-invasive assessment of autoregulation [18, 19].

5 Conclusions

The obtained results demonstrate that NIRS-derived COx is not an acceptable substitute for ICP/ABP-derived PRx monitoring in TBI patients. However, in some TBI cases, NIRS may be useful for optimal MAP determination.

Acknowledgments DB was supported by NIH R01 NS112808.

References

1. Czosnyka M, Miller C, Le Roux P et al (2014) Participants in the international multidisciplinary consensus conference on multimodality monitoring. Monitoring of cerebral autoregulation. Neurocrit Care Suppl 2:S95–S102
2. Rosner MJ, Daughton S (1990) Cerebral perfusion pressure management in head injury. J Trauma 30:933–940
3. Lassen NA (1964) Autoregulation of cerebral blood flow. Circ Res 15(SUPPL):201–204
4. Zeiler FA, Donnelly J, Calviello L et al (2017) Pressure autoregulation measurement techniques in adult traumatic brain injury, part II: a scoping review of continuous methods. J Neurotrauma 34(23):3224–3237
5. Depreitere B, Citerio G, Smith M et al (2021) Cerebrovascular autoregulation monitoring in the management of adult severe traumatic brain injury: a Delphi consensus of clinicians. Neurocrit Care 34(3):731–738
6. Czosnyka M, Brady K, Reinhard M et al (2009) Monitoring of cerebrovascular autoregulation: facts, myths, and missing links. Neurocrit Care 10(3):373–386
7. Czosnyka M, Smielewski P, Kirkpatrick P et al (1997) Continuous assessment of the cerebral vasomotor reactivity in head injury. Neurosurgery 41(1):11–17
8. Brady KM, Lee JK, Kibler KK et al (2007) Continuous time-domain analysis of cerebrovascular autoregulation using near-infrared spectroscopy. Stroke 38:2818–2825
9. Rivera-Lara L, Geocadin R, Zorrilla-Vaca A et al (2017) Validation of near-infrared spectroscopy for monitoring cerebral autoregulation in comatose patients. Neurocrit Care 27(3):362–369
10. Brain Trauma Foundation, American Association of Neurological Surgeons (2007) Guidelines for the management of severe traumatic brain injury. J Neurotrauma 24(Suppl 1):S1–S106
11. Smielewski P, Czosnyka M, Steiner L et al (2005) ICM+: software for on-line analysis of bedside monitoring data after severe head trauma. Acta Neurochir Suppl 95:43–49
12. Marshall LF, Marshall SB, Klauber MR (1991) A new classification of head injury based on computerized tomography. J Neurosurg 75(Special Supplements):S14–S20
13. Stocchetti N, Picetti E, Berardino M et al (2014) Clinical applications of intracranial pressure monitoring in traumatic brain injury: report of the Milan consensus conference. Acta Neurochir 156(8):1615–1622
14. Steiner LA, Czosnyka M, Piechnik SK et al (2002) Continuous monitoring of cerebrovascular pressure reactivity allows determination of optimal cerebral perfusion pressure in patients with traumatic brain injury. Crit Care Med 30(4):733–738
15. Aries MJ, Czosnyka M, Budohoski KP (2012) Continuous determination of optimal cerebral perfusion pressure in traumatic brain injury. Crit Care Med 40(8):2456–2463
16. Sekhon MS, Gooderham P, Menon DK et al (2019) The burden of brain hypoxia and optimal mean arterial pressure in patients with hypoxic ischemic brain injury after cardiac arrest. Crit Care Med 47(7):960–969
17. Tas J, Beqiri E, van Kaam CR et al (2021) An update on the COGiTATE phase II study: feasibility and safety of targeting an optimal cerebral perfusion pressure as a patient-tailored therapy in severe traumatic brain injury. Acta Neurochir Suppl 131:143–147
18. Liu X, Hu X, Brady KM et al (2020) Comparison of wavelet and correlation indices of cerebral autoregulation in a pediatric swine model of cardiac arrest. Sci Rep 10(1):5926
19. Brady KM, Easley RB, Kibler K et al (2012) Positive end-expiratory pressure oscillation facilitates brain vascular reactivity monitoring. J Appl Physiol 113(9):1362–1368

Effects of Exercise-Diet Therapy on Cognitive Function in Healthy Elderly People Evaluated by Deep Learning Based on Basic Blood Test Data

K. Sakatani, K. Oyama, L. Hu, S. Warisawa, and T. Yamashita

Abstract

Background: Recent studies reported that vascular cognitive impairment in the elderly caused by arteriosclerosis plays an important role in cognitive disorders in both vascular dementia and Alzheimer's disease. In addition, systemic metabolic disorders such as oxygen metabolism dysfunction could be risk of dementia. Based on these findings, we have developed a deep neural network-based screening test (DNN-based test) of cognitive function using basic blood test data, which allowed prediction of cognitive function expressed by Mini Mental State Examination (MMSE) scores. Aim: Here, we investigated whether the DNN-based test could be applicable to assessment of the effects of exercise-diet on cognitive function. Methods: We studied the following two groups: (1) seven subjects of the local fitness gym (68.6 ± 3.2 years old). We evaluated cognitive function by the DNN-based test using blood data before and after the intervention (for 3 months). These results were compared with the measured MMSE score. (2) we studied a total of 230 subjects (67.9 ± 7.4 years old) who were members of the Tsuminory health class (Apple classroom). We assessed cognitive function by the DNN-based test before and after the intervention (for 2 months). We compared the predicted MMSE scores by the DNN-based test before and after the 2-month intervention. Results: In the first group, the MMSE score predicted by the DNN-based test increased from 27.1 ± 0.8 to 27.6 ± 0.7 after the intervention period ($p = 0.024$). The measured MMSE score also increased after exercise, but not significant ($P = 0.28$). In the second group, the exercise-diet therapy increased the predicted MMSE scores in 189 cases ($p < 0.001$). In contrast, the therapy significantly reduced the mean MMSE score ($p < 0.001$). Discussion: The MMSE score predicted by the DNN-based test were increased by exercise-diet therapy in most subjects. The DNN-based test may be useful to monitor the effect of exercise-diet therapy on cognitive function aged people.

K. Sakatani (✉) · L. Hu · S. Warisawa
Department of Human and Engineered Environmental Studies, Graduate School of Frontier Sciences, The University of Tokyo, Tokyo, Japan
e-mail: k.sakatani@edu.k.u-tokyo.ac.jp

K. Oyama
Department of Computer Science, College of Engineering, Nihon University, Tokyo, Japan

T. Yamashita
Tsuminori Internal Medicine Clinic, Tokyo, Japan

F. Scholkmann et al. (eds.), *Oxygen Transport to Tissue XLIII*, Advances in Experimental Medicine and Biology 1395, https://doi.org/10.1007/978-3-031-14190-4_24

Keywords

Vascular cognitive impairment · Dementia · Mild cognitive impairment · Deep neural network

1 Introduction

As the world's population ages rapidly, dementia is becoming a major global health problem. Early detection of mild cognitive impairment (MCI) is important for the effective treatment and prevention of dementia. Therefore, screening tests for cognitive function are critical. Currently, the Mini Mental State Examination (MMSE) are commonly used to screen for cognitive impairment [1]. However, it is impractical to screen a large number of subjects over a short time period, given that it is subjective in nature and conducted on a one-to-one basis between the inspector and subject.

To resolve this problem, based on the findings that systemic metabolic disorders, including lifestyle-related diseases and anemia, affect cognitive function [2, 3], we have developed a deep neural network (DNN) model that can estimate cognitive function using basic blood test data that do not contain dementia-specific biomarkers; the estimated cognitive function was expressed by the MMSE score [4].

In the present study, we evaluated the usefulness of the DNN-based model in monitoring the effect of exercise-diet therapy on cognitive function in the elderly; exercise-diet therapy has been reported to be effective in improving cognitive function and preventing dementia onset [5]. We estimated cognitive function by the DNN model using data from blood tests performed before and after the exercise-diet therapy. In a pilot study, we compared the effect of the exercise-diet therapy on the MMSE score estimated by the DNN model and the MMSE score actually measured.

2 Methods

2.1 Subjects and Study Protocol

We studied the following two groups: (i) members of the local fitness gym (Fukushima, Japan); seven subjects (two males and five females, average age 68.6 ± 3.2 years old). Exercise was freely performed by each person using exercise equipment in the fitness gym. Approximately 1 h of exercise was performed 2–3 times a week. The blood sampling and MMSE were performed before and after the intervention period (for 3 months). (ii) members of the Tsuminory health education class "Apple class" (Kagoshima, Japan); 230 subjects (31 males and 199 females, average age 67.9 ± 7.4 years old). Subjects were divided into four classes according to the MMSE score evaluated by the DNN-based test of cognitive function: Class A (28≦, ≦30, n = 183), B (24≦, ˂28, n = 44), C (20≦, ˂24, n = 2), D (˂20, n = 1). We compared the MMSE scores assessed by the DNN-based test before and after the exercise-diet therapy performed in Apple class (2 months).

2.2 Blood Test

We performed a blood test in all the subjects, including a complete blood count and basic metabolic panel before and after the exercise-diet therapy. The blood test items are shown in Table 1.

2.3 Deep Learning-Based Assessment of Cognitive Function

We employed the DNN-based screening test that predicts cognitive impairment expressed by MMSE score based on basic blood test data and subject age [4]. Briefly, we used the H_2O open source machine learning library to implement the DNN [6]. Input to the DNN in this study consists of 24 variables including the subject's age and 23 blood test items

Table 1 Blood test items to be input into the DL-based test of cognitive function

Complete blood count	General biochemical examination	
WBC count	Total protein	BUN
RBC count	Albumin	Creatinine
Hemoglobin	A/G ratio	Uric acid
Hematocrit	AST (GOT)	Glucose
MCV	ALT (GPT)	Na
MCH	r-GTP	K
MCHC	Total cholesterol	CI
Platelet count	Triglyceride	

MCV mean corpuscular volume, *MCH* mean corpuscular hemoglobin, *MCHC* mean corpuscular hemoglobin concentration, *BUN* blood urea nitrogen

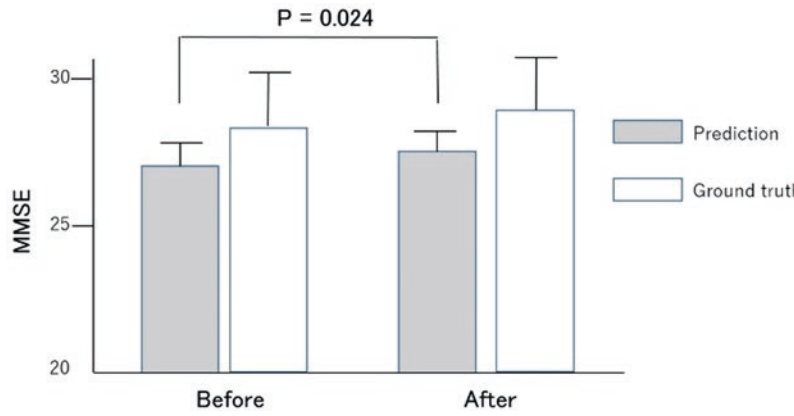

Fig. 1 Comparison of measured and predicted MMSE scores before and after exercise-diet therapy. Grey bars indicate MMSE scores predicted by the DNN-based test of cognitive function while white bars indicate measured MMSE scores. The error bars indicate SD

(Table 1) in the input layer. The DNN has two hidden layers with 400 neurons each.

3 Results

In the first group, the MMSE score predicted by the DNN-based test increased from 27.1 ± 0.8 to 27.6 ± 0.7 after the intervention period ($p = 0.024$). The measured MMSE score also increased from 28.4 ± 2.2 to 29.0 ± 1.9 after the intervention period, but there was no significant difference ($p = 0.28$) (Fig. 1).

In the second group, the exercise-diet therapy increased the predicted MMSE scores in 189 cases: the mean MMSE score increased from 28.0 ± 1.7 to 28.4 ± 1.2 significantly after the exercise-diet therapy ($p < 0.001$). In 26 cases, the cognitive class was elevated after the therapy; Class B → A (23 cases), C → B (two cases), D → C (one case). In Class A (n = 163), mean MMSE scores increased from 28.4 ± 1.1 to 28.6 ± 1.2 ($p < 0.05$). In contrast, the therapy significantly reduced the mean MMSE score from 27.7 ± 0.7 to 26.1 ± 0.8 in Class A (20 subjects) and B (one subject) ($p < 0.001$). In the remaining 20 subjects, the predicted MMSE scored did not change significantly ($p > 0.05$) (Table 2).

4 Discussion

This is the first study to apply AI technology (i.e., deep learning) to interventions to prevent dementia. In our previous studies, we developed the DNN-based test of cognitive function based on the relation between cognitive function and systemic metabolic disorders including lifestyle diseases and other metabolic disorders (Fig. 2). In contrast to the previous study that estimated cognitive function from blood test data at a given point in time [4], this study estimated cognitive function from blood test data before and after the period of the exercise-diet therapy and evaluated the effect of the therapy.

What is important is that although it is difficult to treat neurodegeneration, it is possible to treat and prevent systemic metabolic diseases such as lifestyle-related diseases and prevent the onset of dementia. For example, the exercise-diet therapy is well known to be effective for cognitive impairment [5].

Table 2 Change of MMSE scores after exercise-diet therapy in Apple class

Changes of MMSE scores		Before	After	p value
Increases (n = 189)	With increases of Class (n = 26)	25.4 ± 2.6	27.4 ± 1.3	$p < 0.001$
	Class A (n = 163)	28.4 ± 1.1	28.6 ± 1.2	$p < 0.05$
Decreases (n = 21)		27.7 ± 0.7	26.1 ± 0.8	$p < 0.001$
No change (n = 20)		26.0 ± 0.8	25.7 ± 0.8	$p > 0.05$

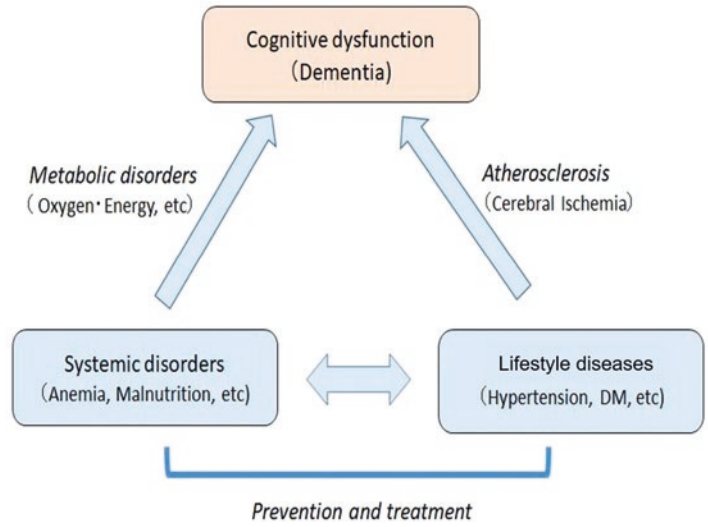

Fig. 2 Relations between cognitive dysfunction and systemic metabolic disorders. Mechanisms of cognitive dysfunction in the elderly with systemic metabolic disorders and arteriosclerosis induced by lifestyle diseases. The systemic disorders can be prevented and treated, which leads to the prevention and improvement of cognitive impairment in elderly people

In the first group, although the number of subjects was small (n = 7), a statistically significant increase was observed in predicted MMSE scores after a 3-month exercise-diet therapy ($p = 0.024$). The average value of measured MMSE scores increased after the therapy, however, there was no statistical significance. In the second group, the DNN-based test showed significant increases of predicted MMSE scores in 163 subjects. In addition, the cognitive class was elevated in 46 subjects. The DNN-based test predicts cognitive function based on general blood test data which reflect systemic metabolic function. Therefore, the present results suggest that the mechanism of the effect of exercise-diet therapy on cognitive function involves the systemic metabolic changes induced by the exercise-diet therapy.

Finally, we discuss the advantages and limitations of the DNN-based test of cognitive impairment. First, the DNN-based test, unlike the MMSE, is an objective assessment of cognitive function. This is an inexpensive and non-invasive test because it uses blood test data rather than dementia-specific biomarkers such as amyloid beta. In addition, this test may contribute to personalised care for the prevention of dementia, because the blood test data reflect systemic metabolic abnormalities which could affect cognitive function. Such abnormalities include anemia [3], malnutrition [7], renal function impairment [8] and liver dysfunction [9]. Importantly, these systemic disorders can be detected via basic blood tests of health examination. However, it should be noted that this test may overlook changes in cognitive function induced by direct brain stimulation such as computer games [10], since it does not measure the brain function directly. In addition, it should be noted that the number of women was 2.5–6 times higher than that of men. The effects of the exercise-diet therapy in this study need to be carefully evaluated because there are differences in cognitive function and degree of cerebral atrophy between men and women [11]. Further research, including a prospective cohort study of large numbers of subjects, should be conducted to scientifically validate the DNN-based test of cognitive function.

In summary, this study suggests that DNN-based test of cognitive function may help objectively assess the effect of exercise-diet therapy on cognitive function in the elderly. The combination of the DNN-based test and exercise-diet interventions may be useful to prevent the onset of dementia.

Acknowledgments The part of the present study was supported by the Koriyama Health Promotion Foundation and Xebio Cooperation in Japan.

References

1. Arevalo-Rodriguez I, Smailagic N, Roqué IFM et al (2015) Mini-Mental State Examination (MMSE) for the detection of Alzheimer's disease and other dementias in people with mild cognitive impairment (MCI). Cochrane Database Syst Rev 21(3):362. CD010783
2. Van Der Flier WM, Skoog I, Schneider JA et al (2018) Vascular cognitive impairment. Nat Rev Dis Primers 4:18003
3. Hong CH, Falvey C, Harris TB et al (2013) Anemia and risk of dementia in older adults: findings from the Health ABC study. Neurology 81:528–533
4. Sakatani K, Oyama K, Hu L (2020) Deep learning-based screening test for cognitive impairment using basic blood test data for health examination. Front Neurol 11:588140
5. Ngandu T, Lehtisalo J, Solomon A et al (2015) A 2 year multidomain intervention of diet, exercise, cognitive training, and vascular risk monitoring versus control to prevent cognitive decline in at-risk elderly people (FINGER): a randomised controlled trial. Lancet 385(9984):2255–2263
6. Sze V, Chen YH, Yang TJ, Joel S (2017) Efficient processing of deep neural networks: a tutorial and survey. Proc IEEE 105:3295–3329
7. Sugimoto T, Arai H, Sakurai T (2022) An update on cognitive frailty: its definition, impact, associated factors and underlying mechanisms, and interventions. Geriatr Gerontol Int 22(2):99–109
8. Miranda AS, Cordeiro TM, Dos Santos Lacerda Soares TM et al (2017) Kidney-brain axis inflammatory crosstalk: from bench to bedside. Clin Sci (Lond) 131:1093–1105
9. Kunutsor SK, Laukkanen JA (2016) Gamma glutamyl transferase and risk of future dementia in middle-aged to older Finnish men: a new prospective cohort study. Alzheimers Dement 12:931–941
10. Djabelkhir L, Wu YH, Vidal JS et al (2017) Computerized cognitive stimulation and engagement programs in older adults with mild cognitive impairment: comparing feasibility, acceptability, and cognitive and psychosocial effects. Clin Interv Aging 12:1967–1975
11. Li R, Singh M (2014) Sex differences in cognitive impairment and Alzheimer's disease. Front Neuroendocrinol 35(3):385–403

NIRS Studies Show Reduced Interhemispheric Functional Connectivity in Individuals with Multiple Sclerosis That Exhibit Cortical Hypoxia

Ateyeh Soroush, Damilola D. Adingupu, Taelor Evans, Scott Jarvis, Lenora Brown, and Jeff F. Dunn

Abstract

Many with multiple sclerosis (MS) have low cortical microvascular oxygen levels (hypoxia), which have been previously proposed to exacerbate inflammation in MS. We do not know if hypoxia impacts or relates to brain function. We hypothesise that within the MS population, those who have hypoxia may show reduced brain functional connectivity (FC). We recruited 20 MS participants and grouped them into normoxic and hypoxic groups (n = 10 in each group) using frequency-domain near-infrared spectroscopy (fdNIRS). Functional coherence of the haemodynamic signal, quantified with functional near-infrared spectroscopy (fNIRS) was used as a marker of brain function and was carried out during resting-state, finger-tapping, and while completing two neurocognitive tasks. Reduced FC was detected in the hypoxic MS group. fNIRS measures of haemodynamic coherence in MS could be a biomarker of functional impairment and/or disease progression.

Keywords

Cortical microvascular tissue haemoglobin saturation · S_tO_2 · fNIRS · Controlled oral word association test (COWAT) · Paced auditory serial addition test (PASAT)

1 Introduction

Multiple sclerosis (MS) is a chronic neurological disease characterised by inflammation and degeneration within the central nervous system

A. Soroush · D. D. Adingupu · T. Evans
J. F. Dunn (✉)
Hotchkiss Brain Institute (HBI), University of Calgary, Calgary, Canada

Department of Radiology, University of Calgary, Calgary, Canada

Department of Clinical Neurosciences, University of Calgary, Calgary, Canada

Experimental Imaging Center (EIC), Cumming school of Medicine, University of Calgary, Calgary, Canada
e-mail: dunnj@ucalgary.ca

S. Jarvis
Department of Radiology, University of Calgary, Calgary, Canada

Department of Clinical Neurosciences, University of Calgary, Calgary, Canada

L. Brown
Hotchkiss Brain Institute (HBI), University of Calgary, Calgary, Canada

Department of Clinical Neurosciences, University of Calgary, Calgary, Canada

F. Scholkmann et al. (eds.), *Oxygen Transport to Tissue XLIII*, Advances in Experimental Medicine and Biology 1395, https://doi.org/10.1007/978-3-031-14190-4_25

(CNS) [1]. According to the most extensive global study to date, there are 2.8 million people worldwide who have MS [2]. The demyelination and lesions associated with MS can affect how brain regions communicate with each other and the damage can alter the brain functional connectivity (FC). However, controlling for factors that may affect inflammation, such as cortical microvascular oxygen levels, in MS is extremely important for the assessment of FC.

Hypoxia, which is defined as low cortical microvascular oxygenation [3], has been associated with MS [4]. Previous studies have shown that lesion formation occurs most commonly in brain regions that have poor blood flow, or perfusion, and are thus susceptible to hypoxia [5]. Frequency-domain near-infrared spectroscopy (fdNIRS), a type of non-invasive optical imaging, has previously shown that about 40% of the MS population have hypoxia [6]. Hypoxic individuals with MS are those with significantly lower cortical microvascular tissue haemoglobin saturation (S_tO_2), measured by fdNIRS, when compared to a healthy control group. We have proposed that hypoxia in MS may contribute to inflammation [4] and reduced brain function.

We utilised functional near-infrared spectroscopy (fNIRS) to obtain changes in oxygenated haemoglobin (ΔHbO) and used this measure to compute the continuous wavelet coherence to quantify FC as a marker of brain function. FC is the statistical association between time series of physiological signals from different parts of the brain. The concept of FC, using wavelet coherence [7], is based on the assumption that brain regions exhibiting a similar temporal and frequency evolution of activity, share information and are thereby connected in a functional manner [8].

Previous studies have assessed brain FC using functional magnetic resonance imaging (fMRI) and fNIRS, and reported reductions in brain network connectivity in MS population during rest and non-rest activity states [9, 10]. However, very little is known about the effects of hypoxia on FC in MS. We studied the FC in different brain regions during resting-state and non-rest tasks. We hypothesise that hypoxia in MS is associated with reduced brain functional communication, as measured by quantifying coherence of frequencies of regional haemodynamic response.

2 Methods

2.1 Participants

We recruited 20 individuals with MS (51.6 ± 8.7 years). Based on the methodology used in a previous literature [6], we grouped the participants into hypoxic and normoxic groups (n = 10/group). The method used for grouping is explained in detail in Sect. 2.2. Ethics approval for the investigation was given by the University of Calgary Conjoint Health Research Ethics Board (REB19-1105).

2.2 Protocol and Devices

An fdNIRS device, OxiplexTS (model 96208, ISS Inc., Champaign, IL), was used to quantify the cortical microvascular S_tO_2 and for grouping participants into hypoxic and normoxic. An fdNIRS probe, with 4 sources and 1 detector, was placed on each participant's forehead (~1.5 cm above the eyebrows, ~1 min each side) to measure the S_tO_2. We used a NIRScout fNIRS device (NIRX, California, US) with 16 sources and 16 detectors, distributed over frontal and sensorimotor areas. The distance between each pair of source and detector was between 28 and 30 mm. Participants underwent an 8-min resting-state in which they were sat in a chair, looking at a plus sign displayed on a monitor. A 4-min finger-tapping period (with frequency of 1 Hz, 10 s on, 30 s off, 6 trials) was followed by two neurocognitive tasks (i.e., the controlled oral word association test (COWAT), and paced auditory serial addition test (PASAT)).

The COWAT [11] is a verbal fluency test wherein participants were asked to list as many words as they could that began with a specific letter of the alphabet (i.e., F, A, and S) in three 1-min trials. In the fourth trial, participants were asked to list as many animals as they could that

began with any letter of the alphabet. The PASAT [12] is a test designed to assess attention, concentration, and auditory processing speed. In this test, a recorded series of 61 integer numbers (between 1 and 9) were played aloud at the rate of one number every 3 s. The participants were asked to add each spoken number to the number that was presented previously.

2.3 Data Processing

Processing was done using MATLAB (version 2020b, MathWorks, Natick, MA, USA) and Homer3 packages. Raw fNIRS time series data were converted to optical density (OD) using the modified Beer-Lambert law. The OD was converted to ΔHbO using the differential pathlength factor (DPF), which is an age-dependent value. A Savitzky-Golay filter with window length of 11 ms and order of 5 was used for motion detection and correction. Individual channels with a signal-to-noise ratio (SNR) below 5 were discarded. A bandpass filter (0.015–0.25 Hz) was utilised to remove cardiac and respiratory frequencies. Channels were grouped into two main regions of frontal and sensorimotor cortices (left and right areas) with two pairs channels in each area. Square wavelet coherence was used as a measure of FC between hemispheres in each region. Results were split into two frequency windows to investigate the effect of frequency on results and control for the task frequency of activation: a low frequency window (LFW) = 0.015–0.075 Hz and a high frequency window (HFW) = 0.075–0.25 Hz. The values were then averaged across time and frequency. Therefore, for each participant we had 16 values (during 4 tasks, in 2 brain regions, and within 2 frequency windows).

2.4 Statistical Processing

Statistical analyses were done in Rstudio (version 1.3.1056) (R Core Team, 2020). An independent-samples t-test was conducted to determine the effect of interhemispheric coherence on groups. Data were statistically analysed separately within each frequency window, during each task and for each brain region.

3 Results

The S_tO_2 values for controls are reported in an accompanying ISOTT paper [13]. In the MS group, those with S_tO_2 values that were less than 2 SDs below the control mean were classified as hypoxic (<=55.1%) and the rest were in the normoxic group. There were 10 hypoxic individuals with MS in the 20 volunteers.

Figure 1 shows the reduction in FC in the hypoxic MS group compared with the normoxic MS group. It is shown that during finger-tapping, using LFW, there was a significant reduction in the hypoxic MS group in the coherence between left and right sensorimotor cortex (normoxic = 0.65 ± 0.11, mean ± SD; hypoxic = 0.52 ± 0.14, $p = 0.048$).

The FC obtained during the COWAT, using the HFW, was reduced between left and right sensorimotor areas in the hypoxic MS group (normoxic = 0.61 ± 0.17, mean ± SD; hypoxic = 0.43 ± 0.14, $p = 0.020$).

FC was also reduced during the PASAT, between left and right sensorimotor areas, using the HFW (normoxic = 0.67 ± 0.19, mean ± SD; hypoxic = 0.49 ± 0.14, $p = 0.028$).

4 Discussion

This study shows that the presence of hypoxia relates to the interhemispheric FC in individuals with MS, during task execution. Our data also suggest that the frequency activation of a task could impact the FC results when the task activation frequency is within the frequency window in which FC reduction was observed. Moreover, we show that lower interhemispheric FC in the hypoxic MS group is significant in brain regions associated with the performed task.

Jimenez et al. [10] previously reported decreased interhemispheric FC during finger-tapping in individuals with MS. They hypothe-

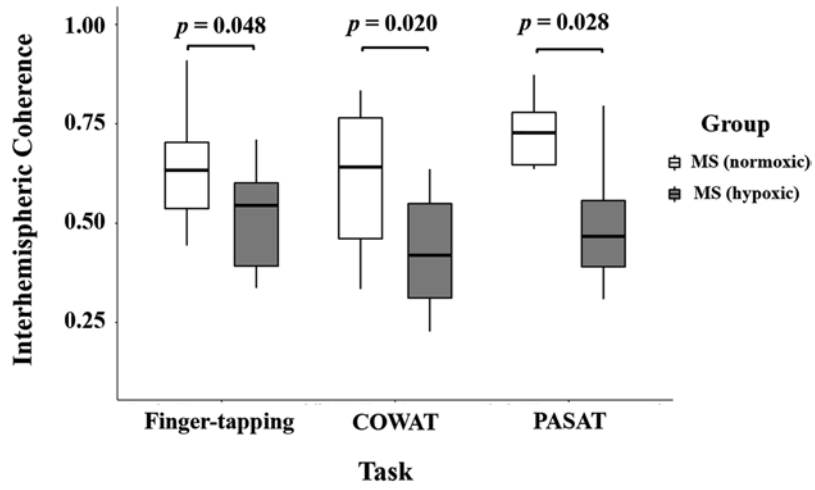

Fig. 1 Interhemispheric coherence values, between left and right sensorimotor regions, for normoxic MS and hypoxic MS groups. Results are shown during finger-tapping using the low frequency window (LFW), COWAT using the high frequency window (HFW), and PASAT using the high frequency window (HFW)

sised that impaired communication following white matter degeneration and axonal loss is the main factor leading to the lower coherence in the MS population. In our case, using the same finger-tapping task, we show that the presence of hypoxia relates to the reduced FC though we do not report the difference with healthy controls.

There was also a reduction in FC in the hypoxic MS group, between the left and right sensorimotor areas, during the COWAT task. Having a change in the sensorimotor area during a cognitive task is possible, as there is a reported relationship between the sensorimotor cortex and cognitive function in the human cerebellum [14]. During the PASAT the hypoxic group showed reduced FC. The auditory cortex as well as brain regions associated with cognition are involved during the PASAT. Based on the montage used in this study, the closest pairs of channels to the primary and secondary auditory cortices are in the sensorimotor area and so we may be detecting some auditory activation.

When studying FC, one also must take into account whether the task is presented at a similar frequency to the analysis. In the PASAT, the participant computed the sum of two numbers every 6 s. This a possible task frequency of activation ~0.17 Hz which falls within the HFW. We do not know if the brain activates continuously during the PASAT or if there would be such frequency associated with the oscillation.

When interpreting the reduced FC in hypoxic MS compared to the normoxic MS group, there are several complications. As a result, it is not yet clear whether hypoxia is causing the reduction of FC or whether both changes are associated with a common pathophysiology—such as inflammation. Therefore, future work on the underlying mechanism driving FC changes in MS and hypoxia is warranted. Moreover, in terms of treatments, the efficacy of hyperoxygenation while controlling for hypoxia is still unknown and requires further assessments.

5 Conclusions

This study provides strong evidence that hypoxia in MS, as measured with fdNIRS, is associated with reduced brain function (as measured with FC). The group classified as having hypoxia may have impairments that are either caused by the hypoxia, made more severe by the hypoxia or correlate with the hypoxia-meaning that they may have a similar cause, but the hypoxia may not actually be the cause of the reduced FC. Taking the proposed relationship between tissue hypoxia and inflammation [4] into account, we have hypothesised that hypoxia may contribute to reduced FC. Future research on inflammatory biomarkers should be conducted to investigate if microvascular hypoxia, and consequently reduced brain FC, is a result of inflam-

mation in MS. fNIRS measures of haemodynamic coherence in MS could provide novel information on brain function and be a biomarker of functional impairment and/or disease progression.

Acknowledgments We would like to thank all the participants who took part in this research. This research was supported by the Canadian Institutes of Health Research and the National Multiple Sclerosis Society of the USA.

References

1. Ghasemi N, Razavi S, Nikzad E (2017) Multiple sclerosis: pathogenesis, symptoms, diagnoses and cell-based therapy. Cell J 19:1
2. Walton C, King R, Rechtman L et al (2020) Rising prevalence of multiple sclerosis worldwide: insights from the Atlas of MS, third edition. Mult Scler 26:1816
3. Lacerte M, Shapshak AH, Mesfin FB (2020) Hypoxic brain injury. CPD Anaesth 9:157–159
4. Yang R, Dunn JF (2019) Multiple sclerosis disease progression: contributions from a hypoxia–inflammation cycle. Mult Scler 25:1715
5. Haider L, Zrzavy T, Hametner S et al (2016) The topograpy of demyelination and neurodegeneration in the multiple sclerosis brain. Brain 139:807
6. Yang R, Dunn JF (2015) Reduced cortical microvascular oxygenation in multiple sclerosis: a blinded, case-controlled study using a novel quantitative near-infrared spectroscopy method. Sci Rep 51(5):1–9
7. Gao JF, Yang Y, Huang WT et al (2016) Exploring time- and frequency- dependent functional connectivity and brain networks during deception with single-trial event-related potentials. Sci Rep 6:1–13
8. Biswal B, Yetkin FZ, Haughton VM et al (1995) Functional connectivity in the motor cortex of resting human brain using echo-planar MRI. Magn Reson Med 34:537–541
9. González Torre JA, Cruz-Gómez ÁJ, Belenguer A et al (2017) Hippocampal dysfunction is associated with memory impairment in multiple sclerosis: a volumetric and functional connectivity study. Mult Scler 23:1854–1863
10. Jimenez JJ, Yng R, Nathoo N et al (2014) Detection of reduced interhemispheric cortical communication during task execution in multiple sclerosis patients using functional near-infrared spectroscopy. J Biomed Opt 19:076008
11. Arnett PA, Smith MM, Barwick FH et al (2008) Oralmotor slowing in multiple sclerosis: relationship to neuropsychological tasks requiring an oral response. J Int Neuropsychol Soc 14:454–462
12. Rosti E, Hämäläinen P, Koivisto K et al (2006) The PASAT performance among patients with multiple sclerosis: analyses of responding patterns using different scoring methods. Mult Scler 12:586–593
13. Adingupu DD, Evans T, Soroush A et al (2022) Non-invasive detection of persistent cortical hypoxia in Multiple Sclerosis using frequency domain near-infrared spectroscopy (fdNIRS). Adv Exp Med Biol (in press)
14. Ashida R, Cerminara NL, Edwards RJ et al (2019) Sensorimotor, language, and working memory representation within the human cerebellum. Hum Brain Mapp 40:4732–4747

Eye Tracking Parameters Correlate with the Level of Cerebral Oxygen Saturation in Mild Traumatic Brain Injury: A Preliminary Study

Alexey O. Trofimov, Veronica Sofronova, Ksenia Trofimova, Anton Dubrovin, Dmitry Martynov, Cyrill Lidji-Goryaev, Oxana Semyachkina-Glushkovskaya, and Denis E. Bragin

Abstract

Aim: The aim of this study was to assess the relationship between oculomotor synergies and brain oxygen status at mild traumatic brain injury (mTBI) using simultaneous comparison of eye-tracking (ET) parameters and cerebral oxygen saturation.

Material and methods: This non-randomised single-centre prospective study included 77 patients with mTBI (mean age was 36.3 ± 4.8 years, 48 men, 29 women, median GCS 13.7 ± 0.7). Cerebral oximetry was used to detect oxygen saturation level ($SctO_2$) in the frontal lobe pole (FLP) region. Eye movements were measured simultaneously using the EyeTracker. Calculated parameters were: vertical and horizontal angular eyeball velocity (AV); left vertical speed (LVS); right vertical speed (RVS); left horizontal speed (LHS); and right horizontal speed (RHS). The indices of vertical and horizontal eye version (version index, Vx) were calculated as the Pearson correlation coefficient between the corresponding AV of the right and left eyes. Significance was pre-set to $p < 0.05$.

Results: $SctO_2$ in the FLP varied from 62% to 79%. The average $SctO_2$ values were 69.26 ± 6.96% over the left FLP and 70.25 ± 7.58% over the right FLP ($p = 0.40$). The total analysis of the eye-tracking data revealed the following values of gaze parameters: LVS – 0.327 ± 0.263 rad/sec; LHS – 0.201 ± 0.164 rad/sec; RVS – 0.361 ± 0.269 rad/sec; and RHS – 0.197 ± 0.124 rad/sec. The calculated vertical version index (VVx) was 0.80 ± 0.12. The calculated horizontal version index (HVx) was 0.82 ± 0.11. The VVx and HVx were correlated with $SctO_2$ levels in the FLP ($p = 0.038$; $r = 0.235$; $p = 0.048$; $r = 0.218$, respectively $p = 0.035$; $r = 0.241$; $p = 0.039$;

A. O. Trofimov (✉) · V. Sofronova · K. Trofimova · A. Dubrovin · C. Lidji-Goryaev
Department of Neurological Diseases, Privolzhsky Research Medical University, Nizhny Novgorod, Russia

D. Martynov
State Technical University Named After R.E. Alekseev, Nizhny Novgorod, Russia

O. Semyachkina-Glushkovskaya
Department of Physiology, Saratov State University, Saratov, Russia

D. E. Bragin
Lovelace Biomedical Research Institute, Albuquerque, NM, USA

Department of Neurology, University of New Mexico School of Medicine, Albuquerque, NM, USA

F. Scholkmann et al. (eds.), *Oxygen Transport to Tissue XLIII*, Advances in Experimental Medicine and Biology 1395, https://doi.org/10.1007/978-3-031-14190-4_26

r = 0.235, respectively). Conclusions: VVx and HVx correlate with the $SctO_2$ level in the FLP ($p < 0.01$) in mTBI. No significant correlation was detected between the level of the $SctO_2$ level and vertical and horizontal AV of the eyeballs. Eye tracking can help quantify the severity of ocular conjugation impairments after mTBI, as well as explore the contribution that cerebral oxygen status disorders make to this process.

Keywords

Oculomotor synergies · Cerebral oximetry · Oculography · Near-infrared spectroscopy (NIRS) · Brain oxygen status

1 Introduction

Achievements in neuroscience have significantly reduced morbidity in mild traumatic brain injury (mTBI). However, mTBI is still accompanied by an increase in the frequency of posttraumatic encephalopathies. In recent years, mTBI treatment perspectives have been related to the non-invasive study of white matter fibre pathways impairments [1]. Among these techniques, the least studied is oculography or eye tracking (ET) [2]. Eye tracking is a promising technology for assessing conjugated eye movements and oculomotor synergies [3]. Considering that the oculomotor analyser tracts anatomically coincide with other brain fibre tracts, ET allows to assess their condition in several brain pathologies, including in TBI [4]. It has been previously shown that brain oxygenation in traumatic brain injury (TBI) depends on the perfusion parameters [5]. However, the significance of cerebral oxygenation disorders in the development of dysfunction of the fibre pathways, especially at mild traumatic brain injury, remains unclear.

The aim of our study was to assess the relationship between oculomotor synergies and brain oxygen status at mTBI using simultaneous comparison of ET parameters and cerebral oxygen saturation.

2 Materials and Methods

2.1 Study Design and Population

This non-randomised single-centre prospective study was approved by the Ethics Committee of Privolzhsky Research Medical University and conformed to the standards of the Declaration of Helsinki. Informed consent was obtained from each patient and their family.

The study involved 77 patients (48 men, 29 women, all right-handed) with diffuse (i.e., absence of any CT and/or MRI parenchymal lesions), blunt, mild TBI at 1–2 days after head injury. The diagnosis of mTBI was based on the presence and duration of acute symptoms observed after the trauma: a loss or change in consciousness, post-traumatic amnesia, vestibular and oculomotor disorders.

In all patients, the injury resulted from a fall on the back of the head or the frontal region. The nature of the injury omitted any lateralisation of the lesions.

All patients were treated in the emergency department from January 2018 to April 2021. The mean age was 36.3 ± 4.8 years (range 18–61 years). The median Glasgow Coma Score (GCS) was 14.3 ± 0.7, height 172.3 ± 8.5 cm and weight 78.6 ± 7.2 kg. All patients were free of any known ophthalmological diseases or injury and were not taking ocular medications.

2.2 Eye Tracking Configuration

Binocular eyes movement (saccades and smooth pursuits) were recorded continuously at 20 Hz as a series of visual cues configured in mobile eye-tracking system software and were presented on a tablet screen (EyeTracker, BVG Software group LLC, the Netherlands).

The room lights and electronic devices were switched off during eye-tracking follow-ups.

The protocol included a calibration procedure when the tablet screen was black for 10 s to allow the participant an opportunity to adapt their eyes.

The circle marker (diameter 0.3 cm) was presented on the monitor for 20 s. The marker moved

across the screen randomly at different speeds, making it possible to track the saccades and the smooth pursuits. The circle colour changed from white to red every 2 s so the patient could maintain the attention on the circle centre [6].

The low-quality frames (i.e., unrecognised pupils, incorrect initial frames and blinking frames) were excluded manually using the network refinement function. A 300 best consecutive eye tracking was analysed before the tablet screen was switched off. The total procedure duration was 30 s.

The calculated parameters were: the vertical and horizontal angular velocity (AV); left vertical speed (LVS); right vertical speed (RVS); left horizontal speed (LHS); and right horizontal speed (RHS).

The indices of vertical and horizontal eye version (version index, Vx) were calculated as the Pearson correlation coefficient between the corresponding AV of the right and left eyes.

2.3 Near-Infrared Spectroscopy

Near-infrared spectroscopy was simultaneously performed by a space-resolved absolute cerebral oximeter Fore-Sight 2030 (CAS Medical Systems Inc., Branford, USA). It included the detection of brain oxygen saturation values ($SctO_2$) in the region of the frontal lobe pole (FLP) by transcutaneous optode. Data were obtained using a multimodality monitoring system providing 1-sec-by-1-sec average values.

2.4 Statistical Analysis

Data were evaluated for normality using the Shapiro-Wilk criterion. Continuous variables are expressed as mean ± standard deviation. The statistical analysis was performed using non-parametric statistics and regression analysis methods. The level of significance was set at 0.05. All analyses were performed using the software package Statistica 7.0 (Statsoft Inc., USA).

3 Results

Oxygen saturation in the FLP varied within the range from 61% to 89%. The average $SctO_2$ values were 69.26 ± 6.96% over the left FLP, and 70.25 ± 7.58% over the right FLP (p = 0.40) (Fig. 1). Values below the ischemic threshold

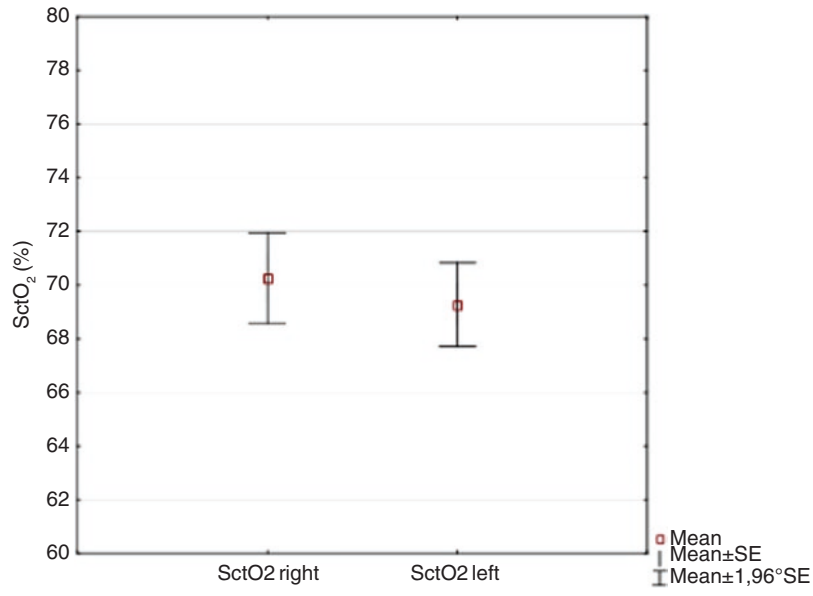

Fig. 1 Comparison of $SctO_2$ values between the right ($SctO_2$ right) and left ($SctO_2$ left) sides

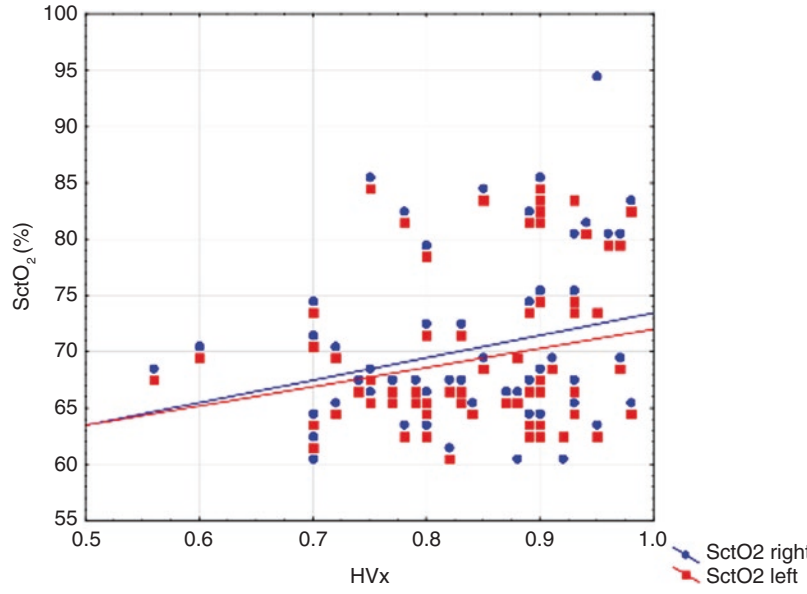

Fig. 2 Horizontal version index (HVx) plotted against $SctO_2$ values on the left side (red squares) and right side (blue circles) in the patients with mild TBI ($p = 0.038$; $r = 0.235$; $p = 0.048$; $r = 0.218$, respectively)

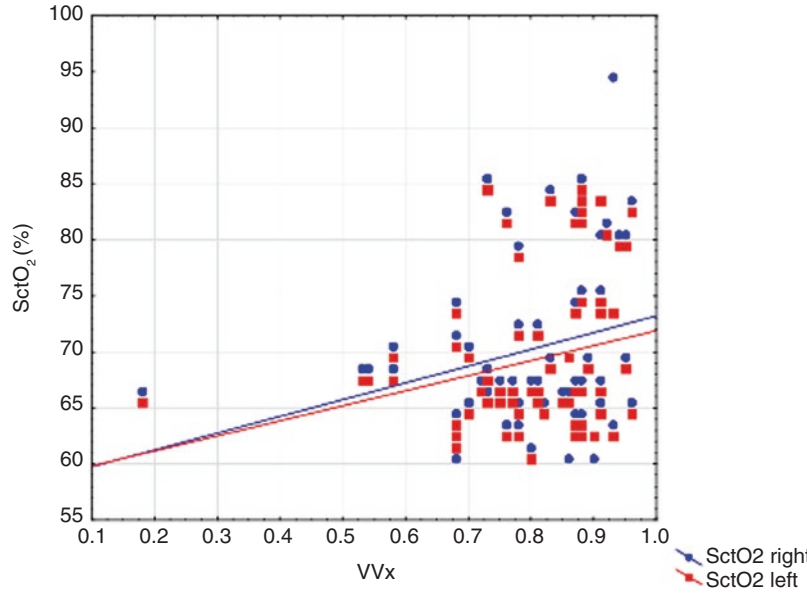

Fig. 3 Vertical version index (VVx) plotted against $SctO_2$ values on the left side (red squares) and right side (blue circles) in the patients with mild TBI ($p = 0.035$; $r = 0.241$; $p = 0.039$; $r = 0.235$, respectively)

($SctO_2$ less than 60%) were not detected. The total analysis of the eye tracking data revealed the following values of gaze parameters: LVS – 0.327 ± 0.263 rad/sec; LHS – 0.201 ± 0.164 rad/sec; RVS – 0.361 ± 0.269 rad/sec; and RHS – 0.197 ± 0.124 rad/sec. The calculated vertical version index (VVx) was 0.80 ± 0.12. The calculated Horizontal version index (HVx) was 0.82 ± 0.11.

Quantitative analysis of vertical and horizontal eye version indices showed that HVx and VVx were correlated with the cerebral saturation levels in the both FLP ($p = 0.038$; $r = 0.235$; $p = 0.048$; $r = 0.218$, respectively $p = 0.035$; $r = 0.241$; $p = 0.039$; $r = 0.235$, respectively) (Figs. 2 and 3).

4 Discussion

As noted earlier, ET allows the detection and quantification of oculomotor synergies impairments and, consequently, neural network functioning, making ET a promising tool for screening diagnosis of mTBI [6, 7].

Previous studies have shown that the SCAT-5 test is a very useful tool for diagnosing concussion because it includes a physical examination, an assessment of consciousness using the GCS, and a range of cognitive and sensorimotor tests. However, SCAT-5 test is rather cumbersome and complex. In addition, it cannot be used to assess visual impairments thoroughly [8].

The aim of our study was to evaluate the relationship between oculomotor synergies and brain oxygen status at mTBI using simultaneous comparison of ET parameters and cerebral oxygen saturation.

We have shown that in mTBI patients without lateralisation brain lesions vertical and horizontal eye version indices were significant correlated with cerebral saturation levels in both frontal lobe poles.

In our opinion, one of the possible reasons for identified oculomotor synergies impairments at mTBI is the development of relative brain hypoxia due to impaired cerebral autoregulation, which is confirmed by early studies [9]. At the same time, the mechanisms underlying autoregulatory dysfunction remain poorly understood.

As shown earlier, the autoregulation impairments at mTBI are significantly less than in severe TBI. Perhaps this is why despite the correlations between VRx and $SctO_2$ being statistically significant, the power of the correlation is relatively weak (p less than 0.3) [10].

To confirm our assumption, it is necessary to evaluate the significance and power of the correlation between VRx and cerebral saturation at severe TBI, which requires further research.

It should be noted that the statistical outliers are detected in the left-lower and right-upper quadrants at Figs. 2 and 3.

Their appearance has several explanations. On the one hand, they can be associated with the saccade period. On the other hand, this may be a consequence of convergence disorders characteristic of the acute period of TBI.

Also, a third possible explanation is that the best oculomotor synergies are as-associated with the best saturation, and vice versa, a drop in cerebral oxygenation leads to disturbances in eye vergence. It should be also noted that similar changes in ET values were recently observed in patients with COVID-19, which confirms our assumptions about the direct relationship between oculomotor dysfunction and cerebral hypoxia [11]. In addition, recent research on ET in aviation has shown that this tool can be used to diagnose cerebral hypoxia, which opens up promising prospects for its use in brain injuries [12].

Further research is needed for the understanding of these phenomena.

However, our study had several limitations. First, the serious limitation of our study is the relatively small group (77 patients). Second, we did not measure oxygenation in both brain lobes. Accordingly, we cannot say how ET parameters and oxygen saturation in these lobes correlated with each other. Third, we did not have ET and $SctO_2$ longitudinal assessments in mTBI patients to see the pattern of oculomotor impairment at different time points and how these dysfunctions evolved. Thus, further studies are required to delineate the brain oxygen status role in the oculomotor synergies impairments at mild TBI.

5 Conclusion

The eye tracking allows us to quantify the severity of convergence disorders after mTBI and study the contribution that disturbances in brain oxygen status make to this process. The version indices of the eye movement (VVx and HVx) significantly correlate with the $SctO_2$ level in the FLP ($p < 0.01$) in mTBI. No significant correlation was detected between the level of the $SctO_2$

level and vertical and horizontal AV of the eyeballs.

Acknowledgments AT and KT were supported by a Grant-in-Aid for Exploratory Research from the Privolzhsky Research Medical University. OSG was supported by RSF 20-15-00090, RSF 19-15-00201, grant 075-15-2019-1885; DB was supported by NIH R01 NS112808.

References

1. Astafiev SV, Shulman GL, Metcalf NV et al (2015) Abnormal white matter blood-oxygen-level-dependent signals in chronic mild traumatic brain injury. J Neurotrauma 32(16):1254–1271
2. Murray NP, Claire-Marie Roberts MH, Tyagi A et al (2021) Oculomotor training for poor saccades improves functional vision scores and neurobehavioral symptoms. Arch Rehabil Res Clin Transl 3(2):100126
3. Hunfalvay M, Roberts C, Murray N et al (2019) Horizontal and vertical self-paced saccades as a diagnostic marker of traumatic brain injury. Concussion (London, England) 4(1):CNC60
4. Cifu DX, Wares JR, Hoke KW et al (2015) Differential eye movements in mild traumatic brain injury versus normal controls. J Head Trauma Rehabil 30(1):21–28
5. Trofimov AO, Kalentiev G, Voennov O et al (2016) Comparison of cerebral oxygen saturation and cerebral perfusion computed tomography in cerebral blood flow in patients with brain injury. Adv Exp Med Biol 876:145–149
6. Mucha A, Collins M, Elbin R et al (2014) A brief vestibular/ocular motor screening (VOMS) assessment to evaluate concussions. Am J Sports Med 42(10):2479–2486
7. Contreras R, Ghajar J, Bahar S et al (2011) Effect of cognitive load on eye-target synchronization during smooth pursuit eye movement. Brain Res 1398(29):55–63
8. Sussman E, Ho A, Pendharkar A, Ghajar J (2016) Clinical evaluation of concussion: the evolving role of oculomotor assessments. Neurosurg Focus 40(4):E7
9. Piper C, Fortune B, Cull G et al (2013) Basal blood flow and autoregulation changes in the optic nerve of rhesus monkeys with idiopathic bilateral optic atrophy. Invest Ophthalmol Vis Sci 54(1):714–721
10. Wetzel P, Lindblad A, Mulatya C et al (2019) Eye tracker outcomes in a randomized trial of 40 sessions of hyperbaric oxygen or sham in participants with persistent post concussive symptoms. Undersea Hyperb Med J Undersea Hyperb Med Soc Inc 46(3):299–311
11. Wagner M, den Boer M, Jansen S et al (2022) Video-based reflection on neonatal interventions during COVID-19 using eye-tracking glasses: an observational study. Arch Disease Child. Fetal Neonatal Ed 107(2):156–160
12. Peißl S, Wickens D, Baruah R (2018) Eye-tracking measures in aviation: a selective literature review. Int J Aerosp Psychol 28(3–4):98–112

Critical Closing Pressure of Cerebral Circulation at Concomitant Moderate-to-Severe Traumatic Brain Injury

Kseniia A. Trofimova, Darya I. Agarkova, Alex O. Trofimov, Cyrill Lidji-Goryaev, Oxana Semyachkina-Glushkovskaya, Andrew Y. Abashkin, and Denis E. Bragin

Abstract

Background: Critical closing pressure (CrCP) is the pressure below which local pial blood pressure is inadequate to prevent blood flow cessation. The state of cerebral CrCP in patients with concomitant moderate-to-severe traumatic brain injury (cTBI) after brain lesions surgery remains poorly understood. Aim: The aim of our study was to establish the dynamics of CrCP after intracranial surgery in traumatic brain injury (TBI) patients with polytrauma. Material and methods: Results of the treatment of 70 patients with moderate-to-severe cTBI were studied (Male: Female – 39:31, mean age –33.2 ± 12.2 years). Depending on intracranial surgery, patients were divided into 2 groups. All patients were subjected to transcranial Doppler of both middle cerebral arteries, and evaluation of mean arterial pressure (MAP). Based on the data obtained, CrCPs were calculated. Significance was preset to $P < 0.05$. Results: Mean CrCP values in each group were significantly higher than a reference range ($p < 0.01$). There was no significant difference in CrCP values between the left and right hemispheres in the group 1 ($p = 0.789$). In the group 2, mean CrCP values on the unoperated side remained significantly lower than on the operated side ($p = 0.000011$) even after intracranial surgery. In group 1, mean CrCP values were significantly lower than on the surgery side in the group 1 ($Z = 3,4$; $p = 0.043$). Conclusion: CrCP values in concomitant moderate-to-severe TBI after removing brain lesions and without surgery were significantly higher than referral data. Even after removal of brain

K. A. Trofimova (✉) · D. I. Agarkova · C. Lidji-Goryaev
Department of Neurological Diseases, Privolzhsky Research Medical University, Nizhny Novgorod, Russia

A. O. Trofimov
Department of Neurological Diseases, Privolzhsky Research Medical University, Nizhny Novgorod, Russia

Department of Physiology, Saratov State University, Saratov, Russia

O. Semyachkina-Glushkovskaya
Department of Physiology, Saratov State University, Saratov, Russia

A. Y. Abashkin
Department of Trauma, BSMP, Dzerzhinsk, Russia

D. E. Bragin
Lovelace Biomedical Research Institute, Albuquerque, NM, USA

Department of Neurology, University of New Mexico School of Medicine, Albuquerque, NM, USA

F. Scholkmann et al. (eds.), *Oxygen Transport to Tissue XLIII*, Advances in Experimental Medicine and Biology 1395, https://doi.org/10.1007/978-3-031-14190-4_27

lesions volumes in patients with concomitant moderate-to-severe TBI, CrCP values on the surgery side remained markedly higher than on the side opposite to the removed lesion volumes.

Keywords

Intracranial hematoma · Intracranial pressure (ICP) · Cerebral perfusion pressure (CPP) · Microvascular perfusion

1 Introduction

According to current guidelines, based on a large body of research, adequate microvasculature perfusion maintenance is an essential component of intensive therapy of head injury. However, cerebral perfusion pressure (CPP) stabilisation at severe multiple trauma and shock, as caused by road traffic accidents, often resembles a Sisyphean task.

CPP can be calculated as a difference between mean arterial pressure (MAP) and brain parenchymal pressure, which is usually considered equal to intracranial pressure (ICP) [1].

Furthermore, ICP gradients development in the injured brain can seriously complicate the calculation of local CPP, which was confirmed by Sun et al. [2].

According to Kaczmarska et al., cerebral microvascular perfusion might be more accurately described by the closure margin, or 'effective' perfusion pressure, defined as the difference between MAP and the pressure below which arterial and arteriolar vessels collapse and local blood flow ceases [3].

This parameter has been defined as zero flow pressure or critical closing pressure (CrCP) [4]. It is believed that when arterial blood pressure reaches the CrCP value, the pulse fluctuations smooth out, followed by an avalanche-like collapse of the microvascular bed [5]. Previously, Richards et al. showed that CrCP is highly correlated with invasively established CPP and ICP values [6].

Therefore, the measurement of CrCP is of practical importance, since it allows a non-invasive assessment of the cerebral perfusion state when invasive monitoring of ICP is difficult or impossible [7].

It should be noted that the state of cerebral CrCP in patients with concomitant moderate-to-severe TBI (cTBI) after brain lesions volume surgery remains poorly understood.

The aim of our study was to establish the dynamics of CrCP after intracranial surgery in TBI patients with polytrauma.

2 Methods

This non-randomised single-centre study complies with the Declaration of Helsinki. The protocol was approved by the local Ethics Committee of Nizhny Novgorod Clinical Hospital named after N.A. Semashko. All patients and their families provided written informed consent. The inclusion and exclusion criteria are in Table 1.

2.1 Population

The study involved 39 men and 31 women with concomitant moderate-to-severe TBI; mean age of 33.2 ± 12.2 years treated at Nizhny Novgorod Regional Trauma Centre Level I of Regional Clinical Hospital named after N.A. Semashko.

Table 1 Inclusion and exclusion criteria

Inclusion criteria	Exclusion criteria
1. Between 16 and 70 years old	1. Less than 16 and more than 70 years old
2. Polytrauma with moderate-to-severe TBI within 3–5 days after a brain injury	2. CT Marshall grade III, VI (any non-evacuated intracranial hematoma, parenchymal volume lesions, etc.)
3. GCS less than 12 on admission	3. Injury severity score less than 9 and more than 36
4. Injury severity score between 9 and 36	4. Any cardiovascular injury/diseases history
5. CT Marshall grades I, II, V	

The recruitment period was from January 2013 to December 2020. All patients were polytraumatised. They all received therapy according to the Guideline of TBI treatment and Advanced Trauma Life Support [8]. The patients were divided into two groups. The first group included 37 TBI patients without volume lesions. The second group comprised 33 TBI patients after intracranial surgery within the first 3 days of the injury. Glasgow Coma Scale (GCS) severity was 10.4 ± 1.5 and 9.7 ± 1.7 in the first and second group, respectively. The injury severity scores (ISS) were 31 ± 9 and 32 ± 8 in the first and second group, respectively. Among 33 patients that underwent meningeal hematomas surgery, the epidural hematomas were removed in 7 patients, subdural hematomas in 32, and multiple hematomas in 4 patients.

2.2 Critical Closing Pressure Calculation

Cerebral circulation CrCP was calculated using Eq. 1 proposed by Ogoh [9]:

$$\mathrm{CrCP} = \mathrm{ABPs} - \frac{\mathrm{ABPs} - \mathrm{ABPd}}{\mathrm{Vs} - \mathrm{Vd}} \times \mathrm{Vs} \quad (1)$$

where ABPd – diastolic arterial pressure (mmHg), ABPs – systolic arterial pressure (mmHg), CrCP – critical closing pressure (mmHg), Vd – diastolic cerebral blood flow velocity (cm/s), Vs – systolic cerebral blood flow velocity (cm/s).

Reference range CrCP was chosen according to Ogoh S. as 33 ± 2 mmHg.

Diastolic and systolic arterial blood pressure was monitored noninvasively (IntelliView MP5, Philips Medizin Systeme, Germany). Cerebral blood flow velocity (CBFV) in both middle cerebral arteries (MCA) was bilaterally measured using ultrasound Doppler with a 2-Mhz probe for 20 minutes (Sonomed 300 M, Spectromed, Russia) [9]. We used the intensive care monitor 'Centaurus-CrCP' (Ver. 3.0, Privolzhsky Research Medical University, Russia). PaO_2, $PaCO_2$, and core temperature were within normal ranges. All patients did not require sedation or pharmacological support of blood pressure and were normotensive.

2.3 Statistical Analysis

Continuous variables are expressed as median [interquartile range]. The data were evaluated for normality distribution using the Shapiro-Wilk test. The differences in CrCP values were assessed using a nonparametric Sign test. The significance level was set at 0.05. All analyses were performed using the software package Statistica 7.0 (Statsoft Inc., USA).

3 Results

Mean CrCP values in each group were significantly higher than a reference range ($p < 0.01$).

We did not find a significant difference in CrCP values between the left and right hemispheres in the first group (94 [86;107] mmHg vs. 94 [87;108] mmHg, respectively, $Z = -0.267$; $p = 0.789$).

In the second group, mean CrCP values on the unoperated side ('non-surgery' side) remained significantly lower than on the operated side ('surgery' side) (91 [85;110] mmHg vs. 87 [78;110] mmHg, respectively, $Z = 4.4$; $p = 0.000011$) even after intracranial surgery.

There was no statistically significant difference between mean CrCP on the 'non-surgery' side compared to mean CrCP values in the first group ($Z = 0.182$; $p = 0.855$).

In addition, in the first group, mean CrCP values were significantly lower than on the surgery side in the second group ($Z = 3,4$; $p = 0.043$).

CrCP values in the 'surgery' side at various types of removed intracranial volume lesions showed no significant differences ($p > 0.05$).

Also, we did not find significant effects of patient age on CrCP value ($p > 0.05$).

4 Discussion

For the first time, a theoretical model that describes the collapse of small vessels with a regional arterial fall was proposed by Burton in 1951 [4].

It has been noted that a drop in CrCP by half leads to perfusion collapse in half of the total number of capillaries proportionally. Thus, the importance of CrCP is evident [10–12].

The aim of our study was to establish the dynamics of CrCP after intracranial surgery in TBI patients with polytrauma.

We have shown that CrCP values were significantly higher than normal in all concomitant moderate-to-severe TBI patients.

We assume that one of the possible reasons may be a decrease in the catecholamines concentration due to shock relief in the subacute stage of polytrauma, which leads to cerebral vasodilation. This CrCP rise is confirmed by previous studies [7].

Another possible reason might be related to the increase of pleural cavities pressure due to the lung contusion, haemo- or pneumothorax, which was found in our study in all patients, and is consistent with previous research [13].

We have shown that CrCP significantly differs in TBI patients after intracranial surgery.

Significant CrCP increase ($p = 0.00032$) on the side of surgical intervention apparently has several reasons. We suggest that cerebral microvascular vasospasm or microthrombosis in the craniectomy area is the most possible reason [5]. Although evident signs of 'dopplerographic' vasospasm were found in only 27 patients (81.2%), the putative CBF turbulence caused by proximal vasospasm may lead to an underestimation of its frequency [14].

Postoperative CT scans did not reveal any volume brain lesion, which reflects the ICP constancy as well the absence of any ICP gradients [2, 15]. Therefore, CrCP increase probably relates to vascular wall tone increase, which was reported in previous research [13, 15].

5 Conclusion

CrCP values in concomitant moderate-to-severe TBI after removal volume lesions and without surgery were significantly higher than referral data.

Even after removing volume brain lesions in the patients with concomitant moderate-to-severe TBI, CrCP values on the surgery side remained significantly higher than the side opposite to where volume lesions were removed.

Acknowledgments KT and AT were supported by a Grant-in-Aid for Exploratory Research from the Privolzhsky Research Medical University. OSG was supported by RSF 20-15-00090, RSF 19-15-00201, grant 075-15-2019-1885; DB was supported by NIH R01 NS112808.

References

1. Rosner M, Rosner S, Johnson A (1995) Cerebral perfusion pressure management protocol and clinical results. J Neurosurg 83:949–962
2. Sun G, Fu T, Liu Z, Zhang Y, Chen X, Jin S, Chi F (2021) The rule of brain hematoma pressure gradient and its influence on hypertensive cerebral hemorrhage operation. Sci Rep 11(1):4599. https://doi.org/10.1038/s41598-021-84108-w
3. Kaczmarska K, Kasprowicz M, Grzanka A (2018) Critical closing pressure during a controlled increase in intracranial pressure. Acta Neurochir Suppl 126:133–137
4. Burton A (1951) On the physical equilibrium of small blood vessels. Am J Phys 16284:319–329
5. Soehle M, Czosnyka M, Pickard J (2004) Critical closing pressure in subarachnoid hemorrhage effect of cerebral vasospasm and limitations of a transcranial Doppler-derived estimation. Stroke 35:1393–1398
6. Richards H, Czosnyka M (1999) Assessment of critical closing pressure in the cerebral circulation as a measure of cerebrovascular tone. Acta Neurochir 141(11):1221–1227
7. Bouzat P, Sala N, Payen J, Oddo M (2013) Beyond intracranial pressure: optimization of cerebral blood flow, oxygen, and substrate delivery after traumatic brain injury. Ann Intensive Care 3(1):1–9
8. Carney N, Totten A et al (2017) Guidelines for the management of severe traumatic brain injury, 4th ed. Neurosurgery 80(1):6–15
9. Ogoh S, Fisher J, Young CN, Fadel PJ (2011) Impact of age on critical closing pressure of the cerebral circulation during dynamic exercise in humans. Exp Physiol 96:417–425
10. Aaslid R (1992) Cerebral hemodynamics, transcranial Doppler. Edited by Newell D, Aaslid R. Raven Press, New York
11. Kaczmarska K, Uryga A, Placek M et al (2020) Critical closing pressure during experimental intracranial hypertension: comparison of three calculation methods. Neurol Res 42(5):387–397

12. Minhas J, Haunton V, Robinson T (2019) Determining differences between critical closing pressure and resistance-area product: responses of the healthy young and old to hypocapnia. Pflugers Archiv Eur J Physiol 471(8):1117–1126
13. Varsos G, Richards H, Kasprowicz M et al (2014) Cessation of diastolic cerebral blood flow velocity: the role of critical closing pressure. Neurocrit Care 20:40–48
14. O'Brien N, Lovett M, Chung M (2020) Non-invasive estimation of cerebral perfusion pressure using transcranial Doppler ultrasonography in children with severe traumatic brain injury. Childs Nerv Syst:1–9
15. Nogueira R, Panera R, Teixeira M (2017) Cerebral hemodynamic effects of cheyne-stokes respiration in a patient with stroke. J Stroke Cerebrovasc Dis 26(5):e80–e82

Part III

Methods

Hybrid Convolutional Neural Network (hCNN) for Image Reconstruction in Near-Infrared Optical Tomography

Meret Ackermann, Jingjing Jiang, Emanuele Russomanno, Martin Wolf, and Alexander Kalyanov

Abstract

Near-infrared optical tomography (NIROT), a promising imaging modality for early detection of oxygenation in the brain of preterm infants, requires data acquisition at the tissue surface and thus an image reconstruction adaptable to cephalometric variations and surface topologies. Widely used model-based reconstruction methods come with the drawback of huge computational cost. Neural networks move this computational load to an offline training phase, allowing much faster reconstruction. Our aim is a data-driven volumetric image reconstruction that generalises well to different surfaces, increases reconstruction speed, localisation accuracy and image quality. We propose a hybrid convolutional neural network (hCNN) based on the well-known V-net architecture to learn inclusion localisation and absorption coefficients of heterogenous arbitrary shapes via a joint cost function. We achieved an average reconstruction time of 30.45 s, a time reduction of 89% and inclusion detection with an average Dice score of 0.61. The CNN is flexible to surface topologies and compares well in quantitative metrics with the traditional model-based (MB) approach and state-of-the-art neuronal networks for NIROT. The proposed hCNN was successfully trained, validated and tested on in-silico data, excels MB methods in localisation accuracy and provides a remarkable increase in reconstruction speed.

Keywords

Image reconstruction · V-net architecture · NIROT · Preterm infant brain oxygenation

1 Introduction

Near-infrared optical tomography (NIROT) is sensitive to tissue oxygenation and enables 3D reconstructions to localise hypoxic regions in the brain based on a spatial arrangement of light emitters and detectors on the head's surface. Non-invasive and independent from extrinsic agents, it is an apt imaging modality for preterm infants. Their delicate brains require targeted imaging technologies to instantly detect even small hypoxic volumes, enabling early intervention to prevent permanent disabilities and severe neurodevelopmental disorders [1–3].

For this purpose, NIROT needs to be applicable at the bedside and the images need to be provided in real-time. NIROT image reconstruc-

M. Ackermann (✉) · J. Jiang · E. Russomanno · M. Wolf · A. Kalyanov
Biomedical Optics Research Laboratory, Neonatology, University Hospital Zurich and University of Zurich, Zurich, Switzerland
e-mail: meret.ackermann@usz.ch

F. Scholkmann et al. (eds.), *Oxygen Transport to Tissue XLIII*, Advances in Experimental Medicine and Biology 1395, https://doi.org/10.1007/978-3-031-14190-4_28

tions (IR) are commonly approached using model-based (MB) numerical optimisation based on the radiative transfer equation [4, 5]. Yet these approaches are too slow for real-time imaging and a significant increase in speed is unrealistic due to the high computational efforts after data acquisition. A key advantage of neural networks (NN) is that they shift the computational load to offline training and are thus much faster at processing high-dimensional data of the NIROT setups. We propose a hybrid CNN (hCNN) that learns IR from the inherent pattern of 2-iteration rough numerical IRs. The strength of a deep CNN is its attention to both local patterns in small receptive fields (RF) and global information in deep layers, which is known to be important for NIROT IRs [6]. With this in mind, we extended the V-net of Milletari et al. [7] to simultaneously learn a segmentation and regression task by minimising a joint cost function to obtain inclusion localisations and absorption coefficients (μ_a). We aimed for major gains in IR speed as well as high quality IRs in diverse geometries in a fraction of the time required today.

2 Methods

The diffusion approximation-based finite element algorithm and open-source software NIRFASTer for parallel computing on GPU and CPU were used to create synthetic input and ground truth (GT) data [8–10]. Head geometries with observed cephalometric variations of neonates at a gestational age of 31–32 weeks were implemented [11, 12]. 55 unique surfaces of 23 geometries with altered source-detector positions were considered. The 3D meshes had a diameter of 60 mm and maximal depths of 41.08–38.87 mm. Within a geometry, the depth varied by 4.19–13.3 mm (mean: 7.09 mm) as a result of the different head curvatures. The field of view, a circle of 25 mm diameter with 437 detectors at the centre of 8 circular arranged sources (~44 mm diameter) was placed on the surface of the 55 fine meshes (65,370–70,214 nodes) for measurements in reflection mode (Fig. 1a). Up to 5 spherical inclusions (4–10 mm in diameter) were placed within the sensitive region for the setup between 2 mm from the tissue boundary to 31.2 mm below the detector plane, and within a radius of 12 mm from the field of view's centre. Overlapping of inclusions was allowed. Intersecting regions had the optical properties (OP) of one of the inclusions. μ_a for bulk tissue was set from 0.005 to 0.01 mm^{-1} and for each inclusion from 1.2 to 5 times higher. The reduced scattering coefficient (μ'_s) was homogenous from 0.8 to 0.9 mm^{-1}. All OP lie in ranges observed in preterm head tissues and contrasts due to hypoxia [13, 14]. Localisation, size and OP were set at random within the defined boundaries.

For accurate forward simulation the sources were placed inside the mesh ~$1/\mu'_s$ from the surface. The modulation frequency was 100 MHz and Gaussian noise of 2% was added to amplitude and phase. As input, rough IRs of 2 iterations were generated with the bulk OPs as initial guess, a coarser mesh (factor ~ 4.35 lower node density), and a Tikhonov regularisation parameter (λ_T) of 1e-3 derived from 5 geometries (L-curve method). The input and GT meshes were mapped and cropped to 3D images of 32 × 32 × 32 voxels at a resolution of 1 mm. The μ_as to be predicted were taken as a single channel of 8-bit prediction depth with a sensitive range (0.0025–0.0529 mm^{-1}) set at unequally distributed precision levels, where 0 denotes pixels outside the model boundaries. The values were scaled to range from 0 to 1. Segmentation was derived by thresholding specific to the μ_as of each GT image to label background, bulk, and inclusions. The input data was normalised over the training data, the observed μ_as range was scaled to be between 0.001 and 1. The outside of tissue was set to 0.

A deep CNN was devised to learn reconstruction of the modelled tissue μ_as. As inclusions occupy only a small region of the total volume, it is required to correct for the contribution of each label during training. Thus the Dice coefficient-based loss function Eq. 1, ideal for unbalanced segmentation tasks, was used [7].

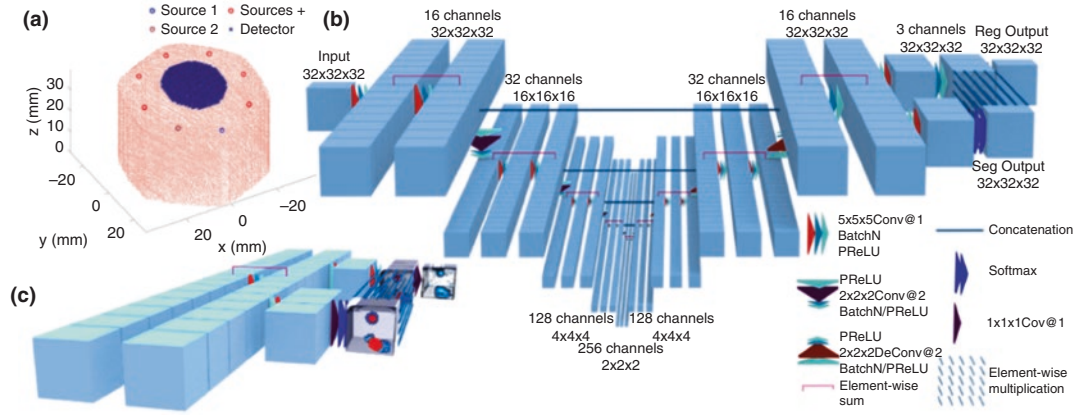

Fig. 1 (**a**) Mesh of modelled preterm infant head surface illustrating the source-detector placement. (**b**) Schematic illustration of the hCNN (**c**) Magnification of the last hCNN layers

$$L_{DICE}(x_i, s_i, \theta_i) = 1 - \left[2 \frac{\sum_{k=1}^{K} wik \sum_{m=1}^{m} Y(x_i, \theta)_{km} s_i km}{\sum_{k=1}^{K} wik \sum_{m=1}^{m} Y(x_i, \theta)_{km}^2 + s_i^2 km} \right] \quad (1)$$

Here θ are the network weights, x_i is a single training input, S_i the related labelled and Y the predicted segmented volume. The loss function over K classes and M voxels, is balanced by w_k, the inverse of the region size of the respective label.

$$w_k = 1 \quad (2)$$

To localise not only changes in tissue μ_as but also predict absolute values, the loss function was joined with the half mean squared error of voxel wise predicted absorption coefficients $y_{i,}$ versus the respective true values t_i.

$$L_{MSE}(x_i, t_i, \theta) = \frac{\sum_{m=1}^{M} \left(y|m(x_i, \theta) - t_{im} \right)^2}{2} \quad (3)$$

The joint loss function was minimised to find optimal weights θ^* over a batch of N datapoints. λ_{L2} and β are hyperparameters, the former for L2 regularisation, the latter introduced to weight the two objective functions and consider the scale difference.

$$\theta = \arg\min_{\theta} \frac{1}{N} \sum_{i=1}^{N} \{ L_{DICE}(\theta, x_i, S_i) + \beta L_{MSE}(\theta, x_i, t_i) + \lambda_{L2} L2 \sum_{i=1}^{N} \theta_i^2 \quad (4)$$

The implemented hCNN (Fig. 1b) enlarges the RF over 5 stages, then deconvolves the input over 4 stages to the original image size, each stage mirroring the layers of the resolution decreasing stage. Skip connections pass the input of each stage to the related last convolution to learn a residual function. In addition, the feature map of the convolution preceding downscaling, and the input of the corresponding mirroring stage are concatenated along the channel dimension. The output of the last mirroring stage is passed to two strands (Fig. 1c). The first convolves the feature map for dimensionality reduction, followed by a softmax function to extract the probabilistic segmentation. The second passes the feature map to a last convolution, batch normalisation and nonlinear activation, then the segmentation probabilities are multiplied elementwise, and a dense extraction predicts the μ_as.

23,000 image pairs (rough IR, GT and labelled output) were split in training, validation and test data (17,200, 3300 and 2500) of 42, 8 and 5 surfaces. The hCNN was implemented in MATLAB

drawn on MathWork's DL toolbox and trained on a workstation with a 12-Core AMD Ryzen 93,900X CPU (3.80 GHz 2 × 32 GB RAM) and NVIDIA RTX 3090 GPU (24 GB RAM)). θ were initialised by independent sampling from a normal distribution with 0 mean and a standard deviation of 0.01. Convolutional layers were zero-padded, λ_{L2} was 1e-3, and the optimiser was stochastic gradient descent with momentum. A mini batch size of 8, a momentum of 0.99 and initial learning rate of 1e-4 decreased by one magnitude after 4 epochs was selected. Training was done for 8 epochs and took 4 h.

The performance in quantitative metrics and IR speed was compared to IRs in NIRFASTer. 250 simulated measurements and the associated coarse meshes were used to run both IRs, initialised at the respective bulk OP. λ_T for the MB and hCNN IRs was set to 100 and 1e-3 respectively and evaluated just as prior for the hCNN. The stopping criterium for the MB IR was an improvement of less than 2% compared to the previous iteration. The common peak signal-to-noise ratio (PSNR), structural similarity index (SSIM), and root mean square error (RMSE) were used as evaluation metrics to compare the IR performances. The test data set was further evaluated for localisation accuracy using the Dice coefficient.

3 Results

The proposed hCNN was successful in 247 of 250 volumetric IRs. We achieved a mean ± SD IR time of 30.45 ± 4.88 s corresponding to an average reduction of 89% compared to the conventional IR. The time varied depending on the measurement surface but showed little variance for different tissue OP of the same surface and mean and variance values for different curvatures remained in a small range (Fig. 2a). The MB approach converged only for 206 of 250 IRs. For 3 tissue models, the MB IR failed within 2 iterations and thus did not provide input for the hCNN. We reached a RMSE of 1.71e-3 ± 4.9e-4, PSNR of 55.75 ± 2.69 and SSIM of 0.99 ± 4.9e-3 (Fig. 2b). The evaluation of the larger sample shows the representativeness of the 247 samples (Fig. 2c). The hCNN attains an inclusion localisation with an average Dice score of 0.62 ± 0.16. The wide range is probably due to either undetected inclusions (Fig. 3c) or deep inclusions reconstructed, but not properly located (Fig. 3b, d). For MB IR, conversely, deep inclusions are not detected at all in scenarios with inclusions at different depths (Fig. 3d) or they can only be suspected as a slight, unbounded shadow (Fig. 3c). Reported Dice scores for MB IRs for simpler cases and the same noise level range from 0.1 to 0.48 [15].

4 Discussion and Conclusion

Representativeness and data abundance are critical for deep learning. The current lack of patient data in neonatology and a clinically reliable IR will remain a challenge. In-vivo application will add complexity due to tissue heterogeneities, artefacts, and more intricate noise patterns. Yet, NNs often rise to just such challenges, capturing intrinsic patterns inherently difficult to model. We anticipate that the proposed architecture, trained, validated, and tested on in-silico data, will demonstrate its performance in real measurements. When establishing deep learning methods, the application on different surfaces, the remarkable reduction of IR time and a sound validation will be crucial for clinical acceptance.

To the best of our knowledge, we are the first to present a data-driven 3D NIROT IR adaptable to varying geometries. We have shown that the proposed hCNN, significantly improves the IR time. Together with reduced speed variance and increased IR robustness, key requirements for clinical monitoring are met. Inclusion detection and spatial confinement are remarkably solid. The accuracy of the reconstructed absolute μ_as compares well with the traditional method. Visual evaluations reveal sound IRs in challenging tasks such as overlapping scenarios (Fig. 3b) superimposed and low contrast inclusions (Fig. 3e).

Acknowledgments We gratefully acknowledge funding by the Swiss National Science Foundation (159490 and

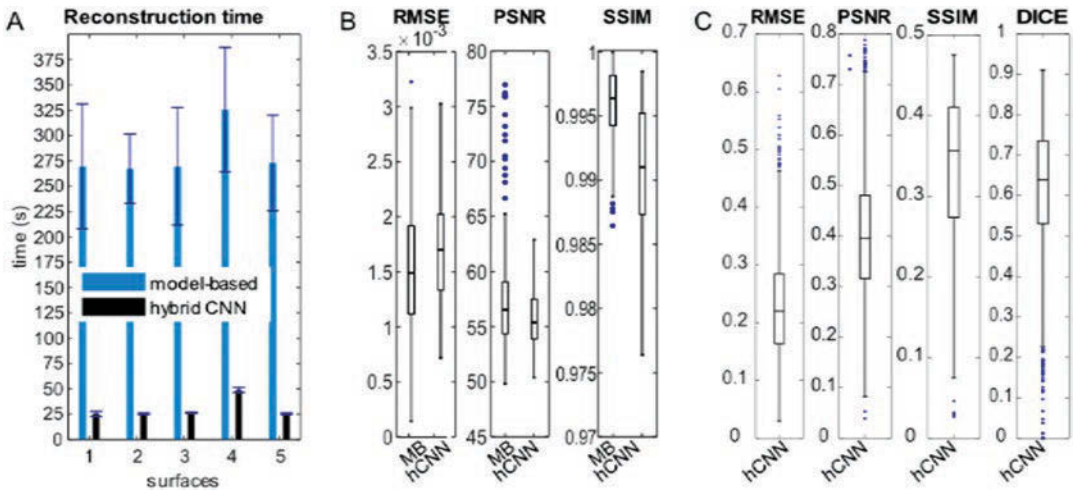

Fig. 2 (**a**) MB and hCNN reconstruction times starting at the first NIRFASTer iter-ation (**b**) Evaluation of the MB and hCNN IR. (**c**) Assessment of 2'500 hCNN IRs

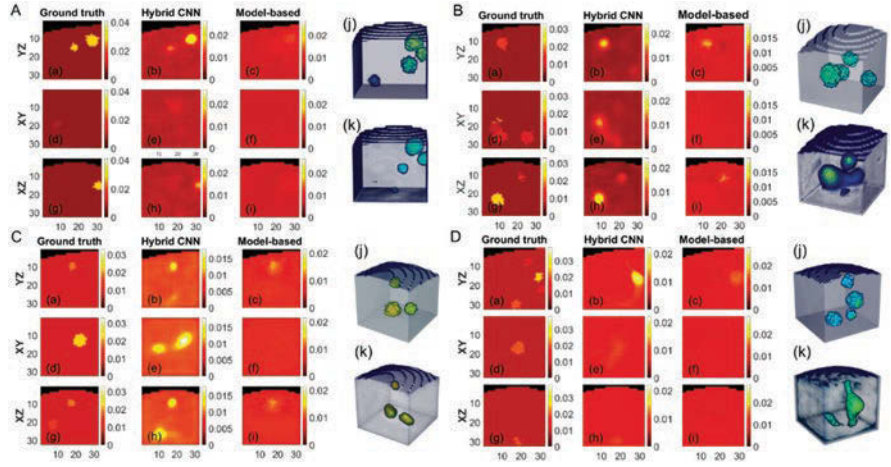

Fig. 3 Selection of IRs and GTs of 4 different surfaces (**a** and **b**) shown in cross sections through point XYZ (**a**–**i**) and 3-dimensional GT to be predicted (**j**) and hCNN IR (**k**) of size 32 mm × 32 mm × 32 mm. (**a**) X = 29, Y = 19, Z = 4, (**b**) X = 21, Y = 14, Z = 5, (**c**) X = 16, Y = 19, Z = 4, (**d**) X = 16, Y = 20, Z = 3. Units are in mm^{-1} for colour bars and in mm for axes and coordinates

197079), Innovationspool of the University Hospital Zurich and Innosuisse (52181.1). MW declares that he is president of the board and co-founder of OxyPrem AG as conflict of interest.

References

1. Back SA (2017) White matter injury in the preterm infant: pathology and mechanisms. Acta Neuropathol 134(3):331–349. https://doi.org/10.1007/s00401-017-1718-6
2. Badurdeen S, Roberts C, Blank D et al (2019) Haemodynamic instability and brain injury in neonates exposed to hypoxia-ischaemia. Brain Sci 9(3). https://doi.org/10.3390/brainsci9030049
3. Liao S, Ferradal S, White B et al (2012) High-density diffuse optical tomography of term infant visual cortex in the nursery. J Biomed Opt 17(8):081414
4. Arridge SR (2011) Methods in diffuse optical imaging. Philos Trans R Soc A Math Phys Eng Sci 369(1955):4558–4576
5. Zhu C, Liu Q (2013) Review of Monte Carlo modeling of light transport in tissues. J Biomed Opt 18(5):050902

6. Lu W, Duan J, Veesa JD et al (2019) New nonlocal forward model for diffuse optical tomography. Biomed Opt Express 10(12):6227–6241
7. Milletari F, Navab N, Ahmadi S-A (2016) V-net: fully convolutional neural networks for volumetric medical image segmentation. In: 2016 fourth international conference on 3D vision (3DV). IEEE, pp 565–571
8. Dehghani H, Eames ME, Yalavarthy PK et al (2009) Near infrared optical tomography using NIRFAST: algorithm for numerical model and image reconstruction. Commun Numer Methods Eng 25(6):711–732
9. Doulgerakis-Kontoudis M, Eggebrecht AT, Wojtkiewicz S et al (2017) Toward real-time diffuse optical tomography: accelerating light propagation modeling employing parallel computing on GPU and CPU. J Biomed Opt 22(12):125001
10. Friston KJ (1994) Functional and effective connectivity in neuroimaging: a synthesis. Hum Brain Map 2(1–2):56–78
11. Hall JG (1989) Handbook of normal physical measurements. Oxford Medical Publications. Oxford University Press, Oxford
12. Kurmanavicius J, Wright EM, Royston P et al (1999) Fetal ultrasound biometry: 1. Head reference values. BJOG Int J Obstet Gynaecol 106(2):126–135
13. Arri S, Muehlemann T, Biallas M et al (2011) Precision of cerebral oxygenation and hemoglobin concentration measurements in neonates measured by near-infrared spectroscopy. J Biomed Opt 16(4):047005
14. Ijichi S, Kusaka T, Isobe K et al (2005) Developmental changes of optical properties in neonates determined by near-infrared time-resolved spectroscopy. Pediatr Res 58(3):568–573
15. Jiang J, Di Costanzo MA, Lindner S et al (2021) Localization of deep ischemia and hemorrhage in preterm infants' head with near-infrared optical tomography: a numerical case study. In: Nemoto EM, Harrison EM, Pias SC, Bragin DE, Harrison DK, LaManna JC (eds) Oxygen transport to tissue XLII. Springer, Cham, pp 131–136. https://doi.org/10.1007/978-3-030-48238-1_21

Cross-Frequency Coupling Between Brain and Body Biosignals: A Systemic Physiology Augmented Functional Near-Infrared Spectroscopy Hyperscanning Study

S. Guglielmini, G. Bopp, V. L. Marcar, Felix Scholkmann, and M. Wolf

Abstract

Background: Understanding the brain and body processes during interaction or cooperation between two or more subjects is an important topic in current neuroscientific research. In a previous study, we introduced a novel approach that enables investigation of the coupling of biosignals (brain and systemic physiology, SP) from two subjects: systemic physiology augmented functional near-infrared spectroscopy (SPA-fNIRS) hyperscanning.

Aim: The aim was to extend our signal analysis approach by the cross-frequency time-dependent wavelet transform coherence (WTC) of the fNIRS and SP biosignals to gain new insights into the nature and cause of functional hyperconnectivity.

Subjects and methods: 24 pairs of adults took part in a closed-eye versus prolonged eye-contact task of 10 min each. Brain and body activity was measured continuously by SPA-fNIRS hyperscanning. We calculated the time-dependent WTC of the biosignals for four different frequency bands: very low-frequency band (VLF, 0.002–0.08 Hz), low-frequency band 1 (LF1, 0.015–0.15 Hz), low-frequency band 2 (LF2, 0.08–0.15 Hz) and heart rate band (HR, 1–2 Hz). We then performed the cross-frequency correlated-coherence coupling analysis.

Results: A stronger cross-frequency coupling during the eye-contact condition (between 99 pairs of biosignals) was found than during the eye-closed condition (between 50 pairs of biosignals). Prolonged eye contact led to entrainment of the brain and body between different frequency bands and two

Authors S. Guglielmini and G. Bopp have shared first authorship.

S. Guglielmini (✉) · G. Bopp · M. Wolf
Biomedical Optics Research Laboratory, Department of Neonatology, University Hospital Zurich, University of Zurich, Zurich, Switzerland
e-mail: Sabino.Guglielmini@usz.ch

V. L. Marcar
Biomedical Optics Research Laboratory, Department of Neonatology, University Hospital Zurich, University of Zurich, Zurich, Switzerland
Comprehensive Cancer Center Zürich, University Hospital Zürich, Zürich, Switzerland

F. Scholkmann
Biomedical Optics Research Laboratory, Department of Neonatology, University Hospital Zurich, University of Zurich, Zurich, Switzerland

Institute of Complementary and Integrative Medicine, University of Bern, Bern, Switzerland

F. Scholkmann et al. (eds.), *Oxygen Transport to Tissue XLIII*, Advances in Experimental Medicine and Biology 1395, https://doi.org/10.1007/978-3-031-14190-4_29

subjects. The strongest hyperconnectivity was between the LF1-VLF frequency band.

Discussion and Conclusion: With this exploratory study, we reveal further benefits of the SPA-fNIRS approach for future hyperscanning studies.

Keywords

SPA-fNIRS hyperscanning · Cross-frequency time-dependent wavelet transform coherence · Social interactions · Eye contact

1 Introduction

Social interactions are a key factor in establishing and maintaining interpersonal relationships and are indispensable for human development [1]. Through such interactions it is possible to understand our counterpart in order to comprehend his or her views, goals and motivations [2]. Social interaction is based on the extraordinary ability of humans to empathise with each other [3]. To gain a more advanced understanding of social interactions, it is crucial to understand the individual underlying signal transduction pathways. Signals sent by one person may be perceived by the senses of another person and then transmitted via the body to the brain, where they are processed [4]. The neural and physiological processes associated with social interaction are increasingly investigated. Since an interpersonal interaction involves two or more individuals, it should ideally be studied by collecting data from all participants [5], requiring a complex measurement setup and data analysis framework. The setup of capturing brain-to-brain coupling is termed 'hyperscanning' which can be efficiently realised, for example with optical neuroimaging employing functional near-infrared spectroscopy (fNIRS) [6]. Systemic physiology augmented fNIRS (SPA-fNIRS) hyperscanning is an extension of this approach enabling brain-to-brain, brain-to-body and body-to-body coupling between subjects to be investigated [7]. The data analysis framework normally includes methods to determine the similarity between two time series at each frequency depending on time. Wavelet transform coherence (WTC) is a suitable choice for this. Furthermore, the interactions between signals in different frequency bands can be determined to quantify the cross-frequency coupling [6].

In our previous study, brain-physiology coupling analyses were performed by correlating the time-dependent WTC of the fNIRS and systemic physiology (SP) signals in the same frequency bands. We found significant changes in the correlation of coupling between several brain and body signals. In the present study, the aim was to propose and test a new framework based on the cross-frequency time-dependent WTC to determine the cross-frequency coupling of fNIRS and SP signals to help better understand interpersonal functional hyperconnectivity.

2 Material and Methods

Twenty-four pairs of subjects participated in the study (age: 32.8 ± 13.7 years, age range: 18–65 years, 21 males, 27 females). Written informed consent was obtained from all the participants and the study protocol was approved by the Ethics Committee of the Canton of Zurich (KEK-ZH-Nr. E50/2002).

The two subjects from each pair sat one in front of the other and the experimental paradigm consisted of a first phase in which each pair kept their eyes closed for 10 min and a second phase in which they made eye contact.

Several SP and fNIRS signals were concurrently measured (Fig. 1a): heart rate (HR), mean arterial blood pressure (MAP), pulse pressure (PP), systolic blood pressure (SBP), diastolic blood pressure (DBP), arterial oxygenation (SpO_2) by a non-invasive continuous blood pressure device (SOMNOtouch™ NIBP, SOMNO Medics, Germany), electrodermal activity and skin temperature at the left and right wrist (EDA (left), temp (left), EDA (right), temp (right)) by two wristbands (Empatica, Boston, USA) and $P_{ET}CO_2$ by a capnograph (Nonin Life Sense; Nonin Medical, USA). Furthermore, changes in [O_2Hb], [HHb] and [tHb] were measured on the

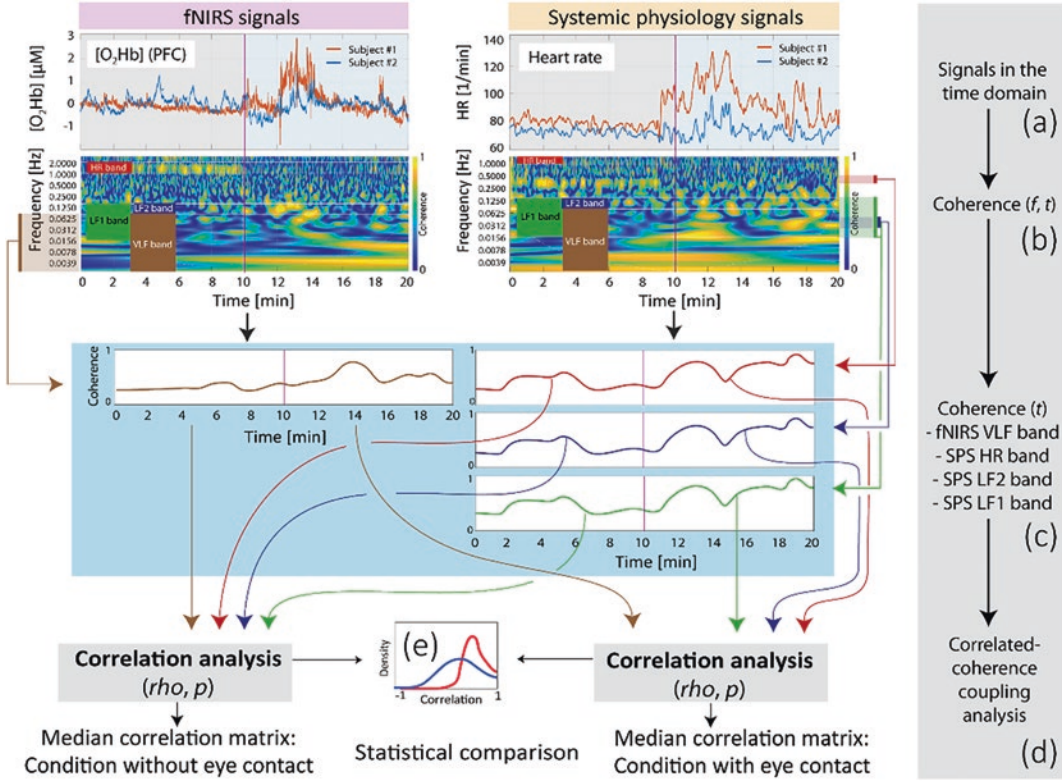

Fig. 1 Cross-frequency coupling analysis pipeline. (**a**) Two biosignals pairs acquired for subject #1 and #2. (**b**) The two respective scalograms obtained performing the WTC. (**c** and **d**) A time-dependent WTC of the first biosignal in one of the 4 frequency bands is selected and correlated with those of the other three frequency bands. (**e**) The cross-correlation distribution of each type of time-series over the two conditions is tested with Kolmogorov-Smirnov test

prefrontal cortex with fNIRS (NIRSport, NIRX, Berlin, Germany) and grouped according three regions of interest (left, right and entire prefrontal region). Nine fNIRS signals were considered: [O_2Hb] (left), [HHb] (left), [tHb] (left), [O_2Hb] (right), [HHb] (right), [tHb] (right), [O_2Hb] (left+right), [HHb] (left + right) and [tHb] (left + right).

The WTC of each biosignal measured on subject 1 and subject 2 was applied (Fig. 1b). Afterwards the average of the WTC in four frequency bands was calculated: very low-frequency band (VLF, 0.002–0.08 Hz), low-frequency band 1 (LF1, 0.015–0.15 Hz), low-frequency band 2 (LF2, 0.08–0.15 Hz) and heart rate band (HR, 1–2 Hz) (Fig. 1c). The Spearman correlation between each time-dependent WTC signal was calculated (Fig. 1d). Additionally, the significance level (p-value) was determined, generating a 59 × 59 matrix of WTC time-series correlation coefficients for each individual pair and each condition (eyes-closed, eye contact). In the analysis, we considered only the correlation of pairs of biosignals belonging to different frequency bands, i.e., a cross-frequency correlation was investigated. A group average was performed by calculating the median of all the individual correlation matrices, obtaining a single correlation matrix for each condition (Fig. 2). For the group average, only correlation coefficients were used that were statistically significantly different from 0 ($p < 0.05$) to ensure that the group average was based only on meaningful physiological changes from the individual measurements. To investigate whether the correlation distribution of each pair of time-series during the eye-contact condition was statistically different from the one during the eyes-closed condition, a Kolmogorov-Smirnov

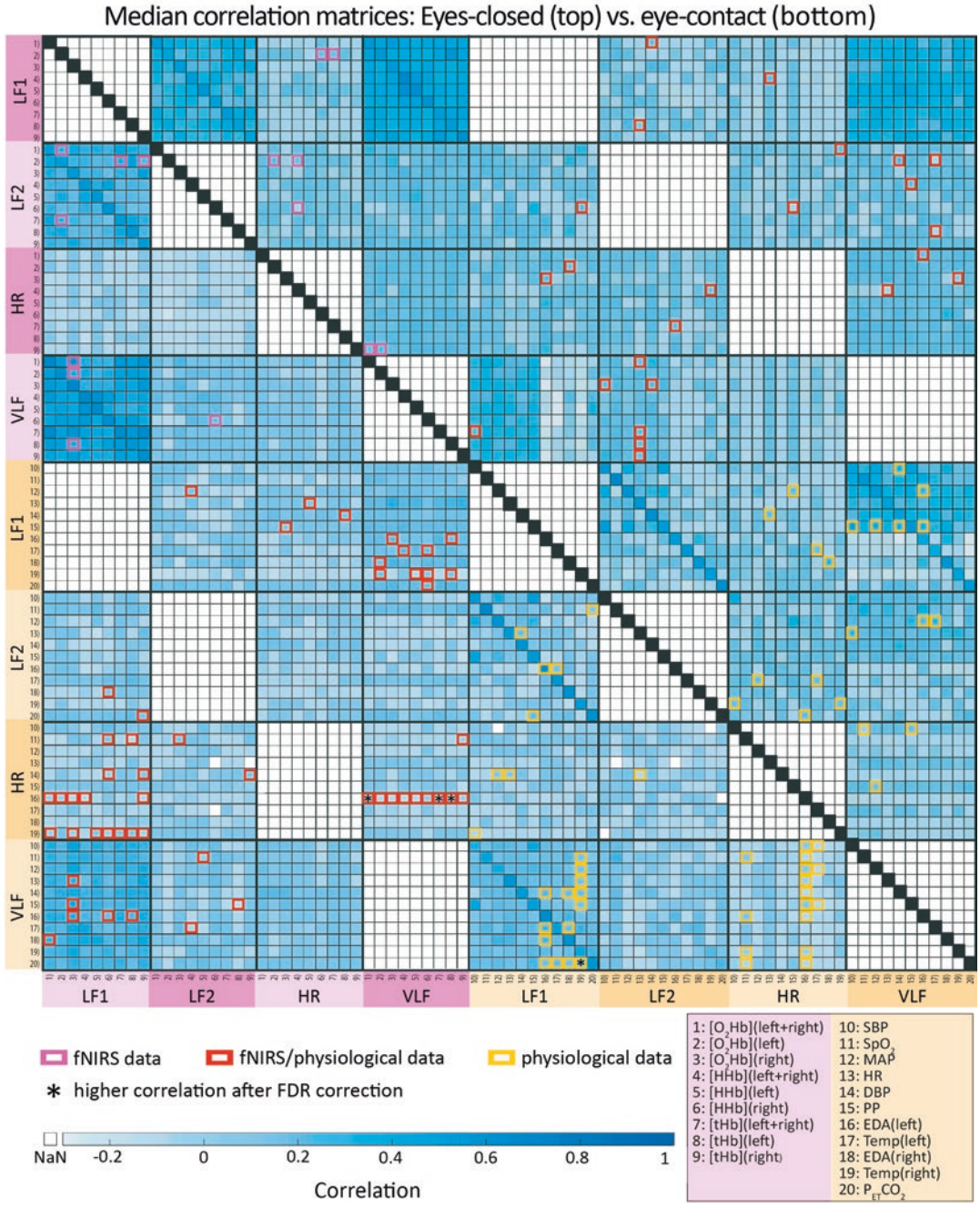

Fig. 2 Median correlation matrices for both the eyes-closed condition (top right) and the eye-contact condition (bottom left). Biosignal pairs showing a significant difference in correlation were marked in the matrix corresponding to the condition in which a higher correlation was found. Biosignal pairs showing higher correlation after performing FDR correction were marked with an asterisk

test was performed (Fig. 1e). Finally, a false discovery rate correction (FDR) was applied to the *p*-values to correct the multiple comparison situation. This analysis was conducted in MATLAB (The MathWorks, Inc., Natick, MA, USA).

3 Results

The results are visualised in Fig. 2, separated into three groups: fNIRS, physiological and fNIRS-physiological data. A marked matrix value index indicates a statistically significant difference and a higher distribution media than the other condition. Moreover, while the results during the eye-contact condition are clustered between LF1-VLF and LF1-HR, during the eye-closed condition they are scattered between the various frequency pairs. Significant results were obtained after performing FDR correction were marked with an asterisk. We found a statistically significant ($p < 0.05$) cross-frequency coupling between temp (right, LF1) and $P_{ET}CO_2$(VLF), [O_2Hb] (left + right, VLF) and EDA (left, HR), [HHb] (right, VLF) and EDA (left, HR), [tHb] (left + right, VLF) and EDA (left, HR), [tHb] (left, VLF) and EDA (left, HR). All these biosignals showed a higher correlation during the eye-contact condition compared to the eye-closed condition.

4 Discussion

The aim was to propose a new framework to investigate the influence of the visual channel in a prolonged eye-contact versus eye-closed task by assessing the cross-frequency coupling between different biosignals (brain and systemic physiology).

Our results showed a stronger cross-frequency coupling during the eye-contact condition compared to the eye-closed condition. The findings suggest that an increased stress level during the eye-contact condition led to an activation of the sympathetic autonomic nervous system and thus to a simultaneous change of the respective signals in an identical direction in both subjects, resulting in a higher number of more highly correlated biosignal pairs in the eye-contact condition.

Several cross-frequency coupling clusters were identified in the eye-contact condition, specifically between the fNIRS signals in the LF1/VLF band and SP signals in the VLF/LF1 frequency band. An additional cross-frequency coupling cluster was detected between the fNIRS signals in LF1/VLF and SP signals in the HR band. Finally, a cluster between SP signals in VLF and LF1 was found. A statistically significant correlation emerged between EDA (left) in the HR band and fNIRS signals in the VLF band in the eye-contact compared to eyes closed condition. These results are in line with the observations of Holper et al. [7], who found a coherence between fNIRS and EDA within the HR band.

A possible improvement of the analysis is the evaluation of the WTC in random pairs that will be investigated in future studies to control spurious correlations in the signals. In addition, the use of an eye-tracking device would be useful in the future for similar studies enabling to determine the duration of eye contact between the pairs and when it occurs.

Our study is the first to investigate cross-frequency coupling using SPA-fNIRS hyperscanning data and shows the applicability of this approach for SPA-fNIRS studies. The findings of this study indicate that prolonged eye contact is followed by entrainment of brain and body activities occurring at different frequencies, in addition to the coupling in identical frequency bands as reported in our previous work. The strongest hyperconnectivity was found between the LF1-VLF frequency band. This should be considered in future hyperscanning research.

Acknowledgments We gratefully acknowledge funding by the Swiss National Science Foundation (159490) and

Innosuisse (28314.1). MW declares that he is president of the board and co-founder of OxyPrem AG.

References

1. Nguyen T et al (2020) Chapter 1 – Studying parent-child interaction with hyperscanning. In: Hunnius S, Meyer M (eds) Progress in brain research. Elsevier, pp 1–24
2. Wheatley T et al (2012) From mind perception to mental connection: synchrony as a mechanism for social understanding. Soc Personal Psychol Compass 6(8):589–606
3. Carlson SM, Koenig MA, Harms MB (2013) Theory of mind. Wiley Interdiscip Rev Cogn Sci 4(4):391–402
4. Hari R et al (2015) Centrality of social interaction in human brain function. Neuron 88(1):181–193
5. Nguyen T, Hoehl S, Vrtička P (2021) A guide to parent-child fNIRS hyperscanning data processing and analysis. Sensors (Basel, Switzerland) 21(12):4075–4075
6. Hyafil A et al (2015) Neural cross-frequency coupling: connecting architectures, mechanisms, and functions. Trends Neurosci 38(11):725–740
7. Holper L, Wolf M, Tobler PN (2014) Comparison of functional near-infrared spectroscopy and electrodermal activity in assessing objective versus subjective risk during risky financial decisions. NeuroImage 84:833–842

Machine Learning Distinguishes Familiar from Unfamiliar Pairs of Subjects Performing an Eye Contact Task: A Systemic Physiology Augmented Functional Near-Infrared Spectroscopy Hyperscanning Study

S. Guglielmini, G. Bopp, V. L. Marcar, Felix Scholkmann, and M. Wolf

Abstract

Background: Eye contact is an important aspect of human communication and social interactions. Changes in brain and systemic physiological activity associated with interactions between humans can be measured with systemic physiology augmented functional near-infrared spectroscopy (SPA-fNIRS) hyperscanning, enabling inter-brain and inter-body synchronisation to be determined. In a previous study, we found that pairs of subjects that are socially connected show higher brain and body synchrony. *Aim*: To enable a deeper understanding, our aim was to build and automatically detect the best set of features to distinguish between two different groups (familiar and unfamiliar pairs). *Material and methods*: We defined several features based on the Spearman correlation and wavelet transform coherence (WTC) of biosignals measured on 23 pairs of subjects (13 familiar and 10 unfamiliar pairs) during eye contact for 10 min. Additional custom features that identify the maximum brain-to-body coupling instants between pairs were generated. *Results*: After testing on combinations of different feature extraction methods, four subsets of features with the strongest discrimination power were taken into account to train a decision tree (DT) machine learning (ML) algorithm. We have obtained 95.65% classification accuracy using a leave-one-out cross-validation. The coupling features which represent the two maximum mean values resulting from the sum of 7 time-dependent WTC signals (oxyhaemoglobin concentration of the

S. Guglielmini (✉) · G. Bopp · M. Wolf
Biomedical Optics Research Laboratory, Department of Neonatology, University Hospital Zurich, University of Zurich, Zurich, Switzerland
e-mail: Sabino.Guglielmini@usz.ch

V. L. Marcar
Biomedical Optics Research Laboratory, Department of Neonatology, University Hospital Zurich, University of Zurich, Zurich, Switzerland

Comprehensive Cancer Center Zürich, University Hospital Zurich, Zurich, Switzerland

F. Scholkmann
Biomedical Optics Research Laboratory, Department of Neonatology, University Hospital Zurich, University of Zurich, Zurich, Switzerland

Institute of Complementary and Integrative Medicine, University of Bern, Bern, Switzerland

F. Scholkmann et al. (eds.), *Oxygen Transport to Tissue XLIII*, Advances in Experimental Medicine and Biology 1395, https://doi.org/10.1007/978-3-031-14190-4_30

right prefrontal region, total haemoglobin concentration of the left and right prefrontal region, heart rate, electrodermal activity on the left and right wrist, and skin temperature on the right wrist) played an essential role in the classification accuracy. *Conclusion*: Training the DT-ML algorithm with combined brain and systemic physiology data provided higher accuracy than training it only with brain or systemic data alone. The results demonstrate the power of the SPA-fNIRS hyperscanning approach and the potential in applying ML to investigate the strength of social bonds in a wide range of social interaction contexts.

Keywords

SPA-fNIRS hyperscanning · Cross-frequency time-dependent wavelet transform coherence · Social interactions · Eye contact

1 Introduction

Social interactions play a key role in our daily life. Forms of social interaction are very broad and involve different aspects including cooperation, competition and emulation [1]. Humans exchange thoughts and ideas through verbal communication, but also through nonverbal communication such as gestures and facial expressions, which can provide us with additional information for social interactions [2]. Eye contact is an essential aspect of human nonverbal communication representing one of the main channels by which we communicate interest, attention and engagement [3]. The length of gaze, the frequency, the degree of pupil dilation and the speed of blinking are all important aspects of nonverbal communication [4]. Associated with social interactions is a coupling of brain activity of the interacting subjects which can be measured by neuroimaging with the hyperscanning approach. Recently there has been an increase in research on functional near-infrared spectroscopy (fNIRS)-based hyperscanning of social interactions [5, 6]. A challenge with the traditional fNIRS hyperscanning approach is that there is a change in systemic physiology (SP), e.g., blood pressure, [7–9], also occurs, which possibly affects fNIRS signals. The solution is to measure brain activity (with fNIRS) and SP activity in parallel. For the case of hyperscanning, we termed this approach "systemic physiology augmented fNIRS (SPA-fNIRS) hyperscanning" [10].

In our previous SPA-fNIRS hyperscanning study [10], we found that pairs of subjects that are socially connected (i.e., familiar pairs) show stronger brain-to-brain and body-to-body coupling during eye contact. Identifying the set of biosignals that determines functional hyperconnectivity is a challenge in which machine learning (ML) can play a key role. To enable a deeper understanding, our aim was to build and automatically detect the best set of features able to distinguish between familiar and unfamiliar pairs using SPA-fNIRS hyperscanning data. Furthermore, we investigated whether ML with a DT leads to higher discrimination accuracy of the two groups when a combination of SP and brain signals was employed compared to only brain or SP signals.

2 Material and Methods

A group of 13 healthy familiar pairs (boyfriends/girlfriends, spouses, siblings) and a group of 10 healthy unfamiliar pairs (colleagues and strangers) took part in the study (age: 33.3 ± 13.7 years, 20 males, 26 females). Written informed consent was obtained from all of the participants and the study protocol was approved by the Ethics Committee of the Canton of Zurich (KEK-ZH-Nr. E50/2002).

The following SP and fNIRS signals measured during 10 min of eye contact and analysed in our previous study [10] were considered: the heart rate (HR) measured by a non-invasive continuous blood pressure device (SOMNOtouch™ NIBP, SOMNO Medics, Germany), electrodermal activity and skin temperature of the left/right wrist (electrodermal activity (EDA) (left/right) and temp (left/right) by two wristbands

(Empatica, Boston, USA)). Furthermore, changes in [O_2Hb], [HHb] and [tHb] were measured on the prefrontal cortex by optical neuroimaging with fNIRS (NIRSport, Berlin, Germany) and grouped according three regions of interest (left, right and entire prefrontal region). Nine fNIRS signals were considered: [O_2Hb] (left), [HHb] (left), [tHb] (left), [O_2Hb] (right), [HHb] (right), [tHb] (right), [O_2Hb] (left+right), [HHb] (left + right) and [tHb] (left + right). For the fNIRS signals, the short channel regression was performed.

Seventy-two features were calculated for each pair based on the Spearman correlation coefficients and wavelet transform coherence (WTC) of the 14 mentioned biosignals. The WTC for each biosignal was averaged over four frequency bands (very low-frequency band (VLF, 0.002–0.08 Hz), low-frequency band 1 (LF1, 0.015–0.15 Hz), low-frequency band 2 (LF2, 0.08–0.15 Hz), and heart rate band (HR, 1–2 Hz)) obtaining 20 SP and 50 fNIRS features. Two additional custom features have been built. First, the sum of three time-dependent WTC fNIRS in the LF1 band ([O2Hb] (right), [tHb] (left), [tHb] (right)) and four SP signals (HR (0.003–0.4 Hz), EDA (left), EDA (right), Temp (right) (0.045–0.25 Hz) was performed. The resulting time-dependent WTC was divided into 30-s blocks and the two blocks with the maximum coherence were extracted. Then, the average of each block was calculated separately, obtaining two additional features (Fig. 1b). The purpose of the two coupling features (CF) was to detect the instants of strongest brain-to-body coupling during the 10 min of eye contact.

Four groups of subset features were considered in the analysis. The first subset was composed of the two CF. The dimensionality of the SP, fNIRS, and SPA-fNIRS sets of features was reduced applying a hybrid approach [11] obtaining the other three subsets: SP, fNIRS, and SPA-fNIRS+CF. In a first step, Fisher's discriminant ratio (FDR) [12] was chosen as a selection method with the aim of eliminating some features that are considered irrelevant for the classification of the two groups and obtain a better classification accuracy. Thereafter, the sequential backward selection (SBS) algorithm [13] was adopted. SBS belongs to the class of wrapper methods, which are iterative algorithms that evaluate all possible reduced feature subset candidates obtained after the first step and provide significant and relevant feature sets. The subset of the strongest discrimination power was selected for further analysis. Therefore, two additional subsets of features were obtained consisting of two SP features and four fNIRS features, respectively. The last subset consisted of three features and was obtained by adding to the two CF the feature with greater discriminative power among the subset of SPA-fNIRS features (Fig. 1c). To classify the two groups of pairs, we applied a state-of-the-art classifier: DT. DT is a non-parametric supervised ML algorithm that builds a predictive model by learning simple decision-making rules derived from the data features [14]. The classifier was trained and evaluated with the MATLAB Statistics and Machine Learning Toolbox (The MathWorks, Inc., Natick, MA, USA). DT was tested by the leave-one-out cross-validation: Training includes all data except those of one pair and is tested on the data of this left out pair. This procedure is repeated until all pairs have been left out. The accuracy is obtained by dividing the number of correctly classified test data points by the total number of test data (Fig. 1d).

3 Results

The classification performance of the respective four subsets as well as the features automatically selected are summarised in Table 1. The results show that the most accurate classification was achieved when the two CF and the coherence of [O_2Hb] (left, LF1) were fed as inputs to the classifier (95.65%), i.e., both brain and SP features were included. DT was therefore able to correctly classify 22 pairs out of 23. Limited to only brain or SP, the accuracy of the DT was much lower. Only fNIRS features provided slightly higher accuracy than only SP features. High performance was obtained when only CF was used, achieving an accuracy of 86.96%.

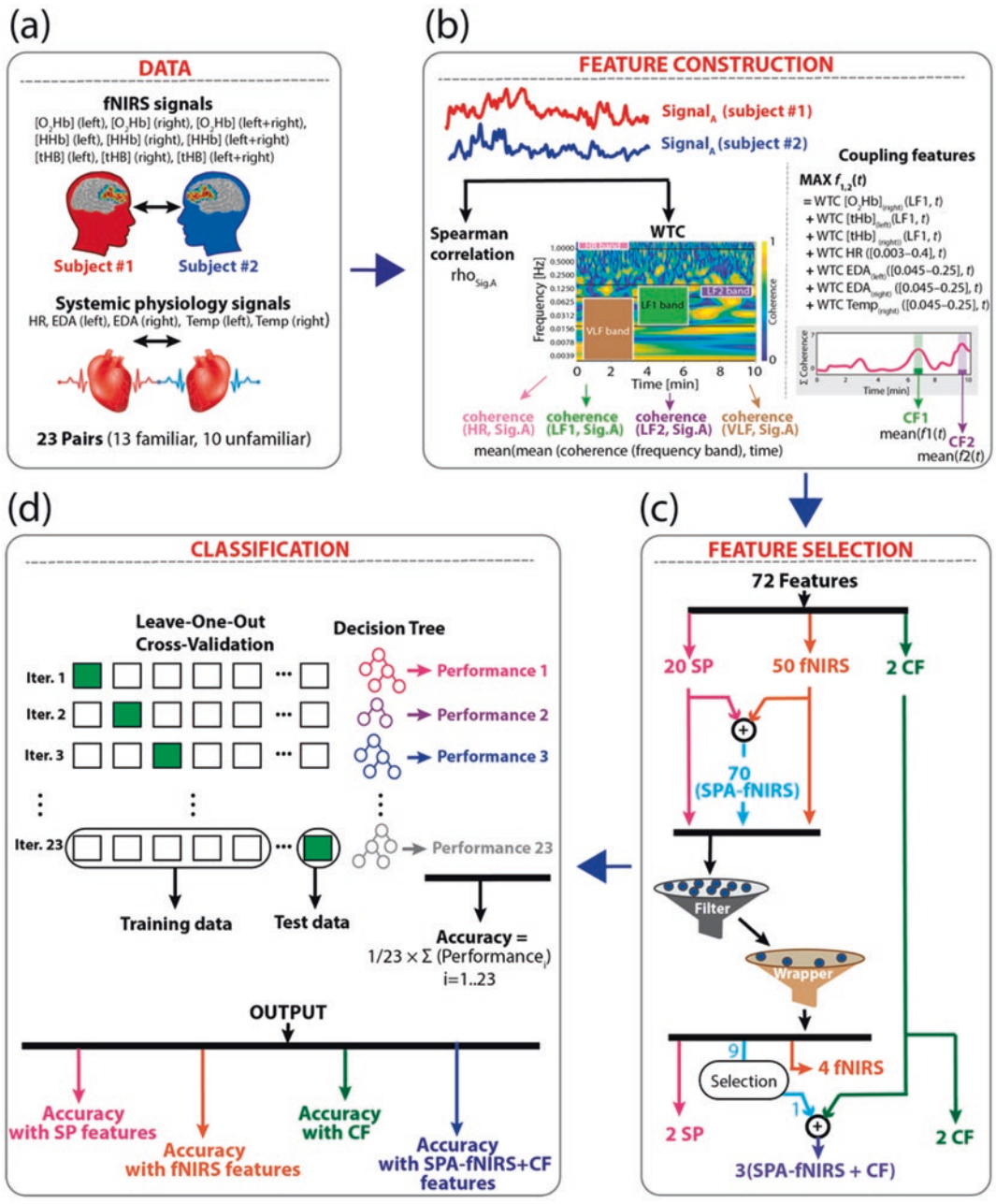

Fig. 1 Group detection pipeline. (**a**) Input data acquired in 23 pairs (13 familiar and 10 unfamiliar pairs); (**b**) Feature construction: 72 features were built based on Spearman correlation coefficients, WTC and CF; (**c**) Feature selection: Four subsets of feature were generated; (**d**) Classification: the DT accuracy was performed using leave-one-out cross-validation on each subset

Table 1 Four cases with the respective features used to build a DT model and its average accuracy: SP, fNIRS, CF, SP-FNIRS+CF

Case	Selected features	Accuracy (%)
SP	EDA (left, LF2), EDA (right, LF2)	52.17
fNIRS	[HHb] (left, LF1), [HHb] (left, VLF), [O_2Hb] (left, LF1), [O_2Hb] (right, LF1)	65.22
CF	The two CF	86.96
SP-fNIRS + CF	The two CF, [O_2Hb] (left, LF1)	95.65

4 Discussion, Conclusions and Outlook

To the best of our knowledge, this is the first SPA-fNIRS hyperscanning study exploring whether the social bonding state of pairs determined the brain-to-brain, brain-to-body and body-to-body coupling during a prolonged eye contact interaction task. In concordance with other studies [15, 16], we found a stronger functional hyperconnectivity in familiar pairs compared to unfamiliar pairs, which enabled us to distinguish the two groups with high accuracy (95.65%). This result was achieved using the two CF features and the coherence of [O_2Hb] in the LF1 frequency band, i.e., 0.015–0.15 Hz. The Mayer wave frequency (0.1 Hz) – due to a spontaneous oscillation of the cardiovascular system [17, 18] – falls within this frequency band. The new signal-processing approach we proposed is based on brain, body and brain-body features. We found that by applying SPA-fNIRS hyperscanning data, it is possible to automatically identify a global coupling involving SP and fNIRS signals. In fact, the two maximum 30 s mean values of the sum of seven time-dependent WTC signals ([O_2Hb] of the right prefrontal region, [tHb] of the left and right prefrontal region, HR, EDA (left), EDA (right), and temp (right)) representing the instants of strongest brain-to-body coupling during the 10 min task within pairs have played an essential role in the classification accuracy. We conclude that with the combination of brain and SP features, DT achieved higher accuracy compared to training with only brain or systemic features alone. The next step in our research will be to increase the sample size and further extend our approach to consider behavioural data (e.g., facial expressions, eye movements) as well. The results demonstrate the power of the SPA-fNIRS hyperscanning approach and the potential in applying ML to investigate the strength of social bonds in a wide range of social interaction contexts.

Acknowledgments We gratefully acknowledge funding by the Swiss National Science Foundation (159490) and Innosuisse (28314.1). MW declares that he is president of the board and co-founder of OxyPrem AG.

References

1. Bardis PD (1979) Social interaction and social processes. Soc Sci 54(3):147–167
2. Fichten CS et al (1992) Verbal and nonverbal communication cues in daily conversations and dating. J Soc Psychol 132(6):751–769
3. Argyle M, Dean J (1965) Eye-contact, distance and affiliation. Sociometry 28(3):289–304
4. Binetti N et al (2016) Pupil dilation as an index of preferred mutual gaze duration. R Soc Open Sci 3(7):160086
5. Balters S et al (2020) Capturing human interaction in the virtual age: a perspective on the future of fNIRS hyperscanning. Front Hum Neurosci 14(458)
6. Scholkmann F et al (2013) A new methodical approach in neuroscience: assessing inter-personal brain coupling using functional near-infrared imaging (fNIRI) hyperscanning. Front Hum Neurosci 7(813)
7. Scholkmann F et al (2017) Effect of short-term colored-light exposure on cerebral hemodynamics and oxygenation, and systemic physiological activity. Neurophotonics 4(4):045005
8. Zohdi H et al (2021) Color-dependent changes in humans during a verbal fluency task under colored light exposure assessed by SPA-fNIRS. Sci Rep 11(1):9654
9. Zohdi H, Scholkmann F, Wolf U (2021) Individual differences in hemodynamic responses measured on the head due to a long-term stimulation involving colored light exposure and a cognitive task: a SPA-fNIRS study. Brain Sci 11(1)
10. Guglielmini S et al (2021) Looking at each other causes entrainment of spontaneous activity of the brain and body physiology between subjects: a systemic physiology augmented functional near-infrared spectroscopy (SPA-fNIRS) hyperscanning study. Neurophotonics
11. Ostojic D et al (2020) Reducing false alarm rates in neonatal intensive care: a new machine learning approach. Adv Exp Med Biol 1232:285–290

12. Webb, A.R., Statistical pattern recognition. 2002
13. Aha DW, Bankert RL (1996) A comparative evaluation of sequential feature selection algorithms. In: Fisher VD, Lenz H-J (eds) Learning from data: artificial intelligence and statistics. Springer, New York, pp 199–206
14. Breiman, L., Friedman, J.H.; Olshen, R.A.; Stone, C.J., Classification and regression trees. 1984
15. Kinreich S et al (2017) Brain-to-brain synchrony during naturalistic social interactions. Sci Rep 7(1):17060
16. Pan Y et al (2017) Cooperation in lovers: an fNIRS-based hyperscanning study. Hum Brain Mapp 38(2):831–841
17. Julien C (2006) The enigma of Mayer waves: facts and models. Cardiovasc Res 70(1):12–21
18. Julien C (2019) An update on the enigma of Mayer waves. Cardiovasc Res 116(14):e210–e211

Assessing Neurovascular Coupling Using Wavelet Coherence in Neonates with Asphyxia

Tim Hermans, Katherine Carkeek, Anneleen Dereymaeker, Katrien Jansen, Gunnar Naulaers, Sabine Van Huffel, and Maarten De Vos

Abstract

Brain monitoring is important in neonates with asphyxia in order to assess the severity of hypoxic ischaemic encephalopathy (HIE) and identify neonates at risk of adverse neurodevelopmental outcome. Previous studies suggest that neurovascular coupling (NVC), quantified as the interaction between electroencephalography (EEG) and near-infrared spectroscopy (NIRS)-derived regional cerebral oxygen saturation (rSO_2) is a promising biomarker for HIE severity and outcome. In this study, we explore how wavelet coherence can be used to assess NVC. Wavelet coherence was computed in 18 neonates undergoing therapeutic hypothermia in the first 3 days of life, with varying HIE severities (mild, moderate, severe). We compared two pre-processing methods of the EEG prior to wavelet computation: amplitude integrated EEG (aEEG) and EEG bandpower. Furthermore, we proposed average real coherence as a biomarker for NVC. Our results indicate that NVC as assessed by wavelet coherence between EEG bandpower and rSO_2 can be a valuable biomarker for HIE severity in neonates with peripartal asphyxia. More specifically, average real coherence in a very low frequency range (0.21–0.83 mHz) tends to be high (positive) in neonates with mild HIE, low (positive) in neonates with moderate HIE, and negative in neonates with severe HIE. Further investigation in a larger patient cohort is needed to validate our findings.

Keywords

NIRS · Hypoxic-ischemic encephalopathy (HIE) · Cerebral oxygenation · Regional oxygen saturation (rSO_2) · Peripartal asphyxia

T. Hermans (✉) · S. Van Huffel
Department of Electrical Engineering (ESAT), STADIUS, KU Leuven, Leuven, Belgium
e-mail: tim.hermans@esat.kuleuven.be

K. Carkeek
Department of Development and Regeneration, KU Leuven, Leuven, Belgium

Neonatal Intensive Care Unit, UZ Leuven, Leuven, Belgium

Neonatal Intensive Care Unit, Cliniques Universitaires Saint Luc, Bruxelles, Belgium

A. Dereymaeker · G. Naulaers
Department of Development and Regeneration, KU Leuven, Leuven, Belgium

Neonatal Intensive Care Unit, UZ Leuven, Leuven, Belgium

K. Jansen
Department of Development and Regeneration, KU Leuven, Leuven, Belgium

Child Neurology, UZ Leuven, Leuven, Belgium

M. De Vos
Department of Electrical Engineering (ESAT), STADIUS, KU Leuven, Leuven, Belgium

Department of Development and Regeneration, KU Leuven, Leuven, Belgium

F. Scholkmann et al. (eds.), *Oxygen Transport to Tissue XLIII*, Advances in Experimental Medicine and Biology 1395, https://doi.org/10.1007/978-3-031-14190-4_31

1 Introduction

Neonatal hypoxic ischaemic encephalopathy (HIE) is the most frequent and important complication of peripartal asphyxia, a phenomenon occurring when the neonatal brain shows signs of hypoxia during labour and delivery due to a lack of cerebral blood flow and oxygen supply. In these patients, it is important to monitor the neonatal brain as soon as possible after birth to assess the severity of HIE and to continue monitoring over the first days of life to identify neonates at risk of adverse neurodevelopmental outcome.

The two techniques most frequently used for continuous brain monitoring in neonates are electroencephalography (EEG) and near-infrared spectroscopy (NIRS), measuring cerebral activity and cerebral oxygenation, respectively. The interaction between EEG and NIRS can be interpreted as a measure for neurovascular coupling (NVC). NVC is a regulatory mechanism that maintains a balance between cerebral oxygen demand and supply by managing cerebral blood flow [1]. Recent studies have shown the potential of quantifying NVC using EEG and NIRS in neonates, showing that NVC is impaired in neonates with non-favourable outcome [1–3].

In this study, we reviewed and expanded on the work of Chalak et al., who proposed the use of wavelet coherence to quantify NVC [3]. Wavelet coherence is a signal processing method to detect transient linear relationships between two signals as a function of frequency and time. In other words, wavelet coherence identifies the frequencies and time points at which two signals strongly co-vary. There are two important challenges in this wavelet approach that will be explored in this paper. Firstly, because EEG dynamics are much faster than NIRS, the raw EEG data needs to be compressed to an EEG feature with similar dynamics as the NIRS signal. Secondly, wavelet coherence analysis yields a large amount of information, which in turn needs to be condensed to an interpretable biomarker.

In this paper, wavelet coherence will be applied to EEG and NIRS signals measured in neonates with HIE of varying severity. Two different methods for EEG pre-processing will be compared and an interpretable biomarker for NVC derived from the wavelet result will be proposed.

2 Methods

Clinical data were retrospectively collected from UZ Leuven neonatal intensive care unit (NICU) between 2010 and 2020. Eighteen patients were included that had a gestational age >36 weeks, were treated with therapeutic hypothermia for HIE, and had had one cerebral magnetic resonance imaging (MRI) scan taken between 3–9 days of life. The MRI scans were scored by four neonatologists using the scoring system proposed by Weeke et al. [4]. Based on the total Weeke scores, the patients were divided into three groups: mild (score is 0), moderate (score is 1 or 2) and severe (score is greater than 2). This study was conducted with the approval of the hospital Ethical Review Board for a retrospective, anonymous data analysis.

Bipolar EEG (C3-C4, taken from a multichannel EEG) and single-channel NIRS (regional oxygen saturation, rSO_2 [%]) were simultaneously recorded during hypothermia treatment in the first 3 days of life. Sampling frequencies of the raw EEG and NIRS data were 250 Hz and 1 Hz, respectively. The data recorded between 6 and 66 h after start hypothermia were used for further analysis.

rSO_2 was pre-processed in two steps. First, flat lines were removed, and artefacts were automatically detected based on anomaly detection and physiological thresholds (<15% and >100%). For anomaly detection, the running line length (running average of the absolute first time-derivative) was computed in a moving window of 10 s, and samples were marked as artefacts where the line length exceeded its median plus 4 • 1.482 • MAD computed in windows of 1 h, where MAD is the median absolute deviation. Second, the rSO_2 signal was down-sampled to 1/3 Hz since the signal contained no significant spectral content above 1/6 Hz.

Two different EEG features were computed for coupling with rSO_2: amplitude integrated

EEG (aEEG) and EEG bandpower. aEEG was emulated with a sampling frequency of 1/3 Hz and the bandwidth of the aEEG was used as input for wavelet coherence, as in previous studies [3, 5]. EEG bandpower was computed in four steps. First, the raw EEG was filtered with a bandpass filter (1–40 Hz), and subsequently down-sampled to 80 Hz. Second, amplitudes <0.5 μV or >200 μV were marked as artefacts. Third, the time-varying signal power was computed using the continuous wavelet transform and the wavelet power was averaged in the frequency band 2–16 Hz, analogous to the 2–16 Hz bandpass filter which is applied in the aEEG emulation algorithm. Finally, the power was averaged in non-overlapping windows of 3 s to obtain a sampling frequency of 1/3 Hz and then log-transformed.

Wavelet coherence was computed between the pre-processed EEG and rSO_2 signals using a complex Morlet wavelet with a centre frequency of 6 rad/s [6]. The complex wavelet makes it possible to not only compute the amount and strength of coupling, but also the phase of the coupling, e.g., in-phase (positive relationship) or anti-phase (inverse relationship).

For computational purposes, all missing values in EEG and rSO_2 were replaced by linear interpolation. Ultimately, coherence values that significantly overlapped with missing values were removed and not considered in any further calculations. Prior to wavelet coherence, second order polynomial trends were removed followed by z-score normalisation. A Monte Carlo analysis using 100 surrogates was done to detect significant magnitude squared coherence values ($p < 0.05$) [6].

Wavelet coherence yields time-frequency maps, i.e., coherence values as function of time and frequency. These time-frequency maps were summarised over time in two different ways, yielding two 'frequency profiles'. The first frequency profile (% significant coherence) describes the amount of coupling detected for each frequency. It is computed per frequency as the percentage of time in which the (magnitude squared) coherence was significant. The second frequency profile (real coherence) describes the dominant phase of the coherence (in-phase, anti-phase) and its consistency. It is computed per frequency as the real part of the time-averaged complex coherence, excluding non-significant coherence values from the average.

The latter frequency profile (real coherence) was further condensed to a single biomarker for NVC by averaging the real coherence over frequencies 0.21–0.83 mHz. This mean real coherence was compared between the three patient groups. This frequency band was selected using the real coherence frequency profile, as largest differences were seen between the patient groups in these frequencies.

3 Results

The amount of detected coupling with each EEG feature for each patient group is depicted in Fig. 1. In all cases, coupling is primarily detected in lower frequencies (<10 mHz) and for higher frequencies, the percentage of detected coupling is close to 5%, which is the expected value for noise (since we used $p < 0.05$ in the Monte Carlo analysis). In general, the results for aEEG and bandpower are similar, but slightly more coupling is detected using the bandpower compared to the aEEG. Visually, no clear distinction can be seen between the patient groups.

Figure 2 shows the time-averaged real coherence for both EEG features and for each patient group. The curves differ between the aEEG and bandpower feature. Furthermore, between 0.21 and 0.83 mHz (grey shaded background), the real coherence computed using bandpower differs between patient groups, being highest (positive) in the mild group and lowest (negative) in the severe group. This is emphasised in Fig. 3, where the average real coherence between 0.21–0.83 mHz obtained using EEG bandpower is shown for each patient group.

4 Discussion and Conclusions

This study investigated the use of wavelet coherence to assess NVC and HIE severity in neonates with peripartal asphyxia and led to four main

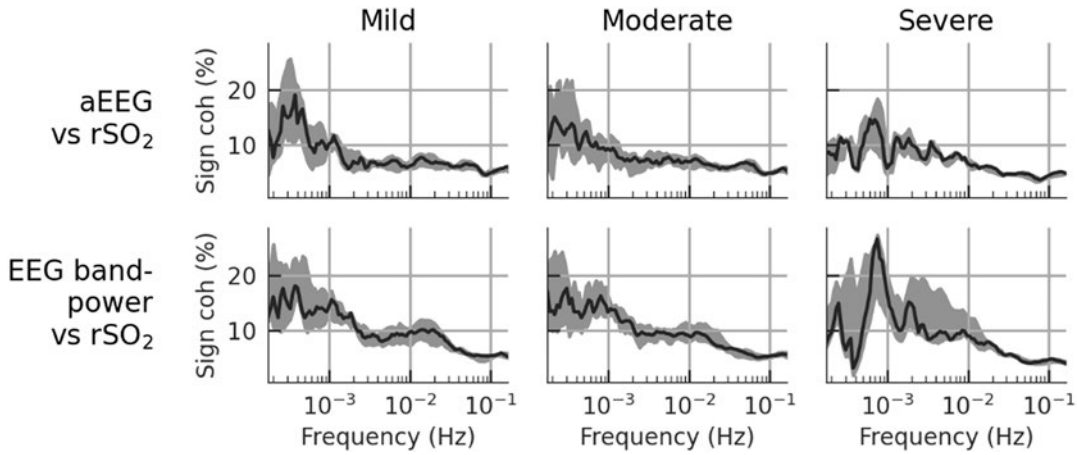

Fig. 1 The percentage of time with significant coherence ($p < 0.05$) as function of frequency for each patient group, computed from aEEG (top) or EEG bandpower (bottom). The black line is the median, and the shaded area is the interquartile range

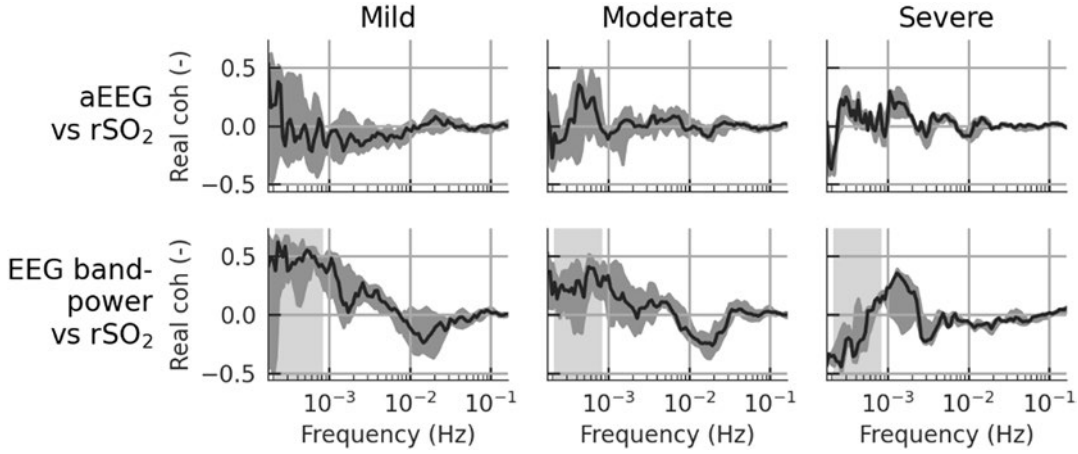

Fig. 2 The average real coherence as function of frequency for each patient group, computed from aEEG (top) or EEG bandpower (bottom). The black line is the median, and the shaded area is the interquartile range. The grey shading in the bottom plot indicates the 0.21–0.83 mHz band

findings. Firstly, coupling was detected primarily in low frequencies (<10 mHz), with little coupling detected in higher frequencies (Fig. 1). Secondly, the 'phase' of the coupling appears to be more important than the 'amount' of coupling, as real coherence (Fig. 2) showed a more pronounced difference between patient groups than the percentage of significant coherence (Fig. 1). Thirdly, extraction of EEG bandpower seemed to be a more suitable EEG feature than aEEG for coupling with rSO_2. This is illustrated in Figs. 1 and 2, showing that slightly more coupling is detected, and real coherence differs more between patient groups when using EEG bandpower compared to aEEG. Finally, real coherence computed using EEG bandpower averaged over 0.21–0.83 mHz is a potential biomarker for HIE severity, where real coherence is highest (positive) for mild HIE and lowest (negative) for severe HIE (Fig. 3).

Positive real coherence relates to an in-phase coupling, meaning that there is a positive correla-

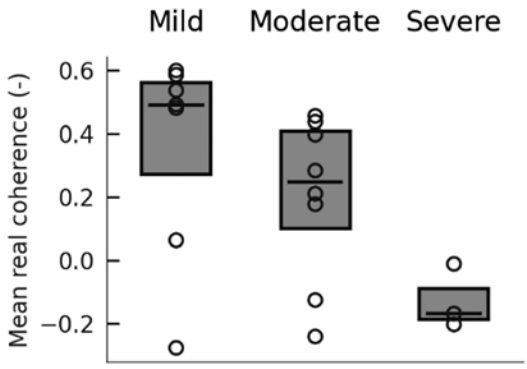

Fig. 3 Average real coherence between 0.21 and 0.83 mHz for each patient group, computed using EEG bandpower. The box represents the median and interquartile range

tion between EEG activity and rSO_2. In contrast, negative real coherence relates to an anti-phase coupling, meaning that there is a negative correlation. Under static conditions (constant cerebral blood flow (CBF) and constant arterial oxygen saturation (SaO_2)), rSO_2 is expected to decrease when EEG activity increases. This is because rSO_2 primarily represents venous oxygenation, which would drop in response to increased cerebral activity due to increased O_2 uptake.

In a healthy brain, conditions are not static, however, and CBF is regulated in response to EEG activity via NVC to maintain sufficient cerebral oxygen supply. Therefore, we hypothesise that a simultaneous increase of rSO_2 and EEG activity reflects an increase in CBF (assuming constant SaO_2). Following this reasoning, average real coherence can be interpreted as a biomarker for NVC, where positive values represent active regulation of CBF in response to changes in cerebral activity and negative values represent insufficient or a lack of such regulation.

Several limitations of this study need to be considered. Firstly, the patient group was small and heterogenous, which complicates (statistical) comparisons between patient groups. Furthermore, factors such as seizure activity, medication, sleep-wake cycling and variations in SaO_2 were not taken into account. These limitations should be tackled in future research to further validate this methodology.

The results in this study support previous findings by Chalak at el. who also found an increased amount of in-phase coherence between aEEG bandwidth and rSO_2 in neonates with normal outcome compared to neonates with abnormal outcome [3]. Additionally, the low frequency range (<1 mHz) in which we found most coupling was in the same frequency range identified by Chalak et al. (0.25–1 mHz).

Furthermore, a recent study by Das et al. compared the use of aEEG bandwidth with preprocessed EEG for wavelet coherence [5]. They showed that both methods yield similar results in terms of the magnitude squared coherence. Our results are in keeping with these findings (Fig. 1), but additionally show that the real coherence can differ between aEEG and EEG bandpower (Fig. 2), indicating that the phase information can depend on the EEG feature that is used.

Acknowledgments This project receives funding from the European Union's Horizon 2020 Framework Programme under grant agreement No.813843 and from the Flemish Government (AI Research Program). SVH, MDV and TH are affiliated to Leuven.AI - KU Leuven institute for AI, B-3000, Leuven, Belgium.

References

1. Hendrikx D, Smits A, Lavanga M et al (2019) Measurement of neurovascular coupling in neonates. Front Physiol 10:65
2. Govindan RB, Massaro A, Chang T et al (2016) A novel technique for quantitative bedsid-monitoring of neurovascular coupling. J Neurosci Methods 259:135–142
3. Chalak LF, Tian F, Adams-Huet B et al (2017) Novel wavelet real time analysis of neurovascular coupling in neonatal encephalopathy. Sci Rep 7:45958
4. Weeke LC, Groenendaal F, Mudigonda K et al (2018) A novel magnetic resonance imaging score predicts neurodevelopmental outcome after perinatal asphyxia and therapeutic hypothermia. J Pediatr 192:33–40.e2
5. Das Y, Wang X, Kota S et al (2021) Neurovascular coupling (NVC) in newborns using processed EEG versus amplitude-EEG. Sci Rep 11:9426
6. Torrence C, Webster PJ (1999) Interdecadal changes in the ENSO–monsoon system. J Clim 12:2679–2690

Basic Examination of Haemoglobin Phase of Oxygenation and Deoxygenation in Resting State and Task Periods in Adults Using fNIRS

Nursyarizah Amirah Jasni and Hiroki Sato

Abstract

Functional near-infrared spectroscopy (fNIRS) is a neuroimaging technique used to measure the relative changes in concentrations of oxygenated haemoglobin (oxy-Hb) and deoxygenated haemoglobin (deoxy-Hb) in the cerebral cortex. While most previous studies using fNIRS have relied only on a single oxy-Hb or deoxy-Hb parameter to infer about neural activation, the phase difference between the oxy- and deoxy-Hb signals (haemoglobin phase of oxygenation and deoxygenation: hPod) has been reported to be an important biomarker for analysing haemodynamic characteristics of the brain in infants. In this study, we examined the basic characteristics of adult hPod to develop a new analysis method to detect more sensitive signals that reflect neural activation in adults using fNIRS. We measured the hPod of 12 healthy adults in the frontal and occipital cortex during rest and upon exposure to visual stimuli and the verbal working memory (WM) task. We found that the average hPod values during the entire measurement period ranged between π and 1.5π rad in all conditions. This result indicates that the phase differences in adults were generally close to a stable antiphase pattern (hPod values around π), regardless of the presence or absence of tasks and stimuli. However, when dynamic changes in hPod values were analysed, significant differences between the resting state and WM tasks were observed during activation period in the frontal and occipital regions. These results suggest that the analysis of dynamic hPod change is useful for detecting a subtle activation for cognitive tasks.

Keywords

Optical brain imaging · hPod · Verbal WM task · Dynamic hPod · Neurovascular coupling

1 Introduction

Functional near-infrared spectroscopy (fNIRS) is an optical brain imaging tool that can be used to measure the relative changes in the concentration of the oxy-Hb and deoxy-Hb in the cerebral tissue [1, 2]. In most conventional studies that used fNIRS, oxy-Hb and deoxy-Hb signals were studied individually as a single parameter to infer about neural activation. However, the phase difference between the spontaneous low-frequency oscillations of the cerebral oxy- and deoxy-Hb concentrations is related to the cerebral blood

N. A. Jasni · H. Sato (✉)
Department of Bioscience and Engineering, College of Systems Engineering and Science, Shibaura Institute of Technology, Saitama, Japan
e-mail: hiroki@shibaura-it.ac.jp

F. Scholkmann et al. (eds.), *Oxygen Transport to Tissue XLIII*, Advances in Experimental Medicine and Biology 1395, https://doi.org/10.1007/978-3-031-14190-4_32

volume, blood oxygenation and flow velocity [3–6].

Previous studies have shown that both oxy-Hb and deoxy-Hb signals are crucial in evaluating the neural activity by monitoring changes occurring in the oxy- and deoxy-Hb concentrations, which represent the haemodynamic changes based on neuronal activation through neurovascular coupling.

For both the preterm and term infants, Watanabe et al. [7] suggested that the time-averaged haemoglobin phase of oxygenation and deoxygenation (hPod), which reflects the phase difference between oxy-Hb and deoxy-Hb signals, is sensitive to the developmental status of the haemodynamic and metabolic processes of the brain. The hPod values are defined as the phase values obtained by time-averaging the instantaneous phase difference of spontaneous low-frequency oscillatory changes in oxy- and deoxy-Hb signals. The hPod contains integrated information regarding the interplay between neural activity, blood flow, and metabolism [6, 8]. A previous study also showed that the hPod is an important biomarker for analysing haemodynamic characteristics of the brain and reflects the early brain development in infants [9, 10]. However, most hPod studies have been used to evaluate brain development in infants, and little work has been done thus far to understand the hPod in adults.

The task-induced brain activity can be better detected using the phase information between changes in oxy- and deoxy-Hb [11, 12]. Therefore, it is important to clarify how the stimulus-induced activity and the spontaneous activity produce differentiated values of hPod in functionally different regions of the cortex.

Here, we studied the general pattern of hPod occurring in adults during the resting and active states. We further attempted to explain the statistical differences in the hPod values between the resting state and the presence of tasks and stimuli in the frontal and occipital regions of the cortex.

From the data obtained, the hPod values were analysed using two different methods. First, we calculated the hPod values by taking average of the entire measurement duration and called it 'main hPod'. We hypothesised that the main hPod values of adults are in an antiphase pattern, as reported previously.

Second, we proposed a new approach that measured the dynamic changes in the hPod values based on the dynamic features of the haemodynamic changes during rest, visual stimuli, and WM tasks and called it 'dynamic hPod'. Pierro et al. [13] in a preliminary study revealed that the brain activation during task performance or stimuli-induced phase lag differed in the oxy-Hb signals (from 0 to π). Therefore, we hypothesised that the dynamic hPod pattern changes according to the haemodynamic response curves induced by tasks or stimuli.

2 Methods

2.1 Participants

Twelve healthy adults consisting of six females and six males (age: 22.2 ± 1.04 years) participated in the experiment. Two males were left-handed, as determined by the Edinburgh Handedness Inventory [14], while the other 10 participants were right-handed. All data were included in the analysis as the inclusion or exclusion of the left-handed participants did not affect our primary findings in the hPod study.

The study was approved by the Ethics Committee of Shibaura Institute of Technology, and consent was obtained from all participants prior to the initiation of the experiment.

2.2 fNIRS Device and Data Acquisition

An fNIRS system (ETG-4000, Hitachi Medical Corporation, Japan) was used to measure the relative concentrations of the oxy-Hb and deoxy-Hb signals [mM•mm] during the resting state and during the presence of visual stimuli and verbal WM tasks.

The fNIRS system was equipped with 18 near-infrared light sources and 15 detectors. The light source consisted of near-infrared laser

diodes with wavelengths of 695 and 830 nm. The transmitted signal was detected by photodiodes located 30 mm from the sources.

The optodes, sources, and detectors were arrayed in a 3 × 3 lattice pattern (each right and left frontal area) and embedded in a soft silicone holder that was placed on the participant's forehead, while 3 × 5 arrays of eight source and seven detection fibres were set on a probe and placed on the occipital area of the participants' head.

The probabilistic registration method was used to estimate the locations of measurement channels in the stereotaxic brain coordinate system or the Montreal Neurological Institute (MNI) space. In addition, a probabilistic registration method was used to generate 3-D topographical maps [15].

We estimated 24 measurement channels for the frontal area of the cortex, with 12 channels for each hemisphere (Fig. 1a), and 22 channels for covering the occipital area of the cortex (Fig. 1b).

2.3 Experimental Paradigm

The tasks were organised into three sessions: resting state, presence of visual stimuli, and verbal WM task. During the resting state, the participants were seated on a comfortable chair in a dim, quiet room and instructed to focus on the fixation cross displayed on the monitor. Subsequently, the participants received computer-automated instructions that were followed by a brief practice session to familiarise them with the WM task (Fig. 2a). The measurements were conducted while the participants performed the WM task [16]. Thereafter, visual stimuli consisting of black-and-white checkerboards with 4-Hz pattern reversals were displayed for 8500 ms (Fig. 2b) [17]. Each task consisted of 10 trials, and the tasks were separated by a short break (approximately 1 min). The duration of the measurement for each task was approximately 5 min; the entire experiment took approximately 45 min.

For the resting state, the participants were asked to focus on a fixation point, and the measurement periods were similar with the visual stimuli (target measurement: 8500 ms). In the verbal WM task (refer to Fig. 2a), each trial started with a 1500 ms presentation of the target stimuli, followed by a delay of 7000 ms. A probe stimulus was presented for 2000 ms or until the participant responded. The intervals between the target and probe stimuli onsets were randomised from 14000 to 16000 ms. Fixation cross was presented during the interval and delay period. A visual cue (changing the colour of fixation) was presented at the beginning of the trial onset. Auditory cues, 1000 and 800 Hz tones of 100-ms

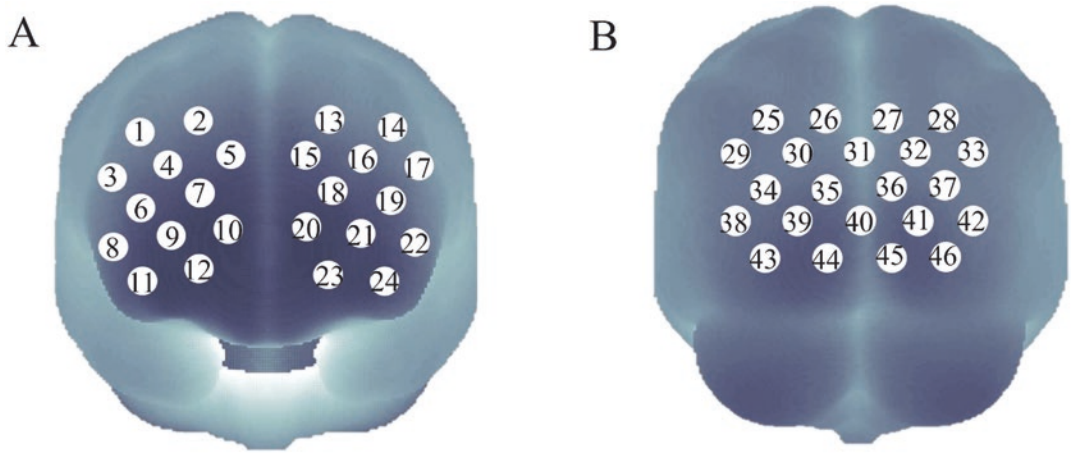

Fig. 1 Schematic arrangements of fNIRS channels. (**a**) Frontal area of the cortex: 1–24 measurement channels; 12 channels for each hemisphere. (**b**) Occipital area of the cortex: 22 measurement channels (25–46 channels)

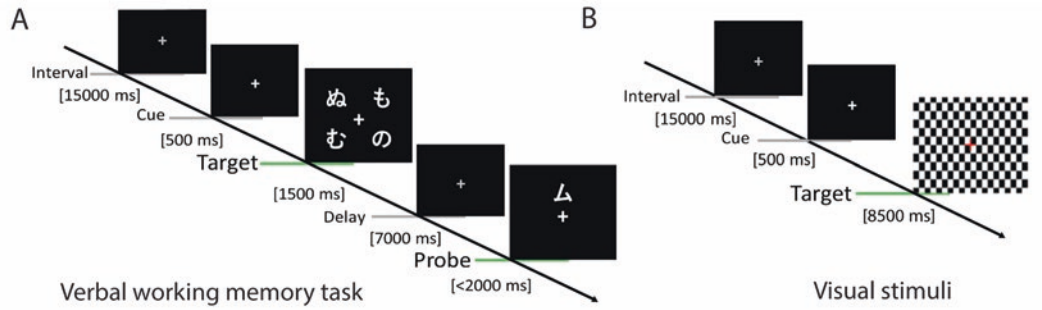

Fig. 2 Schematic of (**a**) verbal WM task trial, wherein four Japanese characters in hiragana are presented as target stimuli, and a Japanese character in katakana is presented as probe stimuli. (**b**) Visual stimuli trial, comprising black-and-white checker-boards with 4 Hz pattern reversals

duration, were presented at the onset of the target stimuli and probe stimulus, respectively. For the visual stimuli, the checkerboard pattern was displayed for 8500 ms after the interval and fixation cross displayed for 500 ms (Fig. 2b).

2.4 Data Analysis

A plug-in-based analysis software, Plat-form for Optical Topography Analysis Tools (POTATo, run on MATLAB, The MathWorks) [18], was used for performing the analyses.

First, a high-pass filter (0.02 Hz) and low-pass filter (0.8 Hz) were applied to the Hb-signals to remove low-frequency drift/oscillation and high-frequency noise components.

Next, the time-continuous data of the Hb-signals for each channel were separated into 10 task blocks, which were defined as a 24.7 s period starting from 2.0 s before the onset of the target stimuli and ending at 14.0 s after probe stimuli containing the verbal WM task trials (Fig. 2a). In addition, even for the visual stimuli, the time-continuous data of the Hb-signals were separated into 10 task blocks, which were defined as a 24.7 s period starting from 2.0 s before the checker-board pattern was displayed and 14.0 s after visual stimuli were presented (Fig. 2b). Time continuous data of the Hb-signals during resting state were also processed according to task sequence in the WM tasks and the visual stimuli.

The value of the hPod was calculated according to the method reported by Watanabe et al. [7]. A Hilbert transformation was applied to the time series of the oxy-Hb and deoxy-Hb for each channel to obtain the instantaneous phases of each Hb-signal. Then, the phase difference between the instantaneous phases of the oxy- and deoxy-Hb signals for each block was calculated and represented by a vector with a phase value and length of 1. These calculations were performed to obtain both the main and dynamic hPods.

To calculate the 'main hPod', the time series of the vectors were averaged over the measurement time of the resting state and tasks. In our analysis, the data obtained during the resting state were considered as the control condition. To assess the statistical significance of the main hPod values between resting state and tasks, we first averaged the hPod values of the participants for each measurement channel. Then, the hPod values in frontal (24 measurement channels) and occipital regions (12 measurements) were averaged. Then, the statistical significance of the hPod values (averaged hPod values of 12 participants) was examined using a group-level t-test (significance level was set to $p < 0.05$, one-tailed).

However, for the 'dynamic hPod', the time series of the vectors were averaged over each 2 s of the measurement time to obtain the dynamic changes in the hPod. Similar to the main hPod calculation, the data obtained during the resting state were considered as the control condition. To assess the statistical significance of the dynamic hPod values between resting state and tasks, we

first averaged the hPod values of the task-related duration (refer to Figs. 4 and 5: grey vertical areas indicate the onset of the target and probe) within participants. Then, the statistical significance of the dynamic hPod values during the task periods was examined by a group-level t-test (significance level was set to $p < 0.05$, one-tailed) across participants. All the statistical analyses were performed for each channel.

3 Results

3.1 hPod Vector Representation (Main hPod)

The time series of the vectors were averaged over the measurement time. The π values and a value smaller than 1.5π indicate an antiphase pattern, while the values of 0 and 2π and angular values larger than 1.5π indicate a pattern close to an in-phase pattern.

The main hPod phase values during rest and tasks ranged between π and 1.5π rad (Fig. 3). The phase values of hPod in the frontal and occipital regions were 1.14π rad and 0.993π rad (during the resting state), 1.26π rad and 1.07π rad (during the application of visual stimuli), and 1.17π rad and 1.047π rad (while performing the verbal WM task).

A group-level t-test showed no significant differences in either region between the resting and WM tasks (frontal: $t(11) = 1.79$, $p = 0.31$, occipital: $t(11) = 1.79$, $p = 0.086$) or between the rest and visual stimuli (frontal: $t(11) = 1.79$, $p = 0.23$; occipital: $t(11) = 1.79$, $p = 0.127$).

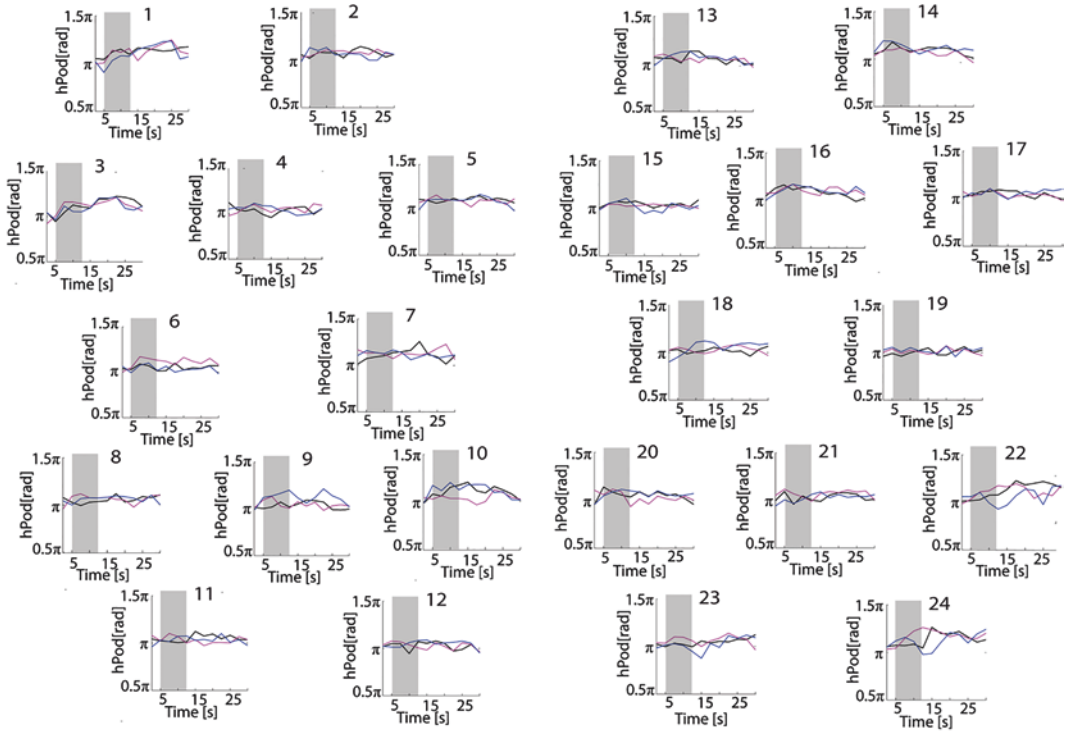

Fig. 4 Dynamic hPod in adults in the frontal area Vector representations averaged hPod values during the resting state, during the verbal working memory task, and the visual stimuli across participants (black, blue, and magenta lines, respectively) are shown. The grey vertical areas indicate the onset of the target and the probe, respectively

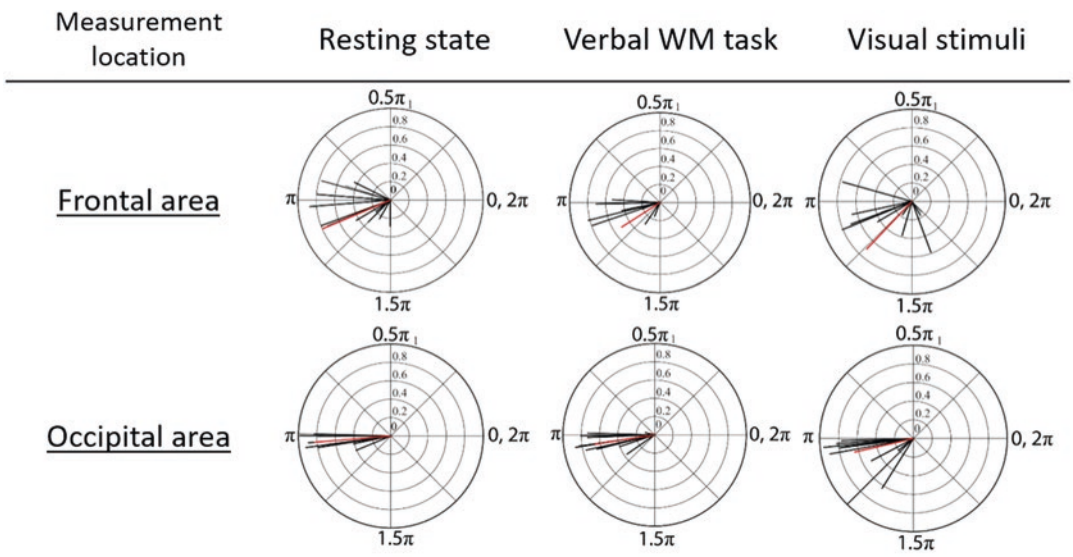

Fig. 3 Main hPod of adults in the resting state and during tasks. Black and red arrows denote the vector representations of individual and averaged hPod values, respectively

3.2 Dynamic Changes in hPod (Dynamic hPod)

The dynamic changes in the hPod followed a stable antiphase pattern, and no significant difference was found between the hPod values during the resting and active states in most regions of the cortex (Figs. 4 and 5). However, a group-level t-test showed a significant difference between the resting state and the WM tasks in the frontal (ch9, uncorrected t (8) = 2.13, p = 0.023) and occipital regions (ch37, uncorrected t (2) = 3.92, p = 0.031) (Fig. 6). No significant difference was found in any of the channels between the resting state and upon exposure to visual stimuli in both the frontal and occipital regions (uncorrected $p > 0.05$).

4 Discussion

Our results showed that the 'main hPod' values in adults were in an antiphase pattern, and no significant difference was observed between the hPod values during the resting state and while performing tasks in both regions of the cortex. These results conform with those of previous studies that focus on healthy adults. Previous studies have reported a similar antiphase relationship between the oxy- and deoxy-Hb oscillations in many regions of the brain in both resting and task experiments [7, 19, 20]. Our findings show that the phase differences in adults were close to an antiphase pattern (hPod values around π), regardless of the presence or absence of tasks and stimuli.

The dynamic changes in the hPod followed a stable antiphase pattern, and no significant difference was observed between the hPod values in both resting and task experiments in most regions of the cortex. However, the hPod values between the resting state and WM tasks during the 'activation period' were statistically different in the two measurement channels (ch 9 and ch 37), while multiple comparisons were not corrected. Previous studies report activation of the prefrontal cortex (PFC), a cortical region related to the cognitive function, during WM tasks [16, 21]. In functional studies, brain activation during task performance or upon exposure to stimuli induced phase lag differences in the deoxy-Hb signal (from 0 to π) [22, 23]. The phase lag of Hb signals during the cortical activation could affect the hPod values during the WM tasks and lead to larger hPod values.

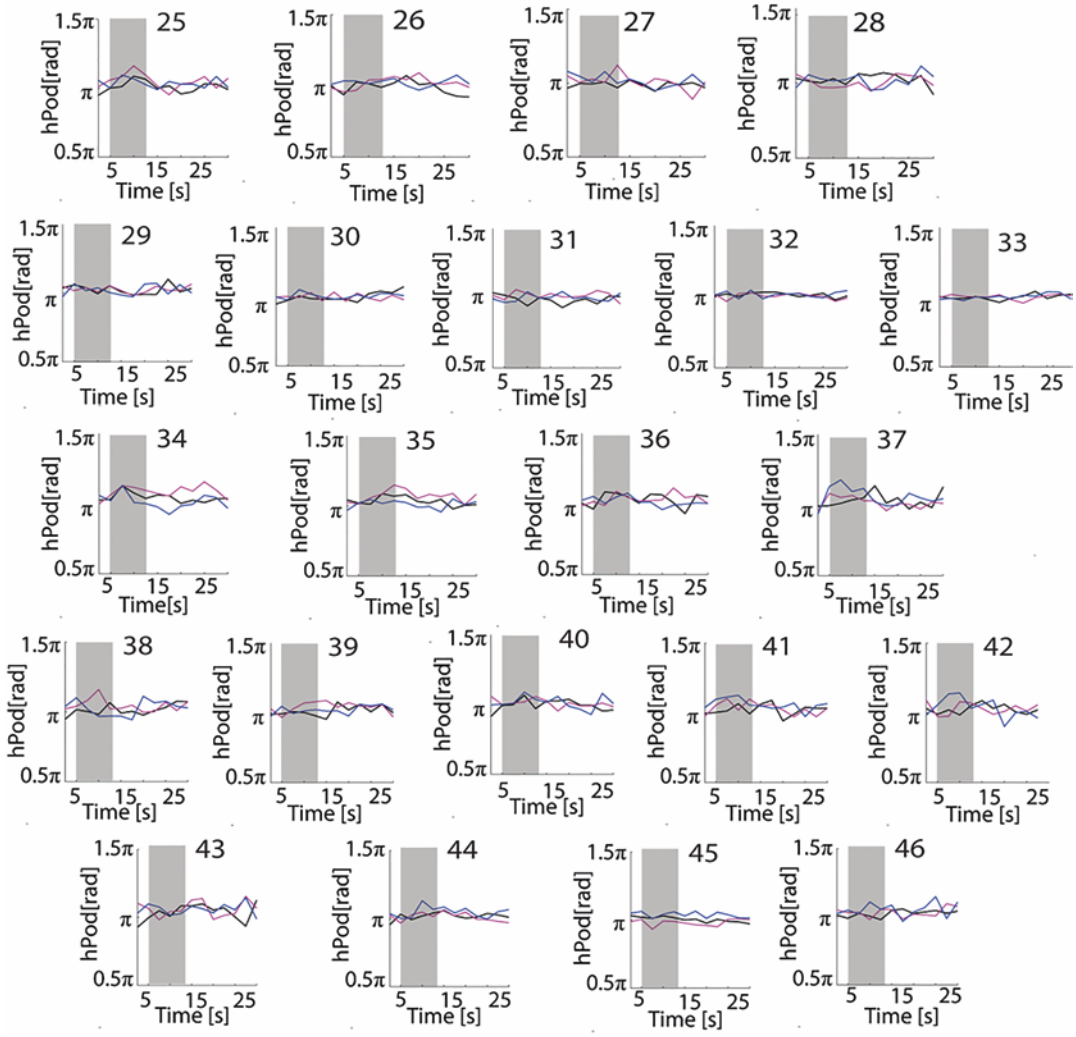

Fig. 5 Dynamic hPod in the occipital area
Black, blue, and magenta lines indicate the vector representations of averaged hPod values during the resting state, verbal working memory task, and visual stimuli across participants, respectively. The grey vertical areas indicate the onset of the target and probe, respectively

However, there are some limitations that should be addressed. First, in this study, the number of datasets was relatively small, which might have resulted in statistical insignificance after multiple comparison corrections. In future studies, more subjects from a wider age range and health conditions, healthy elderly subjects, and participants with psychiatric disorders should be recruited. This is because the hPod index has the potential to be used as an indicator to detect brain aging processes in older adults and early detection of higher brain dysfunction in unhealthy subjects [24].

In addition, to determine hPod, the NIRS data were band pass filtered (0.02–0.8 Hz). Hence, the resulting signal might contain sources of spontaneous low-frequency oscillations, including the Mayer wave (0.1 Hz). The Mayer waves can mask the cortical haemodynamic responses associated with the neural activity of interest and should be removed in normal functional studies [25]. However, [26] showed systemic low-fre-

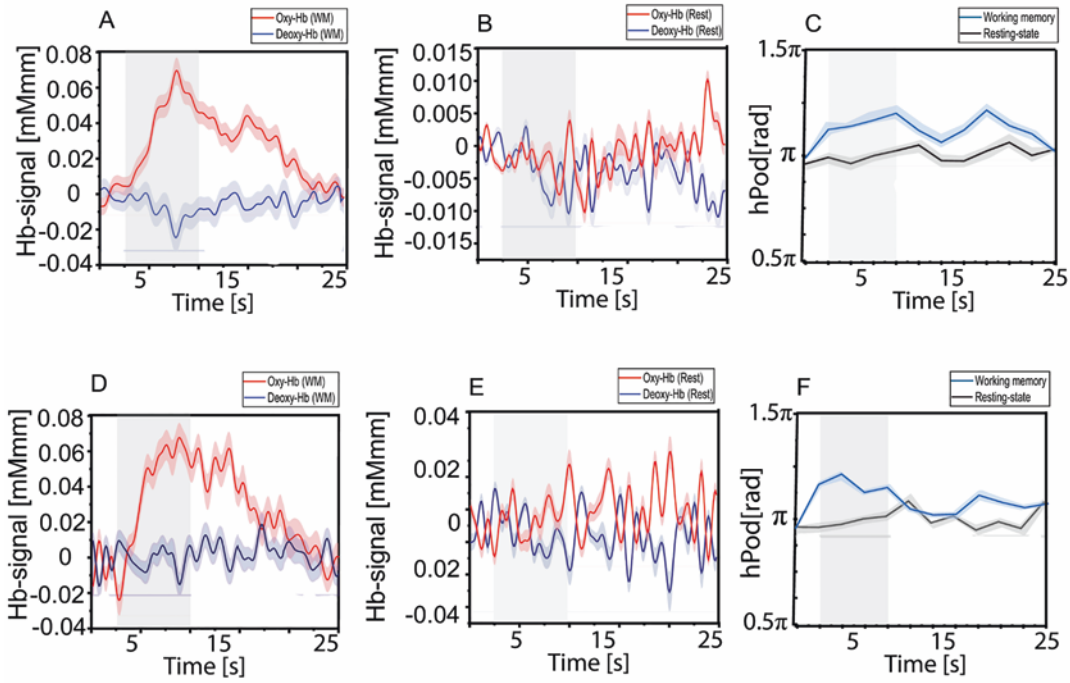

Fig. 6 (**a, b, d, e**) Time courses for the Hb-signal changes. (**c, f**) Dynamic hPod values between the resting state and WM tasks for the representative channels with statistical significance ch 9 and ch 37, uncorrected $p < 0.05$). These time courses represent the grand average with shadow areas showing standard errors across participants. The two grey vertical areas indicate the onsets of the Target and the Probe, respectively

quency oscillation effects on resting state networks of the brain without clarifying the relationship between the Mayer wave and low-frequency component of haemoglobin signals. In a previous study on haemoglobin phase of oxygenation and deoxygenation (hPod), Mayer wave components were included in the data analysis [10]. Therefore, we did not remove the Mayer wave component in this study. For the future perspective, it will be necessary to separate the Mayer wave component and examine the effects of the Mayer wave on the hPod.

As reported previously, the phase differences between haemoglobin signals in the cerebral cortex reflect the neurovascular coupling mechanism, which is related to cerebral blood flow and blood oxygenation [27, 28]. Thus, factors that contribute to the antiphase pattern of the hPod in adults related to physiological changes should be investigated thoroughly using a haemodynamic model [29].

5 Conclusion

We examined the basic characteristics of adult hPod during rest and upon exposure to visual stimuli and WM task to develop a new analysis approach using fNIRS to detect more sensitive signals that reflect neural activation. Our results showed that the 'main hPod' (i.e., average hPod values during the entire measurement period) ranged between π and 1.5π rad in all conditions, which were generally close to a stable antiphase pattern (i.e., hPod values of approximately π), regardless of the presence or absence of tasks and stimuli. However, 'dynamic hPod' showed significant changes during the activation period of the WM task, compared to the resting state in the frontal and occipital regions. These results suggest that the analysis of dynamic hPod changes is useful to detect subtle neural activation during cognitive tasks.

Acknowledgments We thank Drs. Gentaro Taga, Fumitaka Homae, Yunjie Tong, and Liang Zhenhu for their technical instruction and discussion. This work was supported, in part, by the Precise Measurement Technology Promotion Foundation and KAKENHI (20K11367).

References

1. Scholkmann F, Kleiser S, Metz AJ, Zimmermann R, Mata Pavia J, Wolf U, Wolf M (2014) A review on continuous wave functional near-infrared spectroscopy and imaging instrumentation and methodology. NeuroImage 85(Pt 1):6–27
2. Koizumi H, Yamamoto T, Maki A, Yamashita Y, Sato H, Kawaguchi H, Ichikawa H (2003) Optical topography: practical problems and new applications. Appl Opt 42:3054–3062
3. Obrig H, Villinger A (2003) Beyond the visible-imaging the human brain with light. J Cereb Blood Flow Metab 23(1):1–18
4. Pierro ML, Sassaroli A, Bergheton PR, Ehrenberg BL, Fantini S (2012) Phase-amplitude investigation of spontaneous low-frequency oscillations of cerebral hemodynamics with near-infrared spectroscopy: a sleep study in human subjects. NeuroImage 63:1571–1584
5. Fantini S (2012) A haemodynamic model for the physiological interpretation of in vivo measurements of the concentration and oxygen saturation of haemoglobin. Phys Med Biol 47:N249–N257
6. Liang Z, Minagawa Y, Yang HC et al (2018) Symbolic time series analysis of fNIRS signals in brain development assessment. J Neural Eng 15(6):066013. https://doi.org/10.1088/1741-2552/aae0c9. PMID: 30207540; PMCID: PMC6239960
7. Watanabe H, Shitara Y, Aoki Y et al (2017) Hemoglobin phase of oxygenation and deoxygenation in early brain development measured using fNIRS. Proc Natl Acad Sci E1737–E1744:7–1
8. Taga G, Watanabe H, Homae F (2018) Developmental changes in cortical sensory processing during wakefulness and sleep. NeuroImage 178:519–530
9. Issard C, Gervain J (2018) Variability of the hemodynamic response in infants: influence of experimental design and stimulus complexity. Dev Cogn Neurosci 33:182–193. https://doi.org/10.1016/j.dcn.2018.01.009
10. Taga G, Watanabe H, Homae F (2017) Spatial variation in the hemoglobin phase of oxygenation and deoxygenation in the developing cortex of infants. Neurophotonics 5(1):1–7
11. Yoshino K, Kato T (2012) Vector-based phase classifications of initial dips during word listening using near-infrared spectroscopy. Neuroreport 23(16):947–951
12. Taga G, Watanabe H, Homae F (2011) Spatiotemporal properties of cortical haemodynamic response to auditory stimuli in sleeping infants revealed by multi-channel near-infrared spectroscopy. Philos Trans R Soc A 369(1995):4495–4511
13. Pierro M, Sassaroli A, Zheng F, Fantini S (2011) Phase characterization of oscillatory components of the cerebral concentrations of oxy-hemoglobin and deoxy-hemoglobin. Optical Tomography and Spectroscopy of Tissue IX, Proc. SPIE 7896. https://doi.org/10.1117/12.875010
14. Oldfield RC (1971) The assessment and analysis of handedness: the Edinburgh inventory. Neuropsychologia 9(1):97–113
15. Singh AK, Okamoto M, Dan H, Jurcak V, Dan I (2005) Spatial registration of multichannel multi-subject fNIRS data to MNI space without MRI. Neuroimage 27(4):842–851
16. Aoki R (2013) Correlation between prefrontal cortex activity during working memory tasks and natural mood independent of personality effects: an optical topography study. Phys Res Neuroimaging 212:79–87
17. Hohberger B, Kremers J, Horn FK (2019) Steady-state visually evoked potentials elicited by multifrequency pattern-reversal stimulation. Trans Vis Sci Technol 8(1):1–3 4–13
18. Sutoko S, Sato H, Maki A, Kiguchi M, Hirabayashi Y, Atsumori H, Obata A, Funane T, Katura T (2016) Tutorial on platform for optical topography analysis tools. Neurophoton 3:1. https://doi.org/10.1117/1.NPh.3.1.010801
19. Lloyd-Fox S, Begus K, Halliday D, Pirazzoli L, Blasi A, Papademetriou M, Darboe MK, Prentice AM, Johnson MH, Moore SE, Elwell CE (2017) Cortical specialisation to social stimuli from the first days to the second year of life: a rural Gambian cohort. Dev Cogn Neurosci 25:92–104. https://doi.org/10.1016/j.dcn.2016.11.005
20. Issard C, Gervain J (2017) Adult-like processing of time-compressed speech by newborns: a NIRS study. Dev Cogn Neurosci 25:176–184
21. Ogawa Y, Kotani K et al (2014) Relationship between working memory performance and neural activation measured using near-infrared spectroscopy. Brain Behav 4(4):544–551 19–8
22. Yamada T (2019) Continuous wave functional near-infrared spectroscopy: various signal components and appropriate management. J Rehabil Neurosci 19:10–19
23. Sassaroli A, Zheng F, Pierro M, Bergethon P, Fantini S (2011) Phase difference between low-frequency oscillations of cerebral deoxy- and oxy-hemoglobin concentrations during a mental task. J Innov Opt Health Sci 4(2):151–158
24. Liang Z, Tian H, Yang HC, Arimitsu T, Takahashi T, Sassaroli A, Fantini S, Niu H, Minagawa Y, Tong Y (2021) Tracking brain development from neonates to the elderly by hemoglobin phase measurement using functional near-infrared spectroscopy. IEEE J Biomed Health Inform 25(7):2497–2509. https://doi.org/10.1109/JBHI.2021.3053900. Epub 2021 July 28. PMID: 33493123

25. Luke R, Shader, MJ. McAlpine D (2021) Characterization of Mayer-wave oscillations in functional near infrared spectroscopy using a physiologically informed model of the neural power spectra. Neurophotonics, 8(4), 041001
26. TongY, Hocke LM, Nickerson LD, Licata SC, Lindsey KP, Frederick BD (2013) Evaluating the effects of systemic low frequency oscillations measured in the periphery on the independent component analysis results of resting state networks. Neuroimage, 76, 202–215
27. Fantini S (2002) A haemodynamic model for the physiological interpretation of in vivo measurements of the concentration and oxygen saturation of hemoglobin. Phys Med Biol 47(18):N249–N257
28. Mayhew J et al (2000) Spectroscopic analysis of neural activity in brain: increased oxygen consumption following activation of barrel cortex. NeuroImage 12(6):664–675
29. Kainerstorfer J, Sassaroli A, Hallacoglu B, Pierro M, Fantini S (2014) Practical steps for applying a new dynamic model to near-infrared spectroscopy measurements of hemodynamic oscillations and transient changes: implications for cerebrovascular and functional brain studies. Acad Radiol 21(2):185–196

Development and Validation of Robust and Cost-Effective Liquid Heterogeneous Phantom for Time Domain Near-Infrared Optical Tomography

A. Kalyanov, J. Jiang, E. Russomanno, M. Ackermann, A. Di Costanzo Mata, R. Mindel, L. Miller, and M. Wolf

Abstract

Diffused light imaging techniques, such as near-infrared optical tomography (NIROT), require a stable platform for testing and validation that imitates tissue optical properties. The aim of this work was to build a robust, but flexible liquid phantom for BORL time-domain NIROT system Pioneer. The phantom was designed to assess penetration depth and resolution of the system, and to provide a heterogeneous inner structure that can be changed in controllable manner with adjustable optical properties. We used only in-house produced 3D-printed elements and mechanics of a budget 3D-printer to build the phantom, and managed to keep the overall costs below $500. We achieved stable and repeatable movement of an arbitrary structure in 3+1 degree of freedom inside the phantom and demonstrated its performance in a series of tests. Thus, we presented a universal and cost-effective solution for testing NIROT, that can be easily customised to various systems or testing paradigms.

Keywords

NIROT · Diffused light imaging · NIRS · Optical properties

1 Introduction

Developing an imaging technique based on diffused light, i.e., near-infrared optical tomography (NIROT), requires a robust setup for testing and validation. Before clinical application in vivo, the optical imaging techniques need to be tested and validated in tissue phantoms that imitate tissue properties, e.g., optical properties and structure. Several technologies were used to build such phantoms, which can be roughly categorised as solid [1] and liquid phantom [2, 3].

One of the strongest advantages of solid phantoms is the temporal stability and arbitrary shape. They also enable complex internal structures. These phantoms can be built from gelatin or agar [4], resin [5–7], or silicone [8]. At the same time, the temporal stability is the drawback when a

A. Kalyanov (✉) · J. Jiang · M. Ackermann · A. Di Costanzo Mata · R. Mindel · L. Miller · M. Wolf
BORL, Neonatology, University of Zurich and University Hospital Zurich, Zürich, Switzerland
e-mail: alexander.kalyanov@uzh.ch

E. Russomanno
BORL, Neonatology, University of Zurich and University Hospital Zurich, Zürich, Switzerland

D-ITET, ETH Zurich, Zürich, Switzerland

F. Scholkmann et al. (eds.), *Oxygen Transport to Tissue XLIII*, Advances in Experimental Medicine and Biology 1395, https://doi.org/10.1007/978-3-031-14190-4_33

specific dynamic is required. Therefore, several liquid phantoms were constructed to simulate changes in optical properties [2, 3], or to create dynamic internal structure [5].

The aim of this work was to build a robust but flexible liquid phantom for our time domain NIROT Pioneer [9, 10]. The phantom was designed to serve for system validation and characterisation, including penetration depth and resolution. It provided a heterogeneous inner structure that can be changed in a controllable manner with adjustable optical properties and to achieve high stability in time.

2 Method

We based our design on a previously presented **liquid phantom** developed in our laboratory [2, 3]. The design included a rectangular liquid container with silicone windows on two sides for optical sensors. The container was placed on a heat plate with a magnetic stirrer to keep the liquid homogeneous. Internal heterogeneities, i.e., inclusions of arbitrary shape were inserted and moved to defined locations by means of 3+1D movement mechanism, adopted from a 3D printer. The inclusion holder enters the container from the top. This design enables the use of various liquids with added inks as a bulk, and inclusion of any water resistant material as heterogeneous objects. Silicone windows may have various optical properties. Very thin windows have no influence on the readings; conversely thick windows act as a layer of tissue.

We produced the **container** in-house using the 3D printer Ultimaker 2 (Ultimaker, Denmark). The size of the container was 22×22 cm^2 in area and 25 cm in height. The inner volume was ~3 l. We printed the container with polyethylene terephthalate glycol (PETG) black filament, 100% infill, 0.8 mm nozzle size. This material was shown to be water resistant with excellent layer to layer adhesion. In contrast to acrylonitrile butadiene styrene (ABS), PETG prints have very few holes between layers, and the 100% infill ensured water tightness. The CAD model and a photo of the actual container are shown in Fig. 1.

We used two windows of different geometry. Up to four windows of any shape could be implemented. Here, we employed one rectangular window fit for a frequency domain (FD) near-infrared spectroscopy (NIRS) device (Imagent, ISS, USA, self-calibrating probe), which served as reference. The circular window was used to access the phantom with the TD NIROT Pioneer.

We produced **silicone windows** with specified optical properties according to a previously developed recipe [8]. We used Elastosil Vario40 (Wacker, Germany) instead of Silpuran 2420 (Wacker, Germany), because the latter is too soft for this task. Otherwise the same inks (White 9010 and carbon black powder) were applied. We produced a set of circular and rectangular windows and a complete bulk reference phantom from one mixture of silicone. The reference phantom was measured to obtain the achieved optical properties. The spectrum of the window employed in this study is shown in Fig. 2. The CAD of the mold for the circular window, and the window itself are shown in Fig. 1c, d. We achieved 1.5 mm thickness of the window. The geometry of the mold enabled us to align the window surface with the inner surface of the container.

The **moving stage** for inclusions inside the liquid phantom was based on an affordable 3D printer (Creality Ender 3, China). The printer had a metal frame, with moving parts riding along rails. We modified the frame to be able to move the whole inclusion holder in XYZ-axis, while the liquid phantom container stayed motionless. We achieved this by attaching the printing head frame to the building plate. We placed the liquid container in front of the moving mechanism. We attached the inclusion holder to the printing head (Fig. 3a). It was located over the container and enabled inclusion positioning in a range [−15, 15] mm in XY-axis, and [1.5 70] mm in depth. The XYZ movement was implemented with dedicated motors of the 3D printer and controlled through the printer logic. These axes required minimum modification in the firmware, since their coordinates were in millimeters. We implemented software stops to prevent the holder crashing into container walls.

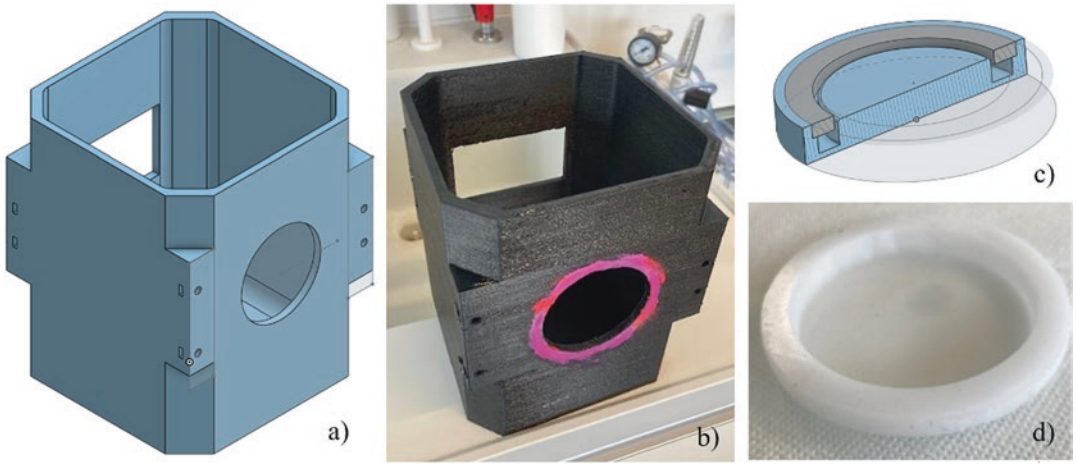

Fig. 1 Liquid phantom container: CAD (**a**) and photo (**b**) of phantom. CAD of the mold (**c**) and a photo of the circular window (**d**)

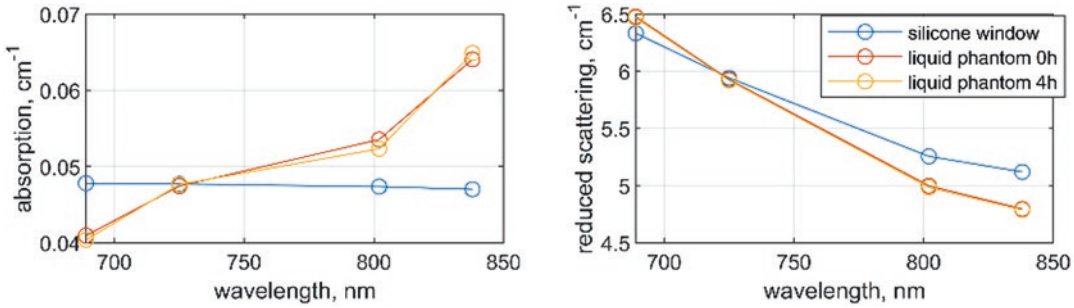

Fig. 2 Optical properties of the silicone window used in this study (blue), and liquid phantom right after preparing the mixture in the phantom container (red) and the same mixture after 4 h at a room temperature (yellow)

We also implemented two **inclusion holders** with adjustable distance between them (Fig. 3b). An extruder motor controlled the distance. We also used an additional threaded rod in pair with the motor. This movement required us to implement conversion and scaling of the target coordinates (in mm) to the units that the extruder motor channel of the firmware needs. The inclusion holder was made as a half-frame (Fig. 3c). We placed inclusions on a fishing line in the center of the frame's height, and as close to the front as possible. We used a sewing needle to put the rope through a silicone inclusion. The friction was high enough to hold the inclusion in place without additional fixation. The rope was attached to the top and the bottom part of the frame and tightened.

We tested **precision and repeatability** of an inclusion's movement in dry conditions, outside of the container. We placed a graph paper with 1 mm grid behind the inclusion holder, and made marks on the ropes to indicate the position. We used a digital camera to capture the actual position of the holder during movement and compared it to the graph paper. The XY- and YZ- axis movements were performed in random pattern and repeated 3 times. The E-axis (distance between 2 inclusions) movement was performed in monotonic manner, but in both directions: i.e., inclusions moving away from each other, and moving closer to each other. We repeated this cycle 3 times.

The **liquid phantom** included 3 l distilled water, 90 ml Intralipid® to achieve the desired scattering (μ_s') and ~4 ml of diluted Indian Ink

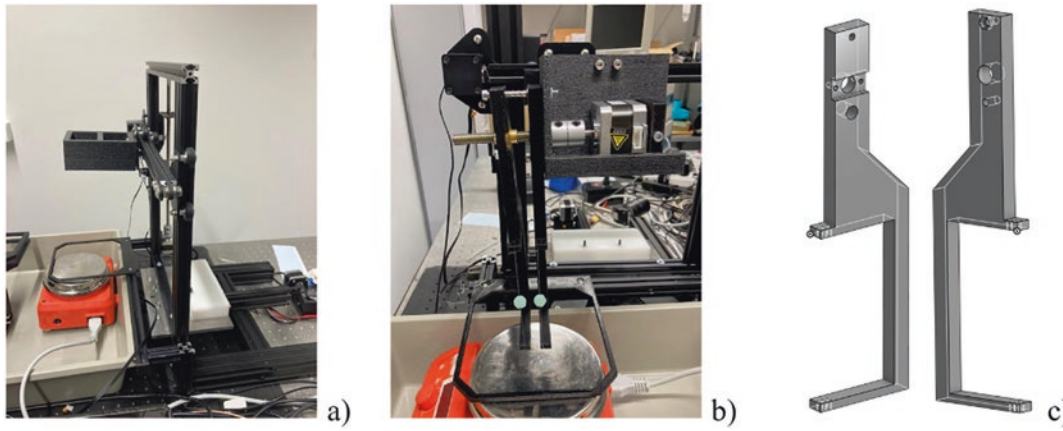

Fig. 3 Moving stage without inclusion holder seen from the side (**a**), the same stage with the holder and 2 inclusions, front view (**b**), and the CAD of the left and right holders (**c**)

(1:20 Indian Ink to water) to reach a certain absorption (μ_a). We controlled the optical properties of the liquid in real time by means of the reference NIRS measurement. The mixture was constantly mixed by a magnetic stirrer. The optical properties are shown in Fig. 2. Here we aimed at matching the optical properties of the liquid to the ones of the silicone window at 725 nm: μ_a = 0.048 cm^{-1}, μ_s' = 5.9 cm^{-1}. However, the water absorption feature became prominent at long wavelengths and must be taken into account.

We were able to keep both scattering and absorption stable over time and to change them over a wide range. Additionally, it is possible to add blood to the liquid phase of the phantom, which enables oxygenation-deoxygenation cycles to be performed.

3 Results

We measured the precision and repeatability of the movement of the inclusion. The results are shown in Fig. 4a, b. We discovered only little offset in XY positioning, less then 0.5 mm. In YZ positions the offset was higher, but still within 1 mm. We expected this high precision in these 3 axes, because the original 3D-printer design was very little modified. The offset of the E-axis reached 2 mm. However, it was repeatable (Fig. 4c). Thus, a simple linear correction can be applied.

We performed a NIROT measurement of a single inclusion. The inclusion had 10 mm diameter, 7× absorption contrast. It was placed 15 mm deep, in the center of the field of view. We successfully reconstructed this inclusion in the expected location (Fig. 5).

4 Discussion and Conclusion

We presented a liquid phantom with movable internal heterogeneity. We believe that this phantom cannot only be used as a universal platform for testing NIROT systems, but also for functional NIRS devices. It enables a wide range of inclusion locations, placement of multiple inclusions, as well as changeable distance between two inclusions. We confirmed its stability in time thanks to constant mixing of the liquid by means of the magnetic stirrer. The setup was also equipped with a heat plate to keep the liquid at a specified temperature.

The overall concept of the phantom is intuitive and simple. We consider our solution as only one of many options. However, we found it nontrivial to find affordable components to build such system. We managed to stay within a $500 budget (without the price of 3D printed components and the heater with magnetic stirrer). We believe the affordability makes our concept very attractive.

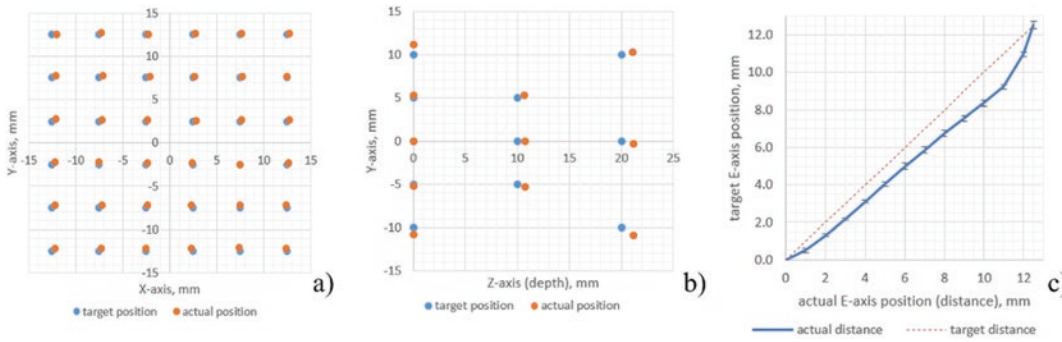

Fig. 4 Comparison of target and actual position of inclusion in cross (**a**) and longitudinal section (**b**). Average distance between two inclusions (**c**)

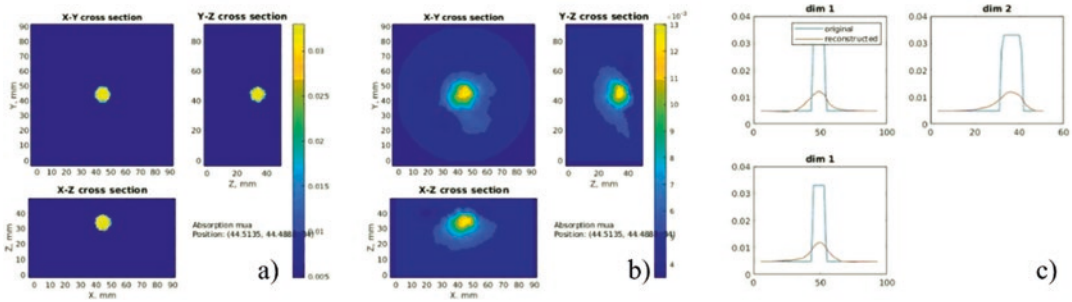

Fig. 5 NIROT imaging of a single inclusion inside the liquid phantom. Expected location of the inclusion (**a**) shown as distribution of absorption coefficient, and the reconstructed tomogramm cross sections (**b**) and 1D distribution (**c**). All axes are in mm, absorption coefficients are in mm^{-1}

We highlight that the most problematic element of the movement stage is the E-axis, since the donor 3D printer lacks the 4th axis mechanics. We 3D-printed several plastic elements to fix the motor and the gear, and to enable the movement of the inclusion holders (see Fig. 3b, c), but we report a lack of precision in manufacturing, and also a lack of stability of plastic elements. We expect that the precision and stability of E-axis movement can be significantly increased by producing these parts out of metal in an appropriate workshop. We propose to use the phantom with human blood to mimic tissue oxygenation. It is equipped with a temperature control and a mixing unit that are definitely required for the blood/water solution. One drawback of the current design is that we cannot introduce a lid, thus we expect significant heat loss, which may limit the functionality. In addition, for deoxygenation experiments, there may be a problem that oxygen diffuses into the phantom.

To conclude, in this work we presented a robust and cost-effective solution for a flexible liquid phantom, that can be used for testing diffuse optical imaging systems, such as NIROT. The demonstrated design can easily be customised in a lab equipped with a workshop and a 3D-printer. We demonstrated performance of the phantom in a series of experiments. We confirmed that the system is applicable for a wide range of tasks. We hope that our experience will be useful for many research groups all around the globe.

Acknowledgments We gratefully acknowledge funding by the Swiss National Science Foundation (159490 and 197079), the Innovationspool of the University Hospital Zurich; Consejo Nacional de Ciencia y Tecnología CONACyT (CVU-627802). AK declares that he is part-time employee by OxyPrem AG as conflict of interest. MW declares that he is president of the board and co-founder of OxyPrem AG as conflict of interest.

References

1. Jiang J, Lindner S, Di Costanzo-Mata A et al (2021) In phantom validation of time-domain near-infrared optical tomography pioneer for imaging brain hypoxia and hemorrhage. Adv Exp Med Biol 1269:341–346
2. Kleiser S, Ostojic D, Andresen B et al (2018) Comparison of tissue oximeters on a liquid phantom with adjustable optical properties: an extension. Biomed Opt Express 9:86–101
3. Kleiser S, Nasseri N, Andresen B et al (2016) Comparison of tissue oximeters on a liquid phantom with adjustable optical properties. Biomed Opt Express 7:2973–2992
4. Cubeddu R, Pifferi A, Taroni P et al (1997) A solid tissue phantom for photon migration studies. Phys Med Biol 42:1971–1979
5. Pifferi A, Torricelli A, Cubeddu R et al (2015) Mechanically switchable solid inhomogeneous phantom for performance tests in diffuse imaging and spectroscopy. J Biomed Opt 20:121304
6. Wabnitz H, Jelzow A, Mazurenka M et al (2014) Performance assessment of time-domain optical brain imagers, part 2: nEUROPt protocol. J Biomed Opt 19:086012
7. Pifferi A, Torricelli A, Bassi A et al (2005) Performance assessment of photon migration instruments: the MEDPHOT protocol. Appl Opt 44:2104–2114
8. Tomm N, Ahnen L, Isler H et al (2019) Characterization of the optical properties of color pastes for the design of optical phantoms mimicking biological tissue. J Biophotonics 12:e201800300
9. Jiang JJ, Mata AD, Lindner S et al (2020) Image reconstruction for novel time domain near infrared optical tomography: towards clinical applications. Biomed Opt Express 11:4723–4734
10. Jiang J, Mata ADC, Lindner S et al (2020) Dynamic time domain near-infrared optical tomography based on a SPAD camera. Biomed Opt Express 11:5470–5477

Effect of Exercise Therapy on Stress Response Evaluated by IoMT Monitoring System

Masamichi Moriya, L. Hu, Shin'ichi Warisawa, and Kaoru Sakatani

Abstract

The Internet of Medical Things (IoMT) system plays a role in various areas of social activity, including healthcare. Telemetry of cardiovascular function, such as blood pressure and pulse, in daily life is useful in the treatment of cardiovascular disease and stress management. However, until now, brain function monitoring technology has not been installed in the IoMT system.

In this study, we used near-infrared spectroscopy (NIRS) installed in the IoMT system to evaluate whether consumers who are not medical experts can measure their own brain function correctly. In addition, the IoMT system was used to assess the long-term effects of physical exercise on physical and mental health.

We studied a total of 119 healthy adults recruited from a fitness gym in Koriyama, Japan. After receiving instruction in the usage of the IoMT monitoring system including NIRS, the subjects monitored their physical and mental conditions by themselves when they visited the gym. We evaluated the relations between blood pressure (BP), pulse rate (PR), body weight (BW) and age. In addition, we evaluated the left/right asymmetry of the prefrontal cortex (PFC) at rest and BP. We calculated the laterality index at rest (LIR) for assessment of left/right asymmetry of PFC activity; a positive LIR (>0) indicates right-dominant PFC activity associated with higher stress responses, while a negative LIR (<0) indicates left-dominant PFC activity associated with lower stress responses. We studied 47 out of 119 cases who monitored their physiological conditions before and after physical exercise for 6 months for this study.

The results showed that the systolic blood pressure and mean blood pressure ($p < 0.05$) were significantly reduced after the physical exercise for 6 months; body weight did not change significantly ($p > 0.05$). In addition, NIRS demonstrated that LIR changed to plus values from minus values after exercise ($p < 0.01$).

These results show that (1) consumers who are not-medical experts can measure their own brain function correctly using NIRS; (2) after

M. Moriya (✉)
Department of Physical Therapy, Faculty of Health Care and Medical Sports, Teikyo Heisei University, Tokyo, Japan

Department of Human and Engineered Environmental Studies, Graduate School of Frontier Sciences, The University of Tokyo, Tokyo, Japan
e-mail: m.moriya@edu.k.u-tokyo.ac.jp

L. Hu · S. Warisawa · K. Sakatani
Department of Human and Engineered Environmental Studies, Graduate School of Frontier Sciences, The University of Tokyo, Tokyo, Japan

F. Scholkmann et al. (eds.), *Oxygen Transport to Tissue XLIII*, Advances in Experimental Medicine and Biology 1395, https://doi.org/10.1007/978-3-031-14190-4_34

long-term physical exercise, systemic blood pressure decreased, associated with modulation of PFC activity (i.e., from right-dominant PFC activity to left-dominant activity), indicating that long-term physical exercises caused relaxation in the brain and the autonomic nervous system.

Keywords

Internet of Medical Things system · Telemetry · NIRS · Brain function

1 Introduction

The Internet of Medical Things (IoMT) system is believed to be the next revolutionary technology and bring great benefits to various domains of society including healthcare [1]. The IoMT system has gained increasing attention due to the development of solutions for tele-monitoring [2] and tele-treatment [3]; support older adults to work on their functional status by exercising independently but remotely supervised by professionals when needed. Furthermore, the need for IoT is increasing due to the COVID-19 pandemic, and many reports have been made in a short period of time [4–6]. There is a possibility that advanced information technologies, including the Internet of Things (IoT), will be applied to healthcare.

In our previous study, we developed the IoT-based health monitoring system, which allows for the long-term measurement of blood pressure (BP), pulse rate (PR), body weight (BW), and even mental stress measured from prefrontal cortex (PFC) activity using a wearable near-infrared spectroscopy (NIRS) device [7]. In the pilot study, we observed that the IoT monitoring system, which was set up in a local fitness gym, allowed non-medical persons (members of the gym) to measure physical and mental health conditions by themselves. In IoMT studies, stress evaluations using electrocardiogram (ECG) signals have been reported [8], but there are no studies in which non-medical personnel measure brain activity and check stress on their own.

Here, we report on the large longitudinal cohort study employing the IoMT monitoring system. The purpose of this study is to investigate the effect of IoMT introduction on the physical and mental health conditions of exercise.

2 Methods

2.1 Subjects and Study Protocol

We studied 119 volunteers (average age 69.0 ± 7.5 years old); the mean BW was 56.3 ± 9.2 kg, while BMI was 22.9 ± 3.1. All subjects were recruited from the local fitness gym, which is attached to the Koriyama Health Promotion Foundation. Subjects were non-medical persons. The subjects provided written informed consent as required by the Human Subjects Committee in the gym.

The IoMT health monitoring system was set up in the fitness gym. The protocol is that, after instruction on how to use the IoMT system, the subjects were asked to monitor their physiological conditions by themselves when they visited the fitness gym. The participants were requested to sit in front of a tablet PC placed on a table where the on-screen instructions and measurement items are presented. Following the instructions displayed on the screen, the subjects were firstly asked to scan their membership card with identification barcode, and then to measure PFC activity at rest using a NIRS device for 1 min, followed by measurements of their BP, PR, and BW.

2.2 System Design

We employed the IoMT-based healthcare monitoring system, which allows long-term measurements of BP, PR and BW, as well as NIRS measurements of PFC activity [7]. Briefly, the system is composed of a tablet-based data receiver collecting physical and mental data using several kinds of medical instruments and

a remote control system used to store and analyse the data collected from the tablet. The objective health measurements include BP and PR using a sphygmomanometer (TM-2657, A&D Corp., Japan), and BW using an electronic scale (AD-6209PBT-C, A&D Corp., Japan). In addition, we measured PFC activity using a wearable NIRS (HOT-1000, Hitachi High-Technologies Corporation, Japan). The HOT-1000 is a two-channel NIRS, which uses a single LED (800 nm) for measurements of total haemoglobin (t-Hb) concentration changes [9]. These devices have a Bluetooth communication function so that the measured data can be transported to the tablet receiver automatically. After being collected in the receiver, the data can be sent to the remote Amazon's AWS Cloud system at the end of each measurement session. We analysed the collected data at a remote University of Tokyo graduate school.

2.3 Data Processing

We compared 47 out of 119 cases who monitored their BP (systolic blood pressure; SBP, diastolic blood pressure; DBP, mean blood pressure; MBP), PR, BW, and LIR before and after physical exercise for 6 months. In addition, we evaluated the relation between BP and the left/right asymmetry of the PFC activity at rest; the left/right asymmetry was assessed by calculating the LIR as follows:

$$\mathrm{LIR} = \frac{\sum t\left\{\begin{matrix}\left(\Delta\mathrm{oxyRt} - \Delta\mathrm{oxyRmin}\right) \\ -\left(\Delta\mathrm{oxyLt} - \Delta\mathrm{oxyLmin}\right)\end{matrix}\right\}}{\sum t\left\{\begin{matrix}\left(\Delta\mathrm{oxyRt} - \Delta\mathrm{oxyRmin}\right) \\ +\left(\Delta\mathrm{oxyLt} - \Delta\mathrm{oxyLmin}\right)\end{matrix}\right\}}$$

The index defined by the above equation provides values in the range of [−1, +1]. LIR>0 indicates the right dominant activity, while LIR<0 indicates the left dominant activity. Previous studies demonstrated that LIR>0 is associated with high-stress responses, while LIR<0 is associated with low-stress responses [10, 11].

3 Results

We studied 47 out of 119 non-medical individuals who were able to monitor the physiological status of exercise for 6 months (Table 1). Other subjects (72 cases) are still measuring. We found that the systolic blood pressure, mean blood pressure ($p < 0.05$) and diastolic blood pressure ($p < 0.01$) were significantly reduced after the physical exercise for 6 months; body weight did not change significantly ($p > 0.05$). In addition, NIRS demonstrated that LIR changed to minus values (left-dominant with low-stress responses) from plus values (right-dominant with high-stress responses) after exercise ($p < 0.01$).

There was a statistically significant positive correlation but weak between LIR and SBP ($r = 0.1$, $p < 0.01$), LIR and MBP ($r = 0.1$, $p < 0.05$) (Fig. 1). It is shown that the more right-dominant the PFC activity at rest is, the higher the BP is.

4 Discussion

The present study is an implementation research evaluating the usefulness of the IoT-based health monitoring system. We observed that the subjects could monitor their physiological and mental conditions by themselves for long periods using the IoT monitoring system. By analysis of the data, we found that the SBP, MBP ($p < 0.05$), DBP and PR ($p < 0.01$) were significantly reduced after physical exercise for 6 months. In our previous study, we observed gradual decreases in BP in a number of subjects, suggesting positive effects of fitness on health conditions. It suggests that the physical activities on the gym affect positively on the reduction of their BP and on promoting their health; this is consistent with the reported study on the effect of exercise on hypertension [12]. In addition, LIR turned into minus values after 6 months, suggesting that exercise reduces stress. A meta-analysis of previous data suggest that exercise is effective in improving anxiety symptoms in people with a current diagnosis of anxiety and/or stress-related disorders [13].

Table 1 Comparison before and after physical exercise

	Before	After 6 months	p-value
SBP (mmHg)	118.7 ± 14.4	114.7 ± 16.14.	$p<0.05$
DBP (mmHg)	70.2 ± 8.8	67.2 ± 9.0	$p<0.01$
MBP (mmHg)	92.2 ± 10.1	88.7 ± 12.8	$p<0.05$
PR (bpm)	80.1 ± 13.3	78.7 ± 12.6	$p<0.01$
BW (kg)	55.1 ± 9.6	55.0 ± 9.7	n.s.
LIR	0.07 ± 0.3	-0.13 ± 0.3	n.s.

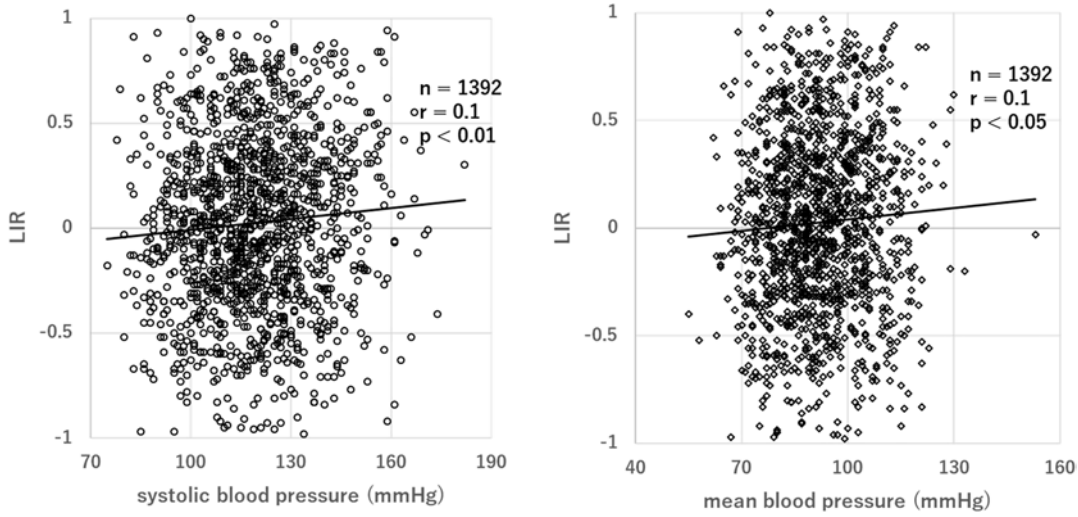

Fig. 1 Correlation between LIR and SBP, LIR and MBP

Interestingly, SBP and MBP positively correlated with LIR. This is consistent with the reported NIRS studies; the right PFC activity predominantly modulates sympathetic activities while the left PFC activity predominantly modulates parasympathetic activities [14–17]. This result should be emphasised given that the present study is the first research into laypersons' implementation of brain functional monitoring by NIRS. The subjects put the NIRS probes on the forehead by themselves according to the instruction on the PC screen. Nevertheless, there was a significant positive correlation between LIR and BP. These observations suggest that non-medical personnel can use NIRS to monitor brain function and manage brain health by themselves. However, the present study did not investigate whether non-medical personnel were able to wear NIRS correctly, and this may be one of the reasons for the weak correlation. Because we evaluated long-term effects of physical exercise on the physical and mental health conditions, it remains to be addressed: (1) What exercises are more effective, and (2) Does exercise time and frequency affect outcomes. These questions are beyond the scope of this study and it is expected that these questions would be addressed as the IoMT system is continued.

The present study suggests that the IoT-based health monitoring system is useful for healthcare outside the medical facility, and resolves the shortage of medical staff in developed and developing countries. Furthermore, various efforts are underway to reduce contact due to the influence of COVID-19 [18, 19]. This IoMT system also has significant implications from the perspective of reducing contact opportunities.

Finally, this study includes data measurement by the subject her/himself and remote analysis. We are preparing to build a system that feeds back the analysed data to the subject.

Acknowledgments Part of the present study was supported by the Koriyama Health Promotion Foundation and Xebio Cooperation in Japan. We gratefully acknowledge funding by the Furukawa Medical & Welfare Foundation.

References

1. Gubbi J, Buyya R, Marusic S et al (2013) Internet of Things (IoT): a vision, architectural elements, and future directions. Future Gen Comput Syst 29:1645–1660
2. De Luca R, Bramanti A, De Cola MC et al (2015) Tele-health-care in the elderly living in nursing home: the first Sicilian multimodal approach. Aging Clin Exp Res 28:753–759
3. Morone G, Paolucci T, Luziatelli S et al (2016) Wii Fit is effective in women with bone loss condition associated with balance disorders: a randomized controlled trial. Aging Clin Exp Res 28:1187–1193
4. Umair M, Cheema MA, Cheema O et al (2021) Impact of COVID-19 on IoT adoption in healthcare, smart homes, smart buildings, smart cities, transportation and industrial IoT. Sensors (Basel) 21:3838
5. Al Bassam N, Hussain SA, Qaraghuli AAI et al (2021) IoT based wearable device to monitor the signs of quarantined remote patients of COVID-19. Inform Med Unlocked 24:100588
6. Sarfraz Z, Sarfraz A, Iftikar HM et al (2021) Is COVID-19 pushing us to the Fifth Industrial Revolution (Society 5.0)? Pak J Med Sci 37:591–594
7. Ishida M, Ushioda S, Nagasawa Y et al (2020) Development of IoT-based monitoring system for healthcare: a preliminary study. Adv Exp Med Biol 1232:291–297
8. Sangaiah AK, Arumugam M, Bian GB (2020) An intelligent learning approach for improving ECG signal classification and arrhythmia analysis. Artif Intell Med 103:101788
9. Komuro Y, Sato Y, Lin L et al (2018) Reliability of wearable two channel CW-NIRS in measurements of brain function. Adv Exp Med Biol 1072:301–305
10. Davidson RJ, Jackson DC, Kalin NH (2000) Emotion, plasticity, cortex, and regulation: perspectives from affective neuroscience. Psychol Bull 126:890–909
11. Ishikawa W, Sato M, Fukuda Y et al (2014) Correlation between asymmetry of spontaneous oscillation of hemodynamic changes in the prefrontal cortex and anxiety levels: a near-infrared spectroscopy study. J Biomed Opt. 19:027005
12. Boyer JL (1970) Exercise therapy in hypertensive men. JAMA 213:131
13. Sakatani K (2012) Optical diagnosis of mental stress: review. Adv Exp Med Biol 737:89–95
14. Stubbs B, Vancampfort D, Rosenbaum S (2017) An examination of the anxiolytic effects of exercise for people with anxiety and stress-related disorders: a meta-analysis. Psychiatry Res 249:102–108
15. Tanida M, Sakatani K, Takano R (2004) Relation between asymmetry of prefrontal cortex activities and the autonomic nervous system during a mental arithmetic task: near infrared spectroscopy study. Neurosci Lett 369:69–74
16. Tanida M, Katsuyama M, Sakatani K (2007) Relation between mental stress-induced prefrontal cortex activity and skin conditions: a near-infrared spectroscopy study. Brain Res. 1184:210–216
17. Tanida M, Katsuyama M, Sakatani K (2008) Effects of fragrance administration on stress-induced prefrontal cortex activity and sebum secretion in the facial skin. Neurosci Lett. 432:157–161
18. Meier JV, Noel JA, Kaspar K (2021) Alone together: computer-mediated communication in leisure time during and after the COVID-19 pandemic. Front Psychol 12:666655
19. de Melo Ghisi GL, Xu Z, Liu X (2021) Impacts of the COVID-19 pandemic on cardiac rehabilitation delivery around the world. Glob Heart 16(1):43

Improved Optical Tissue Model for Tissue Oximetry Imaging Applications

Gennadi Saiko

Abstract

Introduction: Chronic, non-healing wounds are a growing concern in healthcare delivery. Tissue oxygenation is recognised as critical to successful wound healing. However, the quality and quantity of the information extracted by hyperspectral imaging depend on the optical tissue model. This article aims to develop a simplified and computationally efficient approach comparable in quality with the two-layer model. Methods: We have considered the epidermal layer as a 'thin-film' within the dermal layer. By considering the mismatched boundary and developing a four-flux model for light transport within the tissue, we have obtained a quasi two-layer model with a closed-form solution similar to the single-layer model. Results: We have compared the developed model with the two-layer model (reference) and the single-layer model for the broad range of physiologically relevant parameters. The thickness of the epithelium: 50, 80, and 120 μm. Melanin concentration: 1, 2, 4, 8, 16, and 32%. Blood concentration: 0.2%, 1%, and 7%. Oxygen saturation: 60%, 80%, and 99%. Our initial results show that the accuracy of the proposed quasi two-layer model significantly (by a factor of 10) outperforms the single-layer model and is in close agreement with the two-layer model. Conclusions: The proposed quasi two-layer model significantly (by the factor of 10) outperforms the single-layer model and is closely aligned with the two-layer model.

Keywords

Quasi two-layer model · Tissue optics · Turbid tissues · Skin layers · Hyperspectral imaging

1 Introduction

Chronic, non-healing wounds are a growing concern in healthcare delivery. Chronic low extremity wounds, including leg ulcers (venous and arterial), diabetic foot ulcers (DFUs), and pressure injuries (PIs), can be debilitating for the affected individual and place a massive financial burden on healthcare systems [1, 2]. Early diagnosis is an essential step in the cost-effective management of non-healing wounds. Early detection of barriers to effective wound healing permits timely interventions and changes to treatment algorithms. There are no early indicators that can predict successful wound healing despite the recognised need and focused research. Tissue oxygenation is recognised as critical to success-

G. Saiko (✉)
Swift Medical Inc, Toronto, Canada
e-mail: gennadi.saiko@swiftmedical.com

F. Scholkmann et al. (eds.), *Oxygen Transport to Tissue XLIII*, Advances in Experimental Medicine and Biology 1395, https://doi.org/10.1007/978-3-031-14190-4_35

ful wound healing. However, at present, only surrogate measures of wound oxygenation are available clinically and include arterial duplex studies, dye-based imaging modalities (angiography and fluorescence angiography), laser Doppler and transcutaneous oximetry. None of these methodologies directly measures the wound base but instead measures the oxygenation of the surrounding or distant non-wounded skin. Moreover, none of these technologies are available within the confines of the wound healing clinic, and thus access to these studies becomes a barrier in and of itself. Direct measurement of wound oxygenation and perfusion (total haemoglobin) with an affordable hand-held device would be a valuable adjunct in managing complicated chronic wounds.

Near-Infrared Spectroscopy (NIRS) and imaging are promising clinical modalities that may measure wound oxygenation and perfusion in the wound bed and peri-wound remotely and non-invasively. In particular, hyperspectral imaging can be used to assess DFU development risk [3] and the severity of peripheral arterial disease [4].

In hyperspectral/multispectral imaging, a camera captures a series of images and reconstructs the reflectance spectrum (hyperspectral imaging) or its proxy (multispectral imaging) for each pixel. Some inference about tissue chromophore concentrations can be derived from the reflectance spectrum using a particular light transport model, e.g., modified Beer-Lambert or Single Backward Scattering [5].

The quality and quantity of the extracted information depend on the optical tissue model. However, popular Beer-Lambert and modified Beer-Lambert models are empirical models. There are several shortcomings with these simple models. Firstly, they do not consider the mismatched boundary, which significantly changes light distribution in the tissue. Secondly, they do not account for the complex multi-layer morphology of the tissue. Therefore, the more accurate data, the more realistic models are required, which emulate optical tissue properties.

To overcome these deficiencies, several more realistic modes have been proposed. In [6], the authors proposed a two-layer model to estimate blood saturation, melanin content, and epidermis thickness from spectral diffuse reflectance measurements. However, due to computational complexity, the method is suitable for a single-point assessment and cannot be extended to imaging geometry. The purpose of this article is to develop a simplified approach comparable with the two-layer model, which can be used in real-time imaging.

2 Methods

The skin is a multi-layer structure. Typically, it is subdivided into three primary layers: epidermis, dermis, and subcutaneous tissue. In addition, though, each of these layers can be split into several respective sub-layers.

However, if we consider the spectrum's visible range, the light penetration depth does not exceed 2 mm, and subcutaneous tissue does not contribute much to the reflectance. In this case, we can consider the skin as a two-layer structure: the bloodless epidermis and underlying, blood-containing tissue, which has optical properties of the dermis.

2.1 One-Layer Model

In healthy skin, the epidermis is not more than 100–120 μm thick. The dermis is around 2 mm thick. Since light does not penetrate more than 2 mm into it, we can approximate the dermis as a semi-infinite layer. If we ignore the surface layer (epidermis), we can consider tissue semi-space with the optical parameters of the dermis. The reflectance of the semi space with mismatches boundary can be written as [7].

$$R_{\_} = r_{01} + \frac{\left(1 - r_{01}\right)\left(1 - r_{10}\right)R_d}{1 - r_{10}R_d} \tag{1}$$

Here r_{01} is the specular reflectance for the light coming from air to the tissue, r_{10} is the specular reflectance of the light coming from the tissue into the air, R_d is the diffuse reflectance of the bulk tissue.

The simplest tissue model beyond Beer-Lambert and modified Beer-Lambert models is the Kubelka-Munk (K-M) approach. The diffuse reflectance of the semi space with absorption and scattering coefficients, K and S in the K-M model

$$R_d = a - \sqrt{a^2 - 1} \tag{2}$$

where $a = \frac{S+K}{S}$. In [8], the authors expressed K-M absorption and scattering coefficients K and S through tissue scattering and absorption coefficients μ_a and μ'_s.

The advantage of the K-M model is that it is pretty simple. In particular, we can measure R, find R_d by inverting Eq. 1, and find K/S by solving Eq. 2.

However, the optical properties of the epidermis are very different from those of the dermis, especially for dark skin tones. In general, the skin contains melanin located in the bottom, basal layer of the epidermis. Its concentration there varies from 1% to 43% [9]. Thus, the predictions from the one-layer model can significantly deviate from the two-layer model.

2.2 Quasi Two-Layer Model

In general, the two-layer models (see, for example, [6]) present technical challenges with regard to extracting the tissue's optical parameters in imaging mode. Therefore, some simplifications of this model tailored to computational efficiency would be helpful for imaging scenarios.

The thickness of the healthy epidermis ranges from 50 to 130 μm [10]. If we consider the optical properties of the epidermis, one can see that its optical density in the normal epidermis case does not exceed 1, but typically it is smaller.

It gives us some hints on how we can simplify the two-layer geometry. For example, we can consider a semi space (dermal layer) with a 'thin-film' of epidermis located just below the boundary, which is characterised by two parameters: absorption ρ and scattering χ, which depends on absorption μ_a and reduced scattering μ'_s of the epidermal layer (denoted by sub-index 1):

$$\rho = \int_{L_1} \mu_{a1} dz \tag{3a}$$

$$\chi = \frac{1}{2} \int_{L_1} \mu'_{s1} dz \tag{3b}$$

Here we have integration over the epidermis layer with the thickness L_1. In the sequence of scattering events in the dermis, the photon will ultimately forget about the initial direction, and we can expect that χ photons will be reflected, ρ absorbed, and $1\text{-}\rho\text{-}\chi$ will pass through the film.

In this case, we can extend the two-flux K-M model to a four-flux model, illustrated by the following diagram (see Fig. 1). In particular, we have four fluxes inside the tissue (two inbound, I_1, I_3, and two outbound, I_2 and I_4) and can write balance equations for them:

$$I_1 = (1 - r_{01}) I_0 + r_{10} I_2 \tag{4a}$$

$$I_2 = \chi I_1 + (1 - \rho - \chi) I_4 \tag{4b}$$

$$I_3 = \chi I_4 + (1 - \rho - \chi) I_1 \tag{4c}$$

$$I_4 = R_d I_3 \tag{4d}$$

This system can be solved, and the reflectance of the tissue will be

$$R = r_{01} + \frac{(1 - r_{01})(1 - r_{10})\left[\chi + \left((1 - \rho - \chi)^2 - \chi^2\right) R_d\right]}{1 - \chi\left(R_d + r_{10}\right) - \left((1 - \rho - \chi)^2 - \chi^2\right) R_d r_{10}} \tag{5}$$

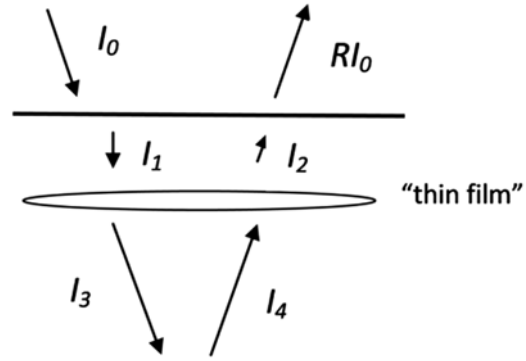

Fig. 1 Four fluxes in a quasi two-layer model

This equation is the generalisation of Eq. 1 for the quasi two-layer model. In the case of $\rho = 0$, $\chi = 0$, Eq. 5 is reduced to Eq. 1.

3 Results

To assess the quasi two-layer model's accuracy, we have performed its comparison with a reference (two-layer) model described in [6]. The deviations of reflectance predicted by the quasi two-layer model and single layer model from the reference model at 532 nm (difference in reflectance) are presented in Fig. 2a and Fig. 2b, respectively.

Our model has four variable parameters: thickness of the epithelium, L_1 (50–120 μm), melanin concentration, c_{mel} (1–41% of the basal layer), blood concentration in the dermis, *c* (0.2–7%), and blood oxygen saturation, *SO2* (60–99%). We have selected the following values to compare models. The thickness of the epithelium: 50, 80, and 120 μm. Melanin concentration: we selected 1, 2, 4, 8, 16, and 32% to emulate six Fitzpatrick skin types (I–VI). Blood concentration: 0.2%, 1%, and 7%. Oxygen saturation: 80%.

4 Discussion and Conclusions

Our initial results show that the proposed quasi two-layer model significantly (by a factor of 10) outperforms the single-layer model in accuracy and is in close agreement with the two-layer model. It emulates tissue reflectance typically within 1% of the values derived from the two-layer model. In many imaging scenarios, it is within an experimental error. So, we can set a 1% discrepancy (in absolute values) as a threshold for the model's applicability.

In the 80–100 μm thickness range, the model provides tissue reflectance within 1% of the reference model for the whole range of other parameters (melanin, blood concentration, and oxygen saturation, SO_2). Compared with the reference model, the quasi two-layer model provides slightly lower values for small thicknesses (50 μm) and slightly higher values for large thicknesses (120 μm).

We found that SO_2 barely impacts results. Any increase in the dermis' blood content signifies the impact of the dermis and decreases the discrepancy.

For the thin epithelium (50 μm) for small blood concentrations (0.2%), the model is beyond 1% discrepancy only for darkly pigmented skin

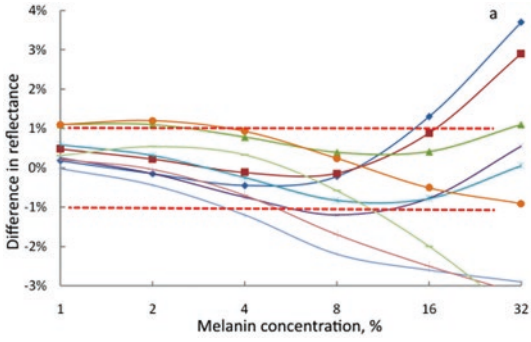

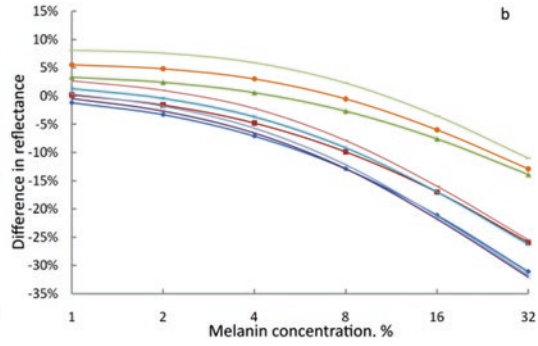

Fig. 2 The difference between reflectance of the two-layer (reference) model and quasi two-layer model (Panel a) and single layer model (Panel b) as a function of the melanin concentration: ◊ (50um, 0.2%), □ (50um, 1%), Δ (50um, 7%), x (80um, 0.2%), * (80um, 1%), ○ (80um, 7%),| (120um, 0.2%), + (120um, 1%), – (120um, 7%), where the first and second values are epidermis thickness and dermal blood content. SO_2 was set to 80%. Dotted red lines indicate the ±1% deviation from the two-layer model predictions

(16–32%). For high blood concentrations (7%), the model is beyond 1% discrepancy only for the very dark skin (32%).

For the mid-range thickness of the epithelium (80 μm), the model is within a 1% discrepancy for all skin tones and blood concentrations.

For the thick epithelium (120 μm) for small blood concentrations (0.2%), the model is within a 1% discrepancy only for lightly pigmented skin (1–2%). For high blood concentrations (7%), the model is beyond a 1% discrepancy only for darkly pigmented skin (16–32%).

The proposed method's advantage is that its expression for tissue reflectance has the same form as the single-layer model. Thus, it can be reversed. Moreover, it contains just several algebraic operations; it can be easily applied on a per-pixel basis in imaging scenarios.

In summary, the proposed quasi two-layer model significantly outperforms the single-layer model and is closely aligned with the two-layer model. Moreover, due to its computational simplicity, it can be easily adapted to image processing algorithms. However, the algorithm performance optimisation is beyond the scope of the current article.

References

1. Fife CE, Carter MJ (2012) Wound care outcomes and associated cost among patients treated in US outpatient wound centers: data from the US wound registry. Wounds 24(1):10–17
2. Sen CK, Gordillo GM, Roy S et al (2009) Human skin wounds: a major and snowballing threat to public health and the economy. Wound Repair Regen 17(6):763–771
3. Saiko G, Lombardi P, Au Y et al (2020) Hyperspectral imaging in wound care: a systematic review. Int Wound J 17:1–17
4. Chin JA, Wang EC, Kibbe MR (2011) Evaluation of hyperspectral technology for assessing the presence and severity of peripheral artery disease. J Vasc Surg 54(6):1679–1688
5. Saiko G, Douplik A (2014) Reflectance of biological turbid tissues under wide area illumination: single backward scattering approach. Int J Photoenergy 2014:241364
6. Yudovsky D, Pilon L (2010) Rapid and accurate estimation of blood saturation, melanin content, and epidermis thickness from spectral diffuse reflectance. Appl Opt 49(10):1707–1719
7. Saunderson JL (1942) Calculation of the color of pigmented plastics. J Opt Soc Am 32(12):727–736
8. van Gemert MJC, Star WM (1987) Relations between the Kubelka-Munk and the transport equation models for anisotropic scattering. Lasers Life Sci 1(98):287–298
9. Jacques SL (1996) Origins of tissue optical properties in the UVA, visible, and NIR regions. In: Alfano RR, Fujimoto JG (eds) Advances in optical imaging and photon migration, vol 2. Optical Society of America, Washington, DC, pp 364–370
10. Lee Y, Hwang K (2002) Skin thickness of Korean adults. Surg Radiol Anat 24(3):183–189

In Vitro Validation of a New Tissue Oximeter Using Visible Light

Nassim Nasseri, Stefan Kleiser, Ursula Wolf, and Martin Wolf

Abstract

There is a clinical need to measure local tissue oxygen saturation (StO_2), oxy-, deoxy- and total haemoglobin concentration ([O_2Hb], [HHb], [tHb]) in human tissue. The aim was to validate an oximeter called OxyVLS applying visible light spectroscopy (VLS) to determine these parameters without needing to assume a reduced scattering coefficient (μ'_s). This problem is solved by appropriate calibrations. Compared to near-infrared spectroscopy (NIRS), OxyVLS determines the oxygenation in a much smaller more superficial volume of tissue, which is useful in many clinical cases. OxyVLS was validated in liquid phantoms with known StO_2, [tHb], and μ'_s and compared to frequency domain NIRS as a reliable reference. OxyVLS showed a high accuracy for all the mentioned parameters and was even able to measure μ'_s. Thus, OxyVLS was successfully tested in vitro.

Keywords

Local tissue oxygen saturation · Visible light spectroscopy · StO_2 · Liquid phantom

1 Introduction

There is a clinical need to determine the local tissue O_2 saturation (StO_2). For example, in bone surgery StO_2 affects fracture repair [1] and low StO_2 leads to osteonecrosis [1]. Identifying this during surgery enables preventive measures. But the currently used microsphere technique [1] is expensive and radioactive [2]. In reconstructive surgery, local measurement of flap StO_2 may increase the rate of flap salvage [3]. Currently flap viability is tested by clinical observation, capillary refilling, temperature and pinprick [4–6], which depend on the surgeon's expertise. Thus, a quantitative method for local oximetry (1 cm^3) is needed.

Visible light spectroscopy (VLS) is mostly sensitive to capillaries [7] and suitable for local oximetry of such small volumes, due to its penetration depth of a few mm. VLS-oximetry based on least squares fitting of spectra (500–630 nm)

N. Nasseri
Biomedical Optics Research Laboratory, Department of Neonatology, University Hospital Zurich, University of Zurich, Zurich, Switzerland

Institute of Complementary and Integrative Medicine, University of Bern, Bern, Switzerland

S. Kleiser · M. Wolf (✉)
Biomedical Optics Research Laboratory, Department of Neonatology, University Hospital Zurich, University of Zurich, Zurich, Switzerland
e-mail: martin.wolf@usz.ch; martin.wolf2@uzh.ch

U. Wolf
Institute of Complementary and Integrative Medicine, University of Bern, Bern, Switzerland

F. Scholkmann et al. (eds.), *Oxygen Transport to Tissue XLIII*, Advances in Experimental Medicine and Biology 1395, https://doi.org/10.1007/978-3-031-14190-4_36

has determined the StO_2 [8–14]. Although VLS is a promising tool for oximetry, it had limited clinical use, because the unknown scattering coefficient (μ'_s) impedes the absolute measurement of chromophore concentrations. Wodick and Lübbers have described how StO_2 and chromophore concentrations can be measured independently of μ'_s [15–17]. This should enable a clinically applicable VLS oximeter.

The aim was to implement this and extend the method in an oximeter called OxyVLS to locally measure StO_2, $[O_2Hb]$ and [HHb]. We also propose a method to estimate μ'_s.

2 Methods

The **OxyVLS** consists of a Maya2000 Pro spectrometer (500–930 nm spectral range, 0.2 nm resolution) with a tungsten halogen source (7 W) and a 400 µm reflection probe (all by Ocean Optics, Dunedin, FL, USA). The probe has an outer diameter of 6.4 mm and a length of 76.2 cm.

OxyVLS was validated in a **liquid phantom** developed for testing oximeters in-vitro under realistic conditions as described in [18]. In short it consisted of 2500 mL phosphate-buffered saline (0.9% NaCl), initially 20 mL human blood (haemoglobin content = 220 g/L, htc = 67%), 74 mL Intralipid® 20% solution (IL), sodium bicarbonate buffer (8.4%) and glucose. The blood concentration was increased twice simulating different reasonable values for tissue [19–21]. The average μ'_s was 6.8 at 692 nm and 5.4 at 834 nm as measured by OxiplexTS (ISS). The liquid was oxygenated by streaming O_2 and deoxygenated by adding yeast.

To analyse the spectra we applied the **interval analysis** [15, 16]. The attenuation spectrum of tissue containing haemoglobin (A) is different from the spectrum of pure haemoglobin in a cuvette (G). This difference is due to inhomogeneous haemoglobin distribution in tissue, other absorbers, and μ'_s [22]. According to [15, 16], the transfer function (H) is one to one. An example of such a transfer function is shown in Fig. 1a. The small deviation from a one-to-one function is due to the wavelength dependency of μ'_s [17]. The interval between wavelength pairs of the same attenuation stays unchanged even if the shape of the spectrum changes due to the transfer function (H). This enabled us to calculate the StO_2 by minimising the residual sum of squares between the interval signal and the interval signal obtained from haemoglobin in a cuvette with known StO_2 (data from [23]). The only assumption we made is that H is a one-to-one function.

To calculate **$[O_2Hb]$, [HHb]** and **[tHb]** in phantom, we employed the spectra from the [tHb] = 26.3 µM as reference. Based on this reference, we calculated [tHb] after increasing the [tHb]. Figure 1b shows the linear regression of the attenuation in the reference and the attenuation in phantom. The same linear relationships were found at all StO_2. The slope of a linear fit represents the proportion of [tHb] to the reference [tHb]. From [tHb] we obtained $[O_2Hb]$ and [HHb] by the StO_2.

Our recorded spectra showed that the change in $\boldsymbol{\mu'_s}$ alters the y-intercept of the transfer function. By calculating the y-intercept of the normalised regression line, we obtained a measure of μ'_s. Here, the fits were normalised by dividing the y-values of each line by its corresponding slope. **Data** were **processed** by re-sampling the data to 1 Hz. Obvious artefacts were removed. The blood bags were analysed by the ABL 800 (Radiometer, Copenhagen, Denmark) to determine the [tHb] in the phantom.

3 Results

As shown in Fig. 2a there is good agreement between **StO_2** of OxyVLS and of OxiplexTS. The effect of changes in [tHb] on this relationship is marginal. The **[tHb]** was measured to be 26.3, 43.9 and 69.5 µM from the injected haemoglobin concentration, 22.6, 35.4 and 53.8 by OxiplexTS and 26.0, 36.8 and 48.7 by OxyVLS in the phantom. Figure 2b shows [tHb] and **$[O_2Hb]$** measured by the two instruments. Figure 3 shows the trend of $\boldsymbol{\mu'_s}$ at 692 nm and at 834 nm in relation

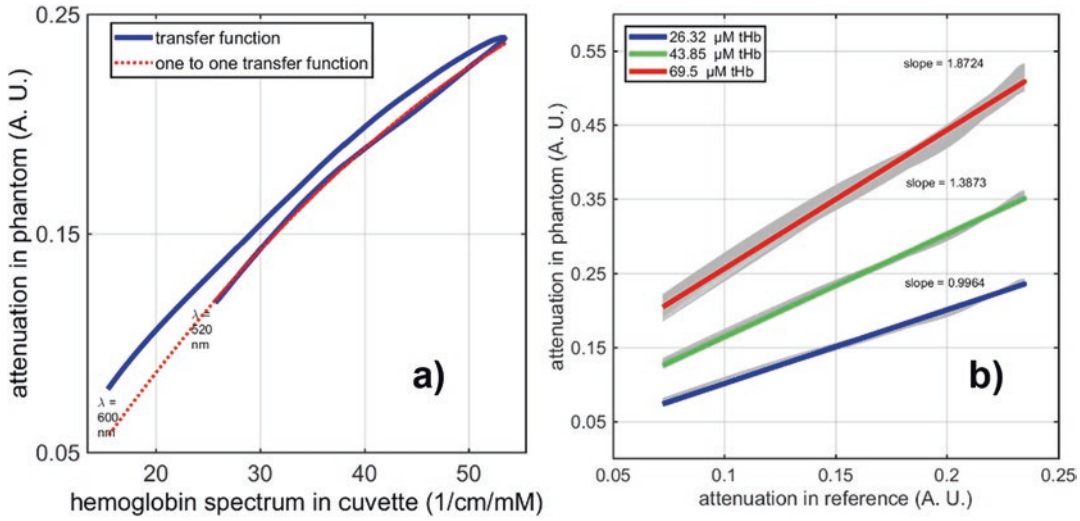

Fig. 1 (**a**) Transfer function between HHb measured in the phantom (StO_2 = 0.1%) and the pure spectrum at StO_2 = 0.1%. (**b**) Linear regression of the attenuation of haemoglobin in the reference dataset (x-axis) from 520 to 600 nm and the attenuation of the phantom at 3 different [tHb] (y-axis) at StO_2 = 0.1%. Grey represents the measured spectra and the linear fit is in colour

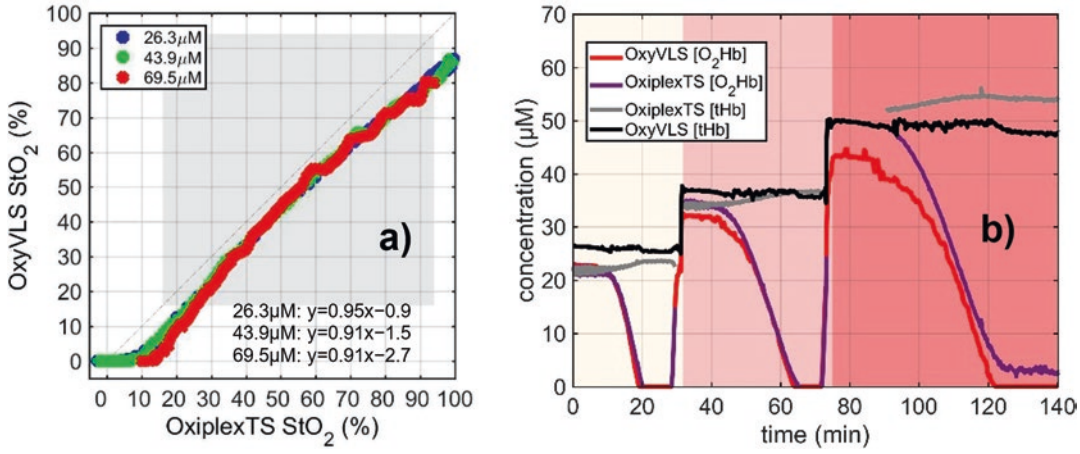

Fig. 2 (**a**) StO_2 measured by OxyVLS (y-axis) and OxiplexTS (x-axis) agree well irrespective of the [tHb]. (**b**) [O_2Hb], and [tHb] measured by OxyVLS in com- parison to OxiplexTS. The shading indicates [tHb] = 26.3 μM, 43.9 μM, 69.5 μM. From 75 to 90 min the OxiplexTS data is missing due to a technical problem

to the y-intercept of the linear fits after normalisation. The mean μ'_s increased in the phantom from 6.6 to 6.9 to 7.5 cm^{-1} at 692 nm and from 5.5 to 5.6 to 5.8 cm^{-1} at 834 nm measured by OxyiplexTS. The corresponding values of OxyVLS were increases from 6.6 to 6.9 to 7.6 cm^{-1} at 692 nm and from 5.5 to 5.6 to 5.8 cm^{-1} at 834 nm.

4 Discussion and Conclusion

OxyVLS and OxiplexTS showed reasonable agreement for changes in StO_2, [tHb], [O_2Hb] and [HHb]. Both oximeters underestimated [tHb] at higher concentrations. This may be due to the blood bag not having been homogenised before taking blood samples. As we later discovered, the

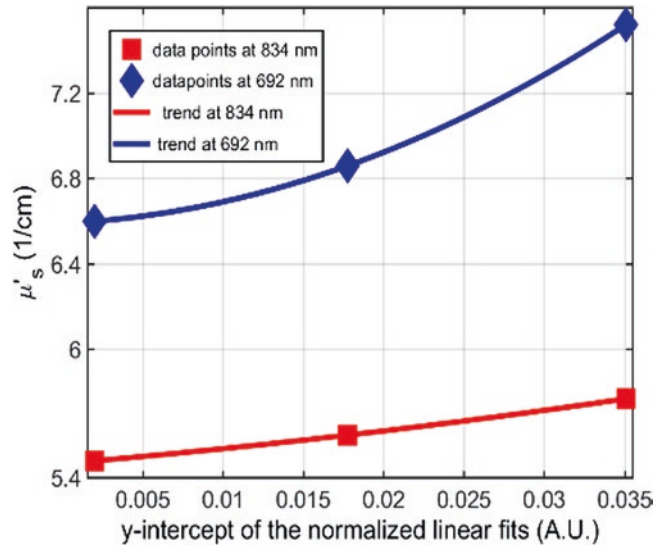

Fig. 3 Y-axis: Trend of μ'_s measured by OxiplexTS at 692 nm and 834 nm. X-axis: the y-axis intercept shown in Fig. 1

distribution of erythrocytes in the bag is not sufficiently homogeneous without homogenising. Thus, the explanation may be that the haemoglobin reference we obtained from the ABL 800 may not have been accurate. OxyVLS slightly underestimated [O_2Hb] at high StO_2, probably due to the high μ_a of haemoglobin for visible light causing low signal-to-noise ratio. The reason for OxyVLS slightly underestimating StO_2 and hence [O_2Hb] and [HHb] is that the distance between the two peaks at 542 nm and 576 nm is due to a difference of only 1 nm between the measured and the reference spectrum taken from the literature [23]. This issue could be solved by proper calibration.

In conclusion, visible light spectroscopy (OxyVLS) measured absolute values of [O_2Hb], [HHb], [tHb], StO_2 and μ'_s in a liquid phantom simulating human tissue and the results agreed well with frequency domain NIRS oximeters. It was not necessary to assume the μ'_s for these calculations. Visible light spectroscopy is expected be a valuable tool for clinical application in flap and bone tissue oximetry and many other applications.

Acknowledgments MW declares that he is president of the board and co-founder of OxyPrem AG. SK is CTO and co-founder of OxyPrem AG.

References

1. McCarthy I (2006) The physiology of bone blood flow: a review. J Bone Joint Surg Am 88(Suppl 3):4–9
2. Prinzen FW, Bassingthwaighte JB (2000) Blood flow distributions by microsphere deposition methods. Cardiovasc Res 45:13–21
3. Holzle F, Rau A, Loeffelbein DJ et al (2010) Results of monitoring fasciocutaneous, myocutaneous, osteocutaneous and perforator flaps: 4-year experience with 166 cases. Int J Oral Maxillofac Surg 39:21–28
4. Disa JJ, Cordeiro PG, Hidalgo DA (1999) Efficacy of conventional monitoring techniques in free tissue transfer: an 11-year experience in 750 consecutive cases. Plast Reconstr Surg 104:97–101
5. Gardiner MD, Nanchahal J (2010) Strategies to ensure success of microvascular free tissue transfer. J Plast Reconstr Aesthet Surg 63:e665–e673
6. Keller A (2007) Noninvasive tissue oximetry for flap monitoring: an initial study. J Reconstr Microsurg 23:189–197
7. Liu H, Chance B, Hielscher AH et al (1995) Influence of blood vessels on the measurement of hemoglobin oxygenation as determined by time-resolved reflectance spectroscopy. Med Phys 22:1209–1217
8. Benaron DA, Parachikov IH, Cheong WF et al (2005) Design of a visible-light spectroscopy clinical tissue oximeter. J Biomed Opt 10:44005
9. Ho JK, Liakopoulos OJ, Crowley R et al (2009) In vivo detection of myocardial ischemia in pigs using visible light spectroscopy. Anesth Analg 108:1185–1192
10. Fox PM, Zeidler K, Carey J et al (2013) White light spectroscopy for free flap monitoring. Microsurgery 33:198–202

11. Friedland S, Benaron D, Coogan S et al (2007) Diagnosis of chronic mesenteric ischemia by visible light spectroscopy during endoscopy. Gastrointest Endosc 65:294–300
12. Harrison DK (2003) Optical measurements of tissue oxygen saturation in lower limb wound healing. Adv Exp Med Biol 540:265–269
13. Harrison DK (2012) Clinical applications of tissue oxygen saturation measurements. Adv Exp Med Biol 737:191–196
14. Kessler M, Frank K, Hoper J et al (1992) Reflection spectrometry. Adv Exp Med Biol 317:203–212
15. Wodick R, Lubbers DW (1973) Quantitative analysis of reflection spectra and other spectra of inhomogenous light paths conducted in multicomponent systems with the aid of interval analysis, I. Interval analysis applied to multicomponent systems with unknown, inhomogeneous light paths (author's transl). Hoppe Seylers Z Physiol Chem 354:903–915
16. Wodick R, Lubbers DW (1973) Quantitative analysis of reflection spectra and other spectra with inhomogenous light paths conducted in multicomponent systems with the aid of interval analysis, II. Determination wavelength-dependent interferences and their constituent and unknown components in multicomponent systems by interval analysis (author's transl). Hoppe Seylers Z Physiol Chem 354:916–922
17. Lubbers DW (1973) Spectrophotometric examination of tissue oxygenation. Adv Exp Med Biol 37A:45–54
18. Kleiser S, Nasseri N, Andresen B et al (2016) Comparison of tissue oximeters on a liquid phantom with adjustable optical properties. Biomed Opt Express 7:2973–2992
19. Arri SJ, Muehlemann T, Biallas M et al (2011) Precision of cerebral oxygenation and hemoglobin concentration measurements in neonates measured by near-infrared spectroscopy. J Biomed Opt 16:047005
20. Wolf U, Wolf M, Choi JH et al (2003) Mapping of hemodynamics on the human calf with near infrared spectroscopy and the influence of the adipose tissue thickness. Adv Exp Med Biol 510:225–230
21. Ijichi S, Kusaka T, Isobe K et al (2005) Developmental changes of optical properties in neonates determined by near-infrared time-resolved spectroscopy. Pediatr Res 58:568–573
22. Lubbers DW, Wodick R (1969) The examination of multicomponent systems in biological materials by means of a rapid scanning photometer. Appl Opt 8:1055–1062
23. Zijlstra WG, Buursma A, van Assendelft OW (2000) Visible and near infrared absorption spectra of human and animal haemoglobin determi- nation and application. VSP, Utrecht

Photon and Proton Dose Painting Based on Oxygen Distribution – Feasibility Study and Tumour Control Probability Assessment

Ana Ureba, Jakob Ödén, Iuliana Toma-Dasu, and Marta Lazzeroni

Abstract

Solid tumours may present hypoxic sub-regions of increased radioresistance. Hypoxia quantification requires of clinically implementable, non-invasive and reproducible techniques as positron emission tomography (PET). PET-based dose painting strategies aiming at targeting those sub-regions may be limited by the resolution gap between the PET imaging resolution and the smaller scale at which hypoxia occurs. The ultimate benefit of the usage of dose painting may be reached if the planned dose distribution can be performed and delivered consistently. This study aimed at assessing the feasibility of two PET-based dose painting strategies using two beam qualities (photon or proton beams) in terms of tumour control probability (TCP), accounting for underlying oxygen distribution at sub-millimetre scale.

A tumour oxygenation model at submillimetre scale was created consisting of three regions with different oxygen partial pressure distributions, being hypoxia decreasing from core to periphery. A published relationship between uptake and oxygen partial pressure was used and a PET image of the tumour was simulated. The fundamental effects that limit the PET camera resolution were considered by processing the uptake distribution with a Gaussian 3D filter and re-binning to a PET image voxel size of 2 mm. Prescription doses to overcome tumour hypoxia were calculated based on the processed images, and planned using robust optimisation.

Normal tissue complication probabilities and TCPs after the delivery of the planned doses were calculated for the nominal plan and the lowest bounds of the dose volume histograms resulting from the robust scenarios planned, taking into account the underlying oxygenation at submillimetre scale. Results were presented for the two beam qualities and the two dose painting strategies: by contours (DPBC) and by using a voxel grouping-based approach (DPBOX).

In the studied case, DPBOX outperforms DPBC with respect to TCP regardless the beam quality, although both dose painting strategy plans demonstrated robust target coverage.

A. Ureba (✉)
Department of Oncology-Pathology, Karolinska Institutet, Medical Radiation Physics, Stockholm, Sweden
e-mail: ana.ureba@ki.se

J. Ödén
RaySearch Laboratories AB, Solna, Sweden

I. Toma-Dasu · M. Lazzeroni
Department of Oncology-Pathology, Karolinska Institutet, Medical Radiation Physics, Stockholm, Sweden

Department of Physics, Stockholm University, Medical Radiation Physics, Stockholm, Sweden

F. Scholkmann et al. (eds.), *Oxygen Transport to Tissue XLIII*, Advances in Experimental Medicine and Biology 1395, https://doi.org/10.1007/978-3-031-14190-4_37

Keywords

Radioresistance · Dose Painting · TCP · PET

1 Introduction

Radiotherapy planning is a multi-step process, which starts with the decision of irradiation of a malignant tumour and ends with the delivery of a planned dose distribution to treat the lesion. A frequent feature of solid tumours is the presence of the hypoxic microenvironment, mainly due to the imbalance between blood supply and oxygen consumption rate of the tumour cells. Hypoxia is known as a negative prognostic factor inducing chemo- and radio-resistance. A desirable strategy in a radiotherapy treatment may be overcoming hypoxia by spatially modulating the radiation dose distribution to scale the dose in those intra-tumour radioresistant areas while maintaining, or possibly deescalating, the dose in the remaining tumour and normal tissues [1–4].

Imaging techniques routinely used in the clinic such as functional magnetic resonance or positron emission tomography (PET) with hypoxia-specific tracers, are non-invasive and may be used for identifying spatial differences in physiological features as hypoxia. Still, there is no clinical protocol to adapt to routine clinical practice these image modalities as techniques that provide surrogate values for quantifying oxygen level in the tumour [1, 5]. PET imaging has been extensively used to delineate biological targets aiming to boost more aggressive regions [6]. Despites having been shown that PET imaging by means of dedicated tracers (i.e. FMISO, Cu-ATSM, HX4 or FAZA) provides information on the chronic hypoxic areas, there is no consensus on the translation of the PET uptake information to oxygen concentration [2, 7]. One of the main issues is the resolution gap between the millimetre scale of the PET images and the typical micrometre scale at which hypoxia manifests. Hence, the limitations of the PET image acquisition process compromise the ability of PET images to represent the tumour microenvironment heterogeneity [8, 9]. However, improved quantification capability may be foreseen in the advent of new PET scanners and reconstruction algorithms, which promise enhanced spatial resolution and signal-to-noise ratio [10].

The beam quality plays a fundamental role in counteracting hypoxia in terms of the structure of the particle track, more specifically, the particle energy deposition in the medium and the particle interaction density tracks through the medium. In particular, the ability of light and heavy ions to sharply deposit their energy at the end of their range may be required for dose sculpting. Therefore, given the physical characteristics of their energy deposition, the use of proton beams may be advantageous when aiming at sculpting the dose distribution to overcome radioresistance in the tumour sub-regions [2, 3].

This study aimed to determine the clinical feasibility of two different dose prescription strategies based on hypoxia PET imaging for both photons and protons and at assessing the treatment outcome prediction in terms of tumour control probability (TCP) by taking into account the underlying oxygen distribution at sub-millimetre scale.

2 Methods

A 3D *in-silico* tumour model with heterogeneous oxygen partial pressure (pO_2) distribution at sub-millimetre scale (0.2 mm) was located in the head and neck region of a clinical patient PET-CT image. The simulated radiotherapy target consisted of three self-contained regions: the clinical target volume (CTV), the gross tumour volume (GTV) and the hypoxic core (HC). A pO_2 distribution having a hypoxic fraction (HF) of 9% CTV-GTV (CTV rim excluding GTV), 24% for GTV-HC (GTV rim excluding HC) and 58% for HC was assigned to each region. Temporal changes due to fast re-oxygenation were considered, after each fraction of treatment and simulated by resampling the pO_2 values within each volume as described in previous studies [11].

The uptake distribution of the PET tracer FMISO was calculated from the pO_2 values by applying a non-linear conversion function (Ƒ), which describes the relationship between the

tracer uptake and the pO_2 distribution based on the inhibition of a chemical reaction [7]. In order to mimic the fundamental limits of the PET imaging system, a Gaussian 3D filter (Full Width Half Maximum of 11 mm) was applied on the resulting uptake distribution at 0.2 mm voxel side length and re-binned increasing the voxel side length to 2 mm. Then, to identify the hypoxic volume and to calculate the dose required to overcome radioresistance from the PET image, the following steps were taken: the inverse of the non-linear conversion function ($\mathcal{F}^{-1}$) was used to convert the FMISO uptake into a new pO_2 map at 2 mm scale and the hypoxic target volume (HTV) was contoured at 10 mmHg threshold.

Assuming that the unique factor which affects radioresistance is the hypoxia level [7], the prescription doses needed to overcome tumour radioresistance for a 10 fraction treatment were voxel wise calculated aiming at 95% TCP on the CTV.

Two different dose prescription strategies were adopted: Dose Painting by Contour (DPBC) with three levels of uniform dose, in HTV, in the GTV-HTV and in the CTV-GTV using the expression derived by Toma-Dasu et al. [7, 11]; and Dose Painting by BOXes (DPBOX) consisting of dividing the volumes in 10 mm side length cubic sub-volumes and assigning the maximum dose within each box [8].

Treatment plans with two different beam qualities, photons and protons, were made in a research version of the treatment planning system RayStation (v10B, RaySearch Laboratories AB). A TrueBeam STx from Varian (Varian, Palo Alto, CA, USA) was used to optimise volumetric modulated arc therapy 6 MV photon plans using two full arcs. The intensity modulated proton therapy plans were optimised using a typical pencil beam scanning dedicated nozzle from IBA (Ion Beam Applications S.A., Louvain-la-Neuve, Belgium) using a 4-field configuration (60°, 120°, 240°, 300°) with energy range of 70–230 MeV. The proton dose was weighted by its relative biological effectiveness (RBE) with a constant RBE of 1.1, whereas RBE = 1.0 was used for photons, both in accordance with clinical practise. To account for setup and density uncertainties, robust minimax optimisation was used for the targets by considering ±3 mm setup errors for all plans and 0% and ± 3.5% density change for proton plans, which resulted in 27 different scenarios for the photon plans and 81 different scenarios for the proton plans. Based on dose distribution scenarios from robust optimisation, upper and lower bound limits with one sigma error from average dose distribution were calculated for each plan and plotted in their corresponding dose volume histogram.

The plans aimed at fulfilling the dose constraints for the following organs at risk: $D_{max} \leq 33$ Gy (RBE) for spinal cord, $D_{max} \leq 34$ Gy (RBE) for brainstem, $D_{mean} \leq 15$ Gy (RBE) unilateral or $D_{mean} \leq 18$ Gy (RBE) bilateral for parotid glands, and $D_{2\%} < 43$ Gy (RBE) for mandible.

For each plan and dose prescription strategies described above, the TCPs of the nominal and the lower bound limit were evaluated using the underlying pO_2 distributions at submillimetre scale (0.2 mm voxel size) using the LQ-Poisson model [12]. The following values for the model parameters were used: $\alpha = 0.035$ Gy^{-1}; $\alpha/\beta = 10$ Gy and $\rho_0 = 3.5\ 10^6$ cm^{-3} for the radiobiological parameters and initial clonogenic cell density [12, 13]. For each nominal plan, normal tissue complication probabilities (NTCPs) for the organs at risk were calculated with the Lyman-Kutcher-Burman model considering the following end points: myelopathy, necrosis, xerostomia and osteoradionecrosis for spinal cord, brainstem, parotid glands and mandible, respectively [14]. A crossed comparison between beam quality and dose prescription strategies were evaluated in terms of NTCP changes (ΔNTCP) and a possible clinical benefit for each organ at risk was considered if ΔNTCP was higher than 10 pp (percentage point).

3 Results and Discussion

After simulating the main limitations of the PET imaging system, the average pO_2 value for the three volumes (HTV, GTV and CTV) was 8, 15, 20 mmHg. HF was zero for the CTV-HTV and

100% for the HTV. The HTV was 15 cm^3, 16% smaller than the original HC.

The dose distribution required to overcome tumour hypoxia was physically feasible and the plans were robust in terms of target coverage (Fig. 1). However, the mandible and both parotids did not satisfy the organs at risk constraints since they partially overlapped the CTV and the target coverage was prioritised during plan optimisation. This resulted in NTCP values for the

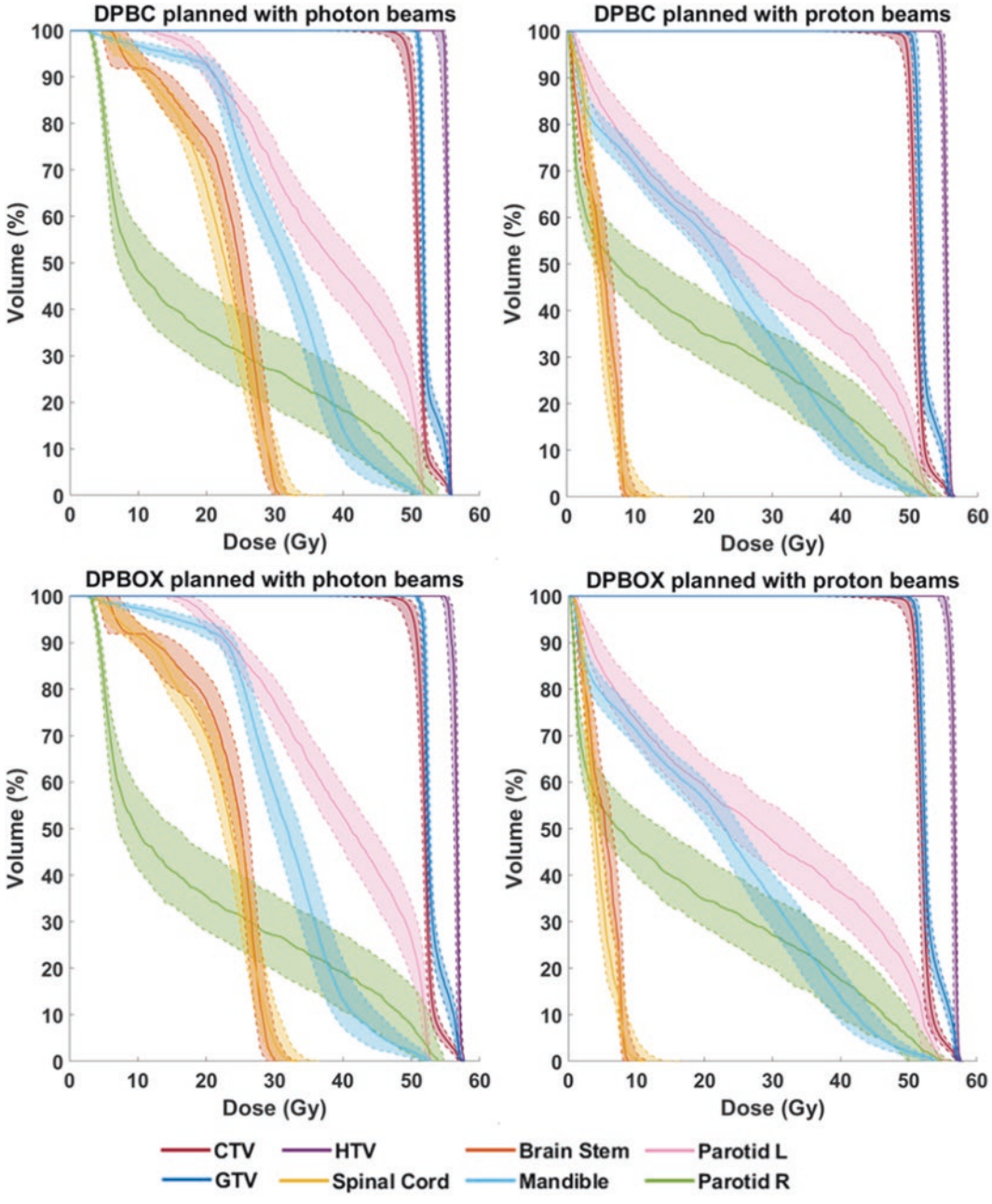

Fig. 1 Dose-volume histograms of the robust plans with photon and proton beams based on the two dose painting strategies studied. Solid lines show the nominal plan (0 mm/0%), while dashed lines show the confidence interval as one sigma of the average dose distribution of robust scenarios

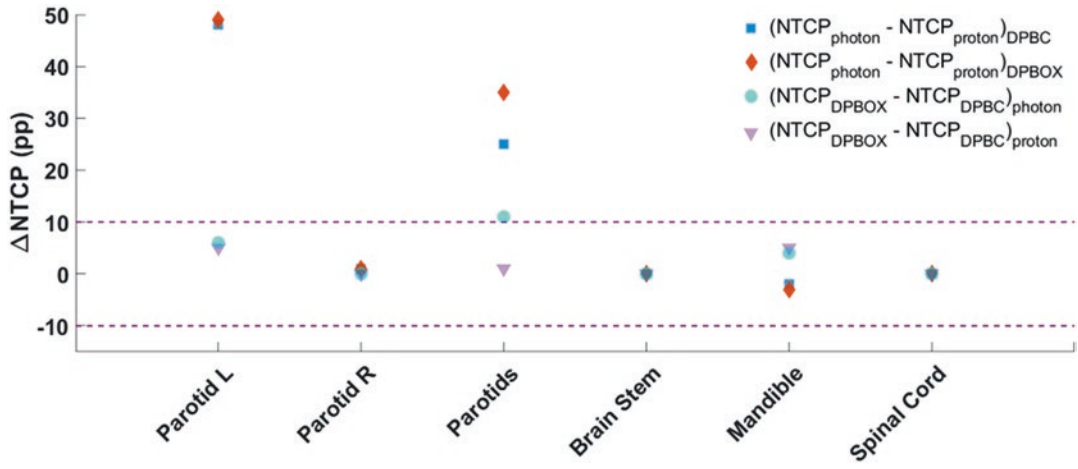

Fig. 2 Normal tissue complication probability change (ΔNTCP) (pp: percentage point)

mandible being 6 and 8% for DPBC and 10 and 13% for DPBOX, for photons and protons, respectively. DPBOX plans had small volumes with higher doses (Fig. 1).

ΔNTCP showed therapeutic gain in terms of beam quality in favour of protons while it resulted in no clinical gain in terms of dose painting strategies (Fig. 2). Proton plans showed the ability of better sparing the parotid glands regarding dose-volume distribution and NTCP (Figs. 1 and 2).

TCP accounting for the underlying heterogeneity in tumour radiosensitivity due to cell oxygenation at sub-millimetre scale was >95% for DPBC and > 97% for the DPBOX in the GTV for both beam qualities and lowest bound. These results seem promising and pointing to that dedicated-PET-based dose painting approaches aiming at targeting chronic hypoxia, may be successfully implemented in a clinical workflow. Furthermore, presented results show that the resolution gap between the hypoxia in tissue and dedicated-PET image may be bridged by prescription doses derived from quantifying PET images. Nevertheless, for the clinical usage of the PET image for dose prescription, well-defined protocols for image acquisition, reconstruction and segmentation are still required for PET image quantification.

4 Conclusions

The robust optimisation strategies utilised in this study resulted in clinically acceptable plans for both the photon and the proton beams. In the studied patient case, DPBOX outperforms the DPBC with respect to TCP regardless the beam quality. In terms of NTCP proton plans demonstrated to spare better the parotids compared to photon plans.

Acknowledgments Financial support from the Cancer Research Funds of Radiumhemmet and The Swedish Research Council (2020-04618) is gratefully acknowledged.

References

1. Troost EG, Koi L, Yaromina A et al (2017) Therapeutic options to overcome tumor hypoxia in radiation oncology. Clin Transl Imaging 5(5):455–464
2. Håkansson K, Smulders B, Specht L et al (2020) Radiation dose-painting with protons vs. photons for head-and-neck cancer. Acta Oncol 59(5):525–533
3. Leeman JE, Romesser PB, Zhou Y et al (2017) Proton therapy for head and neck cancer: expanding the therapeutic window. Lancet Oncol 18(5):e254–e265
4. Epel B, Maggio MC, Barth ED et al (2019) Oxygen-guided radiation therapy. Int J Radiat Oncol Biol Phys 103(4):977–984

5. Thorwarth D (2018) Biologically adapted radiation therapy. Z Med Phys 28(3):177–183
6. Verma V, Choi JI, Sawant A et al (2018) Use of PET and other functional imaging to guide target delineation in radiation oncology. Semin Radiat Oncol 28(3):171–177
7. Toma-Dasu I, Uhrdin J, Antonovic L et al (2012) Dose prescription and treatment planning based on FMISO-PET hypoxia. Acta Oncol 51(2):222–230
8. Ureba A, Kjellsson-Lindblom E, Toma-Dasu I et al (2021) Assessment of the probability of tumour control for prescribed doses based on imaging of oxygen partial pressure. Adv Exp Med Biol 1269:185–190
9. Grimes DR, Warren DR, Warren S (2017) Hypoxia imaging and radiotherapy: bridging the resolution gap. Br J Radiol 90:20160939
10. Berg E, Cherry SR (2018) Innovations in instrumentation for positron emission tomography. Semin Nucl Med 48(4):311–331
11. Toma-Dasu I, Dasu A, Brahme A (2009) Dose prescription and optimisation based on tumour hypoxia. Acta Oncol 48(8):1181–1192
12. Fowler JF (2009) Sensitivity analysis of parameters in linear-quadratic radiobiologic modeling. Int J Radiat Oncol Biol Phys 73(5):1532–1537
13. Webb S, Nahum AE (1993) A model for calculating tumour control probability in radiotherapy including the effects of inhomogeneous distributions of dose and clonogenic cell density. Phys Med Biol 38(6):653
14. Burman C, Kutcher GJ, Emami B et al (1991) Fitting of normal tissue tolerance data to an analytic function. Int J Radiat Oncol Biol Phys 21(1):123–135

Part IV

Tumor Oxygenations

Effect of Acidosis-Induced Signalling Pathways on Mitochondrial O_2 Consumption of Tumour Cells

C. Degitz, S. Reime, and O. Thews

Abstract

Signalling pathways such as ERK1/2, p38 or PI3K are activated in tumour cells by extracellular acidosis, which is a common phenomenon in human tumours. These signalling pathways can modulate the mitochondrial function and activity. The aim of the study was to evaluate the impact of extracellular acidosis on the mitochondrial O_2 consumption and, in consequence, the potential role of ERK1/2, p38 and PI3K cascades on modulating the respiratory function. The O_2 consumption rate (OCR) was measured at pH 7.4 and extracellular acidosis (pH 6.6) in combination with inhibition of the respective signalling pathway. The activity of the pathways was determined by phosphorylation-specific western blot using the cytosolic and mitochondrial fraction of cell lysates. The experiments were performed on a rat tumour cell line (subline AT1 of the rat R-3327 prostate carcinoma) and normal cells (NRK-49F fibroblasts). Acidosis increased the OCR of AT1 cells, especially the basal OCR and the O_2 consumption, which is related to ATP production. In normal NRKF cells OCR was unaffected by low pH. Inhibition of ERK1/2 and PI3K, but not p38, reduced the acidosis-induced increase of the OCR significantly in AT1 tumour cells. In this cell line acidosis also led to an ERK1/2 and PI3K activation, predominantly in the mitochondrial fraction. These results indicate that extracellular acidosis activates cellular respiration in tumour cells, presumably by activating the ERK1/2 and/or the PI3K signalling cascade. This activation of ERK1/2 and PI3K is located primarily in the mitochondrial compartment of the cells.

Keywords

ERK1/2 · p38 · PI3K · MAP kinases · AT1 cells · NRKF cells

1 Introduction

The metabolism of solid tumours differs to that of physiological healthy tissue. Whereas normal cells use glycolysis primarily in times of hypoxia, cancer cells utilise this metabolic pathway even under normoxia [1]. This so called "Warburg effect" together with a chaotically structured and uncontrolled angiogenesis resulting from fast tumour growth, lead to two main characteristics of the microenvironment in solid tumours: acidosis and hypoxia [2]. Earlier studies have shown that extracellular acidosis activates certain signalling pathways in different tumour cell lines,

C. Degitz · S. Reime · O. Thews (✉)
Julius-Bernstein-Institute of Physiology, University of Halle, Halle, Germany
e-mail: oliver.thews@medizin.uni-halle.de

F. Scholkmann et al. (eds.), *Oxygen Transport to Tissue XLIII*, Advances in Experimental Medicine and Biology 1395, https://doi.org/10.1007/978-3-031-14190-4_38

including the MAP kinases ERK1/2 and p38 as well as PI3K [3, 4]. Preliminary results also indicated that the extracellular pH could affect mitochondrial function [5]. In this study, the overall oxygen consumption rate of AT-1 and NRKF cells during extracellular acidosis (pH 6.6) was measured, including closer analysis of the impact on different sub-processes of mitochondrial and non-mitochondrial O_2 consumption. In a second step, the effect of the signalling pathways p38, ERK1/2 and PI3K on cellular respiration under acidic and control conditions was analysed. Since these signalling pathways can act directly at mitochondria [6–8], the localisation of p38, ERK1/2 and PI3K activation in the cytosolic or the mitochondrial compartment was analysed. All results of AT1 tumour cells were compared to the normal NRKF fibroblast cell line.

2 Methods

2.1 Cell Line

The subline AT1 of the rat R-3327 Dunning prostate carcinoma was grown in RPMI medium supplemented with 10% foetal calf serum (FCS). The rat normal kidney fibroblast cell line NRK-49F (NRKF) was grown in DMEM medium supplemented with 5% FCS. Cells were grown at 37 °C under humidified 5% CO_2 atmosphere and were split twice a week.

2.2 Experimental Settings

For the experiments, cells were cultivated in Petri dishes for 24 h. Then media was changed to HEPES- and MES-buffered media without FCS adjusted to pH 7.4 (control) or 6.6 (acidosis) for another 3 h after which the measurements were performed. In addition, cells were incubated with or without the according inhibitors of the different signalling pathways.

Western blotting was performed according to standard protocols. In brief, cells were lysed (0.5 M Tris-HCl pH 6.8; 10% SDS; 10% 2-mercaptoethanol; 20% glycerol; 0.01% bromophenol blue), separated by sodium dodecyl sulphate polyacrylamide gel electrophoresis, and transferred to a nitrocellulose membrane. Subsequently, membranes were incubated with antibodies specific for ERK1/2, pERK1/2, Akt, pAkt, vDAC and HSP90. The bound primary antibody was visualised by IRDye secondary antibodies (Licor Biosciences, Lincoln, NE, USA) with the imaging system Odyssey (Licor Biosciences, Lincoln, NE, USA). Quantitative analyses were performed with Image Studio Lite software (Licor Biosciences, Lincoln, NE, USA).

To isolate the mitochondrial protein fraction, standard protocols were used according to Monick at al [9]. In brief, cells were suspended in homogenising buffer containing protease inhibitors (0.25 M sucrose, 0.2 mM EDTA, 10 mM Tris-HCL, 1 µl protein inhibitor cocktail (Sigma-Aldrich, Munich, Germany)) and homogenised in a Dounce homogeniser 20–40 times. After a short centrifugation (3000 rpm) to remove unlysed cells and nuclei, the supernatant was centrifuged for 10 min at 12000 rpm. The supernatant from this step equals the cytosolic fraction. The pellet was re-suspended in protein lysis buffer (0,05 M Tris (pH = 7.4), 0,15 M NaCl, 1% Nonidet P40 with 1:500 protease inhibitor cocktail, 1 mM sodium orthovanadate, 15 mM NaF) and sonicated. After centrifugation (5 min at 14000 rpm), the supernatant equals the mitochondrial fraction.

The oxygen consumption rate (OCR) was measured using the Agilent Seahorse XFe96 Analyzer (Agilent Technologies, Santa Clara, USA). To differentiate mitochondrial O_2 metabolism and its components from non-mitochondrial O_2 consumption, inhibitors of different complexes of the respiratory chain were added (XF Cell Mito Stress Test Kit, Agilent Technologies, Santa Clara, USA). The basal O_2 consumption was defined by the OCR under control conditions minus the non-mitochondrial consumption (after adding rotenone and antimycin A). The oxygen consumption linked to ATP synthesis was calculated from the difference of the basal OCR and OCR after oligomycin treatment, whereas the proton leak resulted from OCR with oligomycin minus non-mitochondrial consumption.

3 Results

Exposing AT-1 cells to extracellular acidosis (pH 6.6) led to a marked ERK1/2 phosphorylation (Fig. 1), indicating an activation of this signalling pathway. In NRKF cells acidosis had no stimulating effect on ERK1/2.

Analyses of cellular respiration showed that in the AT-1 cell line the basal O_2 consumption rate (OCR) was approximately three times higher than in the normal NRKF cells under control conditions. While O_2 consumption in AT-1 cells was more than doubled under acidic conditions, in NRKF cells OCR was not influenced by lowering the extracellular pH (Fig. 2). Besides the basal OCR, especially oxygen consumption for ATP synthesis was increased by acidosis in the tumour cell line (pH 7.4: 2.85 ± 0.22, pH 6.6: 4.56 ± 0.38 fmol/min/cell). In comparison, non-mitochondrial oxygen consumption and proton leak increased only slightly (data not shown). The gain in OCR therefore seems to be mainly due to an enhanced mitochondrial metabolism.

The inhibition of the p38 MAPK pathway (by SB203580) had practically no effect on OCR of NRKF cells and AT-1 cells, neither under control conditions nor under acidosis (Fig. 2). Inhibiting PI3K signalling by LY294002 did not influence the OCR under control conditions (pH 7.4) in both cell lines. However, under acidosis a significant decrease was observed in AT1 tumour cells but not in NRKF cells (Fig. 2). Both basal mitochondrial and O_2 consumption for ATP production decreased by around 20%, but did not reach the control level at pH 7.4. A similar effect was observed in AT1 cells by inhibition of ERK1/2 using U0126. At control pH, U0126 did not influence OCR of AT-1 cells, whereas during acidosis it led to a significant decrease by 25% (Fig. 2, both basal OCR and O_2 consumption for ATP production).

To analyse whether these signalling factors act directly at the mitochondria, the activation of the pathways by acidosis was measured in the cytosolic and the mitochondrial fraction in AT1 tumour cells separately. As quality control for successful isolation of the cell compartments, the amount of the mitochondria-specific protein vDAC-1 was measured (Fig. 3). Acidosis *per se* led to a strong activation of ERK1/2 and PI3K (the later assessed by Akt phosphorylation) predominantly in the mitochondrial fraction, whereas in the cytosolic fraction almost no change in either signalling pathway was seen (Fig. 4). Phosphorylation of ERK1/2 in the mitochondrial fraction increased by about 49% and by 77% for Akt. Inhibition of ERK1/2 by U0126 significantly reduced ERK phosphorylation preferentially in the mitochondrial fraction at both pH values. Inhibition of PI3K (by LY294002)

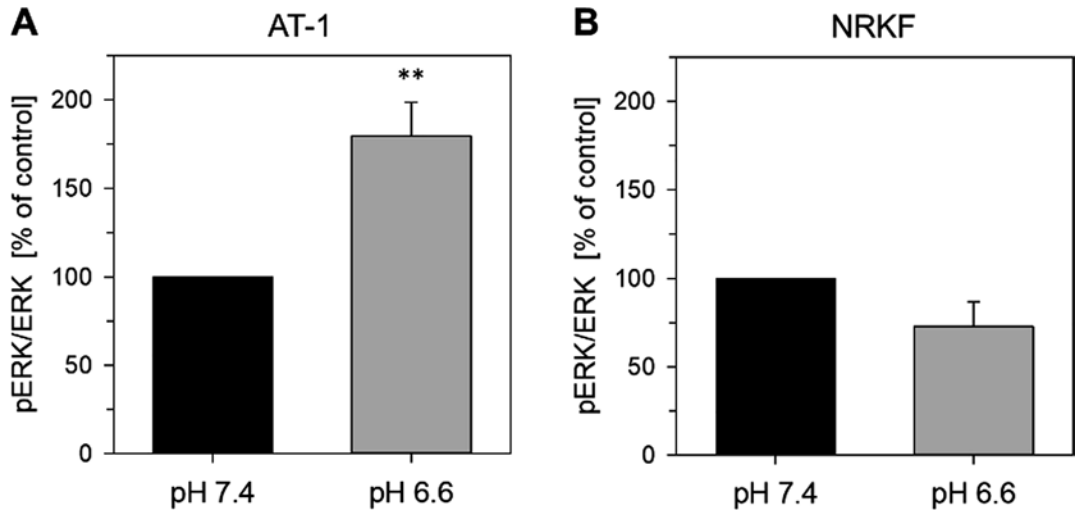

Fig. 1 Relative activation of ERK1/2 in (**a**) AT-1 and (**b**) NRKF cells in the whole cell protein fraction after 3 h under acidic and control conditions. (**) $p < 0.01$, n = 6–8

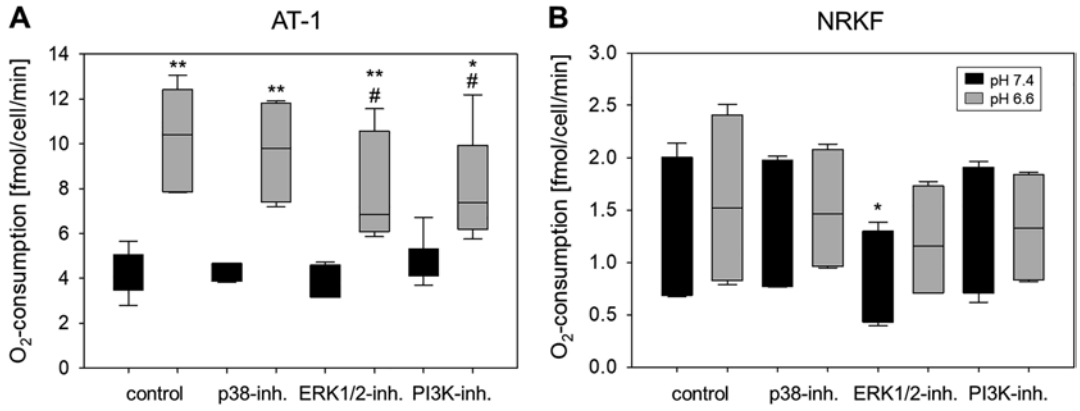

Fig. 2 Impact of inhibition of the p38-, ERK1/2- and PI3K-pathways on basal mitochondrial O_2 consumption rate under acidosis (pH 6.6) and control pH (pH 7.4) for 3 h in (**a**) AT-1 tumour cells and (**b**) NRKF cells. (**) $p < 0.01$, (*) $p < 0.05$ vs. pH 7.4; (#) $p < 0.05$ vs. respective control, n = 4–6

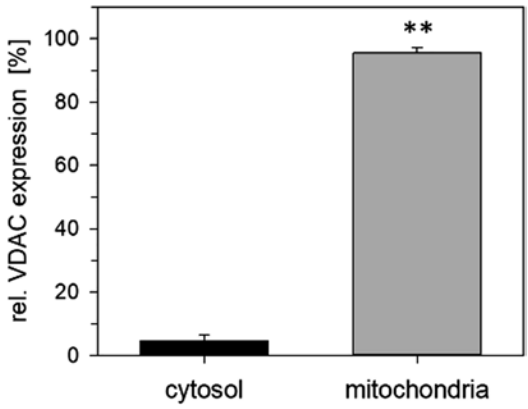

Fig. 3 Relative expression of vDAC in isolated protein fraction of cytosol and mitochondria in AT-1 cells. (**) $p < 0.01$, n = 4

reduced Akt phosphorylation in both cell fractions similarly at control pH, as well as under acidic conditions (Fig. 4).

4 Conclusion

MAP kinase signalling pathways are important for the malignant behaviour of tumour cells, tumour growth and metastasis [10, 11]. It has been shown that acidosis activates those pathways in different cell lines [3]. Whereas in AT-1 tumour cells ERK1/2 activation by acidosis was found in the present study, in NRKF fibroblasts ERK phosphorylation did not increase at low pH. A closer look into this activation in AT1 cells by analysing the cytosolic and mitochondrial protein fractions separately, showed that acidosis seems to activate ERK1/2 predominately in the mitochondrial fraction, whereas in the cytosol pERK/ERK was not altered by acidosis. Additionally, the inhibition of ERK1/2 at pH 7.4 was much stronger in the mitochondrial fraction. Inhibition of the PI3K pathway occurred in both fractions. These results indicate that in tumour cells the acidosis-induced activation of ERK1/2 (and maybe partially also PI3K) is mainly located at the mitochondria. Looking at the oxygen consumption rate of NRKF and AT1 cells, these two cell lines are influenced differently by acidosis. Whereas low pH enhanced the OCR in AT-1 tumour cells (especially basal and ATP production-related OCR), NRKF cells were not affected by lowering the pH. Presently further experiments are necessary to analyse whether this is a fundamental difference between tumour and normal cells, or rather a specific property of the cell lines used.

Combining these two findings in AT1 cells, it becomes obvious that acidosis activates ERK1/2 and Akt predominately at the mitochondria and enhances the mitochondrial O_2 consumption. When inhibiting ERK1/2 and PI3K at low pH, the enhancing effect of acidosis on the OCR was reduced. These results indicate that acidosis induced ERK1/2 or PI3K activation mediated the increase in O_2 consumption directly at the mitochondrial site.

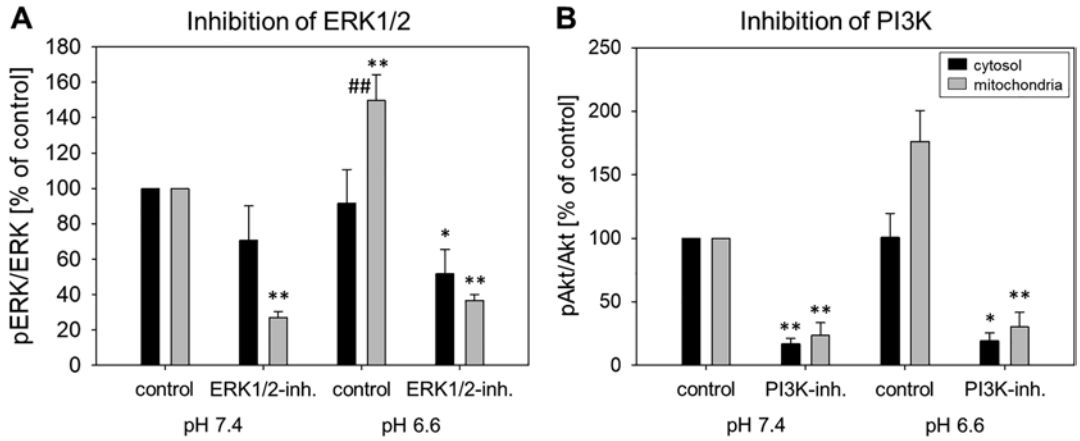

Fig. 4 Impact of inhibition of the p38-, ERK1/2- and PI3K-pathways on relative activation of (**a**) ERK1/2 and (**b**) PI3K during acidosis (pH 6.6) and control pH (pH 7.4) for 3 h in AT-1 tumour cells. (**) $p < 0.01$, (*) $p < 0.05$ vs. pH 7.4; (##) $p < 0.01$ cytosol vs. mitochondria, n = 6

A direct link between ERK1/2 and mitochondria has also been discussed by others. For instance in brain mitochondria, ERK1/2 was located in the outer membrane and intermembrane space [6]. Additionally, it has been demonstrated that ERK1/2 is involved in the process of mitochondria fission [12]. However, further studies are needed to analyse whether these processes play a role in the increased OCR during acidosis in AT1 tumour cells. For Akt it is already known that this signalling factor is translocated to mitochondria and stimulates ATP production via oxidative phosphorylation [8]. Therefore, it seems probable that acidosis-induced PI3K-Akt activation mediates OCR at least in AT-1 cells. Finally, the present study demonstrates that p38 signalling seem to play only a minor/neglectable role for the pH-dependent modulation of oxygen consumption.

Acknowledgments The study was supported by the Deutsche Forschungsgemeinschaft DFG (grant TH482/6-1).

References

1. Vander Heiden MG, Cantley LC, Thompson CB (2009) Understanding the Warburg effect: the metabolic requirements of cell proliferation. Science 324(5930):1029–1033
2. Hui L, Chen Y (2015) Tumor microenvironment: sanctuary of the devil. Cancer Lett 368(1):7–13
3. Riemann A et al (2011) Acidic environment leads to ROS-induced MAPK signaling in cancer cells. PLoS One 6(7):e22445
4. Davis RJ (2000) Signal transduction by the JNK group of MAP kinases. Cell 103(2):239–252
5. Rauschner M et al (2021) Impact of the acidic environment on gene expression and functional parameters of tumors in vitro and in vivo. J Exp Clin Cancer Res 40(1):1–14
6. Wortzel I, Seger R (2011) The ERK Cascade: distinct functions within various subcellular organelles. Genes Cancer 2(3):195–209
7. Trempolec N et al (2017) Induction of oxidative metabolism by the p38α/MK2 pathway. Sci Rep 7(1):11367
8. Rohlenova K, Neuzil J, Rohlena J (2016) The role of Her2 and other oncogenes of the PI3K/AKT pathway in mitochondria. Biol Chem 397(7):607–615
9. Monick MM et al (2008) Constitutive ERK MAPK activity regulates macrophage ATP production and mitochondrial integrity. J Immunol 180(11):7485–7496
10. Papa S et al (2012) The oxidative phosphorylation system in mammalian mitochondria. Adv Exp Med Biol 942:3–37
11. Ersahin T, Tuncbag N, Cetin-Atalay R (2015) The PI3K/AKT/mTOR interactive pathway. Mol BioSyst 11(7):1946–1954
12. Prieto J et al (2016) Early ERK1/2 activation promotes DRP1-dependent mitochondrial fission necessary for cell reprogramming. Nat Commun 7:11124

Feasibility of Non-invasive Measurement of Tumour NAD(H) by *In Vivo* Phosphorus-31 Magnetic Resonance Spectroscopy

Kavindra Nath, Fernando Arias-Mendoza, He N. Xu, Pradeep K. Gupta, and Lin Z. Li

Abstract

Importance of the redox status of nicotinamide adenine dinucleotide (NAD), including its oxidized (NAD^+) and reduced (NADH) forms, has been shown in many biological processes. However, NAD(H) redox status assessment is traditionally limited to biochemical assays *in vitro* or optical redox imaging (ORI) for superficial tissues *in vivo* and for deep tissues *ex vivo*. In recent years, phosphorous-31 magnetic resonance spectroscopy (^{31}P-MRS) was utilized to quantify NAD^+, NADH, and the redox ratio NAD^+/NADH in normal tissues *in vivo*. The quantification is based on the spectral fitting of the upfield shoulder of the αATP peak that contains signals of NAD^+ (a quartet) and NADH (a singlet), assuming pH-independence of peak positions. To evaluate the feasibility of measuring tumour NAD(H) redox status *in vivo*, we fitted single voxel ^{31}P-MR spectra of subcutaneous mouse xenografts of human breast cancer cell lines acquired on a 9.4-T horizontal bore preclinical MR scanner. We found larger variations in the chemical shift offsets of NAD^+ and NADH from αATP in these tumours than the literature values of normal tissues. Furthermore, our ^{31}P-MR spectra of αATP, NAD^+, and NADH solution phantoms indicated that the chemical shift of αATP and thus the offsets between NAD(H) and αATP were pH dependent. Therefore, whether tumour pH should be incorporated into the spectral fitting model should be further evaluated. Additionally, spectral resolution and signal-to-noise ratio should be improved by optimising ^{31}P-MRS protocols, increasing data acquisition time, and using a more sensitive coil for signal detection.

Keywords

Optical redox ratio · xenograft of MAD-MB-231 breast cancer cell line · xenografts of MCF-7 and BT474 breast cancer cell line · Solution phantoms

1 Introduction

According to the Kyoto Encyclopedia of Genes and Genomes (KEGG) database, there are over 2400 unique biochemical reactions containing over 2200 compounds, among which oxygen is involved in ~320 reactions, ATP in ~260 reactions, H^+ in ~540 reactions, and the cohort of

K. Nath · F. Arias-Mendoza · H. N. Xu · P. K. Gupta · L. Z. Li (✉)
Britton Chance Laboratory of Redox Imaging and Laboratory of Molecular Imaging, Department of Radiology, Perelman School of Medicine, University of Pennsylvania, Philadelphia, PA, USA
e-mail: linli@pennmedicine.upenn.edu

F. Scholkmann et al. (eds.), *Oxygen Transport to Tissue XLIII*, Advances in Experimental Medicine and Biology 1395, https://doi.org/10.1007/978-3-031-14190-4_39

NAD^+, NADH, $NADP^+$ and NADPH in ~490 reactions [1]. This testifies to the importance of these molecules in biological activities. Furthermore, the NAD(P) redox statuses are closely coupled with oxygen consumption, bioenergetics, and signalling activities and play essential roles in biology [2]. Thus, methods for detecting tissue NAD(P)(H) are much needed and valuable for biomedical research.

In the 1950s and 60s, Britton Chance and his co-workers established that mitochondrial NADH and oxidised flavoproteins (Fp) containing flavin adenine dinucleotide (FAD) emit fluorescence that can be used to study metabolism and redox state [3]. FAD is a cofactor coupled with NAD(H) redox status. The optical redox ratio Fp/(NADH+Fp) has been shown to correlate linearly with the redox ratio NAD^+/(NAD^++NADH) measured in tissue by liquid chromatography mass spectrometry [4]. Therefore, our group and several others have been investigating the potential of using the optical redox status as a disease biomarker, e.g., for tumour diagnosis and treatment response [3, 5]. Traditionally, tissue NADH redox status can be optically imaged by the Chance redox scanner [5], which is invasive and limited to frozen tissues.

In 2014, Lu et al. published a non-invasive measurement of the NAD(H) redox status using phosphorus-31 magnetic resonance spectroscopy (^{31}P-MRS) *in vivo* [6]. Their approach is to fit the upfield shoulder of the αATP peak with the known spectral patterns of NAD^+ and NADH in normal tissues. With a neutral nitrogen atom within the nicotinamide ring in NADH, the nuclear spins of two ^{31}P atoms have identical chemical shifts showing a single peak in the spectrum. For the NAD^+, the nitrogen atom has a positive charge that breaks the symmetry of the magnetic field causing a chemical shift difference (δ) between the two ^{31}P spins, which are also *J*-coupled. As a two spin AB system, the ^{31}P-MR spectrum of NAD^+ can be modelled as a quartet with a formula based on δ and the coupling constant *J*, which can be measured in solutions. Utilizing this information and showing that the chemical shifts of the αATP and NAD(H) peaks are insensitive to pH and magnesium ion concentration, Lu et al. quantified NAD^+ and NADH and the redox ratio NAD^+/NADH in normal cat brains. Similar approaches have been used to measure the *in vivo* NAD^+ and NADH in the human brain and muscle [7–9].

Motivated by our previous findings using ORI, we sought to measure NAD^+ and NADH in tumours using the ^{31}P-MRS *in vivo*. In a separate manuscript published in this volume, we investigated the feasibility of NAD(H) quantification in human cancers using ^{31}P-MR spectra obtained at 1.5 Tesla (T) [10]. Here we examined ^{31}P-MR spectra obtained from human breast cancer xenografts at a 9.4 T horizontal bore preclinical MR scanner and fitted the αATP spectral region to extract NAD^+ and NADH. Since the NAD(H) chemical shift offsets from the αATP peak appear to vary beyond the range given in the literature, we also investigated the pH dependence of the chemical shifts of αATP and NAD(H) peaks in solution phantoms.

2 Methods

All animal protocols were approved by the Institutional Animal Care and Use Committee at the University of Pennsylvania. Human breast cancer cell lines, MAD-MB-231 and MCF-7, were grown and passaged in RPMI 1640 culture medium. Inoculations of ~10^7 cells in 100 μL culture medium were subcutaneously implanted into the flanks of female athymic nude mice [11]. HCC1806 and BT474 were passaged in DMEM culture medium and each inoculation consisted of ~10^6 cells. Before inoculation of BT-474 and MCF-7 cells, a 60-day release oestrogen pellet (0.72 mg) was implanted subcutaneously around the chest or neck region [11]. When tumour size was in the range of 150–500 mm^3, *in vivo* ^{31}P-MRS was acquired from subcutaneous tumour xenografts using a 9.4 T/31 cm horizontal bore Varian system with a home-built dual-frequency (^{1}H/^{31}P) slotted-tube resonator (13 mm in diameter) [12, 13]. *In vivo* localized ^{31}P-MR spectra were acquired from a single voxel using the Image Selected *In vivo* Spectroscopy (ISIS) method with the time of repetition (TR) 4 s, num-

ber of spectral points (NP) 512, sweep width (SW) 10,000–12,000 Hz, number of acquisitions (NA) 256. The voxel contained most of the tumour while minimising contamination from surrounding tissues.

For the phantom studies, ATP solution was made by dissolving ATP powder in phosphate buffered saline (PBS with Ca^{2+}/Mg^{2+}). The stock solutions of NAD^+ and NADH were made at their maximum solubility by dissolving the powder forms in deionized water (MiliQ) and Tris-HCl buffer (10 mM pH 8.5), respectively. The NAD^+ and NADH stock solutions were further diluted to the desired concentrations with PBS (with Ca^{2+}/Mg^{2+}). The solutions' pH was adjusted from 6 to 8. A 2 ml Eppendorf tube containing such solutions was positioned in the slotted-tube resonator perpendicularly to the main magnetic field. Sometimes, a long-stem spherical microcell (volume 18 μL) containing 85% phosphoric acid (H_3PO_4) was inserted axially inside the 2 ml tube as an external reference with stable chemical shift. Phantoms were scanned by the ISIS protocol (TR 4 s, NP 2048, SW 7978.7 Hz, NA = 32) in the same 9.4 T/31 cm horizontal magnet but interfaced with a Bruker system due to upgrade.

For the spectra of tumour xenografts, the raw data were zero filled to 4096 and Fourier transformed with a Lorentzian filter of 30 Hz followed by baseline correction with the custom-made 3D*i*CSI program. The chemical shift of αATP was set at −10.07 ppm (parts per million). The resulting ^{31}P-MR spectra were further analysed with a MATLAB algorithm by fitting the spectrum of the αATP region with multiple Lorentzian functions, using chemical shift position, amplitude, and half line width (HLW) as independent variables. αATP was fit as a doublet with a *J* coupling constant 15.5 Hz, NADH as a singlet and NAD^+ as a quartet as previously described [6]. NAD and NADH were assumed to have identical HLWs and allowed to vary independently with chemical shifts. The chemical shift offsets of the central positions of NAD^+ and NADH from the αATP peak were limited within ±0.2 ppm of the literature values [6]. A zero-order baseline shift was also included in the model. Peak areas were obtained to represent the signal intensity of NAD^+, NADH and αATP. For the phantom spectra, raw data was zero filled to 4096, but no filtering was used with Fourier transform, and the chemical shifts of the centroid of NAD^+ quartet and the NADH and αATP peaks were obtained.

3 Results and Discussion

We fitted the αATP regions of spectra from 13 breast cancer xenografts with the models of αATP, NAD^+, and NADH peaks. Five spectra have a signal-to-noise ratio (SNR) of the αATP signal below 8, making the fitting results less reliable (data not shown). The spectral fitting of the αATP region of the remaining eight xenografts with SNR ~ 8.5–19 were shown in Fig. 1a–h. Sometimes our fitting indicated the presence of a singlet peak about 1 ppm upfield (i.e., to the right side) of the αATP peak (Fig. 1g, h). This could correspond to the mitochondrial NADH (mNADH) peak previously suggested by Conley et al. in their *in vivo* human muscle study [8]. Adding to the model an extra Lorentzian function representing this single peak, we improved the overall spectral fitting in Fig. 1i, j compared to Fig. 1g, h. This was found necessary for an HCC1806 and a BT-474 tumour. Whether mNADH should be included for other tumours will be investigated further in the future.

We summarised in Table 1 the mean values, standard deviations (SD), and ranges of the chemical shift offsets in the eight tumours shown in Fig. 1 in comparison to the reported literature values. The $\delta_{ATP\text{-}NADH}$ and $\delta_{ATP\text{-}NAD}$ are the relative chemical shift offsets of NAD^+ (centroid) and NADH to the αATP peak, respectively, and the $\delta_{NADH\text{-}NAD}$ is the chemical shift difference between NADH and NAD^+. Thus, while the mean values of chemical shift offsets in breast tumours are close to those in the literature reported for phantoms and normal tissues, there are large variations among individual tumours, particularly for $\delta_{ATP\text{-}NADH}$ and $\delta_{NADH\text{-}NAD}$. We acknowledge that the large fitting variations can be attributed to insufficient SNR and spectral resolutions.

The significant chemical shift variations observed in tumours led us to investigate whether

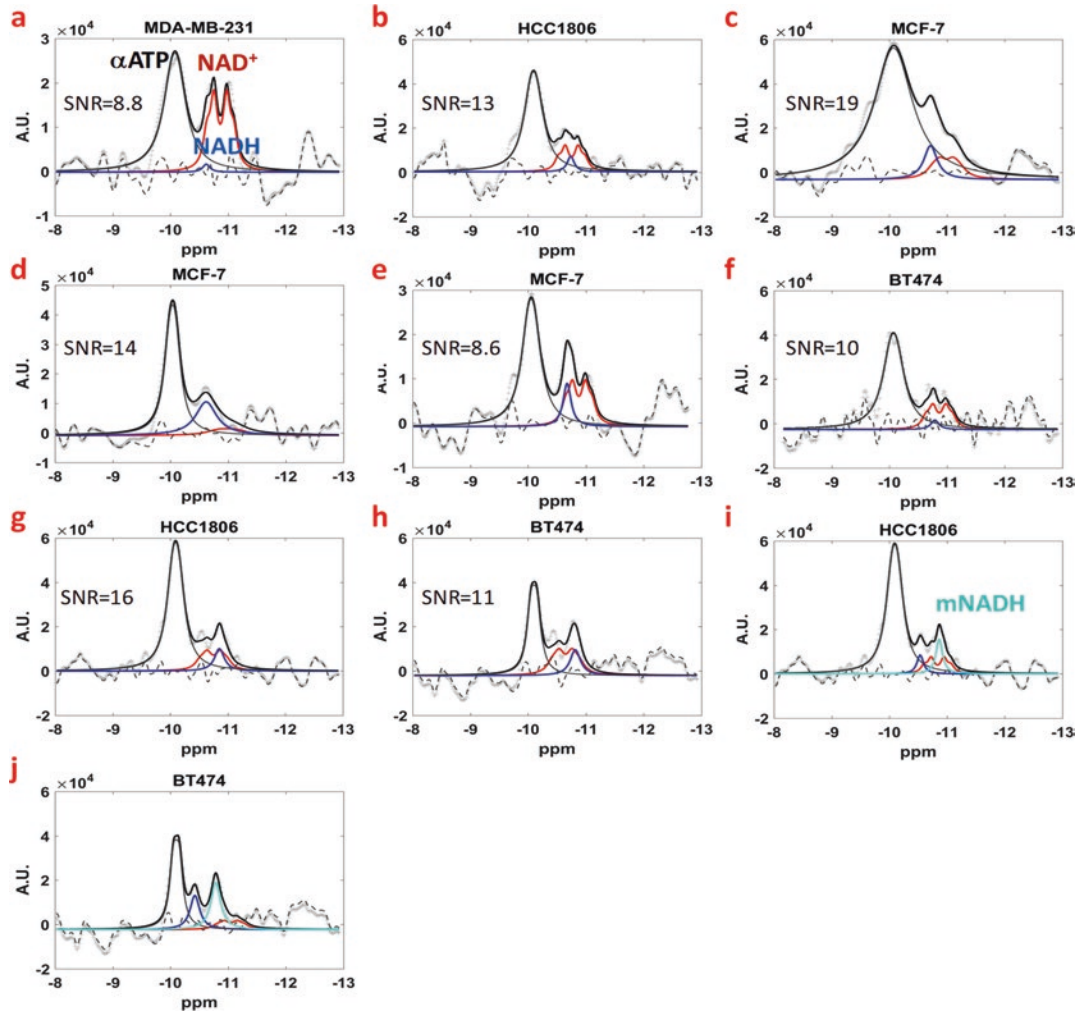

Fig. 1 Spectral fitting of the αATP region of the ^{31}P-MRS spectra from breast cancer mouse xenografts. (**a**–**j**) Spectral fitting of eight tumors with the names of cancer cell lines and the SNRs displayed on individual spectra. Each spectrum shows the raw data in arbitrary units (A.U.) in light grey, global fit in black, αATP in grey, NAD$^+$ in red, NADH in blue, and residues in dashed lines. Panel (**i**) and (**j**) show the fitting for spectra in (**g**) and (**h**), respectively, when the mitochondrial NADH (mNADH) is included in cyan. The x axes are in the range between –8 and –13 parts per million (ppm)

Table 1 Chemical shift offsets between NAD$^+$ (centroid), NADH and αATP in eight xenografts

Chemical shift offsets (ppm)	$\delta_{ATP\text{-}NAD}$	$\delta_{ATP\text{-}NADH}$	$\delta_{NADH\text{-}NAD}$
Mean	0.82	0.56	0.26
SD	0.10	0.13	0.18
Range (min-max)	0.66–0.94	0.32–0.72	0.02–0.62
Literature reference [6, 9]	0.74	0.56	0.18

the chemical shifts of NAD(H) and αATP are pH-dependent since tumours have pH variations and are commonly acidic [13]. Using solution phantoms with pH values ranging from 6 to 8, we corroborated that the NAD$^+$ and NADH chemical shifts are insensitive to pH (Fig. 2a). However, we found that the αATP peak position can vary up to 0.3 ppm from pH 6–8, thus $\delta_{ATP\text{-}NADH}$ and $\delta_{ATP\text{-}NAD}$ are pH dependent and decrease signifi-

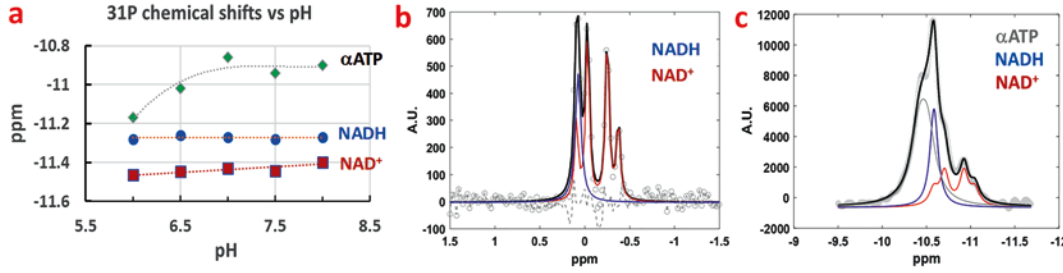

Fig. 2 ^{31}P-MRS studies of ATP, NAD^+ and NADH phantoms. (**a**) pH dependence of chemical shifts in ppm; each point representing a separate phantom using external 85% H_3PO_4 as 0 ppm reference; (**b**) spectral fit for a mixture of NAD^+ (10 mM) and NADH (10 mM) at pH 6.2, $\delta_{NADH\text{-}NAD}$ = 0.22 ppm; (**c**) spectral fit for a mixture of ATP (3 mM), NAD^+(1 mM) and NADH (1 mM) in PBS buffer without Ca^{2+}/Mg^{2+} at pH 6.4, $\delta_{ATP\text{-}NAD}$ = 0.35 ppm, $\delta_{ATP\text{-}NADH}$ = 0.12 ppm. The studies in panel (**b**) and (**c**) did not use external H_3PO_4 reference and thus the chemical shifts are relative

cantly under acidic pH. Our results show that under the neutral and basic range (pH 7–8), the mean $\delta_{ATP\text{-}NADH}$ 0.37 ± 0.04 ppm and the mean $\delta_{ATP\text{-}NAD}$ 0.52 ± 0.04 ppm are significantly less than that given by literature, whereas the mean $\delta_{NADH\text{-}NAD}$ 0.16 ± 0.02 ppm is consistent with previous reports (Table 1) [6]. Figure 2b exemplifies the fitting of the spectra from NAD^+-NADH mixtures using the MATLAB algorithm, with $\delta_{NADH\text{-}NAD}$ 0.22 ppm. Figure 2c demonstrated the separation of ATP, NAD^+, and NADH peaks in a mixture at pH 6.4, with $\delta_{ATP\text{-}NAD}$ 0.35 ppm and $\delta_{ATP\text{-}NADH}$ 0.12 ppm.

Lu et al. reported $\delta_{ATP\text{-}NAD}$ = 0.74 ppm, $\delta_{NADH\text{-}ATP}$ = 0.56 ppm, and no pH (~6–8) dependency of the chemical shifts of αATP, NAD^+, and NADH in solutions [6]. In this study, the solvent was pH-adjusted deionised water and phosphocreatine was added as an internal chemical shift reference, which might be pH dependent. Conversely, in our study, the solvent was pH-adjusted PBS to mimic physiological conditions, and an independent 85% H_3PO_4 phantom was included in the measurement as an external chemical shift reference (Fig. 2a). Another study reported that under low magnetic field (40.5 MHz) using 1.0 M H_3PO_4 as external reference but specifying no solvent conditions, $\delta_{ATP\text{-}NAD}$ was found to increase from 0.19 ppm to 0.35 ppm when pH varied from strong acidic to strong basic [14]. Thus, it is crucial to address these discrepancies and investigate whether chemical shifts alter significantly with pH of solvents used and in the presence of other biological molecules to determine NAD^+ and NADH properly. In this regard, we acknowledge the potential experimental errors in the delicate measurement of chemical shifts in phantoms by a preclinical scanner. Therefore, we should repeat our measurements with a high-resolution NMR system.

In summary, based on this explorative study of breast cancer xenografts supported by the phantom study, we found that the chemical shift offsets between NAD(H) and αATP are pH dependent and can vary significantly beyond the range reported in the literature. Despite the possibility of quantifying NAD(H) in tumours *in vivo*, more investigations are needed to address several essential questions. For example, it remains unknown whether the chemical shifts of NAD(H) are dependent on tissue microenvironment such as extracellular and intracellular pH *in vivo* and the extent of this dependency. It is also known that other phosphorus-containing species (e.g., uridine diphosphate glucose) could resonate near the spectral region of αATP but their contributions to the ^{31}P MR spectra in tumours remain unclear [9]. To answer these questions and obtain a more reliable spectral fitting of NAD(H), we need to achieve higher SNR and spectral resolution for *in vivo* ^{31}P-MRS, which could be attained using reduced spectral bandwidth, longer data acquisition time, and more sensitive detection coils among other improvements.

Acknowledgments We thank Stephen Pickup, Weixia Liu, Jerry D. Glickson, Rong Zhou, and David Nelson for support of the project. We also thank Qi Zhao for developing the 3D*i*CSI program. This work was supported by the US NIH Grant R01CA191207 (L. Z. Li).

References

1. Goodman RP, Calvo SE, Mootha VK (2018) Spatiotemporal compartmentalization of hepatic NADH and NADPH metabolism. J Biol Chem 293:7508–7516
2. Hassinen IE (2019) Signaling and regulation through the NAD^+ and $NADP^+$ networks. Antioxid Redox Signal 30:857–874
3. Xu HN, Li LZ (2014) Quantitative redox imaging biomarkers for studying tissue metabolic state and its heterogeneity. J Innov Opt Health Sci 7:1430002
4. Varone A, Xylas J, Quinn KP et al (2014) Endogenous two-photon fluorescence imaging elucidates metabolic changes related to enhanced glycolysis and glutamine consumption in precancerous epithelial tissues. Cancer Res 74:3067–3075
5. Li LZ, Xu HN, Ranji M et al (2009) Mitochondrial redox imaging for cancer diagnostic and therapeutic studies. J Innov Opt Health Sci 2:325–341
6. Lu M, Zhu XH, Zhang Y et al (2014) Intracellular redox state revealed by in vivo ^{31}P MRS measurement of NAD^+ and NADH contents in brains. Magn Reson Med 71:1959–1972
7. Zhu X-H, Lu M, Lee B-Y et al (2015) In vivo NAD assay reveals the intracellular NAD contents and redox state in healthy human brain and their age dependences. Proc Natl Acad Sci 112:2876–2881
8. Conley KE, Ali AS, Flores B et al (2016) Mitochondrial NAD(P)H In vivo: identifying natural indicators of oxidative phosphorylation in the (31)P magnetic resonance spectrum. Front Physiol 7:45–45
9. Kim SY, Cohen BM, Chen X et al (2017) Redox dysregulation in schizophrenia revealed by in vivo NAD+/NADH measurement. Schizophr Bull 43:197–204
10. Arias-Mendoza F, Nath K, Xu HN et al (2022) Assessment of nicotinamide adenine dinucleotide in human tissues by in vivo phosphorus-31 magnetic resonance spectroscopic imaging at 1.5 Tesla. Adv Exp Med Biol in press
11. Xu HN, Nioka S, Glickson JD et al (2010) Quantitative mitochondrial redox imaging of breast cancer metastatic potential. J Biomed Opt 15:3431714
12. Nath K, Nelson DS, Heitjan DF et al (2015) Lonidamine induces intracellular tumor acidification and ATP depletion in breast, prostate and ovarian cancer xenografts and potentiates response to doxorubicin. NMR Biomed 28:281–290
13. Nath K, Nelson DS, Ho AM et al (2013) ^{31}P and ^{1}H MRS of DB-1 melanoma xenografts: lonidamine selectively decreases tumor intracellular pH and energy status and sensitizes tumors to melphalan. NMR Biomed 26:98–105
14. Moon RB, Richards JH (1973) Determination of intracellular pH by ^{31}P magnetic resonance. J Biol Chem 248:7276–7278

Acidosis-Induced Regulation of Egr1 and Ccn1 *In Vitro* and in Experimental Tumours *In Vivo*

M. Rauschner, S. Reime, A. Riemann, and O. Thews

Abstract

Extracellular acidosis is a characteristic of solid tumours, resulting from hypoxia-induced glycolytic metabolism as well as from the "Warburg effect" (aerobic glycolysis). The acidic environment has shown to affect functional tumour properties (proliferation, migration, invasion) and thus the aim of the study was to identify signalling mechanisms, mediating these pH-dependent effects. Therefore, the serum response factor (Srf) and the activation of the serum response element (SRE) by acidosis were analysed in AT-1 prostate carcinoma cells. Furthermore, the expression of downstream targets of this cascade, namely the early growth response 1 (Egr1), which seems to be involved in tumour proliferation, and the cellular communication network factor 1 (Ccn1), which both contain SRE in their promotor region were examined in two tumour cell lines. Extracellular acidification led to an upregulation of Srf and a functional activation of the SRE. Egr1 expression was increased by acidosis in AT-1 cells whereas hypoxia had a suppressive effect. In experimental tumours, *in vivo* Egr1 and Ccn1 were also found to be acidosis-dependent. Also, it turned out that pH regulated expression of Egr1 was followed by comparable changes of p21, which is an important regulator of the cell cycle.

This study identifies the Srf-SRE signalling cascade and downstream Egr1 and Ccn1 to be acidosis-regulated *in vitro* and *in vivo*, potentially affecting tumour progression. Especially linked expression changes of Egr1 and p21 may mediate acidosis-induced effects on cell proliferation.

Keywords

Tumor proliferation · Serum response factor (Srf) · Cyr61 · AT-1 cells

1 Introduction

Due to rapid growth, solid tumours exhibit an insufficient vascular network, causing hypoxia-induced glycolytic metabolism. This change in metabolism and the "Warburg effect" cause an acidification of extracellular tumour pH [1], which can affect amongst others cell proliferation, invasiveness and metastasis [2, 3], but the mechanism of how acidosis leads to these functional effects is still under investigation. In this study, we analysed the impact of the extracellular pH on the serum response factor (Srf) cas-

M. Rauschner · S. Reime · A. Riemann
O. Thews (✉)
Julius-Bernstein-Institute of Physiology, University of Halle, Halle, Germany
e-mail: oliver.thews@medizin.uni-halle.de

F. Scholkmann et al. (eds.), *Oxygen Transport to Tissue XLIII*, Advances in Experimental Medicine and Biology 1395, https://doi.org/10.1007/978-3-031-14190-4_40

cade which plays an important role in tumour progression. This transcription factor binds to serum response elements in the promotor regions of genes and is involved in the regulation of immediate early genes [4]. Furthermore, Srf is described to modulate gene expression in cancer [5], effecting either adhesion and migration with myocardin-related transcription factors as coactivators [6] or proliferation in association with ternary complex factors (TCFs) [7]. To further analyse potential downstream signalling cascades the early growth response 1 (Egr1) and cell communication network factor 1 (Ccn1), also known as Cyr61, were analysed since these genes contain Srf binding sites [8, 9] and their role in tumour progression has been described in multiple studies [10, 11]. A first link of immediate early genes and low pH was shown by an acidosis-induced activation of Egr1 in normal renal epithelial cells [12]. However, Egr1 as well as Ccn1 have not been studied in relation to extracellular acidosis in tumours. Hence, the aim of the study was to investigate, whether Egr1 and Ccn1 are also acidosis-regulated in cancer cell lines *in vitro* and *in vivo*, and thereby developing a deeper insight in the mechanism from tumour acidosis to malignant progression (Fig. 1a).

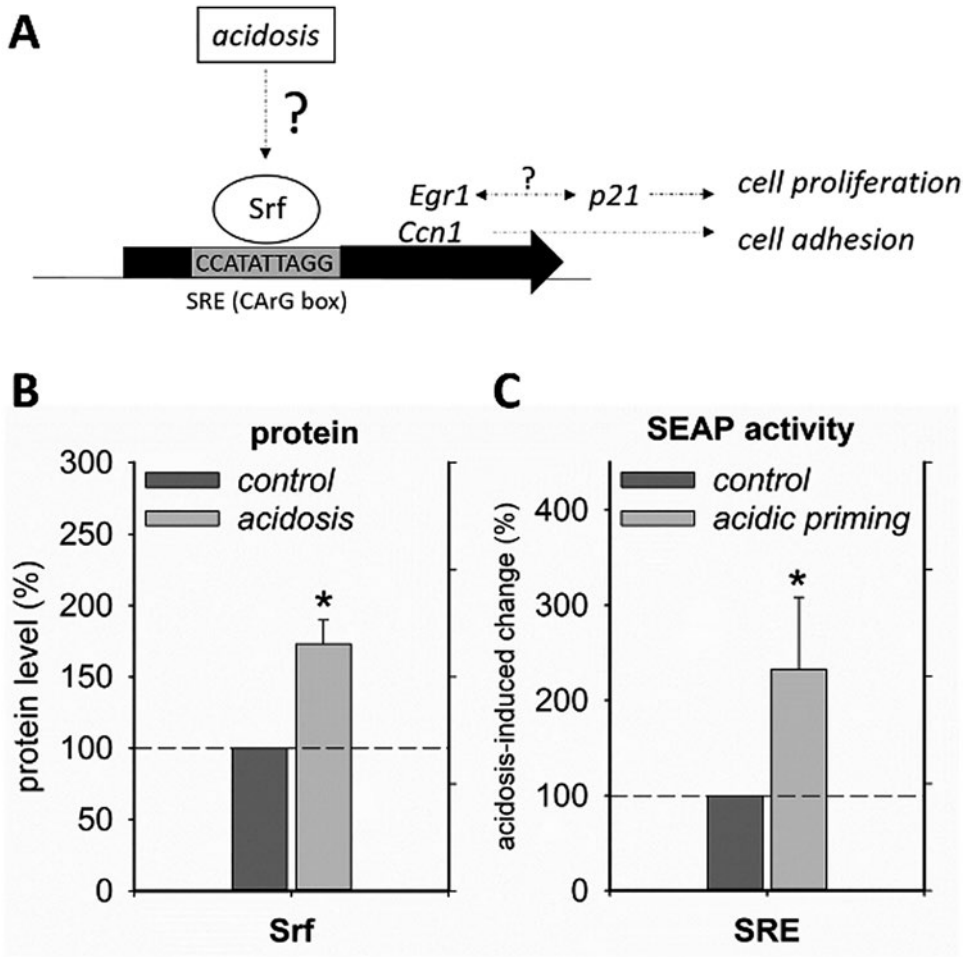

Fig. 1 (**a**) Possible mechanism how acidosis may lead to tumour progression via activation of serum response factor (Srf) and serum response element (SRE). Impact of acidosis on (**b**) serum response factor (Srf) protein expression and (**c**) SRE activity measured by secreted alkaline phosphatase (SEAP) in AT-1 cells. Cells were incubated 24 h at pH 6.6 (acidosis Srf expression) or 24 at pH 6.6 followed by 6 h at pH 7.4 (acidic priming SRE activity). Mean ± SEM, n = 4. (*) $p < 0.05$

2 Methods

2.1 Cell Culture and In Vivo Tumour Models

The subline AT-1 of the rat R-3327 Dunning prostate carcinoma was cultured in RPMI supplemented with 10% foetal calf serum (FCS) and the rat mammary carcinoma cell line Walker-256 which was grown with additional 10 mM L-glutamine, 20 mM HEPES and 0.15% $NaHCO_3$. Solid tumours were induced by subcutaneous implantation of tumour cells (6×10^6 cells in 0.5 mL isotonic saline) on the hind foot dorsum of male Copenhagen or Wistar rats. Tumour volume was determined with a caliper and tumours were analysed at a volume of 0.5–1.0 mL. To induce a more pronounced tumour acidosis *in vivo*, animals were treated with a combination of respiratory hypoxia (10% O_2) and a single injection of meta-iodobenzylguanidine (MIBG), an inhibitor of the respiratory chain at complex I [13]. The combination of hypoxia + inhibition of mitochondrial respiration forces the glycolytic metabolism of the tumour cells which leads to a lower pH in both tumour lines *in vivo* by about 0.5 (AT-1: from 7.02 ± 0.04 to 6.48 ± 0.08, Walker-256: from 7.16 ± 0.03 to 6.65 ± 0.07 [14]). After 24 h animals were sacrificed and tumours surgically removed. All experiments had previously been approved by the regional animal ethics committee and were conducted in accordance with German law on animal protection and the UKCCCR Guidelines [15]. After excision, tumours were minced and lysed with the TRIzol reagent (Thermo Fisher Scientific, Waltham, MA, USA) for RNA extraction.

2.2 Experimental Settings

Treatment of cells included incubation in serum-free media at pH 7.4 (control) or pH 6.6 (acidosis) under normoxic or hypoxic ($pO_2 \approx 1.5$ mmHg) conditions for 24 h. Serum response element activity was determined with secreted alkaline phosphate (SEAP) reporter gene assay. In brief, AT-1 cells were transfected with reporter plasmids and lacZ using the Mercury Pathway Profiling System (Clontech, CA, USA) and Lipofectamine 2000 Reagent (Thermo Fisher Scientific, Waltham, MA, USA). Secreted alkaline phosphate activity was measured with the AttoPhos AP Fluorescent Substrate System (Promega, Madison, WI, USA) and ß-galactosidase activity was determined for normalisation. The expression of Egr1, Ccn1 or p21 was assessed under control or acidotic conditions by quantitative PCR. In brief, 1 µg RNA was subjected to reverse transcription with SuperScript II reverse transcriptase (Invitrogen, Carlsbad, CA, USA) and expression changes were studied by qPCR using the Platinum SYBR Green qPCR Supermix (Invitrogen, Carlsbad, CA, USA) with hypoxanthine-guanine phosphoribosyltransferase (HPRT) as housekeeping gene. The acidosis-induced change of mRNA expression was described by the threshold cylce (Ct) determined by PCR which was then normalised to the expression of the housekeeper gene and the expression under control conditions at normal pH (ΔΔCt). An increase of the ΔΔCt value by "1" corresponds to a doubling of the mRNA level. Acidosis-induced regulation of Egr1 on the protein level was determined by western blot analysis. Protein lysates were separated by 12% SDS-PAGE and transferred to nitrocellulose membranes. Incubation was performed with respective primary antibodies for Egr1, Srf and β-Actin (Cell Signaling Technology, Danvers, MA, USA) as housekeeping gene. Samples were detected by the Odyssey Imaging System (LI-COR Biosciences, Lincoln, NE USA). All experiments were performed at least in triplicates and results are presented as mean ± SEM.

3 Results

To identify which transcription factors were activated under acidosis, a reporter gene assay measuring secreted alkaline phosphatase activity (SEAP) was used. Figure 1 shows that the protein level of the associated transcription factor Srf was increased under acidic conditions by about 73% (Fig. 1b). As a result, the serum response

element (SRE) was strongly (+133%) activated after acidic priming in AT1 prostate carcinoma cells (Fig. 1c). Since Egr1 and Ccn1 genes contain serum response elements [8, 9], an effect of acidosis on the expression of these genes was expected. Ccn1 was significantly upregulated by low pH in both cell lines (Fig. 2a). However, for Egr-1 the effect was cell line-dependent. Although in AT-1 cells expression was up-regulated, the expression in Walker-256 cells was markedly reduced (Fig. 2a). On protein level in AT-1 cells, acidosis increased Egr1 expression, whereas hypoxia led to a reduction to 50% (Fig. 2b). Surprisingly, in AT-1 tumours *in vivo* Egr1 and Ccn1 were significantly downregulated in more acidic tumours (Fig. 3a). Since it has been described that Egr-1 can affect cell proliferation and survival via the p21 signalling pathway, the impact of acidosis on this factor was measured. It was found that in both cell lines the expression of Egr-1 and p21 was changed by acidosis in the same direction (Fig. 3b). p21 was significantly increased in AT-1 but downregulated in Walker cells by acidosis. Again surprisingly, the expression in experimental tumours was changed in the opposite direction.

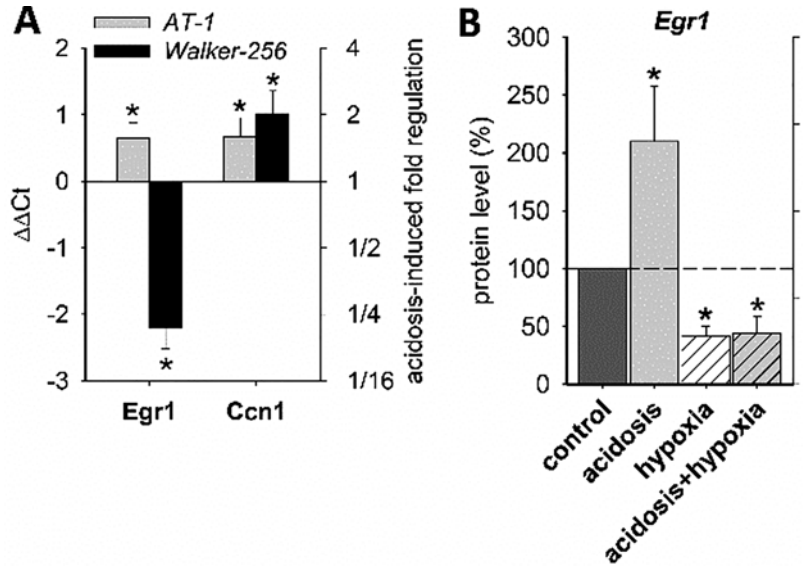

Fig. 2 (**a**) Impact of acidosis on Egr1 and Ccn1 mRNA expression in AT-1 and Walker-256 cells. (**b**) Impact of acidosis and/or hypoxia on Egr1 protein expression in AT-1 cells. Treatments for 24 h; values normalised to control conditions (pH 7.4 normoxia). Mean ± SEM, n = 5–10. (*) $p < 0.05$

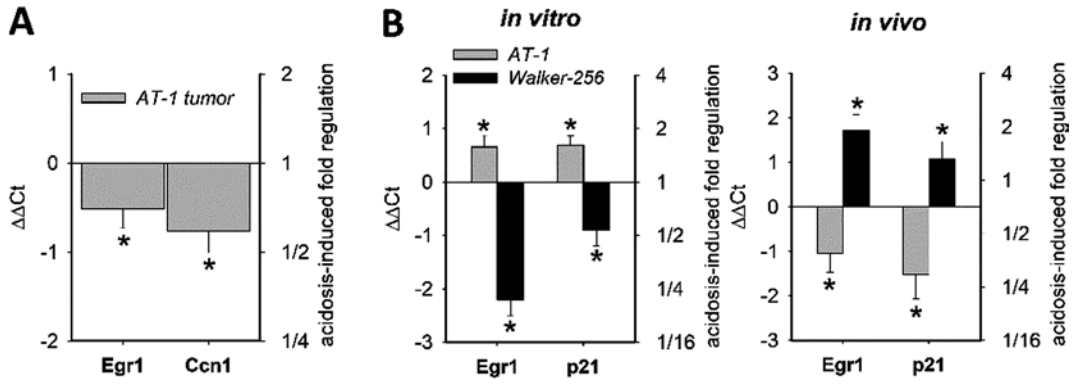

Fig. 3 Impact of acidosis (24 h) on (**a**) Egr1 and Ccn1 mRNA expression in AT-1 tumours and (**b**) Egr1 and p21 mRNA expression in AT-1 and Walker cells (*in vitro*) and tumours (*in vivo*).Values normalised to control conditions. Mean ± SEM, n = 5–10. (*) $p < 0.05$

4 Conclusion

Our study showed that acidosis increased the expression of Srf in tumour cells and by this induced the activation of SRE (AT-1, Fig. 1). Since Srf is an important transcription factor mediating tumour progression, it might be involved in mechanisms from tumour acidosis to malignant progression. Egr1 and Ccn1, which are genes downstream Srf/SRE, were upregulated by acidosis in AT-1 cells (Fig. 2a) whereas hypoxia had an opposing effect (Fig. 2b). Therefore, the upregulation seems to be acidosis-specific. The pH-dependent induction of Egr1 and Ccn1 was described by others [12, 16], however the present study shows that the effect on Egr1 seems to be cell line-dependent. Since Egr1 and Ccn1 genes contain serum response elements [8, 9], acidosis could at least in AT-1 cells regulate the expression via the Srf/SRE pathway. Because Egr1 has been described to modulate tumour growth and survival especially in prostate cancers [10], this mechanism can contribute to the impact of acidosis on the malignant progression of tumours. Although Egr1 is described to be increased in prostate cancers [10], studies for mammary cancer cells showed reduced levels of Egr1 [17], which might explain the acidosis-induced downregulation in Walker-256 cells (Fig. 2a). Ccn1 as a matrix associated protein was shown to be involved in prostate cancer development and found to be elevated in patient samples [11], also emphasising its potential role in the mediation of acidosis-induced tumour progression.

Figure 3a illustrates that Egr1 and Ccn1 expression was regulated in the opposite direction in tumours *in vivo* than in cell culture. One possible explanation for this opposing behaviour might be the method used to acidify the tumours *in vivo*. For this, stronger hypoxia in the tumour tissue was induced by inspiratory hypoxia (in addition to the inhibition of the respiratory chain by MIBG). However, hypoxia *per se* was found to decrease the expression of Egr1 also *in vitro* (Fig. 2b). Another possible explanation of the differences *in vitro* and *in vivo* might be that Srf is regulated by the cytoskeleton dynamics (e.g., G- or F-actin) but also by cytokines or TNF-α. Since these factors are present *in vivo* but not *in vitro* it is conceivable that Srf is regulated by acidosis, but this effect is overwritten by other activation mechanisms. In addition, it is known that Egr1 expression is also regulated by other signalling cascades (e.g., Erk1/2). The present results also indicate that the cyclin-dependent kinase inhibitor p21 is upregulated by acidosis via upregulation.

In conclusion, this study identifies the Srf-SRE signalling cascade and downstream Egr1 and Ccn1 to be acidosis-regulated *in vitro* and *in vivo*, potentially affecting tumour progression. Especially a linked expression of Egr1 and p21 might mediate acidosis-induced effects on cell proliferation.

Acknowledgments The study was supported by the Deutsche Forschungsgemeinschaft DFG (grant TH482/6-1).

References

1. Justus CR, Dong L, Yang LV (2013) Acidic tumor microenvironment and pH-sensing G protein-coupled receptors. Front Physiol 4:354
2. Rauschner M et al (2021) Impact of the acidic environment on gene expression and functional parameters of tumors in vitro and in vivo. J Exp Clin Cancer Res 40(1):10
3. Thews O, Riemann A (2019) Tumor pH and metastasis: a malignant process beyond hypoxia. Cancer Metastasis Rev 38(1–2):113–129
4. Chai J, Tarnawski AS (2002) Serum response factor: discovery, biochemistry, biological roles and implications for tissue injury healing. J Physiol Pharmacol 53(2):147–157
5. Muller S et al (2019) IGF2BP1 promotes SRF-dependent transcription in cancer in a m6A- and miRNA-dependent manner. Nucleic Acids Res 47(1):375–390
6. Medjkane S et al (2009) Myocardin-related transcription factors and SRF are required for cytoskeletal dynamics and experimental metastasis. Nat Cell Biol 11(3):257–268
7. Gualdrini F et al (2016) SRF co-factors control the balance between cell proliferation and contractility. Mol Cell 64(6):1048–1061
8. Latinkic BV, O'Brien TP, Lau LF (1991) Promoter function and structure of the growth factor-inducible immediate early gene cyr61. Nucleic Acids Res 19(12):3261–3267

9. Qureshi SA et al (1991) v-Src activates mitogen-responsive transcription factor Egr-1 via serum response elements. J Biol Chem 266(17):10802–10806
10. Adamson ED, Mercola D (2002) Egr1 transcription factor: multiple roles in prostate tumor cell growth and survival. Tumour Biol 23(2):93–102
11. D'Antonio KB et al (2010) Extracellular matrix associated protein CYR61 is linked to prostate cancer development. J Urol 183(4):1604–1610
12. Yamaji Y et al (1994) Acid activation of immediate early genes in renal epithelial cells. J Clin Invest 94(3):1297–1303
13. Kalliomäki T, Hill RP (2004) Effects of tumour acidification with glucose+MIBG on the spontaneous metastatic potential of two murine cell lines. Br J Cancer 90(9):1842–1849
14. Riemann A, Reime S, Thews O (2019) Acidic extracellular environment affects miRNA expression in tumors in vitro and in vivo. Int J Cancer 144(7):1609–1618
15. Workman P et al (2010) Guidelines for the welfare and use of animals in cancer research. Br J Cancer 102(11):1555–1577
16. Hirschfeld M et al (2011) Expression of tumor-promoting Cyr61 is regulated by hTRA2-beta1 and acidosis. Hum Mol Genet 20(12):2356–2365
17. Huang RP et al (1997) Decreased Egr-1 expression in human, mouse and rat mammary cells and tissues correlates with tumor formation. Int J Cancer 72(1):102–109

Perfusion-Limited Hypoxia Determines the Outcome of Radiation Therapy of Hypoxic Tumours

Filippo Schiavo, Iuliana Toma-Dasu, and Emely Kjellsson Lindblom

Abstract

Despite advancements in functional imaging, the resolution of modern techniques is still limited with respect to the tumour microenvironment. Radiotherapy strategies to counteract e.g., tumour hypoxia based on functional imaging therefore carry an inherent uncertainty that could compromise the outcome of the treatment. It was the aim of this study to investigate the impact of variations in the radiosensitivity of hypoxic tumours in small regions in comparison to the resolution of current imaging techniques on the probability of obtaining tumour control. A novel *in silico* model of three-dimensional tumour vasculature and oxygenation was used to model three tumours with different combinations of diffusion-limited, perfusion-limited and anaemic hypoxia. Specifically, cells in the transition region from a tumour core with diffusion-limited hypoxia to the well-oxygenated tumour rim were considered with respect to their differential radiosensitivity depending on the character of the hypoxia. The results showed that if the cells in the transition region were under perfusion-limited hypoxia, the tumour control probability was substantially lower in comparison to the case when the cells were anaemic (or under diffusion-limited hypoxia). This study therefore demonstrates the importance of differentiating between different forms of hypoxia on a scale currently unattainable to functional imaging techniques, lending support to the use and importance of radiobiological modelling of the cellular radiosensitivity and response at microscale.

Keywords

Radiotherapy · Radioresistance · Oxygen enhancement ratio (OER) · In silico model

1 Introduction

Solid tumours often contain cells in hypoxic conditions [1]. This is a result of the underdeveloped vasculature characteristic of neoplasms, as they rapidly outgrow their own capillary network and thus prevent the formation of an adequate blood supply [2]. As hypoxic cells may require up to three times the radiation dose for isoeffect in comparison to oxic conditions, tumour hypoxia has long been considered a major threat to the success of radiotherapy [3]. However, the direct effect from an increased radioresistance as typi-

F. Schiavo (✉) · I. Toma-Dasu · E. K. Lindblom
Department of Physics, Stockholm University, Stockholm, Sweden

Department of Oncology and Pathology, Karolinska Institutet, Solna, Sweden
e-mail: fillippo.schiavo@fysik.su.se

F. Scholkmann et al. (eds.), *Oxygen Transport to Tissue XLIII*, Advances in Experimental Medicine and Biology 1395, https://doi.org/10.1007/978-3-031-14190-4_41

cally quantified by the oxygen enhancement ratio (OER) [4] is likely not enough to characterise the radioresistance *in vivo*. There are several pathophysiological mechanisms that cause hypoxia [5], and, depending on the origin, cells radiosensitivity could differ substantially: a chronic deprivation of oxygen due to its limited diffusion distance may lead to higher sensitivity because of a diminished viability, while cells acutely hypoxic as a result of a cyclic loss of perfusion inside vessels could represent the most resistant type, indicating the importance of accounting for the type of hypoxia when assessing the level of radioresistance [6].

While this distinction could be crucial in the outcome prediction for a given treatment and hence for selecting the best treatment approach, the resolution of modern functional imaging techniques is still generally rather limited, considering the microscopic scale on which critical variations in the radiosensitivity occur [7].

To bridge this gap between imaging and response prediction, *in silico* modelling of key physiological features such as the oxygenation offers a unique opportunity to study the microscopic effects on the outcome. A novel and complex model of tissue oxygenation has therefore been recently developed [8] and applied to simulate tumours with combinations of diffusion-limited, perfusion-limited and anaemic hypoxia (the latter resulting from limitations either in diffusion from the vessels or perfusion through the vessels), with the specific aim of assessing the impact on the outcome of the transition region between a chronically hypoxic subvolume and its better oxygenated surroundings.

2 Methods

A 3D model of tissue vasculature and oxygenation was used to simulate tumours with different kinds of hypoxia. A complex network of realistic vessels is constructed inside a cubic geometrical structure enclosing a spherical tumour. By means of fractal theory, vessels are "grown" evenly from around the tumour towards its centre. Inside a spherical central subregion with a specified radius, diffusion-limited hypoxia was simulated by reducing the density of vessels, reflecting the *in vivo* increased intervascular distance [5]. The oxygen transport equation was then solved at voxel level with a finite difference method assuming stationary blood flow from the vessels as sources of oxygen diffusion with no convection and assuming an isotropic tumour tissue. Two tumour models containing either perfusion-limited or anaemic hypoxia were also created by randomly closing a fraction of vessels or halving their original oxygen partial pressure of 40 mmHg, respectively. Anaemic hypoxia was hence assumed to produce the same effect (a further reduction in the oxygen diffusion distance) independently on its cause, while the cell viability was accounted for in the TCP calculations. The radius of the simulated tumours was 3 mm, and the resolution was 10 μm (Fig. 1). Single-fraction radiotherapy with doses of 18–30 Gy, as representative of the fractional doses typically delivered in hypofractionated stereotactic body radiotherapy (SBRT) treatments [9–12], was simulated assuming a homogeneous dose distribution in the modelled tumours. The impact from the different kinds of hypoxia on the treatment outcome was then evaluated by calculating the tumour control probability (TCP). The response of the different forms of hypoxia was accounted for in the voxel-wise calculation of the surviving fraction by using the linear-quadratic model with inducible repair [13]. For all three tumour models, a core volume with a radius of 1.0 mm was considered as under diffusion-limited hypoxia, and the surviving fraction in this region was hence calculated by Eq. 1:

$$SF_{DL} = \exp\left(-\frac{\alpha_S}{OMF} D - \frac{\beta}{OMF} D^2 \right) \quad (1)$$

where α_S and β are the radiosensitivity parameters, OMF is the oxygen-modifying factor dependent on the local oxygen tension [14], and D is the radiation dose. For the tumours also containing anaemic hypoxia or perfusion-limited hypoxia, a transition region between the tumour core under diffusion-limited hypoxia and the well-oxygenated rim of the tumour was consid-

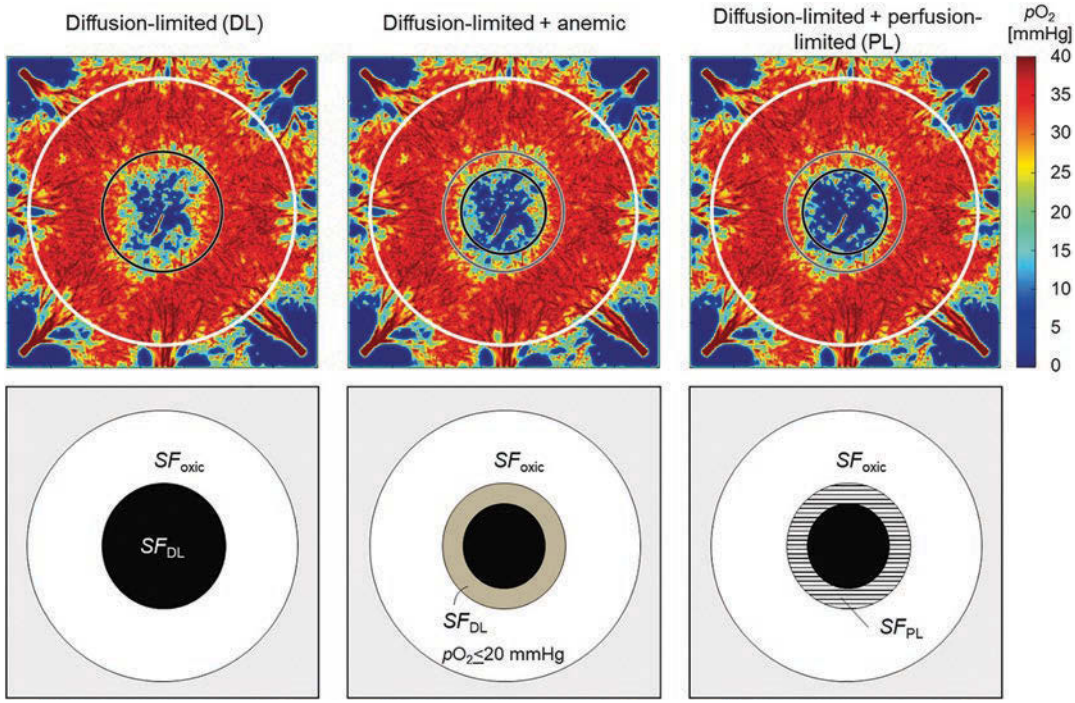

Fig. 1 Cross-sections of the tumour models showing the pO_2 maps (upper panel) and the regions in which the different expressions for calculating the cell survival were used (lower panel)

ered explicitly. In this region, with a radius extending from 1.0 mm to 1.4 mm, the surviving fraction was calculated depending on the nature of the hypoxia (i.e. perfusion-limited or anaemic). Thus, for the tumour under perfusion-limited hypoxia:

where the parameters α_R and D_C describe the inducible repair as originally defined by Denekamp and Dasu [13]. For the tumour containing diffusion-limited and anaemic hypoxia, survival in the transition region was calculated by assuming that voxels with an oxygen partial pressure below 20 mmHg were supplied mainly by the anaemic vessels and thus chronically hypoxic, and others being acutely hypoxic, i.e., under perfusion-limited hypoxia:

$$SF_{DL+PL} = \exp\left\{-\frac{\alpha_R}{OMF}\left[1+\left(\frac{\alpha_S}{\alpha_R}-1\right)e^{-\frac{D}{D_C \bullet OMF}}\right]D-\frac{\beta}{OMF}D^2\right\} \tag{2}$$

$$SF_{DL+anemic} = \begin{cases} \exp\left\{-\frac{\alpha_R}{OMF}\left[1+\left(\frac{\alpha_S}{\alpha_R}-1\right)e^{-\frac{D}{D_C \bullet OMF}}\right]D-\frac{\beta}{OMF}D^2\right\} & for\ pO_2 > 20\,mmHg \\ \exp\left(-\frac{\alpha_S}{OMF}D-\frac{\beta}{OMF}D^2\right) & for\ pO_2 \le 20\,mmHg \end{cases} \tag{3}$$

Cell survival in the well-oxygenated external rim was calculated by Eq. 4:

$$SF_{oxic} = \exp\left\{-\alpha_R\left[1+\left(\frac{\alpha_S}{\alpha_R}-1\right)e^{-\frac{D}{D_C}}\right]D-\beta D^2\right\} \quad (4)$$

Assuming a homogeneously distributed population of cells $N_0 = 5{\cdot}10^5$ before irradiation, the total TCP was calculated using an LQ-Poisson-based model as in previous studies [6].

The impact on the TCP from the size of the transition region was also studied by varying the size of the tumour core under diffusion-limited hypoxia between 0 and 1.4 mm. The numerical values of the modelling parameters used in the simulations were $\alpha_R = 0.33\ Gy^{-1}$, $\alpha_S = 0.66\ Gy^{-1}$, $\beta = 0.033\ Gy^{-2}$, $D_C = 0.27$ Gy, and $OMF_{max} = 3$.

3 Results and Discussion

The hypoxic fraction defined based on a 10 mmHg threshold in the hypoxic volume was 12.4%, 16.5% and 21.2% for the tumour with diffusion-limited, diffusion-limited + anaemic and diffusion- + perfusion-limited hypoxia, respectively. In the transition region (the area between the grey and black circles in Fig. 1), the hypoxic fraction was about 3% for both the tumours with diffusion-limited + anaemic hypoxia and diffusion- + perfusion-limited hypoxia. The highest TCP was consistently found in the tumour with diffusion-limited hypoxia only (Table 1). For the tumours with anaemic or perfusion-limited hypoxia in the transition region, the TCP was lower for 18-22 Gy. For the tumour with perfusion-limited hypoxia, the TCP was substantially lower than for the other two cases except for the highest dose.

Table 1 Tumour control probability in the three modelled tumours after single doses of 18–30 Gy. The relative size of the transition region is 29% with respect to the to the maximal radius of 1.4 mm

	TCP (%)			
Dose (Gy)	18	20	22	30
DL	57.8	78.0	84.5	86.8
DL + Anaemic	48.0	74.2	83.4	86.8
DL + PL	25.8	62.3	79.7	86.8

DL Diffusion-limited, *PL* Perfusion-limited

For all tumours there was a marked decrease in TCP when reducing the dose from 22 Gy to 18 Gy, which was even steeper when going from 20 Gy to 18 Gy, a reduction by only 2 Gy. Furthermore, the relative decrease is biggest for the tumour with perfusion-limited hypoxia in the transition region, indicating a higher sensitivity to dose heterogeneities. The impact of perfusion-limited hypoxia is dependent on the viability of the cells whether the duration of the loss of perfusion is specifically accounted for or not. However, given the lack of experimental data available in the literature the distinction was limited to chronic and acute terms for characterising the cells' viability and hence radiosensitivity. In light of the sharp dose gradients in SBRT, the oxygenation in the transition region could be crucial with respect to the outcome of the treatment. This is further demonstrated in Fig. 2, which displays the change in TCP as the transition region becomes progressively larger, corresponding to a decrease of the more radiosensitive tumour core under diffusion-limited hypoxia. While the tumours with diffusion-limited and diffusion-limited + anaemic hypoxia are minimally affected by this change, the TCP for the tumour with diffusion- + perfusion-limited hypoxia drops to zero as the proportion of perfusion-limited hypoxic cells increases. Depending on the position and size of the transition region, the outcome of an SBRT treatment could therefore be highly affected by where the sharp dose gradients are located within the target.

The vasculature and oxygenation model here adopted could represent a further step in the personalisation of radiotherapy given the opportunity to consider different oxygenation scenarios in the treatment planning process. An example of this could be related to the choice of the steep dose gradient localisation, which is characteristic of stereotactic approaches, where the hypothesis of even a small fraction of radioresistant cells may favour the choice of plans that minimise the presence of cold spots close to the periphery of the target.

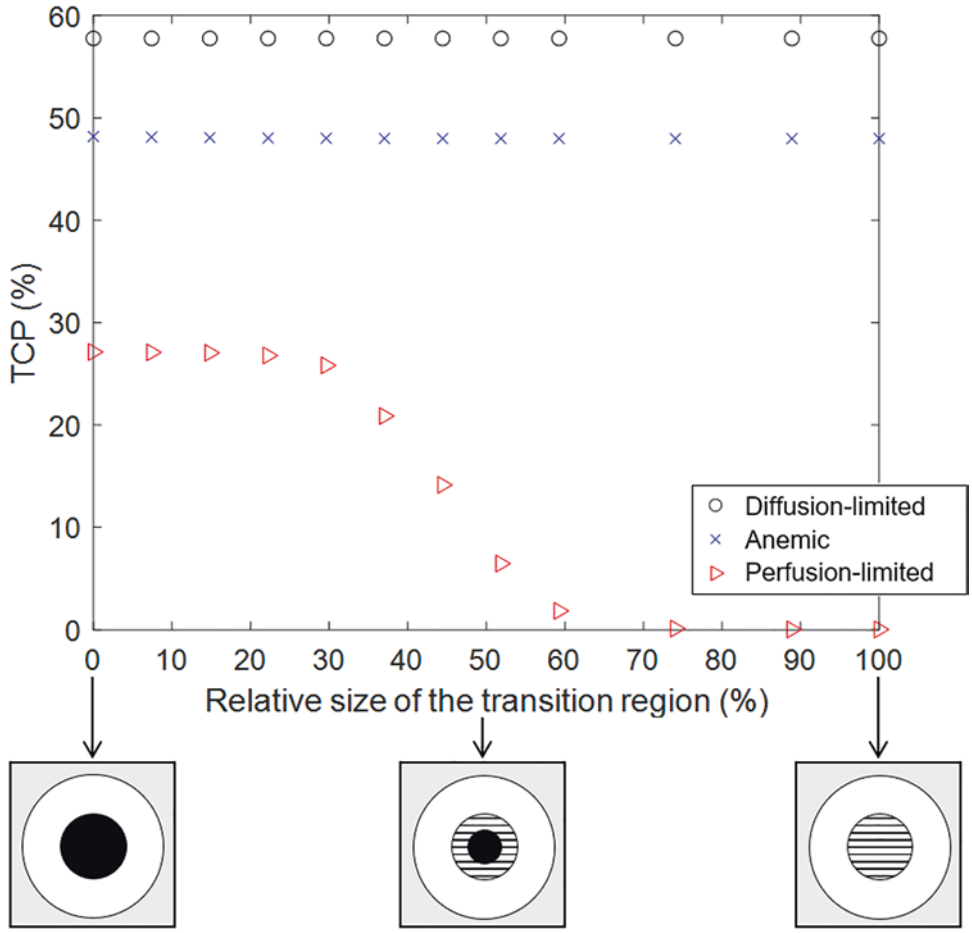

Fig. 2 The TCP for the three modelled tumours after exposure to a dose of 18 Gy, as a function of the radius of the transition region relative to the maximal radius of 1.4 mm

4 Conclusions

The ability to differentiate between different forms of hypoxia could have a crucial impact on the outcome of radiotherapy. Even a very limited tumour compartment of resistant cells, too small to identify by modern imaging techniques, could substantially reduce the probability of obtaining tumour control in radiotherapy. Radiobiological modelling of cellular response depending on oxygen supply on the microscale enables the studying of mechanisms and effects invisible to current imaging techniques, and therefore represents a powerful tool in bridging the gap between imaging and reality in radiotherapy.

Acknowledgments Financial support from the Cancer Research Funds of Radiumhemmet and The Swedish Research Council (2020-04618) is gratefully acknowledged.

References

1. Rasey JS, Koh WJ, Evans ML et al (1996) Quantifying regional hypoxia in human tumors with positron emission tomography of [18F]fluoromisonidazole: a pretherapy study of 37 patients. Int J Radiat Oncol Biol Phys 36(2):417–428
2. Vaupel P, Kallinowski F, Okunieff P (1989) Blood flow, oxygen and nutrient supply, and metabolic microenvironment of human tumors: a review. Cancer Res 49:6449–6465
3. Overgaard J (2007) Hypoxic radiosensitization: adored and ignored. J Clin Oncol 25(26):4066–4074

4. Hall EJ, Giaccia AJ (2012) Radiobiology for the radiologist, 7th edn. Lippincott Williams & Wilkins
5. Vaupel P, Mayer A (2014) Hypoxia in tumors: pathogenesis-related classification, characterization of hypoxia subtypes, and associated biological and clinical implications. Adv Exp Med Biol 812:19–24
6. Lindblom E, Toma-Dasu I, Dasu A (2018) Accounting for two forms of hypoxia for predicting tumour control probability in radiotherapy – an in silico study. Adv Exp Med Biol 1072:183–187
7. Ljungkvist AS, Bussink J, Kaanders JH et al (2006) Dynamics of hypoxia, proliferation and apoptosis after irradiation in a murine tumor model. Radiat Res 165(3):326–336
8. Schiavo F, Kjellsson Lindblom E, Toma-Dasu I (2022) Towards the virtual tumor for optimizing radiotherapy treatments of hypoxic tumors: A novel model of heterogeneous tissue vasculature and oxygenation. J Theor Biol 547:111175
9. Timmerman RD, McGarry R, Yiannoutsos C et al (2006) Excessive toxicity when treating central tumors in a phase II study of stereotactic body radiation therapy for medically inoperable early-stage lung cancer. J Clin Oncol 24(30):4833–4839
10. Timmerman RD, Paulus R, Pass HI et al (2018) Stereotactic body radiation therapy for operable early-stage lung cancer: findings from the NRG Oncology RTOG 0618 trial. JAMA Oncol 4(9):1263–1266
11. Olsen JR, Robinson CG, El Naqa I et al (2011) Dose–response for stereotactic body radiotherapy in early-stage non-small-cell lung cancer. Int J Radiat Oncol Biol Phys 81(4):e299–e303
12. Fritz P, Kraus HJ, Blaschke T et al (2008) Stereotactic, high single-dose irradiation of stage I non-small cell lung cancer (NSCLC) using four-dimensional CT scans for treatment planning. Lung Cancer 60:193–199
13. Denekamp J, Dasu A (1999) Inducible repair and the two forms of tumour hypoxia – time for a paradigm shift. Acta Oncol 38:903–918
14. Toma-Dasu I, Dasu A (2013) Modelling tumour oxygenation, reoxygenation and implications on treatment outcome. Comput Math Methods Med 2013:141087

Improved Oxygenation of Human Skin, Subcutis and Superficial Cancers Upon Mild Hyperthermia Delivered by WIRA-Irradiation

Andreas R. Thomsen, Michael R. Saalmann, Nils H. Nicolay, Anca-L Grosu, and Peter Vaupel

Abstract

Clinical trials have shown that mild hyperthermia (HT) serves as an adjunct to cancer treatments such as chemo- and radiotherapy. Recently, a high efficacy of mild HT immediately followed by hypofractionated radiotherapy (RT) in treatment of recurrent breast cancer has been documented if temperatures of 39–43 °C are achieved for 40–60 min. In the present study, temperature and oxygenation profiles were measured in superficial tissues of healthy volunteers exposed to water-filtered infrared-A- (wIRA)- irradiation, to verify that adequate thermal doses together with the improved tumor oxygenation necessary for radiosensitisation are obtained. Experiments were performed using a wIRA-system equipped with two wIRA-radiators, each with a thermography camera for real-time monitoring of the skin surface temperature. Temperatures within the abdominal wall were measured with fibre optic sensors at defined tissue depths (subepidermal, and 1–20 mm inside the tissue). The corresponding tissue pO_2 values were assessed with fluorometric microsensors. In selected situations, hyperspectral tissue imaging was used to visualise the oxygenation status of normal skin and superficial tumours in patients. Pretreatment skin surface temperature was 34.6 °C. Upon wIRA exposure, average skin surface temperatures reached 41.6 °C within 5–12 min. Maximum tissue temperatures of 41.8 °C were found at a tissue depth of 1 mm, with a steady decline in deeper tissue layers (41.6 °C @ 5 mm, 40.8 °C @ 10 mm, 40.6 °C @ 15 mm, and 40.1 °C @ 20 mm). Effective HT levels ≥39 °C were established in tissue depths up to 25 mm. Tissue heating was accompanied by a significant increase in tissue pO_2 values [e.g., at a tissue depth of 13 mm mean pO_2 rose from 46 mmHg to 81 mmHg (@ T = 40.5 °C). In the post-heating phase (+ 5 min), pO_2 was 79 mmHg (@ T = 38 °C) and 15 min post-heat pO_2 was 72 mmHg (@ T = 36.8 °C)]. pO_2 values remained elevated for 30–60 min post-heat. Non-invasive monitoring of normal skin and

A. R. Thomsen (✉) · N. H. Nicolay · A.-L. Grosu · P. Vaupel
Department of Radiation Oncology, University Medical Center, University of Freiburg, Freiburg, Breisgau, Germany

German Cancer Consortium (DKTK) Partner Site Freiburg, German Cancer Research Center (DKFZ), Heidelberg, Germany
e-mail: andreas.thomsen@uniklinik-freiburg.de

M. R. Saalmann
Department of Radiation Oncology, University Medical Center, University of Freiburg, Freiburg, Breisgau, Germany

F. Scholkmann et al. (eds.), *Oxygen Transport to Tissue XLIII*, Advances in Experimental Medicine and Biology 1395, https://doi.org/10.1007/978-3-031-14190-4_42

of recurrent breast cancers confirmed the improved O_2 status by wIRA-HT. In conclusion, wIRA-irradiation enables effective tissue heating (T = 39–43 °C) associated with distinct increases in blood flow and pO_2. These adjustments unequivocally meet the requirement for effective radiosensitisation.

Keywords

Hypofractionated radiotherapy · Water-filtered infrared-A-(wIRA) irradiation · Radiosensitizatiom · Thermography

1 Introduction

Clinical trials have shown that mild hyperthermia (HT) (HT-level: 39–43 °C) –*inter alia*- promotes healing of acute and chronic wounds [1], prevents postoperative wound infection [2], can be beneficial in patients with fibromyalgia or circumscript cutaneous scleroderma [3], and can improve skin graft transplantation. In addition, mild HT can reduce the infectious burden of thermosensitive bacteria (e.g., M. ulcerans, C. trachomatis) [4]. Furthermore, mild HT is increasingly used as an adjunct to established cancer treatments as chemotherapy [5–7] and radiotherapy [8, 9]. In the treatment of recurrent breast cancer, mild HT, immediately followed by hypofractionated radiotherapy (RT), was recently shown to allow for reduced radiation doses (20 Gy at single doses of 4 Gy once per week, instead of 50–60 Gy at 2 Gy five times per week). The mentioned protocol, which resulted in temperatures of 39–43 °C for 40–60 min, was associated with a high efficacy and low toxicity [10, 11]. In the present study, systematic measurements were performed to assess temperature and oxygenation profiles in superficial tissues exposed to water-filtered infrared-A- (wIRA)- irradiation, to verify that adequate thermal doses together with improved tumour oxygenation necessary for radiosensitisation are obtained.

2 Methods

2.1 Delivery of wIRA-Hyperthermia

Superficial hyperthermia was applied using the TWH 1500 wIRA-hyperthermia system (hydrosun®, Müllheim, Germany) with two irradiators, controlled independently by two thermographic cameras and safety pyrometers. Irradiators were positioned at a distance of 34 cm between irradiator exit and skin surface, which results in an approximate irradiance of 200 mW/cm^2.

For application of hyperthermia, the lower abdominal wall (10 treatment sessions) and the lumbar region (2 treatment sessions) of healthy volunteers (1 female, and 2 males, age: 35–49 years) were exposed to wIRA-irradiation for approximately 60 min. Measurements were performed in 3 healthy individuals during 12 different sessions, using 7 pre-selected locations per session. Time interval between measurements in each individual was >1 week. A second series of investigations was performed in 2 tumour patients. Here, wIRA therapy was accompanied by hyperspectral imaging. Participation in this procedure has been found to be ethically sound by the local ethics authority, and volunteers gave their informed consent.

2.2 Non-invasive Monitoring of Skin Surface Temperatures (Thermography)

Using this therapeutic approach, maximum skin surface temperature is continuously regulated by a control circuit for each of the two irradiators, which is a key element of the TWH 1500 system: When thermography assesses a hot spot, i.e., a temperature above a defined maximum (*switch-off temperature*: 43 °C), the power supply to the respective irradiator is instantly switched off via a relay. As soon as the temperature of the hot spot drops (to *switch-on temperature:* 42.5 °C), the irradiator is turned back on [12]. In steady state

conditions, between 1 and 4 on-off cycles take place per minute. The resulting peaks in temperature traces are visible in thermography records, but also in superficial skin layers, measured invasively as described below.

A typical example of serially assessed thermographic images during the onset (0–10 min) of wIRA-HT of the skin surface and *in situ* positioning of the temperature probes is shown in Fig. 1.

2.3 Minimally Invasive Measurement of Tissue Temperatures (Thermometry) and Tissue Oxygenation

Tissue temperatures within skin and subcutis of the abdominal wall were measured using fibre-optic sensors (OTG-M600, Opsens, Quebec, Canada). Corresponding tissue oxygen partial pressures (pO_2) were assessed with the OxyLite-Pro system (Oxford Optronix, Abington, UK). Characteristic traces of subcutaneous temperatures and pO_2 before, during and after wIRA-HT are shown in Fig. 2.

Fibre-optic temperature probes (diameter: 0.7 mm) and oxygen sensors (diameter: 0.4 mm) were transepidermally inserted via 1.1 mm i.v. catheters (Vasofix™ Safety, Braun, Melsungen, Germany) down to defined tissue depths of 1–20 mm, so that dermis and subcutis are addressed. Position of invasive catheters and probes is visible on thermography images, e.g. in Fig. 1.

In selected situations, hyperspectral tissue imaging (TIVITA™, Diaspective Vision, Am Salzhaff, Germany) was used to visualise the HbO_2 saturation (stO_2) in the microcirculation of the sub-papillary/upper dermis layers [13] of healthy volunteers (n = 3 sessions) and in superficial chest wall tumours (2 patients).

Registration of pre-heating and post-heating temperature and oxygen levels completed the data collection upon wIRA-exposure.

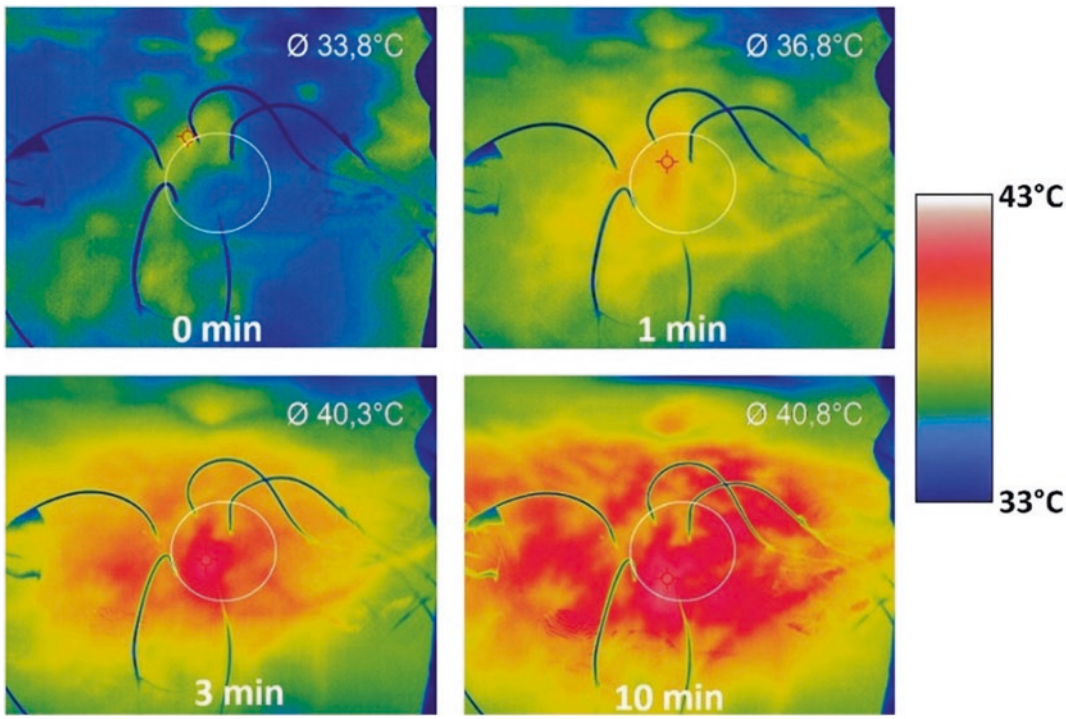

Fig. 1 Thermography images from the first 10 min of wIRA-hyperthermia of the abdominal wall of a healthy volunteer. Cables from invasive probes are visible. Respective mean region of interest (ROI, depicted with a circle) temperatures are presented in the upper right corners

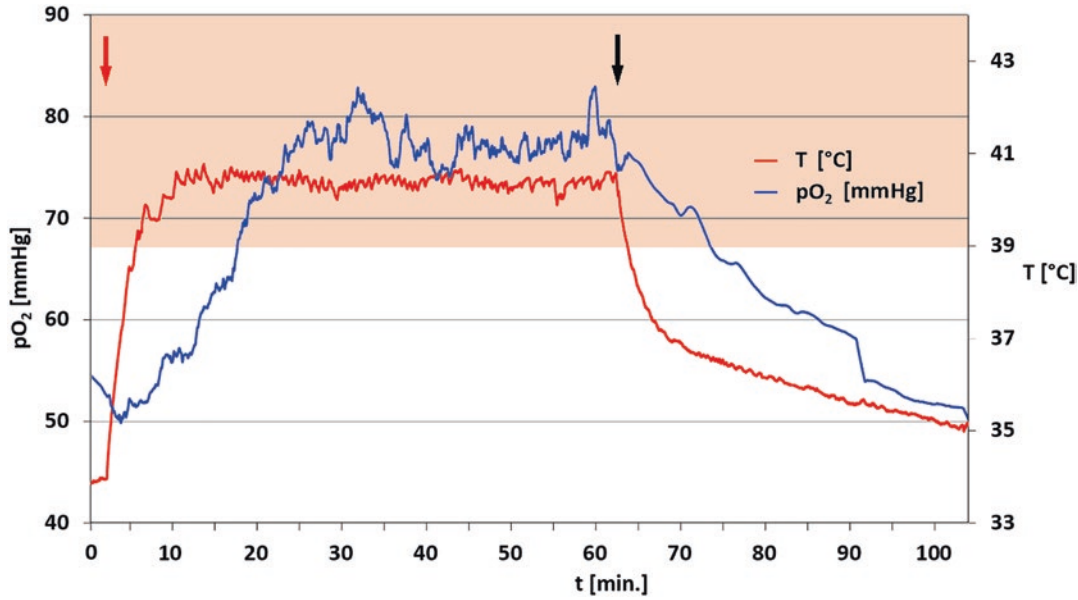

Fig. 2 Tissue temperature (red trace) and pO_2 (blue trace) during a representative treatment of a healthy volunteer (depth 8 mm). The temperature range of mild hyperthermia (39–43 °C) is marked in light red. Start and termination of wIRA-irradiation are marked by arrows

3 Results

Heating of skin and deeper tissue layers by wIRA-irradiation resulted in temperatures >39 °C within 2 min (surface and ≤ 5 mm) to 12 min (17–20 mm). Maximum temperatures of about 42 °C were found in subepidermal regions, with a steady decline in deeper layers reaching 40.1 °C at a depth of 20 mm. Upon the start of heating, increases in tissue temperatures were steepest close to the body surface, where T > 40 °C were achieved within 4 ± 2 min, whereas up to 30 min of wIRA-heating were required to reach this temperature at a depth of 20 ± 1 mm. Temperature distribution pre-heating and during steady state hyperthermia in different tissue layers are shown in Fig. 3.

In all tissue depths addressed (subepidermal, 8–10 mm, and 17–20 mm), wIRA-HT caused a marked, highly significant increase in oxygenation. Mean tissue oxygen tensions in the subcutis rose from 43 to 81 mmHg at tissue depths of 8–10 mm, and from 46 to 77 mmHg at tissue depths of 17–20 mm (Figs. 3 and 4). Oxygenation reached a maximum within 25–30 min of wIRA-HT and remained at this significantly higher level in the further course of treatment. Upon cessation of wIRA-irradiation, oxygenation only slowly decreased, and remained at significantly elevated levels within the typical time frame of subsequent radiotherapy protocols (Fig. 4).

Non-invasive monitoring of HbO_2 saturation (stO_2) in the subepidermal microvasculature assessed a baseline value of 41 sat.%. Upon steady-state hyperthermia, HbO_2 saturation was significantly elevated to a mean of 74 sat.%. in the abdominal wall of healthy volunteers (Fig. 3 and 5a). This effect was equally visible in the skin affected by locally invasive recurrent breast cancer (Fig. 5b). When wIRA-irradiation was terminated, stO_2 values decreased slowly and remained distinctly elevated, even after skin temperatures had dropped to baseline.

4 Conclusions

wIRA-irradiation enables effective tissue heating (T = 39–43 °C) associated with distinct increases in blood flow and pO_2 values. As mentioned above, tissue oxygenation status before, during

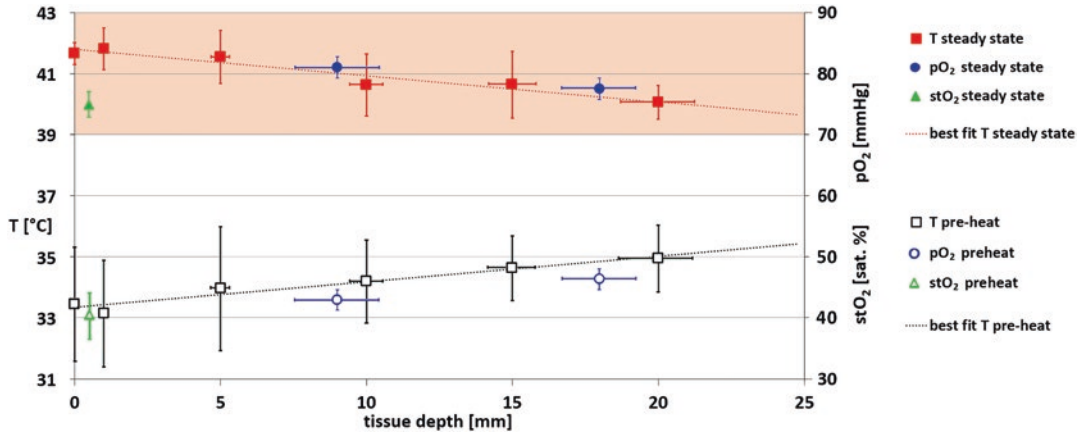

Fig. 3 Presentation of temperatures (T), oxygen tension (pO_2) in different tissue depths, and superficial HbO_2 saturation (stO_2) in healthy volunteers prior to wIRA-HT (open symbols) and in the steady state phase (closed symbols). Mean values ±SD obtained from n = 12 sessions (T, pO_2) and n = 3 sessions (stO_2) are shown. The temperature range of mild hyperthermia (39–43 °C) is marked in light red

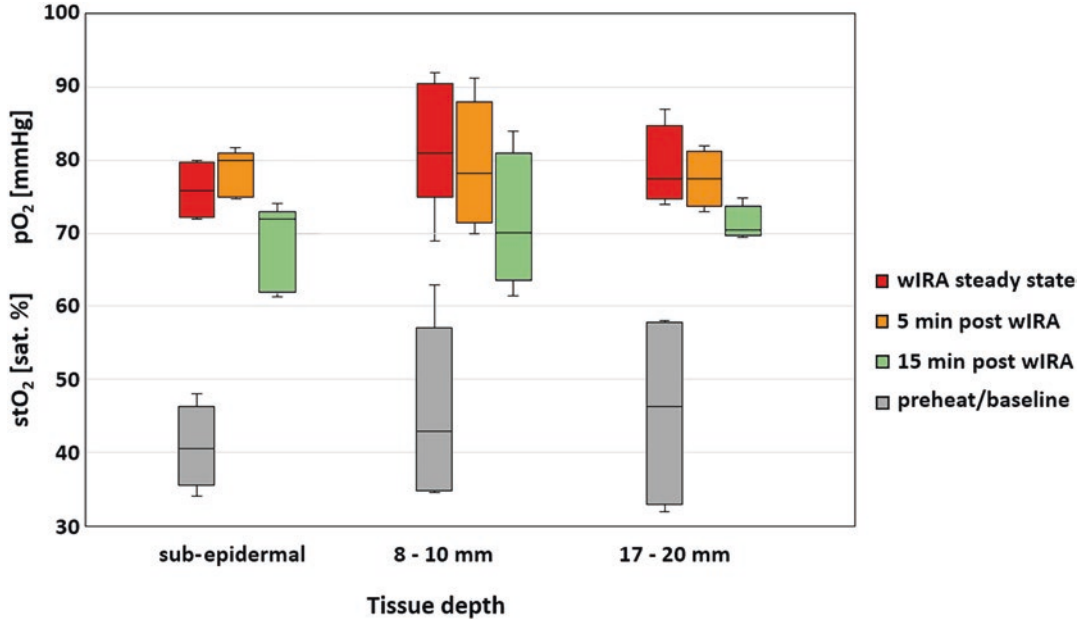

Fig. 4 stO_2 values (sub-epidermal) and pO_2 values (in tissue depths of 8–10 mm and 17–20 mm) during and post wIRA-hyperthermia in healthy volunteers. Post-heating pO_2 and stO_2 remained at significantly elevated levels within the time frame of subsequent radiotherapy. Subepidermal stO_2 was assessed using hyperspectral skin imaging (n = 3), pO_2 in the subcutis with invasive probes (n = 6 for 8–10 mm, n = 4 for 17–20 mm tissue depths). Boxes show medians with first and third quartiles, whiskers show ranges

and after wIRA-hyperthermia was assessed by two different approaches in our experiments:

(A) By an indirect, non-invasive approach, using hyperspectral analysis of oxygen saturation (stO_2) of haemoglobin present in subepidermal microvasculature (Fig. 5). While measurement in deeper tissue layers is technically not possible, this method offers the advantage of non-invasive imaging of larger skin areas.

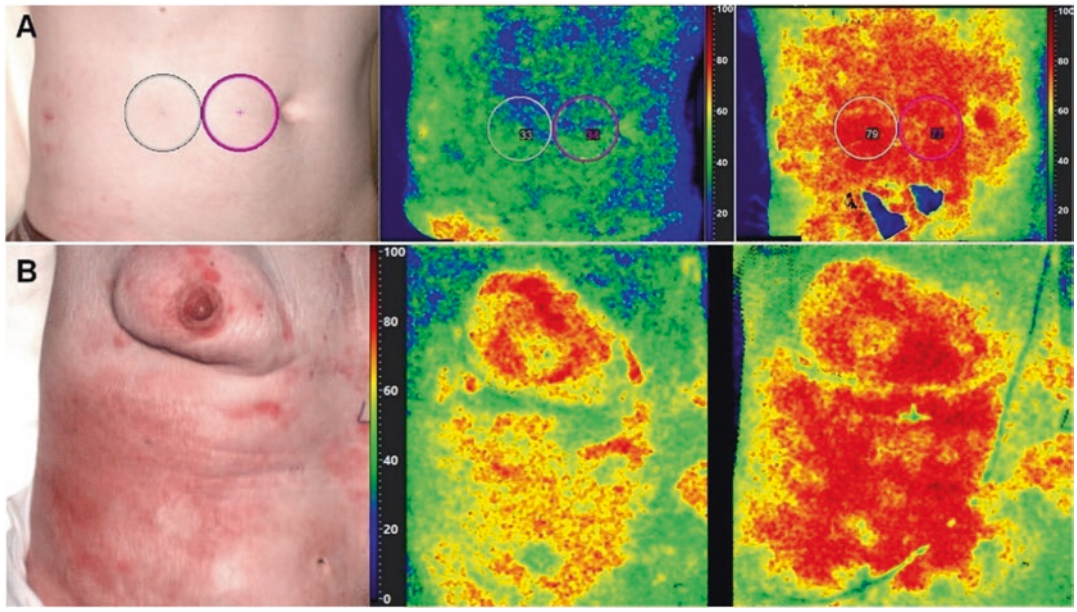

Fig. 5 Imaging of HbO_2 saturations in the upper dermis of the abdominal wall of a healthy volunteer (**a**), and in the outer tissue layer (≈ 1 mm) of a large-size, inflammatory recurrent breast cancer (**b**). Topographic aspect of the treatment area (left panels), stO_2 imaging before (central panels) and at the end of wIRA-hyperthermia (right panels). The malignant inflammatory condition in a patient treated evidently causes higher stO_2 baseline values. The second patient presented with a large, ulcerated tumour covered with fibrin exudate, which partially prevented an adequate stO_2 reading

(B) By direct, minimally invasive micro-sensor measurements of tissue oxygen pressures (pO_2, Figs. 2, 3 and 4). In principle, invasive measurements are not restricted to a certain tissue depth.

The combined use of these two methods confirmed that wIRA-hyperthermia not only improves tissue oxygenation in the upper dermis, but also in deeper tissue layers. With both methods used, the assessed data reflect integral values from small tissue subvolumes, i.e., distinctions between extracellular and intracellular space are not possible.

Hyperspectral skin imaging was found to be a versatile, non-invasive method to assess HbO_2 saturations in the subpapillary microvasculature of the upper dermis, so that it represents a useful supplement to invasive pO_2 measurements in the lower dermis and subcutis.

Compared to pre-heating values, wIRA-HT causes a significant improvement of the tissue O_2 status. Both hyperspectral imaging of stO_2 and direct measurement of tissue pO_2 show that this effect covers the period needed for subsequent radiotherapy.

These findings unequivocally meet the requirement for effective radiosensitisation [14]. In addition, HT- levels ≥39 °C increase vascular permeability, and thus intratumor delivery of anticancer agents, and can stimulate antitumor immunity. To inhibit repair of RT-induced DNA damage, HT levels ≥41 °C are necessary [5, 15].

It is concluded that wIRA-HT is a reliable treatment modality for efficiently heating skin and subcutaneous tissue up to a depth of approx. 25 mm. In the set temperature range (mild hyperthermia, 39–43 °C), tissue oxygenation is sustainably improved in all tissue depths examined (~0.5–20 mm), so that oxygen-mediated radiosensitisation can be exploited.

Acknowledgments This work was supported by the Dr. med. h.c. Erwin Braun Foundation, Basel, Switzerland.

We thank Dr. Petra Mayr (Oxford Optronix, UK), for valuable technical advice.

References

1. Hoffmann G, Hartel M, Mercer JB (2016) Heat for wounds – water-filtered infrared-A (wIRA) for wound healing – a review. Ger Med Sci 14:Doc08. https://doi.org/10.3205/000235
2. Künzli BM, Liebl F, Nuhn P et al (2013) Impact of preoperative local water-filtered infrared A irradiation on postoperative wound healing: a randomized patient- and observer-blinded controlled clinical trial. Ann Surg 258:887–894. https://doi.org/10.1097/SLA.0000000000000235
3. Foerster J, Storch A, Fleischanderl S et al (2006) Neutrophil respiratory burst is decreased in scleroderma and normalized by near-infrared mediated hyperthermia. Clin Exp Dermatol 31:799–806. https://doi.org/10.1111/j.1365-2230.2006.02243.x
4. Borel N, Sauer-Durand AM, Hartel M et al (2020) wIRA: hyperthermia as a treatment option for intracellular bacteria, with special focus on Chlamydiae and Mycobacteria. Int J Hyperth 37:373–383. https://doi.org/10.1080/02656736.2020.1751312
5. Oei AL, Kok HP, Oei SB et al (2020) Molecular and biological rationale of hyperthermia as radio- and chemosensitizer. Adv Drug Deliv Rev 163–164:84–97. https://doi.org/10.1016/j.addr.2020.01.003
6. Oei AL, van Leeuwen CM, Ahire VR et al (2017) Enhancing synthetic lethality of PARP-inhibitor and cisplatin in BRCA-proficient tumour cells with hyperthermia. Oncotarget 8:28116–28124. https://doi.org/10.18632/oncotarget.15922
7. van den Tempel N, Odijk H, van Holthe N et al (2018) Heat-induced BRCA2 degradation in human tumours provides rationale for hyperthermia-PARP-inhibitor combination therapies. Int J Hyperth 34:407–414. https://doi.org/10.1080/02656736.2017.1355487
8. Datta NR, Kok HP, Crezee H et al (2020) Integrating loco-regional hyperthermia into the current oncology practice: SWOT and TOWS analyses. Front Oncol 10:819. https://doi.org/10.3389/fonc.2020.00819
9. Bakker A, van der Zee J, van Tienhoven G et al (2019) Temperature and thermal dose during radiotherapy and hyperthermia for recurrent breast cancer are related to clinical outcome and thermal toxicity: a systematic review. Int J Hyperth 36:1024–1039. https://doi.org/10.1080/02656736.2019.1665718
10. Notter M, Piazena H, Vaupel P (2017) Hypofractionated re-irradiation of large-sized recurrent breast cancer with thermography-controlled, contact-free water-filtered infra-red-A hyperthermia: a retrospective study of 73 patients. Int J Hyperth 33:227–236. https://doi.org/10.1080/02656736.2016.1235731
11. Notter M, Thomsen AR, Nitsche M et al (2020) Combined wIRA-hyperthermia and hypofractionated re-irradiation in the treatment of locally recurrent breast cancer: evaluation of therapeutic outcome based on a novel size classification. Cancers 12:606. https://doi.org/10.3390/cancers12030606
12. Vaupel P, Piazena H, Müller W et al (2018) Biophysical and photobiological basics of water-filtered infrared-A hyperthermia of superficial tumors. Int J Hyperth 35:26–36. https://doi.org/10.1080/02656736.2018.1469169
13. Wild T, Becker M, Winter J et al (2018) Hyperspectral imaging of tissue perfusion and oxygenation in wounds: assessing the impact of a micro capillary dressing. J Wound Care 27:38–51. https://doi.org/10.12968/jowc.2018.27.1.38
14. Thomsen AR, Saalmann MR, Nicolay NH et al (2022) Temperature profiles and oxygenation status in human skin and subcutis upon thermography-controlled wIRA-hyperthermia. In: Vaupel P (eds) Water-filtered infrared A (wIRA) irradiation. Springer, Cham. https://doi.org/10.1007/978-3-030-92880-3_5
15. Hall EJ, Giaccia AJ (2019) Radiobiology for the radiologist, 8th edn. Wolters Kluwer, Philadelphia/Baltimore/New York/London/Buenos Aires

Blood Supply and Oxygenation Status of the Liver: From Physiology to Malignancy

Peter Vaupel and Gabriele Multhoff

Abstract

To maintain a multitude of vital functions, blood flow to the *normal liver* and the hepatic oxygenation status has to be kept on a high level (1.0–1.2 mL/g/min and 30–40 mmHg, respectively). There is a longitudinal oxygen partial pressure (pO_2) gradient within the liver sinusoids between periportal inflow and outflow into the central vein leading to a zonation of the O_2 status, which is associated with a zoning of liver functions. Oxygenation of *metastatic lesions* of colorectal cancers in the liver is poor due to a dysfunctional vascularity and inadequate blood supply. *Hepatocellular carcinomas* (HCCs) are highly vascularised (arterialised), metabolically very active and present with a predominantly arterial blood supply. HCCs are generally believed to be very hypoxic. However, confirmation of severe hypoxia based on reliable, direct pO_2 measurements in HCCs is still missing.

P. Vaupel (✉)
Department of Radiation Oncology, University Medical Center, University of Freiburg, Freiburg, Breisgau, Germany
e-mail: vaupel@uni-mainz.de

G. Multhoff
Department of Radiation Oncology and Central Institute for Translational Cancer Research (TranslaTUM), Klinikum rechts der Isar, Technical University Munich (TUM), Munich, Germany
e-mail: gabriele.multhoff@tum.de

Keywords

Hepatocellular carcinoma · Hepatic blood flow · Hepatic arterial buffer response · Hepatic pO_2 distribution

1 Introduction

The liver is the largest parenchymal organ in the human body. It performs hundreds of vital functions, some of which are rather complex. These include (a) multiple roles in the metabolism of carbohydrates, amino acids and proteins, and lipids, (b) synthesis of most plasma proteins and clotting factors, (c) production, activation and inactivation of hormones, (d) production of growth factors, (e) storage functions for fat-soluble vitamins, vitamin B_{12} and folate, copper, iron and glycogen, (f) immune functions (von Kupffer cells are part of the macrophage lineage supporting natural killer (NK) cells with IL-15), (g) foetal erythropoiesis, postnatal decomposition of aged red blood cells, (h) drug metabolism, biotransformation, (i) conversion of toxic ammonia into urea, (j) deactivation of toxins, filtration and elimination of xenobiotic macromolecules, (k) bile production, secretion of bile acids and excretion of bilirubin, and (l) production of essential enzymes.

To maintain this plethora of vital functions, liver blood flow must be kept at a physiologically

F. Scholkmann et al. (eds.), *Oxygen Transport to Tissue XLIII*, Advances in Experimental Medicine and Biology 1395, https://doi.org/10.1007/978-3-031-14190-4_43

high level, has to undergo temporary regulations (e.g., in fasting vs. postprandial phases), and has to guarantee an adequate oxygen (O_2) supply.

This chapter presents principles of hepatic blood flow, the delivery of O_2 to the normal liver, the parenchymal O_2 status, and functional, zonal distributions of oxygenation. In addition, these parameters are discussed in the context of metastatic lesions within the liver, and highly controversial data described for hepatocellular carcinomas (HCCs) are critically questioned. The incidence of HCC is rising constantly, mostly due to an increase in HCCs due to metabolic liver disease [1]. Worldwide, HCC was the sixth most common cancer, and the third most common cause of cancer-related deaths in 2020 [2]. The incidence is highest in East Asia, followed by Micronesia, Northern Africa and Southeast Asia. HCC is characterised by severe therapy resistance and/or escape from anti-tumour immune responses, very often believed/claimed to be caused by severe/extreme hypoxia [e.g., 3–7].

2 Hepatic Blood Flow and Oxygen Supply

The liver receives ≈27% of the cardiac output (i.e., 1.0–1.2 mL/g/min) and consumes 20% of the total oxygen used by the body at rest (≈0.06 mL O_2/g/min).

The liver has a dual blood supply. About 75% of the blood is received via the (hepatic) portal vein which drains nutrient-rich, partially deoxygenated blood from the gastro-intestinal tract, pancreas and the spleen. In portal-venous blood, the oxygen partial pressure (pO_2) is 50 mmHg, HbO_2 saturation (sO_2) is up to 85%, and O_2 content (cO_2) is 17.5 mL O_2/dL blood (i.e., 50–60% of total hepatic O_2 supply). Approximately 25% of the blood supply is received via the hepatic artery (pO_2 = 90 mmHg, sO_2 = 95%, cO_2 = 19.5 mL O_2/dL blood (i.e., 40–50% of the total hepatic O_2 supply). The mean pO_2 of the blood exiting the liver via the hepatic vein is 37 mmHg, sO_2 = 65% and cO_2 = 13.0 mL O_2/dL blood. In the fasting state, the hepatic O_2 extraction rate is 25–30%.

Knowing the pO_2 values for the source vessels at the portal triad, the inflow pO_2 of the liver sinusoids (i.e., large calibre liver capillaries with discontinuous endothelium) is about 60–65 mmHg, and the outflow pO_2 is ≈30–35 mmHg around the central vein. Accordingly, the longitudinal pO_2 gradient within the sinusoids is ≈30 mmHg. Note: Direct arterio-venous anastomoses between the branches of the hepatic arterioles and the central vein are common in the normal liver.

The proportion of blood flow supplied to the liver by the portal vein may increase to almost 90% after a meal.

The valve-free portal vein system is a low-pressure (8–10 mmHg), low resistance circuit with blood pressures in the sinusoids of 6–8 mmHg [8], i.e., the mean 'driving' perfusion pressure is relatively low (≈3 mmHg).

Liver blood flow is intrinsically regulated by the intimate Hepatic Arterial Buffer Response (HABR): When portal venous flow is reduced (such as in liver fibrosis, cirrhosis), arterial flow rapidly increases almost linearly [9] and thus allows for 'buffering' of up to 60% of the decreased portal flow, i.e., blood flows in the portal venous and hepatic arterial systems vary reciprocally, without inducing full compensation. Complete compensation can be achieved via an appropriate increase in O_2 extraction. Currently, it is postulated that adenosine is the key mediator in this regulation [10]. The main physiological role of this response is to maintain the O_2 supply to the liver, and thereby also the liver functions and metabolic homeostasis.

3 Hepatic pO_2 Distribution

Direct pO_2 measurement in the liver of animals using pO_2 microsensors dates back to the late 1960s and early 1970s [11, 12]: Mean pO_2 values were 30–35 mmHg (range: 6–50 mmHg) in dogs, and ≈30 mmHg (range: 3–65 mmHg) in rats. The first reliable, direct pO_2 measurements in the human liver were reported in 1995 [13]. In sporadic measurements, the median pO_2 ranged from 35 to 40 mmHg with no values below 2.5 mmHg. In the mid-2000s, mean pO_2 values of

30–40 mmHg confirmed the well-adapted oxygenation status of the normal liver (for recent, comprehensive reviews see [14, 15]).

The longitudinal pO_2 gradient between the portal triad and central vein, as described above, creates a functional zonation of the underlying hepatocytes: In the *periportal zone* (zone 1), the tissue pO_2 values are 45–50 mmHg. Oxphos, gluconeogenesis, β-oxidation, cholesterol biosynthesis, ammonia detoxication, and protein secretion are localised in this zone. The *midlobular/intermediate zone* (zone 2), which is characterised by tissue pO_2 values of 25–40 mmHg, controls xenobiotic metabolism and iron homeostasis. In the *perivenous/pericentral zone* (zone 3) pO_2 values are 15–20 mmHg, fostering bile acid production, glutamine synthesis, glycolysis, cytochrome p-450 activity, and HIF-expression [16, 17].

Wnt ligands produced by sinusoidal endothelial cells and Wnt/β-catenin signalling are necessary for preserving the metabolic zonation in the adult liver [18].

4 Oxygenation of Metastatic Lesions in the Liver

Hepatic metastases of colorectal cancers are characterised by dysfunctional vascularity and inadequate blood flow [19]. Macroscopic metastases receive their primary blood supply from the hepatic artery, with the portal venous contribution being of minor importance [20]. As a consequence of inadequate blood supply, severe hypoxia and hypoxia-induced activation of HIF are common features. Using pO_2 microsensors, direct pO_2 measurements in 4 metastatic lesions revealed the following data: Weighted mean: 6 mmHg, hypoxic fraction $pO_2 \leq 5$ mmHg: 45%, and hypoxic fraction $pO_2 \leq 10$ mmHg: 75%. These data clearly show that metastatic lesions from colorectal cancers in the liver have a substantially poorer oxygenation than the primary tumours (weighted median pO_2 values: 6 vs. 25 mmHg; for a review see [21]).

Note: Due to an incorrect citation by McKeown [22], the mean pO_2 in metastatic rectal cancers in the liver has erroneously been assigned to human hepatocellular carcinomas, leading to fatal misinterpretations and conclusions concerning the oxygenation status of the latter tumour type (see below). Unfortunately, several other flaws in this review [22] must be mentioned in this context: (a) correct units for pO_2 are missing, (b) incorrect unit is used for pO_2 (%), (c) Henry's law and Dalton's law are used inappropriately (both are only valid for gas mixtures or gases dissolved in homogeneous solutions, and (d) an assumption is made that Bunsen's solubility coefficient α is valid for heterogeneous tissues. The coefficient α greatly depends on the water content of the tissue, on the lipid content, and on the volume of the extravascular space [15].

5 Oxygenation of HCCs

Tumorigenesis of HCCs is associated with arterial hyper-vascularisation (i.e., arterial inflow becomes dominant, arterial fraction ≈58%, 'arterialisation' of HCCs is correlated with IL-6 and IL-8 levels), highly active metabolism ('hypermetabolism'), and a strongly enhanced and accelerated aerobic glycolysis (Warburg effect) [23–26].

Two studies involved direct pO_2 measurements in *rodent HCC models* and provided conflicting results: Hypoxia was detected in a rat hepatoma heterotopically transplanted into skeletal muscle [27], while chemically induced HCC nodules in mice failed to demonstrate reduced pO_2 values compared to the normal liver (mean pO_2 was ≈30 mmHg in normal liver and in HCCs [28]).

Non-invasive blood oxygenation level-dependent (BOLD)-MRI and tissue oxygenation level-dependent (TOLD)-MRI were used in the late 2010s to characterise the oxygenation status of *HCCs in humans* [29–32]. These studies are indicative of pronounced heterogeneities within and between HCCs. Declining T2* values were assessed in liver haemangiomas > HCCs > metastatic liver tumours > cholangiocarcinomas, i.e., the oxygenation status deteriorates in this order. None of these articles report 'severe hypoxia' in

HCCs. Results described by Park et al. [32] confirm severe hypoxia in cholangiocarcinomas using directly assessed pO_2 data [33].

Direct, reliable measurements of the oxygenation status in *human HCCs in situ* to prove that HCCs are typically severely hypoxic tumours have not yet been published.

6 Severe Hypoxia in HCCs: Fact or Myth?

As mentioned before, highly aggressive growth patterns, therapeutic resistances and/or escape from anti-tumour immune responses of HCCs are claimed to be the result of severe/extreme tissue hypoxia. So far, the latter, detrimental condition has not been evidenced in HCCs by directly measuring pO_2 values. Instead, it relies on the detection of hypoxia-related factors in the cancer tissue (e.g., mostly HIF and HIF-related proteins or HIF-related mechanisms). Unfortunately, the notion of severe hypoxia as a well-established characteristic of HCC was greatly supported by an incorrect citation in the review by McKeown [22]. Due to overinterpretation of *in vitro* data, insufficient discussion of non-hypoxic HIF expression as a driving force for hypervascularisation, metabolic reprogramming, speculation, inappropriate translation and continuous perseverations of unproven pO_2 data, HCCs are still believed to be very hypoxic. Because direct evidence of severe hypoxia in human HCCs is sparse, its role remains elusive [34, 35] and reliable data are not available [34, 36].

Acknowledgement The authors thank Professor A. Graham Pockley, Nottingham Trent University (UK), for linguistic support.

References

1. Llovet JM, Kelley RK, Villanueva A et al (2021) Hepatocellular carcinoma. Nat Rev Dis Primers 7:6
2. Cicalese L (2021) What is the global incidence of hepatocellular carcinoma (HCC) worldwide? https://www.medscape.com
3. Chen C, Lou T (2017) Hypoxia inducible factors in hepatocellular carcinoma. Oncotarget 8:46691–46703
4. Xiong XX, Qui XY, Xing D et al (2017) Advances in hypoxia-mediated mechanisms in hepatocellular carcinoma. Mol Pharmacol 92:246–255
5. Lin C-A, Chang L-L, Zhu H et al (2018) Hypoxic microenvironment and hepatocellular carcinoma treatment. Hepatoma Res 4:26
6. Ma L, Craig AJ, Heinrich S (2021) Hypoxia is a key regulator in liver cancer progression. J Hepatol 75:736–7373
7. Bao MH-R, Wong CC-L (2021) Hypoxia, metabolic reprogramming, and drug resistance in liver cancer. Cell 10:1715
8. Eipel C, Abshagen K, Vollmar B (2010) Regulation of hepatic blood flow: the hepatic arterial buffer response revisited. World J Gastroenterol 16:6046–6057
9. Lautt DW, Legare DJ, Waleed RE (1990) Quantitation of the hepatic arterial buffer response to graded changes in portal blood flow. Gastroenterology 8:1024–1028
10. Lautt WW, Legare DJ, d'Almaida MS (1985) Adenosine as putative regulator of hepatic arterial flow (the buffer response). Am J Physiol Heart Circ Physiol 248:H331–H338
11. Kessler M, Görnandt L, Therman M et al (1973) Oxygen supply and microcirculation of liver in hemorrhagic shock. In: Kessler M, Bruley DF, Clark LC et al (eds) Oxygen supply. Urban & Schwarzenberg, München/Berlin/Wien, pp 252–255
12. Görnandt L, Kessler M (1973) pO_2 histograms in regenerating liver tissue. In: Kessler M, Bruley DF, Clark LC et al (eds) Oxygen supply. Urban & Schwarzenberg, München/Berlin/Wien, pp 288–289
13. Kallinowski F, Buhr HJ (1995) Tissue oxygenation of primary, metastatic and xenografted rectal cancers. In: Vaupel P, Kelleher DK, Günderoth M (eds) Tumor oxygenation. Fischer, Stuttgart/Jena/New York, pp 205–209
14. Keeley TP, Mann GE (2019) Defining physiological normoxia for improved translation of cell physiology to animal models and humans. Physiol Rev 99:161–234
15. Vaupel P, Flood AB, Swartz HM (2021) Oxygenation status of malignant tumors vs. normal tissues: critical evaluation and updated data source based on direct measurements with pO_2 microsensors. Appl Magn Reson. https://doi.org/10.1007/s00723-021-01383-6
16. Kietzmann T (2017) Metabolic zonation of the liver: the oxygen gradient revisited. Redox Biol 11:622–630
17. Kietzmann T (2019) Liver zonation in health and disease: hypoxia and hypoxia-inducible transcription factors as concert masters. Int J Sci 20:2347
18. Ma R, Martinez-Ramirez AS, Borders TL et al (2020) Metabolic and non-metabolic liver zonation is established non-synchronously and requires sinusoidal Wnts. elife. https://doi.org/10.7554/eLife.46206
19. Burke D, Davies MM, Zweit J et al (2001) Continuous angiotensin II infusion increases tumour:normal

blood flow ratio in colo-rectal liver metastases. Br J Cancer 85:1640–1645
20. Lin G, Hägerstrand I, Lunderquist A (1984) Portal blood supply of liver metastases. Am J Roentgenol 143:53–55
21. Vaupel P, Höckel M, Mayer A (2007) Detection and characterization of tumor hypoxia using pO_2 histography. Antioxid Redox Signal 9:1221–1235
22. McKeown SR (2014) Defining normoxia, physoxia and hypoxia in tumours: implications for treatment response. Br J Radiol 87(1035):20130676
23. Taouli B, Johnson RS, Hajdu CH et al (2013) Hepatocellular carcinoma: perfusion quantification with dynamic contrast-enhanced MRI. Am J Roentgenol 201:795–800
24. Chen Y-W, Pan H-B, Tseng H-H et al (2013) Assessment of blood flow in hepatocellular carcinoma: correlation of computed tomography perfusion imaging and circulating angiogenic factors. Int J Mol Sci 14:17536–17552
25. Asayama Y, Yoshimitsu K, Nishihara Y et al (2008) Arterial blood supply of hepatocellular carcinoma and histologic grading: radiologic-pathologic correlation. Am J Roentgenol 190:W28–W34
26. Karmacharya MB, Sultan LR, Sehgal CM (2021) Photoacustic monitoring of oygenation changes induced by therapeutic ultrasound in murine hepatocellular carcinoma. Sci Rep 11:4100
27. Cater DB, Schoeniger EL, Watkinson DA (1963) Effect of breathing high pressure oxygen upon tissue oxygenation in rat and mouse tumours. Acta Radiol Ther Phys Biol 1:356–365
28. Tanaka H, Yamamoto M, Hashimoto N et al (2006) Hypoxia-independent overexpression of hypoxia-inducible factor 1α as an early change in mouse hepatocarcinogenesis. Cancer Res 66:11263–11270
29. Patterson AJ, Priest AN, Bowden DJ et al (2016) Quantitative BOLD imaging at 3T: temporal changes in hepatocellular carcinoma and fibrosis following oxygen challenge. J Magn Reson Imaging 44:739–744
30. Hectors SJ, Wagner M, Bana O et al (2017) Quantification of hepatocellular carcinoma Heterogeneity with multiparametric magnetic resonance imaging. Sci Rep 7:2452
31. Guo Y, Xiao Z, Yang L et al (2020) Hypoxia-inducible factors in hepatocellular carcinoma (Review). Oncol Rep 43:3–15
32. Park HJ, Kim YK, Min JH (2014) Feasibility of blood oxygenation level- dependent MRI at 3 T in the characterization of hepatic tumors. Abdom Imaging 39:142–152
33. Graffman S, Björk P, Ederoth P et al (2001) Polarographic pO_2 measurements of intraabdominal adenocarcinoma. Acta Oncol 40:105–107
34. Xiong XX, Qiu XY, Hu DX et al (2017) Advances in hypoxia-mediated mechanisms in hepatocellular carcinoma. Mol Pharmacol 92:246–255
35. Morse MA, Sun W, Kim R et al (2019) The role of angiotensin in hepatocellular carcinoma. Clin Cancer Res 25:912–920
36. Cramer T, Vaupel P (2022) Severe hypoxia is a typical characteristic of human hepatocellular carcinoma: scientific fact or fallacy? J Hepatol 76:975–980

Optical Redox Imaging Is Responsive to TGFβ Receptor Signalling in Triple-Negative Breast Cancer Cells

He N. Xu, Annemarie Jacob, and Lin Z. Li

Abstract

Co-enzyme nicotinamide adenine dinucleotide NAD(H) regulates hundreds of biochemical reactions within the cell. We previously reported that NAD(H) redox status may have prognostic value for predicting breast cancer metastasis. However, the mechanisms of NAD(H) involvement in metastasis remain elusive. Given the important roles of TGFβ signalling in metastatic processes, such as promoting the epithelial-to-mesenchymal transition, we aimed to investigate the involvement of the mitochondrial NAD(H) redox status in TGFβ receptor signalling. Here we present the initial evidence that NAD(H) redox status is responsive to TGFβ receptor signalling in triple-negative breast cancer cells in culture. The mitochondrial NAD(H) redox status was determined by the optical redox imaging (ORI) technique. Cultured HCC1806 (less aggressive) and MDA-MB-231 (more aggressive) cells were subjected to ORI after treatment with exogenous TGFβ1 or LY2109761, which stimulates or inhibits TGFβ receptor signalling, respectively. Cell migration was determined with the transwell migration assay. Global averaging quantification of the ORI images showed that 1) TGFβ1 stimulation resulted in differential responses between HCC1806 and MDA-MB-231 lines, with HCC1806 cells having a significant change in the mitochondrial redox status, corresponding to a larger increase in cell migration; 2) HCC1806 cells acutely treated with LY2109761 yielded immediate increases in ORI signals. These preliminary data are the first evidence that suggests the existence of a cell line-dependent shift of the mitochondrial NAD(H) redox status in the TGFβ receptor signalling induced migratory process of breast cancer cells. Further research should be conducted to confirm these results as improved understanding of the underlying mechanisms of metastatic process may contribute to the identification of prognostic biomarkers and therapeutic targets.

Keywords

NAD(H) and Flavoproteins (Fp) · HCC1608 and MDA-MB-231 cells · Cell migration assay · The redox ratio

1 Introduction

Metastasis causes approximately 90% of cancer deaths. Metastatic cells differ from non-metastatic ones in numerous dimensions, e.g.,

H. N. Xu (✉) · A. Jacob · L. Z. Li
Britton Chance Laboratory of Redox Imaging, Department of Radiology, University of Pennsylvania, Philadelphia, PA, USA
e-mail: hexu2@pennmedicine.upenn.edu

F. Scholkmann et al. (eds.), *Oxygen Transport to Tissue XLIII*, Advances in Experimental Medicine and Biology 1395, https://doi.org/10.1007/978-3-031-14190-4_44

genetic mutations, gene expression profile, metabolic profile, signalling pathway activities. Nicotinamide adenine dinucleotide (NAD including the oxidised NAD^+ and reduced NADH forms) is an essential co-enzyme that acts as the electron acceptor or donor for hundreds of reactions within the cell [1]. A change in the NAD^+/NADH ratio (redox shift) can profoundly affect metabolism, including reactions of glycolysis and the TCA cycle [2] and breast cancer progression to metastasis [3]. In our previous work, we also found that the NAD(H) redox status of breast cancer cells is associated with their invasive potential, e.g., the more invasive/metastatic breast cancer cells were in a more oxidised state [4, 5] and less responsive to treatment [6].

Transforming growth factor-β (TGFβ) receptors signal through the canonical SMAD pathway and several non-canonical pathways [7] and has been implicated in the metastatic processes and dramatically impact cancer progression [8]. It acts as a tumour promoter in later stage of breast cancer, in part by enhancing tumour cell motility and invasiveness and the capacity to form metastases [9]. A retrospective study including 180 women with non-metastatic invasive triple-negative breast cancer (TNBC) found that high expression of cytoplasmic TGF-β1 was associated with higher histologic tumour grade and lymph node status, more axillary lymph node dissection, as well as reduced disease-free survival [10]. TGFβ signalling stimulates both glycolysis and mitochondrial respiration, drives the epithelial-to-mesenchymal transition (EMT) and promotes cancer stem cell maintenance [11].

To better understand the role of NAD(H) redox status in tumour metastatic risk, we aimed to investigate its involvement in TGFβ signalling. NAD and its redox status regulate reactive oxygen species (ROS) in mitochondria and critically support cell metabolism. Stimulated mitochondrial ROS is essential for TGFβ signalling-induced EMT [11]. As such, our working hypothesis is that metabolic reprograming induced by TGFβ signalling to promote cancer metastasis associates with a shift in the mitochondrial NAD(H) redox status. As the first step, we employed the optical redox imaging (ORI) technique to image the NAD(H) redox status while modulating the TGFβ receptor signalling using exogeneous TGFβ1 or TGFβ receptor inhibitor LY2109761. ORI detects the intrinsic fluorescence of NADH and Fp (oxidised flavoproteins containing flavin adenine dinucleotide FAD) and has been widely applied to study the mitochondrial redox status, cellular metabolism, or treatment response [6, 12]. The optically-determined redox ratio Fp/(NADH+Fp) was found to linearly correlate with NAD^+/($NADH+NAD^+$) determined by liquid chromatography-mass spectrometer in precancerous epithelial tissues [13].

2 Methods

Human recombinant TGFβ1 (GenScript Inc., Z03411-10) and LY2109761 (Cayman Chemical Company) were reconstituted with deionised H_2O containing 0.1% bovine serum albumin (BSA) or ethanol, respectively, aliquoted, then stored in −80 °C freezer. HCC1806 and MDA-MB-231 cell lines purchased from ATCC were routinely cultured in RPMI1640 supplemented with 10% fetal bovine serum (FBS) in a 5% CO_2 incubator at 37 °C. For TGFβ1 treatment, ~30,000 cells/dish in 0.5 mL RPMI 1640 containing 10% FBS (complete medium) were seeded in the glass bottom dishes (Cellvis, D35-20-1.5-N) and allowed to attach for 4 h, then 0.5 mL RPMI1640 containing 0.1% BSA (starvation medium) were added to the dishes. Cells administered with TGFβ1 (10 ng/mL) or nothing (control) were incubated for 72 h. To avoid high fluorescence background in the completed RPMI 1640, approximately 45 min before imaging, the culture medium was switched to $LCIS^+$ (Live Cell Imaging Solution, Life Technologies spiked with 11 mM D-glucose and 2 mM L-glutamine). During imaging, no TGFβ1 was present in the LCIS. For TGFβ signalling inhibition experiments, ~50,000 cells/dish in RPMI1640 with 10% FBS were seeded in the glass bottom dishes and incubated for 24 h. LY2109761 (14.5 μM final) or ethanol (0.3%, control) was administered to $LCIS^+$ and immediately imaged.

ORI was performed using a Zeiss Axio Observer 7 fluorescence microscope and data were processed to extract global averaging means and standard deviations (SD) according to the same protocol we reported previously [6]. To assess single cell parameters, 25 cells/dish were selected to obtain the mean values for a specific dish and the region of interest (ROI) was drawn on cell periphery and nuclear area. A clearly discernible presence of nucleus was the criterion for cell selection.

For the migration assay, cells were first serum-starved in the starvation medium for 24 h. The cells were then resuspended in the starvation medium and 300 μL suspension of ~75,000 cells were transferred to the Transwell® insert (Sigma-Aldrich, CLS3422,). RPMI 1640 containing 10% FBS was added to the bottom chamber. After 24 h incubation, the cells that did not transmigrate across the insert's membrane were completely removed using cotton swabs. The migrated cells were then fixed in chilled 70% ethanol (10 min) and stained with 300 nM DAPI (5 min). The membrane was then carefully removed from the insert with a surgical knife and placed in a glass-bottom dish and covered with a round cover-glass for imaging. The membrane side that has DAPI-stained cells was facing the lens and the whole area of membrane was tile-imaged with a wide-field microscope (EVOS FL Auto Imager). DAPI-stained nuclei were then counted using ImageJ. The number of migrated cells were normalised to the total seeded cells to obtain the percentage of cell migration.

To compare the group means, Student's t-tests were performed (two-tailed unequal variance). $P < 0.05$ was considered statistically significant.

3 Results and Discussion

TGFβ1 binds with a type II receptor (TGFβRII) which then activates type I receptor (TGFβRI) on the cell surface to initiate the intracellular signalling that promotes downstream cell migration. In comparison with HCC1806 control cells (Fig. 1a, upper panel), many TGFβ1-stimulated HCC1806 cells (Fig. 1a, lower panel) showed a distinct morphology, more spread and flower-like, and large Fp aggregates (pointed by the yellow arrows) whereas the same localised NADH signal change was less prominent. Analysis based on single cells found that compared to control cells, both nuclear and whole cell areas were larger ($p = 0.010$ and 0.035, respectively) in TGFβ1-stimulated cells and so was the nuclear to whole cell area ratio ($p = 0.031$) with the nuclear to cytoplasmic area ratio having an upward trend ($p = 0.1$) (Fig. 1b). The nucleus as the largest and stiffest organelle of the cell dominates the biomechanical process of migration with increased size and contour irregularity, and often shifted position [14–17]. In future we can confirm whether the morphological changes (nuclear and whole cell) we observed were directly associated with the migratory process by staining the EMT markers such as Snail, E-Cadherin, and Vimentin. We did not observe pronounced morphological contrasts between stimulated and control MDA-MB-231 cells.

Figure 2a is the global averaging result of exogeneous TGFβ1 effects on both TNBC lines. TGFβ1 led to a 20% ($p = 0.027$) and a 9% ($p = 0.0099$) decrease in Fp and the redox ratio, respectively in HCC1806 cells. In MDA-MB-231 cells, there was no significant change in Fp signal but there was a 17% increase in NADH ($p = 0.033$) and a downward trend of the redox ratio ($p = 0.060$).

Our transwell migration assay showed that TGFβ1 stimulation significantly increased cell migration of both TNBC lines (Fig. 2b, c), with a more prominent effect on the less aggressive HCC1806 cells (160% increase) compared to that on MDA-MB-231 cells (~50% increase).

We also examined the effects of acutely inhibiting TGFβ receptor signalling on the mitochondrial redox status. LY2109761 is a selective TGFβ receptor type I/II dual inhibitor. Figure 3 shows the typical images (Fig. 3a) acquired immediately after LY2109761 was administered and the quantitative analysis (Fig. 3b) for HCC1806 cells. From Fig. 3a, we can see the distinct large aggregates of intense NADH and Fp signals. Global averaging quantification yielded a 67% increase in Fp ($p = 0.00058$), a 124%

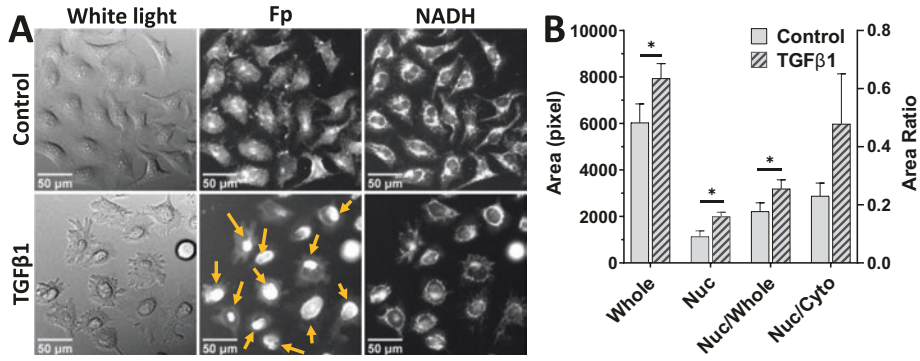

Fig. 1 Exogeneous TGFβ1 effects on HCC1608 cells. (**a**) Representative white light, Fp, NADH images; (**b**) Single cell-based analysis results, where "nuc" stands for nuclear, "cyto" stands for cytoplasmic (Mean ± SD, N = 3 dishes, pixel size = 0.29 × 0.29 μm^2, *p < 0.05)

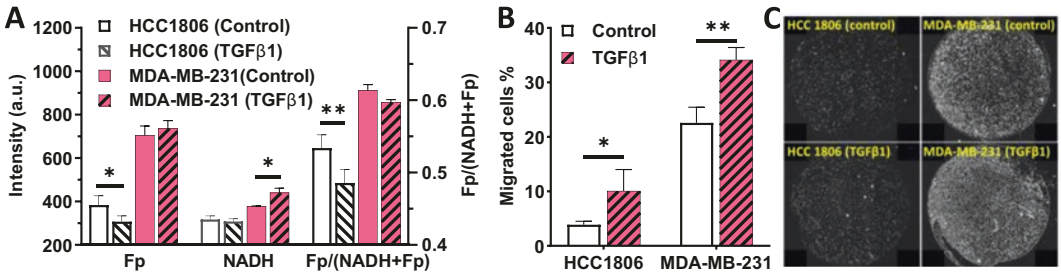

Fig. 2 TGFβ1 stimulation affects the mitochondrial redox status and promotes cell migration. (**a**) Differential redox responses to TGFβ1-induced signalling between HCC1806 (N = 4 dishes) and MDA-MB-231 (N = 3 dishes) lines; (**b**) differential increase in cell migration (N = 6 and 3 for HCC1806 and MDA-MB-231 lines, respectively); (**c**) Representative DAPI images of migrated cells on the entire migration chamber membranes (6.5 mm diameter). (Mean ± SD, *p < 0.05, **p < 0.01)

increase in NADH (p = 0.0018), and no significant change in the redox ratio Fp/(NADH+Fp) despite a downward trend. In future, we can quantify the redox ratios for the same individual cells before and immediately after LY2109761 inhibition to confirm whether the NAD(H) redox state is affected significantly. As the cell migratory process is a long-term process, we can also examine whether long-term LY2109761 inhibition (e.g., 24 h treatment) may affect the redox ratio.

NADH and Fp signals detected by ORI are mainly originated from mitochondria and both Fp and NADH increased simultaneously and formed large aggregates. It would be interesting to investigate whether such changes may reflect an emergent property of mitochondrial network dynamics. Since TGFβ signalling regulates mitochondrial dynamics [18] and cell metabolism [11], the immediate and dramatic ORI responses to LY2109761 inhibition could indicate that these cells are highly dependent on the constitutive TGFβ receptor signalling activity for their metabolism.

We can also measure cell migration under the inhibition of LY2109761 in future. It has been reported by others that 10 μM LY2109761 treatment for 24 h dramatically reduced cell migration and invasion for several breast cancer lines (including TNBC lines MDA-MB-231 and Hs578T) in a cell-line dependent manner [19]. It would be interesting to investigate (e.g. by using the same passage cells) how the ORI measures correlate with LY2109761's inhibitory effects on cell migration of breast cancer lines with various aggressiveness.

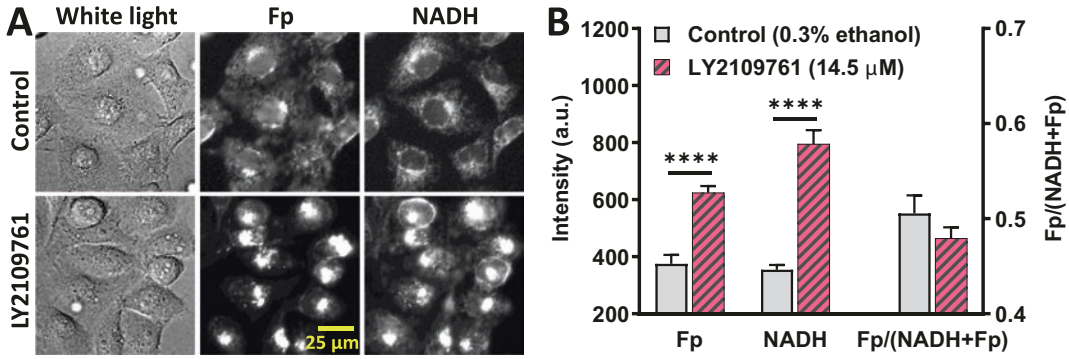

Fig. 3 Acute LY2109761 treatment effects on the NADH and Fp redox status of HCC1806 cells; (**a**) typical white light and redox images, where distinct mitochondrial aggregates indicated by intense Fp and NADH signals can be seen in LY2109761 treated cells in comparison with control cells; (**b**) Global averaging results (Mean ± SD, N = 3 dishes/group, ****$p < 0.0001$)

In our previous work, we have demonstrated that the basal level of mitochondrial redox ratio of breast cancer cells positively correlate with cell invasiveness, with MDA-MB-231 cells having the largest redox ratio and highest invasiveness and HCC1806 cells having significantly smaller redox ratio and lower invasion [4, 5]. In this report, we showed that the mitochondrial redox status of HCC1806 cells responded to the stimulation of TGFβ receptor signalling that promotes cell migration/invasion and became more reduced, whereas there was no significant change in the redox ratio in the more aggressive MDA-MB-231 cells under the same stimulation.

This study provides new evidence supporting the notion that the mitochondrial redox status is involved in the regulation of breast cancer progression [3–5]. TGFβ signalling drives EMT, a critical step for cancer progression. EMT involves extensive metabolic changes [20]. Targeting TGFβ-induced metabolic changes during EMT has been proposed for novel cancer treatments [11]. Further research in this direction may improve our understanding of cancer progression and identify potential metabolic targets for cancer therapeutics.

Acknowledgments This work was supported by McCabe Pilot Award (H. N. Xu) and NIH Grant R01CA191207 (L. Z. Li). The work was also supported in part by the National Center for Advancing Translational Sciences of the National Institutes of Health under Award Number UL1TR001878, and by the Institute for Translational Medicine and Therapeutics of the University of Pennsylvania. The content is solely the responsibility of the authors and does not necessarily represent the official views of the NIH. We thank the Cell and Developmental Biology (CDB) Microscopy Core, Perelman School of Medicine, University of Pennsylvania.

References

1. Goodman RP, Calvo SE, Mootha VK (2018) Spatiotemporal compartmentalization of hepatic NADH and NADPH metabolism. J Biol Chem 293:7508–7516
2. Thapa M, Dallmann G (2019) Role of coenzymes in cancer metabolism. Semin Cell Dev Biol 98:44–53
3. Santidrian AF, Matsuno-Yagi A, Ritland M et al (2013) Mitochondrial complex I activity and NAD^+/NADH balance regulate breast cancer progression. J Clin Invest 123:1068–1081
4. Xu HN, Nioka S, Glickson JD et al (2010) Quantitative mitochondrial redox imaging of breast cancer metastatic potential. J Biomed Opt 15:036010
5. Feng M, Xu HN, Jiang J et al (2021) Potential biomarker for triple-negative breast cancer invasiveness by optical redox imaging. Adv Exp Med Biol 1269:247–251
6. Podsednik A, Jiang J, Jacob A et al (2021) Optical redox imaging of treatment responses to Nampt inhibition and combination therapy in triple-negative breast cancer cells. Int J Mol Sci 22:5563
7. Massagué J (2012) TGFβ signalling in context. Nat Rev Mol Cell Biol 13:616–630
8. Padua D, Massagué J (2009) Roles of TGFβ in metastasis. Cell Res 19:89–102
9. Muraoka RS, Dumont N, Ritter CA et al (2002) Blockade of TGF-beta inhibits mammary tumor cell viability, migration, and metastases. J Clin Invest 109:1551–1559

10. Zhang M, Wu J, Mao K et al (2017) Role of transforming growth factor-β1 in triple negative breast cancer patients. Int J Surg 45:72–76
11. Hua W, Ten Dijke P, Kostidis S et al (2020) TGFbeta-induced metabolic reprogramming during epithelial-to-mesenchymal transition in cancer. Cell Mol Life Sci. 77:2103–2123
12. Heikal AA (2010) Intracellular coenzymes as natural biomarkers for metabolic activities and mitochondrial anomalies. Biomark Med 4:241–263
13. Varone A, Xylas J, Quinn KP et al (2014) Endogenous two-photon fluorescence imaging elucidates metabolic changes related to enhanced glycolysis and glutamine consumption in precancerous epithelial tissues. Cancer Res 74:3067–3075
14. Fischer EG (2020) Nuclear morphology and the biology of cancer cells. Acta Cytol 64:511–519
15. Calero-Cuenca FJ, Janota CS, Gomes ER (2018) Dealing with the nucleus during cell migration. Curr Opin Cell Biol 50:35–41
16. Cascione M, De Matteis V, Toma CC et al (2018) Morphomechanical alterations induced by transforming growth factor-β1 in epithelial breast cancer cells. Cancers 10:234
17. Fischer T, Hayn A, Mierke CT (2020) Effect of nuclear stiffness on cell mechanics and migration of human breast cancer cells. Front Cell Dev Biol 8:393
18. Kumar S, Pan CC, Shah N et al (2016) Activation of Mitofusin2 by Smad2-RIN1 complex during mitochondrial fusion. Mol Cell 62:520–531
19. Kim S, Lee J, Jeon M et al (2015) Zerumbone suppresses the motility and tumorigenecity of triple negative breast cancer cells via the inhibition of TGF-β1 signaling pathway. Oncotarget 7:1544–1558
20. Li L, Li W (2015) Epithelial–mesenchymal transition in human cancer: comprehensive reprogramming of metabolism, epigenetics, and differentiation. Pharmacol Ther 150:33–46

Evaluation of Betulinic Acid Derivatives as PET Tracers for Hypoxia-Induced Carbonic Anhydrase IX (CA IX) Expression

V. Haupt, D. Gündel, E. Prell, M. Kahnt, S. Sommerwerk, A. Riemann, R. Paschke, R. Csuk, A. Odparlik, and O. Thews

Abstract

Non-invasive visualisation of the expression of hypoxia-related proteins, such as carbonic anhydrase IX (CA IX), by positron emission tomography (PET) could provide important information on the oxygenation status of tumours. Since betulinic acid derivatives bind specifically to CA IX the aim of the study was the development betulinic acid-based ^{68}Ga-labelled PET tracers and to evaluate the hypoxia detecting properties *in vitro* and *in vivo*. The binding of betulinic acid (B-DOTA) and betulinyl-3-sulfamate (BS-DOTA) was assessed in two rat tumour cell lines (AT1 prostate and Walker-256 mammary carcinomas). AT1 cells express CA IX in a hypoxia-dependent manner whereas Walker-256 cells, expressing almost no CA IX in wildtype, were transfected with the rat Car9 gene. *In vivo* measurements were carried out in a small animal PET/CT in AT1 tumours in rats breathing room air, 8% or 100% O_2. In AT1 cells hypoxia-induced overexpression of CA IX led to a stronger binding of BS-DOTA but not of B-DOTA. The BS-DOTA binding correlated linearly with the CA IX protein expression and could be blocked by an excess of unlabelled tracer. In the transfected Walker-256 cells no specific binding of either of the tracers was seen. *In vivo* the intratumoral accumulation of BS-DOTA was increased in animals kept under inspiratory hypoxia and reduced by hyperoxia. Therefore, betulinyl-3-sulfamate could be used as a PET tracer of CA IX expression in tumours and to provide information about the oxygenation status. However, accumulation data indicated that binding not only depends on hypoxia-induce CA IX expression but also on the tumour-line-specific basal expression and on the initial oxygenation status of the tumour.

Supplementary Information The online version contains supplementary material available at [https://doi.org/10.1007/978-3-031-14190-4_45].

V. Haupt · A. Riemann · O. Thews (✉)
Julius-Bernstein-Institute of Physiology, University of Halle, Halle (Saale), Germany
e-mail: oliver.thews@medizin.uni-halle.de

D. Gündel · E. Prell · A. Odparlik
Department of Nuclear Medicine, University Hospital Halle, Halle (Saale), Germany

M. Kahnt · S. Sommerwerk · R. Csuk
Department of Organic Chemistry, University of Halle, Halle (Saale), Germany

R. Paschke
Biozentrum, University of Halle, Halle (Saale), Germany

F. Scholkmann et al. (eds.), *Oxygen Transport to Tissue XLIII*, Advances in Experimental Medicine and Biology 1395, https://doi.org/10.1007/978-3-031-14190-4_45

Keywords

B-DOTA · BS-DOTA · AT-1 cells · Walker-256 cells · Tumor oxygenation status

tracer binding in experimental rat tumours. Different levels of CA IX expression were obtained in these tumours by housing the animals in a hypoxic or hyperoxic atmosphere.

1 Introduction

Tumours show pronounced hypoxia resulting in heterogeneously distributed pO_2 with well-oxygenated regions adjacent to hypoxic areas [1]. Assessing the pre-therapeutic oxygenation could be helpful to identify patients with more hypoxic tumours and adapt treatment accordingly. Several attempts have been suggested to measure the oxygenation status of the tissue by positron emission tomography (PET). Therefore, direct hypoxia markers such as 2-nitroimidalzole derivatives which bind to cells in the absence of oxygen labelled with suitable isotopes were used (for instance ^{18}F-fluoromisonidazole (FMISO) [2]). An alternative strategy is the indirect detection of O_2-deficiency by assessing the expression of hypoxia-dependent cellular proteins which may provide additional information on pathophysiological processes such as glucose metabolism or acid-base-regulation. One of the genes regulated by the transcription factor HIF-1α is the carbonic anhydrase IX (CA IX) which is highly upregulated in many tumours and which expression is correlated with the O_2 status [3]. For specific binding anti-CA IX antibody or fragments have been used which were labelled with different isotopes [4, 5]. Also, small peptides specifically binding to CA IX and labelled with ^{18}F were tested probes [6]. Recently, it was shown that betulinic acid derivatives bind specifically to CA IX with high affinity and can inhibit the enzymatic activity [7]. The question arises whether these compounds could be used as a basis for PET tracers of the CA IX. The aim of the present study was to label betulinic acid and betulinyl-3-sulfamate with ^{68}Ga after linking the compound to the chelator DOTA. These tracers were then evaluated in two different tumour cell lines under different conditions *in vitro*. Preliminary *in vivo* experiments were performed to demonstrate the

2 Methods

2.1 Cell Line

The subline AT1 of the rat R-3327 Dunning prostate carcinoma and the Walker-256 mammary carcinoma cells were grown in RPMI medium supplemented with 10% foetal calf serum (FCS) at 37 °C under humidified 5% CO_2 atmosphere. For hypoxia experiments cells were transferred to a hypoxia chamber (HypoxyLab, Oxford Optronix, Oxford, UK) at an O_2 fraction of 0.2% ($pO_2 \approx 1.5$ mmHg). Animal experiments were performed in male rats (body weight 194–277 g) in accordance with the German Law for Animal Protection (approved by the regional animal ethics committee). AT1 tumours were induced by subcutaneous injection of cells (4×10^7 cells/0.4 ml isotonic saline) into the dorsum of the hind foot. Tumours were investigated when they reached a volume of 0.3–1.5 ml. AT1 tumours with this volume are strongly hypoxic (mean pO_2 1.1 ± 2.1 mmHg) [8]. For modulation of the tumour oxygenation *in vivo* animals were kept at room air (21% O_2), hypoxic (8% O_2) or hyperoxic (100% O_2) conditions.

2.2 Tracer Synthesis

Betulinic (B) acid and betulinyl-3-sulfamate (BS) were synthesised and linked to the chelator DOTA (for details of the chemical synthesis see Supplementary Material). For labelling, ^{68}Ga was eluted from a ^{68}Ge/^{68}Ga generator (Eckert & Ziegler Eurotope, Berlin, Germany) into a sodium acetate-buffered solution containing B-DOTA (50 µg) or BS-DOTA (50 µg) (for details see Supplementary Material). After sterile filtration, the tracer was used for the *in vitro* and *in vivo* experiments.

2.3 Experimental Settings

With AT1 cells the following experimental groups were analysed: (1) control cells kept at room air (normoxia), (2) cells kept under hypoxia ($pO_2 \approx 1.5$ mmHg) for 24 h (hypoxia), (3) cells kept under hypoxic conditions and additionally treated with unlabelled tracer (10 µg/ml final concentration) 30 min prior to adding the labelled tracer. For Walker-256 the experimental groups were as followed: (1) wild type cells, (2) CA IX-transfected cells (for details of transfection see Supplementary Material), (3) CA IX-transfected cells additionally treated with unlabelled tracer. For binding studies cells were incubated with the labelled tracer for 30 min, centrifugated, the supernatant decanted, the cell pellet resuspended in PBS and the activity of the cell pellet and the supernatant was determined in a γ-counter. Additionally, the CA IX expression was measured by qPCR and Western blot.

For PET imaging the rats were anaesthetised with pentobarbital and placed in supine position in the scanner. PET imaging was performed on a nanoScan PET/CT (Mediso GmbH, Münster, Germany). The radiotracer BS-DOTA with an activity of 19.7–22.9 MBq was administered as a bolus injection (volume 300 µl) via the tail vein catheter and the PET measurements were performed 50 min after injection in 3D mode for 10 min (spatial resolution ~1.0–1.5 mm). Afterwards the PET data were reconstructed using 3D-OSEM algorithm. The calculated SUV values were then normalised to control for animals breathing room air.

3 Results

3.1 Cellular Metabolism CA IX Expression

Both cell lines produced substantial amount of lactic acid by glycolytic metabolism even under normoxic conditions. The glucose consumption as well as the lactate formation increased under hypoxic conditions ($pO_2 \approx 1.5$ mmHg) leading to an extracellular acidification (Supplementary Fig. S2). H^+ intracellularly generated by glycolysis was exported by the HIF-1 regulated CA IX. As shown in Fig. 1, mRNA and protein expression of CA IX increased significantly by hypoxia in AT1 cells *in vitro* and *in vivo*. In contrast, Walker-256 expressed CA IX at a very low level (only 10% of AT1) and could not be induced substantially by hypoxia (Fig. 1). Therefore Walker-256 cells were transfected with a Car 9 containing plasmid leading to an increase of the CA IX protein expression by about 500% (data not shown).

3.2 Tracer Binding on Tumour Cells In Vitro and In Vivo

The tracer binding to cells was quantified by the fraction of the cell-bound ^{68}Ga activity to the

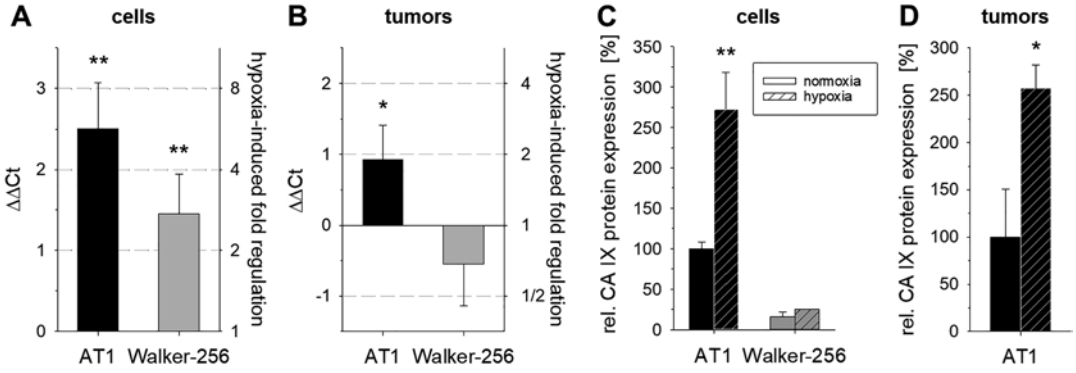

Fig. 1 CA IX expression on mRNA (A + B) and protein (C + D) level in AT1 and Walker-256 cells (A + C) and tumours (B + D) under control (normoxia) and hypoxic conditions. n = 4–12; (*) $p < 0.05$, (**) $p < 0.01$ normoxia *vs.* hypoxia

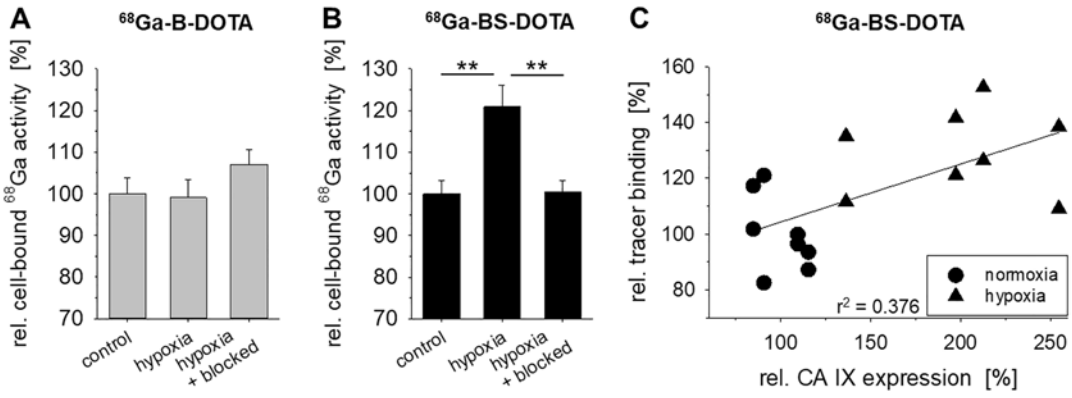

Fig. 2 (A + B) Binding of B-DOTA and BS-DOTA to AT1 cells kept at room air (control) or hypoxia ($pO_2 \approx 1.5$ mmHg) for 24 h. In the "blocked" experiments cells were additionally incubated with an excess of unlabelled tracer. (C) Correlation between BS-DOTA binding and CA IX expression in AT1 cells. 4–12; (**) $p < 0.01$

total activity in the sample. Compared to control conditions (room air) the binding of the B-DOTA tracer was unaffected by incubating the cells in strong hypoxia (Fig. 2a). However, binding of BS-DOTA to AT1 cells was significantly higher if the cells were kept at $pO_2 \approx 1.5$ mmHg for 24 h (hypoxia) (Fig. 2b) which could be blocked by unlabelled tracers. The binding correlated linearly with the CA IX expression (Fig. 2c). Walker-256 cells showed no specific binding of either tracer (Supplementary Fig. S3).

For *in vivo* testing ^{68}Ga-BS-DOTA (21.5 ± 0.5 MBq) was injected i.v. and PET imaging was performed. The analysis of the accumulation (SUV) revealed that the binding of the tracer to the tumour tissue was low (Fig. 3a). The uptake varied when animals were kept under hypoxic or hyperoxic conditions. The hypoxia group showed a SUV 8% higher than controls whereas the hyperoxia group had 5% lower values (Fig. 3b). A correlation with pO_2 measurements of a previous study [8] showed an inverse correlation between tumour pO_2 and tracer accumulation (Fig. 3c).

4 Conclusion

Betulinic acid derivatives bind specifically to the carbonic anhydrase IX [9] which offers the possibility to use this moiety for designing PET tracers of CA IX expression. Since CA IX expression is under the control of the transcription factor HIF-1α this tracer could be used as a marker for imaging the oxygenation status of tumours. In the present study the pure betulinic acid (coupled to DOTA chelator) was compared to betulinyl-3-sulfamate. From the binding studies of the tracers in two cell models it became obvious that in AT1 cells only the tracer with the sulfamate group (BS-DOTA) showed hypoxia-dependent binding resulting in a linear relation between CA IX expression and BS-DOTA binding. However, the increase in tracer binding in the hypoxia group was much lower than the increase in CA IX protein expression indicating that either not all CA IX molecules have been marked with tracer molecules or that not all CA IX molecules are incorporated into the outer cell membrane but stay in intracellular compartments. The functionality of the BS-DOTA tracer was shown by the fact that the increase of binding at low pO_2 could be blocked completely by an excess of unlabelled tracer. The tracer based upon pure betulinic acid (B-DOTA) showed no specific binding in both cell lines. In AT1 tumours *in vivo* the BS-DOTA accumulation showed differences (but not statistically significant) if animals were kept under different oxygen conditions. A reason for these insignificant results could be the fact that AT1 tumours are poorly oxygenated even under control conditions ($pO_2 = 1.2 \pm 0.7$ mmHg) [8]. Even with pure O_2 breathing the pO_2 increased only to 3.4 ± 1.0 mmHg. For this reason, it can be

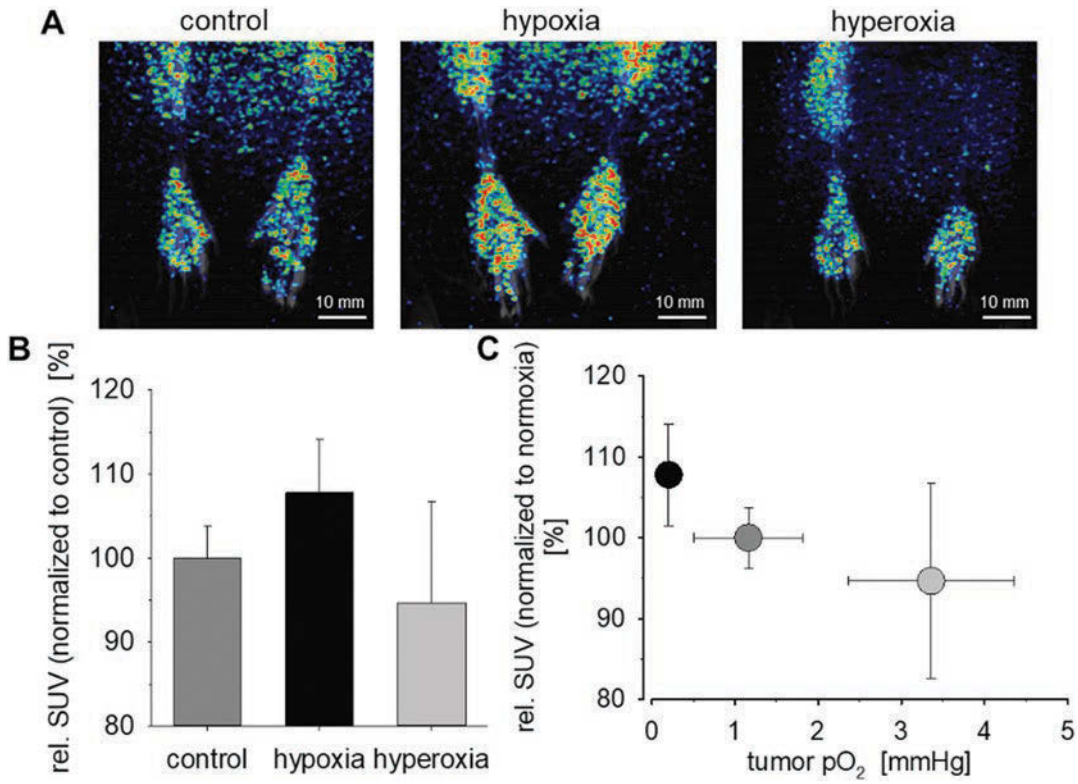

Fig. 3 (**a**) Examples of PET images of BS-DOTA binding in AT1 tumours. (**b**) Accumulation of BS-DOTA in AT1 tumours *in vivo* in animals kept at room air (control), hypoxia (8% O_2) or hyperoxia (100% O_2) for 24 h (n = 4). (**c**) Correlation between intratumoral pO_2 and BS-DOTA accumulation (pO_2 measurements from a previous study [8])

expected that the CA IX expression is strongly stimulated under control but even under hyperoxic conditions so that no marked differences of the tracer accumulation between the three groups could be expected.

Betulinyl-3-sulfamate linked with DOTA and labelled with ^{68}Ga might be used as a PET tracer of CA IX expression in tumours and to provide information about the oxygenation status. Since pure betulinic acid showed no specific binding it could be an indication that a sulfamate group is essential for the specific binding. However, although BS-DOTA binding was O_2-dependent *in vitro* and *in vivo*, some limitations of this approach for hypoxia imaging must be discussed. Firstly, the overall uptake of the tracer in tumours was rather low which might be due to the DOTA sidechain. Secondly, the binding depended not only on the hypoxia-induced CA IX expression but also on the tumour-line-specific basal CA IX expression and on the initial oxygenation status of the tumour. Therefore, betulinic acid compounds seem to be of only limited use for visualisation of the tumour oxygenation status.

References

1. Thews O, Vaupel P (2015) Spatial oxygenation profiles in tumors during normo- and hyperbaric hyperoxia. Strahlenther Onkol 191:875–882
2. Peeters SG, Zegers CM, Lieuwes NG et al (2015) A comparative study of the hypoxia PET tracers [^{18}F]HX4, [^{18}F]FAZA, and [^{18}F]FMISO in a preclinical tumor model. Int J Radiat Oncol Biol Phys 91:351–359
3. Pastorekova S, Gillies RJ (2019) The role of carbonic anhydrase IX in cancer development: links to

hypoxia, acidosis, and beyond. Cancer Metastasis Rev 38:65–77
4. Cepa A, Ralis J, Kral V et al (2018) In vitro evaluation of the monoclonal antibody ^{64}Cu-IgG M75 against human carbonic anhydrase IX and its in vivo imaging. Appl Radiat Isot 133:9–13
5. Fiedler L, Kellner M, Oos R et al (2018) Fully automated production and characterization of ^{64}Cu and proof-of-principle small-animal PET imaging using ^{64}Cu-labelled CA XII targeting 6A10 fab. ChemMedChem 13:1230–1237
6. Jia L, Li X, Cheng D et al (2019) Fluorine-18 click radiosynthesis and microPET/CT evaluation of a small peptide-a potential PET probe for carbonic anhydrase IX. Bioorg Med Chem 27:785–789
7. Vanchanagiri K, Emmerich D, Bruschke M et al (2018) Synthesis and biological investigation of new carbonic anhydrase IX (CAIX) inhibitors. Chem Biol Interact 284:12–23
8. Frank J, Gündel D, Drescher S et al (2015) Injectable LiNc-BuO loaded microspheres as in vivo EPR oxygen sensors after co-implantation with tumor cells. Free Radic Biol Med 89:741–749
9. Winum JY, Pastorekova S, Jakubickova L et al (2005) Carbonic anhydrase inhibitors: synthesis and inhibition of cytosolic/tumor-associated carbonic anhydrase isozymes I, II, and IX with bis-sulfamates. Bioorg Med Chem Lett 15:579–584

Role of the mTOR Signalling Pathway During Extracellular Acidosis in Tumour Cells

M. Wolff, M. Rauschner, S. Reime, A. Riemann, and O. Thews

Abstract

The metabolic microenvironment of solid tumours is often dominated by extracellular acidosis which results from glycolytic metabolism. Acidosis can modulate gene expression and foster the malignant progression. The aim of the study was to analyse the effects of extracellular acidosis on the mTOR signalling pathway, an important regulator of anabolic and catabolic processes like cell proliferation and autophagy. The study was performed in two tumour cell lines, AT-1 prostate and Walker-256 mammary carcinoma cells. Cells were incubated at pH 7.4 or 6.6 for 3 h and 24 h. Then RNA and protein were extracted and analysed by qPCR and western blot. mTOR and P70-S6 kinase (P70-S6K), an important downstream target of mTOR, as well as the autophagic flux were studied. The effect of acidosis on P70S6K phosphorylation was compared to pharmacological mTOR inhibition with LY294002 and rapamycin. In both cell lines the total mTOR expression was not altered by acidosis, however, the mTOR phosphorylation was reduced after 3 h but not after 24 h. The P70S6K phosphorylation was reduced at both time points comparable to changes by pharmacological mTOR inhibitors. The autophagic flux, also a target of mTOR and measured by LC3-II expression, was increased in both cell lines after 24 h of acidosis. The results of this study indicate that mTOR signalling is inhibited by extracellular acidosis which then lead to a reduced activity of the P70-S6 kinase (modulating gene expression) and increased autophagy possibly mediated by ULK1/2 activity. These finding may offer new perspectives for therapeutic interventions in acidic tumours.

Keywords

AT1 cells · Walker-256 cells · Warburg effect · Malignant progression

1 Introduction

Many solid tumours show an adverse tumour microenvironment with hypoxia and extracellular acidosis [1]. Hypoxia results from chaotic structured and dysfunctional tumour vascularisation leading to glycolytic metabolism [2]. However, even in many well oxygenated tumours glycolytic metabolism is found ("Warburg effect") [3]. Glycolysis leads to lactic acid production with H^+ accumulation in the extracellular space leading to pH even below

M. Wolff · M. Rauschner · S. Reime · A. Riemann · O. Thews (✉)
Julius-Bernstein-Institute of Physiology, University of Halle, Halle, Germany
e-mail: oliver.thews@medizin.uni-halle.de

F. Scholkmann et al. (eds.), *Oxygen Transport to Tissue XLIII*, Advances in Experimental Medicine and Biology 1395, https://doi.org/10.1007/978-3-031-14190-4_46

6.0 [4]. Tumour acidosis has been described to contribute to the malignant progression (e.g., invasion, metastasis) but the underlying molecular mechanisms are still not fully understood. One interesting signalling pathway is mTOR. mTOR is a serin-threonine kinase, involved in the regulation of anabolic processes, like cell growth and proliferation, but also in the regulation of catabolic processes like autophagy [5]. There is indication that mTOR activity is affected by the extracellular pH [6]. The mTOR complex 1 (mTORC1) is activated by the small G-Protein Rheb, which is under the control of PI3K/Akt and ERK1/2 signalling pathways which has been shown to be regulated by the extracellular pH [7]. Activated mTORC1 has multiple downstream targets. One of them is the P70-S6 kinase, which promotes mRNA biogenesis, translation and synthesis of ribosomal proteins [5]. mTORC1 also suppresses autophagy by inhibition of ULK1/2 [8]. The aim of the study was to analyse whether extracellular acidosis leads to alterations of the mTOR expression or activation in two different tumour lines. The study should also test whether these changes affect downstream targets of mTOR such as the P70-S6 kinase (proliferation) or the ULK1/2 pathways leading to autophagy.

2 Methods

2.1 Cell Line

The subline AT-1 of the rat R-3327 Dunning prostate carcinoma and the rat mammary carcinoma cell line Walker-256 were grown in RPMI medium supplemented with 10% foetal calf serum (FCS). For Walker-256 cells the medium contained additionally 20 mM HEPES and 0.15% $NaHCO_3$. Cells were grown at 37 °C under humidified atmosphere containing 5% CO_2. To study the changes in expression cells were incubated in FCS lacking medium buffered with 10 mM HEPES/10 mM MES adjusted to pH 7.4 or 6.6 for 3 h and 24 h. For measuring the P70-S6 kinase and mTOR on protein level experiments were performed in FCS containing media.

2.2 Experimental Settings

After the incubation at different pH levels for either 3 h or 24 h the protein expression of mTOR, phosphor-mTOR, P70-S6 kinase, phosphor-P70-S6K, and LC3 were measured. Western blot analyses were performed according to standard protocols using an Odyssey scanner (LI-COR Biosciences, Bad Homburg, Germany). Primary antibodies were obtained from Cell Signalling (Danvers, USA), secondary antibodies also obtained from LI-COR. For mTOR inhibition LY294002 (50 µM) and rapamycin (500 nM) were used. The autophagic flux was calculated from the changes in the LC3-II expression in the presence and absence of the protease inhibitors aloxistatin and pepstatin A (10 µg/ml each) according to the literature [9]. The autophagic flux was calculated from the LC3-II expression with inhibitors minus control expression with DMSO.

3 Results

The expression of total mTOR protein in AT-1 as well as in Walker-256 cells was almost unaffected by extracellular acidosis after 3 h as well as after 24 h (grey bars in Fig. 1). At pH 7.4 the absolute mTOR expression was not different between 3 h and 24 h. Measuring the mTOR expression on mRNA level confirmed this finding showing no relevant differences in mRNA expression (data not shown). However, exposing the cells to an acidic environment affected mTOR phosphorylation. After 3 h at pH 6.6 mTOR phosphorylation of AT-1 cells was reduced by 31% which was comparable to the finding in Walker-256 cells (black bars in Fig. 1). After 24 h this effect disappeared in both cell lines, indicating a time dependent impact of pH on mTOR inhibition. The direct downstream target of mTOR, the P70-S6 kinase (P70-S6K), also showed in both cell lines no relevant changes in total protein expression, but a reduced phosphorylation after 3 h and after 24 h (Fig. 2). In AT-1 cells phosphorylation was reduced by 71% after 3 h ($p < 0.01$) and by 52% after 24 h. Similar results were found in the

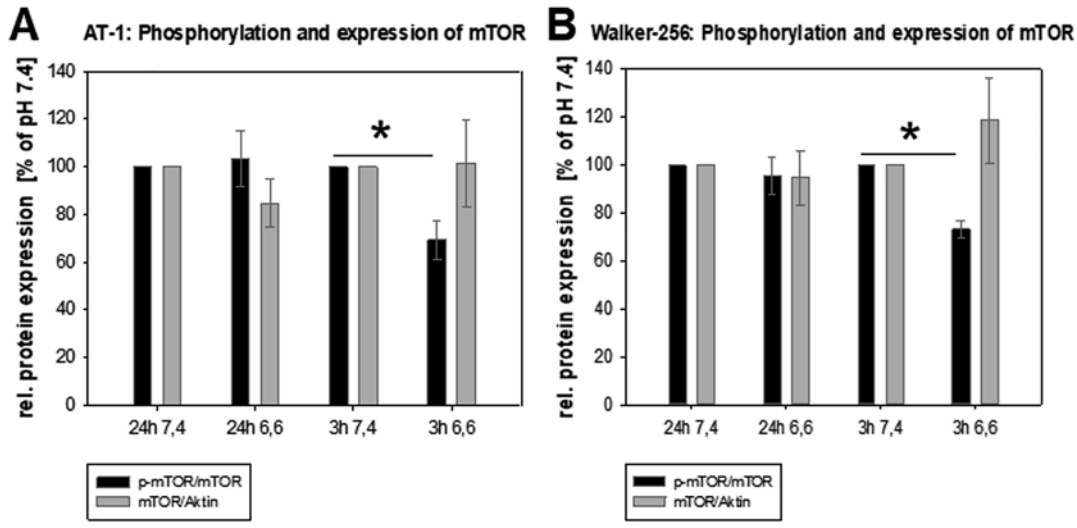

Fig. 1 Impact of extracellular pH (7.4 and 6.6) for 24 or 3 h on mTOR expression and phosphorylation of (**a**) AT-1 and (**b**) Walker-256 cells. Normalised to respective value at pH 7.4. (*) $p < 0.05$; n = 4–6

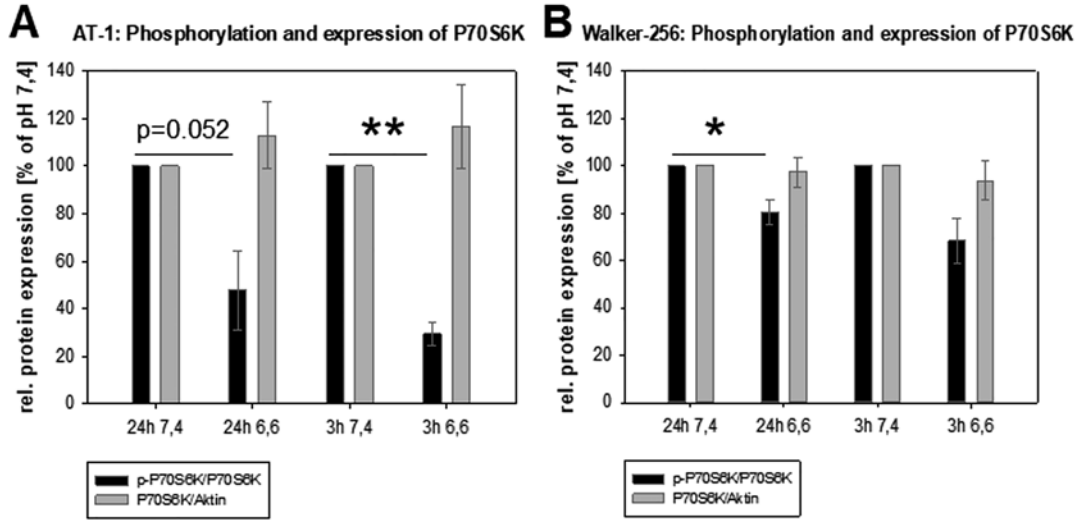

Fig. 2 Impact of extracellular pH (7.4 and 6.6) for 24 or 3 h on P70-S6 kinase (P70S6K) expression and phosphorylation of (**a**) AT-1 and (**b**) Walker-256 cells. Normalised to respective value at pH 7.4. (*) $p < 0.05$, (**) $p < 0.01$; n = 4

Walker-256 cells, in which phosphorylation was reduced by 20% after 24 h ($p < 0.05$). These result fit well to the observed decreased mTOR activation. In order to analyse whether the decrease of mTOR activation leads to a comparable reduction in P70-S6K phosphorylation, the acidosis effect was compared with the impact of known pharmacological mTOR-inhibitors (LY294002, rapamycin) (Fig. 3). In both cells lines the inhibitory effect of acidosis on P70-S6 kinase was in the same range (≈50%) as with both mTOR inhibitors. LC3B-II protein levels were measured to study the effects of acidosis on autophagy. The LC3B-II measurement showed an increase in LC3B-II protein level expression in both cell lines but only after 24 h acidosis, indicating an increase in autophagic activity (Fig. 4). In AT-1 cells the increase was

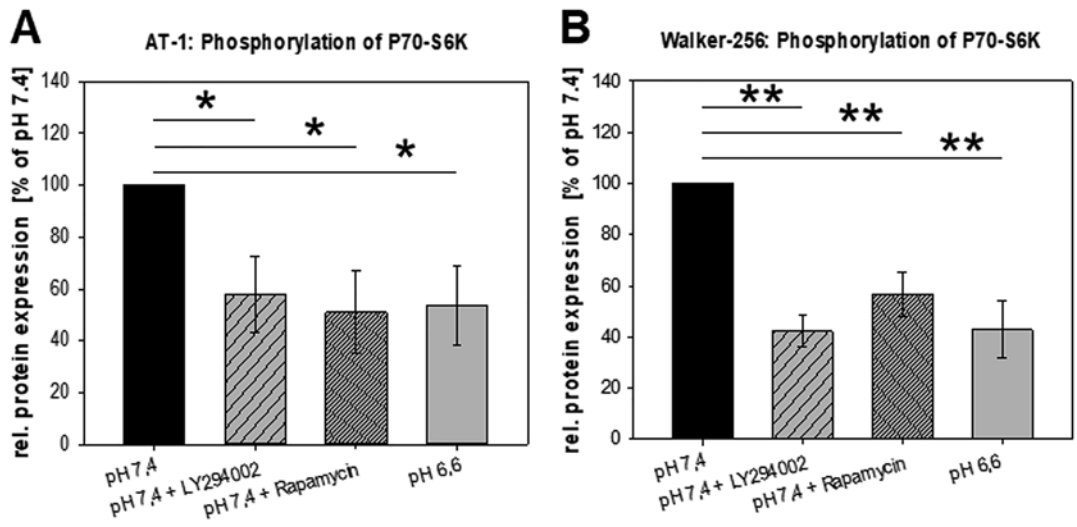

Fig. 3 Relative phosphorylation of the P70-S6 kinase of (**a**) AT-1 and (**b**) Walker-256 cells after 24 h at pH 7.4 or 6.6 and impact of mTOR inhibition by LY294002 and rapamycin. (*) $p < 0.05$, (**) $p < 0.01$ n = 5–7, n = 6

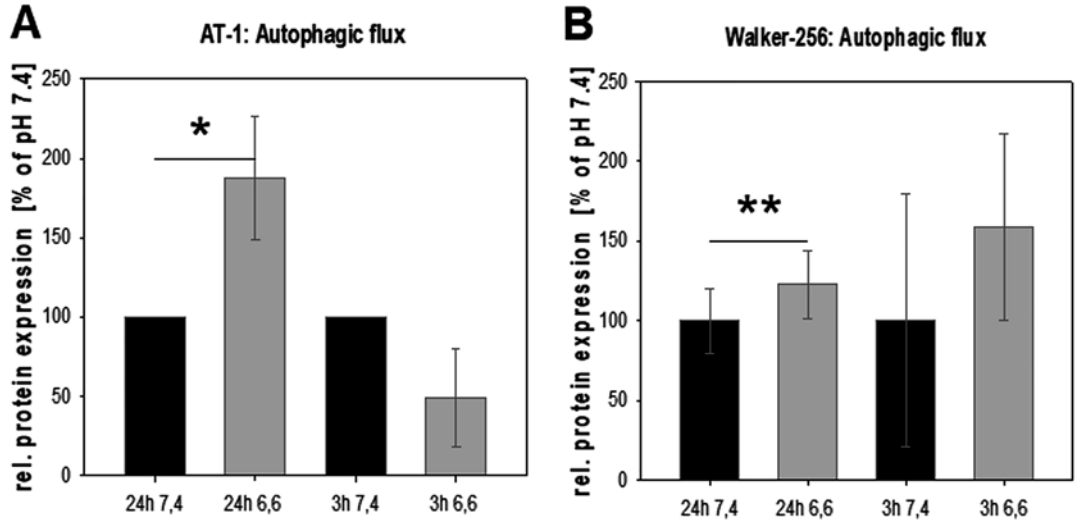

Fig. 4 Impact of extracellular pH (7.4 and 6.6) for 24 or 3 h on the autophagic flux measured by the autophagy marker LC3-II of (**a**) AT-1 and (**b**) Walker-256 cells. (*) $p < 0.05$; n = 4-5

up to 88% and in Walker-256 cells 23%. After 3 h acidosis the results were non-uniform, showing a marked variability between the replicates. In AT-1 cells on average a decrease in autophagic flux 50% (n.s.) was observed, whereas in Walker-256 cells the flux increased by 60% (n.s.)

4 Conclusion

Acute extracellular acidosis (3 h) inhibits mTOR activation in AT-1 prostate carcinoma cells as well as in Walker-256 mammary carcinoma cells. However, these effects disappear after 24 h. In parallel to mTOR inhibition a reduction of the

phosphorylation of the downstream P70-S6 kinase was found. The degree of inhibition was comparable to that obtained with pharmacological mTOR inhibitors. The inhibition of the P70-S6 kinase was detectable after 3 h and 24 h, therefore lasting longer than the initial mTOR inhibition. An acidosis dependent inhibition of the P70-S6 kinase has also been described by Balgi et al. [6]. However, these authors did not analyse the direct impact on mTOR phosphorylation and they took only much shorter time intervals into account (5–30 min). Especially the differences between 3 h and 24 h could be of interest since the extracellular tumour acidosis outlasts longer periods (hours to days). pH-dependent inhibition of mTOR activity and therefore decreased protein synthesis may contribute to explain acidosis-mediated decrease in cell proliferation. In addition, the present results indicate that that acidosis activates autophagic processes. Further studies will need to prove that this mechanism is mediated by decreased mTOR activation which may lead to increased ULK1/2 activation, in turn a strong activator of autophagy. The role of increased autophagy in tumour biology has been discussed controversially as it can act as a tumour suppressor but also as a promotor [10]. Therefore, it is important to further analyse the role of extracellular acidosis in this process which may lead to new therapeutic targets.

Acknowledgments The study was supported by the HaPKoM program of the Medical Faculty, University of Halle (PK40) and the Deutsche Forschungsgemeinschaft DFG (grant TH 482/6-1).

References

1. Corbet C, Feron O (2017) Tumour acidosis: from the passenger to the driver's seat. Nat Rev Cancer 17(10):577–593. https://doi.org/10.1038/nrc.2017.77
2. Thews O, Riemann A (2019) Tumor pH and metastasis: a malignant process beyond hypoxia. Cancer Metastasis Rev 38(1–2):113–129. https://doi.org/10.1007/s10555-018-09777-y
3. Vander Heiden MG, Cantley LC, Thompson CB (2009) Understanding the Warburg effect: the metabolic requirements of cell proliferation. Science 324(5930):1029–1033. https://doi.org/10.1126/science.1160809
4. Vaupel P, Kallinowski F, Okunieff P (1989) Blood flow, oxygen and nutrient supply, and metabolic microenvironment of human tumors: a review. Am Assoc Cancer Res 49(23):6449–6465
5. Laplante M, Sabatini DM (2009) mTOR signaling at a glance. J Cell Sci 122(Pt 20):3589–3594. https://doi.org/10.1242/jcs.051011
6. Balgi AD, Diering GH, Donohue E, Lam KKY, Fonseca BD, Zimmerman C, Numata M, Roberge M (2011) Regulation of mTORC1 by pH. PLoS One 6(6):e21549. https://doi.org/10.1371/journal.pone.0021549.g001
7. Riemann A, Schneider B, Ihling A, Nowak M, Sauvant C, Thews O, Gekle M (2011) Acidic environment leads to ROS-induced MAPK signaling in cancer cells. PLoS One 6(7):e22445. https://doi.org/10.1371/journal.pone.0022445
8. Dossou AS, Basu A (2019) The emerging roles of mTORC1 in macromanaging autophagy. Cancers (Basel) 11(10). https://doi.org/10.3390/cancers11101422
9. Mizushima N, Yoshimori T (2007) How to interpret LC3 immunoblotting. Autophagy 3(6):542–545. https://doi.org/10.4161/auto.4600
10. Yun CW, Lee SH (2018) The roles of autophagy in cancer. Int J Mol Sci 19(11). https://doi.org/10.3390/ijms19113466

Part V

Tissue Oxygenation

Feasibility Study of Remote Contactless Perfusion Imaging with Consumer-Grade Mobile Camera

Timothy Burton, Gennadi Saiko, and Alexandre Douplik

Abstract

A non-invasive, contactless, inexpensive and easy-to-operate perfusion imaging method using a consumer-grade mobile camera (iPhone 8) developed in our group can visualise blood flow in tissue. *Methods*: Ischemia was induced in one hand using a blood pressure cuff inflated over the systolic blood pressure to stop the blood flow. Using an iPhone, data was collected from 5 subjects, beginning with no occlusion (a baseline), followed by one hand occluded, and then release of the occlusion to restore blood circulation. This protocol was repeated for each hand for a total of 10 videos. The data were analysed to extract the oscillating and quasi-constant components of the photoplethysmogram signal representing blood flow. In addition, we introduced a scoring parameter to reflect perfusion (i.e., perfusion score). *Results*: The proposed perfusion score was used to create a pseudo colour map of perfusion across the protocol, demonstrating the ability to detect ischemia caused by occlusion. The difference in perfusion score was statistically significant between ischemia and baseline/recovery. *Conclusions*: Pilot results on healthy volunteers demonstrate the feasibility of perfusion imaging using a consumer-grade camera. A further developed method can be used to assess the viability of transplanted tissue.

Keywords

Flap viability · Vascular imaging · PPG imaging · Photoplethysmogram

1 Introduction

Perfusion imaging is the visualisation of blood flow in tissue. The ideal perfusion imaging approach is non-invasive and contactless, inexpensive, and does not require a skilled technician to operate. In particular, the contactless property enables use in sterile and telehealth environments and when tissue is sensitive to contact. Our present work focuses on demonstrating the feasibility of perfusion imaging using an affordable consumer-grade camera.

A primary application of perfusion imaging is assessing transplanted tissue viability, such as the flaps grafted during a mastectomy operation. Mastectomy flap necrosis currently occurs at significant rates (10–30% [1]), indicating the need for a perfusion imaging approach to identify tis-

Authors Timothy Burton and Gennadi Saiko have equally contributed to this chapter.

T. Burton · G. Saiko (✉) · A. Douplik
Ryerson University, Toronto, ON, Canada
e-mail: gsaiko@ryerson.ca

F. Scholkmann et al. (eds.), *Oxygen Transport to Tissue XLIII*, Advances in Experimental Medicine and Biology 1395, https://doi.org/10.1007/978-3-031-14190-4_47

sue at risk to enable rapid intervention. The current standard of care is clinical bedside monitoring (assessment of tissue colour, capillary refill, and dermal edge bleeding) [1], limited by subjectivity. A comprehensive review of available objective flap monitoring techniques is presented in [2]. It includes fluorimetry, the Cook-Swartz implantable Doppler probe, microdialysis, implanted oximetry probes, CO_2 monitoring, glucose and lactate measurements, among others. The shortcomings of these techniques are their complexity and invasiveness. So, minimally invasive or non-invasive alternatives that can be operated with minimal training are of value. For example, fluorimetry is a minimally invasive technique initially based on fluorescein dye and is typically performed as an indocyanine green angiography [3]. The indocyanine green dye is injected into the venous system and excited with a laser, which causes fluorescence to identify perfusion. While indocyanine green angiography is minimally invasive, it requires highly qualified personnel and relies on costly, complex instrumentation.

Alternatively, perfusion can be detected strictly non-invasively by observing the periodic pulse wave in blood vessels caused by cardiac contraction. The pulse wave distends vessels due to increased local arterial pressure. Therefore, it affects the local light absorption along the vessel, where haemoglobins are the primary light absorbers (chromophores) in the visible spectrum range. Vessel distension is maximal at the peak of the pulse wave amplitude and minimal at the pulse wave trough. When localised vessel distension is maximal, light absorption increases in this vessel component due to the larger fraction of the blood. Correspondingly, light reflection from the tissue decreases due to that increased absorption. The opposite effect occurs at the trough of the pulse wave; minimal vessel distension results in lower light absorption and increased light reflection within the local portion of the vessel. Hence, the light reflection is modulated by pulse wave and, consequently, can be linked to blood perfusion. Photoplethysmographic (PPG) methods can measure such a periodic light reflection pattern. PPG-based methods are typically skin contact-based and single-point measurements [4]. With advancements in imaging technologies, PPG methods can be extended into imaging modalities [5]. For example, PPG imaging has been shown to be effective for perfusion mapping using a system composed of two polarisers and an LED at a specific wavelength, with data captured with a scientific-grade camera [6]. The authors [7] used a high-speed camera to detect pulse wave propagation.

In contrast, we used an iPhone 8 containing a consumer-grade camera and an LED with an uncontrolled emission spectrum. Compared to scientific-grade equipment, such mobile consumer devices are both low-cost and widely available. In addition, while consumer mobile devices, and the iPhone in particular [8, 9], have been previously used for single-point PPG measurement, we are unaware of their use for imaging.

2 Methods

We used an occlusion model of ischemia in hands, where one hand was occluded with a blood pressure cuff on the upper arm and the other was left unoccluded as a control. The hands were placed side by side and recorded using an iPhone 8 at 60 frames per second. The iPhone was placed about 10 cm above the hands. Hands were illuminated with the onboard LED. The hands were rotated by 180° with respect to the camera. The collection protocol began with a 10-s baseline section. In the occlusion section, the cuff was then inflated above the systolic pressure and maintained for 30 s. The cuff was rapidly deflated for the recovery section and then held for 30 s. The resultant data was approximately 85-s 1920 × 1080 pixel RGB before cropping to the interest region. The study was approved by the Ryerson REB, and pilot data was captured from five healthy subjects with various skin tones, with each hand occluded once for a total of 10 videos.

First, the video data was processed to extract the local PPG signals by Gaussian blurring the spatial averaging over 5 × 5 pixel regions. Next, local signals were averaged to generate signals for each hand. Signals from the occluded hand and the non-occluded hand of a subject were compared, and signals differed in both the oscillating (AC) and quasi-constant (DC) components during the occlusion section of the protocol, as shown in Fig. 1. The DC component was similar across hands during baseline and recovery sections, but the amplitude dropped during occlusion. Wavelets were used to analyse the AC components of the signals, which is an appropriate tool given the non-stationary characteristic of the data [10]. A wavelet coherence map, which compares the local wavelet power of each signal over time and frequency, visualised the time-frequency similarity of the signals. The coherence in the 1.2-3 Hz frequency band present during both baseline and recovery sections reduced during occlusion, as shown in Fig. 2, which captures the dissimilarity in the AC component caused by occlusion.

The PPG signal was post-processed using these meaningful components. A continuous wavelet transform band-pass filtered the signal from 1.2-3 Hz to capture the AC information. The signal mean (normalised by dividing by 255, given that the iPhone camera ADC was 8-bit) was added back to capture the DC information. The perfusion score was the summation of the interquartile signal range and mean. Note that the range of these statistics is similar, meaning that a more complex compression process was not required. The perfusion score was calculated for each 5 × 5 non-overlapping block and overlaid as a transparent pseudo-colour map on the first video frame. In addition, for statistical comparison, the average perfusion score was generated from each hand.

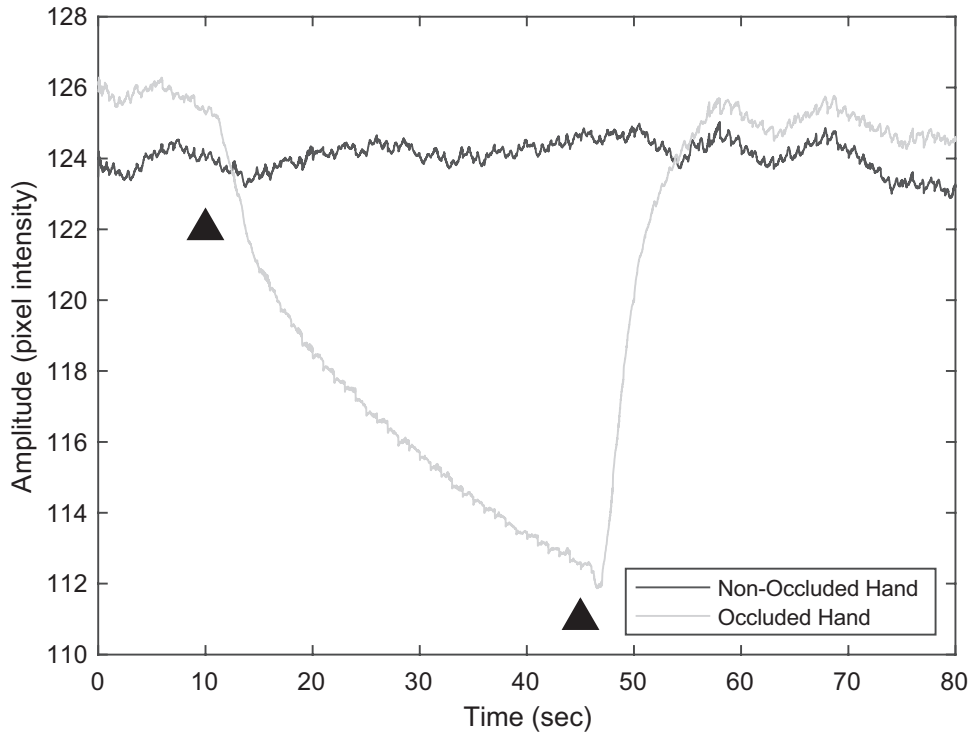

Fig. 1 The effect of the protocol on the signal, with the first triangle denoting the boundary between the baseline and ischemia sections and the second triangle denoting the boundary between the ischemia and recovery sections

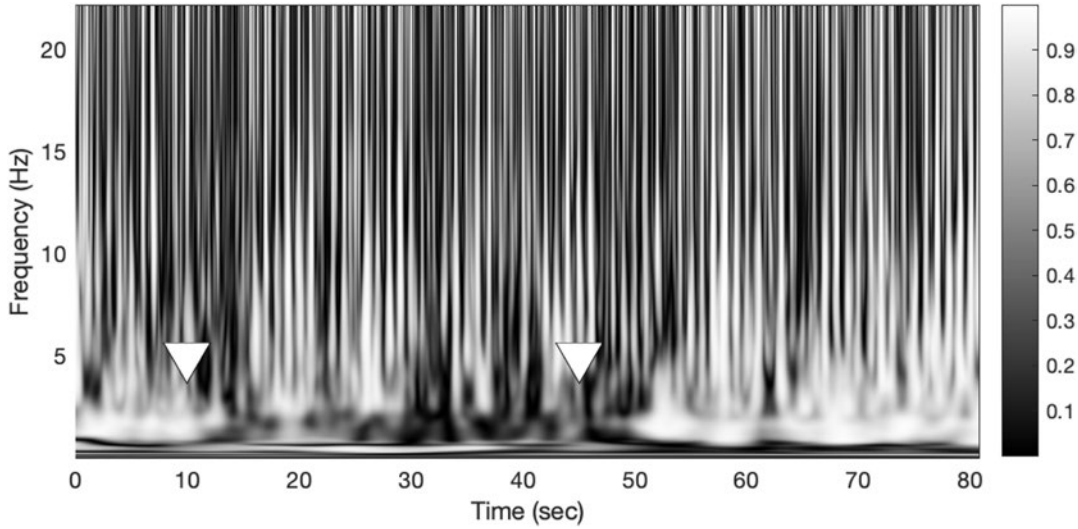

Fig. 2 Wavelet coherence analysis of the signals from the two hands

3 Results

Figure 3 shows the first video frame (left) and resultant perfusion map (right) for the same video used in Figs. 1 and 2. The colouring by perfusion score of the occluded right hand is less intense than the non-occluded left hand, representing the reduced perfusion caused by the occlusion. The average perfusion score was calculated for both hands during each protocol section. Then, the score of the occluded hand was subtracted from the non-occluded hand for a quantitative assessment. Figure 3 shows a difference between the scores of 0.0008 during the baseline section, 0.0925 during the occlusion section (a 115.6-fold increase from baseline), and 0.0263 during the recovery section (3.5-fold decrease from occlusion). The score differences were calculated across all 10 videos for the colour channel with the highest contrast. Paired t-tests were used to test for differences between the means of the scores during each pair of the protocol sections across the 10 videos since each video was collected using the same protocol. Both the baseline and occlusion sections ($p < 0.01$) and occlusion and recovery sections ($p < 0.01$) were found to be significantly different, whereas the baseline and recovery sections were not significantly different ($p = 0.34$).

4 Discussion

The perfusion score and mapping described here is effective in identifying ischemia in hands occluded with a blood pressure cuff in pilot data from five subjects. The contrast between the hands during the occlusion section of the protocol was statistically significantly different from the non-ischemic sections (baseline and recovery). Further, the lack of significant difference between the baseline and recovery sections is likely representative of the normal health status of the subjects, given that the occluded hand reperfused quickly to normalise the perfusion scores. In future work, the protocol will be modified to induce ischemia more effectively before collecting a larger dataset to explore the variability across subjects. The iPhone 8, as used in the present work, acquires data at 8-bit depth. Thus, older and newer models with similar bit depth and resolution are expected to provide similar results. However, upgrading to the most recently released model (iPhone 13) offers 12-bit depth at the same spatial and temporal resolutions, which has the potential to increase the acquisition quality dramatically. Finally, perfusion score and mapping will be improved to enhance detection and visualisation of ischemia.

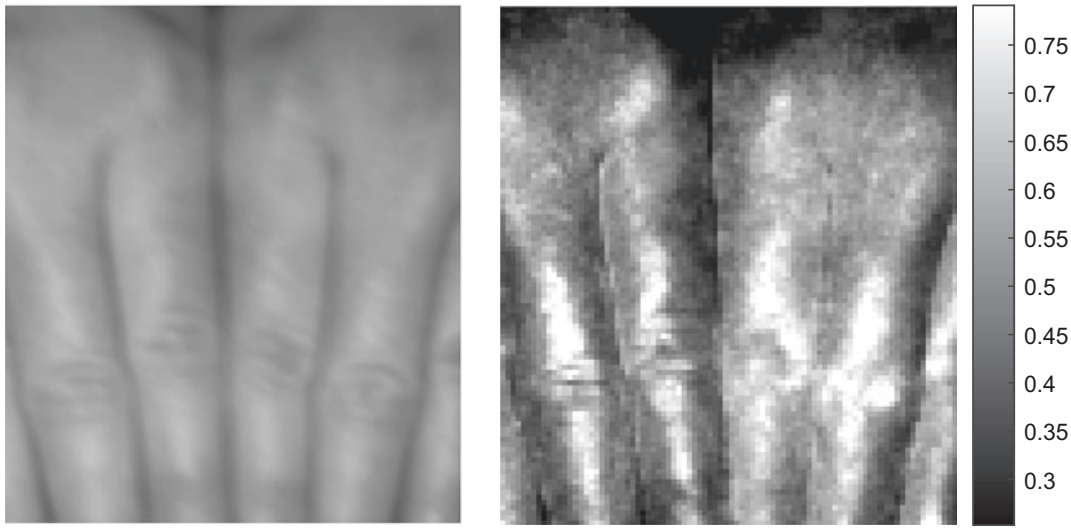

Fig. 3 Left pane: an image of the hands (the right hand is occluded). Right pane: a perfusion map of the hands generated by localised perfusion scores. The colour scale shows the range of perfusion scores

5 Conclusion

In this pilot study, the iPhone video acquisition paired with the data processing described was effective in identifying occlusion-induced ischemia. However, further work will be performed to both improve and stabilise the detection and generate a more robust assessment of the performance using a larger number of subjects.

Acknowledgments The authors thank the volunteers who participated in this study and Meiyun Cao for assistance in the lab, and all the Ryerson photonics group members for their support. The authors acknowledge funding from NSERC Alliance (Douplik & Saiko), NSERC Discovery (Douplik), NSERC RTI (Douplik), and Ryerson Healthy Fund (Douplik).

References

1. Moyer HR, Losken A (2012) Predicting mastectomy skin flap necrosis with indocyanine green angiography: the gray area defined. Plas Reconstr Surg 129(5):1043–1048
2. Chae MP, Rozen WM, Whitaker IS et al (2015) Current evidence for postoperative monitoring of microvascular free flaps. A systematic review. Ann Plast Surg 74:621–632
3. Ritschl LM, Schmidt LH, Fichter AM et al (2018) Prediction of flap necrosis by using Indocyanine green Videoangiography in cases of venous occlusion in the epigastric flap model of the rat. J Reconstr Microsurg Open 3:e62–e69
4. Castaneda D, Esparza A, Ghamari M et al (2018) A review on wearable photoplethysmography sensors and their potential future applications in health care. Int J Biosen Bioelectr 4(4):195–202
5. Sun Y, Thakor H (2015) Photoplethysmography revisited: from contact to noncontact, from point to imaging. IEEE Trans Biomed Eng 63(3):463–477
6. Kamshilin AA, Teplov V, Nippolainen E et al (2013) Variability of microcirculation detected by blood pulsation imaging. PLoS One 8(2):e57117
7. Saiko G, Dervenis M, Douplik A (2021) On the feasibility of pulse wave velocity imaging for remote assessment of physiological functions. Adv Exp Med Biol 1269:393–397
8. Matsumura K, Rolfe P, Lee J, Yamakoshi T (2014) iPhone 4s photoplethysmography: which light color yields the most accurate heart rate and normalized pulse volume using the iPhysioMeter application in the presence of motion artifact? PLoS One 9(3):e91205
9. Nam Y, Nam Y-C (2017) Photoplethysmography signal analysis for optimal region-of-interest determination in video imaging on a built-in smartphone under different conditions. Sensors 17(10):2385
10. Rhif M, Abbes AB, Farah IM et al (2019) Wavelet transform application for/in non-stationary time-series analysis: a review. Appl Sci 9(7):1345

Stability of a Novel PEGylation Site on a Putative Haemoglobin-Based Oxygen Carrier

C. E. Cooper, M. Bird, X. Sheng, M. Simons, L. Ronda, A. Mozzarelli, and B. J. Reeder

Abstract

PEGylation of protein sulfhydryl residues is a common method used to create a stable drug conjugate to enhance vascular retention times. We recently created a putative haemoglobin-based oxygen carrier using maleimide-PEG to selectively modify a single engineered cysteine residue in the α subunit (αAla19Cys). However, maleimide-PEG adducts are subject to deconjugation via retro-Michael reactions, with consequent cross-conjugation to endogenous plasma thiols such as those found on human serum albumin or glutathione. In previous studies mono-sulfone-PEG adducts have been shown to be less susceptible to deconjugation. We therefore compared the stability of our maleimide-PEG Hb adduct with one created using a mono-sulfone PEG. The corresponding mono-sulfone-PEG adduct was significantly more stable when incubated at 37 °C for 7 days in the presence of 1 mM reduced glutathione, 20 mg/mL human serum albumin, or human serum. In all cases haemoglobin treated with mono-sulfone-PEG retained >90% of its conjugation whereas maleimide-PEG showed significant deconjugation, especially in the presence of 1 mM reduced glutathione where <70% of the maleimide-PEG conjugate remained intact. Although maleimide-PEGylation of Hb seems adequate for an oxygen therapeutic intended for acute use, if longer vascular retention is required reagents such as mono-sulfone-PEG may be more appropriate.

Keywords

Vascular retention time · Recombinant human hemoglobin · Mono-sulfone-PEG adduct · Maleimide-PEG adduct

1 Introduction

In order to use a haemoglobin-based oxygen carrier (HBOC) as an oxygen therapeutic, it is necessary to increase the size of the haemoglobin (Hb) molecule to prevent renal clearance [1]. This can be achieved by PEGylation. However, whilst previously used non-specific PEGylation methods can create stable HBOC, these HBOC are heterogeneous mixtures with significantly altered protein function [1]. We therefore recently

C. E. Cooper (✉) · M. Simons · B. J. Reeder
School of Life Sciences, University of Essex, Colchester, UK
e-mail: ccooper@essex.ac.uk

M. Bird · X. Sheng
Abzena Ltd., Babraham, Cambridge, UK

L. Ronda · A. Mozzarelli
University of Parma, Parma, Italy

Institute of Biophysics, Pisa, Italy

F. Scholkmann et al. (eds.), *Oxygen Transport to Tissue XLIII*, Advances in Experimental Medicine and Biology 1395, https://doi.org/10.1007/978-3-031-14190-4_48

engineered a HBOC with homogenous PEGylation at a single site, by removing the existing reactive sulfhydryl on the β subunit (βCys93) and introducing a new surface cysteine sulfhydryl on the α subunit. The novel PEGylation site chosen (αAla19Cys) was on the surface of the protein, distant from the heme binding site and the α/β dimer/dimer interface. The resultant mutant Hb (βCys93Ala/αAla19Cys) had unaltered functional oxygen-binding properties to wild type Hb and no increase in the autoxidation or heme loss that has prevented the use of previous recombinant Hb as viable oxygen therapeutics [2]. Our PEGylation method used maleimide-PEG to conjugate to a surface sulfhydryl. However, maleimide-PEG adducts are subject to deconjugation via retro-Michael reactions and cross-conjugation to endogenous thiol species *in vivo*, such as human serum albumin (HSA) or reduced glutathione (GSH). We therefore compared our maleimide-PEG adduct with one created using a mono-sulfone-PEG less susceptible to deconjugation [3]. In the presence of high (1 mM) GSH, Hb treated with mono-sulfone-PEG retained >90% of its conjugation whereas maleimide-PEG showed significant deconjugation, with <70% of the maleimide-PEG conjugate remaining intact following 7 days incubation at 37 °C [4]. In this paper we compare the stability data in the presence of GSH with more physiological levels of competing thiols species such as HSA and IgG-depleted serum.

2 Methods

Recombinant human Hb with the βCys93Ala/αAla19Cys mutations was expressed in a pET-Duet system in an *E. coli* BL21 host and purified by ion exchange chromatography and gel filtration as described previously [2]. The purified Hb was then PEGylated at αAla19Cys with a 20 kDa maleimide-PEG or mono-sulfone-PEG [4]. Hb-PEG solutions were prepared at 2 mg/mL in CO purged PBS buffer containing 20 mg/mL HSA or 50% v/v IgG depleted human serum. Blank samples consisting of HSA, serum or HbCO in PBS were prepared as controls. Each sample was supplemented with 0.05% w/v sodium azide. Aliquots (60 μL) of the samples were then prepared. One aliquot per sample was directly frozen at −80 °C (t = 0 days). The remaining aliquots were incubated at 37 °C. At t = 1, 3 and 7 days samples were removed from storage at 37 °C and frozen at −80 °C. Once all timepoint samples had been acquired, the samples were thawed and analysed by size exclusion chromatography (SEC). Analytical SEC used TOSOH TSKgel Super SW 3000 analytical (4.6 mm × 15 cm) and guard (4.6 mm × 3.5 cm) columns. Hb-PEG and control samples were isocratically eluted with PBS. For each analysis 30 μg (15 μL) of sample was injected and elution was performed over 10 min at 30 °C with visible detection at 538 nm. The stabilities of maleimide- and mono-sulfone PEG Hb conjugate linkages were assessed by evaluating the levels of the Hb-PEG and free Hb peaks in isolation (i.e., ignoring all other species present). Chromatograms were baseline subtracted using HSA and serum blanks to account for the absorbance of interfering matrix related peaks. For normalisation and to aid comparison, the percentage of Hb-PEG was expressed as a relative percentage compared to the t = 0 days value. Each SEC sample was run in triplicate. The figures show a representative example.

3 Results

Human serum albumin (HSA) contains a free reactive cysteine with the potential to participate in cross-conjugation reactions with a Hb-PEG bond *in vivo*. As HSA runs at a similar weight to Hb-PEG on SDS-PAGE, size exclusion chromatography (SEC) was used to monitor the stability of the Hb-PEG bond by monitoring the heme absorbance at 538 nm. As shown previously [2], SEC of Hb-PEG solutions separates free unPEGylated protein from Hb-PEG (Fig. 1).

The intensity of the Hb-PEG heme peak, measured by SEC, showed that the fraction of Hb-PEG following incubation in PBS for 7 days remained at 95% of the Day 0 value, consistent with the SDS-PAGE data shown previously [2]. Figure 2 compares the stability of PEG:Hb conjugates in the presence of HSA. Compared to

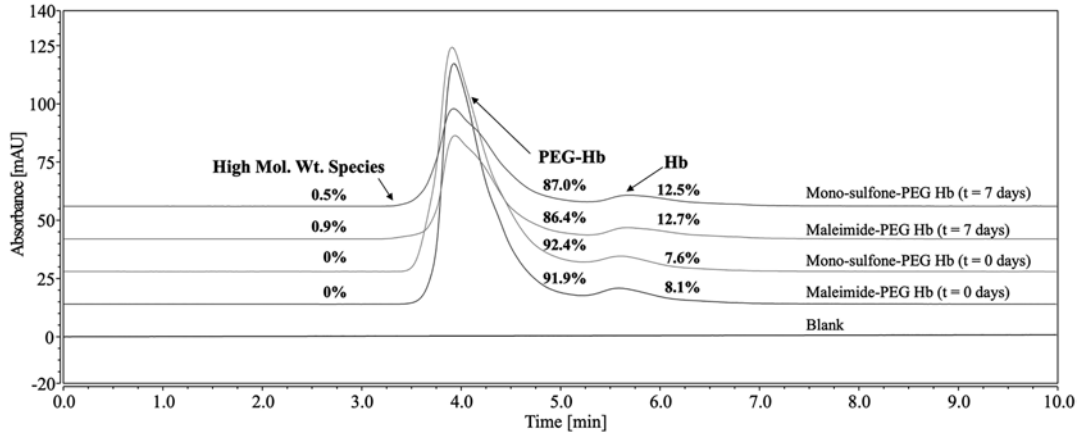

Fig. 1 SEC of Hb-PEG conjugates in PBS. Comparison with SEC standards reveals Hb peaks at 5.5 min comprise unPEGylated Hb dimer and peaks at 4 min Hb-PEG peaks. A small fraction of unidentified higher molecular weight species elutes at 3.5 min panel). Arrows identify peak of Hb species indicated. % values reflect the contribution of that species to the overall intensity

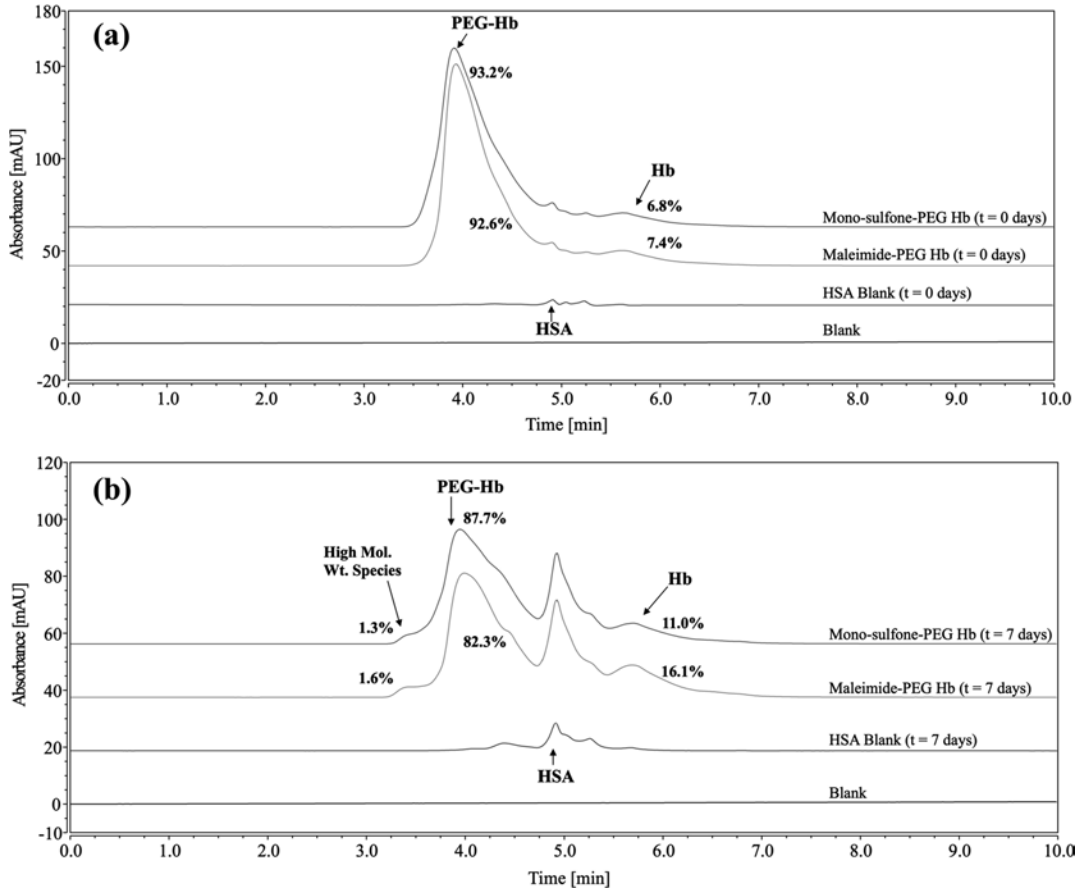

Fig. 2 SEC of Hb-PEG conjugates in HSA. SEC of Hb mutants following incubation in HSA at 37 °C immediately (**a**) and after 7 days incubation (**b**). Arrows identify peak of Hb species indicated. % values reflect contribution of that species to the overall intensity

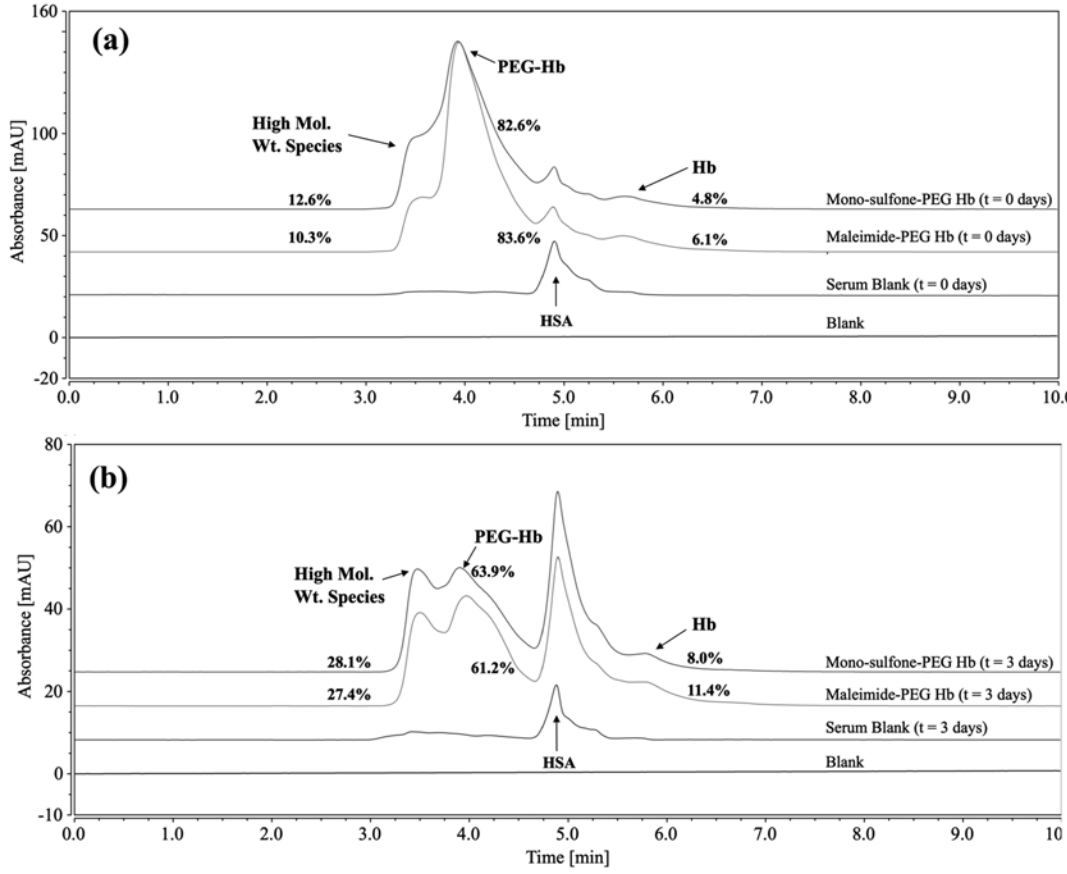

Fig. 3 SEC of Hb-PEG conjugates in human serum. SEC of Hb mutants following incubation in human serum at 37 °C immediately (**a**) and after 3 days incubation (**b**). Arrows identify peak of Hb species indicated. % values reflect the contribution of that species to the overall intensity

PBS, the extent of Hb-PEGylation following incubation in HSA is lower, suggesting cleavage of the Hb-PEG bond. Figure 3 shows the effect of a 37 °C incubation in human serum on the Hb-PEG bond. Distinct Hb-PEG and unPEGylated peaks can be seen, again allowing for quantification of the Hb-PEG/Hb ratio with time. However, unlike for HSA, it was not possible to analyse a sample on day 7 due to significant protein precipitation.

Figure 4 shows a side-by-side comparison of the stability of Hb-maleimide-PEG and Hb-mono-sulfone-PEG following incubation with PBS, GSH, HSA and serum. The mono-sulfone-PEG is stable in all conditions over a 7-day period. In contrast, in the presence of species containing competing thiols, the Hb-maleimide-PEG conjugation is labile. However, even in the most competitive conditions (1 mM GSH), 70% of the Hb-maleimide-PEG conjugation is retained after 7 days.

4 Discussion

The creation of a new cysteine residue in Hb (βCys93Ala/αAla19Cys) enables efficient PEGylation with no detectable effect on protein function or stability [2]. Although maleimide PEGylation is efficient and relatively stable, the use of alternative PEG reagents such as mono-sulfones [4] leads to a product with enhanced stability, with minimal deconjugation detectable in the presence of plasma reducing

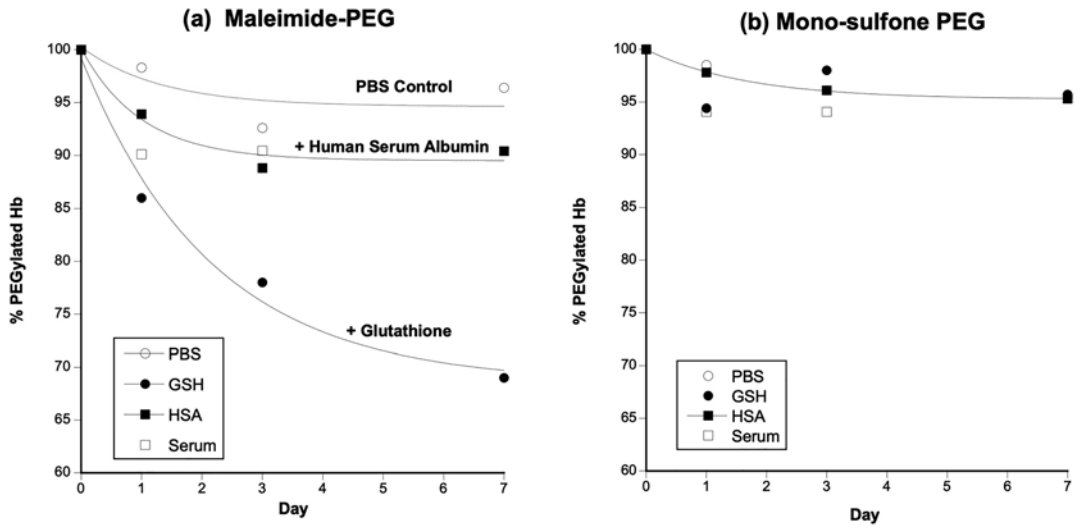

Fig. 4 Kinetics of stability of Hb-PEG conjugates. Graphs show the % drop in Hb PEGylation for maleimide-PEG Hb (**a**) and mono-sulfone-PEG Hb (**b**), assuming 100% PEGylation at t = 0 analysed by either SDS-PAGE (PBS, GSH; [4]) or SEC (HSA, serum; this paper). Curve fits are mono exponential decay; for mono-sulfone PEG, only the fit to the HSA data is shown for clarity as the fits superimpose. Note for the SEC data, the contribution of the higher molecular weight species was ignored, due to the uncertainty as to the PEGylation status of this species. This had minimal effect for the HSA calculation but did lead to greater uncertainty for the serum data

agents and free sulfhydryl residues, even after a week of incubation at 37 °C. This enhanced stability may not be relevant for current HBOC, which are targeted as acute therapeutics with circulatory half-lives of at most 2–3 days [1]. In these cases, HBOCs are likely cleared primarily by phagocytosis rather than by filtration in the kidney following loss of conjugation. However, if a longer lived HBOC with half-lives of weeks rather than days is required, this paper shows more stable PEG linkages such as mono-sulfone are likely to prove more suited than maleimide PEG.

Acknowledgments This research was funded in whole or in part by the UK research councils BBSRC (BB/L004232/1) and MRC (MR/L01310X/1). For the purpose of Open Access, the authors have applied a CC BY public copyright licence to any Author Accepted Manuscript (AAM) version arising from this submission.

Disclosure Cooper and Reeder have patents relating to the use of recombinant haemoglobin as a component of an oxygen therapeutic. Bird and Sheng were employees of Abzena Ltd. at the time this work was undertaken.

References

1. Bettati S, Mozzarelli A (eds) (2011) Chemistry and biochemistry of oxygen therapeutics: from transfusion to artificial blood. Wiley
2. Cooper CE, Silkstone GGA, Simons M et al (2020) Engineering hemoglobin to enable homogenous PEGylation without modifying protein functionality. Biomater Sci 8:3896–3906
3. Badescu G, Bryant P, Swierkosz J et al (2014) A new reagent for stable thiol-specific conjugation. Bioconjug Chem 25:460–469
4. Cooper CE, Bird M, Sheng X et al (2021) Stability of Maleimide-PEG and Mono-sulfone-PEG conjugation to a novel engineered cysteine in the human hemoglobin alpha subunit. Front Chem 9:707797

Oxygen Storage in Stacked Phospholipid Membranes Under an Oxygen Gradient as a Model for Myelin Sheaths

Wouter Vervust and An Ghysels

Abstract

Axons in the brain and peripheral nervous system are enveloped by myelin sheaths, which are composed of stacked membrane bilayers containing large fractions of cholesterol, phospholipids, and glycolipids. The oxygen availability to the nearby oxygen consuming cytochrome *c* oxidase in the mitochondria is essential for the well-functioning of a cell. By constructing a rate network model based on molecular dynamics simulations, and solving it for steady-state conditions, this work calculates the oxygen storage in stacked membranes under an oxygen gradient. It is found that stacking membranes increases the oxygen storage capacity, indicating that myelin can function as an oxygen reservoir. However, it is found that the storage enhancement levels out for stacks with a large number of bilayers, suggesting why myelin sheaths consist of only 10–300 membranes rather than thousands. The presence of additional water between the stacked bilayers, as seen in cancer cells, is shown to diminish myelin oxygen storage enhancement.

Keywords

Oxygen storage capacity · Oxygen reservoir · Oxygen transport · Smoluchowski transport equation

1 Introduction

The transport of molecular oxygen throughout the body is primarily realised by blood cells in the cardiovascular system [1]. The final destination of oxygen is the cytochrome *c* oxidase (COX), a protein embedded in the inner mitochondrial membrane, where oxygen is consumed in the energy conversion cycle. The binding site for oxygen is located at the center of the inner mitochondrial membrane [2]. Passive diffusive transport through several membranes, including the plasma membrane, is responsible for the last steps of oxygen from blood cells to the COX binding site. Cancer cells are known to show hypoxia which can fluctuate across the tumour cell, and tumour oxygenation can enhance radiation therapy of cancer cells [3]. Interestingly, nerve cell axons are surrounded by myelin, which is composed of stacked membrane bilayers containing large fractions of cholesterol, phospholipids, and glycolipids [4, 5]. Understanding the mechanisms of oxygen pathways from capillaries to tissue mitochondria is thus important for completely unraveling the physiological role of oxygen [6].

W. Vervust · A. Ghysels (✉)
IBiTech – Biommeda research group, Ghent University, Ghent, Belgium
e-mail: an.ghysels@ugent.be

F. Scholkmann et al. (eds.), *Oxygen Transport to Tissue XLIII*, Advances in Experimental Medicine and Biology 1395, https://doi.org/10.1007/978-3-031-14190-4_49

In this paper, a bottom-up approach will be used to study the role of membranes starting from the molecular scale. Phospholipid membranes form a barrier for oxygen, but the oxygen solubility in the phospholipid tail region is higher than in water, such that a high concentration of oxygen is found in the hydrophobic matrix [7, 8]. This high partitioning toward the membrane suggests that the omnipresence of phospholipid membranes provides the cell with an oxygen reservoir. Therefore, this paper wants to establish the view that a phospholipid membrane has a dual function: slowing oxygen transport, while also storing oxygen. Moreover, the inhomogeneity and anisotropy of the membrane facilitate oxygen transport in the interleaflet region of a lipid bilayer, compared to the transport orthogonal to the membrane surface [9]. The interleaflet space of bilayers can thus form a connected network of efficient diffusive pathways throughout the cell. The timely delivery of oxygen is especially important in the brain and the peripheral nervous system. This paper will in addition investigate how stacked membranes can serve as an oxygen reservoir in the nervous system, given a certain partial oxygen pressure.

In the methods section, kinetic modelling based on the Smoluchowski equation is introduced. It is explained how kinetic parameters were extracted from previous molecular dynamics (MD) simulations. The kinetic parameters will be used to predict the steady-state oxygen distribution given an oxygen gradient. In the results and discussion section, the enhancement in oxygen storage due to the stacking will be computed, where the number of stacked bilayers is varied. The conclusion section summarises our findings.

2 Methodology

Smoluchowski Equation for Transport Due to the membrane's inhomogeneity along the membrane's normal (z-coordinate, Fig. 1), the oxygen concentration c is z-dependent. It relates to the free energy profile $F(z) = -k_BT\ln c(z)$, with k_B the Boltzmann constant and T the temperature. Diffusive transport through an inhomogeneous medium is governed by the Smoluchowski equation, which is determined by the free energy $F(z)$ and diffusion $D(z)$ profiles [10]. Discretisation in N bins along z transforms the Smoluchowski equation into a set of linearly coupled equations, which can be summarised by a rate model with rate matrix R

$$\frac{\partial c_i(t)}{\partial t} = \sum_{N}^{j=1} R_{ij} c_j(t), \tag{1}$$

where $c_i(t)$ is the concentration in bin i at time t, and where the kinetic parameters in the rate matrix R are uniquely determined by the $F(z)$ and $D(z)$ profiles [10]. In this work, we will solve the rate equations with different profiles, representing different stacked bilayers.

Construction of the Rate Model from Molecular Simulations Bayesian analysis (BA) of MD trajectories at the atomic scale can be used to obtain the F and D profiles – and thus the rate matrix R – of a membrane [9–11]. In practice, the transitions observed in conventional MD trajectories are compared to the transitions expected by the rate model with a proposed rate matrix R. A Monte Carlo procedure is then used to extract the rate matrix with the highest likelihood of producing the observed MD trajectories.

Previously published MD simulations and their F and D profiles are used in this work to investigate the storage capacity of stacked bilayers. The considered membranes are a homogeneous 1-palmitoyl-2-oleoyl-sn-glycero-3-phosphocholine (POPC) bilayer (see Fig. 1) and a model system for inner mitochondrial membrane (labeled MITO) from Ref. [9]. MD simulations were run with the CHARMM36 force field at 310 K with a simulation box containing 72 lipid molecules, as depicted in Fig. 1a [12, 13]. The z-axis was discretised into 100 bins ($z \oplus 0.68^{-}$), and BA was performed on the oxygen trajectories, resulting in the F and D profiles shown in Fig. 1b, c.

In a next step, the single-membrane profiles are extended to artificially construct the F and D profiles of n stacked membranes by concatenat-

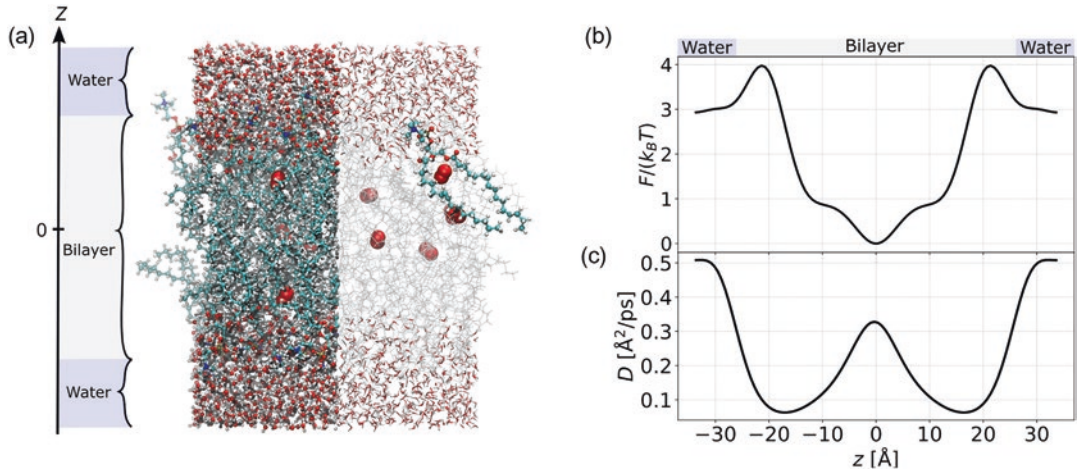

Fig. 1 MD simulations of the (POPC) membrane. (**a**) Simulation box with indication of the z-axis. For clarity, water and phospholipid molecules are shaded in the right part of the box with one high-lighted POPC molecule (ball-and-stick) and red oxygen molecules (van der Waals spheres). (**b**) Free energy $F(z)$ in units k_BT. (**c**) Diffusivity $D(z)$. $F(z)$ and $D(z)$ were obtained from Bayesian analysis of the MD trajectories

ing the membrane part of the profiles n times, to imitate myelin sheaths (Fig. 2a). The following three configurations are compared (Fig. 2b):

1. A water layer without any membrane (Fig. 2b top), representing oxygen diffusion to the mitochondria without shielding of membranes.
2. A single bilayer and water (Fig. 2b centre).
3. A series of n stacked bilayers (Fig. 2b bottom), representing myelin sheaths.

The oxygen storage S is measured under an oxygen gradient (see below), which gives $S(0)$, $S(1)$ and $S(n)$ for the setups with zero, one, and n bilayers, respectively. The amount of water is varied in setup 1 and setup 2 to match the size of setup 3, as is depicted in Figs. 2b. This allows for comparison between equally sized configurations in the results and discussion section. The stacking periodicity d can be increased to simulate a more disorganised structure with a larger aqueous phase between the membrane layers.

Steady-State Solution Under Oxygen Gradient The oxygen storage S in the membranes is measured under an oxygen gradient, where one side (to the left in Fig. 2) has a partial oxygen pressure and the other side (to the right of Fig. 2) has zero partial oxygen pressure, referring to full depletion of oxygen by COX. The concentration profile is assumed to have reached the steady-state regime, where the concentration no longer changes over time, but a net oxygen flux might still occur.

We solve the rate model (Eq. 1) for the steady-state solution, i.e., the right hand side of Eq. 1 vanishes, with bin 1 (to the left) at fixed concentration $c_1 = c^*$ and bin N (to the right) at fixed concentration $c_N = 0$, for all times t. This is done by constructing the vector v of length $N - 2$, which has all elements equal to zero except for its first element $v_1 = -R_{2,1}$. The rate matrix is stripped of its first and N^{th} rows and columns, to form the cropped rate matrix R' [14]. The steady-state concentration c_i^{SS} in each bin i is then obtained by matrix multiplication of R' and the vector v, and scaling with the concentration c^*,

$$c_i^{ss} = \begin{cases} c^*, & i = 1 \\ c^* \sum_{j=2}^{N-1} \left[R'^{-1} \right]_{i-1,j-1} v_j, & i = 2,\ldots,N-1 \\ 0, & i = N \end{cases} \quad (2)$$

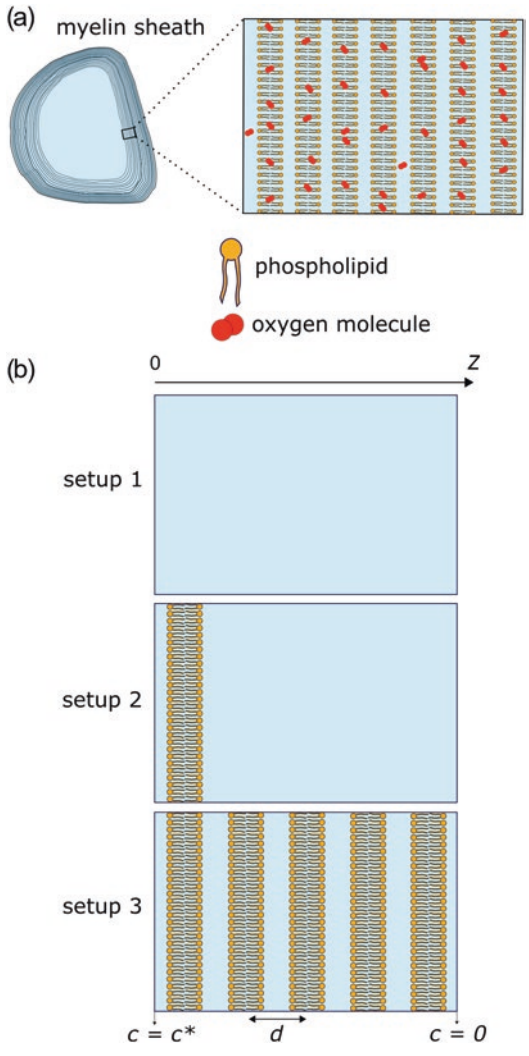

Fig. 2 (**a**) Myelin sheaths wrapped around a neural cell consist of stacked membranes [5]. (**b**) Considered configurations with steady-state boundary conditions: $c = c^*$ to the left and $c = 0$ to the right. Setup 1 is pure water, setup 2 has one bilayer, setup 3 has n bilayers (depicted is $n = 5$). Stacking periodicity d is indicated with arrow

where R'^{-1} is the matrix inverse of R'. Finally, the storage capacity S corresponding to a concentration profile $c(z)$ is computed by integrating over the concentration profile and multiplying with the membrane surface area A,

$$S = A\int c(z)dz \approx A\sum_i c_i \quad z \tag{3}$$

where in the second equation, the integral was approximated by the discretisation with bin width Δz.

3 Results and Discussion

First, we calculated the concentration profile under an oxygen gradient (Eq. 2) in the setups without bilayer, with one bilayer, and with n stacked bilayers. The steady-state profiles for the POPC membrane are shown for $n = 5$ in Fig. 3a. The setup of pure water gives a simple linear slope (black line), while the presence of a membrane clearly introduces a high peak in oxygen concentration (blue dashed line). Increasing the number of stacked membranes creates additional peaks (green line), whose height drops linearly with each additional peak.

The stacking enhancement of adding bilayers is quantified by $E(n) = S(n)/S(1)$, which is the ratio between storage in n stacked bilayers versus storage in 1 bilayer (setup 2 and setup 3 in Fig. 2). The membrane area A (Eq. 3) drops out of this ratio, and $E(n)$ has no unit. Fig. 3b depicts the stacking enhancement $E(n)$ for the POPC and MITO membranes, which shows that the stacking enhancement increases with the number n of stacked membranes. This indeed suggests that myelin sheaths may function as a reservoir for oxygen storage in the nervous system, making oxygen readily available to COX in the nearby mitochondria.

Interestingly, stacked bilayers not only have more peaks in Fig. 3a, but the first peak of the stacked bilayers (green) is also higher compared to the case of a single bilayer (blue dashed). This again favours the enhancement in stacked membranes compared to a single bilayer. The higher peak is explained by the fact that the nearby second peak also provides a source of oxygen.

Moreover, the slope of the curve in Fig. 3b becomes less steep with increasing n, meaning that stacking an additional membrane onto a thick layer of stacked membranes has less impact. In other words, stacking a 51st membrane on top of 50 stacked membranes has less impact on the stacking enhancement than stacking an 11th membrane on top of 10 stacked membranes. Therefore, it seems plausible that, for a certain stacking number, a trade-off may be reached between stacking enhancement and the extent of the physical space occupied by the membranes. Indeed, in electron microscopy images, myelin

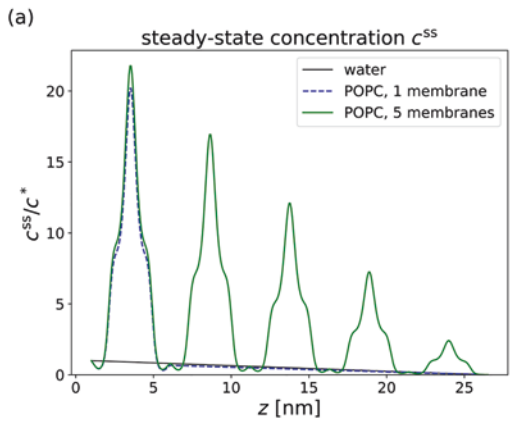

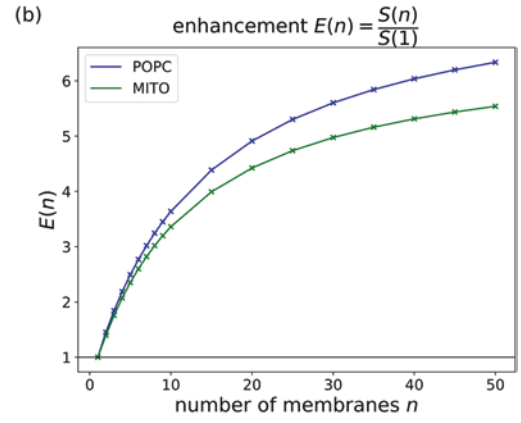

Fig. 3 (**a**) Steady-state concentration profile under oxygen gradient (in units c^*) with $c = c^*$ to the left and $c = 0$ to the right, for $n = 5$. Setup 1 with only water (black), setup 2 with 1 POPC membrane (blue dashed) and setup 3 with $n = 5$ stacked POPC membranes (green), as shown in Fig. 2b. (**b**) Stacking enhancement $E(n) = S(n)/S(1)$ is the ratio of storage capacity between n stacked bilayers and one bilayer, under a steady-state oxygen gradient over the membrane(s). $S(1)$ and $S(n)$ correspond to setup 2 and setup 3 in Fig. 2, respectively

sheaths often consist of about 10–300 bilayers but not thousands [5].

The storage efficiency also depends on the intrinsic storage capacity of a single bilayer. The ratio $S(1)/S(0)$ is a measure for the content in a single bilayer compared to a slab of pure water with the same dimension. For POPC, this ratio amounts to $S(1)/S(0) \approx 8$ in the steady-state regime using a membrane thickness of approximately 5.2 nm. Because of the linearity of the rate model and the symmetry of the considered setups, we can conclude that the latter ratio is equivalent to the ratio of storage in a membrane versus storage in the water phase in equilibrium. This is also known as the membrane partitioning constant K_m, of which the study was initiated over a century ago with Overton's rule. In short, $S(1)/S(0) = K_m = c_{mem}/c_{wat}$, with c_{mem} and c_{wat} the equilibrium oxygen concentration in the membrane and water phase, respectively.

Concretely, the POPC membrane stores about 8 times more oxygen molecules than can be stored in pure water. For example, let us assume a partial oxygen pressure of ~10 mmHg, which lies in the reported 10–34 mmHg range for brain tissue [15]. At atmospheric pressure and body temperature, the partial oxygen pressure is 159 mmHg, and the solubility of oxygen in water is approximately 7.187 mg/L [16]. Therefore, the 10 mmHg partial oxygen pressure corresponds to an oxygen concentration of $(10/159) \cdot 7.187$ mg/L = 0.45 mg/L. Next, the steady-state profile over 10 stacked POPC membranes under this oxygen gradient ($c^* = 0.45$ mg/L to the left of the stack, while $c = 0$ to the right of the stack) is computed with Eq. 2, and similarly for pure water. Finally, the storage per area (S/A) follows from Eq. 3, resulting in about 1791/μm^2 oxygen molecules available in the membrane stack, compared to 226/μm^2 oxygen molecules in a similarly sized slab of water.

Next, it is tested how the bilayer spacing influences the enhancement provided by the stacked membranes. The pathophysiology of cancer cells may show abnormal microvasculature and defective microcirculatory function, such as an increase in interstitial fluid [17, 18]. Moreover, abnormal myelination can also occur following trauma to a central nervous system tract, where myelin sheath swelling and decompaction have been observed, even in myelin that is spatially separated from the primary injury [19, 20]. Here, structural loss in the membrane stacking is modeled by increasing the thickness of the aqueous phase between the stacked bilayers. These additional water layers will decrease the total permeability [21], but they might also affect the storage capacity. Fig. 4 shows the

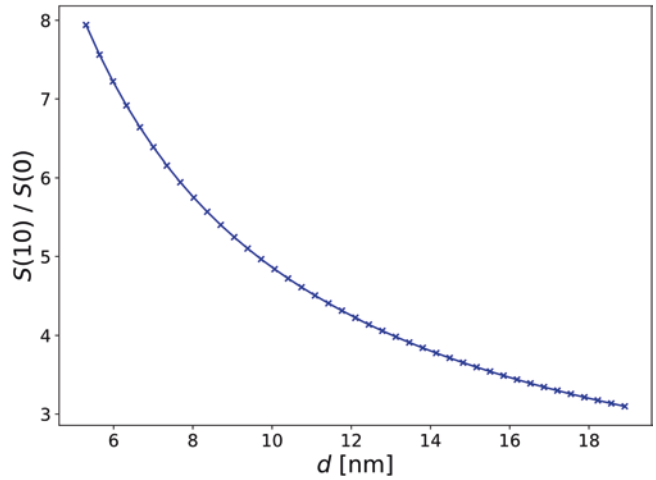

Fig. 4 Enhancement $S(n)/S(0)$ in stacked membranes for $n = 10$, as a function of stacking periodicity d

enhancement $S(n)/S(0)$ for $n = 10$ stacked bilayers, comparing the storage in 10 bilayers with the storage in pure water, while the stacking periodicity d (indicated in Fig. 2b) is gradually increased. At the left of the figure, the periodicity $d = 5.2$ nm corresponds to 10 stacked POPC membranes without additional water, as was simulated in Fig. 3b. Figure 4 clearly shows that an increase in stacking periodicity d can cause a strong decrease in the storage enhancement by the stacked bilayers, indicating that additional water between the myelin layers affects the storage efficiency in a negative way. This can be understood by comparing the contributions to the total storage by the membrane and by the interstitial water. The oxygen storage in water becomes larger for increasing d, simply because there is more interstitial water. In contrast, the oxygen storage in the membranes is fairly independent of d. Thus, for increasing periodicity d, the relative contribution of the bilayers to the total oxygen storage becomes smaller, and consequently a highly distorted membrane stack will gradually lose its function as a compact oxygen reservoir.

4 Conclusion

A phospholipid membrane has a higher solubility for molecular oxygen compared to pure water. By calculating the steady-state concentration over a membrane under an oxygen gradient, we have shown that the oxygen storage capacity S can be even more enhanced by stacking multiple bilayers, as is the case in myelin sheaths of axons in the nervous system. The stacking enhancement levels out when many membranes are stacked, meaning that beyond a certain number of stacked membranes, stacking even more would have limited efficiency. This could explain why myelin sheaths appear to consist of 10–300 stacked bilayers but not thousands. Finally, the enhancement is negatively affected by an increase of the aqueous phase between the bilayers, which can for instance occur in cancer cells with more disordered stacking geometry.

Acknowledgments We thank Kenneth Smith (University College London, UK) for scientific discussions and pointing us towards myelin sheaths. Funding was received from the FWO – Flanders (Research Project G002520N).

References

1. Popel AS (1989) Theory of oxygen transport to tissue. Crit Rev Biomed Eng 17:257–321
2. Tsukihara T, Aoyama H, Yamashita E et al (1995) Structures of metal sites of oxidized bovine heart cytochrome c oxidase at 2.8 A. Science 269:1069–1074
3. Colliez F, Gallez B, Jordan BF (2017) Assessing tumor oxygenation for predicting outcome in radiation oncology: a review of studies correlating tumor hypoxic status and outcome in the preclinical and clinical settings. Front Oncol 7:10

4. Morell P, Quarles RH (1999) Characteristic composition of myelin. Basic Neurochem Mol Cell Med Asp 6:69–94
5. Arroyo EJ, Scherer SS (2000) On the molecular architecture of myelinated fibers. Histochem Cell Biol 113:1–18
6. Pias SC (2021) How does oxygen diffuse from capillaries to tissue mitochondria? Barriers and pathways. J Physiol 599:1769–1782
7. Dotson RJ, Smith CR, Bueche K et al (2017) Influence of cholesterol on the oxygen permeability of membranes: insight from atomistic simulations. Biophys J 112:2336–2347
8. Ghysels A, Krämer A, Venable RM et al (2019) Permeability of membranes in the liquid ordered and liquid disordered phases. Nat Commun 10:1–12
9. Ghysels A, Venable RM, Pastor RW, Hummer G (2017) Position-dependent diffusion tensors in anisotropic media from simulation: oxygen transport in and through membranes. J Chem Theory Comput 13:2962–2976
10. Hummer G (2005) Position-dependent diffusion coefficients and free energies from Bayesian analysis of equilibrium and replica molecular dynamics simulations. New J Phys 7
11. Krämer A, Ghysels A, Wang E et al (2020) Membrane permeability of small molecules from unbiased molecular dynamics simulations. J Chem Phys 153:124107
12. Brooks BR, Brooks CL III, Mackerell AD Jr et al (2009) CHARMM: the biomolecular simulation program. J Comput Chem 30:1545–1614
13. Klauda JB, Venable RM, Freites JA et al (2010) Update of the CHARMM all-atom additive force field for lipids: validation on six lipid types. J Phys Chem B 114:7830–7843
14. Vervust W, Ghysels A (2022) An electric RC circuit model to describe oxygen storage and transport in myelin sheaths. To be submitted
15. Mulkey DK, Henderson RA III, Olson JE et al (2001) Oxygen measurements in brain stem slices exposed to normobaric hyperoxia and hyperbaric oxygen. J Appl Physiol 90:1887–1899
16. Clever LH, Battino R, Miyamoto H et al (2014) IUPAC-NIST solubility data series. 103. Oxygen and ozone in water, aqueous solutions, and organic liquids (supplement to solubility data series volume 7). J Phys Chem Ref Data Monogr 43:33102
17. Molls M, Anscher MS, Nieder C, Vaupel P (2009) The impact of tumor biology on cancer treatment and multidisciplinary strategies. Springer
18. Vaupel P (2006) Abnormal microvasculature and defective microcirculatory function in solid tumors. In: Vascular targeted therapies in oncology. Wiley, pp 9–29
19. Payne SC, Bartlett CA, Harvey AR et al (2011) Chronic swelling and abnormal myelination during secondary degeneration after partial injury to a central nervous system tract. J Neurotrauma 28:1077–1088
20. Payne SC, Bartlett CA, Harvey AR et al (2012) Myelin sheath decompaction, axon swelling, and functional loss during chronic secondary degeneration in rat optic nerve. Invest Ophthalmol Vis Sci 53:6093–6101
21. Davoudi S, Ghysels A (2021) Sampling efficiency of the counting method for permeability calculations estimated with the inhomogeneous solubility–diffusion model. J Chem Phys 154:54106

Confocal Laser and Electron Microscopic Investigation of Gap Junctions in Anaplastic Astrocytomas

Alexander K. Logvinov, Evgeniya Yu. Kirichenko, Salah M. M. Sehweil, Denis E. Bragin, Irina K. Logvinova, and Alexey M. Ermakov

Abstract

Connexin 43 (Cx43) is a multifunction protein that forms gap junction channels and hemichannels and is suggested to play an essential role in oxygen-glucose deprivation, induced via neuroinflammation during astrocytoma expansion into healthy tissue. To prove this assumption we studied connexin 43 localisation and ultrastructure of gap junctions in samples of malignant brain tumour (anaplastic astrocytomas grade III). For confocal laser microscopy, vibratome sections of tumour fragments were incubated in a mixture of primary antibodies to connexin 43 and glial fibrillary acidic protein (GFAP), then in a mixture of secondary antibodies conjugated with a fluorescent label. After the immunofluorescence study, sections were washed in phosphate buffer, additionally postfixed with 1% OsO4 solution, dehydrated and embedded in epoxy resin by a plane-parallel method. Ultra-thin sections obtained from these samples were contrasted with uranyl acetate and lead citrate and viewed under a Jem 1011 electron microscope. Confocal laser examination detected a positive reaction to Cx43 in the form of point fluorescence. These points were of various sizes. Most of them were localised around or at the intersection of small processes containing GFAP. Electron microscopy of the tumour samples containing the most significant number of Cx43 revealed single and closely spaced gap junctions with a typical ultrastructure on the processes and bodies of tumour cells. Sequential analysis in the fields of view revealed 62 gap junctions in the area of 100 μm^2. Numerous gap junctions in anaplastic astrocytomas revealed in our study may indicate electrotonic and metabolic transmission between glioma cells, possibly promoting its progression.

Keywords

Connexin 43 · Glial fibrillary acidic protein (GFAP) · Gliofibrils · Immunofluorescence

A. K. Logvinov
Academy of Biology and Biotechnology, Southern Federal University,
Rostov-on-Don, Russia

E. Y. Kirichenko (✉) · A. M. Ermakov
Department of Bioengineering, Rostov State Technical University,
Rostov-on-Don, Russia

S. M. M. Sehweil
Department of Neurology and Nervous Diseases, Rostov State Medical University, Rostov-on-Don, Russia

D. E. Bragin
Lovelace Biomedical Research Institute, Albuquerque, NM, USA

Department of Neurology, University of New Mexico School of Medicine, Albuquerque, NM, USA

I. K. Logvinova
Rostov State Transport University, Rostov-on-Don, Russia

F. Scholkmann et al. (eds.), *Oxygen Transport to Tissue XLIII*, Advances in Experimental Medicine and Biology 1395, https://doi.org/10.1007/978-3-031-14190-4_50

1 Introduction

Anaplastic astrocytoma is a malignant brain tumour that arises from astrocytes. Gap junctions (GJ) and connexins (Cx) are considered crucial pathogenetic mechanisms of malignant tumour growth and promising targets for targeted therapy [1]. Cx43 is a multifunction protein that forms gap junction channels and hemichannels and thus is suggested to play a key role in oxygen-glucose deprivation, induced by neuroinflammation during the process of astrocytoma expansion into healthy tissue. On the one hand, it has been shown that interaction of intracellular C-domain Cx43 with the pro-oncogenic kinase Src leads to a decrease in the proliferative activity of tumour cells, and the restoration of intercellular interactions through GJ promotes the spread of apoptosis signals in tumour cell population and suppression of tumour growth [2]. On the other hand, the interaction of Cx43 extracellular domains with extracellular matrix and proteins of neighbour cells, as well as intercellular exchange through the GJ, enhance the ability of tumour cells to migrate and promote the transformation of surrounding non-malignant tissue into tumour tissue [3, 4]. However, there is still no clear understanding of the association between astrocytoma and Cx43 along with gap junctions. It is uncertain whether the positive expression of connexins is associated with the formation of functional GJ (nexuses) or the accumulation of protein in the cytosol in astrocytic tumours of various degrees of malignancy.

In previous studies, we demonstrated the presence of GJs in samples of pleomorphic xanthoastrocytoma grade II [5], hemistocytic astrocytoma grade II and glioblastoma grade IV but did not find these contacts in oligodendroglioma grade II [6]. However, the information regarding cell-cell interactions in malignant anaplastic astrocytomas, i.e., diffusely infiltrating grade III astrocytomas that tend to transform into grade IV glioblastomas, is absent in the available literature.

The aim of this work was to study connexin 43 expression, localisation, and ultrastructure of gap junctions in samples of anaplastic astrocytoma grade III.

2 Methods

The studies were carried out after obtaining written informed consent of patients and their relatives. Fragments of surgically resected human brain glial tumours with a confirmed histological diagnosis of anaplastic astrocytoma grade III were used as material for research. Tumour samples ($n = 8$) were fixed in 4% paraformaldehyde. Vibratome (VT 1000E, Leica, Germany) was used to cut 40 μm sections from the samples. Sections were cryoprotected and instantly frozen over liquid nitrogen vapor. For immunohistochemistry, sections were thawed in a phosphate buffer at room temperature. After that, sections of tumour fragments were incubated in a mixture of rabbit polyclonal antibodies to Cx43 (Spring Bioscience, USA) and mouse monoclonal antibodies to glial fibrillar acidic protein (GFAP, Dako, Denmark) with the addition of 0.1% sodium azide for 7 days at 10 °C. Sections were washed in phosphate buffer and incubated for 24 h at 10 °C in a mixture of secondary antibodies conjugated with a fluorescent label: goat anti-Rabbit CF488A antibodies (Sigma-Aldrich, USA) and goat anti-mouse CF555 antibodies (Sigma -Aldrich, USA). After incubation, sections were washed in phosphate buffer, mounted on glass slides in the anti-fading medium Fluorescence Mounting Medium (Dako, Denmark), covered with a cover glass, and examined using a laser scanning confocal microscope (Zeiss LSM880, Germany). After fluorescence study, the cover glass was carefully removed from a part of tumour sections ($n = 6$). They were washed in phosphate buffer and additionally postfixed in 1% OsO4, dehydrated and embedded in epoxy resin by a plane-parallel method. After polymerisation, 1 mm tissue fragments were excised and polymerised to the top of the epoxy resin block of. Single and serial ultra-thin sections obtained from the tumour sections were cut using EM UC 7 ultramicrotome (Leica, Germany) and an ultra 45° diamond knife (Diatome, Switzerland), contrasted with uranyl acetate and lead citrate. Images were taken under an electron microscope Jem 1011 (Jeol, Japan) with an accelerating voltage of 80 kV.

3 Results and Discussion

Confocal microscopy of fluorescently-labeled 40 μm tumour sections showed that GFAP is present in the cytoplasm, as well as in large and small chaotically branching processes of malignant cells (Fig. 1a). A fluorescence study of Cx43 in astrocytoma tissue showed a reaction pattern of expression: positive signals have the form of fluorescent points of various sizes (Fig. 1b). A double fluorescence study made it possible to demonstrate that the majority of Cx43 points are localised around or at the intersection of small processes containing GFAP (Fig. 1c, arrows). Serial optical imaging (0.2 μm step size along the z-direction) revealed that some of the Cx43+ signals could be detected in deeper sections than others, reflecting the heterogeneous size of Cx43+ along the z-axis. Such positive Cx43 + extended areas in the studied volume were also associated with GFAP-positive structures of astrocytomas. Tumour regions containing the most significant number of positive labels for Cx43 were further examined by electron microscopy.

Sequential examination of ultra-thin sections, selected from anaplastic astrocytoma samples revealed numerous single and closely spaced GJ. Figure 1d shows two tumour cells, the cytoplasm, and processes filled with gliofibrils. The process of cell 1 is larger than the process of cell 2. These processes are adjacent to each other and are in contact at several points through extended GJ. Ultrastructural details of the detected GJ were visualised at high magnifications and rotation of the sample using a goniometer (Fig. 1d, d*). Electron microscopic examination showed that GJ of anaplastic astrocytomas did not have visible perforations. In cases where the GJ nexuses were in the cut plane, they were seen as "stuck together" bilipid membranes with an osmiophilic gap between them, which corresponds to a classic seven-layer structure of the GJ. Higher magnification revealed thin electron-transparent bridges between the two membranes crossing the osmiophilic dark contact gap. These structures are, apparently, intercellular pores, providing the transition of ions and micromolecules from the process of one tumour cell to the process of another (Fig. 1g). In addition, we found areas where networks of GJ were formed both between thin processes and between processes of a large area. Moreover, most of the GJ junctions were located in the immediate vicinity of tumour cell bodies. With magnification of 40,000 in one field of view, up to 6 GJs can be detected. They predominantly have an even or slightly curved shape, short and elongated nexuses, connecting along or across the cut processes of different cells. Besides GJ formation between processes of various diameters, we found numerous GJs on the soma of tumour cells. Such contacts can be conditionally divided into two types: GJ between the soma and the process of another cell and GJ between the own compartments of the cell. Figure 1e shows 3 GJs formed on three sides of one process (Fig. 1e). The first GJ is formed between the tumour cell soma and the thinnest process. That process has two more GJs located on opposite sides: one extended and curved, another one with extended elongated nexus. Another type of the GJ location is shown in Fig. 1f. An electronogram shows a vacuolated tumour cell with an eccentrically located nucleus. A curved intracytoplasmic GJ was revealed at higher magnification in the peripheral part of its cytoplasm (Fig. 1f, f*). In order to analyse the total number of gap junctions in areas of astrocytomas selected for the study, we performed the morphometric analysis. Sequential imaging of the visual fields revealed 62 GJs in an area of 100 μm^2, which significantly exceeds the number of GJs in other previously studied tumours of glial origin.

The obtained results show that positive fluorescence signals of connexin 43 correspond to the formation of GJs with a typical ultrastructure in anaplastic astrocytomas grade III. Identification of the significant number of GJs in gliomas supports the hypothetical tumour glial cells' ability to integrate into the surrounding neuronal and neuroglial networks of the brain. This hypothesis was based on the discovery of glutamatergic synapses between glioma cells and the presynaptic terminals of neurons [7, 8]. The existence of such synapses promotes tumour proliferation, growth,

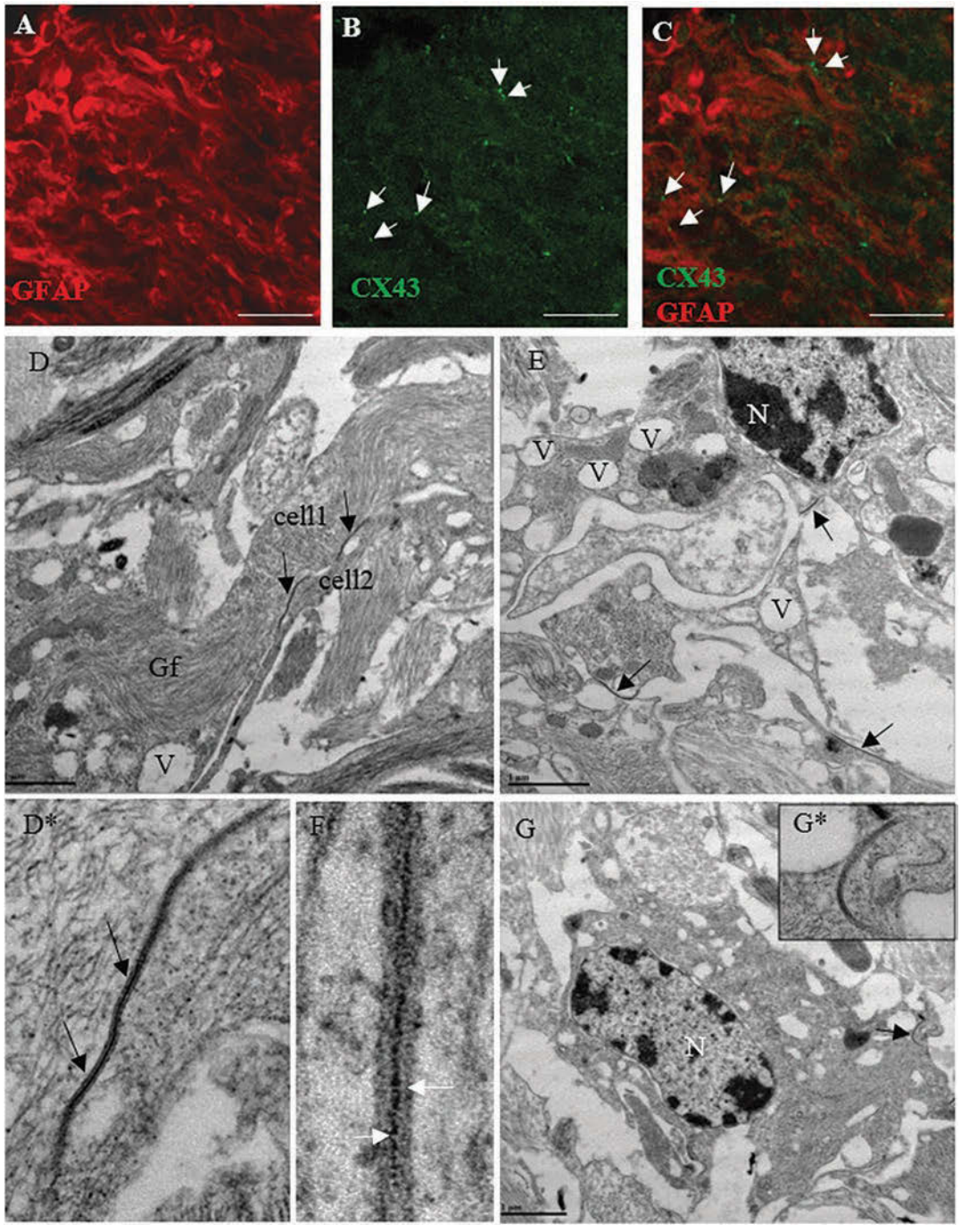

Fig. 1 Immunofluorescence and electron microscopic examination of GJs in grade III anaplastic astrocytomas. (**a**) expression of GFAP, (**b**) GJ protein of astroglia Cx43 (arrows) is located in the form of points in the tumour tissue, (**c**) a combination of GFAP and Cx43. Scale bar 20 microns. (**d**) GJs between the processes of tumour cells, d* – typical ultrastructure of GJ, (**e**) GJ connecting the tumour cell soma and processes: GJ between the soma and the process and another two GJ, formed on the same process from opposite sides, (**f**) ultrastructure of GJ, white arrows indicate bridges penetrating two bilipid membranes, (**g**) GJ formed inside the tumour cell, g* – curved GJ inside the cell soma. Legend: *Gf* gliofibrils, *V* vesicles, *N* nucleus, *GFAP* expression of glial fibrillary acidic protein, Cx43 expression of connexin 43, arrow indicate gap junction (GJ). Magnification: d – 40,000, d* – 200,000, e – 50,000, f – 400,000, g – 40,000, g* – 200,000

and stability. Presumably, an excitatory signal in the synapse between a glutamatergic neuron and glial tumour cell is transmitted to other tumour cells through GJs. This phenomenon was found not only in glioma cells but also in some types of breast cancer that metastasise to the brain [9].

The numerous gap junctions in anaplastic astrocytoma shown in our study may indicate electrotonic and metabolic transmission between glioma cells, promoting its progression. GJs can promote the diffuse transfer of lactate and bicarbonate (end-product of glycolytic metabolism) from more hypoxic tumour cells to normoxic ones by providing metabolic cooperation with low resistance. One possible method to block the glycolysis products release by tumour cells is to inhibit massive intercellular transmission via gap junctions identified in this study.

4 Conclusions

In this work, we have demonstrated for the first time a significant number of GJs in anaplastic astrocytomas. These numerous containing connexin 43 contacts are formed both between processes of different cells and between the soma of one cell and the process of another cell, as well as between the soma and the process of the same cell.

Acknowledgments The work was supported by RSF 22-25-00795. DB was supported by NIH R01 NS112808.

References

1. Tabernero A, Gangoso E, Jaraíz-Rodríguez M et al (2016) The role of connexin43-Src interaction in astrocytomas: a molecular puzzle. Neurosci 26:183–194
2. Herrero-González S, Gangoso E, Giaume C et al (2010) Connexin43 inhibits the oncogenic activity of c-Src in C6 glioma cells. Oncogene 29:5712–5723
3. Bates D, Sin W, Aftab Q et al (2007) Connexin43 enhances glioma invasion by a mechanism involving the carboxy terminus. Glia 55:1554–1564
4. Crespin S, Bechberger J, Mesnil M et al (2010) The carboxy-terminal tail of connexin43 gap junction protein is sufficient to mediate cytoskeleton changes in human glioma cells. J Cell Biochem 110:589–597
5. Kirichenko E, Sehweil-Salah M, Goncharova Z et al (2020) Ultrastructural evidence for presence of gap junctions in rare case of pleomorphic xanthoastrocytoma. Ultrastr Pathol 44:227–236
6. Kirichenko E, Savchenko A, Kozachenko D et al (2017) Ultrastructural characteristics of gap junctions in human glial brain tumors. Archive Pathol 79:3–11
7. Venkataramani V, Ivanov Tanev D, Kuner T et al (2019) Glutamatergic synaptic input to glioma cells drives brain tumour progression. Nature 573:532–538
8. Venkatesh HS, Morishita W, Geraghty AC et al (2019) Electrical and synaptic integration of glioma into neural circuits. Nature 573:539–545
9. Zeng Q, Michael IP, Zhang P et al (2019) Synaptic proximity enables NMDAR signalling to promote brain metastasis. Nature 573:526–531

A Radiation Biological Analysis of the Oxygen Effect as a Possible Mechanism in FLASH

Harold M. Swartz, P. Jack Hoopes, David J. Gladstone, Valentin Demidov, Peter Vaupel, Ann Barry Flood, Benjamin B. Williams, Rongxiao Zhang, and Brian W. Pogue

Abstract

The delivery of radiation at an ultra-high dose rate (FLASH) is an important new approach to radiotherapy (RT) that appears to be able to improve the therapeutic ratio by diminishing damage to normal tissues. While the mechanisms by which FLASH improves outcomes have not been established, a role involving molecular oxygen (O_2) is frequently mentioned. In order to effectively determine if the protective effect of FLASH RT occurs via a differential direct depletion of O_2 (compared to conventional radiation), it is essential to consider the known role of O_2 in modifying the response of cells and tissues to ionising radiation (known as 'the oxygen effect'). Considerations include: (1) The pertinent reaction involves an unstable intermediate of radiation-damaged DNA, which either undergoes chemical repair to restore the DNA or reacts with O_2, resulting in an unrepairable lesion in the DNA, (2) These reactions occur in the nuclear DNA, which can be used to estimate the distance needed for O_2 to diffuse through the cell to reach the intermediates, (3) The longest lifetime that the reactive site of the DNA is available to react with O_2 is 1–10 μsec, (4) Using these lifetime estimates and known diffusion rates in different cell media, the maximal distance that O_2 could travel in the cytosol to reach the site of the DNA (i.e., the nucleus) in time to react are 60–185 nm. This calculation defines the volume of oxygen that is pertinent for the direct oxygen effect, (5) Therefore, direct measurements of oxygen to determine if FLASH RT operates through differential radiochemical depletion of oxygen will require the ability to measure oxygen

H. M. Swartz (✉) · P. J. Hoopes · D. J. Gladstone · B. B. Williams · R. Zhang · B. W. Pogue
Geisel School of Medicine, Dartmouth College, Hanover, NH, USA

Norris Cotton Cancer Center, Dartmouth-Hitchcock Medical Centre, Lebanon, NH, USA

Thayer School of Engineering, Dartmouth College, Hanover, NH, USA
e-mail: harold.swartz@dartmouth.edu

V. Demidov
Geisel School of Medicine, Dartmouth College, Hanover, NH, USA

P. Vaupel
Department of Radiation Oncology, University Medical Center, Freiburg, Germany

A. B. Flood
Geisel School of Medicine, Dartmouth College, Hanover, NH, USA

Norris Cotton Cancer Center, Dartmouth-Hitchcock Medical Centre, Lebanon, NH, USA

F. Scholkmann et al. (eds.), *Oxygen Transport to Tissue XLIII*, Advances in Experimental Medicine and Biology 1395, https://doi.org/10.1007/978-3-031-14190-4_51

selectively in a sphere of <200 nm, with a time resolution of the duration of the delivery of FLASH, (6) It also is possible that alterations of oxygen levels by FLASH could occur more indirectly by affecting oxygen-dependent cell signalling and/or cellular repair.

Keywords

Radiotherapy · Oxygen depletion · Hypoxia · Radiation resistance

1 Introduction and Background

Significant improvement in the effectiveness of radiation therapy (RT) now seems possible due to the observation that delivering radiation doses at extremely high dose rates (FLASH RT) can increase the therapeutic ratio for RT. When compared to conventional rates, at the same total dose, FLASH RT has been shown to reduce normal tissue damage in a variety of tissues in animal models including brain, colon, lung, and skin [1] as well as in an initial human application [2]. Increased normal tissue tolerance may be as high as 1.3–2.0 X compared to conventional dose rates. Importantly, tumour dose-response is not significantly altered with FLASH. In contemplating the possible mechanisms for the FLASH effect, it is useful to keep in mind that FLASH differs from conventional irradiation in at least three ways: the rate of delivery of the radiation (40 Gy/sec vs 0.1 Gy/sec), the time over which each fraction is delivered (0.5 secs. vs. 200 secs[1]), and the number of fractions.

Because of the importance of oxygen on the response of cells and tissues to ionising radiation, many of the leading explanations for the mechanism of the normal tissue-sparing effect of FLASH relate to modification of the oxygen effect [4]. But to date, no definitive evidence has been produced to show if and how oxygen is an important part of the mechanism for the sparing of normal tissue by FLASH. There have been a number of experiments carried out to measure directly the impact of FLASH vs. conventionally delivered irradiation on oxygen depletion using phantoms and preclinical models [5] as well as theoretical analyses and discussions about possible mechanism leading to differential depletion of oxygen [6, 7].

Experimental approaches have usually measured the rate of depletion of oxygen with FLASH versus conventionally delivered radiation They use global measurements of oxygen, based on the expectation that the apparently protective effect of FLASH for normal tissues compared to conventional delivery is because it causes a reduction of oxygen in the normal tissues sufficient to drop the oxygen to a temporary hypoxic level, making these cells more resistant to permanent radiation damage. Based on the usual level of oxygen in normal tissues (about 40 mm Hg), this would require a substantial depletion of oxygen to start to have radiobiologically significant levels of hypoxia (<20 mm Hg) (Fig. 1). Also, in order to explain why there is no similar adverse effect on the relative efficacy of irradiation on tumours, it would appear to require that FLASH does not cause a radiobiologically significant reduction of the direct oxygen effect in tumour tissue even though most tumours have some regions that are already quite hypoxic so that even small changes of oxygen in deep hypoxia would be expected to increase radiation resistance. Therefore, it is not clear that the experiments and calculations that have focused on global depletion of oxygen have focused sufficiently on what needs to be measured or calculated.

Our approach in this paper is to consider the potential role of oxygen as the basis of the FLASH phenomenon starting with the established understanding of the role of oxygen in radiation biophysics and radiation biology [8]. We then use this information to consider what types of measurements and or/calculations of FLASH on oxygen levels are likely to provide the data needed to test rigorously theories that oxygen effects are a principal component of the sparing of normal tissue by FLASH, and have little impact on the response of tumours. We also briefly consider whether it also is possible that there could be an oxygen-dependent mechanism for the FLASH effect that is more

[1]Numbers are for a 20Gy dose FLASH versus 600 mu/min linear accelerator [3].

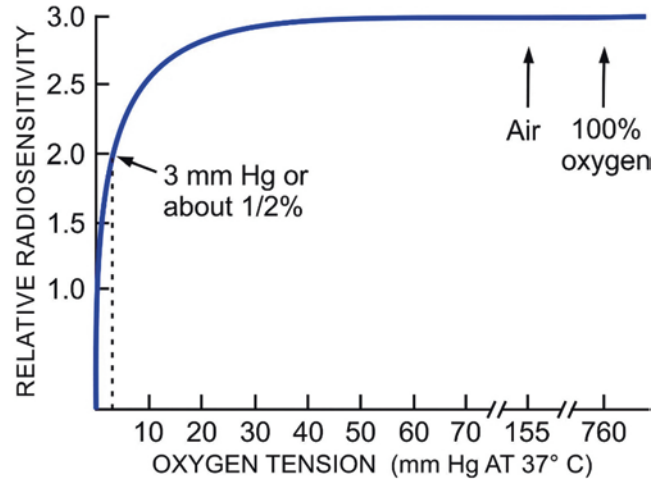

Fig. 1 Classical oxygen effect: There is a very steep rise in radiosensitivity of cells from a minimum at very low (hypoxic) levels of oxygen, quickly levelling off before reaching a plateau at levels of oxygen that are less than usual global average levels. (Adapted from [10])

indirect, mediated by changes in oxygen levels impacting cell signalling and/or repair.

2 The Biological Impact of Oxygen on the Radiation Response of Cells and Tissues

Radiation-induced cell death occurs a significant time interval after irradiation, usually when the cells attempt to divide. Strong historical evidence leads to the widely accepted conclusion that the principal cytotoxic radiation target is unrepaired or misrepaired DNA damage [9].

Similarly, radiobiological knowledge about the classical oxygen effect is well-established with relatively few controversies [10]. As shown in Fig. 1, the response of cells to radiation increases by a factor of about 3 when oxygenated cells are compared to severely hypoxic cells.

Oxygen is by far the largest known modifier of ionising radiation-induced cytotoxicity. It also can impact other types of therapy often used in combination with radiation including immunotherapy, chemotherapy and surgery. Reoxygenation of viable hypoxic cells during radiation therapy is one of the primary motivations for fractionation [11]. Despite the importance of oxygen, quantitative measurement in the clinical setting has been challenging [12, 13]. Therefore, when using radiation to control malignant tumours, maximisation of the therapeutic ratio based on the tumour hypoxia and normal tissue oxygenation status situation is appealing, but has been an ongoing challenge. Tumours are often hypoxic and therefore relatively resistant to ionising radiation, while normal tissues typically have oxygen levels that are well above those needed for full damage by ionising radiation. This situation has had very important impacts on how various types of ionising radiation delivery are used in the treatment of cancer [9, 10]. Many aspects of clinical radiation oncology reflect the need to get a maximum dose to the tumour while avoiding unacceptable levels of damage to normal tissues adjacent to the tumour. Some of this is accomplished by delivering the radiation stereotactically from multiple directions and using techniques that achieve highly conformal dose distributions so that the tumour receives much more dose than the surrounding normal tissues. As tumour cells die more oxygen is available for the remaining cells in the tumour.

3 The Chemical Basis of Oxygen Impacting the Radiation Response of Cells and Tissues

Key reactions leading to the generation of free radical products of DNA can be schematically represented as 6 equations:

$$\mathbf{RH + radiation \rightarrow primary\ products} \rightarrow \mathbf{R\cdot + H\cdot}\left(\text{direct damage}\right) \quad (1)$$

$$\mathbf{RH + OH\cdot \rightarrow R\cdot + H2O}\ \left(\text{indirect damage}\right) \quad (2)$$

$$\mathbf{R\cdot + PSH \rightarrow RH + P\cdot}\left(\text{chemical repair}\right) \quad (3)$$

$$\mathbf{R\cdot + R\cdot \rightarrow R - R}\ \left(\begin{array}{l}\text{crosslink,may}\\ \text{be enzyme repairable}\end{array}\right) \quad (4)$$

$$\mathbf{R\cdot + XY \rightarrow RX + Y\cdot}\ \left(\text{chemical addition,may be enzyme repairable}\right) \quad (5)$$

$$\mathbf{R\cdot + O2 \rightarrow ROO\cdot}\left(\text{damage that is not repairable}\right) \quad (6)$$

where R is the rest of the DNA molecule and H is a site on the DNA where a pair of electrons forms a bond which the high energy of ionising radiation can break into two products, each with an unpaired electron and hence a free radical. The most important impacts of oxygen on radiation damage occur well after the initial absorption of the radiation (which occurs in 10^{-16} sec), starting at about 10^{-10} sec after the initial energy absorption. At this time, it becomes possible for chemical reactions to occur via diffusion, including free radical products of DNA generated either 'directly' as in Eq. (1), or 'indirectly' from reactive radical intermediates of water, especially the hydroxyl radical (Eq. 2). Equation (3) indicates how rapid chemical repair can occur via reaction of a "protective molecule" (such as glutathione) restoring the integrity of the DNA. Equations (4) and (5) indicate how the reactive free radicals in DNA can undergo damaging chemical reactions, rather than the immediate chemical repair. It is possible for some of the damaging reactions as Eqs. (4) and (5) to later be reversed by repair enzymes that are normally present to correct mistakes in the replication of DNA. But the presence of oxygen can shift the reactions in a more damaging direction as described by Eq. (6). O_2, with its two unpaired electrons, reacts rapidly with other free radicals that by definition also have unpaired electrons, effectively competing with reaction in Eq. (3), increasing the amount of damage. This is widely agreed to be the primary radiation chemical basis for the oxygen effect [9, 10].

4 Key Variables to Investigate Whether Impact of FLASH on Outcomes Is Related to Oxygen

Based on these known mechanisms of the direct effect of oxygen as described above, the key variables to study to evaluate the evidence of differential impacts by FLASH and conventional irradiation are the reactants described in Eqs. (3) and (6): [1] The amount of DNA radicals available for interaction with oxygen; [2] The oxygen levels pertinent to the reactions; and [3] The electron donating species. In this analysis we assume that the electron donating species is constant, but note that this could be modified differently by FLASH vs. conventional delivery.

The oxygen level in Eq. (6) must reflect oxygen molecules that are available to react with the reactive intermediates of DNA. The DNA is too large to diffuse, so therefore this amount is the oxygen level already present at the nucleus, plus any oxygen that can diffuse to the nucleus during the lifetime of the reactive intermediate of DNA.

4.1 Amount of DNA Radical Available for Interaction with Oxygen

Assuming that the amount of DNA radicals produced are the same for both types of tissue, the key variable is the lifetime of the radical. The best available data on the lifetime of the DNA intermediate that can react with oxygen are from a series of studies by Epp and colleagues (see [14] and references therein). They used two different approaches to determine the lifetime of the DNA radical. In one set of experiments a double pulse of radiation system was used, in which the first pulse was sufficient to completely deplete O_2 and then by varying the time interval before the second pulse, could determine the apparent lifetime of the species that reacted with O_2 (as indicated by the longest interval that resulted in an oxygen effect on cell death). In the second set of experiments they irradiated isolated cells in the absence of O_2 and then, as precisely as possible,

allowed oxygen to enter the system. Their data indicated that the reactive intermediate has a lifetime of 1–10 μsec.

4.2 Amount of Oxygen Available to React with the DNA Radical

The oxygen level in Eq. (6) must reflect oxygen molecules that are available to react with the reactive intermediates of DNA. The DNA is too large to diffuse, so therefore this amount is the oxygen level already present at the nucleus, plus any oxygen that can diffuse to the nucleus during the lifetime of the reactive intermediate of DNA. Knowing the lifetime of the intermediate that could react with oxygen (from the data of Epp and colleagues) and the rate of diffusion of oxygen we then can calculate the size of the perinuclear volume in which oxygen could diffuse to the nucleus within the lifetime of the reactive intermediate of DNA. Using the data on the lifetime of the intermediate of DNA that can react with oxygen we estimate that the diffusion distance in the cell is about 60–185 nm. The diffusion rates are based on Einstein's diffusion equation [15], the mean water content of the cytosol, i.e., 70% [16], and applying the appropriate O_2 diffusion coefficients [17]. Thus the volume in the cell whose oxygen concentration is germane to the oxygen effect is a sphere with a diameter of 60–185 nm. All other oxygen in the cell is irrelevant for oxygen-dependent damage due to FLASH.

5 Discussion

The above descriptions/discussions principally recapitulate well-known and non-controversial facts about the oxygen effect in ionising radiation. In order to measure directly the impact of different radiation delivery schemes on the pertinent oxygen concentrations, we conclude that the following aspects must be addressed:

1. Measurements need to be made *in vivo* to be able to take into account the effects of biological structures and functions as well as microenvironment that would impact oxygen levels and its transport.
2. There is a need to measure oxygen selectively in or around the nucleus. Note that this is a very important specification because there is no true homogeneous 'oxygen level' in either tumours or normal tissues; both types of tissues have very significant variations among (and within) their different compartments. Therefore, making measurements in other compartments (e.g., extracellular) will not provide direct data on oxygen levels in the nucleus [12, 13]. Instead, it needs to be assessed within a sphere of about 60–185 nm in diameter around the nucleus. This is the oxygen that is potentially available to diffuse to the reactive DNA within its lifetime after induction by ionising radiation.
3. There is a need to follow the dynamics of oxygen change with respect to temporal actions of interest, which is less than 10 μsec and may well be shorter (it is technically difficult to completely eliminate oxygen from experimental apparatus on such a short timescale which may result in incorrect measurements of radiobiological effect of oxygen).
4. It is important to measure the dynamics of oxygen change during each pulse for FLASH and throughout the irradiation period of each radiation fraction.

Currently, there appear to be no oxygen measuring techniques that have the desired properties to accomplish all these goals. Perhaps the clarification of what is needed will stimulate the developments of the necessary capabilities. Optical reporter methods may provide the greatest potential with studies in tumours within the depth of resolution, sensitivity and time of these methods. In particular, there are several plausible oxygen sensing probe types that could be conjugated to targeting molecules [18, 19], and through the combination of targeted delivery with retaining pO_2 sensing, they might be deployed. Alternatively, implicitly produced molecules can be used for O_2 sensing, such as Protoporphyrin IX [20], albeit to measure pO_2 in the mitochon-

dria rather than the nucleus. For *in vivo* measurement, the signal always will decay exponentially with depth, making sensing below 1–2 cm ultimately unlikely. However, this may be sufficient for the whole body mouse imaging, and with localised probes, the signal may be selectively amplified relative to the background interference [21]. Temporally, optical probes offer the advantage of fast acquisition, however ultimately most are limited by the time of collisional interaction with oxygen, and so the diffusion coefficient determines the maximum speed of useful sampling. This is likely to be in the μs range at the fastest, and so ultrafast pO_2 measurements with sub-μs FLASH events could not likely be effectively performed. Still another major limitation is the contribution of the FLASH radioluminescence itself, which can render most optical measurements useless during a pulse. Thus, even optical measurements are likely limited to measuring oxygen only before and after any pulses of radiation [22].

As noted in the introduction, most experimental studies and theoretical calculations in preclinical FLASH studies have focused on measuring/calculating global pO_2 changes rather than at the sites that are really pertinent, the nucleus and immediate region around it. While these data are interesting and may well be useful, they do not provide what is needed for direct pO_2 measurements at the sites and time resolution needed to directly investigate the differential impact of FLASH on oxygen levels.

It also is important to consider how differential O_2 depletion by FLASH versus conventional irradiation could cause an 'indirect oxygen effect'. There are many signalling pathways that are affected by oxygen level. It is likely that these are impacted not only by the absolute level at the sites where the oxygen signalling is activated (such as HIF-1α), but also by the rate and length of the change. These considerations open up a wide range of possibilities for a differential impact of FLASH mediated through transient oxygen level changes that impact cell signalling and gene activation.

Finally, it is important to remember that the dose from FLASH is delivered over a much shorter time than by conventional radiation. It seems possible that this could have a role in the normal tissue sparing seen with FLASH. For example, the potentially greater volume of blood that would circulate through the radiation field with the longer time for conventional radiation, combined with high sensitivity of small lymphocytes to ionising radiation, could impact immune responses and some of those responses are oxygen-dependent [23].

6 Conclusions

There are at least two plausible radiobiological mechanisms for the oxygen effect in FLASH: [1] *Directly* via depletion of oxygen at the critical molecular site (DNA), which therefore reduces the amount of initial oxygen-dependent radiation damage; [2] *Indirectly* via depletion of oxygen at critical sites that leads to alterations in repair and/or cell signaling, that lead to physiologically mediated changes in the response to radiation damage. Not only differences in dose rate (FLASH vs conventional) are important but also the different lengths of time over which radiation is delivered.

Accurate measurements of the direct oxygen depletion within 1–10 microseconds after radiation absorption should be performed in/around the nucleus within 60–185 nm of DNA location. There is no currently available method to make this assessment directly, however optical methods may eventually fill this gap. Very useful studies to test the direct oxygen depletion hypotheses may also be feasible through more indirect approaches such as altering the overall or local oxygen levels and analysing the impact in place of their direct measurement. Testing for the effects of alterations of oxygen on indirect mechanisms is feasible but will be very complex, and here we only describe the broad parameters that need to be considered to tackle this problem. Much more work needs to be done to test these possibilities, but this could be a very productive area of research.

Overall, the above considerations may be useful in developing more definitive tests of the

hypotheses to better understand whether and how differential impacts on oxygen levels are a major part of the mechanisms for the phenomenon of FLASH.

Acknowledgments This work was supported by a project funding from the Norris Cotton Cancer Center at the Geisel School of Medicine at Dartmouth. Disclaimer: BWP declares commercial involvement with DoseOptics LLC that developsCherenkov imaging cameras for RT dosimetry.

References

1. Al-Hallaq H, Cao M, Kruse J et al (2019) Cured in a FLASH: reducing normal tissue toxicities using ultra-high-dose rates. Int J Radiat Onc Biol Phys 104:257–260
2. Bourhis J, Sozzi WJ, Jorge PG et al (2019) Treatment of a first patient with FLASH-radiotherapy. Radiother Oncol 139:18–22
3. Favaudon V, Caplier L, Monceau V et al (2014) Ultrahigh dose-rate FLASH irradiation increases the differential response between normal and tumor tissue in mice. Sci Transl Med 6:245–293
4. Wilson JD, Hammond EM, Higgins GS et al (2020) Ultra-high dose rate (FLASH) radiotherapy: silver bullet or fool's gold? Front Oncol 9:1563. (1-12)
5. Friedl AA, Prise KM, Butterworth KT et al (2021) Radiobiology of the flash effect. Med Phys. Published Ahead of Print. https://doi.org/10.1002/mp.15184
6. Favaudon V, Labarbe R, Limoli CL (2021) Model studies of the role of oxygen in the FLASH effect. Med Phys 00:1–14
7. Pratx G, Kapp DS (2019) A computational model of radiolytic oxygen depletion during FLASH irradiation and its effect on the oxygen enhancement ratio. Phys Med Biol 64:185005
8. Watts ME, Maughan RL, Michael BD (1978) Fast kinetics of the oxygen effect in irradiated mammalian cells. Int J Radiat Biol 33:195–199
9. Lin B, Gao F, Yang Y et al (2021) FLASH radiotherapy: history and future. Front Oncol 11:644400
10. Hall EJ, Giaccia AJ (2018) Radiobiology for the radiologist. Lippincott Williams & Wilkins, 624 p
11. Withers HR (ed) (1975) The four R's of radiotherapy. Academic Press, New York. Lett JT AH, ed. Advances in radiation biology; 5:241–247
12. Swartz HM, Vaupel P, Williams BB et al (2020) 'Oxygen level in a tissue' – what do available measurements really report? Adv Exp Med Bio 1232:145–153
13. Swartz HM, Flood AB, Schaner PE et al (2020) How best to interpret measures of levels of oxygen in tissues to make them effective clinical tools for care of patients with cancer and other oxygen-dependent pathologies. Physiol Rep 8(e14541):1–20
14. Ling CC, Michaels HB, Epp ER et al (1978) Oxygen diffusion into mammalian cells following ultrahigh dose rate irradiation and lifetime estimates of O_2-sensitive species. Radiat Res 76:522–532
15. Vaupel P, Flood AB, Swartz HM (2021) Oxygenation status of malignant tumors vs. normal tissues: critical evaluation and updated data source based on direct measurements with pO_2 microsensors. Appl Magn Reson, 51(10):1481–1487. https://doi.org/10.1007/s00723-021-01414-2
16. Luby-Phelps K (2000) Cytoarchitecture and physical properties of cytoplasm: volume, viscosity, diffusion, intracellular surface area. Int Rev Cytol 192:189–221
17. Vaupel P (1976) Effect of percentual water content in tissues and liquids on the diffusion coefficients of O_2, CO_2, N_2, and H_2. Pflügers Arch 361:201–204
18. Wilson DF, Evans SM, Jenkins WT et al (1998) Oxygen distributions within R3230Ac tumors growing in dorsal flap window chambers in rats. Adv Exp Med Biol 454:603–609
19. Dunphy I, Vinogradov SA, Wilson DF (2002) Oxyphor R2 and G2: phosphors for measuring oxygen by oxygen-dependent quenching of phosphorescence. Anal Biochem 310:191–198
20. Harms FA, Bodmer SI, Raat NJ et al (2012) Validation of the protoporphyrin IX-triplet state lifetime technique for mitochondrial oxygen measurements in the skin. Opt Lett 37:2625–2627
21. Cao X, Gunn JR, Allu SR et al (2020) Implantable sensor for local Cherenkov-excited luminescence imaging of tumor pO2 during radiotherapy. J Biomed Opt 25:112704
22. Cao X, Zhang R, Esipova TV et al (2021) Quantification of oxygen depletion during FLASH irradiation *in vitro* and *in vivo*. Int J Radiat Oncol Biol Phys 111:240–248
23. O'Hara JA, Blumenthal RD, Grinberg OY et al (2001) Response to radioimmunotherapy correlates with tumor pO_2 measured by EPR oximetry in human tumor xenografts. Radiat Res 155:466–473

Assessment of Nicotinamide Adenine Dinucleotide in Human Tissues by *In Vivo* Phosphorus-31 Magnetic Resonance Spectroscopic Imaging at 1.5 Tesla

Fernando Arias-Mendoza, Kavindra Nath, He N. Xu, Pradeep K. Gupta, and Lin Z. Li

Abstract

As a phosphorus-containing molecule, nicotinamide adenine dinucleotide is visible by phosphorus magnetic resonance spectroscopy (^{31}P-MRS). However, the relatively low cellular levels of its oxidised (NAD^+) and reduced (NADH) forms and a significant peak overlap hinder their evaluation in live tissues. This problem is critical when using ^{31}P-MR spectroscopic imaging, where signals are localised from limited tissue volumes. We have reported improvements in spectral resolution of ^{31}P-MRSI of human tissues *in situ* using a strict optimisation of the static magnetic field (B_0 shimming) and ^{1}H-irradiation during ^{31}P acquisition. Given this, we aimed to demonstrate if these improvements allowed us to measure the *in vivo* intracellular levels of NAD^+ and NADH at the relatively low magnetic field of 1.5 tesla (T). Our results show the feasibility of the *in vivo* determination of NAD^+ and NADH from relatively small volumes of human tissues studied at 1.5 T. These results are clinically relevant as the currently available systems for human use mainly operate at 1.5 or 3.0.

Keywords

^{31}P-MR spectroscopic imaging · Breast cancer · Nicotinamide Adenine Dinucleotide$^+$

1 Introduction

Nicotinamide adenine dinucleotide (NAD) is an essential oxidoreduction coenzyme in the intermediary metabolism [1]. As a redox pair, NAD^+ and NADH are closely related to cellular oxygen consumption, bioenergetics, and signalling activities [2]. Traditionally, the NAD(H) redox status assessment was limited to indirect measurements using biochemical assays *in vitro* [3, 4] or direct assessment by optical redox imaging [5, 6]. However, recent reports have shown the non-invasive quantification of NAD^+ and NADH in live tissues *in situ* using phosphorous-31 magnetic resonance spectroscopy (^{31}P-MRS) [7–10].

To our knowledge, previous reports [7–9] except the one from Conley et al., [10] describe

F. Arias-Mendoza (✉) · K. Nath · H. N. Xu
P. K. Gupta · L. Z. Li
Laboratory of Molecular Imaging & Britton Chance Laboratory of Redox Imaging. Department of Radiology, Penn Medicine (University of Pennsylvania Health System), Philadelphia, PA, USA
e-mail: Fernando.Arias-Mendoza@pennmedicine.upenn.edu

F. Scholkmann et al. (eds.), *Oxygen Transport to Tissue XLIII*, Advances in Experimental Medicine and Biology 1395, https://doi.org/10.1007/978-3-031-14190-4_52

the feasibility of determining NAD^+ and NADH by *in vivo* ^{31}P-MRS using magnetic fields higher than 1.5 T. Higher field strengths improve spectral sensitivity. However, they are seldom available for clinical use. Moreover, in these previous studies including Conley's, spectra were obtained from large volumes to improve spectral sensitivity further. Here, we report the feasibility of determining NAD^+ and NADH *in vivo* from relatively small, more clinically relevant volumes (i.e., voxels) of human tissues *in situ* using a 1.5 T clinical scanner. We acquired these data using multivoxel localisation (i.e., ^{31}P-MR spectroscopic imaging [^{31}P-MRSI]) and applied ^{1}H-irradiation and optimal B_0 shimming for signal improvement. Although we focused on the determination of NAD^+ and NADH in brain and breast cancer in this report, we have obtained ^{31}P-MRSI at 1.5 Tof many other human tissues *in situ*, with similar or better spectral qualities, which allows to postulate that the determination of NAD^+ and NADH by ^{31}P-MRSI at 1.5 T can be attained in most human tissues *in situ*.

2 Methods

Under the approval of the Institutional Review Board of the Fox Chase Cancer Center (USA), we acquired non-invasive ^{31}P-MRSI data from *in situ* tissues of human subjects using a 1.5 T clinical magnetic resonance (MR) system (Siemens, Germany) [11–13]. In brief, after acquiring MR images and optimising the static magnetic field (B_0 shimming) [14], ^{31}P signals were localised and acquired using the 3D-chemical shift imaging (3D-CSI) algorithm [15, 16] with eight phase-encoding steps per orthogonal axis, a 45° excitation pulse at the location of the tumour, 512 data points, a spectral width of ±1000 Hz, repetition time of one second, constant amplitude phase-modulated ^{1}H decoupling during the acquisition time, low-level ^{1}H excitation during the rest of the time for nuclear Overhauser effect, and four averages per encoding step. The 3D-CSI field-of-view was 180 or 240 mm per side, giving nominal voxel volumes of 11.4 and 27 mL, respectively.

We use our proprietary custom-made 3D*i*CSI program for spectral processing. In summary, data sets were Fourier-transformed in the spatial domain. In the time domain, data were zero-filled to 1024 points and an apodization filter with a Lorentzian function of 5–7 Hz was used to reduce noise despite signal broadening before Fourier transform and phase-correction. The chemical shift (δ) of αATP was set at −10.07 parts per million (*ppm*). When needed, we use the 3D*i*CSI program to anatomically localise the spectra overlaying the results over the MR images and the voxel-shifting subroutine to center voxels of interest in targeted tissues or anatomical structures.

We used the commercially available OriginPro for subsequent signal analysis and curve fitting of the αATP-NAD(H) spectral region. In brief, we applied a Lorentzian function to each signal varying the amplitude and half-line width (HLW) manually. However, we kept each peak's chemical shift position as close to its theoretical value as possible until the residual spectrum showed minimal amounts of remaining signals. The αATP signal was modelled as a doublet, NADH as a singlet, and NAD^+ as a quartet considering the constraints of scalar couplings and magnetic field strength on chemical shifts [7].

3 Results and Discussion

Figure 1 shows non-localised spectra of the head of a healthy subject. The red spectrum in panel A was acquired without ^{1}H irradiation, while the black spectrum shows the effect of this irradiation. The inset in panel A expands the αNTP-NAD(H) region of both spectra. The αNTP signal is a doublet due to *J*-coupling with the neighbouring β-phosphate (J = 15.5 Hz). Each peak in the doublet of αNTP is further split into a triplet due to the *J*-coupling with the ribose's -CH_2- residue to which the α-phosphate is attached (J = 6.0 Hz). ^{1}H-irradiation collapses the triplets into a single resonance resulting in a sharper, more prominent, and clearer αNTP doublet. As shown in the panel, ^{1}H-irradiation also improves spectral resolution resolving the over-

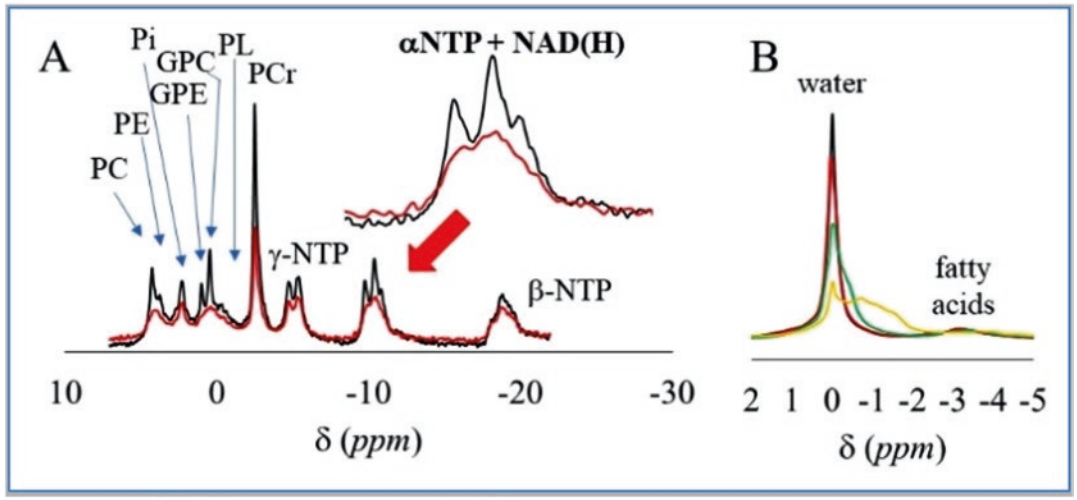

Fig. 1 Non-localised ^{31}P-MRSI of the head of a healthy human subject. Panel **A**. Effect of ^{1}H irradiation on the ^{31}P signals (black) *vs.* no irradiation (red). The inset expands the αNTP-NAD(H) region. Assignments *PC* phosphocholine, *PE* phosphoethanolamine, *Pi* inorganic phosphate, *GPE* glycero-phosphoethanolamine, *GPC* glycero-phosphocholine, *PL* phospholipids, *PCr* phosphocreatine; γ-, α-, β-NTP, the three ^{31}P signals from nucleoside triphosphates. Panel **B**. Effect of B_0 shimming on non-localised ^{1}H MRS. The spectrum in yellow was acquired before optimisation. Spectra in green, red, and black show the progressive reduction of inhomogeneities of the B_0 field during B_0 shimming, and thus sharper and more clearly defined signals were progressively acquired

lapping signals upfield of the αNTP doublet, including NAD^+ and NADH.

Panel B of Fig. 1 depicts non-localised ^{1}H MR spectra. In these spectra, a sizeable ^{1}H resonance from water and a shorter, more diffuse resonance from the -CH_2- units in fatty acids are present. This panel shows how the non-localised water and fatty acid signals become sharper, symmetric, and more precise with B_0 shimming. We repeated three times our automated procedure to improve the B_0 static field of our clinical scanner. The yellow spectrum in panel B was acquired immediately after collecting MR images but before the ^{31}P-MRSI exam. This spectrum shows a broad and asymmetric water signal, and the fatty acids signal is not visible. After each iteration (green, red, and black spectra, respectively), the water signal became more symmetric and narrower, and the fatty acid signal was increasingly apparent. These improvements translated into the subsequent ^{31}P-MRSI exams, as shown in panel A and in the rest of the figures [14].

Regarding NADH, the similarity of the atoms surrounding both phosphates made them resonate as a single peak. In NAD^+, however, the presence of the positive charge in the nitrogen atom of the nicotinamide causes a chemical shift difference ($\delta = 0.3211$ *ppm*) between the two spins, which are also *J*-coupled ($J = 20.03$ Hz). The resulting quartet of NAD^+ has central resonances (s2 and s3) of the same intensity (I_s) and are more prominent than the external resonances (s1 and s4) that also match in intensity (I_w). The theoretical *ppm* position of the centroid of the NAD^+ quartet is constant in a range of field strengths. However, while the central resonances separate, the external resonances get closer when increasing the magnetic field. Conversely, the intensity ratio I_s/I_w decreases when the magnetic field increases. We have also demonstrated that variations in pH modify the spectral positions of NAD^+ and NADH relative to αNTP in a related study also published in this volume [17]. Therefore, scalar couplings and pH (and maybe other factors) must be considered for the proper peak fitting of NAD^+ and NADH by ^{31}P-MRSI.

Panel A of Fig. 2 shows the projection of a 180 mm cubic 3D matrix grid used to acquire ^{31}P-MRSI of a healthy human brain. The matrix had eight phase-encoding steps per side. Thus,

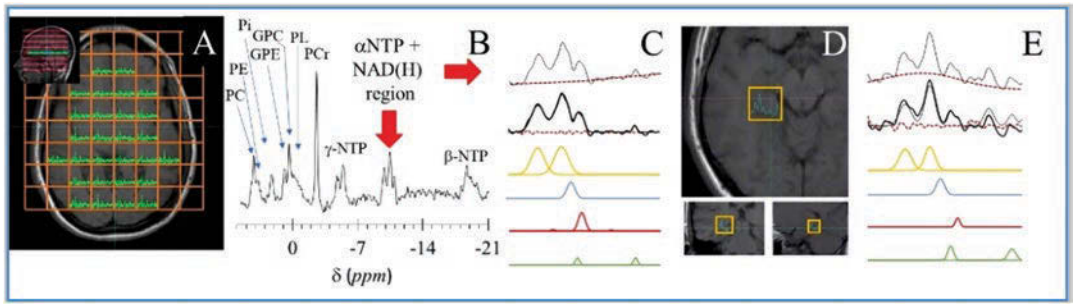

Fig. 2 NAD^+ and NADH assessment in brain tissue of a healthy human subject. Panel **A**. Axial (main) and sagittal (inset) MR images overlaid with the 3D matrix grid of the ^{31}P-MRSI (orange) and the spectra of each voxel (green). Panel **B**. Summed brain spectra from the 28 voxels shown in panel **A**. Peak assignments as in Fig. 1. Panel **C**. Curve fitting steps to determine NAD^+ and NADH. First row, original αNTP+NAD(H) region (grey), and the baseline correction (dashed red). Second row, baseline-corrected spectrum (grey), global curve fitting (black), and residuals (dashed red). Following rows, the doublet of αNTP (yellow), the singlet of NADH (blue), and the quartet of NAD^+ (red; centre resonances are not resolved). The last row shows UDPG (green), where the signal *ca.* -12.30 *ppm* was visible while the signal *ca*. -10.75 *ppm* was calculated from the value of the visible signal. Panels **D** and **E**. Analysis of an individual spectrum from the dataset in **A** centered in the right hippocampus. Panel **D**. Transverse (main), and coronal and sagittal (insets) MR images to guide the voxel positioning (yellow squares). Panel **E**. Similar analysis as in Panel **C** for the single voxel spectrum

the ^{1}H-irradiated brain-localised ^{31}P spectra were acquired from nominal voxel volumes of 11.4 mL. To improve the signal-to-noise ratio (SNR) for the initial analyses of NAD^+ and NADH, we summed the 28 ^{31}P spectra shown in Panel A and the result depicted in Panel B (total volume, 319.2 mL).

The αNTP-NAD(H) region of the summed spectrum in panel A was further analyzed to determine the integral of each signal. Panel C shows the main steps of the integration analysis to determine αNTP (yellow), NADH (blue), and NAD^+ (red). Uridine diphosphate glucose (UDPG; green) was also present, demonstrated by a clear signal around −12.30 *ppm*. This signal must match with an identical signal around −10.75 *ppm*, which was obscured by peak overlap. To prevent overestimating NAD^+ or NADH, we modeled the signal at −10.75 *ppm* and included it in the analysis. In the peak fitting shown in panel C, the s2 and s3 signals of NAD^+ were not resolved, and the s1 signal of NAD^+ was obscured by peak overlap. Like in the procedure for UDPG, we modelled s1 of NAD^+ from the value of s4. Panels D and E of Fig. 2 show the analysis of a single voxel from the dataset in panels A to C. As shown in panel E, we placed the voxel to include the hippocampus employing the voxel shifting property of 3D-CSI. Despite the expected lower spectral resolution due to the small voxel volume (11.4 mL), the peak analysis depicted in panel E demonstrates the feasibility of determining αNTP, NAD^+, NADH and UDPG at this resolution.

Figure 3 shows an example of the *in vivo* ^{31}P-MRSI determination of NAD^+ and NADH in a cancer mass of a patient with invasive ductal carcinoma (IDC) before treatment. Panel A shows a spectrum from a 30 mL voxel centered in the tumour mass located in the right breast. The inset depicts an MR image of the breast overlaid with the projection of the 3D grid of the ^{31}P-MRSI (grey) and the selected voxel (orange square). Panel B shows the curve fitting procedure of the α-NTP-NAD(H) region of the spectrum shown in panel A following the steps described in Fig. 2. The additional signal *ca*. –11.0 *ppm* (purple) has been suggested by Conley et al. [10] to be mitochondrial NAD(P)H.

Table 1 summarises the NAD(H) results from three breast cancer exams. One exam is from a patient with a ductal carcinoma *in situ* (DCIS) before treatment. The other two exams are from a patient with IDC; one before treatment (shown in Fig. 3) and one during treatment. Table 1 shows larger values of the NAD^+/NADH ratio in the more advanced and metastatic IDC, both before and during treatment, compared to the non-

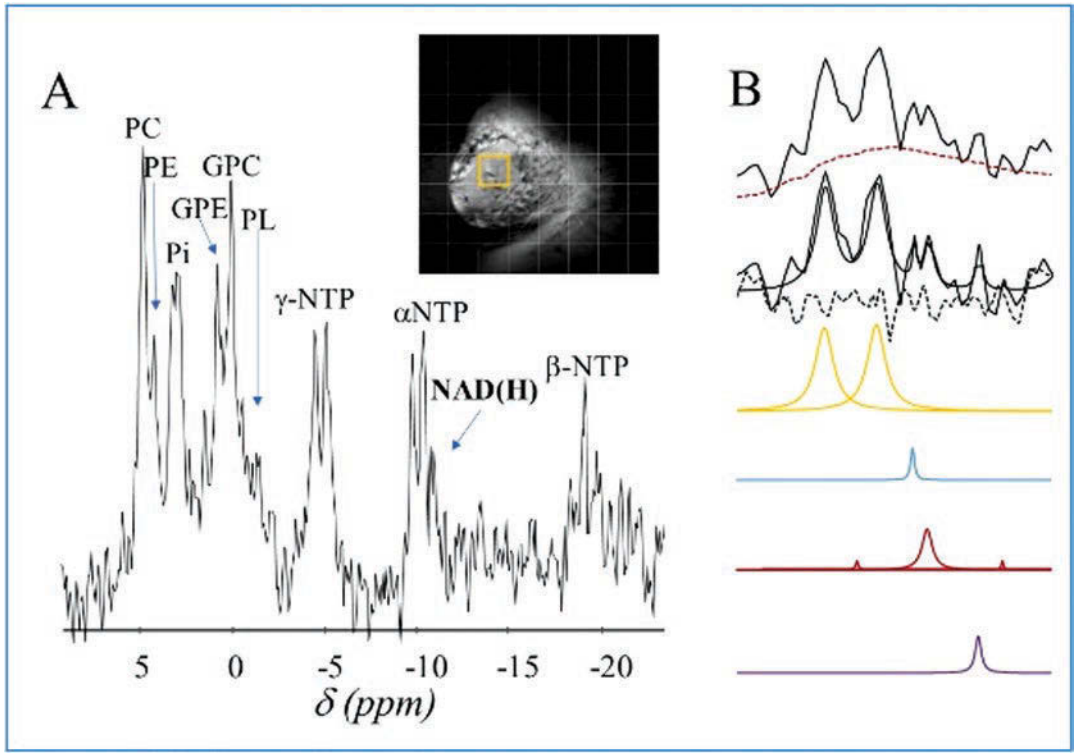

Fig. 3 Localised ^{31}P-MRSI of a patient with breast cancer. Panel **A**. Spectrum from a voxel centered in the tumor of a patient with invasive ductal carcinoma (IDC). The MR image (inset) shows the lesion and the position of the voxel. Assignment as in Fig. 1. Panel **B**. Curve fitting of the αNTP-NAD(H) region as described in panels **C** and **E** of Fig. 2

Table 1 NAD(H) Redox Values in breast cancer patients

Diagnosis	DCIS	IDC	
Relation to treatment	Before	Before	During
NAD^+/NADH	0.99	3.73	2.30
(NAD^+ + NADH)/αNTP	0.55	0.19	0.65

metastatic and mostly curable DCIS. Furthermore, the value of the NAD^+/NADH ratio in the IDC patient is almost 50% lower during the treatment when compared to the pre-treatment value. Conversely, the (NAD^++NADH)/αNTP ratio value is almost three times lower in the IDC patient before treatment compared to the pre-treatment value of the DCIS patient or the value of the IDC patient during treatment. Although these observations are few, they suggest possible NAD(H) differences between metastatic and non-metastatic breast cancer and possible modifications during treatment. These preliminary breast cancer results relate to our study of NAD^+ and NADH in preclinical models of human breast cancer, also reported in this volume [17]. Our interest is to translate our preclinical results into the clinic.

The NAD^+ and NADH determination by ^{31}P-MRSI, however, still requires refinement. Currently, ^{31}P-MRSI measures the total cellular pool of both NAD^+ and NADH and cannot yet distinguish between NAD(H) or NADP(H). It is also well known that the cytoplasmic and mitochondrial compartments maintain their NAD^+ and NADH pools at different redox levels and that the flux of redox equivalents between the two compartments is strictly controlled [1–3]. Furthermore, although both are redox coenzymes, the NAD(H) and NADP(H) systems have different cellular functions and need to be distinguished from each other, which is not yet possi-

ble with the present level of technical development of ^{31}P-MRSI [2, 10].

Summarising, the present study demonstrates the feasibility of determining NAD^+ and NADH in examples of human tissues *in situ* (brain and breast cancer) using ^{31}P-MRSI in a clinical scanner at 1.5. In this study, we preliminarily assessed the differences in the cellular content of NAD^+ and NADH in breast cancer patients suggesting a correlation with invasive potential and treatment response. Furthermore, the preliminary results suggest that the *in vivo* measurement of NAD^+ and NADH could be of clinical value in the follow-up of patients with breast cancer and probably in patients with other types of tumours.

Acknowledgments This work was supported by US NIH Grants R01CA118559 and R21CA152858 (PI: F. Arias-Mendoza) for the data acquisition and US NIH Grant R01CA191207 (PI: L. Z. Li) for the data analysis. The authors wish to thank the Cooperative Group of MRS in cancer (CoGMaC) for their participation acquiring the breast cancer data.

References

1. Goodman RP, Calvo SE, Mootha VK (2018) Spatiotemporal compartmentalization of hepatic NADH and NADPH metabolism. J Biol Chem 293(20):7508–7516. https://doi.org/10.1074/jbc.TM117.000258
2. Hassinen IE (2019) Signaling and regulation through the NAD(+) and NADP(+) networks. Antioxid Redox Signal 30(6):857–874. https://doi.org/10.1089/ars.2017.7479
3. Pina-Garza E, Garcia-Sainz A (1983) Chagoya de Sanchez V, Arias-Mendoza F. [ethanol: catabolism and metabolic effects. I. Introduction]. Gac Med Mex 119(1):1–14
4. Zhang Z, Xu HN, Li S, Chellappa K, Davis JG et al (2020) Rapamycin maintains NAD(+)/NADH redox homeostasis in muscle cells. Aging 12(18):17786–17799. https://doi.org/10.18632/aging.103954
5. Xu HN, Li LZ (2014) Quantitative redox imaging biomarkers for studying tissue metabolic state and its heterogeneity. J Innov Opt Heal Sci 7(2):1430002. https://doi.org/10.1142/S179354581430002X
6. Li LZ, Xu HN, Ranji M, Nioka S, Chance B (2009) Mitochondrial redox imaging for cancer diagnostic and therapeutic studies. J Innov Opt Heal Sci. 2:325–341. https://doi.org/10.1142/S1793545809000735
7. Lu M, Zhu XH, Zhang Y, Chen W (2014) Intracellular redox state revealed by in vivo (31) P MRS measurement of NAD(+) and NADH contents in brains. Magn Reson Med 71(6):1959–1972. https://doi.org/10.1002/mrm.24859
8. Zhu X-H, Lu M, Lee B-Y, Ugurbil K, Chen W (2015) In vivo NAD assay reveals the intracellular NAD contents and redox state in healthy human brain and their age dependences. Proc Natl Acad Sci 112(9):2876–2881. https://doi.org/10.1073/pnas.1417921112
9. Kim SY, Cohen BM, Chen X, Lukas SE, Shinn AK, Yuksel AC et al (2017) Redox dysregulation in schizophrenia revealed by in vivo NAD+/NADH measurement. Schizophr Bull 43(1):197–204. https://doi.org/10.1093/schbul/sbw129
10. Conley KE, Ali AS, Flores B, Jubrias SA, Shankland EG (2016) Mitochondrial NAD(P)H in vivo: identifying natural indicators of oxidative phosphorylation in the (31)P magnetic resonance spectrum. Front Physiol 7:45. https://doi.org/10.3389/fphys.2016.00045
11. Arias-Mendoza F, Smith MR, Brown TR (2004) Predicting treatment response in non-Hodgkin's lymphoma from the pretreatment tumor content of phosphoethanolamine plus phosphocholine. Acad Radiol 11(4):368–376. https://doi.org/10.1016/s1076-6332(03)00721-9
12. Arias-Mendoza F, Payne GS, Zakian KL, Schwarz AJ, Stubbs M, Stoyanova R et al (2006) In vivo ^{31}P MR spectral patterns and reproducibility in cancer patients studied in a multi-institutional trial. NMR Biomed 19(4):504–512. https://doi.org/10.1002/nbm.1057
13. Arias-Mendoza F, Zakian K, Schwartz A, Howe FA, Koutcher JA, Leach MO et al (2004) Methodological standardization for a multi-institutional in vivo trial of localized (31)P MR spectroscopy in human cancer research. In vitro and normal volunteer studies. NMR Biomed 17(6):382-391. https://doi.org/10.1002/nbm.915
14. Hu J, Javaid T, Arias-Mendoza F, Liu Z, McNamara R, Brown TR (1995) A fast, reliable, automatic shimming procedure using 1H chemical-shift-imaging spectroscopy. J Magn Reson B 108(3):213–219. https://doi.org/10.1006/jmrb.1995.1126
15. Brown TR (1992) Practical applications of chemical shift imaging. NMR Biomed. 5(5):238–243. https://doi.org/10.1002/nbm.1940050508
16. Brown TR, Kincaid BM, Ugurbil K (1982) NMR chemical shift imaging in three dimensions. Proc Natl Acad Sci U S A 79(11):3523–3526. https://doi.org/10.1073/pnas.79.11.3523
17. Nath K, Arias-Mendoza F, Xu HN, Gupta P, Li LZ (2022) Feasibility of noninvasive measurement of tumor NAD(H) by *in vivo* phosphorus-31 magnetic resonance spectroscopy. Adv Exp Med Biol

Drag-Reducing Polymers Improve Vascular Hemodynamics and Tissue Oxygen Supply in Mouse Model of Diabetes Mellitus

Denis E. Bragin, O. A. Bragina, F. Monickaraj, A. Noghero, A. O. Trofimov, E. M. Nemoto, and M. V. Kameneva

Abstract

Diabetes mellitus (DM) is a chronic metabolic disease characterised by hyperglycaemia and glucose intolerance caused by impaired insulin action and/or defective insulin secretion. Long-term hyperglycaemia leads to various structural and functional microvascular changes within multiple tissues, including the brain, which involves blood-brain barrier alteration, inflammation and neuronal dysfunction. We have shown previously that drag-reducing polymers (DRP) improve microcirculation and tissue oxygen supply, thereby reducing neurologic impairment in different rat models of brain injury. We hypothesised that DRP could improve cerebral and skin microcirculation in the situation of progressive microangiopathies associated with diabetes using a mouse model of diabetes mellitus. Diabetes was induced in C57BL/6 J mice with five daily consecutive intraperitoneal injections of streptozotocin (50 mg/kg/day). Animals with plasma glucose concentrations greater than 250 mg/dL were considered diabetic and were used in the study following four months of diabetes. DRP (2 ppm) was injected biweekly during the last two weeks of the experiment. Cortical and skin (ear) microvascular cerebral blood flow (mCBF) and tissue oxygen supply (NADH) were measured by two-photon laser scanning microscopy (2PLSM). Cerebrovascular reactivity (CVR) was evaluated by measuring changes in arte-

D. E. Bragin (✉)
Lovelace Biomedical Research Institute, Albuquerque, NM, USA

Department of Neurology, University of New Mexico School of Medicine, Albuquerque, NM, USA

National Research Saratov State University, Saratov, Russia
e-mail: dbragin@lovelacebiomedical.org

O. A. Bragina · A. Noghero
Lovelace Biomedical Research Institute, Albuquerque, NM, USA

F. Monickaraj
Department of Ophthalmology and Visual Sciences, University of New Mexico School of Medicine, Albuquerque, NM, USA

New Mexico VA Health Care System, Albuquerque, NM, USA

A. O. Trofimov
Department of Neurology, Privolzhsky Research Medical University, Nizhny Novgorod, Russia

E. M. Nemoto
Department of Neurology, University of New Mexico School of Medicine, Albuquerque, NM, USA

M. V. Kameneva
McGowan Institute for Regenerative Medicine, University of Pittsburgh, Pittsburgh, PA, USA

F. Scholkmann et al. (eds.), *Oxygen Transport to Tissue XLIII*, Advances in Experimental Medicine and Biology 1395, https://doi.org/10.1007/978-3-031-14190-4_53

riolar diameters and NADH (tissue oxygen supply) during the hypercapnia test. Transient hypercapnia was induced by a 60-second increase of CO_2 concentration in the inhalation mixture from 0% to 10%. Compared to non-diabetic animals, diabetic mice had a significant reduction in the density of functioning capillaries per mm^3 (787 ± 52 vs. 449 ± 25), the linear velocity of blood flow (1.2 ± 0.31 vs. 0.54 ± 0.21 mm/sec), and the tissue oxygen supply ($p < 0.05$) in both brain and skin. DRP treatment was associated with a 50% increase in all three parameters ($p < 0.05$). According to the hypercapnia test, CVR was impaired in both diabetic groups but more preserved in DRP mice ($p < 0.05$). Our study in a diabetic mouse model has demonstrated the efficacy of hemorheological modulation of blood flow by DRP to achieve increased microcirculatory flows and tissue oxygen supply.

Keywords

Hyperglycemia · Glucose intolerance · Cerebrovascular reactivity · Hypoxia · Capillary perfusion

1 Introduction

Diabetes mellitus (DM) is a chronic metabolic disease characterised by hyperglycaemia and glucose intolerance caused by impaired insulin action and/or defective insulin secretion. Long-term hyperglycaemia leads to various structural and functional microvascular changes within multiple tissues, including the brain, which involves blood-brain barrier alteration, inflammation, and neuronal dysfunction [1]. Functional cerebral and peripheral microcirculation, such as decreased baseline regional cerebral blood flow (CBF) and impaired vasoreactivity to CO_2, have been shown in diabetic patients [2, 3]. We have demonstrated previously that drag-reducing polymers (DRP) improve microcirculation and tissue oxygen supply, thereby reducing neurologic impairment in different rat models of brain injury [4, 5]. We hypothesised that DRP could improve cerebral and skin microcirculation and tissue oxygen supply in the situation of progressive microangiopathies associated with diabetes using a mouse model of diabetes mellitus.

2 Materials and Methods

Animal procedures were approved by the Institutional Animal Care and Use Committee of the Lovelace Biomedical Research Institute under the Animal Protocol #FY20-067. Diabetes was induced in C57BL/6 J mice (The Jackson Laboratory, Bar Harbor, ME, USA) with five daily consecutive intraperitoneal injections of streptozotocin (50 mg/kg) as previously described [6]. Animals with plasma glucose concentrations greater than 250 mg/dL were considered diabetic and were used in the study following four months of diabetes. DRP (2 ppm) or saline was injected biweekly during the last two weeks of the experiment. A biweekly injection regimen was chosen as it has been shown previously that DRP concentration in the blood falls to 50% within 48 h [7]. Cortical and skin (ear) microvascular cerebral blood flow (mCBF) and tissue oxygen supply (NADH) were measured by two-photon laser scanning microscopy (2PLSM). Cerebrovascular reactivity (CVR) was evaluated by measuring changes in arteriolar diameters and NADH (tissue oxygen supply) during the hypercapnia test. Transient hypercapnia was induced by a 60-second increase of CO_2 concentration in the inhalation mixture from 0% to 10%.

DRP Preparation Polyethylene oxide (PEO, MW ~4000 kDa) was dissolved in saline to 0.1% (1000 ppm), dialysed against saline using a 50 kD cutoff membrane, diluted in saline to 50 ppm, slow rocked for ~2 h, and then sterilised using a 0.22 μm filter [4].

Two-Photon Laser Scanning Microscopy For long-term in-vivo imaging of the mouse cortex, we used an optical clearing skull window using two clearing solutions without performing a cra-

niotomy [8]. For skin imaging, the ear was shaved and treated with a skin-clearing solution [9] before each imaging. The number of perfused capillaries, microcirculation, and tissue oxygen supply were visualised using Olympus BX 51WI upright microscope and water-immersion XLUMPlan FI 20x/0.95 W objective as previously described [4]. Excitation was provided by a Prairie View Ultima multiphoton laser scan unit powered by a Millennia Prime 10 W diode laser source pumping a Tsunami Ti: sapphire laser (Spectra-Physics, Mountain View, CA). Red blood cell flow velocity was measured in microvessels ranging from 3–50 μm diameter up to 500 μm below the surface of the parietal cortex and ear skin. NADH autofluorescence measurement was used to evaluate mitochondrial activity (metabolic status) and tissue oxygenation [10]. In offline analyses using NIH ImageJ software, three-dimensional anatomy of the vasculature in areas of interest was reconstructed from two-dimensional (planar) scans of the fluorescence intensity obtained at successive focal depths in the cortex (XYZ stack).

Optical Clearing For skull optical clearing, solution 1 (saturated supernatant solution of 75% (ethanol and urea) was applied to the exposed skull for about 10 min to allow the skull to turn transparent [8]. Then, solution 1 was removed, and solution 2 (sodium dodecylbenzenesulfonate) was added to the same area for further clearing within 5 min. For skin imaging, the ear was shaved and treated with skin clearing solution (PEG-400 + thiazone + sucrose) before each imaging [9].

Cerebrovascular Reactivity Testing by Hypercapnia Challenge Changes in arteriolar diameters and NADH were measured during the hypercapnia test as previously described [11]. Transient hypercapnia was induced by a 60-second increase in CO_2 concentration to 10% in the inhalation mixture through the face mask. Each trial consisted of 3 min of baseline data acquisition, followed by 1 min of the hypercapnia challenge, and 3 min of the post-hypercapnic surveillance period.

Statistical analyses were done using GraphPad Prism software (La Jolla, CA, USA) by independent Student's *t*-test or Kolmogorov–Smirnov tests where appropriate. Differences between groups and time were determined using a two-way repeated measures ANOVA analysis for multiple comparisons and post hoc testing using the Mann-Whitney *U* test. Variables are expressed as mean ± standard error. The level of significance was set at 0.05.

3 Results

At the baseline, the number of functioning capillaries per mm^3 was 1020 ± 98 in the brain cortex and 954 ± 76 in the ear skin (Fig. 1). Just before the treatment (14 weeks of diabetes), the number of functioning capillaries fell to 524 ± 69 in the brain cortex and 520 ± 58 in the ear skin without difference between groups (Fig. 1).

Two-week DRP treatment led to a significant increase in the density of functioning capillaries per mm3 (787 ± 52), compared to vehicle-treated 449 ± 25 (Fig. 1, $p < 0.05$). Similarly, the linear capillary blood flow velocity dropped from 1.38 ± 0.18 mm/s in the brain and 1.2 ± 0.19 mm/s in the skin to 0.71 ± 0.21 and 0.76 ± 0.2 in the brain and skin, respectively (Fig. 2). After DRP treatment, capillary blood flow velocity re-stored to 1.2 ± 0.31 mm/sec and 1.0 ± 0.21 in the brain and ear, respectively, compared to 0.54 ± 0.21 and 0.62 ± 0.2 in the saline-treated mice (Fig. 2, $p < 0.05$).

Microvascular flow impairment led to tissue hypoxia as reflected by increased NADH autofluorescence in both brain cortex and skin (Fig. 3). Capillary perfusion improvement in DRP-treated mice led to enhancement of tissue oxygen supply 1.05 ± 0.04 and 1.04 ± 0.03 in the brain cortex and skin, respectively, comparing to 1.32 ± 0.06 and 1.22 ± 0.04 in the saline group (Fig. 3, $p < 005$).

Baseline hypercapnia test showed that cerebral arterioles dilated during inhalation of 10%

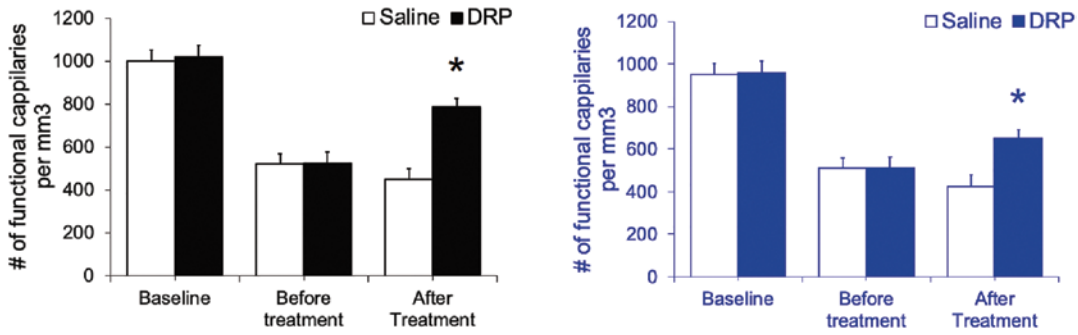

Fig. 1 Number of functional capillaries per mm^3 of tissue. Left: Brain; Right: Ear skin. $N = 10$ mice per group, ($^*p < 0.05$)

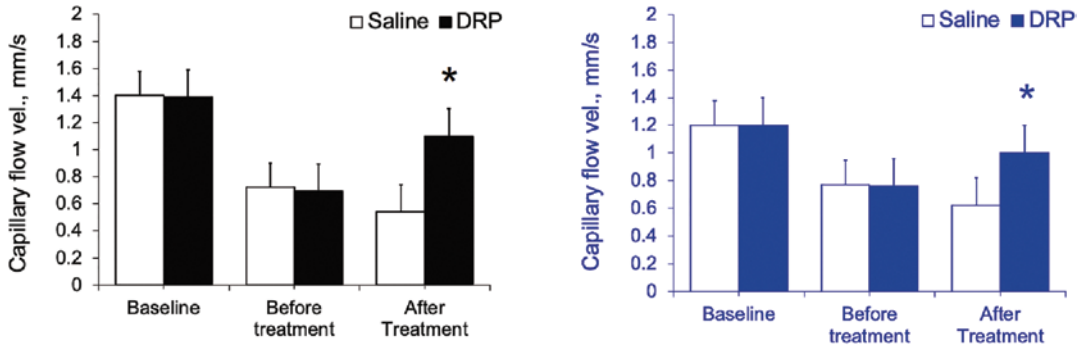

Fig. 2 Capillary flow velocity (mm/s) Left: Brain; Right: Ear skin. $N = 10$ mice per group, ($^*P < 0.05$)

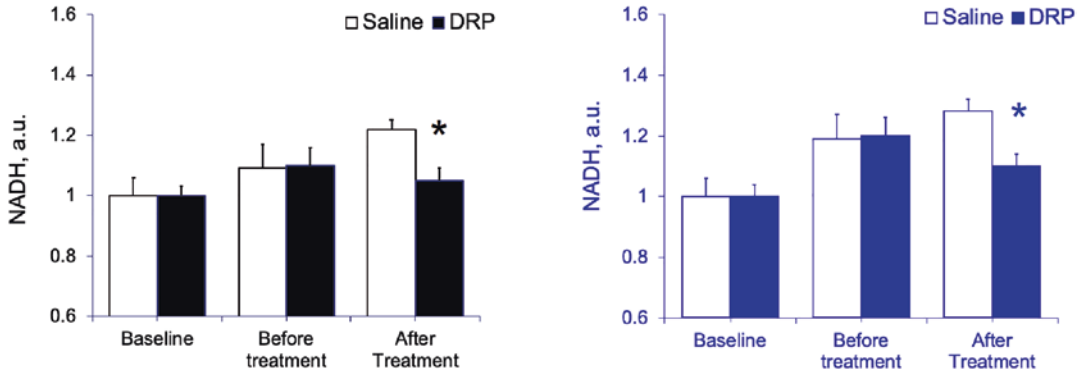

Fig. 3 NADH autofluorescence (inversely reflecting tissue oxygen supply). Left: Brain; Right: Ear skin. $N = 10$ mice per group, ($^*P < 0.05$)

CO_2 (by 44.0 ± 3.5%) and constricted to the pre-hypercapnia diameter after hypercapnia termination reflecting intact CVR (Fig. 4). Diabetes led to the impairment of CVR that was improved by DRP (Fig. 4, $p < 0.05$). Simultaneous NADH autofluorescence imaging did not show any significant changes in tissue oxygen supply during hypercapnia at a baseline due to arteriolar dilatation and increased RBC traffic, reflecting intact microvascular CBF regulation. In diabetic animals, NADH autofluorescence during hypercapnia increased, reflecting decreased tissue oxygen

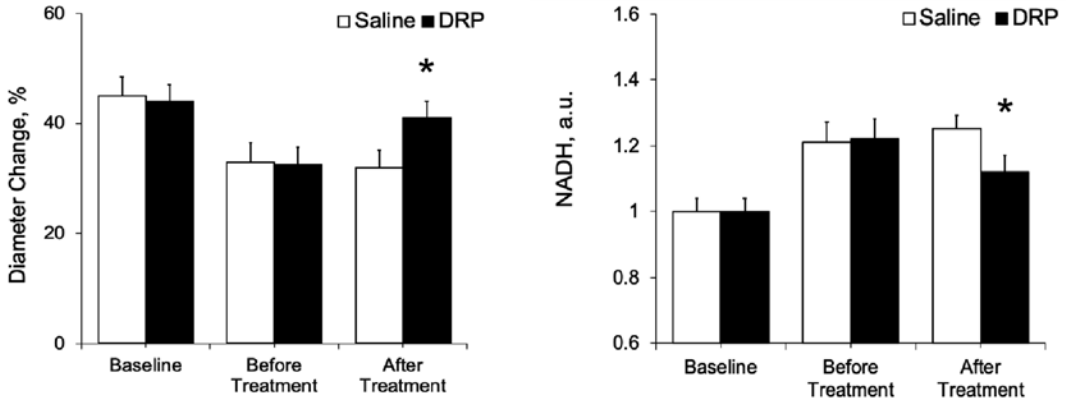

Fig. 4 DRP improves cerebrovascular reactivity as reflected by the change in the diameter of the arterioles during hypercapnia test (left); and NADH autofluorescence dynamics during the hypercapnia test. $N = 10$ mice per group, ($^*P < 0.05$)

supply due to impaired CVR (Fig. 4). DRP mitigated the reduction in tissue oxygen supply during hypercapnia by improving CVR (Fig. 4, $p < 0.05$).

4 Conclusions

Hemorheological modulation of blood flow by DRP increases the number of functioning capillaries, restores capillary perfusion and improves tissue oxygen supply in the brain and skin in a mouse model of diabetes mellitus and can be potentially used as a supportive therapy.

Acknowledgments Support Lovelace Biomedical Startup Funds, RF Governmental Grant 075-15-2022-1094 and NIH R01NS112808.

References

1. Last D, Alsop DC, Abduljalil AM et al (2007) Global and regional effects of type 2 diabetes on brain tissue volumes and cerebral vasoreactivity. Diabetes Care 30:1193–1199. PMID:17290035
2. Morley JE (2008) Diabetes and aging: epidemiologic overview. Clin Geriatr Med 24:395–405
3. Huysman E, Mathieu C (2009) Diabetes and peripheral vascular disease. Acta Chir Belg 109(5):587–594. https://doi.org/10.1080/00015458.2009.11680493. PMID: 19994800
4. Bragin DE, Kameneva MV, Bragina OA, Thomson S, Statom GL, Lara DA, Yang Y, Nemoto EM (2017) Rheological effects of drag-reducing polymers improve cerebral blood flow and oxygenation after traumatic brain injury in rats. J Cereb Blood Flow Metab 37(3):762–775. https://doi.org/10.1177/0271678X16684153. Epub 2016 Dec 22. PMID: 28155574; PMCID: PMC5363490
5. Bragin DE, Peng Z, Bragina OA, Statom GL, Kameneva MV, Nemoto EM (2016) Improvement of impaired cerebral microcirculation using rheological modulation by drag-reducing polymers. Adv Exp Med Biol 923:239–244. https://doi.org/10.1007/978-3-319-38810-6_32. PMID: 27526149; PMCID: PMC4988339
6. Monickaraj F, McGuire PG, Nitta CF, Ghosh K, Das A (2016) Cathepsin D: an Mϕ-derived factor mediating increased endothelial cell permeability with implications for alteration of the blood-retinal barrier in diabetic retinopathy. FASEB J 30(4):1670–1682. https://doi.org/10.1096/fj.15-279802. Epub 2015 Dec 30. PMID: 26718887; PMCID: PMC4799507
7. Chernysheva GA, Smolyakova VI, Plotnikov MB, Cherkashina IV (2006) Pharmacokinetics of high-molecular-weight polyethylene oxide. Khimiko-Farmatsevticheskii Zhurnal 40(9):7–8. *(in Russian)*
8. Zhang C et al (2018) A large, switchable optical clearing skull window for cerebrovascular imaging. Theranostics 8(10):2696–2708. https://doi.org/10.7150/thno.236864

9. Shi R, Guo L, Zhang C, Feng W, Li P, Ding Z, Zhu D (2017) A useful way to develop effective in vivo skin optical clearing agents. J Biophotonics 10(6–7):887–895. https://doi.org/10.1002/jbio.201600221. Epub 2016 Dec 23. PMID: 28009130.6
10. Chance B, Cohen P, Jobsis F et al (1962) Intracellular oxidation-reduction states in vivo. Science 137:499–508.8
11. Bragina OA, Semyachkina-Glushkovskaya OV, Nemoto EM, Bragin DE (2020) Anodal transcranial direct current stimulation improves impaired cerebrovascular reactivity in traumatized mouse brain. Adv Exp Med Biol 1232:47–53. https://doi.org/10.1007/978-3-030-34461-0_7. PMID: 31893393; PMCID: PMC7307636

Haemorheologic Enhancement of Cerebral Perfusion Improves Oxygen Supply and Reduces Aβ Plaques Deposition in a Mouse Model of Alzheimer's Disease

O. A. Bragina, L. O. Sillerud, M. V. Kameneva, E. M. Nemoto, and D. E. Bragin

Abstract

Alzheimer's disease (AD) is a consequence of complex interactions of age-related neurodegeneration and vascular-associated pathologies, affecting more than 44 million people worldwide. For the last decade, it has been suggested that chronic brain hypoperfusion and consequent hypoxia play a direct role in the pathogenesis of AD. However, current treatments of AD have not focused on restoring or improving microvascular perfusion. In a previous study, we showed that drag reducing polymers (DRP) enhance cerebral blood flow and tissue oxygenation. We hypothesised that haemorheologic enhancement of cerebral perfusion by DRP would be useful for treating Alzheimer's disease. We used double transgenic B6C3-Tg(APPswe, PSEN1dE9) 85Dbo/Mmjax AD mice. DRP or vehicle (saline) was i.v. injected every week starting at four months of age till 12 months of age (10 mice/group). In-vivo 2-photon laser scanning microscopy was used to evaluate amyloid plaques development, cerebral microcirculation, and tissue oxygen supply/metabolic status (NADH autofluorescence). The imaging sessions were repeated once a month till 12 months of age. Statistical analyses were done by independent Student's t-test or Kolmogorov–Smirnov tests where appropriate. Differences between groups and time were determined using a two-way repeated measures ANOVA analysis for multiple comparisons and post hoc testing using the Mann-Whitney U test. In the vehicle group, numerous plaques completely formed in the cortex by nine months of age. The development of plaques accumulation was accompanied by cerebral microcirculation disturbances, reduction in tissue oxygen supply and metabolic impairment (NADH increase). DRP mitigated microcirculation and tissue oxygen supply reduction – microvascular perfusion was 29.5 ± 5%, and tissue oxygen supply was

O. A. Bragina (✉)
Lovelace Biomedical Research Institute, Albuquerque, NM, USA
e-mail: obragina@lrri.org

L. O. Sillerud · E. M. Nemoto
Department of Neurology, University of New Mexico School of Medicine, Albuquerque, NM, USA

M. V. Kameneva
McGowan Institute for Regenerative Medicine, University of Pittsburgh, Pittsburgh, PA, USA

D. E. Bragin
Lovelace Biomedical Research Institute, Albuquerque, NM, USA

Department of Neurology, University of New Mexico School of Medicine, Albuquerque, NM, USA

National Research Saratov State University, Saratov, Russia

F. Scholkmann et al. (eds.), *Oxygen Transport to Tissue XLIII*, Advances in Experimental Medicine and Biology 1395, https://doi.org/10.1007/978-3-031-14190-4_54

22 ± 4% higher than in the vehicle group ($p < 0.05$). In the DRP group, amyloid plaques deposition was substantially less than in the vehicle group ($p < 0.05$). Thus, rheological enhancement of blood flow by DRP is associated with reduced rate of beta amyloid plaques deposition in AD mice.

Keywords

Neurodegeneration · Hypoperfusion · NADH autofluorescence · 2-photon laser scanning

1 Introduction

Alzheimer's disease (AD) dementia is a consequence of complex interactions of age-related neurodegeneration and vascular-associated pathologies that presently affect more than five million Americans and are projected to increase to 16 million by 2050 [1]. Therapeutic interventions that can prevent, delay the onset, or slow the progression of this form of dementia are urgently needed. The quantitative neuropathologic criteria for AD diagnostics, as well as the main target of treatment, are the degree of deposition of amyloid plaques and Tau protein neurofibrillary tangles [2]. However, treatments aimed to prevent or remove amyloid plaques have not succeeded in preventing/reducing dementia [3, 4]. For the last decade, it has been suggested that chronic brain hypoperfusion and consequent hypoxia could play a direct role in the pathogenesis of AD or promote its development [5–7]. Individuals with low brain perfusion showed significantly larger white matter lesion volumes [8]; atherosclerosis was significantly more extensive in the AD population and was associated with impaired cognitive function [9–11]. However, current treatments of AD have not focused on restoring or improving microvascular perfusion. We propose a new treatment approach using modulation of haemorheology by drag reducing polymers (DRP). DRP are linear, soluble macromolecules that reduce flow separations at blood vessel bifurcations leading to a reduction of pressure gradients across the arterial system and an increase in the precapillary blood pressure enhancing capillary perfusion [12]. In a previous study, we showed that DRP enhance cerebral blood flow and tissue oxygenation [13]. Here we tested the efficacy of haemorheologic enhancement of cerebral perfusion by drag-reducing polymers for the treatment of Alzheimer's disease.

2 Materials and Methods

Animal procedures were approved by the Institutional Animal Care and Use Committee of the University of New Mexico under the Animal Protocol #200640. As an AD model, we used six-week-old male double transgenic AD mice (B6C3-Tg(APPswe, PSEN1dE9) 85Dbo/Mmjax), obtained from Jackson Laboratory (Bar Harbor, ME, USA). One transgene encoded a mouse/human chimeric amyloid-β (A4) precursor protein containing the double Swedish mutations (APPswe; K595 N/M596 L). The second transgene for human PS1 contained a deletion of exon 9 (dE9), corresponding to an early-onset form of AD. In this model, numerous plaques completely form in the hippocampus and cortex by nine months of age.

The Overall Design of the Study DRP or vehicle (saline) were i.v. injected every week starting four months of age till 12 months of age (10 mice/group). In-vivo 2-photon laser scanning microscopy was used to evaluate amyloid plaques development, cerebral microcirculation, and tissue oxygen supply/metabolic state. The imaging sessions were repeated once a month till 12 months of age.

DRP Preparation Polyethylene oxide (PEO, MW ~4000 kDa) was dissolved in saline to 0.1% (1000 ppm), dialysed against saline using a 50 kD cutoff membrane, diluted in saline to 50 ppm, slow rocked for ~2 hours, and then sterilised using a 0.22 μm filter [13].

Two-Photon Laser Scanning Microscopy For long-term in-vivo imaging of mouse cortex, we used a polished and reinforced thinned-skull window, avoiding skin re-incision/stitching and preventing bone re-grow [14]. Plaques, microcirculation, and tissue oxygen supply were visualised using Olympus BX 51WI upright microscope and water-immersion XLUMPlan FI 20x/0.95 W objective as previously described [13]. Excitation was provided by a Prairie View Ultima multiphoton laser scan unit powered by a Millennia Prime 10 W diode laser source pumping a Tsunami Ti: sapphire laser, centred at 774 nm (Spectra-Physics, Mountain View, CA). Band-pass-filtered epifluorescence (560–660 nm) for fluorescent serum (tetramethylrhodamine isothiocyanate (dextran, 500 kDa in physiological saline, 5% wt/vol) and (425–475) nm for NADH was collected by photomultiplier tubes of the Prairie View Ultima system. Red blood cell flow velocity was measured in microvessels ranging from 3–50 μm diameter up to 500 μm below the surface of the parietal cortex, as described previously [13]. NADH autofluorescence measurement was used to evaluate mitochondrial activity (metabolic status) and tissue oxygenation [13]. The amyloid plaques were evaluated on a separate day from TAMRA and NADH by second harmonic generation (387 nm emission peak) and i.v. labelling with 0.001% of thioflavin S (450 nm emission peak) [15]. In offline analyses using NIH ImageJ software, three-dimensional anatomy of the vasculature in areas of interest was reconstructed from two-dimensional (planar) scans of the fluorescence intensity obtained at successive focal depths in the cortex (XYZ stack). Beta amyloid plaques were counted in an imaging volume of 0.075 mm^3. The data were combined, averaged and normalised from both thioflavin S staining and SHG to four months of age (start of the treatment).

Statistical analyses were done using GraphPad Prism software (La Jolla, CA, USA by independent Student's t-test or Kolmogorov–Smirnov tests where appropriate. Differences between groups and time were determined using a two-way repeated measures ANOVA analysis for multiple comparisons and post hoc testing using the Mann-Whitney U test. Variables are expressed as mean ± standard error. The level of significance was set at 0.05.

3 Results and Discussion

In the vehicle group, numerous plaques completely formed in the cortex by nine months of age. The development of plaques accumulation was accompanied by cerebral microcirculation disturbances, reduction in tissue oxygen supply and metabolic impairment (NADH increase), (Figs. 1, 2). DRP mitigated impairment of microcirculation and tissue oxygen supply – microvascular perfusion was 29.5 ± 5%, and tissue oxygen supply was 22 ± 4% higher than in the vehicle group by the end of the monitoring period (Fig. 1, $p < 0.05$ from the saline group). In the DRP group, amyloid plaques deposition was substantially less than in the vehicle group (Fig. 2, $p < 0.05$ from the saline group).

Our work demonstrated that rheological enhancement of cerebral blood flow and tissue oxygen supply by DRP is associated with a decrease in beta amyloid plaques deposition in the cortex of AD double transgenic B6C3-Tg(APPswe, PSEN1dE9) 85Dbo/Mmjax mice. The mechanisms of this decrease in beta amyloid plaques deposition might include improvement of cerebral microvascular circulation, improved tissue oxygen supply, blood brain barrier preservation, and related reduction in inflammation.

DRPs increase the arteriolar blood volume flow via the increase of flow velocity by reducing flow separations and vortices at vessel bifurcations and decreasing pressure loss across the arterial network due to the viscoelastic properties of DRP [12]. This leads to a rise in pre-capillary blood pressure, thus enhancing capillary perfusion, countering capillary stasis, increasing the density of functioning capillaries and the number of red blood cells passing through capillaries to improve tissue oxygenation [12].

We have also previously shown that DRP attenuates blood brain barrier (BBB) degradation in traumatic brain injury (TBI) [13]. In this

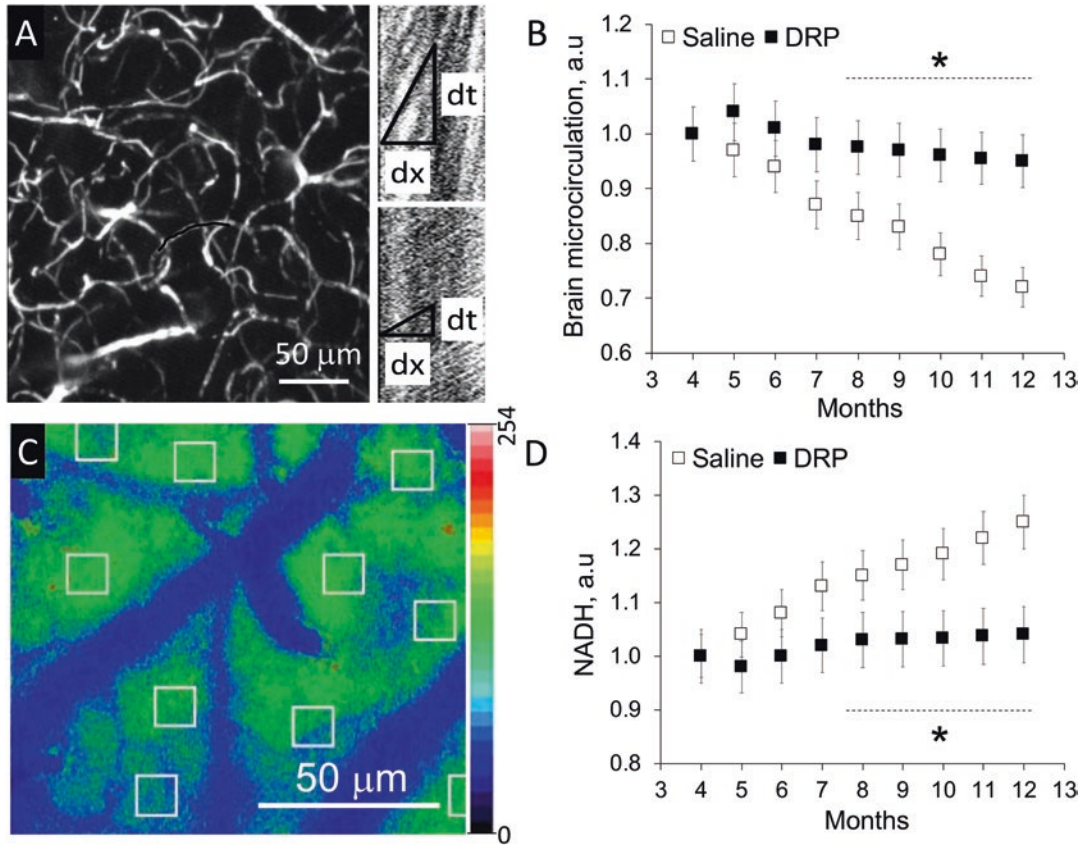

Fig. 1 Weekly treatment with drag reducing polymers (DRP) mitigate microcirculation reduction and improve tissue oxygen supply during Alzheimer's Disease (AD) development. (**a**) Representative micrograph of a region from which microvascular flow was recorded (maximum intensity projection of five planar scans acquired with 10 mm steps, starting at 50 mm from brain surface). Right: Line-scan data for blood flow velocities in the outlined capillary (black line) in the left panel indicating the baseline RBC flow velocity (top scan) and its increase after DRP injection (bottom scan). The slope of the stripes inversely reflects RBC flow velocity. (**b**) Cerebral microvascular perfusion dynamics. (**c**) Representative micrograph of NADH autofluorescence in mouse cortex. (**d**) NADH autofluorescence dynamics. (Data presented as a mean ± SEM, N = 10 per group, $*p < 0.05$)

work, we have also observed better preserved BBB. It is known that the interaction between Aβ and the BBB affects the progression of AD [16]. Beta amyloid deposition leads to the destruction of the integrity and function of the BBB. BBB dysfunction, in turn, promotes beta amyloid production and accelerates its deposit in the brain [16]. Thus, better preserved BBB and reduced inflammation also could be involved in the mitigation of beta amyloid deposition, which could be another mechanism of DRP in delaying AD.

Another recently discussed possible mechanism is the ability of DRP to reduce the near-wall cell-free layer [12], which increases wall shear stress, promoting the release of nitric oxide and vasodilation. Increased near-wall shear stress and occupation of the near-wall space by RBC, due to the presence of DRP in the blood, may explain the significant reduction in the inflammatory reaction potentially due to reduction of the near-wall rolling leukocytes, their attachment to vessel walls, and extravasation that may also add to the reduction of plaques deposition.

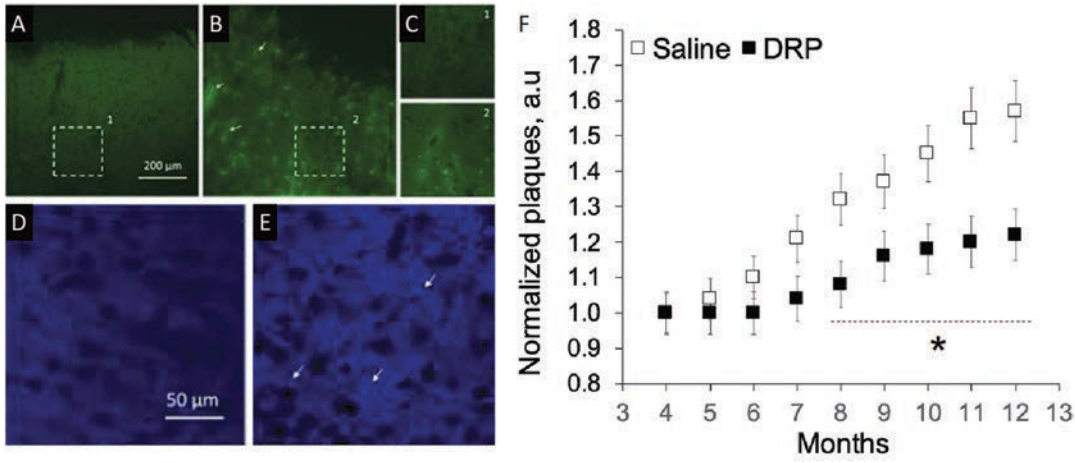

Fig. 2 Weekly treatment with drag reducing polymers (DRP) ameliorates β amyloid plaques deposition formation during Alzheimer's Disease (AD) development. (**a**) Micrograph of thioflavin S stained saline-treated mouse cortex showing no fluorescence at four months and (**b**) Bright β-amyloid plaques fluorescence (thioflavin S) at 12 months of AD development. (**c**) Magnified views of the areas outlined in (**a**) and (**b**). (**d**) Micrographs with no β-amyloid plaques visible from the second harmonic generation (SHG) signal at 4 months in DRP-treated mouse brain and (**e**) Bright β-amyloid plaques (SHG) signal at 12 months of AD development. (**f**) Graph showing attenuation of β-amyloid plaques deposition in DRP group. Data presented as mean ± SEM, N = 10 per group, $^*p < 0.05$, white arrows point to plaques depositions

4 Conclusions

Rheological enhancement of cerebral blood flow and tissue oxygen supply by DRP is associated with a decrease in beta amyloid plaques deposition in the cortex of AD double transgenic B6C3-Tg(APPswe, PSEN1dE9) 85Dbo/Mmjax mice. The mechanisms of this decrease in beta amyloid plaques deposition might include improvement of cerebral microvascular circulation, improved tissue oxygen supply, blood brain barrier preservation, and related reduction in inflammation.

Acknowledgments This work was supported by RF Governmental Grant 075-15-2022-1094, NIH 8P30GM103400 and R01NS112808.

References

1. 2021 Alzheimer's disease facts and figures. Alzheimers Dement 17(3):327–406. (2021)
2. Wood JG, Mirra SS, Pollock NJ et al (1986) Neurofibrillary tangles of Alzheimer disease share antigenic determinants with the axonal microtubule-associated protein tau. Proc Natl Acad Sci U S A 83(11):4040–4043
3. Holmes C, Boche D, Wilkinson D et al (2008) Long-term effects of Abeta42 immunisation in Alzheimer's disease: follow-up of a randomised, placebo-controlled phase I trial. Lancet 9 372(9634):216–223
4. Maarouf CL, Daugs ID, Kokjohn TA et al (2010) The biochemical aftermath of anti-amyloid immunotherapy. Mol Neurodegener 7(5):39
5. Gorelick PB et al (2011) Vascular contributions to cognitive impairment and dementia: a statement for healthcare professionals from the American Heart Association/American Stroke Association. Stroke 42(9):2672–2713
6. Hamel E (2015) Cerebral circulation: function and dysfunction in Alzheimer's disease. J Cardiovasc Pharmacol 65(4):317–324
7. Maier FC, Wehrl HF, Schmid AM et al (2014) Longitudinal PET-MRI reveals β-amyloid deposition and rCBF dynamics and connects vascular amyloidosis to quantitative loss of perfusion. Nat Med 20(12):1485–1492
8. Vernooij MW, van der Lugt A, Ikram MA et al (2008) Total cerebral blood flow and total brain perfusion in the general population: the Rotterdam scan study. J Cereb Blood Flow Metab 28(2):412–419
9. Kalback W, Esh C, Castaño EM et al (2004) Atherosclerosis, vascular amyloidosis and brain hypoperfusion in the pathogenesis of sporadic Alzheimer's disease. Neurol Res 26(5):525–539
10. Roher AE, Esh C, Rahman A et al (2004) Atherosclerosis of cerebral arteries in Alzheimer disease. Stroke 35(11 Suppl 1):2623–2627

11. Roher AE, Tyas SL, Maarouf CL et al (2011) Intracranial atherosclerosis as a contributing factor to Alzheimer's disease dementia. Alzheimers Dement 7(4):436–444
12. Kameneva MV (2012) Microrheological effects of drag-reducing polymers in vitro and in vivo. Int J Eng Sci 59:168–183
13. Bragin DE, Kameneva MV, Bragina OA et al (2016) Rheological effects of drag-reducing polymers improve cerebral blood flow and oxygenation after traumatic brain injury in rats. J Cereb Blood Flow Metab 37(3):762–775
14. Shih AY, Mateo C, Drew PJ et al (2012) A polished and reinforced thinned-skull window for long-term imaging of the mouse brain. J Vis Exp 7(61):3742
15. Kwan AC, Duff K, Gouras GK et al (2009) Optical visualization of Alzheimer's pathology via multiphoton-excited intrinsic fluorescence and second harmonic generation. Opt Express 17(5):3679–3689
16. Wang D, Chen F, Han Z et al (2021) Relationship between amyloid-β deposition and blood-brain barrier dysfunction in Alzheimer's disease. Front Cell Neurosci 19(15):695479

Calorimetric Characterisation of the Binding Reaction Between Human Ferric Haemoglobins and Haptoglobin to Develop a Drug for Removal of Cell-Free Haemoglobin

Khuanpiroon Ratanasopa and Leif Bulow

Abstract

High levels of cell-free haemoglobin (Hb) may occur in plasma as a consequence of e.g., pathological haemolysis or blood transfusion. These Hb molecules can be removed from blood circulation by forming a complex with the acute-phase protein haptoglobin (Hp) and thereby can also the intrinsic toxicity of free Hb be limited. In this study it is shown that ferric HbA, HbF, HbE and HbS, respectively, all bind firmly to Hp at 25 °C. By using isothermal titration calorimetry (ITC), it is demonstrated that ferric HbF has higher affinity to Hp (Ka = 2.79 ± 0.29 ×10^9 $M^{-1)}$ compared with HbA and HbS (1.91 ± 0.24 ×10^9 $M^{-1)}$ and 1.41 ± 0.34 ×10^9 M^{-1} for HbA and HbS, respectively. In addition, the affinity constant for HbE is slightly lower than the other haemoglobins (0.47 ± 0.40 ×10^9 M^{-1}). Since Hp shows a general and high affinity to all Hb variants tested, it can be concluded that Hp may be useful as a therapeutic agent for several different haemolytic conditions by intravenous injection.

Keywords

Pathological haemolysis · Sickle cell anemia · Isothermal titration calorimetry · Hb variants

1 Introduction

Haemoglobin (Hb) is an abundant intracellular protein. Its main function is to carry oxygen from the lungs and transfer it to respiring cells and tissues. The structure of Hb is well known, and the most common form of Hb, adult Hb or HbA, is mainly a tetramer composed of two α and two β subunits [1]. Inside the red blood cells, the iron-containing haemoglobins are protected from oxidation by a powerful enzymatic system embracing inter alia methaemoglobin reductase, catalase, and superoxide dismutase [2]. Upon haemolysis, cell-free Hb is released into plasma and the regular intracellular oxidative protection is not available. Hb is then prone to auto-oxidation and, additionally, can interact with various oxidative agents including NO and hydrogen peroxide. In the first phase, this may generate a non-functional form of Hb called ferric haemoglobin or methaemoglobin (metHb). In addition, metHb can react further with hydrogen peroxide, yielding a highly unstable intermediate species called ferryl Hb,

K. Ratanasopa · L. Bulow (✉)
Department of Chemistry, Pure and Applied Biochemistry, Lund University, Lund, Sweden
e-mail: Leif.Bulow@kilu.lu.se

F. Scholkmann et al. (eds.), *Oxygen Transport to Tissue XLIII*, Advances in Experimental Medicine and Biology 1395, https://doi.org/10.1007/978-3-031-14190-4_55

which is involved in several pathological conditions [1].

Sickle cell anaemia (SCA) or sickle cell disease (SCD) is a haematologic condition caused by a single mutation on the β chain of haemoglobin at position 6, at which glutamine is substituted by valine (E6V). This Hb molecule is referred to as HbS and SCA patients often suffer from plasma hyperviscosity, vascular occlusion and chronic haemolysis [3, 4]. Another common variant is HbE (E26K), which in contrast to SCD is linked to a milder form of haemoglobinopathy. However, when it is inherited together with β-thalassemia, the clinical status often becomes more severe [5]. Blood transfusion is frequently used in clinical management of these patients; however, such treatment may cause complicated side effects [6]. A valuable alternative could be to increase the internal level of foetal Hb, HbF, in these patients. HbF is normally present only in newborns until the age of six months, but its expression can be pharmaceutically re-induced in adults [7]. The deleterious effects of the β-chains can thereby be avoided and many studies focus on exploring intrinsic HbF expression as a simple and beneficial therapy for these conditions [8, 9].

Haptoglobin (Hp) is an abundant acute-phase glycoprotein in human circulation. By forming a complex with cell-free Hb, Hb can be clarified from blood circulation via engulfment of the Hb-Hp complex by CD163 present on macrophages and Kupffer cells in the liver [10]. The uptake of the Hp-Hb complex is followed by lysosomal degradation and haem oxygenase-1 catalyses the conversion of haem into carbon monoxide, biliverdin and iron. It has been demonstrated that Hp is able to attenuate the toxicity of HbA released from red blood cells after intravascular haemolysis [11, 12]. Due to this ability, Hp has a therapeutic potential to treat SCA, β-thalassemia, and other haemolytic disorders [13]. However, the interaction between Hp and Hb has to date only been studied for HbA. Thermodynamic characterisations of the complex formation process are needed to provide a deeper understanding of the molecular events involved in the interaction also with other Hb variants. It is thus important to evaluate the influence of the structural variations of the Hb moiety, which can be instrumental for realising the complete therapeutic potential of Hp. Such thermodynamic data provide essential insights into the clinical aspects, which determine the effectiveness of Hp as a therapeutic drug to remove cell-free Hb. In this report, we have determined the energetics of the complex formation between Hp and HbA, HbS, HbE and HbF, respectively. This study focuses on characterising the complex formation between the ferric forms of these Hbs, which is the most common oxidative state of extracellular Hb, and the most simple and well defined form of Hp, i.e., Hp 1-1 [14].

2 Methods

Samples of adult haemoglobin (HbA) and fetal haemoglobin (HbF) prepared from whole blood and umbilical cord blood, respectively, were supplied by the Biomedical Center of Lund University (Prof. B. Akerstrom, approved by the Ethics Committee Board of Malmö/Lund). Sickle cell haemoglobin (HbS) and haemoglobin E (HbE) were kindly provided by the Food and Drug Administration, USA (Dr. A.I. Alayash). The oxyhaemoglobins were converted to the ferric form just before the ITC measurements by adding a slight excess of potassium ferricyanide ($K_3[Fe(CN)_6]$). The mixture was left for 5 min at room temperature and the cyanide salts were subsequently removed by gel filtration on Sephadex G-25. The presence of ferric haemoglobins and methaemoglobins was verified by spectroscopic scanning between 350 nm to 700 nm. The concentration of ferric haemoglobins was also determined spectrophotometrically after reduction to the deoxy form using sodium dithionite and the extinction coefficient of 133 mM^{-1} cm^{-1} at 430 nm [15].

Haptoglobin 1-1 (Hp) with a purity of 98–100% was purchased from Sigma. The Hp concentration was determined spectrophotometrically using the absorption extinction coefficient $E_{280}^{1\%} = 12$ and the molar mass 85,000. All solutions were prepared and all measurements were made in 20 mM sodium phosphate buffer pH 7.2

containing no extra salt. Hb and Hp solutions were dialysed against the same buffer overnight at 4 °C before use.

The titration complex formation experiments between Hp and the different Hb samples were performed using a MicroCal VP-ITC titration microcalorimeter (GE Healthcare Life Sciences). The experiments consisted of a series of 15 injections of 10 µl 10 µM Hp solution into the 1.463 ml reaction cell containing initially 0.5 µM ferric Hb solution. The injection time was 20 s and with 300 s or 400 s between each injection. Stirring speeds of 394 or 589 rpm were used and the experiments were performed at 25 °C. Blank experiments were performed by injecting buffer into buffer and protein dilution experiments were performed in the same way. The heat effects obtained are small and in order to reduce influences of baseline instability, the peaks were integrated one by one with individual baselines. The titration data were analysed using the Microcal Origin (version 7.0) software to obtain the thermodynamic quantities.

3 Results

Isothermal titration calorimetry (ITC) is one of the most powerful methods for determining the thermodynamics of a binding reaction between two molecules. Figure 1 showing the thermal power plotted against time, illustrates a typical calorimetric titration curve generated by adding Hp 1-1 to ferric HbA. The first six peaks are exothermic and have about the same size. Peak eight has reduced size and the heat evolved from the remaining injections is small. The concentrations of Hp and HbA reach the molar ratio 1:1 during the eighth injection. The peaks are well defined and reach baseline within 1.5 min shortly after the end of injections, clearly demonstrating that the complex forming reaction is fast. Integration of the peaks gives the amount of heat evolved. This was calculated to −2.608 ± 0.044 µcal for the first six injections and −0.088 ± 0.027 µcal for the last seven. The obtained calorimetric data are independent of the injection order between Hp and HbA. Blank experiments from 15 injections of buffer into buffer generated a heat effect of −0.150 ± 0.27 µcal. Similarly, titration experiments of injections of Hp solution into buffer and buffer into Hb solutions gave the same results as the blank buffer-buffer experiments. The heat effects from these control experiments are close to the detection limit of the instrument. Thus, the heat effect for the last seven injections in the binding experiment did not differ significantly from the blank experiments showing that there are no side reactions. The difference in the heat effect before and after mole ratio 1 therefore corresponds to the heat effect from the binding process between Hp and Hb in the buffer solution used. The enthalpy change calculated per mole of added Hp is plotted against mole ratio in the lower part of Fig. 1. The shape of the curve also contains information about the binding constant *(K)* for the binding of one molecule of HbA to one molecule of Hp:

$$\mathrm{Hp} + \mathrm{HbA} \leftrightharpoons \mathrm{Hp} - \mathrm{HbA} \qquad (1)$$

The overall stoichiometry of the binding process between Hp and HbA is thus 1:1, but the actual complex formation involves the binding of two αβ dimers of HbA to each of the two Hb binding sites on Hp:

$$\mathrm{Hp} + (\alpha\beta)_2 \leftrightharpoons \mathrm{Hp} + 2\alpha\beta \leftrightharpoons \mathrm{Hp} - 2\alpha\beta \qquad (2)$$

The binding constants were calculated assuming a single set of identical binding sites and the full drawn line in the figure was calculated using values of K and ΔH. Three independent titration experiments were carried out for HbA, HbF, HbS and HbE, respectively, and average values of ΔH and K from the three series are summarised in Table 1. For all four systems, the fittings resulted in values of binding stoichiometry close to 1. Calculated values of the free energy change, ΔG, and the entropy change, ΔS, using the relation $\Delta G = -RT\ln K = \Delta H - T\Delta S$ are included in Table 1. The enthalpy change for Hp binding to HbA and HbF, are within error of measurements, the same but the binding of HbF is 46% stronger as evidenced by the larger binding constant. The binding of HbS is less exothermic (16%) and the binding constant 26% lower and this is even more

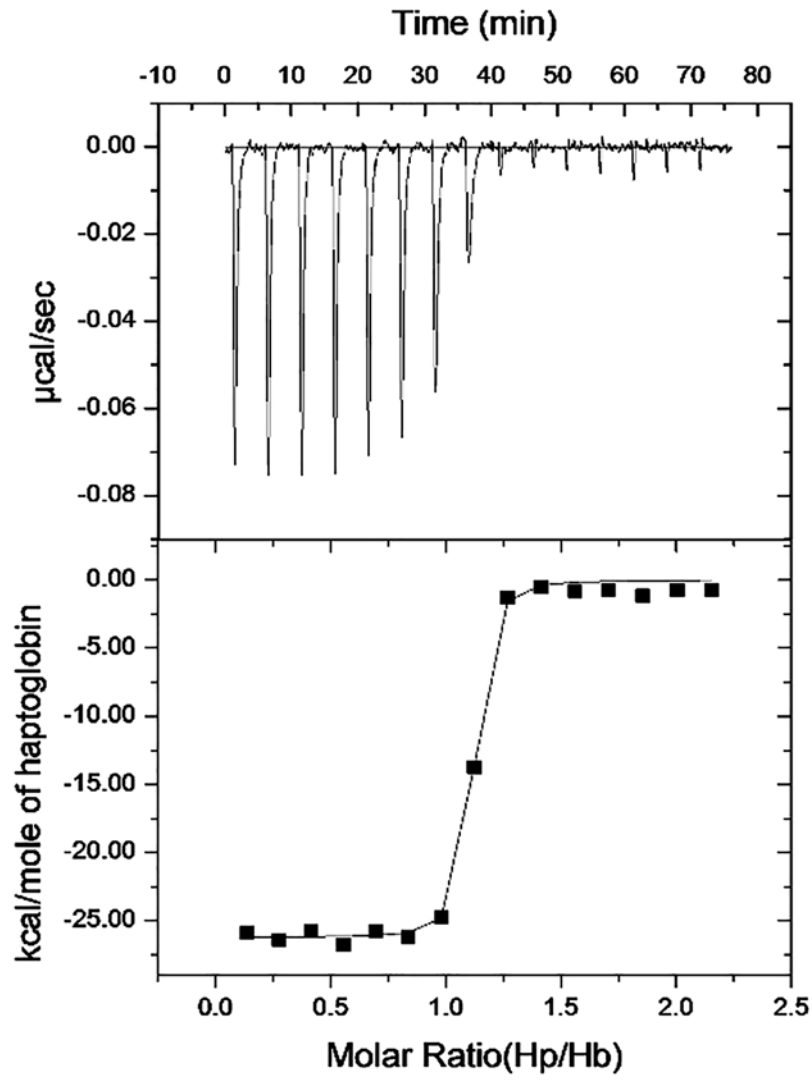

Fig. 1 Isothermal titration calorimetry measurements of the Hp-HbA binding reaction. The upper part shows the thermal power as a function of time for sequential 10 µl injections of 10 µM Hp 1–1 into 0.5 µM ferric HbA and the lower part the observed enthalpy change calculated per mole of added Hp as a function of mole ratio Hp/Hb

Table 1 Values of thermodynamic parameters for the binding of Hp 1–1 to various ferric hemoglobins at 25 °C

	ΔH	Ka	ΔG	ΔS
Ferric hemoglobin	kcal mol^{-1}	10^9 M^{-1}	kcal mol^{-1}	cal mol^{-1} K^{-1}
HbA	−24.88 ± 1.79	1.91 ± 0.24	−12.65	−41.0
HbF	−25.37 ± 0.03	2.79 ± 0.29	−12.87	−41.9
HbS	−20.90 ± 0.09	1.41 ± 0.34	−12.47	−28.3
HbE	−17.46 ± 1.87	0.47 ± 0.40	−11.8	−19.0

pronounced for HbE. The strong exothermic enthalpies generated in all cases indicate substantial changes in hydrophobic hydration upon binding.

The equilibrium constant for the dissociation reaction of Hb tetramers into dimers, can under the experimental conditions be estimated to be in the order of 10^{-5} M. This means that the 0.5 µM Hb solution used at the start of the injection series contains a mixture of Hb tetramers and dimers that will react with the added Hp. The concentration of Hb will decrease further during the titra-

tion series and the dissociation equilibrium will be shifted even further towards dimer formation. However, since we do not observe any significant variation with injection number before molar ratio 1 between Hp and Hb is reached, the potential enthalpy contributions from tetramer dissociation do not significantly contribute to the measured enthalpies under the experimental conditions used.

4 Conclusions

Cell-free Hb easily undergoes various autooxidation reactions, which may be detrimental to many tissues. Particularly if the endogenous protection system is overwhelmed, Hb molecules often accumulate in the kidneys causing tissue damage. Hp is the most well investigated Hb-clearing molecule. The binding process between Hb and Hp has been examined earlier using HbA [14], but due to the extensive numbers of haematological disorders directly related to different Hb variants, it is essential to examine possible differences in the complex formation also for these. Hb variants exhibit small differences in folding and stability, which can influence their binding reaction to Hp. However, the character of the Hb-Hp complex for all Hb variants tested are close to being irreversible. The obtained binding constants, 10^8–10^9 M^{-1}, derived from the ITC measurements are close to the technical limitation of this method. However, the binding constants obtained in this study, are very close to dissociation constants, *Kd*, generated by a previously described H/D exchange and mass spectrometry based protocol. Taken together, there is a great potential for exploring Hp as an intravenously injectable drug for Hb plasma removal in several different haematological conditions.

Acknowledgments This study was supported by grants from the Swedish Research Foundation (VR) and the Swedish Foundation for Strategic Research (SSF).

References

1. Reeder BJ, Svistunenko DA, Cooper CE et al (2004) The radical and redox chemistry of myoglobin and hemoglobin: from in vitro studies to human pathology. Antioxid Redox Signal 6:954–966
2. Olsson MG, Allhorn M, Bulow L et al (2012) Pathological conditions involving extracellular hemoglobin: molecular mechanisms, clinical significance, and novel therapeutic opportunities for α(1)-microglobulin. Antioxid Redox Signal 17:813–846
3. Kato GJ, Hebbel RP, Steinberg MH et al (2009) Vasculopathy in sickle cell disease: biology, pathophysiology, genetics, translational medicine, and new research directions. Am J Hematol 84:618–625
4. Rees DC, Williams TN, Gladwin MT (2010) Sickle-cell disease. Lancet 376:2018–2031
5. Kassim AA, DeBaun MR (2013) Sickle cell disease, vasculopathy, and therapeutics. Annu Rev Med 64:451–466
6. El-Husseini A, Sabry A (2010) Fatal hyperhemolytic delayed transfusion reaction in sickle cell disease: a case report and literature review. Am J Emerg Med 28:1062.e5–1062.e8
7. Akinsheye I, Alsultan A, Solovieff N et al (2011) Fetal hemoglobin in sickle cell anemia. Blood 118:19–27
8. McGann PT, Nero AC, Ware RE (2013) Current management of sickle cell anemia. Cold Spring Harb Perspect Med 3:a011817
9. Musallam KM, Taher AT, Cappellini MD et al (2013) Clinical experience with fetal hemoglobin induction therapy in patients with β-thalassemia. Blood 121:2199–2212
10. Kristiansen M, Graversen JH, Jacobsen C et al (2001) Identification of the haemoglobin scavenger receptor. Nature 409:198–201
11. Baek JH, D'Agnillo F, Vallelian F et al (2012) Hemoglobin-driven pathophysiology is an in vivo consequence of the red blood cell storage lesion that can be attenuated in Guinea pigs by haptoglobin therapy. J Clin Invest 122:1444–1458
12. Cooper CE, Schaer DJ, Buehler PW et al (2012) Haptoglobin binding stabilizes hemoglobin Ferryl iron and the globin radical on tyrosine β145. Antioxid Redox Signal 18:2264–2273
13. Alayash AI, Andersen CBF, Moestrup SK et al (2013) Haptoglobin: the hemoglobin detoxifier in plasma. Trends Biotechnol 31:2–3
14. Ratanasopa K, Chakane S, Ilyas M et al (2013) Trapping of human hemoglobin by Haptoglobin: molecular mechanisms and clinical applications. Antioxid Redox Signal 18:2364–2374
15. Reeder BJ, Grey M, Silaghi-Dumitrescu RL et al (2008) Tyrosine residues as redox cofactors in human hemoglobin: Implications for engineering nontoxic blood substitutes. J Biol Chem 283:30780–30787

Feasibility to Measure Tissue Oxygen Saturation Using Textile-Integrated Polymer Optical Fibers

Tarcisi Cantieni, O. da Silva-Kress, M. González, M. Michler, T. Rastija, R. Grabher, G. Piai, N. Ansari, K. Sharma, E. Morlec, M. Camenzind, L. Boesel, and U. Wolf

Abstract

Tissue oxygen saturation (StO_2) is a crucial factor in the aetiology of pressure injury (PI), since hypoxia leads to necrotization. Pressure on the tissue occludes blood circulation and reduces the StO_2, resulting in hypoxia. PI causes severe suffering, heals slowly and is expensive to treat. Hence it is important to prevent PI by detecting hypoxia, e.g., by near-infrared spectroscopy (NIRS) monitoring of StO_2. For this, the NIRS device has to be wearable for a long time and it is crucial that it provokes no pressure itself. An integration of optical fibres into a textile achieves this. The aim was to investigate the feasibility of such a textile NIRS device.

Knots and loops were tested as textile light emitters (LEs) or detectors (LDs) on a phantom. The light coupling efficiency of the LEs and LDs was investigated.

Results show that knots perform similarly to loops. More loops per fibre increase efficiency both in LEs and in LDs. The best trade-off is at 3 loops. LEs are slightly more efficient than LDs, with an average attenuation from baseline of about −2 dB for loops of 0.5 mm diameter. Adding fibres multiplies the signal by the number of fibres. Inclusions mimicking hypoxia in phantoms were successfully identified. In-vivo arm occlusion tests showed the expected decrease in StO_2. This shows feasibility of optical fibres in a textile to prevent PI.

Keywords

Pressure injury · Hypoxia · NIRS · StO_2

T. Cantieni (✉) · O. da Silva-Kress · U. Wolf
Institute of Complementary and Integrative Medicine, University of Bern, Bern, Switzerland
e-mail: tarcisi.cantieni@unibe.ch

M. González · M. Michler
OST Eastern Switzerland University of Applied Sciences, Institute for Microtechnology and Photonics, Buchs, Switzerland

T. Rastija · R. Grabher · G. Piai
OST Eastern Switzerland University of Applied Sciences, Institute for Electronics, Sensors and Actuators, Buchs, Switzerland

N. Ansari · K. Sharma · E. Morlec · M. Camenzind · L. Boesel
Empa, Swiss Federal Laboratories for Materials Science and Technology, Laboratory for Biomimetic Membranes and Textiles, Dübendorf, Switzerland

F. Scholkmann et al. (eds.), *Oxygen Transport to Tissue XLIII*, Advances in Experimental Medicine and Biology 1395, https://doi.org/10.1007/978-3-031-14190-4_56

1 Introduction

Tissue oxygen saturation (StO_2) is a crucial factor in pressure injury (PI) development [1], since hypoxia may lead to tissue necrotization. Such hypoxia is often caused by pressure on the tissue, which occludes blood circulation and reduces the StO_2. PI cause severe suffering, heal slowly, and are expensive to treat [2]. Hence it is important to prevent them by a device that detects a dangerous situation [3], e.g. by measuring StO_2 using near-infrared spectroscopy (NIRS). For this device to be wearable for a long time, it is crucial that it contains no pressure points itself. Integrating optical fibres into a textile to guide light to and from the tissue achieves this. The aim was to investigate the feasibility of such a textile NIRS device in phantoms and in vivo.

2 Materials and Methods

To investigate the **efficiency to couple light**, light from an LED (700 nm; M700F3 Thorlabs) was guided to our light emitters (LEs) based on polymer optical fibres (POF) to a silicone phantom with optical properties similar to tissue. At a specific source-detector distance (SDD) the detector, a commercial fibre bundle (Thorlabs BFY600LS02) connected to an avalanche photodiode (C12703-01, Hamamatsu, Japan) was perpendicularly placed. In a second step, we also tested the POFs as detectors and the commercial fibre as source. As reference, we applied two commercial fibres, one as an LE, and one as a light detector (LD). In a second experiment the remaining light in a POF as LE was measured, as a measure of outcoupling efficiency.

We investigated loops and knots as LE or LD. The loops were produced by looping a POF (diameter 175 µm, DB-175, Asahi Kasei, Japan) 1–5 times around rods of 0.5 or 1 mm diameter. Simple knots of the same POF were formed tightly together.

Multiple fibres can be bundled: how much does this increase the light intensity? Between 1 and 6 fibres with 3 loops each were stitched into a thin soft patch of tissue and arranged in two concentric circles (radii 1.5 and 3.5 cm). The commercial fibre was placed in the centre as source. The light intensity was measured again on the phantom.

To investigate the **feasibility to detect hypoxic volumes**, we built two two-layered phantoms with optical properties of adipose tissue and muscle [4]. These two phantoms were identical except that one had inclusions that simulated hypoxic volumes at different depths within the muscle. To investigate the detectability of these hypoxic volumes, the patch was applied on both at the same location. The difference in optical density was determined. Two phantom configurations were measured: P1 with an adipose tissue thickness (ATT) of 0.3 cm and a hypoxic volume of 1.2 cm^3 at a depth of 1 cm and P2 with an ATT of 0.7 cm and a hypoxic volume of 2 cm^3 at a depth of 1.5 cm.

Due to the arrangement of stitching points on two concentric rings of the hand-made patch of the previous subsection, the following source-detector distances could be used when utilising the stitching points as either source or detector: 1.5 cm, 2.0 cm, 3.0 cm, 3.5 cm and 4.0 cm. Light source and detecting unit were identical as in the previous subsection.

In order to study detectability, the above-described configurations were simulated using finite element method (Comsol Multiphysics v5.5, Sweden) and compared to the measurements.

To investigate the feasibility of measuring **StO_2 in-vivo**, we taped two POFs with 3 loops of 0.5 mm diameter to a subject's forearm at 0.5 cm, 1.0 cm and 1.5 cm SDD. An arterial occlusion was produced by a pneumatic cuff inflated to 300 mmHg for 200 s.

3 Results and Discussion

Concerning the **efficiency to couple light**: loops performed almost as well as the reference measurement (Fig. 1a). 0.25 mm bending radius was more efficient than 0.5 mm. Taping of the fibre to the phantom may result in slight variation in the

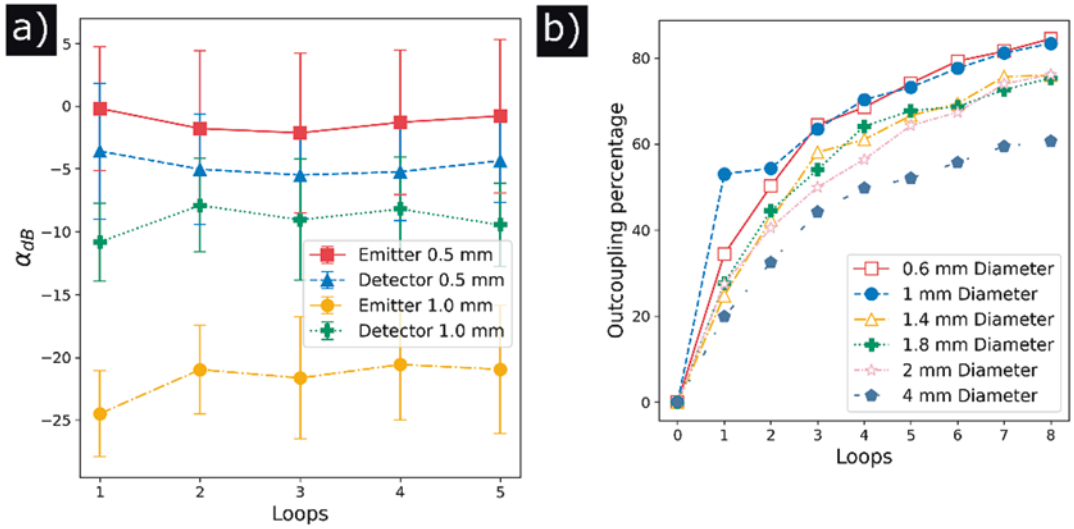

Fig. 1 (**a**) Different numbers of loops and diameters show different attenuation compared to baseline measurements. (**b**) Outcoupling percentage as a function of the number of loops and loop diameter

positioning. Loops and knots have similar efficiency, but loops are easier to produce.

The **outcoupling percentage** is depicted in Fig. 1b as a function of loop numbers and diameters: the outcoupling becomes more efficient the tighter the diameters and the higher the number of loops. Due to the space needed for a higher number of loops while remaining within the borders of a point source, we consider 3 loops as optimal trade-off.

Figure 2a shows the linear increase in intensity as a function of the **number of fibres** for both circles. Although more fibers again need more space, this is a valid option to increase the intensity.

We found a reasonable **contrast caused by a hypoxic inclusion**, very close to our expectations, based on the simulations.

Figure 2b shows the expected decrease [5] in **StO_2 during an arterial occlusion in vivo**. This shows that it is possible to measure StO_2 by a single three-loop-fibre as LE and as LD. We achieved a similar result for an SDD of 0.5 cm. At 1.5 cm, however, the signal-to-noise ratio was too low to calculate StO_2. The sensitivity can easily be increased by adding more fibres to achieve longer SDDs.

4 Conclusion

In conclusion, knots perform similarly to loops. More loops per fibre increase efficiency in both LEs and LDs. The best trade-off is at 3 loops. LEs are slightly more efficient than LDs, with an average attenuation from baseline of about −2 dB for loops of 0.25 mm bending radius. Adding more fibres multiplies the signal by the number of fibres. Inclusions mimicking hypoxia in phantoms were successfully detected with signals as expected by simulations. In-vivo arm occlusion tests showed the expected decrease in StO_2 even using only one fibre for LE and LD at 1 cm distance. We conclude that it is feasible to implement optical fibres in a textile to detect hypoxia and thus to prevent PI.

Acknowledgments We gratefully acknowledge funding of the project by the SNSF and Innosuisse Bridge Discovery (project no. 180983).

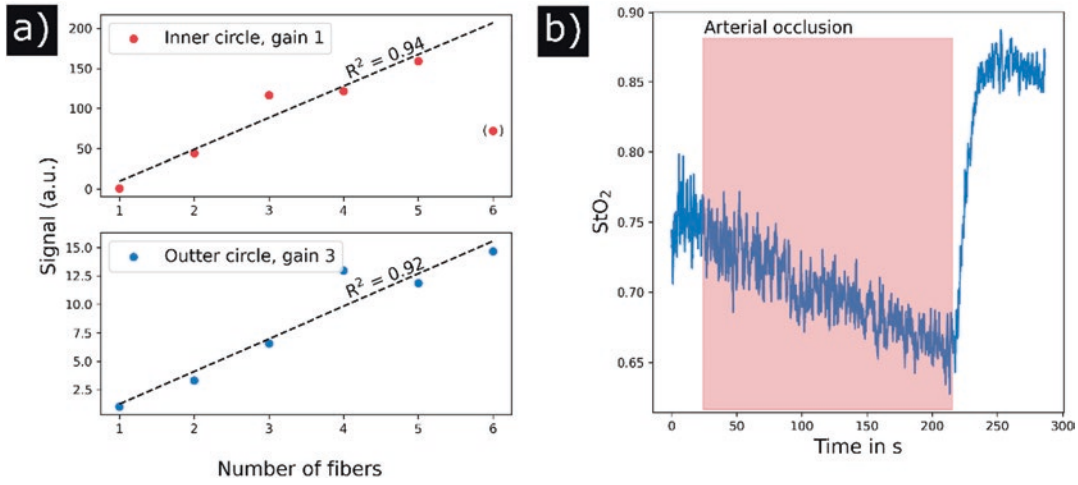

Fig. 2 (**a**) Linearly increasing signal strength for increasing amount of fibres on concentric circles. (**b**) Calculated tissue oxygenation during arterial occlusion based on measurements of a single fibre to a single fibre

References

1. Berg G, Nyberg S, Harrison et al (2010) Near-infrared spectroscopy measurement of sacral tissue oxygen saturation in healthy volunteers immobilized on rigid spine boards. Prehosp Emerg Care 14:419–424
2. Mortenson WB, Miller WC (2008) A review of scales for assessing the risk of developing a pressure ulcer in individuals with SCI. Spinal Cord 46:168–175
3. Damert H-G, Meyer F, Altmann S (2015) Therapieoptionen bei Dekubitalulzera. Zentralblatt für Chirurgie - Zeitschrift für Allgemeine, Viszeral-, Thorax- und Gefäßchirurgie 140:193–200
4. Doornbos RMP, Lang R, Aalders MC et al (1999) The determination of in vivo human tissue optical properties and absolute chromophore concentrations using spatially resolved steady-state diffuse reflectance spectroscopy. Phys Med Biol 44:967–981
5. Rosenberry R, Munson M, Chung S et al (2018) Age-related microvascular dysfunction: novel insight from near-infrared spectroscopy. Exp Physiol 103:190–200

Effect of Atorvastatin on Microcirculation Evaluated by Vascular Occlusion Test with Peripheral Near-Infrared Spectroscopy

Keiichiro Kuronuma, Tsukasa Yagi, Shonosuke Sugai, Satoshi Hayashida, Kazuki Iso, Korehito Iida, Wataru Atsumi, Eizo Tachibana, Satoshi Kunimoto, Yasuyuki Suzuki, Shigemasa Tani, Naoya Matsumoto, Yasuo Okumura, and Kaoru Sakatani

Abstract

The vascular occlusion test (VOT) with peripheral near-infrared spectroscopy (NIRS) is a non-invasive method to evaluate peripheral microcirculation. Statin therapy is widely used for patients with dyslipidaemia and contributes to reducing low-density lipoprotein cholesterol (LDL-C) levels and adverse cardiovascular events. However, it is not yet clear whether statin treatment improves peripheral microcirculation assessed by VOT with NIRS. In the present study, using VOT with NIRS, we evaluated the effect of statin therapy on peripheral microcirculation in patients with dyslipidaemia before and after statin therapy. Methods: A total of six consecutive patients with dyslipidaemia who had not received statin therapy (6 males, mean age 71.8 ± 7.4 years) were enrolled. All patients were administered atorvastatin and their peripheral microcirculation assessed using VOT with NIRS (NIRO-200NX, Hamamatsu Photonics K.K., Japan) before and after statin therapy. The NIRS probe was attached to the right thenar eminence and brachial artery blood flow was blocked for 3 min at 50 mmHg above the resting systolic blood pressure. Maximum and minimum values of NIRS parameters after the VOT were used to determine concentration changes for total haemoglobin (ΔcHb), oxyhaemoglobin (ΔO_2Hb), deoxyhaemoglobin (ΔHHb), and tissue oxygenation index (ΔTOI). Results: During the

K. Kuronuma (✉)
Department of Cardiology, Kawaguchi Municipal Medical Center, Kawaguchi, Japan

Department of Medicine, Division of Cardiology, Nihon University School of Medicine, Tokyo, Japan

T. Yagi · Y. Suzuki · S. Tani · N. Matsumoto · Y. Okumura
Department of Medicine, Division of Cardiology, Nihon University School of Medicine, Tokyo, Japan

S. Sugai · S. Hayashida · K. Iso · K. Iida · W. Atsumi · E. Tachibana · S. Kunimoto
Department of Cardiology, Kawaguchi Municipal Medical Center, Kawaguchi, Japan

K. Sakatani
Department of Human and Engineered Environmental Studies, Universal Sport Health Science Laboratory, Graduate School of Frontier Sciences, The University of Tokyo, Tokyo, Japan

F. Scholkmann et al. (eds.), *Oxygen Transport to Tissue XLIII*, Advances in Experimental Medicine and Biology 1395, https://doi.org/10.1007/978-3-031-14190-4_57

follow-up period (mean 30.3 ± 6.5 days), LDL-C level decreased from 129.7 ± 26.3 to 67.5 ± 20.2 mg/dL (p-value = 0.031), ΔTOI increased from 24.0 ± 5.3 to 33.7 ± 6.3% (p-value = 0.023), and ΔO_2Hb increased from 16.4 ± 5.3 to 20.0 ± 6.6 μmol/L (p-value = 0.007). ΔcHb and ΔHHb did not change significantly. Conclusion: ΔO_2Hb and ΔTOI were significantly increased during the follow-up period. These findings suggest that ΔO_2Hb and ΔTOI could assess the improvement of peripheral microcirculation by statin therapy. Compared to ΔTOI, ΔO_2Hb seems to be a more useful parameter to evaluate peripheral microcirculation.

Keywords

NIRS · Statin therapy · Peripheral microcirculation · Dyslipidemia · Ischemic heart disease

1 Introduction

The vascular occlusion test (VOT) with near-infrared spectroscopy (NIRS) is a non-invasive method to evaluate peripheral microcirculation [1]. Statin therapy is widely used for patients with dyslipidaemia or a history of ischemic heart disease and contributes to reducing low-density lipoprotein cholesterol (LDL-C) levels and adverse cardiovascular events [2]. We previously reported a significant inverse correlation between the body mass index and the changes of peripheral NIRS parameter during a VOT; the correlation was stronger in patients without statin therapy and weaker in patients with statin therapy [3]. Since statin therapy could improve the peripheral endothelial function assessed by flow-mediated dilation (FMD) [4], forearm plethysmography [5], and reactive hyperaemia peripheral arterial tonometry (RH-PAT) [6], we discussed that statin therapy improves peripheral microcirculation and attenuates the correlation between BMI and peripheral microcirculation in our previous study [3]. However, the improvement of peripheral microcirculation by statin treatment has not been shown using VOT with NIRS. In order to address this issue, we evaluated the effect of statin therapy on peripheral microcirculation in the patient with dyslipidaemia before and after statin therapy using VOT with NIRS.

2 Methods

2.1 Subjects

Patients with dyslipidaemia or a history of ischemic heart disease which is recommended intensive statin therapy by the guideline [1] who had never received statin therapy were enrolled between December 2019 to January 2020. The Ethical Committee of Kawaguchi Municipal Medical Center approved this study and protocol.

2.2 Material and Methods

We used NIRO-200NX (Hamamatsu Photonics K.K., Japan) as the NIRS system. The details of VOT were previously described [3]. Briefly, the patient was lying in the supine position during NIRS measurements. The NIRS probe was attached to the right thenar eminence. Then, a pneumatic pressure cuff was placed on the right upper arm, and brachial artery blood flow was blocked for 3 min at 50 mmHg above the resting systolic blood pressure by the cuff. The cuff was deflated rapidly after 3 min of vascular occlusion, to observe reperfusion. Maximum and minimum values after the vascular occlusion were used to determine concentration changes for total haemoglobin (ΔcHb), oxyhaemoglobin (ΔO_2Hb), deoxyhaemoglobin (ΔHHb), and tissue oxygenation index (ΔTOI). All patients were administered 10 or 20 mg of atorvastatin and peripheral microcirculation was assessed using VOT with NIRS before and after statin therapy. The dosage of atorvastatin was at the physician's discretion. The baseline VOT with

NIRS measurements were performed the day before the first statin administration, and follow-up measurements were taken at intervals of approximately 4 weeks.

2.3 Statistical Analysis

Numeric variables are expressed as mean ± standard deviation (SD). Normality was tested using the Shapiro-Wilk test. Differences in continuous variables were analysed with the unpaired, paired Student's t-test, or Wilcoxon's signed-rank test, appropriately. A two-sided p-value of <0.05 was considered statistically significant. All statistical analyses were performed with R version 3.5.3 (R Foundation for Statistical Computing, Vienna, Austria).

3 Results

A total of 6 consecutive patients (6 males, mean age 71.8 ± 7.4 years) were enrolled. All patients, except for one, were administrated 20 mg of atorvastatin. All patients' clinical and examination characteristics are shown in Table 1. The mean follow-up period was 30.3 ± 6.5 days. Paired sample tests showed significant decrease in mean LDL-C level (129.7 ± 26.3 vs. 67.5 ± 20.2 mg/dL, p = 0.031), significant increase in mean ΔO_2Hb and ΔTOI (mean ΔO_2Hb, 16.4 ± 5.3 vs. 20.0 ± 6.6 μmol/L, p-value =0.007; mean ΔTOI, 24.0 ± 5.3 vs. 33.7 ± 6.3 μmol/L, p-value =0.023) (Fig. 1a, b), and no significant difference in ΔcHb and ΔHHb (mean ΔcHb, 9.2 ± 2.3 vs. 7.9 ± 3.2 μmol/L, p = 0.174; mean ΔHHb, 21.1 ± 6.5 vs. 24.4 ± 7.6 μmol/L, p = 0.092). The patients with diabetes mellitus (DM) showed significantly lower ΔO_2Hb compared to those without DM at baseline and after statin treatment (mean ΔO_2Hb, 10.2 ± 3.2 vs. 19.5 ± 2.5 μmol/L, p = 0.016 at baseline; mean ΔO_2Hb = 11.7 ± 1.3 vs. 24.1 ± 2.1 μmol/L, p = 0.002 at follow-up) but ΔTOI was comparable between the patients with and without DM (mean ΔTOI, 24.3 ± 5.5 vs. 23.9 ± 6.1 μmol/L, p = 0.942 at baseline; mean ΔTOI, 34.6 ± 6.3 vs. 33.3 ± 6.1 μmol/L, p = 0.850 at follow-up).

4 Discussion

The major finding of the present study was that ΔTOI and ΔO_2Hb, but not ΔcHb and ΔHHb, increased significantly before and after statin therapy. The findings suggest that ΔTOI and ΔO_2Hb derived by VOT could assess the improvement of peripheral microcirculation by statin therapy.

There are several methods using VOT to evaluate peripheral endothelial function such as brachial artery FMD, forearm plethysmography, and RH-PAT [7, 8]. Those modalities are utilised in clinical settings and previous studies showed that patients with impaired endothelial function are associated with a high risk of adverse cardiovascular events [7, 8]. The VOT with NIRS technique is a similar idea to those modalities assessing a reaction from internal nitrogen oxide provoked by VOT, but the objects to be measured are different in those modalities. Briefly, brachial artery FMD evaluates the difference of brachial arterial diameter measured by ultrasound before and after VOT. Forearm plethysmography measures forearm volume and blood flow, and RH-PAT measures the volume of the index finger using plethysmographic technique before and after VOT [7, 8]. While VOT with peripheral NIRS measures peripheral tissue oxygen saturation before and after VOT. VOT with peripheral NIRS demonstrated a coherent directional change with simultaneously performed forearm plethysmography with excellent reproducibility [9]. Takayama et al. showed an improvement of endothelial function by statin therapy with RH-PAT in a total of 50 patients with an interval of 24 weeks (RH-PAT indexes improved from 1.6 ± 0.3 to 1.8 ± 0.6%, p = 0.04) [6]. In the present study, we could show the significant improvement of endothelial circulation by statin therapy with peripheral NIRS in a total of six patients

Table 1 Clinical and examination characteristics of patients

Patient no.	Age (y) /sex	BMI (kg/m^2)	HTN	DLP	DM	IHD	HbA1c baseline (%)	LDL baseline/ follow-up (mg/dL)	⊿TOI baseline/ follow-up (%)	⊿O2Hb baseline/ follow-up (μmol/L)	⊿cHb baseline/ follow-up (μmol/L)	⊿HHb baseline/ follow-up (μmol/L)
1	75/M	21.4	+	+	–	–	N/A	119/57	33.0/39.7	18.6/24.1	9.6/9.0	18.9/26.0
2	76/M	25.4	+	+	+	+	6.8	121/62	20.4/41.1	7.9/10.8	10.2/5.6	18.9/22.2
3	60/M	20.9	–	+	–	+	5.6	170/107	21.9/36.6	21.9/25.0	8.6/7.2	26.5/35.0
4	67/M	26.0	+	+	+	+	7.1	110/62	28.2/28.0	12.5/12.7	5.5/3.4	14.7/14.6
5	81/M	18.9	–	–	–	+	6.1	104/50	20.4/31.0	16.4/21.2	9.0/10.2	16.2/18.3
6	72/M	29.7	+	+	–	–	5.9	154/67	20.3/26.0	20.9/26.0	12.4/12.3	31.6/30.5

BMI body mass index, *cHb* total haemoglobin, *DLP* Dyslipidemia, *DM* diabetes mellites, *HHb* deoxyhaemoglobin, *HTN* hypertension, *IHD* ischemic heart disease, *LDL* low-density lipoprotein, *M* male, *N/A* not available, *TOI* tissue oxygen index

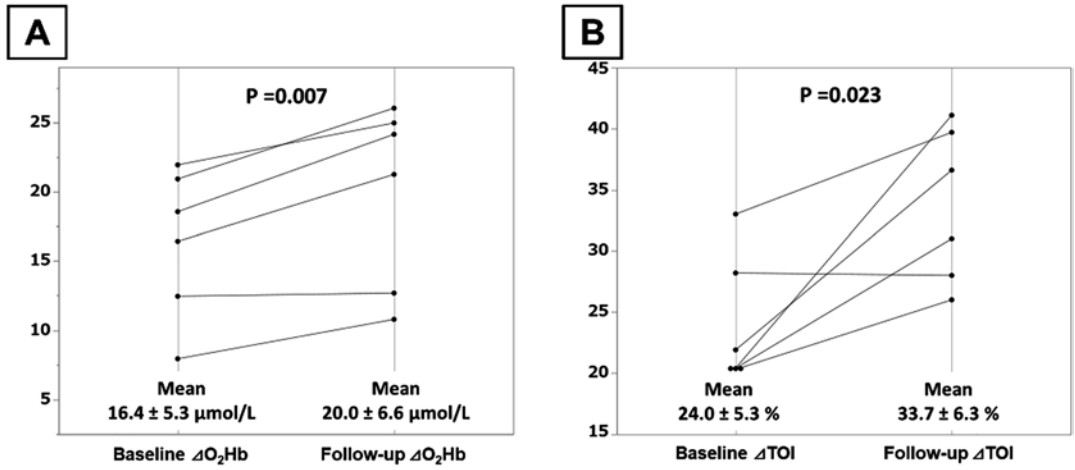

Fig. 1 Changes in oxyhaemoglobin and tissue oxygen index. *O_2Hb* oxyhaemoglobin, *TOI* tissue oxygen index

with an interval of 4 weeks (ΔO_2Hb improved from 16.4 ± 5.3 to 20.0 ± 6.6 µmol/L, $p < 0.01$). The results of the present study, which demonstrated the improvement of endothelial function by statin therapy with a small number of patients, might show superiority of peripheral NIRS for representing an improvement of microvascular endothelial function by statin therapy compared to RH-PAT.

In the present study, two patients had DM, a major risk factor of endothelial dysfunction. Those patients showed the lowest and second-lowest ΔO_2Hb and one of them showed no interval change of ΔO_2Hb between before and after statin therapy. The result is consistent with previous studies showed that patients with high HbA1c, an indication of poorly controlled DM, at baseline did not show an improvement in endothelial function assessed by RH-PAT [6], and statin therapy showed no significant improvement of endothelial function assessed by FMD in patients with DM [10]. Moreover, the value of ΔO_2Hb in a patient with DM was lower than that without DM at the baseline and follow-up period, however, ΔTOI was comparable between the patient with and without DM. Our previous study showed that only ΔO_2Hb was associated with BMI but not other NIRS parameters including ΔTOI [2]. Therefore, ΔO_2Hb seems to be more useful parameter to evaluate peripheral microcirculation compared to ΔTOI.

In conclusion, ΔO_2Hb and ΔTOI derived by VOT could assess the improvement of peripheral microcirculation by statin therapy. Compared to ΔTOI, ΔO_2Hb might be more promising parameter to evaluate peripheral microcirculation. To confirm these findings, additional prospective studies with larger populations would be warranted.

References

1. Butler E, Chin M, Aneman A (2017) Peripheral near-infrared spectroscopy: methodologic aspects and a systematic review in post-cardiac surgical patients. J Cardiothorac Vasc Anesth 31:1407–1416
2. Grundy SM, Stone NJ, Bailey AL et al (2019) 2018 Guideline on the management of blood cholesterol: a report of the American College of Cardiology/American Heart Association Task Force on Clinical Practice Guidelines. Circulation 139:e1082–e1143
3. Kawamorita T, Kuronuma K, Yagi T et al (2020) Application of peripheral near infrared spectroscopy to assess risk factors in patient with coronary artery disease: part 1. Adv Exp Med Biol 1232:331–337
4. Kayikcioglu M, Payzin S, Yavuzgil O et al (2003) Benefits of statin treatment in cardiac syndrome-X. Eur Heart J 24:1999–2005
5. Fichtlscherer S, Schmidt-Lucke C, Bojunga S et al (2006) Differential effects of short-term lipid lowering with ezetimibe and statins on endothelial function in patients with CAD: clinical evidence for 'pleiotropic' functions of statin therapy. Eur Heart J 27:1182–1190

6. Takayama T, Hiro T, Yoda S et al (2018) Effect of aggressive lipid-lowering treatment with Rosuvastatin on vascular endoTHelium function: evaluation of vascular endothelium function (EARTH study). Heart Vessel 33:590–594
7. Flammer AJ, Anderson T, Celermajer DS et al (2012) The assessment of endothelial function: from research into clinical practice. Circulation 126:753–767
8. Daiber A, Steven S, Weber A et al (2017) Targeting vascular (endothelial) dysfunction. Br J Pharmacol 174:1591–1619
9. Harel F, Denault A, Ngo Q et al (2008) Near-infrared spectroscopy to monitor peripheral blood flow perfusion. J Clin Monit Comput 22:37–43
10. Beishuizen ED, Tamsma JT, Jukema JW et al (2005) The effect of statin therapy on endothelial function in type 2 diabetes without manifest cardiovascular disease. Diabetes Care 28:1668–1674

Flow Characteristics of the Conjugate of Anti-CD3 Monoclonal Antibodies and Magnetic Nanoparticle in PBS and Blood Vessels

Sang-Suk Lee, Eun-Jae Kim, Mikyung Kang, Hasung Kang, Sang-Heon Choi, Dain Jeon, Jong-Gu Choi, Yukyoung Choi, Hyunsook Lee, and Mahbub Hasan

Abstract

Previously, anti-CD3 antibodies delivered intravenously have been known for their negative side effects. The experimental conditions for optimal liquid production are derived from the Fc-directed conjugation of anti-CD3 foralumab antibodies and magnetic nanoparticles (Ab-MNPs). The anti-CD3 antibodies are prepared for conjugation with MNPs using SiteClick antibody labelling kits. The successful conjugation of the Ab-MNPs is confirmed using a transmission electron microscopy (TEM) image and an energy dispersive spectroscopy (EDS) analysis. The average values of the moving speed of MNPs and Ab-MNPs in phosphate buffer saline (PBS) were + 3.16 pix/frame and + 6.70 pix/frame in the x-axis, respectively. This implies that MNPs with CD3 antibodies attached to the surface through biocompatible ligand functional groups has better fluidity in PBS. Afterwards, a non-clinical animal testing for the flow characteristics of Ab-MNPs inside a blood vessel is carried out to observe the effects of Ab-MNP delivery through intravenous injection.

Authors Sang-Suk Lee and Eun-Jae Kim have equally contributed to this chapter.

S.-S. Lee (✉) · S.-H. Choi · D. Jeon · J.-G. Choi · Y. Choi · H. Lee
Department of Oriental Biomedical Engineering, College of Health Sciences, Sangji University, Wonju, Republic of Korea
e-mail: sslee@sangji.ac.kr

E.-J. Kim
Department of Medical Laboratory Science, Jeonju Kijeon College, Jeonju, Republic of Korea
e-mail: ejkim@kijeon.ac.kr

M. Kang
Interdisciplinary Program for Bioengineering, Seoul National University, Seoul, Republic of Korea

H. Kang
Department of Medicine, College of Medicine, Seoul National University, Seoul, Republic of Korea

M. Hasan
Department of Oriental Biomedical Engineering, College of Health Sciences, Sangji University, Wonju, Republic of Korea

Department of Biochemistry and Molecular Biology, Bangabandhu Sheikh Mujibur Rahman Science and Tech. University, Gopalganj, Bangladesh

F. Scholkmann et al. (eds.), *Oxygen Transport to Tissue XLIII*, Advances in Experimental Medicine and Biology 1395, https://doi.org/10.1007/978-3-031-14190-4_58

Keywords

Anti-CD3 antibody (Ab) · Foralumab · Magnetic nanoparticles (MNPs) · Conjugates · Phosphate buffer saline (PBS) · Blood vessel · Biocompatibility

1 Introduction

In the current widespread pandemic situation, severe acute respiratory syndrome coronavirus 2 (SARS-CoV-2) is the virus that causes Coronavirus disease 2019 (COVID-19). It is necessary to develop an immunotherapeutic agent that suppresses the cytokine storm syndrome caused by this virus in the body by using an anti-cluster of differentiation 3 (CD3) monoclonal antibody (mAb) [1]. Cytokine is a substance secreted by the immune system in response to a virus and plays an important role in cell-to-cell communication. An oversecretion of cytokines leads to hyperinflammation [2]. A humanised monoclonal antibody therapy targeting CD3 is one of the important signalling molecules for T-cell receptor activation. Monoclonal antibody therapy suppresses T-cells through antibody-mediated complement activation and removal of immune conjugates [3].

Meanwhile, magnetic nanoparticles (MNPs) are receiving a lot of attention for a variety of applications in medical science such as cell separation, gene cloning, biosensing and magnetic resonance imaging (MRI) [4]. MNPs the size of several tens of nanometers, having superparamagnetic properties, have been effectively used to isolate or purify DNA, proteins and peptides by conjugating biomolecules to their surface. When various ligands are introduced after stabilising the surface of MNPs with lipids or polymers, there is an advantage in that DNA/RNA, proteins, bacteria, viruses, cancer cells, etc. can be effectively separated with only a simple magnet [5].

To suppress the overactivation of T-cells, the technology of Ab-MNPs will be used. Ab-MNPs that enter the blood will be concentrated around the target using magnetic pads to increase their efficiency. This study will analyse the structure of the Ab-MNPs and investigate their flow characteristics in phosphate buffer saline (PBS) and rabbit blood vessels.

2 Materials and Methods

Mouse monoclonal antibodies are very useful as diagnostic reagents and for basic research because they have a variety of target antigens and can be mass-produced. Since 1988, many countries have developed humanised antibody manufacturing technology that makes a mouse monoclonal antibody similar to a human antibody. The anti-CD3 monoclonal antibody used in this study has an antibody structure of anti-human CD3 epsilon therapeutic antibody-endotoxin < Endotoxin units (EU)/mg manufactured by creative Biolab, a British antibody development company, as shown in Fig. 1a. This antibody is a human monoclonal antibody (mAb) called "foralumab" that Tiziana LIFE SCIENCES (USA) has completed a clinical trial for nasal administration for the treatment of novel coronavirus infection (COVID-19) [6].

The solution including the Ab-MNPs is prepared by using a SiteClick antibody labelling kit (Thermo Fisher, USA), as shown in Fig. 1b [7]. In this case, since the anti-CD3 antibody conjugated to the MNPs binds to CD3 receptors present in T-cells through the antibody's antigen binding site (Fab), Fc-directed conjugation is used to bind the mAbs to the MNPs for increased efficiency. To make Fc-oriented MNPs, as shown in Fig. 1b, first, an azide is attached to the Fc region of the antibody. Then a dibenzocyclooctyne (DIBO) attached to a sulfodicholorphenol (SDP) ester is attached to the azide through click chemistry. Next, biopure MNPs with an amine group diameter of less than 25 nm fabricated by nanoComposix (USA) are reacted with the modified antibodies so that that the SDP ester of the antibody will bind to the amine group of the MNP to create mAb-MNPs, as shown in Fig. 1c [8].

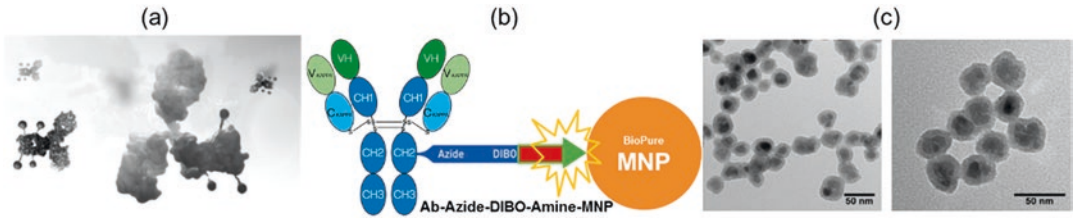

Fig. 1 (**a**) The shape of anti-CD monoclonal foralumab antibody and (**b**) the schematic diagram of conjugation between monoclonal antibody-azide-DIBO and (**c**) amine-magnetic nanoparticles. Scale bar = 50 nm

Transmission electron microscope (TEM) and energy dispersive spectroscopy (EDS) measurements transmit electrons with high energy through a thin sample with a size of nm and analyse the shape structure and the characteristic x-ray energy spectrum emitted from the surface of the sample to confirm elemental components. In addition, in the case of NTA measurement, when a laser beam passes through a liquid sample chamber containing particles, the particles in the path of the beam scatter light and the drifting Brownian motion of the particles can be visualised as an image. A TEM image analysis of the structure of Ab-MNPs are investigated using an EDS analysis. After preparing a humanised antibody from anti-CD3 monoclonal antibody, which is a humanised mouse monoclonal antibody, it is administered to rabbits to maintain the same affinity level so that animal experiments can be performed.

To see the effect of direct injection of Ab-MNPs into the blood vessels of a rabbit, nonclinical animal testing is applied after being approved by the Institution of Animal Care and Use Committees (IACUC) of Sangji University [9]. Ten-week-old New Zealand female rabbits (approximately 1.8 kg) were supplied from the DaeHan Biolink Company (Eumseong, Chungbuk, Republic of Korea). The rabbits used in the anatomical experiment were anaesthetised by injecting 3.0 mL of a mixture of Zoletil® (2.5 mL) and Rompun® (0.5 mL) into the leg muscle of each rabbit. Especially because the Zoletil reagent is classified as a controlled substance, we obtained approval from the Ministry of Food and Drug Safety, Republic of Korea. All anatomical procedures were performed in a general anaesthetic environment.

3 Experimental Results and Discussion

A field emission TEM (JEM-F200, JEOL Ltd., Japan) was used to observe the bonding characteristics between the foralumab antibody and magnetic nanoparticles. For multi-purpose analysis, this device has improved spatial resolution and analysis performance and has a high resolution with a user-centred integrated control system. The sample was well loaded on the TEM grid in an appropriate amount, and the TEM image showed no difference between the MNPs and the Ab-MNPs which included Fe, O, and S elements. TEM images for MNPs, Ab, and Ab-MNPs present in the sample were subjected to rapid EDS with high sensitivity. Intensity images for the main elements O, S, and Fe are shown in Fig. 2a. The EDS spectrum in Fig. 2b shows that the Ab-MNP blue peak has a lower counts value with an overlapped spectrum than the Ab pink peak, but the only MNP black peak has not consisted the Ab pink peak. Also, the S element counts value is higher for Ab-MNP than for MNP. We confirmed that the antibody was conjugated to the MNPs from the elemental analysis.

An NTA device that utilises both the properties of light scattering and Brownian motion was used to confirm the size distribution and number of nanoparticles of Ab-MNPs suspended in PBS [10]. When a laser beam was passed through the sample chamber, particles in the path of this beam scattered light, which can be visualised under a 20× microscope equipped with a camera as shown in Fig. 3.

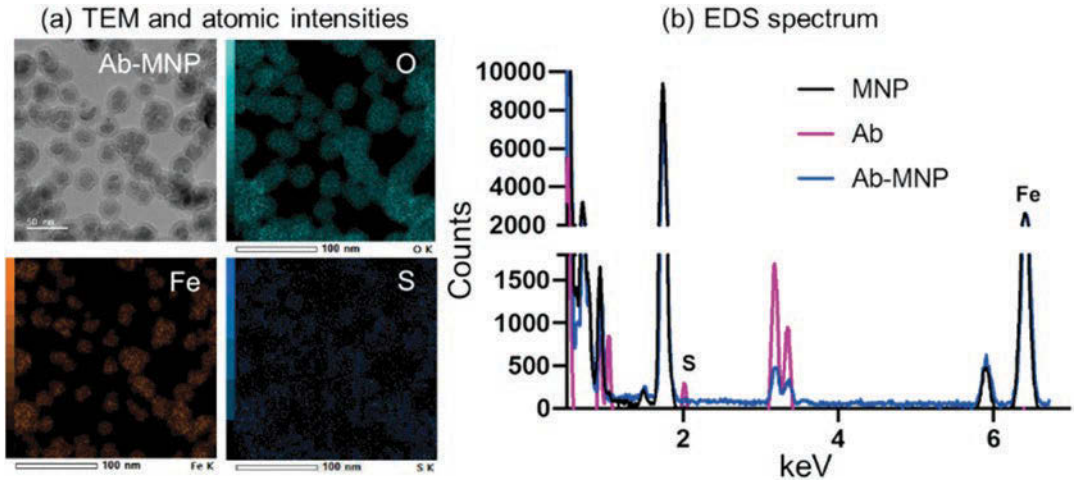

Fig. 2 (**a**) TEM image and atomic intensities of O, S, and Fe for Ab-MNP. (**b**) The EDS spectrum for MNP, Ab, and Ab-MNP and atomic stoichiometric analysis. Here, the S element is a major component constituting the framework of the foralumab antibody(Ab). Here characteristic energies for S and Fe elements are 2.307 keV and 6.398 keV, respectively. Scale bars = 50 nm, 100 nm

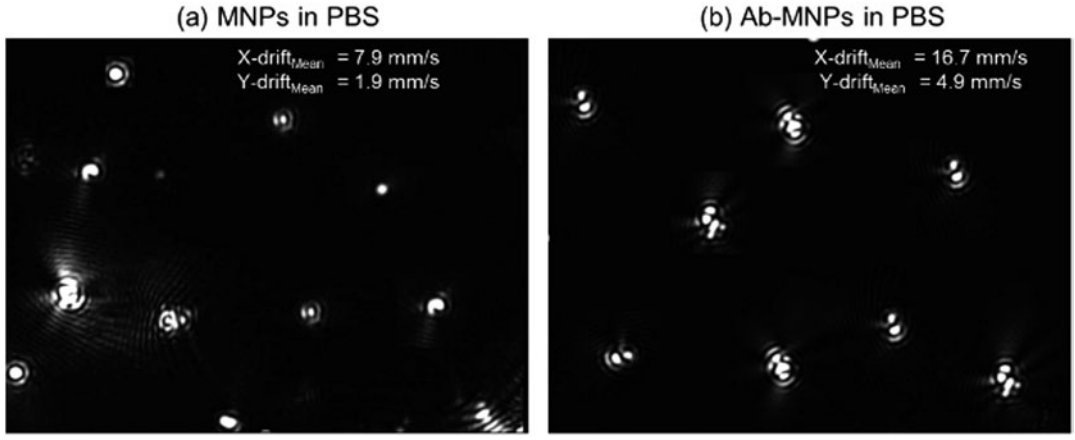

Fig. 3 Flow images with Brown motion of (**a**) MNPs and (**b**) Ab-MNPs in PBS by using the NTA

The mean concentration and size of the Ab-MNP conjugates contained in PBS measured with an NTA were $2.63 \times 10^7 \pm 1.18 \times 10^6$ particles/mL and 258.8 ± 14.2 nm. The average values of the moving speed (1 pix/frame = 2.5 mm/s) of MNPs in PBS were 7.9 and 1.9 in the x-axis and y-axis directions, as shown in Fig. 3a, respectively. Figure 3b shows that the average values of the moving speed of the antibody-attached Ab-MNPs were 16.7 mm/s and 4.9 mm/s in the x-axis and y-axis directions, respectively. As a result, it can be seen that Ab-MNPs, are moving more than twice as fast as MNPs without an antibody. This implies that the CD3 antibody having a biocompatible ligand functional group of Fc-directed foralumab attached to the surface of the MNPs has better fluidity in PBS than the amine-MNPs without mAbs.

To confirm the fluidity of the MNPs attached to the antibody, we performed a non-clinical animal experiment. An 8-week-old 1.8 kg New Zealand rabbit was anaesthetised and laid down

in a stable position, and 75 μl of Ab-MNPs solution, contained in PBS×1, was injected near the artery in the right ear where artery, vein, and capillary were all observed, as shown in Fig. 4. At the time of injection, the arterial blood vessels were cut due to rejection as shown in Fig. 4a at first, but it recovered slowly and showed normal blood vessels as shown in Fig. 4b after 5 min of injection. In addition, it was confirmed that the black coloured MNPs flowed along the blood vessels and circulated blood in the normal colour of blood. The Ab-MNPs showed good movement in the circulatory system and a compatible structure with the living body [11]. Thus, a liquid solution containing Ab-MNPs will not have any side effects when being used for a virus-related treatment. Furthermore, it is expected to induce long-term therapeutic efficacy by rapidly normalising the patient's immune system and treating excessive cytokine secretion.

4 Conclusions

The optimal Fc-directed conjugation of Ab-MNPs was performed using SiteClick antibody labelling kits consisting of antibody concentration, buffer exchange, modification of antibody carbohydrate domain, attachment of azide, and purification and concentration of azide-modified antibody. The successful conjugation of Ab-MNPs is observed by comparison of an EDS spectrum and a TEM image. The average values of the moving speed due to Brown motion of MNPs and Ab-MNPs in PBS were + 3.16/−0.28 pix/frame and + 6.70/+1.98 pix/frame in the x-axis/y-axis, respectively. This implies that

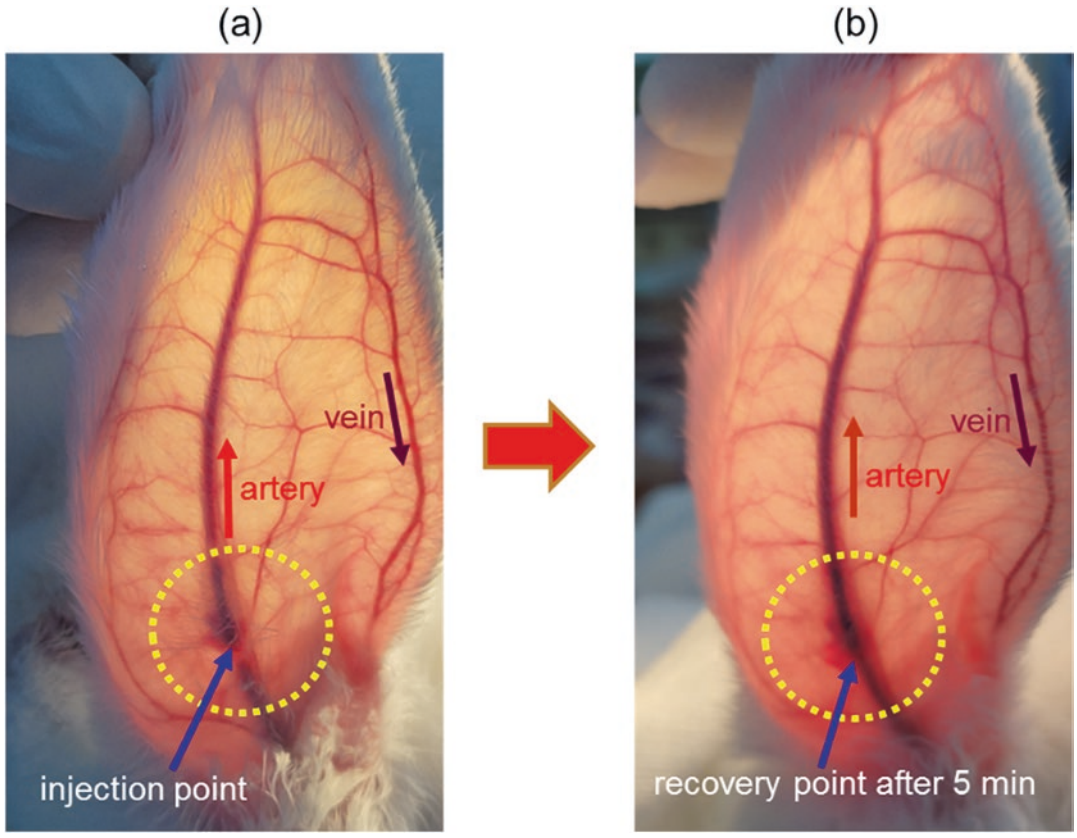

Fig. 4 Appearance in arterial blood vessels of rabbit's left ear at (**a**) immediately and (**b**) 5 min after injection of 75 ul of Ab-MNPs (foralumab-azide-DIBO-amine-MNPs) with recovery flow property

Ab-MNPs have better fluidity in PBS than MNPs without antibodies attached. The Ab-MNPs showed good fluidity in blood circulation when injected into the artery of a rabbit's ear, showing that it had a structure compatible with the living body. It is expected, with the additional use of a simple magnetic patch, that the therapeutic effect of Ab-MNPs will be optimised by reducing the burden on the patient and providing a sense of stability.

Acknowledgments This research was supported by Basic Science Research Program through the National Research Foundation of Korea (NRF) funded by the Ministry of Education (2021R1I1A3054773).

References

1. Ledford H (2021) COVID antibody treatments show promise for preventing severe disease. Nature 591:513–514
2. Lee JS, Park S, Jeong HW et al (2020) Immunophenotyping of COVID-19 and influenza highlights the role of type I interferons in development of severe COVID-19. Sci Immunol 1:1–16
3. https://www.creativebiolabs.net/muromonab-cd3-overview.htm
4. Cardoso VF, Francesko A, Ribeiro C et al (2018) Advances in magnetic nanoparticles for biomedical applications. Adv Healthcare Mater 7:1–35
5. Mengesha AE, Wydra RJ, Hilt JZ et al (2013) Binary blend of glyceryl monooleate and glyceryl monostearate for magnetically induced thermo-responsive local drug delivery system. Pharm Res 30:3214–3224
6. Ogura M, Deng S, Preston-Hurlburt P et al (2017) Oral treatment with foralumab, a fully human anti-CD3 monoclonal antibody, prevents skin xenograft rejection in humanized mice. Clin Immunol 183:240–246
7. https://www.thermofisher.com/order/catalog/product/S10900?kr&en#/S10900?kr&en
8. https://nanocomposix.com/collections/material-magnetite/products/biopure-magnetite-nanoparticles-pvp?variant=15906783264857
9. Shin JY, Ji JO, Lee SS et al (2019) Expression of genes in primo vasculature floating in lymphatic endothelium under lipopolysaccharide and acupuncture electric stimulation. J Acupunct Meridian Stud 12:3–10
10. Schmidt JR, Skinner JL (2004) Brownian motion of a rough sphere and the Stokes−Einstein law. J Phys Chem B 108:6767–6771
11. Butler KS, Lovato DM, Adolphi NL et al (2013) Development of antibody-tagged nanoparticles for detection of transplant rejection using biomagnetic sensors. Cell Transplant 22:1943–1954

Cerebrovascular Reserve (CVR) and Stages of Hemodynamic Compromise

Edwin M. Nemoto and Howard Yonas

Abstract

The concept of hemodynamic compromise (HC) is used to detect brain regions under ischemic stress by impaired ability to dilate in response to a vasodilatory challenge for cerebrovascular reserve (CVR). The vasodilatory challenges are either inhaled CO_2 or a carbonic anhydrase inhibitor acetazolamide (AZ) with measurements of cerebral blood flow (CBF) before and during the challenge. The rationale for CVR is that the brain under ischemic stress is vasodilated and the increase in CBF is attenuated. However, regional oxygen extraction fraction (OEF) by positron emission tomography (PET) is the gold standard for measurement of HC. We showed a strong correlation between CVR and OEF and the OEF response (OEFR) before and after vasodilation in patients with acute ischemic stroke. These observations suggest that CVR measurements alone identify brain regions under ischemic stress without the need for expensive, time consuming and difficult PET OEF.

Keywords

Cerebral blood flow · Regional oxygen extraction fraction · PET · Cerebral perfusion pressure

1 Introduction

The concept of **HC** is shown in Fig. 1 in the CVR response to a vasodilatory challenge and displacement of the CBF autoregulation curve to higher cerebral perfusion pressure (CPP) to the right.

Objective: To evaluate the correlation between CVR, OEF and OEF response (OEFR) in the cerebral cortex of patients suffering large vessel occlusion stroke and thereby show that CVR without OEF will identify HC (Fig. 2).

2 Material and Methods

Patients suffering large vessel occlusive strokes within the past 6 months with occlusive vascular disease, 61 ± 5 years old (mean ± SD). In stroke patients, bilateral carotid occlusions, left middle carotid artery, right internal carotid artery, and left middle carotid artery occlusions were observed. Magnetic Resonance Imaging (MRI): MRI scans performed on either a 3.0 Tesla (Siemens Medical Solutions, Malvern, PA) or 1.5

E. M. Nemoto (✉) · H. Yonas
Department of Neurosurgery, University of New Mexico, Albuquerque, NM, USA
e-mail: enemoto@salud.unm.edu

F. Scholkmann et al. (eds.), *Oxygen Transport to Tissue XLIII*, Advances in Experimental Medicine and Biology 1395, https://doi.org/10.1007/978-3-031-14190-4_59

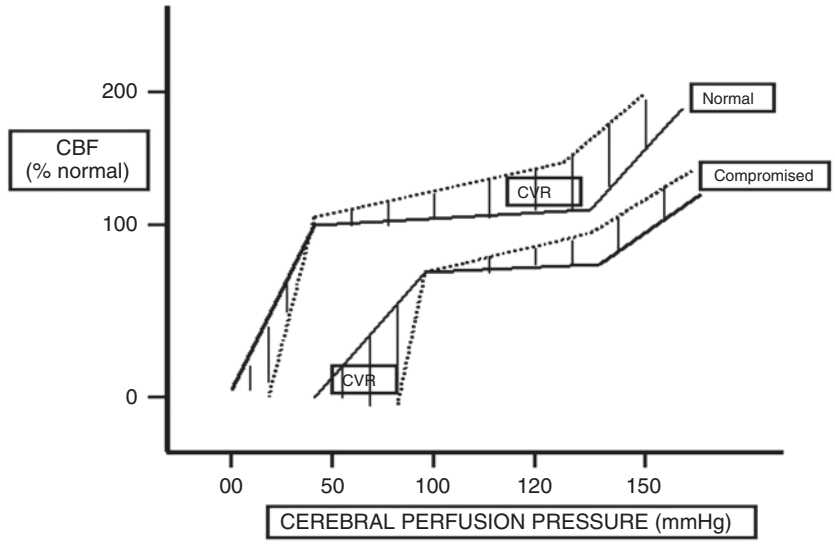

Fig. 1 Illustration of the cerebral blood flow (CBF) autoregulation curves for a normal brain and a compromised brain with a higher critical cerebral perfusion pressure (CPP) of CBF autoregulation

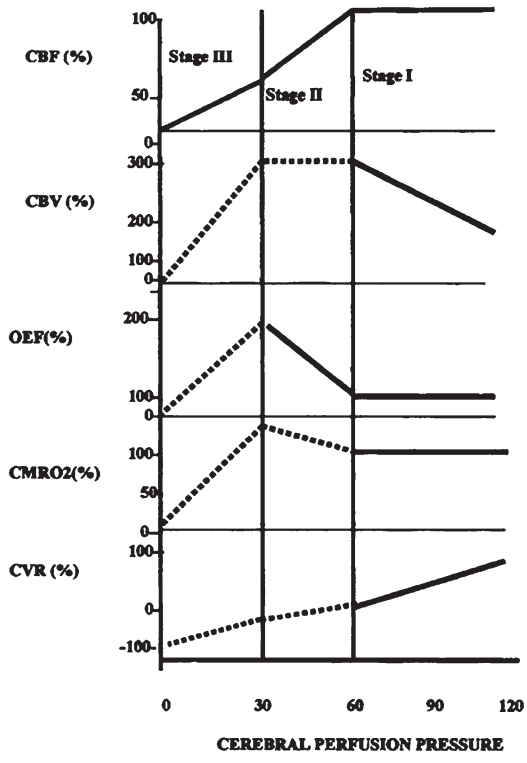

Fig. 2 Phases of HC I–III. Phase I normal. Phase II Ischemic stress. Phase III. Decompensation

Tesla whole body MRI scanner (General Electric Medical Systems, Milwaukee, WI), with echo planar imaging (EPI) capabilities and operating under version VH3 of the scanning software. The imaging protocol consisted of standard imaging sequences. Positron emission tomography (PET): A Siemens/CTI HR+, high-resolution tomograph was performed with ^{15}O-water to measure cerebral blood flow (CBF) and ^{15}O-oxygen to measure cerebral metabolic rate of oxygen ($CMRO_2$). The paradigm for the PET studies was: ^{15}O-oxygen/^{15}O-water/acetazolamide 15 mg/kg i.v. /^{15}O-water/^{15}O-oxygen. ^{15}O-oxygen measurements began 25–30 min after acetazolamide (AZ) with 3 min of data acquisition and within 45 min maximal vasodilatory effect.

- Oxygen extraction fraction (OEF) was calculated after measurement before and after acetazolamide (Diamox) challenge given 15 mg/kg, i.v. OEF threshold was set at 50% based on previous studies.
- *CBF Measurement*:

- Calculation of CBF was done using a two-compartment model approach using the operational Eq. (30):

$$A^*(T) = K_1^W \cdot {}_{\int 0}{}^{T} C_a^*(t) \cdot e^{-k2W\cdot(T-t)} \cdot dt + v_0 \cdot C_a^*(T)$$

where $A^*(T)$ is the radioactivity of the ROI at T, $Ca^*(t)$ the radioactivity in blood at the brain capillary, $K1^W$ the unidirectional blood-brain clearance rate constant of water (=CBF), $k2^W$, the fractional brain-blood clearance rate constant of water, and v_0 the correction constant for the intravascular radioactivity. In order to obtain $Ca^*(t)$, the measured radioactivity in arterial blood was corrected for external dispersion and temporal displacement.

- $CMRO_2$ measurements were initiated with arterial blood sampling as previously described.
- Calculation of CVR, OEF and OEFR.
- Oxygen extraction fraction (OEF) was calculated as the $K1^O$-$K1^W$ ratio for individual regions. Calculation of CVR; CVR was calculated as the percentage increase in CBF after acetazolamide as defined by: $CVR\ (\%) = CBF\ diamox - CBFbslnCBFbsln \times 100$
- OEFR = OEF on AZ/OEF Bsln.

Statistical Analysis

- Graphpad version 6.0 PRISM software (La Jolla, CA). Descriptive summary statistics were obtained using parametric analyses including linear regression analyses, one-way ANOVA and t-tests with a minimum significant difference P value of 0.05.

3 Results

In Figs. 3 and 4 a substantial percentage of hemispheres (37%) were found to be in hemodynamic compromise by CVR but with normal OEF which likely represents Stage III hemodynamic compromise. **The results indicate that CVR alone with a vasodilatory challenge accurately indicates hemodynamic compromise**.

4 Discussion and Conclusions

CVR by definition reflects the vasodilatory capacity of cerebral blood vessels before and after Acetazolamide challenge and as such is superior in detecting hemodynamic compromise. OEF reflects the ratio of oxygen consumption to oxygen delivery and thereby the degree of isch-

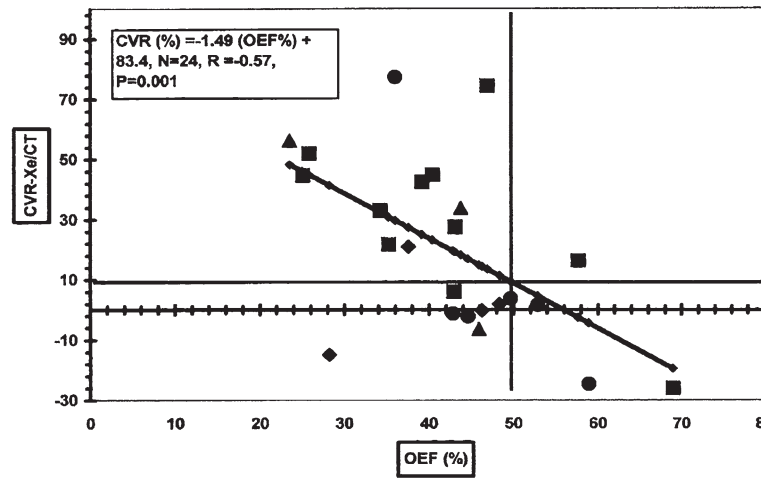

Fig. 3 Illustrates the goodness of fit between the CVR by Xe/CT CBF with acetazolamide challenge and OEF

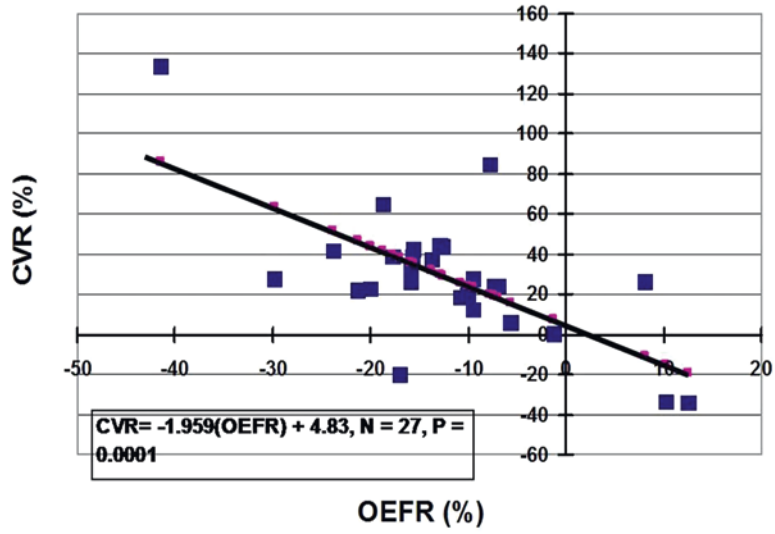

Fig. 4 The fit between CVR and OEFR, the change in OEF before and after i.e. OEFR in response to AZ vasodilatation with P = 0.0016

emic stress in the resting state of the brain without a vasodilatory challenge (Fig. 3). Addition of a vasodilatory challenge to OEF (OEFR) (Fig. 4) significantly improves the correlation with a highly significant P value of 0.0016. With calculation of the relationship between CVR and the OEF response to acetazolamide with OEFR (Fig. 3) further improved the correlation with CVR with a P value of 0.0001.

Acknowledgements Supported by: Supported by NIH and American Heart Association grants NIH-NIGMS Sub-award from P20 GM109089-01A1, NIH-NINDS 1R21NS091600-01A1, NIH-NINDS RO1-NS051639-05, NIH-NINDS R03 NS061216-01A1.

References

1. Yonas H, Smith HA, Durham SR, Pentheny SL, Johnson DW (1993) Increased stroke risk predicted by compromised cerebral blood flow reactivity. J Neurosurg 79(4):483–489
2. Derdeyn CP, Videen TO, Yundt KD, Fritsch SM, Carpenter DA, Grubb RL, Powers WJ (2002) Variability of cerebral blood volume and oxygen extraction: stages of cerebral haemodynamic impairment revisited. Brain 125(Pt 3):595–607

On the Mechanism of Sustained Mitochondrial Membrane Potential Without Functioning Complex IV

Eiji Takahashi and Yoshihisa Yamaoka

Abstract

In intact mitochondria, the transport of electrons, respiration and generation of proton gradients across the inner membrane (proton motive force) are mutually coupled, according to Peter Mitchell's hypothesis on oxidative phosphorylation. Thus, the inhibition of electron transport at either respiratory complex III or IV in the electron transport chain leads to failure in producing proton motive force along with the abolition of respiration. Here, we determined the mitochondrial membrane potential (MMP), as a measure of proton motive force, and cellular respiration in various cultured cells and demonstrated that inhibition of complex IV by KCN abolished mitochondrial respiration while MMP was sustained. These results are unexpected and appear incompatible with Mitchell's chemiosmotic hypothesis.

Keywords

Mitochondria · Electron transport · Mitchell's chemiosmotic hypothesis · Proton motive force

E. Takahashi (✉) · Y. Yamaoka
Graduate School of Advanced Health Sciences, Saga University, Saga, Japan
e-mail: eiji@cc.saga-u.ac.jp

1 Introduction

In eukaryotic cells, reduced nicotinamide adenine dinucleotide (NADH) and reduced flavin adenine dinucleotide (FADH)/succinate produced in the citric acid cycle donate electrons via mitochondrial respiratory complex I and complex II, respectively, to the electron transport chain in the mitochondrial inner membrane. Electrons (or reducing equivalents) are continuously transferred to complex III and subsequently complex IV according to the redox potential of each respiratory complex. Finally, electrons are utilised for reduction of oxygen to water in complex IV. Thus, continuous electron transport is accompanied by the consumption of oxygen (respiration). In parallel, redox reactions in each respiratory complex (except for complex II) translocate protons from the matrix space to intermembrane space, producing concentration gradients of protons across the inner membrane, which serves electro-chemical energy (proton motive force, pmf) for the synthesis of ATP. Thus, Peter Mitchell's chemiosmotic hypothesis for oxidative phosphorylation outlined above predicts tight coupling among the transport of electrons, respiration, and generation of pmf in intact mitochondria. Consequently, pharmacological inhibition of either complex III or complex IV arrests electron transport, respiration, and proton translocation leading to failure in producing pmf and ATP in complex V (F_1F_o).

F. Scholkmann et al. (eds.), *Oxygen Transport to Tissue XLIII*, Advances in Experimental Medicine and Biology 1395, https://doi.org/10.1007/978-3-031-14190-4_60

Here, we report that cultured cells treated with cyanide, a potent inhibitor of complex IV, perfectly sustained mitochondrial membrane potential (MMP), whereas mitochondrial respiration was completely abolished. This is incompatible with Mitchell's chemiosmotic hypothesis.

2 Methods

Cells We used cancer cell lines, Hep3B, MDA-MB-231, and Panc-1, and non-cancer cell lines, COS-7 and HEK293. Cells except for Hep3B were cultured on 22 mm-diameter type I collagen coat cover slip (Corning, 354089). Hep3B was cultured on 25 mm-diameter culture cover glass (Matsunami). Cells except for MDA-MB-231 were cultured in DMEM in 5% CO_2/air. MDA-MB-231 cells were cultured in the Leibovitz's L-15 medium in air.

Mitochondrial Respiration Cellular oxygen consumption (respiration) was determined without detaching cells from culture cover glass as described elsewhere [1]. Briefly, cells on culture cover glass were installed in an 8 μl-airtight measuring cuvette and dynamic changes in O_2 concentration in the surrounding medium was optically measured. The oxygen consumption rate was normalised to the number of cells. More than 3 individual experiments were conducted for each condition.

MMP We assessed MMP as a measure of pmf using a membrane-permeable cationic fluorescent dye, tetramethylrhodamine, methyl ester (TMRM, T-668, Sigma-Aldrich). Cells were incubated with 150 nM TMRM in the culture medium for 20 min. Then, cells were washed twice with hepes-Tyrode solution containing 50 nM TMRM and further incubated for 1.5 h. Loading of TMRM was conducted at 37 °C in the dark. TMRM fluorescence in mitochondria was imaged using a 14-bit cooled CCD camera (CoolSNAP MYO, Photometrics) connected to fluorescence microscopy system (IX-71, Olympus) with 546 nm excitation and 605 nm emission wavelengths. More than 3 individual experiments were conducted for each condition in which >10 images were collected per experiment.

3 Results

Pharmacological Inhibition of Complex IV Abolished Respiration While Sustaining MMP in Various Cell Lines We first compared effects of respiratory inhibition in complex III (10 μM antimycin A, AMA) and complex IV (2 mM KCN) on MMP in Hep3B cells (a cancer cell line) and COS-7 (a non-cancer cell line). Figure 1 demonstrates that both AMA and KCN almost completely abolished respiration. Mitochondrial TMRM fluorescence was imaged 30 min after administration of inhibitors. Antimycin A completely abolished TMRM fluorescence in these cells. In contrast, KCN did not affect TMRM fluorescence. In these cells, TMRM fluorescence was maintained even after 4-days exposure of cells with 2 mM KCN (Supplementary data S1, all Supplementary data are accessible from the public at https://doi.org/10.6084/m9.figshare.15175995.v1). We further tested other cell lines to determine if TMRM fluorescence is resistant to KCN inhibition of respiration. MDA-MB-231, Panc-1, HEK293 cells almost perfectly sustained TMRM fluorescence after KCN (Fig. 2), whereas complex III inhibition by AMA abolished TMRM fluorescence in these cells. Another inhibitor of complex IV, sodium azide (NaN_3) abolished respiration while MMP was maintained in the cell tested. (Supplementary data S2) Now, we have demonstrated that MMP was maintained without functioning complex IV in various cell lines such as Hep3B, COS-7, MDA-MB-231, HEK293, and Panc-1, and proceeded to test hypotheses for sustained MMP without respiration.

Hypothesis #1 When electron transport is compromised due to a lack of oxygen and MMP faces a crisis, reversal action of complex V (F_1F_o-

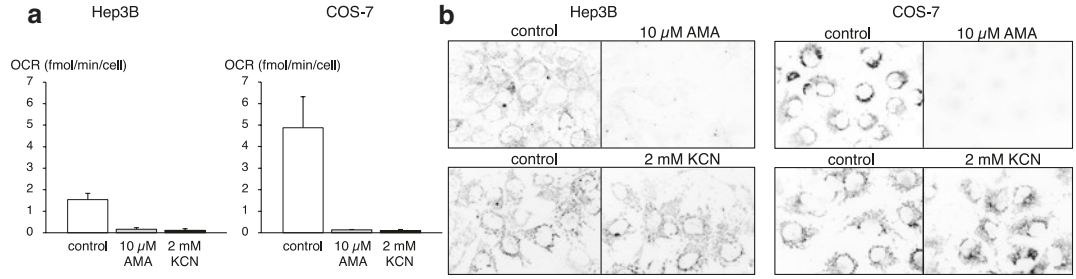

Fig. 1 Mitochondrial respiration (**a**) and representative TMRM fluorescence images (**b**) in Hep3B and COS-7 cells. Number of OCR measurements for control, AMA, and KCN were 7, 4, and 4 in Hep3B cells and 12, 4, and 5 in COS-7 cells, respectively

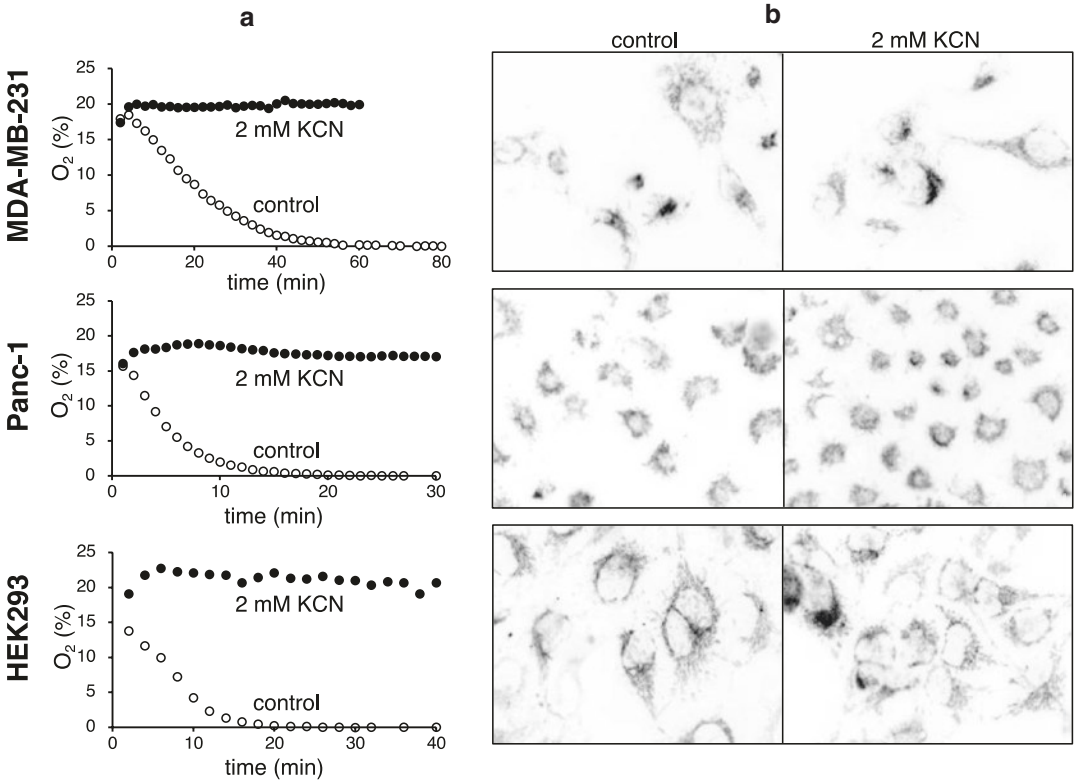

Fig. 2 Representative data for mitochondrial respiration (**a**) and TMRM fluorescence (**b**) in KCN-treated cells. Panel a indicates dynamic changes in O_2 concentration in an 8 μl-airtight measuring cuvette in which cells were placed. Mitochondrial respiration consumes O_2 in the cuvette resulting in slow declines, whereas unchanged O_2 levels in KCN-treated cells indicate abolition of O_2 consumption

ATPase) may restore MMP. To test this possibility, oligomycin, an inhibitor of F_1F_o, was administered in KCN-pretreated cells. In KCN-pretreated Hep3B cells, oligomycin did not affect TMRM fluorescence (Fig. 3). In contrast, in KCN-pretreated COS-7 cells, TMRM fluorescence particularly in perinuclear mitochondria was significantly attenuated (Fig. 3). Remarkably, TMRM fluorescence recovered within 60 min after oligomycin and the second oligomycin at this period no longer attenuated TMRM fluorescence (Fig. 4). These biphasic changes in TMRM

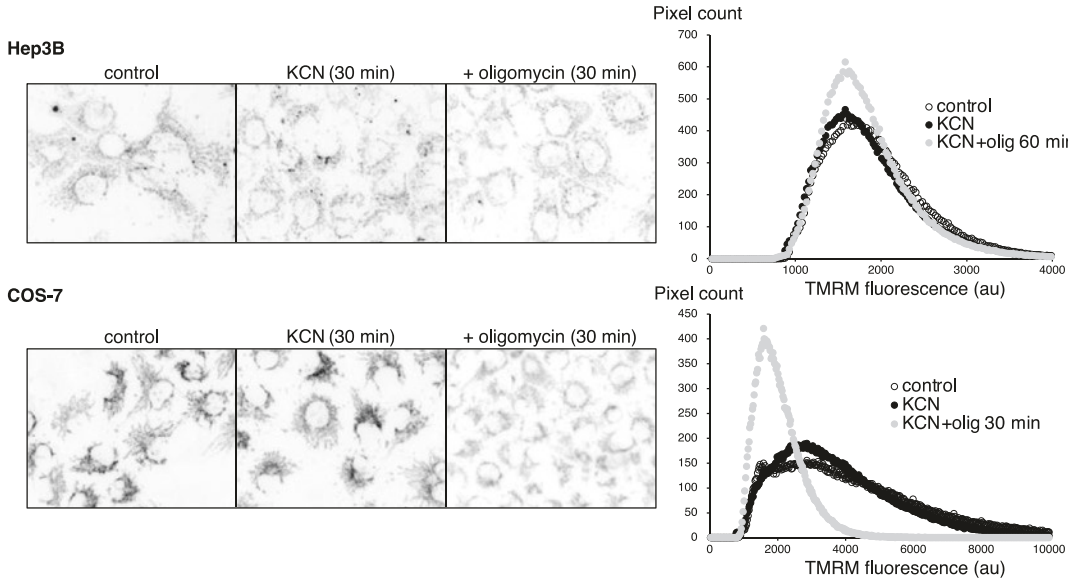

Fig. 3 Effect of oligomycin (olig) on TMRM fluorescence in KCN-pretreated cells. Right panels represent TMRM intensity histograms generated from left panels. Pixels corresponding to mitochondria were extracted by spatial filter and threshold, and intensity of these pixels was plotted

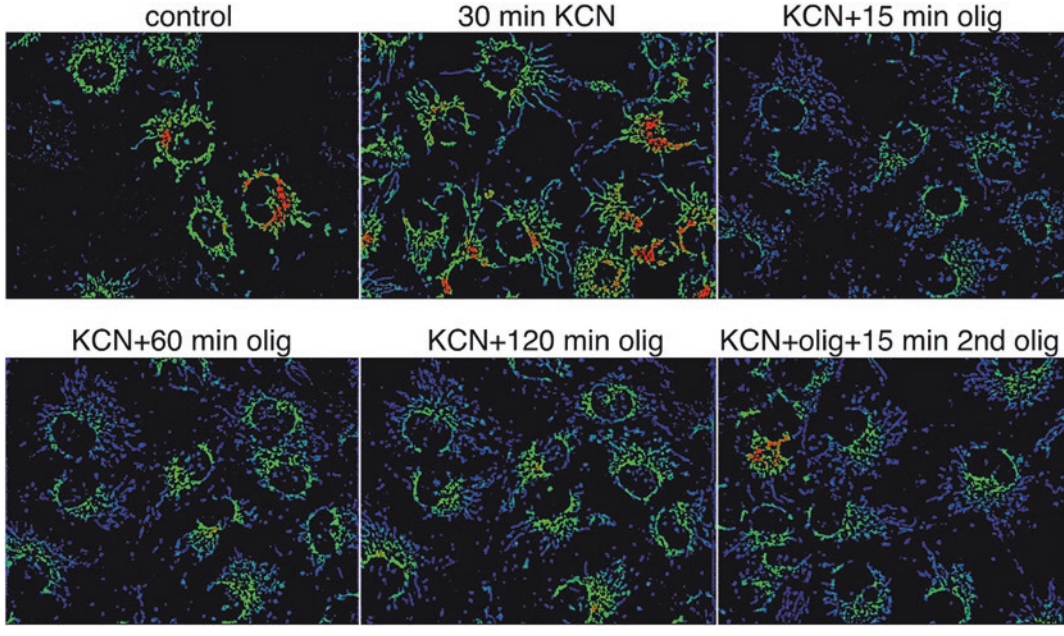

Fig. 4 Recovery of TMRM fluorescence in KCN-pretreated COS-7 cells after depressions caused by oligomycin

fluorescence were demonstrated also in KCN-pretreated MDA-MB-231 and Panc-1 cells (Supplementary data S3 and S4). Oligomycin did not affect TMRM fluorescence in KCN-pretreated HEK293 cells (Supplementary data S5). These results indicate that the reversal of F_1F_o may not be included in sustained MMP in the steady state of KCN inhibition of respiration.

Hypothesis #2 The magnitude of MMP is determined by the balance between proton translocations (from matrix to intermembrane space) in respiratory complexes and proton flux via F_1F_o (from intermembrane space to matrix). Thus, it may be possible at least theoretically that MMP would be maintained with significantly reduced electron transport (and respiration) if forward F_1F_o activity is simultaneously suppressed. We tested this possibility in Hep3B and COS-7 cells. We measured the rate of fall of mitochondrial TMRM fluorescence immediately after administration of AMA. TMRM fluorescence dropped to 87.8 ± 1.1% and 90.5 ± 2.5% in 20 s in Hep3B and COS-7 cells, respectively. Pretreatment with KCN for 30 min did not affect the rate of fall in TMRM fluorescence after AMA (Supplementary data S6 and S7). These results indicate that simultaneous reductions in forward F_1F_o activity in KCN-pretreated cells were unlikely.

Hypothesis #3 Adenine nucleotide translocator (ANT) in the inner membrane exchanges ADP^{3-} and ATP^{4-} between the cytoplasm and matrix space and thus electrogenic. We considered the possibility that ANT might generate MMP in the absence of electron transport and conducted ANT inhibitions by bongkrekic acid in Hep3B and COS-7 cells. The overnight treatment of the cell with 10 μM bongkrekic acid substantially attenuated respiration while TMRM fluorescence was comparable with the control cells. Further treatment with KCN did not significantly affect TMRM fluorescence (Supplementary data S8), excluding contributions of ANTs in sustained MMP without respiration.

Hypothesis #4 Electrons are transferred from complex III to complex IV as a flux of reduced cytochrome *c*. Because cytochrome *c* is water soluble, we hypothesised that in complex IV inhibited cells substantial amount of cytochrome *c* might leak out from the electron transport chain to outside mitochondria instead of reaching at complex IV to reduce molecular oxygens. This mechanism, if exists, would allow proton translocations in complex I and complex III to produce MMP without complex IV. Based on these hypotheses, we monitored the generation of superoxide anions in mitochondria using MitoSox fluorescent probe (ThermoFisher Scientific) in Hep3B and COS-7 cells. In these cells, gradual increases in MitoSox fluorescence were demonstrated after treatment with 10 μM AMA indicating electron leakages from the electron transport chain. However, significant increases in MitoSox fluorescence were not observed upon KCN treatment. (Supplementary data S9 and S10).

Hypothesis #5 Our findings that pharmacological inhibition of complex III certainly abolishes both respiration and MMP whereas MMP was still sustained in the case of complex IV inhibitions may suggest presence of yet unknown electron transport system consisting of complex I, II, and III. To gain insight into this possibility, we tested KCN effects on complex I inhibition by rotenone and complex II inhibition by 2-Thenoyltrifluoroacetone (TTFA) in Hep3B and COS-7 cells. Both 5 μM rotenone and 200 μM TTFA attenuated TMRM fluorescence where the effect depended on the cell type (Supplementary data S11 and S12). It may be noted that KCN did not induce further changes in TMRM fluorescence in rotenone/TTFA treated cells. These results appear to indicate that the magnitude of TMRM fluorescence was determined by electron transport among complex I, II, and III where complex III is indispensable.

4 Discussions

Although controversies on precise molecular mechanisms still exist [2], the chemiosmotic hypothesis for oxidative phosphorylation is a basis for ATP production in mitochondria. In intact mitochondria, electron transport, respiration, and MMP are tightly coupled and, thus, inhibition of electron transport, either by pharmacological inhibition of respiratory complexes or by lack of oxygen, is expected to disrupt MMP

and eventually mitochondrial ATP production. We, however, demonstrated that MMP is maintained against pharmacological inhibitions of respiratory complex IV in a variety of cultured cells. The result is incompatible with the chemiosmotic hypothesis and suggests a possibility that cells in some circumstances might be able to survive without oxygen.

A few papers report changes in MMP during respiratory inhibitions. Picolli et al. [3] demonstrated that a 40% reduction of respiration by 0.3 mM KCN did not affect MitoCapture fluorescence in oligomycin-treated HepG2 cells. Only a slight reduction of the fluorescence was observed with 1 mM KCN where respiration was inhibited by 70%. Hall et al. [4] demonstrated in distal tubule cells that MMP was decreased by 25% in a combination of 1 mM NaCN and N_2 bubbling, in which oligomycin disrupted MMP. In a cellular model of cyanide poisoning, Owiredu et al. [5] showed that 50 μM NaCN resulted in 45–65% reductions in respiration whereas TMRM fluorescence was unchanged. Zuo et al. [6] demonstrated in PC12 cells that 10 mM NaN_3 decreased MMP determined by JC-1 fluorescence only by 7% (comparison with 40 mM NaN_3). Kilbride et al. [7] demonstrated in rat synaptosomes that KCN (<100 μM) inhibition of complex IV enzymatic activity to <30% did not affect JC-1 ratio. At 1 mM KCN, complex IV activity was decreased to 95% with a reduction of JC-1 ratio to ~65% that was further reduced to ~35% by addition of oligomycin.

Cyanide has been used to induce 'chemical anoxia' in cells and organs. This study poses a question as to whether 'chemical anoxia' is equivalent to the lack of oxygen in mitochondria in the context of mitochondrial oxidative phosphorylation. Further study is needed to compare, with respect to MMP and oxidative ATP production, 'true' anoxia and 'chemical' anoxia in various cells.

Cancer cells are prone to rely on aerobic glycolysis for production of ATP (the Warburg effect), in which various signal transduction pathways have been identified, including hypoxia-HIF-1α axis [8]. The present study suggests a possibility that MMP could be generated in oxygen depleted cells. Thus, it would be of special interest as to whether the present findings have implications in the Warburg effect in cancer cells.

Questions always arise as to how accurately TMRM fluorescence reports proton concentration gradients/MMP/pmf in intact cells. However, with comparisons with complex III inhibition by AMA (a positive control), the present study demonstrated that complex IV may not be a prerequisite for MMP generation. We demonstrated a possibility that a combination of complex I, II, and III is sufficient to produce MMP in some cultured cells. Accordingly, the mechanism for oxidative phosphorylation, particularly the role of oxygen, might wait for further elucidation.

References

1. Takahashi E, Yamaoka Y (2017) Simple and inexpensive technique for measuring oxygen consumption rate in adherent cultured cells. J Physiol Sci 67:731–737
2. Morelli AM, Ravera S, Calzia D et al (2019) An update of the chemiosmotic theory as suggested by possible proton currents inside the coupling membrane. Open Biol 9:180221
3. Piccoli C, Scrima R, Boffoli D et al (2006) Control by cytochrome *c* oxidase of the cellular oxidative phosphorylation system depends on the mitochondrial energy state. Biochem J 396:573–583
4. Hall AM, Unwin RJ, Parker N et al (2009) Multiphoton imaging reveals differences in mitochondrial function between nephron segments. J Am Soc Nephrol 20:1293–1302
5. Owiredu S, Ranganathan A, Greenwood JC (2020) In vitro comparison of hydroxocobalamin (B12a) and the mitochondrial directed therapy by a succinate prodrug in a cellular model of cyanide poisoning. Toxicol Rep 7:1263–1271
6. Zuo Y, Jun HJ, Xu X (2019) Sodium azide induces mitochondria-mediated apoptosis in PC12 cells through Pgc-1α-associated signaling pathway. Mol Med Rep 19:2211–2219
7. Kilbride SM, Telford JE, Davey GP (2021) Complex I controls mitochondrial and plasma membrane potentials in nerve terminals. Neurochem Res 46:100–107
8. Vaupel P, Multhoff G (2021) Revisiting the Warburg effect: historical dogma versus current understanding. J Physiol 599:1745–1757

Further Evidence that Gradients of Extracellular pH Direct Migration of MDA-MB-231 Cells In Vitro

Yuki Hada, Daisuke Yamaguchi, Yoshihisa Yamaoka, and Eiji Takahashi

Abstract

We hypothesised that concentration gradients of O_2/H^+ within tissue guide migration of primary cancer cells toward intra-tumour microvessels, thus promoting intravasation and eventual haematogenous metastasis of cancer cells. Previously, we demonstrated in vitro that MDA-MB-231 cells under pH and O_2 gradients (0.2–0.3 units/mm and ~ 6%/mm, respectively) migrate toward higher pH/O_2 regions. The present study was designed to address questions yet unanswered in the previous one, i.e., (1) whether extracellular O_2 gradients could be a cue for directional cell migration in physiologically relevant O_2 environments, and (2) whether average pH level in the bulk extracellular medium affects directional cell migration. In the absence of pH gradients, directional cell migration was not demonstrated at a physiological O_2 level (<5%). We demonstrated that both the migration velocity and directionality are significantly affected by the average extracellular pH level. This result is consistent with our model for directional cell migration that does not necessitate sensing of pH gradient at a single cell level. Thus, in this study, we demonstrated further evidence that gradients of extracellular pH direct migration of MDA-MB-231 cells in vitro.

Keywords

Primary cancer cells · Directional cell migration · Migration velocity · Gap cover glass

1 Introduction

By analogy with chemotaxis, where cell migration is directed by extracellular concentration gradients of chemoattractants, investigators have expected that molecules/ions associated with cellular energy metabolism also direct cell migration. Such extracellular metabolic cues include among many others O_2, CO_2, H^+, HCO_3^-, lactate ion, glucose, and glutamine. This hypothesis is particularly relevant in haematogenous metastasis of cancer cells because, in solid tumour tissue, steep concentration gradients, being perpendicular to microvessels, of metabolic substrate/metabolite such as O_2 and H^+ have been demonstrated in vivo with a μm spatial resolution [1]. If these molecules guide the cell toward nearby blood vessels according to their concentration gradients, primary cancer cells would more efficiently reach the intra-tumour microvessel com-

Y. Hada · D. Yamaguchi · Y. Yamaoka
E. Takahashi (✉)
Graduate School of Advanced Health Sciences, Saga University, Saga, Japan
e-mail: eiji@cc.saga-u.ac.jp

F. Scholkmann et al. (eds.), *Oxygen Transport to Tissue XLIII*, Advances in Experimental Medicine and Biology 1395, https://doi.org/10.1007/978-3-031-14190-4_61

pared to the condition of directionally random cell migration. Thus, the directional cell migration may promote haematogenous metastasis.

In our previous study [2], we combined a novel microfluidic device (gap cover glass, GCG) with the wound-healing assay for cell migration to examine migratory behaviour of MDA-MB-231 cells under the pH/O_2 gradients up to 12 h. We clearly demonstrated directional migration of the cell toward higher pH/higher O_2 regions. Because the addition of hepes (15 mM) in the extracellular medium abolished both extracellular pH gradients and directional cell migration, we concluded that the extracellular pH gradient is at least one of the important cues for the directional migration of MDA-MB-231 cells in vitro.

In addition to the pH gradient, extracellular O_2 concentration gradient is another candidate for the metabolic cue. In the previous study, to ignore the potential effect of O_2 gradients, we intentionally conducted the assay at unphysiologically high O_2 levels (15–21%). In this study, to clarify the possible role of extracellular O_2 gradient as a cue for cell migration, we conducted the migration assay where the average O_2 concentration was set at a physiologically relevant level, ~5%.

Cellular and molecular mechanisms for directional cell migration under extracellular pH gradients have not yet been determined. Our current hypothesis is that the modulation of cell migration velocity by extracellular pH may confer heterogeneities in cell migration directions. Specifically, we suppose that the bell-shaped dependence of migration velocity on pH [3] is essential for inducing directional migrations. Thus, we examined in this study whether extracellular pH in the bulk medium affects not only the velocity but also the directionality of cell migration.

2 Methods

Cells We used a metastatic breast cancer cell line MDA-MB-231. Cells were cultured on type I collagen-coated culture dishes (354456, Corning) in Leibovitz's L-15 medium (11415064, Thermo Fisher Scientific) supplemented with 10% FCS (HyClone Laboratories) and antibiotics (A5955, Sigma-Aldrich) in humidified air at 37 °C. Experiments were usually conducted 4 days after the passage at which cells were 80–90% confluent.

GCG We fabricated a microfluidic device called GCG in which diffusional supply of O_2 and washout of metabolically produced H^+ are physically restricted to the two open-ends (Fig.1a) [4]. Thus, for example, the balance between (restricted) diffusional O_2 supply to cells in the diffusion channel and consumption of O_2 by mitochondrial respiration defines gradients of O_2 concentration along the O_2 diffusion path. At 4–5 × 10^6 cells/ml, spatial gradients of ~6% O_2/mm and 0.2–0.3 units/mm for O_2 and pH, respectively, were consistently produced along the diffusion path (Figs. 1c and d). Details of the GCG and high spatial resolution measurements of O_2 concentration and pH were reported elsewhere [2].

Assay for Cell Migration Under O_2/pH Gradients As described in detail elsewhere [2], we arbitrarily picked 10 cells from the left and right boundaries of the wound space that did not undergo proliferations in the succeeding 12-hour period. We manually tracked, with a 1.5 μm spatial resolution, the migration of individual cells every 2 h for 12 h. Definitions for the left and the right boundaries in relation to the extracellular O_2 and pH gradients are depicted in Fig. 1b. We counted the number of cells migrating to the wound space; the number of cells migrating to the wound space from the left and right boundary, respectively, was designated as N_L and N_R. If the cell migration direction is random, N_L/N_R should be ~1 while a tendency for unidirectional migration toward higher or lower pH/O_2 regions gives $N_L/N_R > 1$ or $N_L/N_R < 1$, respectively. We also calculated accumulated distance of cell migration.

Cell Migration at Physiological O_2 Concentrations Because the O_2 level linearly decreases from the open-end to the centre in GCG, we recorded the migration of the cell

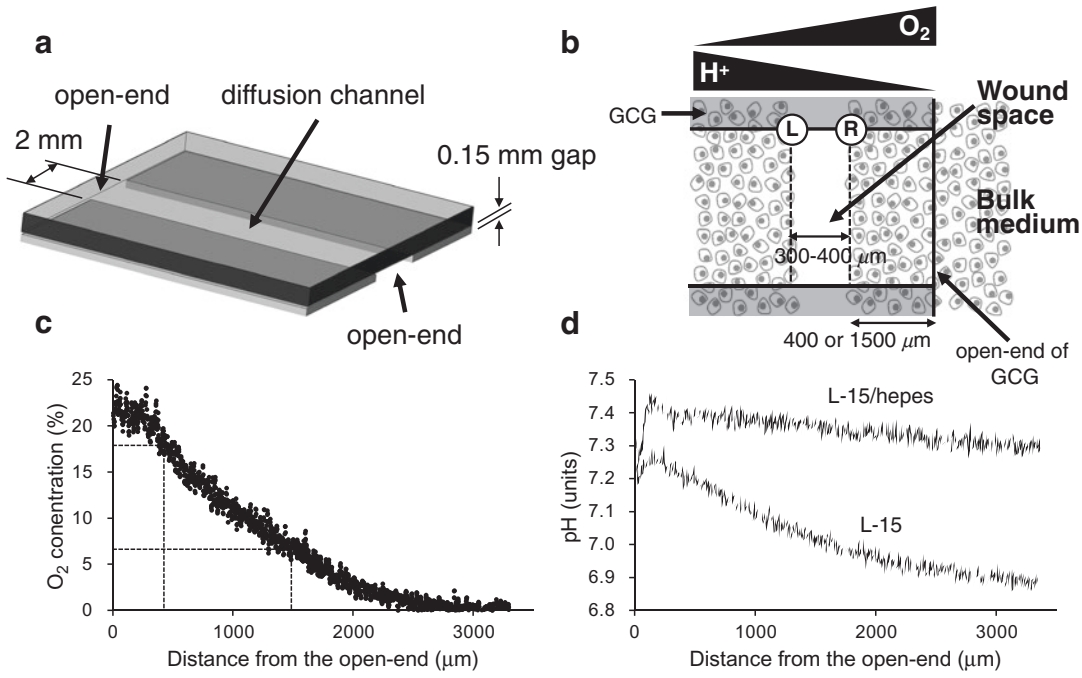

Fig. 1 (**a**). Gap cover glass (GCG). (**b**). Definition of the left (L) and right (R) boundaries in the wound space relative to extracellular O_2/H^+ gradients. (**c**). O_2 concentration gradients in the diffusion channel. (**d**). pH gradients in the diffusion channel. See reference [2] for details

located at ~1500 μm inside the open-end of GCG where the O_2 level dropped to <5% (Fig. 1c). We assessed cell migrations with 15 mM hepes in the extracellular medium to exclude the effect of pH gradients working as a cue for directional cell migration. Hepes in L-15 medium also prevented extracellular pH at these deep regions from being too acidotic; extracellular pH was dropped to <7 without hepes (Fig. 1d). We conducted five measurements at ~1500 μm regions. Additionally, we also conducted five measurements in regions at 300–400 μm inside GCG. The O_2 concentration in the bulk medium (outside GCG) was 21% (air).

Effect of Average pH in the Bulk Medium We tested whether pH levels in the extracellular medium affect directional cell migration in addition to the effect arising from its gradient. Similar to the previous experiment [2], the wound space was created at 300–400 μm inside the open-end of GCG, but in this study pH outside of GCG was set at 6.8, 7.2 or 7.6. The pH of the extracellular L-15/hepes medium was adjusted by adding NaOH. Oxygen concentration in the bulk medium (outside GCG) was 21% (air). We conducted five experiments for each pH condition. Differences in cell migration among three bulk medium pH levels were judged by analysis of variance followed by a post-hoc test, the Tukey-Kramer method.

3 Results

Cell Migration at Physiological O_2 Concentrations Average values for the cell migration activity at ~1500 μm and ~ 400 μm inside the open-end of GCG are summarised in Table 1. In cells in the region ~400 μm inside the open-end of GCG (NEAR), N_L/N_R was significantly larger than unity indicating a directional migration. In this region, both O_2 and pH gradients should present in the extracellular medium (Figs. 1c and d), while the O_2 level must be substantially higher than the physiological level

Table 1 Migration of MDA-MB-231 cells under GCG

	GCG position	Medium	Cell density (x10^6 cells/ml)		Cell number in wound space			Accumulated distance (μm)	
	(μm)		L	R	N_L	N_R	N_L/N_R	L	R
NEAR	423 ± 47	L-15	5.1 ± 0.3	4.9 ± 0.3	49.4 ± 9.9	32.2 ± 10.6	1.57 ± 0.17	175 ± 30	95 ± 16
FAR	1529 ± 51*	L-15/hepes	5.1 ± 0.7	5.1 ± 0.7	33.4 ± 5.2*	35.2 ± 9.7	0.98 ± 0.13*	155 ± 21	193 ± 20*

* $p < 0.05$, comparisons between NEAR and FAR

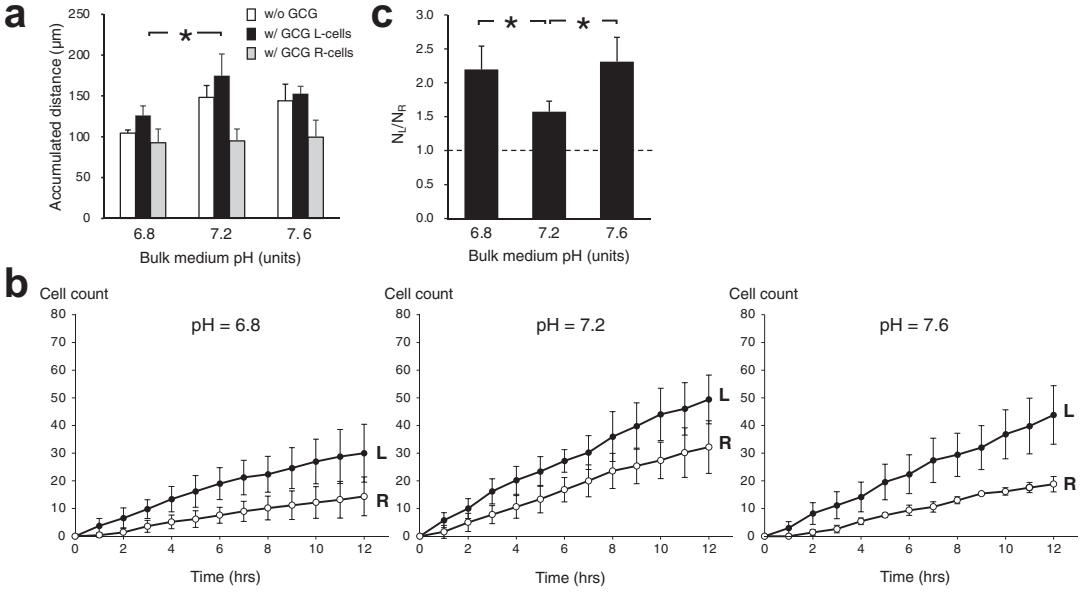

Fig. 2 Migration behaviors of MDA-MB-231 cells under GCG. (**a**). Accumulated distance of cells initially located at the left (L) and right (R) boundaries. Due to the bias for directing the cell to higher pH regions (right side) where the space was crowded with cells (R-side, see Fig. 1b), migrations were significantly hindered in the R-cells. Cell migration was most active in L-15 medium with pH = 7.2. (**b**). Directional migration represented by the number of cells migrating in the wound space from the left and right boundaries. (**c**). Number of cells migrating to the wound space at 12 h. $N_L/N_R > 1$ indicates a directional migration from the left to right, i.e., toward higher pH/O_2. *, $p < 0.05$

(Fig. 1c). In contrast, cells located at ~1500 μm from the open-end of GCG (FAR), such heterogeneous migration was not demonstrated (N_L/N_R ~ 1). In this region, pH gradients should be minimal (due to hepes, Fig. 1d), while O_2 gradients should be present at a physiological extracellular O_2 (~5%, Fig.1c).

Effect of Average pH in the Bulk Medium We determined the migration of MDA-MB-231 cells located 415 ± 55 μm inside from the open-end of GCG. The pH gradients in this region were 0.22, 0.32 and 0.29 units/mm for the bulk medium pH of 6.8, 7.2 and 7.6, respectively (data not shown). Without GCG, accumulated distances of cell migration in 12 h were 105 ± 4 μm, 148 ± 15 μm and 144 ± 21 μm for the medium pH 6.8, 7.2 and 7.6, respectively. Upon introducing GCG, accumulated distances in the L-cells significantly increased ($p < 0.05$, Fig.2a) where cell migration was significantly accelerated at pH = 7.2 compared to cells at pH = 6.8.

With regard to the directionality, cells initially located near the left boundary (L) more actively migrated to the wound space, compared to the cells initially located near the right boundary (R) for all bulk medium pH tested (Fig. 2b). These results indicate a directional cell migration

toward higher pH as shown in Fig. 2c ($N_L/N_R > 1$). Interestingly, the directionality of cell migration as assessed by N_L/N_R was least prominent at pH = 7.2 (Figs.2c).

4 Discussions

In this study, we examined the influence of pH in the bulk extracellular medium to further elucidate our previous demonstrations of directional migration of MDA-MB-231 cells under extracellular pH/O_2 gradients [2]. Directional cell migrations were consistently demonstrated ($N_L/N_R > 1$) under GCG with the bulk medium pH of 6.8, 7.2 and 7.6 indicating that pH gradients with a magnitude of 0.2–0.3 units/mm (Fig.1d) were enough to direct cell migrations. In contrast, cell migration behaviors assessed by accumulated distance and N_L/N_R were significantly affected by the average level of extracellular pH (apart from its spatial gradient). In our previous study, we proposed a hypothesis for directional cell migration under gradients of extracellular pH [2]. In that, the migration of individual cells is random in direction, whereas the speed of migration is affected by extracellular pH of individual cells as demonstrated by others [3, 5]. In fact, our cells demonstrated a pH dependence in accumulated distance upon the extracellular pH (Fig. 2a) that is consistent with the previous reports. In our model, under a linear pH gradient, cells migrated, by chance, to the pH region where cell migration is relatively suppressed (i.e., peripheries of the bell shape) might be virtually trapped within this region, eventually producing a macroscopic heterogeneity of cell distribution in a pH gradient. Accordingly, a bell-shaped dependence of migration velocity upon pH is essential. A distinct feature of this model is that cells should only respond to pH gradients spanning a few hundred μm space and detection of pH gradient corresponding to the cell size (longitudinal length ~ 70 μm) by an individual cell may not be a prerequisite. The present result appears to support this hypothesis, although our model is only qualitative and further elaboration, by computer simulations for instance, is obviously needed.

In the series of our study, an important question to be answered is the role of extracellular gradients of O_2 concentration. In fact, we demonstrated directional cell migration under GCG, where gradients of both pH (0.2–0.3 units/mm) and O_2 (6%/mm) were present. In the previous study [2], we demonstrated that cell migration under GCG was completely abolished in hepes-buffered medium, highlighting substantial effects of extracellular pH gradients. Furthermore, we thought that the effect of O_2 gradients was negligible in these experiments because the average O_2 concentration at individual cells (~15%) is substantially higher than those in in vivo tissues [6] and the O_2 level at which intracellular signals such as HIF-1α, for example, operate [7]. However, this speculation has never been examined experimentally and the possibility of O_2 gradient as a cue for directional migration in vivo is still open to discussion. To answer this important question, we conducted in this study the migration assay at a physiological ~5% O_2 with ~6%/mm O_2 gradient (Fig. 1c) without pH gradients. We assumed that a 6% O_2/mm gradient is physiologically and pathophysiologically relevant because Helmlinger et al. [1] demonstrated in vivo in tumour tissue approximately 9% O_2/mm gradients. We did not demonstrate directional migration of MDA-MB-231 cells, where pH gradients were abolished, indicating that the extracellular O_2 gradient was not a predominant cue in MDA-MB-231 cells under GCG.

From these results, we conclude that extracellular pH gradient ranging 0.2–0.3 units/mm may direct migration of MDA-MB-231 cells in vitro and extracellular gradient of O_2 plays, if any, a minor role.

Acknowledgments This research was funded by JSPS KAKENHI Grant Number 17K07173.

References

1. Helmlinger G, Yuan F, Dellian M et al (1997) Interstitial pH and pO_2 gradients in solid tumors *in vivo*: high-resolution measurements reveal a lack of correlation. Nat Med 3:177–182

2. Takahashi E, Yamaguchi D, Yamaoka Y (2020) A relatively small gradient of extracellular pH directs migration of MDA-MB-231 cells in vitro. Int J Mol Sci 21:2565
3. Stüwe L, Müller M, Fabian A et al (2007) pH dependence of melanoma cell migration: protons extruded by NHE1 dominate protons of the bulk solution. J Physiol 585:351–360
4. Yahara D, Yoshida T, Enokida Y et al (2016) Directional migration of MDA-MB-231 cells under oxygen concentration gradients. Adv Exp Med Biol 923:129–134
5. Jagielska A, Wilhite KD, Van Vliet KJ (2013) Extracellular acidic pH inhibits oligodendrocyte precursor viability, migration, and differentiation. PLoS One 8:e76048
6. Swartz HM, Flood AB, Schaner PE et al (2020) How best to interpret measures of levels of oxygen in tissues to make them effective clinical tools for care of patients with cancer and other oxygen-dependent pathologies. Physiol Rep 8:e14541
7. Jiang BH, Semenza GL, Bauer C et al (1996) Hypoxia-inducible factor 1 levels vary exponentially over a physiologically relevant range of O_2 tension. Am J Phys 271:C1172–C1180

Blood Flow and Respiratory Gas Exchange in the Human Placenta at Term: A Data Update

Peter Vaupel and Gabriele Multhoff

Abstract

Reliable measurements using modern techniques and consensus in experimental design have enabled the assessment of novel data sets for normal maternal and foetal respiratory physiology at term. These data sets include (a) principal factors affecting placental gas transfer, e.g., maternal blood flow through the intervillous space (IVS) (500 mL/min) and foeto-placental blood flow (480 mL/min), and (b) O_2, CO_2 and pH levels in the materno-placental and foeto-placental circulation. According to these data, the foetus is adapted to hypoxaemic hypoxia. Despite flat oxygen partial pressure (pO_2) gradients between the blood of the IVS and the umbilical arteries of the foetus, adequate O_2 delivery to the foetus is maintained by the higher O_2 affinity of the foetal blood, high foetal haemoglobin (HbF) concentrations, the Bohr effect, the double-Bohr effect, and high foeto-placental (=umbilical) blood flow. Again, despite flat gradients, adequate CO_2 removal from the foetus is maintained by a high diffusion capacity, high foeto-placental blood flow, the Haldane effect, and the double-Haldane effect. Placental respiratory gas exchange is perfusion-limited, rather than diffusion-limited, i.e., O_2 uptake depends on O_2 delivery.

Keywords

Placental gas transfer · Foeto-placental blood flow · Foetal haemoglobin · Haemoglobin oxygen affinity

1 Introduction

The physiology of placental respiratory gas exchange was incompletely understood until a decade ago, since *in vivo* measurements of oxygen (O_2) and carbon dioxide (CO_2) levels remained elusive for logistical and ethical reasons. However, in the past two decades reliable measurements using advanced techniques and consensus in experimental design have enabled the assessment of novel data sets for the materno-placento-foetal gas transfer in the term foetus.

P. Vaupel (✉)
Department of Radiation Oncology, University Medical Center, University of Freiburg, Freiburg/Breisgau, Germany
e-mail: vaupel@uni-mainz.de

G. Multhoff
Department of Radiation Oncology and Central Institute for Translational Cancer Research (TranslaTUM), Klinikum rechts der Isar, Technical University Munich (TUM), Munich, Germany
e-mail: gabriele.multhoff@tum.de

F. Scholkmann et al. (eds.), *Oxygen Transport to Tissue XLIII*, Advances in Experimental Medicine and Biology 1395, https://doi.org/10.1007/978-3-031-14190-4_62

2 Methods

Methods used for assessing blood flow data include advanced Doppler ultrasound techniques and phase-contrast magnetic resonance imaging (MRI). The blood gas data are derived from blood samples drawn immediately after delivery by early chordocentesis of double-clamped umbilical cord segments (ideally before placenta-expulsion and before the baby's first breath), by transcutaneous chordocentesis under real-time ultrasound guidance or by blood oxygen level derived (BOLD) measures.

Based on a recent literature research, reliable data describing normal blood flow and respiratory gas exchange in the placenta in term foetus have been evaluated. In general, weighted mean values of the various parameters assessed in >200 term foetuses are presented in this mini review.

3 Basic Morphology of the Mature Placenta

The maternal, O_2-rich blood reaches the large intervillous space (IVS) of the placenta (IVS ≈ 200 mL) through approximately 120 spiral arteries, the terminal branches of the uterine arteries, which eject the maternal blood through orifices in the septated basal plate of the uterine wall into the IVS ('open circulation'). The 'arterialised' IVS bathes the branched chorionic villi which arise from the chorionic plate of the foetal part of the placenta. The villi contain the foetal capillaries which are separated from the maternal blood in the IVS by a 2–3 μm thin endo-epithelial membrane (thus defining the diffusion distance for O_2 and CO_2). The maternal blood in the IVS drains through venous orifices in the basal plate, finally entering the uterine veins.

Foeto-placental blood supply originates from 2 umbilical arteries (with deoxygenated blood). The oxygenated blood travels from the IVS of the placenta to the foetus via a single umbilical vein.

The mature placenta has a mean mass of ≈640 g and a villous surface area of 12–13 m^2, the effective exchange area being 1.8 m^2.

4 Utero-placental and Foeto-placental Units: Blood Flow and Differential Oxygen Affinity of Haemoglobin

Key parameters determining the O_2 transfer are as follows (all values are weighted means, see Fig. 1, e.g., [1–8]).

(a) *Total utero-placental blood flow* (UP-BF): 830 mL/min (=12–14% of maternal cardiac output). BF through combined utero-placental tissues: 330 mL/min (=40% of UP-BF), with evidence of substantial arterio-venous shunt flow (≈25–30%) in the sub-placental myometrium [8].

BF through the IVS: 500 mL/min (145 mL/min/kg foetal mass, i.e., 60% of UP-BF). Renewal of blood within IVS ≈ 2.5 times/min. BF through IVS is highly heterogeneous between different compartments [8, 9].

Note: Maternal supine position is associated with reduced UP-BF and decreased foeto-umbilical venous blood flow, and thus results in a relevant reduction in O_2 delivery to the foetus [10].

(b) *Foeto-umbilical-placental blood flow* (FP-BF): 480 mL/min (140 mL/min/kg foetal mass, i.e., ≈30% of combined ventricular output (CVO = 465 mL/min/kg foetal mass).
(c) *Mean haemoglobin concentration* (cHb) in term maternal blood: 12 g/dL, and in foetal blood: 17 g/dL.
(d) The acute *O_2-half saturation pressure of haemoglobin (p50)* is 30 mmHg for the maternal blood (HbA, borderline alkalosis and anaemia), and 19 mmHg for the foetal blood (70% HbF with low binding of 2,3-bisphosphoglycerate, 2,3-BPG).

5 Key Parameters of the O_2 Supply to the Term Foetus

In addition to the data listed in Figs. 1 and 2, the following parameters are mandatory to describe the O_2 supply to the foetus (e.g., [13–30]): (a)

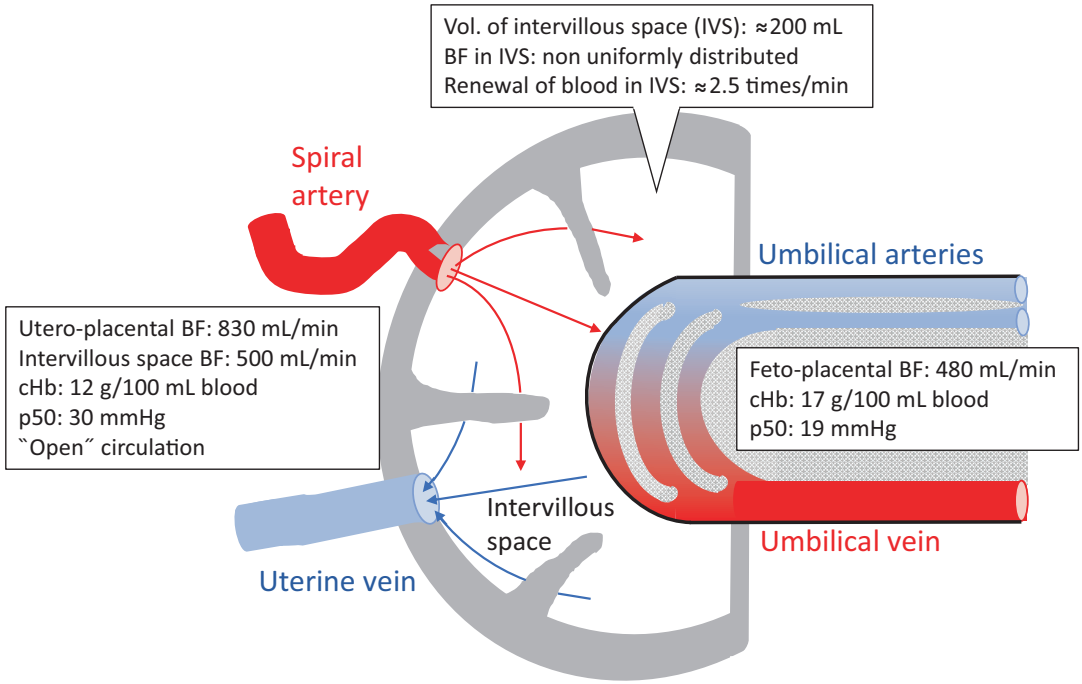

Fig. 1 Blood flow and differential oxygen-haemoglobin binding in the utero-placental and foeto-placental units. BF: blood flow, cHb: haemoglobin concentration, p50: O_2-half saturation pressure

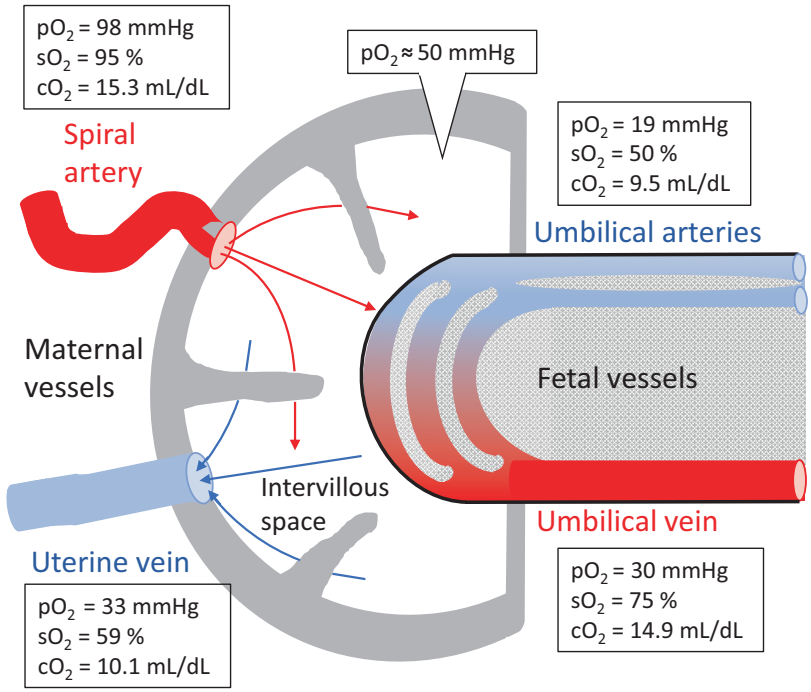

Fig. 2 Oxygenation status in the utero-placental and foeto-umbilical-placental units at term. pO_2: oxygen partial pressure, sO_2: HbO_2 saturation, cO_2: oxygen concentration. Due to spatial heterogeneities, IVS data are best estimates [11, 12]

ΔcO_2 between spiral arteries and uterine veins: 5.2 mL/dL; (b) ΔcO_2 in umbilical circulation; 5.4 mL/dL; (c) O_2 extraction (maternal blood): 34%; (d) O_2 delivered by maternal blood/taken up by the foetus: 26 mL/min (= 7.6 mL/min/kg foetal mass); (e) best estimates for the IVS: $pO_2 \approx 50$ mmHg, $sO_2 \approx 80\%$, $cO_2 \approx 13$ mL/dL; (f) best estimates for foetal (villous) capillaries: $pO_2 \approx 25$ mmHg, $sO_2 \approx 60\%$, $cO_2 \approx 12$ mL/dL; (g) mean ΔpO_2 between IVS and foetal capillaries: ≈25 mmHg, and (h) O_2 diffusion capacity**:** ≈1 mL/min/mmHg.

6 Facilitation of O_2 Transfer to the Foetus

Despite flat gradients between the blood in the IVS and the foetal capillaries ($\Delta pO_2 \approx 25$ mmHg), adequate O_2 delivery is maintained by (a) high O_2 affinity of the foetal blood (HbF), (b) high haemoglobin concentrations, (c) high fractional feto-placental blood flow, (d) the 'placental' Bohr-effect, and (e) the 'foetal' double-Bohr-effect. The two latter mechanisms facilitate the O_2 transfer from the maternal to the foetal blood. The 'placental' Bohr-effect involves the foetal unloading of H^+ and CO_2 into the maternal blood which, in turn, leads to a right-shift of the maternal HbO_2 dissociation curve, and thus to a release of O_2, which is then available for the foetus. The 'foetal' Bohr-effect describes the foeto-maternal CO_2 and H^+ transfer, which leads to a left shift of the foetal HbO_2- dissociation curve, i.e., to an increase in the O_2 affinity and thus O_2 uptake by foetal blood. About 8% of the O_2 exchange in the placenta is associated with the double-Bohr-effect.

7 Key Parameters Governing the CO_2 Transfer from the Foeto-placental Compartment into the Maternal Blood

Beyond the data listed in Figs. 1 and 3, the following parameters additionally determine the CO_2 transfer from the foetus into the maternal compartment (e.g., [14, 24–30]: (a) ΔcCO_2 between umbilical arteries and umbilical vein: 6.0 mL/dL; (b) foetal CO_2 release rate: 29 mL/min (=8.5 mL/min/kg foetal weight); (c) mean ΔpCO_2 between foetal capillaries in the chorionic villi and IVS: ≈6 mmHg, and (d) CO_2 diffusion capacity: 4 mL/min/mmHg.

8 Facilitation of CO_2 Transfer from the Foetus into the Maternal Blood

Despite the very flat pCO_2 gradient (≈ 6 mmHg) between the blood in the villous capillaries and the IVS, an adequate CO_2 transfer is maintained by the following mechanisms: (a) high foeto-placental blood flow, (b) large Krogh's diffusion coefficient, (c) the 'placental' Haldane-effect, and (d) the 'foetal' double-Haldane-effect. The 'placental' Haldaneeffect involves the unloading of oxygen from the maternal blood which increases the affinity of haemoglobin for CO_2 and subsequent CO_2 binding. The 'foetal' double-Haldane-effect includes the O_2 uptake into the villous capillaries which decreases the affinity of haemoglobin for CO_2 and accelerates foetal CO_2 release into the maternal blood of the IVS. About 46% of the CO_2 exchange in the placenta is associated with the double-Haldane-effect. Hyperventilation of the mother, an adaptation in pregnancy, also supports CO_2 transfer from the foetal into the maternal blood in the placenta.

9 Foetal Respiratory Quotient

The foetal respiratory quotient (RQ = CO_2 release/O_2 uptake) at term is 1.11 (indicating a preferential use of glucose for energy metabolism and lipogenesis of the growing foetus [31]).

10 Key Conclusions

We conclude that (a) the foetus is confronted with a hypoxaemic environment (i.e., hypoxaemic IVS), (b) this condition is compensated by the foetus via mechanisms/adaptations that are

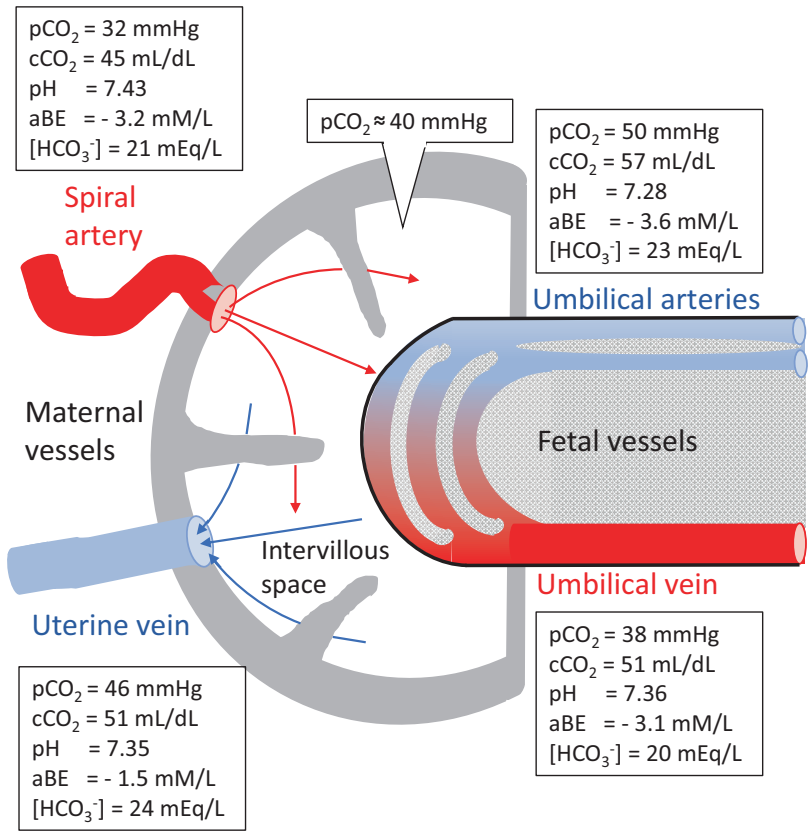

Fig. 3 Parameters determining the CO_2 exchange between foetal and maternal blood, and data reflecting the acute acid-base status in the term placenta. pCO_2: CO_2 partial pressure, cCO_2: CO_2 concentration, aBE: acute base excess

Table 1 Respiratory gas parameters and pH values in unusual environments: Foetus at term *versus* acclimatization to high altitude

Parameters/conditions	Fetus at term	High altitude adaptation (e.g., climbers at Mount Everest), see refs. [32, 33]
Oxygenation status	Hypoxemic hypoxia	Hypobaric hypoxia
Haemoglobin type	HbF	HbA
Arterial pO_2 (mmhg)	30 (umbilical vein)	25
Arterial sO_2 (%)	75 (umbilical vein)	54
cHb (g/dL)	≈17	≈18
Arterial pCO_2 (mmHg)	38 (umbilical vein)	13 (hyperventilation)
Arterial pH	7.36 (umbil. vein)	7.55 (alkalosis)
2,3 bisphosphoglycerate- (2,3 BPG-) level / binding	Decreased	Increased
Hb-O_2 affinity	Increased (due to lower 2.3 BPG)	Increased (due to alkalosis)

different to those observed in high-altitude climbers on Mount Everest (as described in Table 1), (c) placental respiratory gas exchange is perfusion-limited, rather than diffusion-limited, i.e., O_2 uptake by the foetus is dependent on O_2 delivery.

Acknowledgement The authors thank Anett Lange for her help in preparation of this chapter, and Professor A. Graham Pockley, Nottingham Trent University (UK), for linguistic support.

References

1. Sutton MSM, Theard MA, Bhatia SJS et al (1990) Changes in placental blood flow in the normal human fetus with gestational age. Pediatr Res 28:383–387
2. Kiserud T (2005) Physiology of the fetal circulation. Sem Fetal Neonat Med 10:493–503
3. Acharya G, Wilsgaard T, Berntsen GKR et al (2005) Doppler derived umbilical artery absolute velocities and their relationship to fetoplacental volume blood flow: a longitudinal study. Ultrasound Obstet Gynecol 25:444–453
4. Seed M, van Amerom JFP, Yoo SH et al (2012) Feasibility of quantification of the distribution of blood flow in the normal human fetal circulation using CMR: a cross-sectional study. J Cardiovasc Magn Reson 14:79
5. Prsa M, Sun L, van Ameron J et al (2014) Reference ranges of blood flow in the major vessels of the normal human fetal circulation at term by phase-contrast magnetic resonance imaging. Circ Cardiovasc Imaging 7:663–670
6. Acharya G, Sonesson SE, Flo K et al (2016) Hemodynamic aspects of normal human fetoplacental (umbilical) circulation. Acta Obstet Gynecol Scand 95:672–682
7. Krishnamurthy U, Yadav BK, Jella PK et al (2018) Quantitative flow imaging in the human umbilical vessels in-utero using non-gated 2D phase contrast MRI. J Magn Reson Imaging 48:283–289
8. Francis ST, Duncan KR, Moore RJ et al (1998) Non-invasive mapping of placental perfusion. Lancet 351:1397–1399
9. Welsh AW, Fisk NM (2001) Regional variation in power Doppler perfusion measurements within normal placenta. Ultrasound Obstet Gynecol 18(Suppl 1):13
10. Couper S, Clark A, Thompson JMD et al (2021) The effects of maternal position, in late gestation pregnancy, on placental blood flow and oxygenation: an MRI study. J Physiol 599:1901–1915
11. Sørensen A, Peters D, Fründ E et al (2013) Changes in human placental oxygenation during maternal hyperoxia estimated by blood oxygen level-dependent magnetic resonance imaging (BOLD-MRI). Ultrasound Obstet Gynecol 42:310–314
12. Hutter J, Harteveld JLH et al (2020) Perfusion and apparent oxygenation in the human placenta. Magn Reson Med 83:549–560
13. Blickstein I, Green T (2007) Umbilical cord blood gases. Clin Perinatol 34:451–459
14. Armstrong L, Stenson BJ (2007) Use of umbilical cord blood gas analysis in the assessment of the newborn. Arch Dis Child Fetal Neonatal Ed 92(6):F430–F434
15. Wiberg N, Källen K, Olofsson P (2008) Delayed umbilical cord clamping at birth has effects on arterial and venous blood gases and lactate concentrations. BJOG 115:697–703
16. Acharya G, Sitras V (2009) Oxygen uptake of the human fetus at term. Acta Obstet Gynecol 88:104–109
17. Kotaska K, Urinovska R, Klapkova et al (2010) Re-evaluation of cord blood arterial and venous reference ranges for pH, pO_2, pCO_2, according to spontaneous or cesarean delivery. J Clin Lab Anal 24:300–304
18. Higgins C (2014) Umbilical-cord blood gas analysis. Acutecaretesting.org
19. Carter AM (2015) Placental gas exchange and the oxygen supply to the fetus. Compr Physiol 5:1381–1403
20. Manomayangkul K, Siriussawakul A et al (2016) Reference values for umbilical cord blood gases of newborns delivered by elective cesarean section. J Med Assoc Thail 99:611–617
21. Nye GA, Ingram E, Johnstone ED et al (2018) Human placental oxygenation in late gestation: experimental and theoretical approaches. J Physiol 596:5523–5534
22. Saini BS, Morrison JL, Seed M (2020) Gas exchange across the placenta. In: Lapinsky S, Plante L (eds) Respiratory disease in pregnancy. Cambridge University Press, Cambridge/New York
23. Saneh H, Mendez MD, Srinivasan VN (2021) Cord blood gas. In: StatPearls. StatPearls Publishing, Treasure Island
24. De Paco C, Florido J, Garrido MC et al (2011) Umbilical cord blood acid-base and gas analysis after early versus delayed cord clamping in neonates at term. Arch Gynecol Obstet 283:1011–1014
25. Butterwegge M, Kappen R, Rath W (2012) Changes in umbilical cord blood acid-base status after delivery in dependence on time interval- a continuing forensic problem. Z Geburtsh Neonatol 216:253–258
26. Omo-Aghoja L (2014) Maternal and fetal acid-base chemistry: a major determinant of perinatal outcome. Ann Med Health Sci Res 4:8–17
27. Cantu J, Szychowski JM, Li X et al (2014) Predicting fetal acidemia using umbilical venous cord gas parameters. Obstet Gynecol 124:926–932
28. McNamara E-KA (2017) Oxygen transport and delivery. Fetal Neonat Physiol 1:724–737.e2
29. Zaigham M, Källen K, Olofsson (2019) Gestational age-related reference values for Apgar score and umbilical cord arterial and venous pH in preterm and term newborns. Acta Obstet Gynecol Scand 98:1618–1623
30. Saini BS, Portnoy DJRT et al (2020) Normal human and sheep fetal vessel oxygen saturations by T2 magnetic resonance imaging. J Physiol 598:3259–3281
31. Melzer K, Kayser B, Schutz Y (2014) Respiratory quotient evolution during normal pregnancy: what nutritional or clinical information can we get out of it? Eur J Obstet Gynecol Reprod Biol 176:5–9
32. Grocott MPW, Martin DS, Levett DZH et al (2009) Arterial blood gases and oxygen content in climbers on Mount Everest. N Engl J Med 360:140–149
33. Cobb AB, Levett DZH, Mitchell K et al (2021) Physiological responses during ascent to high altitude and the incidence of acute mountain sickness. Physiol Rep 9:e14809

Oxyhaemoglobin Level Measured Using Near-Infrared Spectrometer Is Associated with Brain Mitochondrial Dysfunction After Cardiac Arrest in Rats

Yu Okuma, Koichiro Shinozaki, Tsukasa Yagi, Kei Hayashida, Tomoaki Aoki, Tai Yin, Takeyuki Kiguchi, Taku Iwami, and Lance B. Becker

Abstract

Cerebral blood oxygenation (CBO), measured using near-infrared spectroscopy (NIRS), can play an important role in post-cardiac arrest (CA) care as this emerging technology allows for noninvasive real-time monitoring of the dynamic changes of tissue oxygenation. We recently reported that oxyhaemoglobin (oxy-Hb), measured using NIRS, may be used to evaluate the quality of chest compressions by monitoring the brain tissue oxygenation, which is a critical component for successful resuscitation. Mitochondria are the key to understanding the pathophysiology of post-CA oxygen metabolism. In this study, we focused on mitochondrial dysfunction, aiming to explore its association with CBO parameters such as oxy-Hb and deoxyhaemoglobin (deoxy-Hb) or tissue oxygenation index (TOI). Male Sprague-Dawley rats were used in the study. We applied NIRS between the nasion and the upper cervical spine. Following 10 min of CA, the rats underwent cardiopulmonary resuscitation (CPR) with a bolus injection of 20 μg/kg epinephrine. At 10 and 20 min after CPR, brain, and kidney tissues were collected. We isolated mitochondria from these tissues and evaluated the association between CBO and mitochondrial oxygen consumption ratios. There were no significant differences in the mitochondrial yields (10 vs. 20 min after resuscitation: brain, 1.33 ± 0.68 vs. 1.30 ± 0.75 mg/g; kidney, 19.5 ± 3.2 vs. 16.9 ± 5.3 mg/g, respectively). State 3 mitochondrial oxygen consumption rates, known as ADP-stimulated respiration, demonstrated a significant difference at 10 vs. 20 min after CPR (brain, 170 ± 26 vs. 115 ± 17 nmol/min/mg protein; kidney, 170 ± 20 vs. 130 ± 16 nmol/min/mg protein, respectively), whereas there was no significant difference in ADP non-dependent state 4 oxygen consumption rates (brain, 34.0 ± 6.7 vs. 31.8 ± 10 nmol/min/mg protein; kidney, 29.8 ± 4.8 vs. 21.0 ± 2.6 nmol/min/mg protein, respectively). Consequently,

Y. Okuma (✉)
Feinstein Institute for Medical Research, Northwell Health System, Great Neck, NY, USA

Department of Neurological Surgery, Sonoda Daiichi Hospital, Tokyo, Japan

Department of Neurological Surgery, Fukuyama City Hospital, Fukuyama, Japan

K. Shinozaki · T. Yagi · K. Hayashida · T. Aoki · T. Yin · L. B. Becker
Feinstein Institute for Medical Research, Northwell Health System, Great Neck, NY, USA

T. Kiguchi · T. Iwami
Kyoto University Health Service, Kyoto, Japan

F. Scholkmann et al. (eds.), *Oxygen Transport to Tissue XLIII*, Advances in Experimental Medicine and Biology 1395, https://doi.org/10.1007/978-3-031-14190-4_63

the respiratory control ratio (RCR = state 3/state 4) showed a significant difference over time, but this was only noted in the brain (brain, 5.0 ± 0.29 vs. 3.8 ± 0.64; kidney, 5.8 ± 0.53 vs. 6.2 ± 0.25 nmol/min/mg protein, respectively). The oxy-Hb levels had a dynamic change after resuscitation, and they had a significant association with the RCR of the brain mitochondria (r = 0.8311, p = 0.0102), whereas deoxy-Hb and TOI did not (r = −0.1252, p = 0.7677; r = 0.4186, p = 0.302, respectively). The RCRs of the kidney mitochondria did not have a significant association with CBO (oxy-Hb, r = −0.1087, p = 0.7977; deoxy-Hb, r = 0.1565, p = 0.7113; TOI, r = −0.1687, p = 0.6896, respectively). The brain mitochondrial respiratory dysfunction occurred over time, and it was seen at the time points between 10 and 20 min after CPR. The oxy-Hb level was associated with brain mitochondrial dysfunction during the early post-resuscitation period.

Keywords

NIRS · Cerebral blood oxygenation · Cardiopulmonary resuscitation · Tissue oxygenation index · Mitochondria

1 Introduction

Recent guidelines for cardiopulmonary resuscitation (CPR) state that high-quality CPR plays a key role in improving patient survival from cardiac arrest (CA) [1]. Previously, we introduced that the oxyhaemoglobin (oxy-Hb) levels between CA and during CPR have the potential to evaluate the quality of CPR in a rat CA model [2]. We also showed that near-infrared spectroscopy (NIRS) identified a decrease in oxy-Hb after the return of spontaneous circulation (ROSC), and this result has the potential to aid understanding of the mechanism of how and why adrenaline interferes with the improvement of neurological outcomes post-CA [3]. In this study, we focused on the relationship between mitochondrial function and cerebral blood oxygenation (CBO) parameters, including oxy-Hb, after CA.

2 Methods

2.1 Animal Preparation

The Institutional Animal Care and Use Committees of the Feinstein Institutes for Medical Research approved the study protocol. The details of the methods for a rat asphyxia CA model have been described previously [4, 5]. Briefly, adult male Sprague-Dawley rats (450–550 g, Charles River Laboratories) were anaesthetised with 4% isoflurane (Isosthesia, Butler-Schein AHS) and intubated with a 14-gage angio catheter (Surflo, Terumo Medical Corporation). Anaesthesia was maintained with isoflurane 2% at a fraction of inspired O_2 (FiO_2) of 0.3 under mechanical ventilation. The left femoral artery was cannulated (sterile polyethylene-50 catheter inserted for 20 mm) for continuous arterial pressure monitoring. The oesophageal temperature was maintained at 36.5 ± 1.0 °C during the surgical procedure. The left femoral vein was cannulated with a polyethylene-50 catheter, which was advanced into the inferior vena cava for drug infusion. We attached a NIRS (NIRO-200NX, Hamamatsu Photonics, Japan) from the nasion to the upper cervical spine of the rats. The distance between the emission and the detection probes was 3 cm. We examined the mean arterial pressure (MAP) and oxy/deoxy-Hb and tissue oxygenation index (TOI). The NIRS device recorded the oxygen saturation level (TOI) and the changes in concentration of oxy-Hb and deoxy-Hb in real-time (100 Hz). Data averaged every 20 s were used. After instrumentation setup, the neuromuscular blockade was achieved by slow intravenous administration of 2 mg/kg of vecuronium bromide (Hospira, USA). Asphyxia was induced in the rats by switching off the ventilator, and CA normally occurred 3–4 min after asphyxia started. We defined CA as a MAP below 20 mmHg; CA was completely untreated for 10 min after asphyxia. Mechanical ventilation was restarted at a FiO_2 of 1.0, and manual CPR

was delivered to the CA animals. Chest compressions were performed at a rate of 240–300 per min. At 30 s after the beginning of CPR, a 20 μg/kg bolus of adrenaline was given to the animals through the venous catheter. Following ROSC, to evaluate the brain mitochondrial dysfunction in conjunction with the measurement of CBO, we sacrificed the rats and collected the tissues at two-time points: 10 min and 20 min after CPR. Concerning CBO, we calculated the delta, which was the difference between the current average and the average of the end of the asphyxia period regarded as a baseline.

2.2 Isolation of Mitochondria and Evaluation of Mitochondrial Respiratory Function

All operations were performed at 4 °C. Harvested tissues were immediately placed in a mitochondrial isolation buffer (MESH) composed (in mM) of 210 mannitol, 70 sucrose, 10 Hepes, and 0.2 EGTA at pH 7.3 with 0.2% w/v fatty acid free-BSA (MESH-BSA). The tissue was blot-dried on filter paper, weighed, and placed in MESH-BSA. Low-speed centrifugation was set at 5600 × g for 1 min, and high-speed centrifugation was set at 12,000 × g for 6 min. Finally, the mitochondrial yields were expressed as mg mitochondrial protein/g tissue. For mitochondria isolation, the tissues were diluted in MESH-BSA for homogenisation. The homogenate was centrifuged at low speed, and the supernatant was collected. This supernatant was then centrifuged at high speed. The supernatant was gently decanted with pipettes without disturbing the mitochondria pellet. Finally, the pellet was resuspended in MESH without BSA and centrifuged at high speed. The mitochondria pellet was suspended, and the mitochondrial concentration was determined by the BCA assay using BSA as the standard. Concerning the method of measuring oxygen consumption rate (OCR), we used a Clark-type oxygen electrode (Strathkelvin, Motherwell, UK). Mitochondria were assayed in an assay buffer containing 80 mM KCl, 50 mM MOPS, 1 mM EGTA, 5 mM KH_2PO_4, and 1 mg defatted BSA/mL at pH 7.4. ADP-dependent (state 3), ADP-limited (state 4), and DNP-dependent (uncoupled) OCR were measured at 30 °C in 150 μL of the mitochondrial suspension (0.5 mg/mL) using glutamate + malate as substrates. Rates of substrate oxidation were expressed as nano-atoms oxygen consumed/minute/mg mitochondrial protein [6, 7].

2.3 Statistical Analysis

Data are presented as mean and standard deviation. The Mann–Whitney U test was used to compare variables between two independent groups. Other values were compared between the groups using the one-way analysis of variance with post-hoc analysis using Tukey's test. In the comparison of multiple parameters, correlation coefficient (r) values were collected. All statistical analyses were conducted using JMP (version 10.1 software: SAS Institute, Cary, NC, USA). P-values less than 0.05 were considered statistically significant.

3 Results

ROSC was achieved in all animals. First, we determined the mitochondrial respiratory function by comparing the 10-min post-CPR group with the 20-min post-CPR group. Regarding the yield of isolated tissues, there was no significant difference between the two groups (brain, 1.33 ± 0.68 and 1.30 ± 0.75 mg/g; kidney, 19.5 ± 3.2 and 16.9 ± 5.3 mg/g, respectively). Regarding state 3 OCR, there were significant differences in both brain and kidney tissues between the two groups (brain, 170 ± 26 and 115 ± 17 nmol/min/mg protein; kidney, 170 ± 20 and 130 ± 16 nmol/min/mg protein, respectively). Regarding state 4 OCR, there was no significant difference among the groups (brain, 34.0 ± 6.7 and 31.8 ± 10 nmol/min/mg protein; kidney, 29.8 ± 4.8 and 21.0 ± 2.6 nmol/min/mg protein, respectively). Regarding the respiratory control ratio (RCR), there was a significant difference in

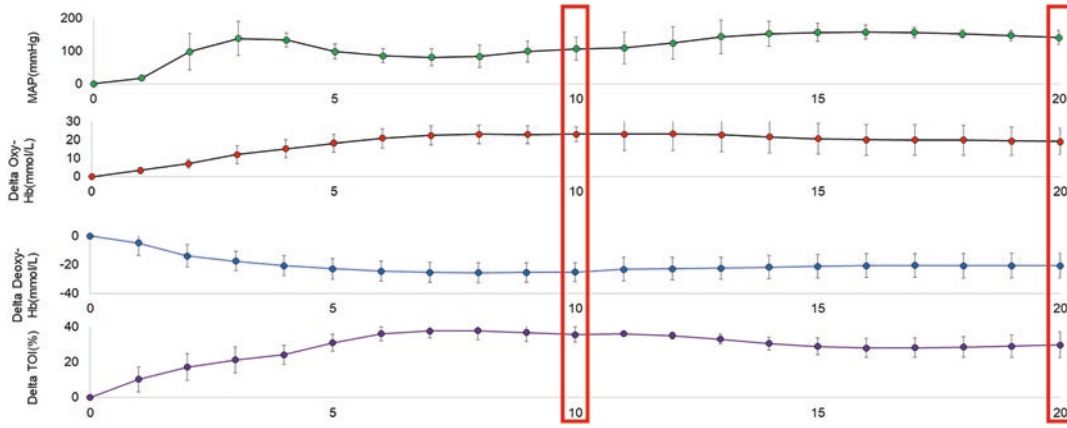

Fig. 1 The dynamic changes of the mean arterial pressure and differences in cerebral blood oxygenation, including oxyhaemoglobin and deoxyhaemoglobin and tissue oxygenation index, during the three types of chest compression. The delta is the difference between the current average and the average at the end of the asphyxia period, which is regarded as the baseline

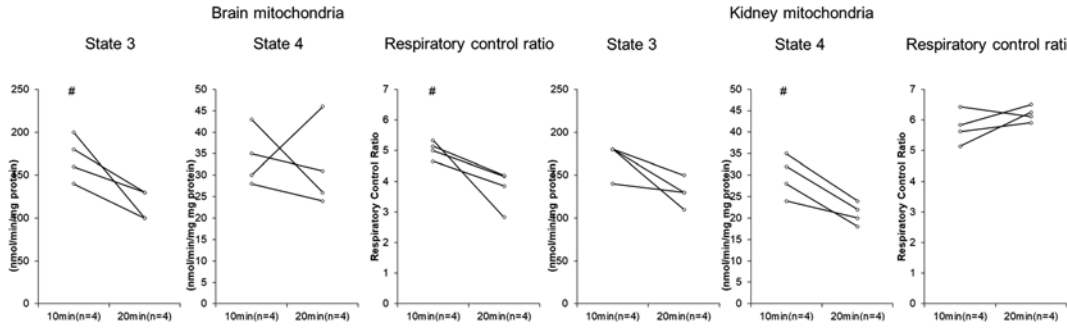

Fig. 2 The evaluation of mitochondrial respiratory function isolated in the brains and kidneys of the animal models. 10 min, 10-min-after-CPR; 20 min, 20-min-after-CPR. #P < 0.05 compared with the 20-min-after-CPR group

the brains between the two groups (brain, 5.0 ± 0.29 and 3.8 ± 0.64; kidney, 5.8 ± 0.53 and 6.2 ± 0.25 nmol/min/mg protein, respectively) (Fig. 1). We next evaluated the MAP and CBO by comparing the 10-min post-CPR group with the 20-min post-CPR group, which did not reveal any significant differences between the groups among all parameters (MAP, 107 ± 35 and 141 ± 21 mmHg, p = 0.107; delta oxy-Hb, 23.1 ± 4.0 and 19.1 ± 7.2 nmol/L, p = 0.552; delta deoxy-Hb, −25.4 ± 6.7 and −20.8 ± 9.0 nmol/L, p = 0.445; delta TOI, 35.8 ± 4.4 and 29.9 ± 7.3%, respectively) (Fig. 2). Finally, we examined the correlation between brain mitochondrial function and CBO. Concerning the brain mitochondria, only oxy-Hb showed a significant correlation with the RCR (r = 0.8311, p = 0.0102), whereas deoxy-Hb and TOI did not show a significant correlation with the RCR (r = −0.1252, p = 0.7677; r = 0.4186, p = 0.302, respectively) Concerning the kidney mitochondria, none of the CBO parameters showed a significant correlation with the RCR (oxy-Hb, r = −0.1087, p = 0.7977; deoxy-Hb, r = 0.1565, p = 0.7113; TOI, r = −0.1687, p = 0.6896, respectively) (Table 1).

Table 1 Relationship between cerebral blood oxygenation (CBO), including oxyhaemoglobin (Oxy-Hb) and deoxyhaemoglobin (Deoxy-Hb), tissue oxygenation index (TOI), and brain mitochondrial function or kidney mitochondrial function, including state 3, state 4, and respiratory control ratio (RCR)

	CBO		Brain mitochondrial function			Kidney mitochondrial function		
	Deoxy-Hb (n = 8)	TOI (n = 8)	State3 (n = 8)	State4 (n = 8)	RCR (n = 8)	State3 (n = 8)	State4 (n = 8)	RCR (n = 8)
Oxy-Hb	−0.069	0.23	0.42	−0.37	**0.83***	0.70	0.59	−0.11
Deoxy-Hb		**−0.91***	−0.49	−0.51	−0.13	−0.12	−0.17	0.16
TOI			0.53	0.30	0.42	0.21	0.22	−0.17
State3				0.58	0.55		**0.94***	−0.41
State4					−0.35			−0.70

*$P < 0.05$

4 Discussion

This experiment reported here demonstrates that the dynamic change of oxy-Hb was associated with the RCR of the brain mitochondria but not that of the kidney. This is the first study of its kind that investigated the relationship between oxy-Hb and mitochondrial dysfunction after CPR. Our previous study has revealed that the values of oxy-Hb during the CPR phase could support the quality of CPR. Some studies have brought up the concept of evaluating brain mitochondrial dysfunction by using NIRS. One of the novel methods utilised CBO and brain cytochrome-c-oxidase [8], and NIRO was reported in a clinical study [9]. Utilising NIRS measurements is difficult due to the large variability of CBO between individuals. To adjust for differences between individuals, we standardised the values of CBO with itself during CA (asphyxiation). Previously, our study showed that the CBO, as detected by NIRS and MAP, had similar levels between 10 and 20 min after CPR. Thus, in this study, we determined whether NIRS could serve as a monitor for the ischemic-reperfusion acute phase 10 and 20 min after CPR. The present study has several limitations. The CBO and mitochondrial dysfunction should be compared not only at two-time points but also at additional time points, which may be realised in future studies. The extent to which ischemic and reperfusion injuries are involved also needs to be evaluated. The evaluation of mitochondrial dysfunction other than that from oxygen consumption measurements, or the evaluation of brain damage based on nonmitochondrial mechanisms, should also be conducted. For example, it might be helpful to measure mitochondrial enzyme activities such as citrate synthetase [10] to further evaluate the health status /quality of the isolated mitochondria at the two time points used in this study. Additionally, it is necessary to investigate whether the levels of oxy-Hb in other organs are correlated with the level of mitochondrial dysfunction in those organs.

5 Conclusion

Oxy-Hb has the potential to correlate with the brain mitochondrial dysfunction and Oxy-Hb may be a useful parameter of the post-CA syndrome.

References

1. Neumar RW, Shuster M, Callaway CW et al (2015) Part 1: Executive summary: 2015 American Heart Association guidelines update for cardiopulmonary resuscitation and emergency cardiovascular care. Circulation 132(18 Suppl 2):S315–S367
2. Okuma Y, Becker LB, Yagi T et al (2021) Evaluation of the quality of chest compression with oxyhemoglobin level by near-infrared spectroscopy in a rat asphyxia cardiac arrest model. Adv Exp Med Biol 1269:265–269
3. Okuma Y, Yagi T, Yin T et al (2021) Effect of adrenaline on cerebral blood oxygenation measured by NIRS in a rat asphyxia cardiac arrest model. Adv Exp Med Biol 1269:39–43
4. Okuma Y, Shinozaki K, Yagi T et al (2019) Combination of cardiac and thoracic pump theories in rodent cardiopulmonary resuscitation: a new method of three-side chest compression. Intensive Care Med Exp 7:62
5. Okuma Y, Aoki T, Miyara SJ et al (2021) The evaluation of pituitary damage associated with cardiac arrest: an experimental rodent model. Sci Rep 11:629
6. Kim J, Perales Villarroel JP, Zhang W et al (2016) The responses of tissues from the brain, heart, kidney, and liver to resuscitation following prolonged cardiac arrest by examining mitochondrial respiration in rats. Oxidative Med Cell Longev 2016:1–7
7. Okuma Y, Becker LB, Hayashida K et al (2021) Effects of post-resuscitation normoxic therapy on oxygen-sensitive oxidative stress in a rat model of cardiac arrest. J Am Heart Assoc 10:e018773
8. Wang X, Tian F, Reddy DD et al (2017) Up-regulation of cerebral cytochrome-c-oxidase and hemodynamics by transcranial infrared laser stimulation: a broadband near-infrared spectroscopy study. J Cereb Blood Flow Metab 37:3789–3802
9. Holper L, Lan MJ, Brown PJ et al (2019) Brain cytochrome-c-oxidase as a marker of mitochondrial function: a pilot study in major depression using NIRS. Depress Anxiety 36:766–779
10. Aoki T, Okuma Y, Becker LB et al (2021) Methodological issue of mitochondrial isolation in acute-injury rat model: asphyxia cardiac arrest and resuscitation. Front Med 8:448

Changes in Oxygenation Levels During Moderate Altitude Simulation (Hypoxia-Induced): A Pilot Study Investigating the Impact of Skin Pigmentation in Pulse Oximetry

Victor Ochoa-Gutierrez, Selene Guerrero-Zuñiga, Julien Reboud, Mauro Pazmino-Betancourth, Andrew R. Harvey, and Jonathan M. Cooper

Abstract

The current COVID-19 pandemic has shown us that the pulse oximeter is a key medical device for monitoring blood-oxygen levels non-invasively in patients with chronic or acute illness. It has also emphasised limitations in accuracy for individuals with darker skin pigmentation, calling for new methods to provide better measurements. The aim of our study is to identify the impact of skin pigmentation on pulse oximeter measurements. We also explored the benefits of a multi-wavelength approach with an induced change of arterial oxygen saturation. A total of 20 healthy volunteers were recruited. We used time domain diffuse reflectance spectroscopy (TDDRS) from a broad band light source, collecting spectra from the index finger along with three different pulse oximeters used simultaneously for monitoring purposes. Five acute hypoxic events were induced by administering 11% FiO_2, produced by a Hypoxico altitude training system, for 120 sec through a face mask with a one-way valve. Our multi-wavelength approach revealed a correlation between the signature of skin pigmentation and the dynamic range of oxygen saturation measurements. Principal component analysis (PCA) showed separation between a range of different pigmented volunteers (PC1 = 56.00%) and oxygen saturation (PC2 = 22.99%). This emphasises the need to take into account skin pigmentation in oximeter measurements. This preliminary study serves to validate the need to better understand the impact of skin pigmentation absorp-

V. Ochoa-Gutierrez (✉)
Division of Biomedical Engineering, School of Engineering, University of Glasgow, Glasgow, UK

School of Physics and Astronomy, University of Glasgow, Glasgow, UK
e-mail: v.ochoa-gutierrez.1@research.gla.ac.uk

S. Guerrero-Zuñiga
National Institute of Respiratory Diseases (INER), Mexico City, Mexico

J. Reboud · J. M. Cooper
Division of Biomedical Engineering, School of Engineering, University of Glasgow, Glasgow, UK

M. Pazmino-Betancourth
Biodiversity, Animal Health & Comparative Medicine, MVLS, University of Glasgow, Glasgow, UK

A. R. Harvey
School of Physics and Astronomy, University of Glasgow, Glasgow, UK

F. Scholkmann et al. (eds.), *Oxygen Transport to Tissue XLIII*, Advances in Experimental Medicine and Biology 1395, https://doi.org/10.1007/978-3-031-14190-4_64

tion on optical readings in pulse oximeters. Multi-wavelength approaches have the potential to enable robust and accurate measurements across diverse populations.

Keywords

Time domain diffuse reflectance spectroscopy · Arterial oxygen saturation · Multiple wavelength spectrophotometer · Skin types

1 Introduction

Oxygen is required to sustain life and normal body function in humans; thus, an accurate measurement of arterial oxygen saturation (SaO_2) is an important physiological parameter to assess the health status of an individual [12]. Altitude response can vary widely among individuals due to differences in ventilatory response to hypoxia. Multiple techniques for non-invasive oxygenation monitoring have been developed, including pulse oximetry. A number of blood properties can be measured non-invasively using optical techniques through the skin. Devices developed for these measurements have proved invaluable in both emergency situations and long-term monitoring of patients in critical conditions. However, they are limited to a narrow oxygen range (80–100%) and do not take skin pigmentation into consideration. Indeed, Sjoding [14], Dyer [7] and Feiner [8] found and Hidalgo [10] mentioned that pulse oximeters can overestimate the blood oxygen level for people with pigmented skin and this is now recognised by The U.S. Food and Drug Administration (FDA) [4]. Pulse oximeters have become particularly widely used to remotely monitor patients with COVID-19 at home where the higher bias on measurements of oxygen level can result in undiagnosed hypoxemia, which can be fatal especially in patients with severe acute disease as can be the case with COVID-19 infection [13]. Therefore, the aim of our study is to identify the impact of skin pigmentation on pulse oximeter measurements and explore the benefits of a multi-wavelength approach during an induced acute change of SpO_2 (defined as SaO_2 quantified with a pulse oximetry) in healthy volunteers.

2 Material and Methods

Our cross-sectional study comprised healthy non-smoking volunteers aged between 18 and 40 years old at the University of Glasgow (located 27 meters above sea level [1]). All participants provided written informed consent and subjects were excluded if they reported symptoms of influenza or respiratory infections up to 10 days before the study, had a history of syncope or could be pregnant. The study was carried out in January and February 2020. Twenty volunteers were eligible, two were excluded for history of syncope, six were excluded due to unreadable data after the study, leaving 12 volunteers for data analysis. Skin pigmentation index was taken from volunteers' photographs (Figs. 1b and 2b) and classified in skin types I through VI according to the Fitzpatrick scale [9], in order to consider differences in the human skin optical properties due to melanin concentration [17]. Their height, weight, blood pressure, temperature, heart and respiratory rates were recorded. All study procedures were conducted in accordance with the Declaration of Helsinki and were approved by the Ethical Committee Review Board of the University of Glasgow (approval number: 300180273). Volunteers were seated throughout the study, their left forearm and hand were placed over a platform on a table and the index finger was placed over a customised 3D printed holder or optical sensor connected to a multiple wavelength spectrophotometer Ocean Optics (Ocean Optics Inc., FL). A pulse oximeter Mightysat Rx® with Bluetooth LE (model P/N 9909, Masimo, Irvine, CA) was placed over the middle finger, a pulse oximeter GO_2 Achieve® (NONIN Medical Inc., Plymouth, MN) over the ring finger and a generic brand pulse oximeter over the little finger (Figs. 1a and 2a). After 30 sec of recording in room air, five acute hypoxic events were induced by administration of 11% oxygen for 120 sec by the Hypoxico altitude training system (Hypoxico

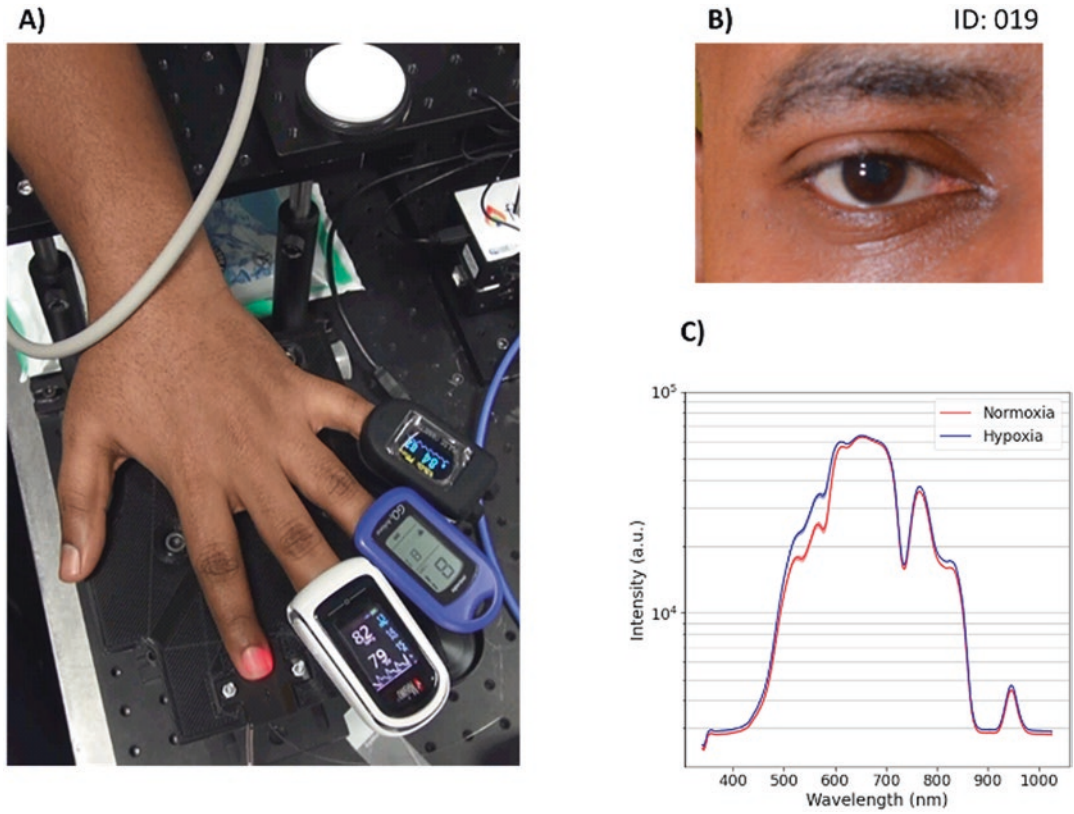

Fig. 1 Volunteer No. 019, high skin pigmentation, type V. (**a**) left hand of volunteer, commercial pulse oximeters placed and reading, index finger optical set-up. (**b**) photo of the volunteer's eye, which shows the presence of melanin in iris colouration, (**c**) averaged spectra HbO_2 (normoxia, red) vs HbO_2 (hypoxia, blue) and standard deviation (shaded over 5 measurements)

Inc., New York, NY) which was previously warmed up for at least 20 min and was set using altitude pre-setting no. 12 (according to the manufacturer recommendation) [11]. For our study the oxygen percentage of the mixture was verified by the oxygen sensorHandi® + (Maxtec, Salt Lake City, UT). The oxygen was administered via a face mask (Ambu®, Ultraseal) connected to a circuit with a one-way valve to allow exhalation and prevent mixture with room air during inspiration. Administration lasted for 120 sec while breathing normally, after this time the subjects could recover without the face mask for 5 min. At the end of each session, the blood pressure, heart rate, respiratory rate and modified Borg dyspnoea scale [5] were measured and recorded. The process was then repeated until five hypoxic events were recorded. Protocols to induce acute hypoxic events in healthy volunteers to assess accuracy of pulse oximeters are not standard [11, 15]; the components of oxygen inspiratory are $PiO_2 = (PB - 47) \times FiO_2$; where PB is barometric pressure (756 mmHg in Glasgow), 47 mmHg is water vapor partial pressure at 37 °C body temperature, and FiO_2 is the dry-gas fraction of oxygen in breathing gas at room air 20.9% [6]. At room air, the inspiratory pressure of oxygen is 148 mmHg, the administration of FiO_2 of 11% created a sudden drop of inspiratory pressure to 78 mmHg; due to variability in lung clearance of the residual gas, acute hypoxic response [16] and cardiovascular

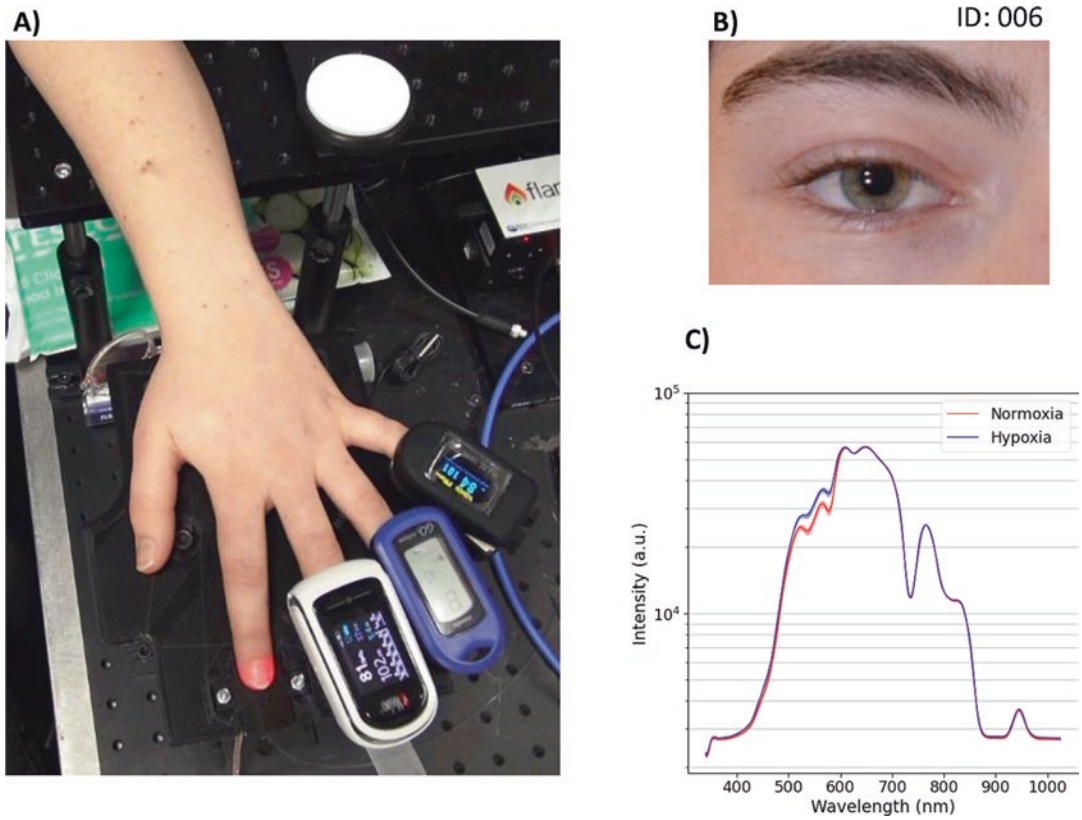

Fig. 2 Volunteer No. 006, low skin pigmentation, type I. (**a**) left hand of volunteer, commercial pulse oximeters placed and reading, index finger optical set-up. (**b**) photo of volunteer's eye, which shows the presence of low melanin in iris colouration, (**c**) averaged spectra HbO_2 (normoxia, red) vs HbO_2 (hypoxia, blue) and standard deviation (shaded over 5 measurements)

response. Administration over 120 sec resulted in a drop to 72% SaO_2 quantified with pulse oximetry. The room temperature was kept constant at 24 °C. Data was processed and analysed with in house MATLAB and Python 3.6 scripts.

3 Results

A spectral profile for all volunteers from different backgrounds and ethnicity was obtained (Figs. 1c and 2c). Skin types according the Fitzpatrick scale were as follows: Type I (n = 3), type II (n = 1), type III (n = 4), type IV (n = 1), type V (n = 1), type NA (Not defined n = 2). To explore the impact of skin pigmentation on SaO_2, a principal components analysis (PCA) was performed. The analysis showed clusters relating to skin pigmentation and oxygenation status. PC2 = 22.99% scores split into normoxia and hypoxia (Fig. 3a) and PC1 = 56.00% scores divided in skin pigmentation Type I-V according to Fitzpatrick (Fig. 3b). There is a difference between subjects with Type I, II and III, compared subjects Type IV and V, especially subject ID: 019 which diverged the most. Moreover, normoxia and hypoxia clusters are well defined between the samples.

4 Discussion and Conclusions

This preliminary study using PCA serves to validate the need to better understand the impact of skin pigmentation absorption on optical readings in pulse oximeters. We saw differences in oxygen

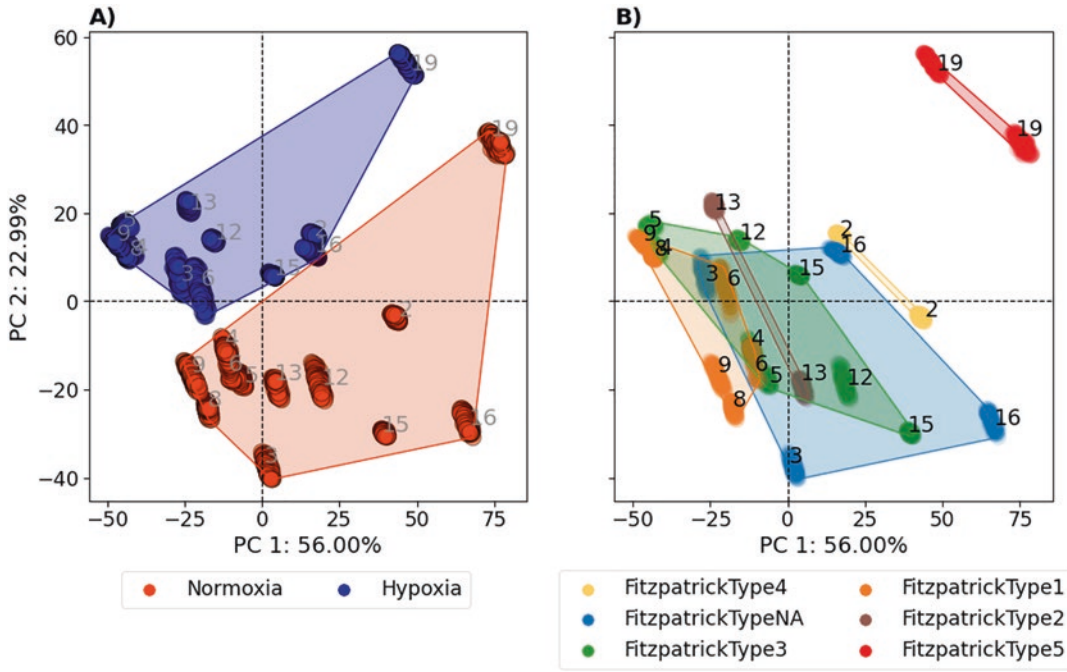

Fig. 3 PCA scatter plots of hyper-spectral measurements (350–1000 nm; VIS-nIRS) from 12 volunteers. Every dot represents *n* spectral measurement. (**a**) Data coloured by oxygenation status. (**b**) Skin pigmentation according Fitzpatrick scale types from I–V

saturation related to skin pigmentation, especially in the type V volunteer. Type III, IV and V spectral distance between normoxia and hypoxia were closer compared to type I, where it was larger. This phenomenon might impact the sensitivity of SaO_2 detection on commercial devices. Future work should use 1) melanin quantification expressed as a percentage to avoid possible skin colour misinterpretations (akin to the colour scales) and 2) a larger sample size to confirm these findings. Regulatory calibration (ISO) [2] and validation (FDA) [3] procedures mention the inclusion of people of colour. However, the percentage of inclusion (13% of darkly pigmented subjects) does not reflect the diversity of the population [13]. There is also a need to acknowledge the variability of skin pigmentation within ethnicities (i.e., type I skin pigmentation can change by sun exposure over time). Avoiding race bias in equipment accuracy would alleviate the subsequent health risks associated with the lack of detection of hypoxemia. In conclusion, our multi-wavelength approach was able to detect hypoxia events, but also emphasised the need to take into account skin pigmentation in oximeter measurements.

Acknowledgments We acknowledge support provided by INER and The University of Glasgow, especially to INER's Principal Dr. Jorge Salas-Hernandez and Dr. Laura Gochicoa-Rangel. V. Ochoa-Gutierrez acknowledges financial support from the Mexican National Science and Technology Council and the Ministry of Energy (CONACyT – SENER) through scholarship No. 593603 and the Secretariat of Public Education (SEP) through scholarship BC-9517/36248.

References

1. Elevation of Glasgow City, UK – Topographic Map – Altitude Map
2. ISO – ISO 80601-2-61:2017 – medical electrical equipment – part 2–61: particular requirements for basic safety and essential performance of pulse oximeter equipment

3. Pulse oximeters – premarket notification submissions [510(k)s]: guidance for Industry and Food and Drug Administration Staff | FDA
4. US Food Administration and Drug (2021) Pulse oximeter accuracy and limitations: FDA safety communication
5. Ambrosino N, Scano G (2004) Dyspnoea and its measurement. Breathe 1(2):100–107
6. Conkin J (2016) Equivalent air altitude and the alveolar gas equation. Aerosp Med Hum Perform 87(1):61–64
7. Dyer O (2020) Pulse oximetry may underestimate hypoxaemia in black patients, study finds. BMJ 371:m4926
8. Feiner JR, Severinghaus JW, Bickler PE (2007) Dark skin decreases the accuracy of pulse oximeters at low oxygen saturation: the effects of oximeter probe type and gender. Anesth Analg 105:S18–S23
9. Fitzpatrick TB (1988) The validity and practicality of sun-reactive skin types I through VI. Arch Dermatol 124(6):869–871
10. Hidalgo DC, Olusanya O, Harlan E (2021) Critical care trainees call for pulse oximetry reform. Lancet Respir Med 9:e37
11. Kolb JC, Farran P, Norris SR, Smith D, Mester J (2004) Validation of pulse oximetry during progressive normobaric hypoxia utilizing a portable chamber. Can J Appl Physiol 29(1):3–15
12. Liu H, Ivanov K, Wang Y, Wang L (2015) A novel method based on two cameras for accurate estimation of arterial oxygen saturation. Biomed Eng Online 14(1):52
13. Lopez L, Hart LH, Katz MH (2021) Racial and ethnic health disparities related to COVID-19. JAMA 325(8):719–720
14. Sjoding MW, Dickson RP, Iwashyna TJ, Gay SE, Valley TS (2020) Racial bias in pulse oximetry measurement. N Engl J Med 383(25):2477–2478
15. Trivedi NS, Ghouri AF, Shah NK, Lai E, Barker SJ (1997) Pulse oximeter performance during desaturation and resaturation: a comparison of seven models. J Clin Anesth 9(3):184–188
16. Weil JV (2003) Variation in human ventilatory control – genetic influence on the hypoxic ventilatory response. Respir Physiol Neurobiol 135(2–3):239–246
17. Hernández-Quintanar L et al (2020) Fiber-optic pulse oximeter for local oxygen saturation determination using a Monte Carlo multi-layer model for calibration. Comput Methods Prog Biomed 187:105237

Part VI

Muscle

The Intramuscular Circulation Is Affected by Neck and Shoulder Pain

Masaru Kanda, Takuya Kitamura, Yusuke Suzuki, Isamu Konishi, Kei Watanabe, and Naritoshi Sato

Abstract

The purpose of this study was to investigate the effects of neck and shoulder pain (NSP) and the position of the head and neck on the intramuscular circulation of the cervical muscles such as the trapezius and levator scapulae muscles in young females. Ten NSP subjects (mean age: 20.9 ± 0.5 years) and ten non-NSP subjects (mean age: 20.6 ± 0.7 years) were recruited to this study. Near-infrared spectroscopy (NIRS) was used to non-invasively measure total haemoglobin (Total-Hb), oxygenated haemoglobin (Oxy-Hb), and deoxygenated haemoglobin (Deoxy-Hb) of the trapezius and levator scapulae muscles. The measurements of Total-Hb, Oxy-Hb, and Deoxy-Hb were taken in the neutral position, immediately after the maximally flexed (extended) position, and after 30 s in the maximally flexed (extended) position. In flexion, no significant main effect or interaction was observed with Total-Hb and Oxy-Hb. A significant interaction was observed with Deoxy-Hb ($p < 0.01$). There was no significant difference in the changes over time in the NSP group ($p = 0.91$). However, in the non-NSP group, a significant increase was noted at the neutral position to immediately after the maximally flexed position ($p < 0.01$) and at the end of maintaining the maximally flexed position ($p < 0.01$). In extension, no significant main effect or interaction was observed with Total-Hb and Oxy-Hb. A significant interaction was observed with Deoxy-Hb ($p < 0.01$). In the NSP group, no significant difference was observed in the changes over time ($p = 0.91$). In the non-NSP group, however, a significant decrease was observed from the neutral position to immediately after the maximally extended position ($p < 0.01$). The results of this study indicate that maintaining either maximal cervical flexion or extension may affect venous blood flow on non-NSP group. However, no effect on NSP group was observed due to existing diminished intramuscular circulation.

Keywords

NIRS · Trapezius · Levator scapulae · Intramuscular circulation

M. Kanda (✉) · Y. Suzuki · I. Konishi · N. Sato
Research Center for Locomotive Syndrome, Niigata University of Health and Welfare, Niigata, Japan
e-mail: kanda@nuhw.ac.jp

T. Kitamura
Research Center for Locomotive Syndrome, Niigata University of Health and Welfare, Niigata, Japan

Niigata University of Rehabilitation, Niigata, Japan

K. Watanabe
Research Center for Locomotive Syndrome, Niigata University of Health and Welfare, Niigata, Japan

Niigata University Medical and Dental General Hospital, Niigata, Japan

F. Scholkmann et al. (eds.), *Oxygen Transport to Tissue XLIII*, Advances in Experimental Medicine and Biology 1395, https://doi.org/10.1007/978-3-031-14190-4_65

1 Introduction

Neck and shoulder pain (NSP), or "katakori" in Japanese, is a very common symptom with a high complaint rate among both males and females in Japan. An epidemiological survey of NSP in the general population indicated that NSP was most common among people in their thirties and younger, and the ratio of females was believed to be high among this group [1].

Regarding poor intramuscular circulation and oxygenation, which is considered to be one of the causes of NSP, it has been reported that compared to the deep tissues of the neck in healthy individuals, the deep tissues of the neck in NSP patients are in an ischaemic state [2]. It has also been suggested that their aerobic capacity is decreased, and their haemodynamics are impaired [3]. According to Sasaki, poor muscular circulation is caused by maintaining the same posture for a long time in an unnatural position, a poor posture, kyphotic posture, and slouching shoulders [4]. However, most studies that measured the muscular blood flow in the cervical muscle group had performed the measurements in the sitting position and analysed the tissue oxygenation rate after the application of an exercise load [2, 5].

Thus, the purpose of this study was to investigate the effects of NSP and the position of the head and neck on the muscular haemodynamics of the cervical muscles such as the trapezius and levator scapulae muscles in young females.

2 Methods

2.1 Participants

Subjects with NSP for more than 1 year in the symptom site defined in the previous study [6] were determined as having NSP. Those that did not were categorised as having no symptoms (non-NSP). The exclusion criteria for both groups were a history of cervical surgery, immunological diseases (rheumatism, etc.), and neurological symptoms of the upper extremities. As a result, there were 10 people in the NSP group (age 20.9 ± 0.5 years, BMI 20.5 ± 1.2 kg/m^2) and 10 in the non-NSP group (age 20.6 ± 0.7 years, BMI 21.8 ± 3.2 kg/m^2) (Table 1). Each participant provided written informed consent after receiving information regarding the potential risks, study objectives, measurement techniques, and benefits associated with the study. This study was approved by the Ethics Committee of Niigata University of Health and Welfare (Approval No. 18446-200,708) and was conducted in accordance with the ethical standards of the 1964 Declaration of Helsinki and its later amendments or comparable ethical standards.

2.2 Experimental Procedure

A seat with a height of 45 cm without a backrest was used for the position during data collection. The starting sitting position was determined as the cervical neutral position. The task motions were to be performed in the following order: (1) neutral position to maximally flexed position and (2) neutral position to maximally extended position. Each position was held for 30 s, with a 1-min rest between measurements. For the neutral position, the foot was opened slightly outwards, and the pelvis was positioned such that the line connecting the anterior superior iliac spine and the posterior superior iliac spine was parallel to the floor [7]. The upper extremity positions were at the side of trunk. For flexion and extension, a timer was used to orally count down 5 s in order to maintain a constant speed during cervical movements. In addition, it was carried out

Table 1 Subjects characteristics

	Participants (n)	Age (year)	Height (cm)	Weight (kg)	BMI
All participants	20	20.8 ± 0.6	160.0 ± 5.6	54.4 ± 7.6	21.2 ± 2.5
Non-NSP	10	20.6 ± 0.7	159.2 ± 4.5	55.5 ± 9.3	20.5 ± 1.2.
NSP	10	20.9 ± 0.6	160.8 ± 6.7	53.2 ± 5.7	21.8 ± 3.2
p value	–	n.s.	n.s.	n.s.	n.s.

after confirming that the movements could be performed properly. The measurements were taken in the neutral position, immediately after the flexed (extended) position, and after 30 s in those positions. The changes in these measurements were compared.

2.3 NIRS Measurements

The measured items were oxygenated haemoglobin (Oxy-Hb), deoxygenated haemoglobin (Deoxy-Hb), and total haemoglobin (Total-Hb) of the trapezius and levator scapulae muscles. A portable near-infrared tissue blood oxygen monitor (Pocket NIRS: Dynasense Co., Ltd., Hamamatsu, Japan) was used. As for the measurement method, the zero set was performed in the resting prone position as the measurement reference value, which measured the relative value in each posture measurement with respect to the reference value 0. Regarding the position of the probe, in an experiment conducted in advance, the muscle thickness and parts of the trapezius and levator scapulae muscles were confirmed in several female subjects using an ultrasonic diagnostic imaging system. In this study, it was set at 1.5 cm medial to the superior angle of the scapula. In addition, the measurements were taken on the side with severe symptoms in the NSP group and on the right side in the non-NSP group.

2.4 Statistical Analysis

For the statistical analysis, Mauchly's sphericity test was performed in advance. If the sphericity could be assumed, the split plot design ANOVA was used. If the assumption could not be made, the degrees of freedom were corrected using the Greenhouse-Geisser epsilon. Using the two-way ANOVA, we analysed two factors: group (presence or absence of NSP) and time (neutral position/immediately after the flexed or extended position/after 30 s in flexed or extended position) (2 × 3). For those with an interaction, the multiple comparison method was used by dividing by the level of each factor. Regarding the standard of the repeated measures factor, a repeated measures analysis of variance or Friedman's test was performed. For the post-hoc test, the corresponding t-test or Wilcoxon's test was performed, and the Bonferroni method was used for correction. The significance level of correction by the Bonferroni method was set at 0.017 (0.05/3). The two-sample t-test or Mann-Whitney test was performed for each level comparison of uncorrelated factors. SPSS version 27.0 (IBM Japan) was used for the statistical processing, and the significance level in all tests was set to 5%.

3 Results

No significant difference was found in the basic attributes between the patients with and without NSP.

In flexion, no significant main effect or interaction was observed with Oxy-Hb and Total-Hb. A significant interaction was observed with Deoxy-Hb ($p < 0.01$). There was no significant difference in the changes over time in the NSP group ($p = 0.91$). However, in the non-NSP group, a significant increase was noted at the neutral position to immediately after the flexed position ($p < 0.01$) and at the end of maintenance of the flexed position ($p < 0.01$). In the comparison between groups, no significant difference was observed in the neutral position ($p = 0.68$), immediately after the flexed position ($p = 0.06$), and at the end of maintenance of flexion ($p = 0.35$).

In extension, no significant main effect or interaction was observed with Oxy-Hb and Total-Hb. A significant interaction was observed with Deoxy-Hb ($p < 0.01$). In the NSP group, no significant difference was observed in the changes over time ($p = 0.91$). In the non-NSP group, however, a significant decrease was observed from the neutral position to immediately after the extended position ($p < 0.01$). In the comparison between the groups, no significant difference was observed in the neutral position ($p = 0.97$), immediately after the extended position ($p = 0.85$), and at the end of extension position ($p = 0.68$).

4 Discussion

Although no significant difference was observed, a decrease in Oxy-Hb was noted in flexion. Therefore, this indicates that oxygen was consumed during flexion from the neutral position and during maintaining the flexion. The trapezius and levator scapulae muscles are the postural muscles of the cervical spine. When the scapula is fixed, it said to have an impact on head and neck extension [8, 9]. Previous studies reported that mild upper extremity work and maximum contraction led to a decrease in Oxy-Hb and Total-Hb and an increase in Deoxy-Hb in the trapezius muscle [10, 11]. In the neck flexion task of this study, Deoxy-Hb was found to increase due to the muscle activity of the trapezius and levator scapulae muscles during movement. However, the muscle activity was not adequate to cause a significant change in Oxy-Hb and Total-Hb. In addition, maintaining flexed position indicates isometric contraction of the trapezius and levator scapulae muscles with stretched position. In other words, the increase in the internal pressure of the muscles [12, 13] caused a decrease in the haemodynamic responses, resulting in venous blood flow stasis and a significant increase in only the Deoxy-Hb. In the NSP, no significant change was observed in the Deoxy-Hb. In a previous study, not only were the haemodynamic responses of the periscapular muscles, the trapezius muscle, and the supraspinatus muscle low, but also the deep tissue circulatory dynamics in the NSP group had also decreased [2]. Therefore, the tissue haemodynamics did not change even when cervical flexion was maintained. In patients with NSP, the aerobic capacity of muscles declines, and the muscle haemodynamics are impaired [3]. In the case of the NSP in this study, the trapezius and levator scapulae muscles might be dysfunctional, and the normal oxygen consumption did not occur during the muscle activity. Therefore, there was no significant change in the muscle haemodynamics in the NSP.

In extension, local compression occurs in the trapezius and levator scapulae muscles. It is likely that the venous blood circulation was promoted by this compression, resulting in a significant decrease in Deoxy-Hb.

In the NSP, there was no significant change in Deoxy-Hb immediately and after 30 s in the extended position. As mentioned above, the muscle haemodynamics may have deteriorated [2] in the NSP. In a previous study, it was reported that degeneration of muscle fibers occurred on both the ventral and dorsal sides of the neck in patients

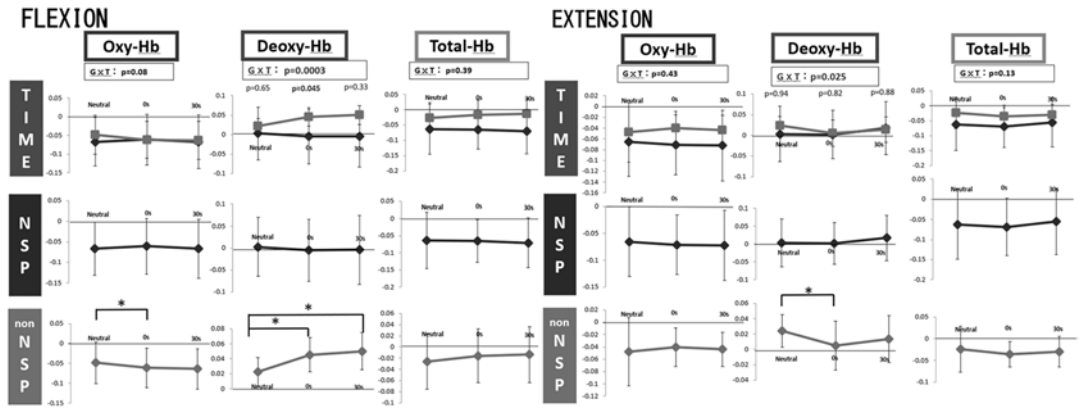

Fig. 1 Effects of the muscular haemodynamics of the cervical muscles in flexion and extension with NSP and non-NSP are shown. G × T: group (presence or absence of NSP) and time (neutral position/immediately after the flexed or extended position/after 30 s in flexed or extended position); neutral, cervical neutral position in sitting; 0 s, immediately after the flexed or extended position; 30 s, after 30 s in flexed or extended position; *NSP* neck and shoulder patient, *Oxy-Hb* oxygenated haemoglobin, *Deoxy-Hb* deoxygenated haemoglobin, *Total-Hb* total haemoglobin

with chronic neck pain [14]. Therefore, the extension did not affect the haemodynamics of these muscle groups in NSP. We expect that understanding the role of oxygenation in NSP, may enable pathway to treat NSP (Table 1 and Fig. 1).

Acknowledgments This study was supported by a Grant-in-Aid for Exploratory Research from the Niigata University of Health and Welfare, Japan.

References

1. Takasawa E, Yamamoto A, Osawa T et al (2010) Prevalence and characteristics of nonspecific neck pain in the general population. Rinsh Seik Geka/Clin Orthop Surg 45:821–825
2. Sakai T, Osaki N, Yasuno T et al (2002) Relations of stiff shoulders with deep hemodynamics values. J Jpn Soc Balneol Climatol Phys Med 65(3):137–146
3. Oda M, Oe N, Yasegawa H (2011) Evaluation of hemodynamics of levator scapulae with NIRS. Gifuken rigaku ryohoshikai gakujutsushi 36(2):49–51
4. Sasaki K (1994) Definition and mechanism of neck and shoulder pain. J Jpn Soc Acup Moxibus 44(4):361–363
5. Takakuwa T, Mishima R, Atsuta Y (2001) 웬 Investigation ofKatakori, evaluation with near-infrared spectroscopy. Orthop Surg 52(4):461–465
6. Shinozaki T, Osawa T, Tsutsumi S et al (2007) Clinical findings of chronic non-specific neck pain based on the questionnaire. Rinsh Seik Geka/Clin Orthop Surg 42(5):409–412
7. Richardson C, Hides J, Hodges PW (2008) Therapeutic exercise for lumbopelvic stabilization. Igaku-shoin Ltd, pp 148–156
8. Liebenson C (2006) Rehabilitation of the spine a practitioner's manual. Lippincott Williams & Wilkins, pp 204–209
9. Calais-Germ B (2014) Anatomy of movement. The Science News, pp 81–83
10. Shiro Y, Arai Y-CP, Matsubara T, Isogai S, Ushida T (2012) Effect of muscle load tasks with maximal isometric contractions on oxygenation of the trapezius muscle and sympathetic nervous activity in females with chronic neck and shoulder pain. BMC Musculoskelet Disord 13:146
11. Sjogaard G, Rosendal L, Kristiansen J et al (2010) Muscle oxygenation and glycolysis in females with trapezius myalgia during stress and repetitive work using microdialysis and NIRS. Eur J Appl Physiol 108:657–669
12. Konno S, Kikuchi S (1993) Relationship between increase of paraspinal compartment pressure and low back pain. Rinsh Seik Geka/Clin Orthop Surg 28(4):419–426
13. Yokozawa H, Muraoka J, Shimizu S et al (2010) Effects of muscle fascicle length and muscle oxygen saturation with static stretching. J Jpn Coll Angiol 108:657–669
14. Uhling Y, Weber BR, Grob D, Müntener M (1995) Fiber composition and fiber transformation in neck muscle of patients with dysfunction of the cervical spine. J Orthop Res 13(2):240–249

Intramuscular Circulation of the Lumbar Multifidus in Different Trunk Positions on Standing

Masaru Kanda, Takuya Kitamura, Yusuke Suzuki, Isamu Konishi, Kei Watanabe, and Naritoshi Sato

Abstract

A deficiency in lumbar muscle blood circulation is considered to be a major risk factor for non-specific low back pain. The aim of this study was to investigate changes in relative circulation over time in the lumbar multifidus in different positions on sitting.

Twelve healthy subjects (7 males, 5 females, average age: 20.9 years) without low back pain for the past 12 months were recruited. Near-infrared spectroscopy (NIRS) was used to non-invasively measure total haemoglobin (Total-Hb) and oxygenated haemoglobin (Oxy-Hb) in the lumbar multifidus at the L5-S1 segment. Subjects were asked to move into either 60-degree trunk-flexed or 20-degree trunk-extended position from the starting (standing in neutral) position in 3 s, timed by a metronome, and to maintain these positions for 30 s. The measurements of Total-Hb and Oxy-Hb were compared at −3 (neutral position), 0, 10, 20, and 30 s in each flexed and extended position on sitting.

In flexion, Total-Hb and Oxy-Hb of the lumbar multifidus were significantly decreased from a neutral (−3 s) to flexed (0 s) position (Total-Hb: $p = 0.002$, Oxy-Hb: $p = 0.004$); however, there were no significant differences in the flexed position. In extension, Total-Hb and Oxy-Hb of the lumbar multifidus were significantly increased from 0 to 10 s (Total-Hb: $p < 0.001$, Oxy-Hb: $p < 0.001$); however, there were no significant differences from the neutral (−3 s) to extended (0 s) position, or from 10 to 30 s.

The results of this study indicate that the intramuscular circulation of the lumbar multifidus decreases immediately once the trunk starts moving into a flexed position on sitting. On the other hand, the intramuscular circulation of the lumbar multifidus increases for up to 10 s once the trunk starts moving into an extended position.

Keywords

Low back pain · NIRS · Muscle blood flow · Haemodynamics

M. Kanda (✉) · Y. Suzuki · I. Konishi · N. Sato
Research Center for Locomotive Syndrome, Niigata University of Health and Welfare, Niigata, Japan
e-mail: kanda@nuhw.ac.jp

T. Kitamura
Research Center for Locomotive Syndrome, Niigata University of Health and Welfare, Niigata, Japan

Niigata University of Rehabilitation, Niigata, Japan

K. Watanabe
Research Center for Locomotive Syndrome, Niigata University of Health and Welfare, Niigata, Japan

Niigata University Medical and Dental General Hospital, Niigata, Japan

F. Scholkmann et al. (eds.), *Oxygen Transport to Tissue XLIII*, Advances in Experimental Medicine and Biology 1395, https://doi.org/10.1007/978-3-031-14190-4_66

1 Introduction

Low back pain (LBP), a common symptom experienced by all age groups [1–3], was reported to be the current primary cause of disability worldwide [4]. It has been reported that occupational LBP, which is the most prevalent orthopaedic disorder, has become a heavy financial and social burden [5]. In addition, LBP has been reported to be the primary cause of disability in the working-age group [4, 6]. In particular, those who are required to work in the trunk-flexed position for an extended period of time have a high probability of experiencing LBP, and the prevalence of LBP is high among caregivers and nurses as they work in the trunk-flexed position for approximately 30% of their daily working hours [7].

The trunk-flexed position reduces muscle blood flow in the lumbar back muscles, which is thought to be a cause of LBP. In the flexed position, the lumbar back muscles are stretched, likely affecting the multifidus, which occupies approximately 80% of the lower lumbar spine compartment [8]. It was reported that the intramuscular pressure of the lumbar back muscles was shown to change with different body positions and changes in the lumbar lordosis angle, and the decrease in muscle blood flow due to increased intramuscular pressure can be a cause of chronic LBP [9]. However, no studies have reported the time-dependent changes during maintaining different trunk positions. Elucidation of these is expected to allow us to implement appropriate interventions to improve LBP. Therefore, this study aimed to examine the time-dependent changes of the intramuscular circulation of the lumbar multifidus of standing subjects in different trunk positions.

2 Methods

2.1 Participants

This was conducted as a cross-sectional study with 12 student volunteers from Niigata University of Health and Welfare (7 males and 5 females with an average age of 20.8 ± 0.4 years) (Table 1). This study was approved by the Ethics Committee of Niigata University of Health and Welfare (18361–200,207) and was conducted in accordance with the ethical standards of the 1964 Declaration of Helsinki and its later amendments or comparable ethical standards.

2.2 Experimental Procedure

The measurements were taken in three standing positions: the trunk-neutral position (hereinafter, neutral position), 60-degree trunk-flexed position (hereinafter, flexed position), and 20-degree trunk-extended position (hereinafter, extended position). With regard to the pelvic position, the anterior superior iliac spine was positioned two fingers below the posterior superior iliac spine [10]. Trunk-flexed and extended angles were measured with a goniometer, in accordance with the method to measure the range of motion of joints. All positions were standardised with the upper extremities at the side of trunk and legs shoulder-width apart. The flexed position was set to 60 degrees, which were used as the standing angle in the previous study [11], and subjects were instructed to flex the trunk without moving the sacrum and to make up for less than 60 degrees with an anterior tilt of the pelvis, which minimised compensatory movements due to hip flexion. In the extended position, maintaining the maximum range of motion (30

Table 1 Subject characteristics

	Participants (n)	Age (year)	Height (cm)	Weight (kg)	BMI
All participants	12	20.8 ± 0.4	165.7 ± 9.6	58.1 ± 8.8	21.2 ± 2.5
Male	7	20.9 ± 0.4	171.7 ± 7.8	63.4 ± 7.4	21.6 ± 2.6.
Female	5	20.8 ± 0.4	157.2 ± 2.6	50.6 ± 2.7	20.5 ± 1.5

degrees) for 30 s was expected to be difficult. Thus, it was set to 20 degrees in this study, and subjects were instructed to extend the trunk without moving the sacrum, as in the flexed position. Prior to measuring Oxy-Hb and Total-Hb, the measurements and movements in the measurement positions were practiced using a standing rod. A metronome was used to keep the speed of movement constant, which confirmed that the movement could be made properly at the time of measurement, and subjects were instructed to maintain the position for 30 s. The measurements were taken immediately, 10, 20, and 30 s after the start of the neutral, flexed or extended position to examine the changes over time.

2.3 NIRS Measurements

This study measured oxyhaemoglobin (Oxy-Hb), which is oxygenated haemoglobin, and total haemoglobin (Total-Hb), which is the sum of Oxy-Hb and deoxyhaemoglobin (Deoxy-Hb), of the lumbar multifidus. For the measurements of Oxy-Hb and Total-Hb, we used a portable near-infrared tissue blood oxygen monitoring device (Pocket NIRS: DynaSense Inc.), which was shown to continuously analyse the changes in oxygen consumption-supply balance in skeletal muscle during various exercises [12]. In the measurements, the zero-setting of the measurement reference value was performed in the prone resting position (hereinafter, prone position), and with respect to the reference value, the relative values in each measurement position were measured. The measurement probe was attached to the outside of the fifth lumbar vertebra and the spinous process of the first sacral vertebra, and the photodetector was attached so that it was positioned outside of the spinous process of the fifth lumbar vertebra.

2.4 Statistical Analysis

The normality was first tested using the Shapiro–Wilk test. In normally distributed data with continuous variables, a repeated measures ANOVA was performed after Bartlett's test. When a significant difference was found, a multiple comparison test was performed with the Bonferroni correction using the Tukey-Kramer method. In non-normally distributed data, a nonparametric multiple comparison test was performed using the Steel-Dwass method after the Quade test. SPSS Statistics 27.0 (IBM Japan, Ltd.) was used for statistical processing, and the significance level in all tests was set to 5%.

3 Results

In the flexed position, Oxy-Hb of the lumbar multifidus decreased significantly from the neutral position (−3 s) to the start of the flexed position (0 s) ($p = 0.008$) and from 20 to 30 s after the start of the flexed position ($p = 0.003$). However, no significant change was observed from 0 to 10 s and from 10 to 20 s after the start of the flexed position. Deoxy-Hb decreased significantly from the neutral position (−3 s) to the start of the flexed position (0 s) ($p = 0.002$). However, no significant change was observed in other measurement points. Total-Hb decreased significantly from the neutral position (−3 s) to the start of the flexed position (0 s) ($p = 0.002$). However, no significant change was observed in other measurement points.

In the extended position, Oxy-Hb of the lumbar multifidus increased significantly during 10 s from the start (0 s) of the extended position ($p = 0.002$). However, no significant change was observed in other measurement points. Deoxy-Hb increased significantly from 20 to 30 s ($p = 0.003$). However, no significant change was observed in other measurement points. Total-Hb increased significantly from the neutral position (−3 s) to the start of the extended position (0 s) ($p = 0.001$) and during 10 s from the start (0 s) of the extended position ($p = 0.001$). However, no significant change was observed from 10 to 20 s and from 20 to 30 s after the start of the extended position.

4 Discussion

In the flexed position, Oxy-Hb, Deoxy-Hb and Total-Hb of the lumbar multifidus decreased significantly from the neutral position (−3 s) to the start of the flexed position (0 s), and Oxy-Hb also

decreased significantly from 20 to 30 s after the start of the flexed position. A previous study showed that with decreasing lumbar lordosis angle, the intracompartmental pressure of the lumbar back muscles increases while muscle blood flow decreases [11]. In addition, it was reported that intramuscular pressure significantly increases in a squatting position or when maximally bending forward [13], and that Oxy-Hb of the multifidus is reduced at trunk flexion of 20 degrees or more [14]. Furthermore, it was reported that a decrease in oxygen supply due to mechanical factors, such as a reduction in blood vessel diameter caused by the extension of capillaries running parallel to the muscles, reduces all of Total-Hb, Oxy-Hb, and Deoxy-Hb [15]. As mentioned above, the lumbar back muscles are stretched in the flexed position, likely affecting the multifidus, which occupies approximately 80% of the lower lumbar spine compartment [8]. Therefore, it is likely that Oxy-Hb, Deoxy-Hb and Total-Hb of the lumbar multifidus decreased in the flexed position for these reasons.

In the extended position, Oxy-Hb and Total-Hb of the lumbar multifidus increased significantly during 10 s from the start (0 s) of the extended position, and Total-Hb also increased significantly from the neutral position (−3 s) to the start of the extended position (0 s). Deoxy-Hb increased significantly from 20 to 30 s after the start of the extended position. A previous study showed that Oxy-Hb increased during extension while Deoxy-Hb remained unchanged, resulting in increasing Total-Hb [16]. In addition, it was reported that Total-Hb of the multifidus increases during trunk extension in the standing position [14]. Also, with regard to circulatory haemodynamics, Oxy-Hb and Total-Hb were shown to increase in the extended position, and with regard to muscle activity, the muscle activity of the multifidus was significantly lower in the extended position than in the neutral position [17]. Therefore, as the extension of the lumbar back muscles was anatomically reduced, expanding the blood vessel diameter, muscle activity decreased, which presumably decreased intramuscular pressure and promoted an increase in haemodynamics. Because this study used the method used in the previous study, it is expected that similar haemodynamics occurred, resulting in an increase in Oxy-Hb and Total-Hb. We expect that understanding the role of oxygenation in lumbar multifidus may enable the pathway to treat LBP (Fig. 1).

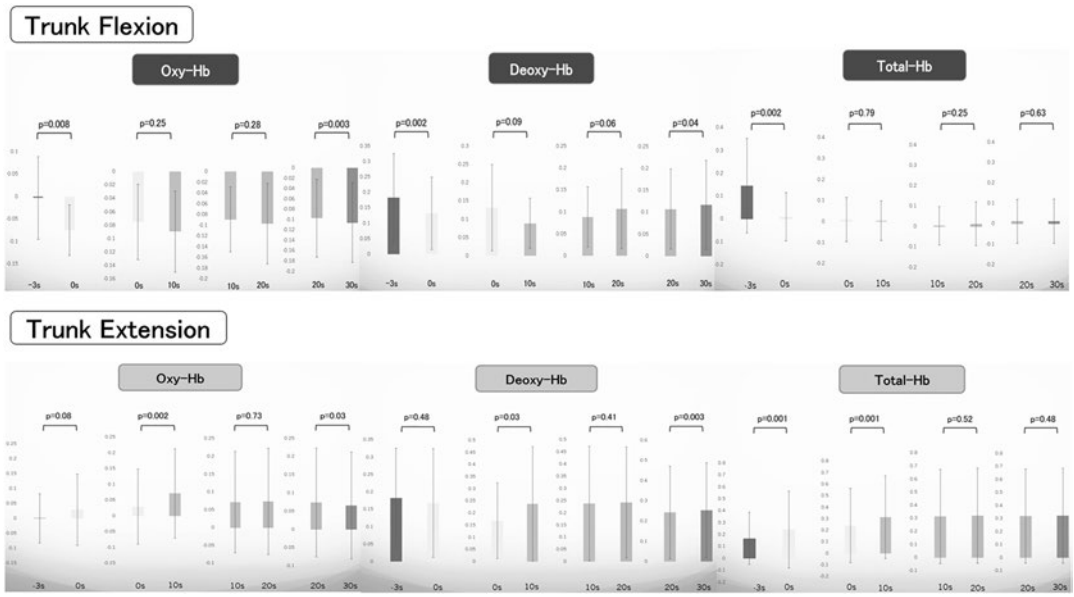

Fig. 1 Changes of the intramuscular circulation of the lumbar multifidus in flexion and extension on standing are shown. −3 s, neutral position in standing; 0 s, immediately after the flexed or extended position; 10 s, after 10 s in flexed or extended position; 20 s, after 20 s in flexed or extended position; 30 s, after 30 s in flexed or extended position; Oxy-Hb, oxygenated haemoglobin; Total-Hb, total haemoglobin

Acknowledgments This study was supported by a Grant-in-Aid for Scientific Research (C) from the Japanese Society for the Promotion of Science.

References

1. Hoy D, Bain C, Williams G et al (2012) A systematic review of the global prevalence of low back pain. Arthritis Rheum 64:2028–2037
2. Kamper SJ, Henschke N, Hestbaek L, Dunn KM, Williams CM (2016) Musculoskeletal pain in children and adolescents. Braz J Phys Ther 16:10
3. Hartvigsen J, Christensen K, Frederiksen H (2003) Back pain remains a common symptom in old age. A population-based study of 4486 Danish twins aged 70–102. Eur Spine J 12:528–534
4. Global Burden of Disease, Injury Incidence, Prevalence Collaborators (2016) Global, regional, and national incidence, prevalence, and years lived with disability for 310 diseases and injuries, 1990–2015: a systematic analysis for the Global Burden of Disease Study 2015. Lancet 388:1545–1602
5. Waddell G (2004) The back pain revolution, 2nd edn. Churchill Livingstone, London
6. Global Burden of Disease 2015 DALYs and HALE Collaborators (2016) Global, regional, and national disability-adjusted life-years (DALYs) for 315 diseases and injuries and healthy life expectancy (HALE), 1990–2015: a systematic analysis for the Global Burden of Disease Study 2015. Lancet 388:1603–1658
7. Kumagai S, Tainaka H, Miyajima K et al (2005) Load on the low back of care workers in nursing homes for the elderly. J Occup Health 47:131–138
8. Konno S, Kikuchi S (1993) Increased intracompartmental pressure in the lumbar back muscles and lower back pain. Rinsh Seik Geka/Clin Orthop Surg 28(4):419–426
9. Konno S (1993) The intracompartmental pressure of the lumbar back muscles and lower back pain. Rinsh Seik Geka/Clin Orthop Surg:2897–2898
10. Fukui T (2005) Theory and technology of orthopedic physiotherapy. Medical View Co., Ltd, pp 145–146
11. Konno S, Kikuchi S (1994) Lumbar intramuscular pressure and chronic lower back pain – compartment syndrome pathology. Gen Rehabil 22:745–749
12. Miura H (2003) Measuring muscle metabolism -near-infrared spectroscopy- muscle science encyclopedia. Asakura Publishing Co., Ltd, pp 430–435
13. Atsuta Y, Takemitsu M (2003) Postural abnormality and lower back pain -elements of myogenic pain. J Musculoskeletal Syst 16(8):791–797
14. Kumamoto T, Seko T, Takahashi Y (2016) Effects of movement from a postural maintenance position on lumbar hemodynamic change. J Phys Ther Sci 28:1932–1935
15. Yokozawa H, Muraoka Y, Shimizu S et al (2002) Changes in muscle bundle length and muscle oxygen dynamics during static stretching. J Jpn Coll Angiol 42:25–29
16. Sakai Y, Matsuyama Y, Ishiguro N (2005) Intramuscular oxygenation of trunk muscle in elderly persons. J Lumbar Spine Disord 11: 148–156
17. Matsuda R, Kumamoto T, Seko T et al (2017) Influences of trunk extension on circulatory dynamics in low back muscles and their activity levels. J Phys Ther Sci 32:559–562

Numerical Optimisation of a NIRS Device for Monitoring Tissue Oxygen Saturation

Oliver da Silva-Kress, T. Cantieni, M. González, M. Michler, T. Rastija, R. Grabher, G. Piai, N. Ansari, K. Sharma, E. Morlec, M. Camenzind, L. Boesel, and U. Wolf

Abstract

The present work aims to develop a wearable, textile-integrated NIRS-based tissue oxygen saturation (StO_2) monitor for alerting mobility-restricted individuals – such as paraplegics – of critical tissue oxygen de-saturation in the regions such as the sacrum and the ischial tuberosity; these regions are proven to be extremely susceptible to the development of pressure injuries (PI).

Using a combination of numerical methods including finite element analysis, image reconstruction, stochastic gradient descent with momentum (SGDm) and genetic algorithms, a methodology was developed to define the optimal combination of wavelengths and source-detector geometry needed for measuring the StO_2 in tissue up to depths of 3 cm. The sensor design was optimised to account for physiologically relevant adipose tissue thicknesses (ATT) between 1 mm and 5 mm. The approach assumes only a priori knowledge of the optical properties of each of the three tissue layers used in the model (skin, fat, muscle) based on the absorption and scattering coefficients of four chromophores (O_2Hb, HHb, H_2O and lipid).

The results show that the selected wavelengths as well as the source-detector geometries and number of sources and detectors depend on ATT and the degree and volume of the hypoxic regions. As a result of a genetic algorithm used to combine the various optimised designs into a single sensor layout, a group of four wavelengths was chosen, coinciding with the four chromophores and agreeing very well with literature. The optimised number of source points and detector points and their geometry resulted in good reconstruction of the StO_2 across a wide range of layer geometries.

O. da Silva-Kress (✉) · T. Cantieni · U. Wolf
Institute of Complementary and Integrative Medicine, University of Bern, Bern, Switzerland
e-mail: oliver.kress@unibe.ch

M. González · M. Michler
Institute for Microtechnology and Photonics, OST Eastern Switzerland University of Applied Sciences, St. Gallen, Switzerland

T. Rastija · R. Grabher · G. Piai
Institute for Electronics, Sensors and Actuators, OST Eastern Switzerland University of Applied Sciences, St. Gallen, Switzerland

N. Ansari · K. Sharma · E. Morlec · M. Camenzind · L. Boesel
Laboratory for Biomimetic Membranes and Textiles, Empa, Swiss Federal Laboratories for Materials Science and Technology, Dübendorf, Switzerland

F. Scholkmann et al. (eds.), *Oxygen Transport to Tissue XLIII*, Advances in Experimental Medicine and Biology 1395, https://doi.org/10.1007/978-3-031-14190-4_67

Keywords

Tissue oxygen saturation (StO_2) · Pressure injury · Hypoxia · Wearable device

1 Introduction

Pressure injuries (PI) are caused by hypoxia due to pressure exerted on the tissue, which occludes the blood flow. Such injuries could be prevented if tissue oxygen saturation (StO_2) were monitored and the pressure removed, before irreversible damage occurs. One method to measure the StO_2 is near-infrared-spectroscopy. PI occur at pressure points such as the sit bones and hypoxia is localised. This means that such a NIRS device needs to be able to detect local hypoxia. The design of NIRS devices for optimal penetration depth, spatial resolution and chromophore reconstruction has been a focus ever since the technology proved to be a valuable, non-invasive and safe method for investigating the oxygen exchange in living subjects in 1942 by G. A. Millikan [1]. As the need for increased spatial resolution and tomographic methods increased, sensor geometries became more complex. Current devices have up to five wavelengths and up to 32 emitters and 32 detectors, most often not prioritising cost, size or mobility [2].

It is important to optimise the geometric arrangement of sources and detectors to be sensitive to such a localised hypoxia. Proper wavelength selection is another crucial step when designing a NIRS system [3, 4]. In combination with emitter and detector geometry optimisation, genetic algorithms are commonplace. However, this global optimiser can be very slow, especially in a multidimensional variable space and when the solution space becomes very large.

Since the present work aims to develop a wearable NIRS device with good spatial and depth resolution of StO_2 in various tissue regions and compositions, the goal is to find a balance between hardware complexity and spatial resolution while ensuring that hypoxia can be safely detected.

2 Methods

A mesh based on the finite element method (FEM) was constructed using the Nirfast finite element analysis package for Matlab. Three tissue layers (skin, fat and muscle), each with concentrations of four chromophores (HHb, O_2Hb, H_2O and lipid), were used as shown in Table 1. The mesh was a 100 × 100 mm rectangular slab with a total depth of 30 mm with a hypoxic sphere placed within the muscle layer at the fat-muscle boundary as shown in Fig. 1a. Nirfast was used to calculate the fluence rate of photons everywhere at the tissue surface due to various numbers and positions of point-sources of different monochromatic wavelengths for each tissue geometry and depth, volume and degree of hypoxia of a hypoxic sphere (the forward calculation) [5]. Nirfast was also used to then spatially reconstruct all chromophore concentrations in the entire tissue mesh, where the initial values were identical to the true values everywhere except for the hypoxic volume of interest. The error between the reconstructed and true [HHb] was calculated using the L^2 norm at each node within the pre-defined hypoxic volume only.

The goal of the optimisation was to minimise this error by iteratively changing the number of sources, the number of detectors, their locations on the tissue surface, and the wavelengths of light. The values of these input variables for each following iteration were chosen according to stochastic gradient descent with momentum (SGDm) to find a global minimum with as few iterations as possible in order to find the sensor configuration which allowed the most accurate reconstruction of the hypoxic volume.

2.1 Optimising a Sensor for a Specific Tissue Physiology

SGDm was used to seek the direction of each iteration in variable space. This approach takes the classic method of gradient descent and includes momentum; a way of keeping the upcoming variable changes from resulting in a

Table 1 Chromophore concentrations of the layered FEM mesh

	O_2Hb (μM)	HHb (μM)	H_2O (%Vol)	Lipid (%Vol)
Skin	0.045	0.015	0.5	0
Fat	0.0004	0.0001	0.2	0.78
Muscle	0.03	0.01	0.75	0

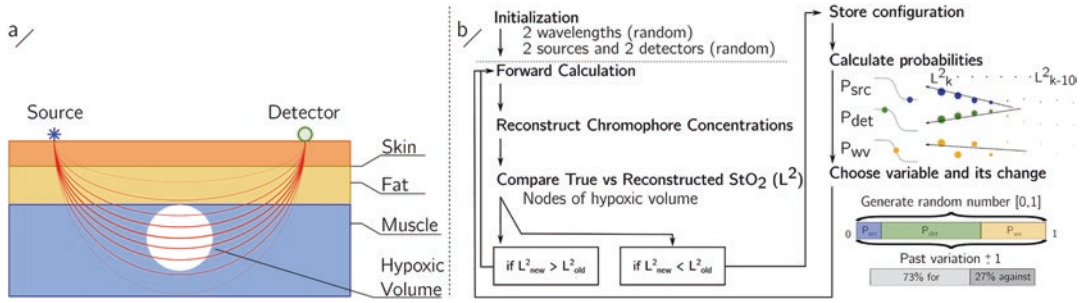

Fig. 1 (**a**) Representative geometry of the finite element tissue mesh and hypoxia placement. (**b**) Outline of the SGDm algorithm

solution which may be trapped in a local minimum by forward projecting the probable effect of a variable change based on past variable changes with exponentially decreasing weight.

The stochastic element chooses the path in variable space based on those probabilities, helping to further avoid local minima and to aid in rate of convergence by sampling a broad region of the solution space (Fig. 1b).

The algorithm also allows the physical constraints of the sensor to be built into the optimisation. These constraints include the number of wavelengths and the number of source and detector points (based on desired hardware complexity), the minimal distance and maximum source-detector separation (SDD) as a function of a limited dynamic range (based on hardware limits). The increase of these variables is countered by an offset sigmoid function which stochastically weighs the benefits of increasing them against the practical cost of doing so. Formally, the objective of the optimisation is to

minimise

$$\Sigma_{i=1}^{N}\left(\left[HHb\right]_i^C\left(S,D,\lambda\right)-\left[HHb\right]_i^T\right)^2$$

subject to

$$2\le N_\lambda \le 4$$

and

$$P_{S,D,\lambda}^{\pm}=\left(1-W_{S,D}\right)\times\left(1-E_{S,D,\lambda}\right)$$

and

$$\lambda=\left[630:10:950\right]$$

for

$$E_{S,D,\lambda}=\frac{1}{1+\exp\left(-N_{S,D}+\delta\right)},\delta=20$$

$$W_{S,D}=Sig\left(\Sigma\left(\frac{1}{\exp\left(N_{S,D}^{\pm}-1:N_{S,D}^{\pm}\right)}\right)\times N_{S,D}^{\pm}\right)$$

where N is the number of nodes within the hypoxic volume, S is the number and position of the source points, D is the number and position of the detection points, λ is the wavelength array, and the superscripts C and T indicate calculated (reconstructed) and true chromophore concentrations, respectively. The number of wavelengths was allowed to be chosen freely between 2 and 4, and the available wavelengths were between 630 nm and 950 nm in 10 nm steps. $P_{S,D,\lambda}^{\pm}$ is the probability that a new configuration can be accepted at each iteration, and is calculated based on the total forward-projected change to W which increases when the number of S or D increases based on an offset sigmoid function and E which

increases based on the increase of past similar L^2 changes of the same variable.

2.2 A Genetic Algorithm Approach to Finding a General Solution

Through the various combinations of tissue parameters, a total of 300 meshes were constructed and the optimum wavelength and source-detector geometries calculated using SGDm. The L^2 of each iteration was encoded in the form of chromosomes, or binary strings. Counting for every iteration and its stored L^2 value for each of the 300 optimisations, a total of over 16,000 chromosomes could be populated for the genetic algorithm. The chromosomes were ranked according to fitness (normalised inverse of L^2) and the top 15% were stochastically selected into the mating population to boost genetic diversity. After the selected population was combined to produce offspring with a P = 1/L chance to mutate, where L is the length of the chromosome, forward calculations were done using 16 FEM meshes, each a combination of the extreme values of the mesh geometry and composition. For each reconstructed set, the mean of the L^2 value was stored. These solutions, with their updated fitness values, were fed back into the general population and the process repeated. This process was allowed to run for 50 generations, or until dominating groups of solutions emerged. In an ideal scenario with constant evolutionary pressure, the chromosomes of the breeding population would all converge. The evolution of the dominating chromosomes can be tracked during optimisation. To avoid degenerate solutions to the source-detector geometry, the hypoxic volume was offset from the centre of the mesh in the surface plane.

3 Results

3.1 SGDm

The algorithm was able to define sensor configurations which could reconstruct hypoxic regions at a depth of up to 30 mm for large hypoxic volumes and degrees of hypoxia. Reconstruction, within the wavelengths and source-detector geometry bounds set before optimisation, was limited by hypoxic volume and depth. Localised hypoxia at a mean depth of at least 2 cm with larger volume and with StO_2 less than 60% of baseline can be reconstructed with less than 5% error in StO_2 using up to 4 wavelengths and up to 10 sources and detectors (Fig. 2).

3.2 Genetic Algorithm

The top two dominating chromosomes in the evolving population were tracked until convergence became clear. Because the two dominant wavelength groups were nearly equal in prevalence, both were considered as suitable groups for the NIRS device (Table 2). Both groups match well with literature, have reasonable spacing between wavelengths and placement on both sides of the isosbestic point of both haemoglobin species [2].

There exists a wide group of source-detector configurations, likely due to small variations of the geometry near the global minimum having little influence on the reconstruction error. These configurations tend towards 4 sources, 8 detectors and a rather unintuitive geometry cantered around the hypoxic volume.

4 Discussion

The hypoxic inclusion was embedded in the muscle layer, meaning that increased ATT resulted in a deeper inclusion. The number of source and detector points resulting from SGDm therefore increased greatly with depth, often reaching the upper limit of the preset hardware bounds. Therefore, it may be possible to exceed the depth limit seen in these simulations by allowing for more sources and detectors.

Because the genetic algorithm used the mean L^2 of tissue geometries with no ATT and high ATT to score fitness, each of the two dominating wavelength groups may correspond to low and high ATT, respectively. This is supported in that the second wavelength group includes 910 nm;

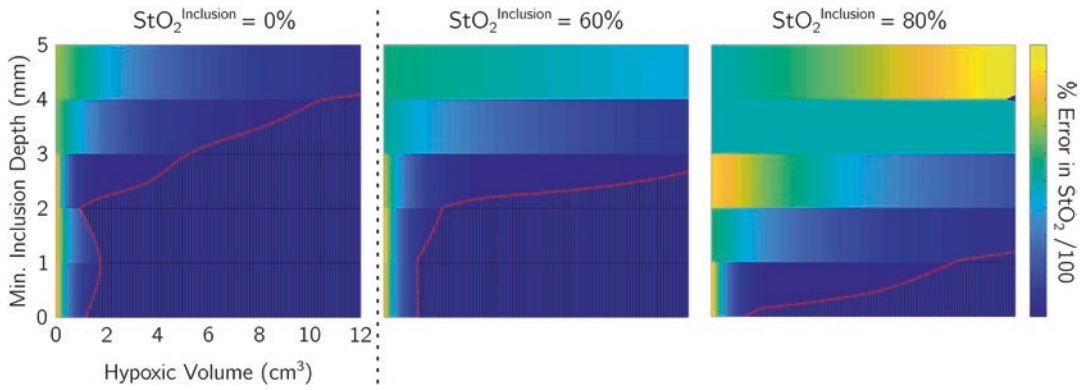

Fig. 2 Percent error in reconstructed StO_2 for different minimum inclusion depths (top of hypoxic sphere) and hypoxic volumes, for three different inclusion StO_2. The regions within the outlined portions show the space where StO_2 could be resolved with less than 5% error

Table 2 The two dominating wavelength groups resulting from 50 generations of evolution

	λ_1	λ_2	λ_3	λ_4
Group 1 (nm)	690	740	810	880
Group 2 (nm)	660	690	880	910

beyond the typical upper regime for NIRS devices, but within the regime where lipid absorption begins to dominate haemoglobin absorption. This effect should be further investigated by decoupling depth of the hypoxia from ATT, allowing the hypoxic region to be placed transregionally in the layer mesh.

Past methods have focused on the optimisation of either the wavelength group or the optode geometry. Corlu et al. presented in 2005 an algorithm to analyse wavelength groups for accurate reconstruction of the same 4 chromophores which revealed a group of 5 wavelengths (650, 710, 865, 912, 928 nm) for a fixed optode geometry [6]. Conversely, Culver et al. used singular value decomposition to optimise the geometry of a fixed number of sources and detectors in 2001 [7]. The wavelength groups calculated in the present work are consistent with good separability and low crosstalk dual-wavelength groups found by Uludağ et al. in 2004 [8]. The present work is unique in that the number of sources and detectors, their arrangement, and the number of wavelengths are simultaneously optimised while the algorithm allows bounding parameters based on desired hardware complexity. In this sense, all specifications of the sensor are optimised in parallel. Using 4 wavelengths also allows an exact solution to the MBLL when four chromophores are considered; a large advantage for practical application.

In conclusion, simultaneously solving for all necessary parameters needed to design a NIRS sensor for StO_2 recovery can be accomplished with relatively fast convergence. It also shows a correlation between the parameters of tissue layer geometry, number and locations of sources and detectors, and the wavelengths used, further suggesting the importance of multivariate parallel optimisation.

One resulting sensor design using wavelength *Group 1*, 4 emitters and 8 detectors is now being used to manufacture the first wearable sensors for the prevention of pressure injuries. The optimisation approach also allows the flexibility to design NIRS sensors for further applications based on measurement area and costs.

As with many global search methods, the process can be computationally expensive. However, the approach converges in relatively few iterations. The most expensive step is the inverse calculation, which can take up to 2 min per iteration or up to 12 h per configuration, or a week for a full solution on a CPU cluster. This can be avoided by evaluating the quality of the forward data differently.

Acknowledgments We gratefully acknowledge funding by the SNSF and Innosuisse Bridge Discovery (project no. 180983). Calculations were performed on UBELIX (http://www.id.unibe.ch/hpc), the HPC cluster at the University of Bern.

References

1. Millikan GA (1942) The oximeter, an instrument for measuring continuously the oxygen saturation of arterial blood in man. Rev Sci Instrum 13(10):434–444. https://doi.org/10.1063/1.1769941
2. Scholkmann F, Kleiser S, Metz AJ et al (2014) A review on continuous wave functional near-infrared spectroscopy and imaging instrumentation and methodology. NeuroImage. https://doi.org/10.1016/j.neuroimage.2013.05.004Ref3
3. Sato H, Kiguchi M, Kawaguchi F et al (2004) Practicality of wavelength selection to improve signal-to-noise ratio in near-infrared spectroscopy. NeuroImage 21(4):1554–1562. https://doi.org/10.1016/j.neuroimage.2003.12.017
4. Uludağ K, Steinbrink J, Villringer A et al (2004) Separability and cross talk: optimizing dual wavelength combinations for near-infrared spectroscopy of the adult head. NeuroImage 22(2):583–589. https://doi.org/10.1016/j.neuroimage.2004.02.023
5. Dehghani H, Eames ME, Yalavarthy PK et al (2009) Near infrared optical tomography using NIRFAST: algorithm for numerical model and image reconstruction. Commun Numer Methods Eng 25(6):711–732. https://doi.org/10.1002/cnm.1162
6. Corlu A, Choe R, Durduran T et al (2005) Diffuse optical tomography with spectral constraints and wavelength optimization. Appl Opt 44(11):2082–2093. https://doi.org/10.1364/AO.44.002082
7. Culver JP, Ntziachristos V, Holboke MJ, Yodh AG (2001) Optimization of optode arrangements for diffuse optical tomography: a singular-value analysis. Opt Lett 26(10):701. https://doi.org/10.1364/OL.26.000701
8. Uludağ K, Steinbrink J, Villringer A, Obrig H (2004) Separability and cross talk: optimizing dual wavelength combinations for near-infrared spectroscopy of the adult head. NeuroImage 22(2):583–589. https://doi.org/10.1016/j.neuroimage.2004.02.023

Upper Trapezius Muscle Tonicity, Assessed by Palpation, Relates to Change in Tissue Oxygenation and Structure as Measured by Time-Domain Near Infrared Spectroscopy

A. Buot, K. Brownhill, and F. Lange

Abstract

Palpation is a diagnostic tool widely used by manual therapists despite its disputed reliability and validity. Previous studies have usually focused on the detection of myofascial trigger points (MTrPs), i.e., the points within muscles thought to have undergone molecular composition, oxygenation and structural changes, altering their tonicity. Time-domain near-infrared spectroscopy (TD-NIRS) could provide new insights into soft tissue oxygenation and structure, in order to objectively assess the validity and reliability of palpation. This pilot study aims at (1) assessing the ability of TD-NIRS to detect a difference between palpably normal and hypertonic upper trapezius (UT) muscles, and (2) to estimate the reproducibility of the TD-NIRS measurement on UT muscles. TD-NIRS measurements were performed on 4 points of the UT muscles in 18 healthy participants (10F, mean age: 27.6 years), after a physical examination by a student osteopath to locate these points and identify the most and least hypertonic. From TD-NIRS, the most hypertonic points had a higher concentration in deoxy- ([HHb]) (0.887 ± 0.253 μM, $p < 0.001$) and total haemoglobin ([HbT]) (1.447 ± 0.772 μM, $p < 0.001$), a lower tissue oxygen saturation (StO_2) (−0.575 ± 0.286%, $p < 0.001$), and a greater scattering amplitude factor (AF) (0.2238 ± 0.1343 cm^{-1}, $p = 0.001$) than the least hypertonic points. Moreover, the intra-class correlation coefficient one-way random-effects model (ICC (1,1)) calculated for each TD-NIRS parameter and for each point revealed an excellent reliability of the measurement (Mean ± SD, 0.9253 ± 0.0678). These initial results, showing that changes in TD-NIRS parameters correlate with changes in muscle tonicity as assessed by palpation, are encouraging and show that TD-NIRS could help to further assess the validity of palpation as a diagnostic tool in manual therapy.

Keywords

Tissue oxygen saturation (StO_2) · NIRS · Myofascial trigger points · Haemodynamics

A. Buot · K. Brownhill
Research Department, University College of Osteopathy, London, UK

F. Lange (✉)
Department of Medical Physics & Biomedical Engineering, University College London, London, UK
e-mail: f.lange@ucl.ac.uk

F. Scholkmann et al. (eds.), *Oxygen Transport to Tissue XLIII*, Advances in Experimental Medicine and Biology 1395, https://doi.org/10.1007/978-3-031-14190-4_68

1 Introduction

Osteopaths are required to recognise the difference between the normal and abnormal function of a tissue [1]. Several techniques are available to determine these changes, among them the sense of touch combined with observation and motion evaluation [1]. Palpation is usually applied to assess tissue motion, soft tissue quality, to provoke pain or tenderness, and to determine bony landmark position. It is a widespread tool to diagnose soft tissue dysfunctions. However, a problem is the continued use of palpation as a diagnostic tool in osteopathic practice, despite lack of robust evidence of validity or reliability.

Myofascial trigger points (MTrPs) are the characteristic features of myofascial pain syndrome (MPS) which is described as "…a regional pain syndrome characterized by myofascial trigger points (MTrP) in palpable taut bands of skeletal muscle that refer pain to a distance, and that can cause distant motor and autonomic effects." [2]. MPS is believed to be the underlying pathophysiology in most patients with chronic non-specific neck pain [2] (when there is no recognisable pathology underlying the pain). There is evidence that chronic load on the muscle causes microtubule proliferation and a restriction of blood flow resulting in local ischemia/hypoxia [3].

Time-domain near-infrared spectroscopy (TD-NIRS) is a non-invasive optical tool that is able to monitor, non-invasively, physiological (i.e., haemodynamic) and structural tissue parameters. Notably, it can measure the concentration of different chromophores, such as oxy- ($[HbO_2]$) and deoxy-haemoglobin ([HHb]) in the tissues (and thus, the total concentration in haemoglobin [HbT]) and the tissue oxygen saturation ($StO_2 = [HbO_2]/[HbT]$) [4]. Moreover, it can give an insight into tissue structure by analysing the scattering information obtained [5].

These capacities of TD-NIRS allow changes in tissue properties to be observed in MPS, which can be used to evaluate palpation validity. Therefore, this pilot study aims to assess the structure and oxygenation of healthy muscles, enabling further study on non-healthy subjects, and to assess the validity of palpation. The two specific aims set for this study are (1) to assess whether scattering and absorption parameters, as measured by TD-NIRS, differ between palpably normal and hypertonic upper trapezius muscles, and (2) to estimate the reproducibility of tissue parameters measured by TD-NIRS, using the upper trapezius muscles.

2 Methods

A total of 18 healthy adults (10F, mean age: 27.6 years) participated in this study. Participants presenting with any self-reported pathology such as acute or chronic neck pain, fibromyalgia, myopathy, radiculopathy, history of shoulder or spine surgery, cardiovascular, pulmonary or metabolic diseases were excluded. The research protocol was reviewed and approved by the Research Ethics Committee of the UCO, London; and signed informed consent was obtained from all participants.

The examiner, a student osteopath and physiotherapist with 6 years' experience, palpated the subjects' upper trapezius muscles to identify the most and least hypertonic sites (4 sites in total, 2 on each side). Palpation was limited to the central region of the upper trapezii within 10 cm of the muscle's midline. The least amount of pressure was used to identify these sites. The participants were asked to report if the pressure used elicited tenderness and their answer was recorded. Then, the examiner marked these 4 sites using a surgical skin marker.

The TD-NIRS measurements were made using an in-house developed instrument previously described in [6]. In the present study, one source and one detector were used, allowing to record 1 channel at a time. A custom 3D printed probe was used to hold the source and detector optical fibre at a separation distance ρ = 3 cm when applied to the skin. The probe was manually centred on each of the 4 marked sites, with the least amount of pressure necessary to maintain skin contact. Measurements were performed in a dark room to decrease the amount of background light. TD-NIRS data were acquired

sequentially for the 4 points, using 16 wavelengths, from 650 to 890 nm in steps of 15 nm, with an acquisition time of 2.5 s per wavelength. To estimate the reproducibility of the measurement, data acquisition of the 4 different sites was repeated 3 times.

The TD-NIRS data was processed offline using Matlab R2018a. We used the classical method to estimate the reduced scattering coefficient μ'_s and the absorption coefficient μ_a, where the distribution of time of flights (DTOF) are fitted to a standard homogeneous model of diffusion theory, after convolution with the IRF. Then, the absorption spectra were used to extract the haemodynamic parameters. Finally, the scattering information were analysed by fitting the scattering spectra obtained between 740 and 870 nm, to an approximation of Mie scattering. This allows to extract 2 parameters, the scattering amplitude factor (AF) and scattering power (SP).

Statistical analyses were performed using Jamovi software (2018). Descriptive statistics were calculated for demographic variables (such as age and sex). For inferential tests, the probability value was set at $p < 0.05$.

To assess the effect of muscle tonicity (most/least hypertonic) on the TD-NIRS parameters, linear mixed effects regression models were used. Participants were treated as random effects (random intercepts) to account for correlations between measurements due to measurements being repeated on the same subject. The TD-NIRS parameters were the response variables, and the muscle tonicity state was the fixed effect.

To estimate the reproducibility of tissue parameters measured by TD-NIRS, their reliability has been calculated using the intraclass correlation coefficient one-way random-effects model (ICC (1,1)).

3 Results

Primary descriptive analysis of haemodynamic TD-NIRS observations showed a bimodal distribution for [HbO_2], [HbT] and StO_2. When plotted against age and sex, it showed that these parameters were strongly dependent on these demographic variables. Hence, age and sex were included in the models as fixed effects. Inclusion of these variables led to the model residuals becoming normally distributed.

Hypertonicity was found to be statistically significant for response variables [HHb] ($F_{(1,198)} = 47.205$, $p < 0.001$), [HbT] ($F_{(1,198)} = 13.53$, $p < 0.001$), and StO_2 ($F_{(1,198)} = 15.42$, $p < 0.001$) (Table 1). Models indicated that the most hypertonic points had [HHb] 0.887 μM and [HbT] 1.447 μM higher than the least hypertonic points, as well as a decreased StO_2 of 0.5%. In contrast, the [HbO_2] in the most and least hypertonic points exhibited no significant difference ($F_{(1,198)} = 2.78$, $p < 0.097$).

A similar process was used for the scattering TD-NIRS observations and the tonicity, as the primary descriptive analysis showed a bimodal distribution, mainly related to sex and age. Modelling with AF as response variable showed that hypertonicity was statistically significant ($F_{(1,198)} = 10.657$, $p = 0.001$) (Table 1). AF was 0.2238 cm^{-1} higher for the most hypertonic points compared to the least hypertonic points. However, for SP as response, tissue tonicity was not statistically significant ($F_{(1,198)} = 0.262$, $p = 0.609$).

The residuals were examined using a Q-Q plot of residuals and found to be normally distributed. The presence of overly influential observations was checked by calculating for Cook's distances. No observation was found to be overly influential (Cook's distance <1).

The intraclass correlation coefficients calculated for repeated observations were calculated for each TD-NIRS parameter. All ICC values indicated an excellent reliability (Table 2).

4 Discussion

Our study showed that the most hypertonic points in the upper trapezius muscle had a greater [HHb] and [HbT], a reduced StO_2, and no changes in [HbO_2] compared to the least hypertonic points as measured by TD-NIRS. This could be interpreted as a local small increased metabolic activity (greater [HHb]), where O_2 demand mar-

Table 1 Main statistical results of the linear mixed effects regression model between haemodynamic and scattering TD-NIRS observations and hypertonicity state, accounting for Age and Sex

	TD-NIRS parameters	ESTIMATE	95% CONFIDENCE INTERVAL		
		Effect most – (least)	Lower	Upper	p
Haemodynamic	[HHb]	0.887	0.634	1.14	<0.001
	[HbO_2]	0.560	−0.099	1.22	0.097
	[HbT]	1.447	0.676	2.22	<0.001
	StO_2	−0.575	−0.863	−0.29	<0.001
Scattering	AF	0.2238	0.0895	0.3582	0.001
	SP	0.0059	−0.0167	0.0285	0.609

Table 2 ICC (1,1) for TD-NIRS parameters according to every point

TD-NIRS parameters	Point 1	Point 2	Point 3	Point 4
[HHb]	0.7327	0.9275	0.8615	0.7793
[HbO_2]	0.9718	0.9797	0.9620	0.9826
[HbT]	0.9563	0.9790	0.9508	0.9854
StO_2	0.9579	0.9470	0.9583	0.9115
AF	0.9070	0.9515	0.8051	0.9678
SP	0.93269	0.9867	0.9234	0.8891

ginally outstrips supply (small decrease in StO_2 and no significant change in [HbO_2]) by means of an increased blood volume/flow (higher [HbT]). This hypothesis would have to be confirmed by adding an independent assessment of the blood flow to clearly differentiate the supply from the demand, which is not straightforward with NIRS measurements only. Techniques such as diffuse correlation spectroscopy (DCS) could be used in combination with TD-NIRS to do so [7]. Moreover, our participants were healthy subjects, so it remains to be seen whether the same findings would be seen in a clinical population to better understand the physiology of MPS and MTrPs.

Regarding the scattering parameters, our results showed an increase of the AF but not of the SP in the most hypertonic points compared to the least. This reflects an augmentation in the effective concentration of the scattering centres with no change in their dimension, indicating a greater density of the *same* scattering structure [5]. Thus, this suggests that the most hypertonic points were optically denser than the least hypertonic points within the upper trapezius muscle according to the TD-NIRS analysis. This is in line with previous works using different instruments such as ultrasound imaging [8], showing a difference in tissue density between MTrPs and normal sites in various muscles. However, as the NIRS measurement is not a direct measure of tissue density, further work would be needed to confirm this hypothesis.

Overall, the TD-NIRS scattering and absorption parameters seems to differ between palpably normal and hypertonic points within the upper trapezius muscles. Several limitations of this preliminary study should be acknowledged. First, in the methodology, the amount of external pressure applied by the examiner was qualitatively assessed, and more quantitative measurement is needed to standardise the measurements, such as the use of a pressure algometer. Secondly, it is worthwhile to realise that baseline muscle tonicity varies between individuals. The use of a scale or a tonicity ratio (between the most hypertonic point and the surrounding muscle tissue) might provide with

more accurate results. Then, in our study, a single practitioner performed all examinations, and inter- and intra-observer variability were not assessed. For the TD-NIRS protocol, subcutaneous adipose tissue thickness (SATT) was not measured in this study as it was thought not be significant over the upper trapezius muscle. However, it might partially explain the difference between male and female, as male tends to have a smaller SATT with respect to female [9]. Further research might see the use of a skinfold calliper to measure SATT, and/or a more complex light propagation model could be used in TD-NIRS to allow for the SATT above the muscle. Finally, in the present study the myoglobin (Mb) species was not considered. Indeed, there is a debate about the contribution of haemoglobin (Hb) and Mb to the in vivo near-infrared (NIR) signal from skeletal muscle, as it is difficult to differentiate Hb and Mb spectra since they are very similar in the NIR range [9].

In conclusion, this study shows, for the first time, a correlation between the resting tonicity state of the upper trapezius muscle, detected by palpation, and a change in the haemodynamic and scattering state measured by TD-NIRS in healthy subjects. These initial results are encouraging and show that TD-NIRS could help to further understand the physiology behind the formation of MPS and MTrPs and assess the validity of palpation as a diagnostic tool in manual therapy.

References

1. www.osteopathy.org.uk/standards/osteopathic-practice/
2. Cerezo-Téllez E, Torres-Lacomba M, Mayoral-Del Moral O et al (2016) Prevalence of myofascial pain syndrome in chronic non-specific neck pain: a population-based cross-sectional descriptive study. Pain Med (Malden, Mass) 17(12):2369–2377
3. Dommerholt J, Bron C, Franssen J (2011) Myofascial trigger points: an evidence-informed review. In: Dommerholt J, Huijbregts P (eds) Myofascial trigger points: pathophysiology
4. Contini D, Zucchelli L, Spinelli L, Caffini M et al (2012) Review: brain and muscle near infrared spectroscopy/imaging techniques. J Near Infrared Spectrosc 20(1):15–27
5. Pifferi A, Farina A, Torricelli A et al (2012) Review: time-domain broadband near infrared spectroscopy of the female breast: a focused review from basic principles to future perspectives. J Near Infrared Spectrosc 20(1):223–235
6. Lange F, Dunne L, Hale L et al (2019) MAESTROS: a multi-wavelength time domain NIRS system to monitor changes in oxygenation and oxidation state of cytochrome-c-oxidase. IEEE J Sel Top Quantum Electron 25(1):7100312
7. Cortese L, Lo Presti G, Zanoletti M et al (2021) The LUCA device: a multi-modal platform combining diffuse optics and ultrasound imaging for thyroid cancer screening. Biomed Opt Express 12(6):3392–3409
8. Jafari M, Bahrpeyma F, Mokhtari-Dizaji M et al (2018) Novel method to measure active myofascial trigger point stiffness using ultrasound imaging. J Bodyw Mov Ther 22(2):374–378
9. Ferrari M, Muthalib M, Quaresima V (2011) The use of near-infrared spectroscopy in understanding skeletal muscle physiology: recent developments. Phil Trans R Soc A 369:4577–4590

Perceived Exertion Correlates with Multiple Physiological Parameters During Cardiopulmonary Exercise Testing

Shinichiro Morishita, Atsuhiro Tsubaki, Kazuki Hotta, Tatsuro Inoue, Sho Kojima, Weixiang Qin, Daichi Sato, Akihito Shirayama, Yuki Ito, and Hideaki Onishi

Abstract

The purpose of this study was to investigate the relationship of the Borg scale score with leg-muscle oxygenated haemoglobin (O_2Hb) and deoxygenated haemoglobin (HHb) levels on near infrared spectroscopy (NIRS) and the work rate, heart rate (HR), oxygen uptake (VO_2) and minute ventilation (VE) during supine cardiopulmonary exercise testing (CPET) in healthy adult men. We also investigated the relationships between the leg-muscle O_2Hb and HHb levels and the work rate during supine CPET. Fifteen healthy male volunteers (mean age, 20.7 ± 0.6 years; mean height, 172.1 ± 5.7 cm; mean body weight, 61.7 ± 6.6 kg) participated in this study. The cardiopulmonary and NIRS parameters were assessed during each minute of supine CPET and at the end of the test. The Borg scale score significantly correlated with the work rate, HR, VO_2, and VE during supine CPET (Rs = 0.86–0.94, $p < 0.05$). Furthermore, the Borg scale score significantly correlated with the leg-muscle O_2Hb and HHb levels during supine CPET (Rs = −0.6, and 0.8, respectively; $p < 0.05$). The leg-muscle O_2Hb and HHb levels had significant correlations with the work rate (R = −0.62 and 0.8, respectively; $p < 0.05$). The Borg scale score may be used to determine the rating of perceived exertion, whole-body fatigue and local-muscle fatigue during supine exercise. Moreover, leg-muscle oxygenation is associated with the work rate in supine exercise, similar to that observed in upright exercise.

S. Morishita (✉)
Department of Physical Therapy, School of Health Science, Fukushima Medical University, Fukushima, Japan

Institute for Human Movement and Medical Science, Niigata University of Health and Welfare, Niigata, Japan

Department of Physical Therapy, Faculty of Rehabilitation, Niigata University of Health and Welfare, Niigata, Japan

A. Tsubaki · K. Hotta · T. Inoue · H. Onishi
Institute for Human Movement and Medical Science, Niigata University of Health and Welfare, Niigata, Japan

Department of Physical Therapy, Faculty of Rehabilitation, Niigata University of Health and Welfare, Niigata, Japan

S. Kojima · W. Qin
Institute for Human Movement and Medical Science, Niigata University of Health and Welfare, Niigata, Japan

D. Sato · A. Shirayama · Y. Ito
Department of Physical Therapy, Faculty of Rehabilitation, Niigata University of Health and Welfare, Niigata, Japan

F. Scholkmann et al. (eds.), *Oxygen Transport to Tissue XLIII*, Advances in Experimental Medicine and Biology 1395, https://doi.org/10.1007/978-3-031-14190-4_69

Keywords

Borg scale score · NIRS · Fatigue · Leg muscle hemoglobin oxygenation

1 Introduction

Supine bicycle ergometry exercises have been performed by patients undergoing haemodialysis [1]. Additionally, supine bicycle ergometry exercises have been used as part of early rehabilitation in intensive care units [2] and are often used in cardiopulmonary exercise testing (CPET) [3].

Previous studies have shown that deoxygenated haemoglobin (HHb) concentration in leg muscles, when measured by near infrared spectroscopy (NIRS), increases in relation to the work rate during upright CPET in healthy adults [4]. The rating of perceived exertion (RPE) using the Borg scale can represent extreme intensities of activity and is significantly correlated with oxygen uptake (VO_2), heart rate (HR) and work rate, which gradually increases during upright CPET in healthy adults [5] .

The purpose of this study was to investigate the relationships of the Borg scale score with the levels of leg-muscle O_2Hb and HHb via NIRS and the work rate, heart rate (HR), oxygen uptake (VO_2) and minute ventilation (VE) during supine CPET in healthy adult male volunteers. We also investigated the relationships between the leg-muscle O_2Hb and HHb levels and the work rate during supine CPET.

2 Methods

2.1 Participants

Fifteen healthy male volunteers (mean age, 20.7 ± 0.6 years; mean height, 172.1 ± 5.7 cm; mean body weight, 61.7 ± 6.6 kg) participated in this study. No participant exhibited symptoms of neurological or cardiovascular disease, and all were free from medication at the time of the study. Each participant provided written informed consent after receiving information regarding the potential risks, study objectives, measurement techniques and benefits associated with the study. This study was approved by the Ethics Committee of Niigata University of Health and Welfare (Approval No. 18124–190,116) and was conducted in accordance with the ethical standards of the 1964 Declaration of Helsinki and its later amendments or comparable ethical standards.

2.2 Experimental Procedure

Participants performed supine CPET with ramp-exercise protocols to determine the VO_2 and VE. The protocol consisted of a 4-min rest period, 4-min warm-up period, cardiopulmonary exercise, and 2-min cool-down period. A ramp program with an incremental increase in the workload of 20 watts/minute on a stationary bicycle (Aerobike 75XLIII; Konami, Tokyo, Japan) accompanied by electrocardiography (ECG; DS-7520, Fukuda Denshi, Tokyo, Japan) and an exhaled gas analyser (AE-310S; Minato Medical Science, Osaka, Japan) were used. All participants were instructed to maintain a cadence of 50 rotations per minute (rpm) during supine CPET. Exhaustion was defined as follows [6]: (1) a plateau in VO_2; (2) respiratory exchange ratio > 1.1; (3) HR values near the age-predicted maximal heart rate, calculated as 220 - (0.65 × age); and (4) a decrease in the cycling cadence to <50 rpm, despite strong verbal encouragement. The highest value obtained for VO_2 was considered the VO_2 peak. We evaluated the HR (using ECG), work rate (in watts), and VO_2 and VE (using an exhaled gas analyser) for each minute of supine CPET and at the end of the exercise test. Additionally, the anaerobic thresholds (ATs) during supine CPET were determined using the V-Slope method [7]. All participants were asked, “How hard do you feel you are working?” using the Borg scale and their responses were recorded every minute. The Borg CR-10 scale, comprising a rating between 0 (nothing at all) and 10 (very very strong), was used in this study.

2.3 NIRS Measurements

NIRS was used to determine the muscle oxygen consumption during supine CPET. We evaluated the O_2Hb and HHb levels for each minute of supine CPET and at the end of the exercise test. O_2Hb and HHb levels were measured in the left vastus lateralis muscle using NIRS (OMEGAFLOW BOM-L1 TRW, OMM Corp., Tokyo, Japan). The probe and detector were set in an optically dense rubber holder to ensure stability in their relative positions. They were secured to the thigh using adhesive tape in order to minimise motion artefacts and contamination of the signal by ambient light. The HHb level can be used to quantify muscle oxygen extraction [8]. O_2Hb and HHb parameters were presented as the relative changes from those at rest.

2.4 Statistical Analysis

The Spearman rank correlation coefficient (Rs) was used to evaluate the relationships between the Borg scale score and the work rate, HR, VO_2 and VE as well as the O_2Hb and HHb levels during supine CPET. In addition, the Pearson correlation coefficient (R) was used to evaluate the relationships between O_2Hb and HHb levels and the work rate during supine CPET. Statistical analyses were performed using SPSS 21.0 (SPSS Japan Inc., Tokyo, Japan). Statistical significance was set at $p < 0.05$.

3 Results

All participants completed supine CPET (Table 1). The Borg scale score had a significant correlation with the work rate, HR, VO_2, and VE during supine CPET (Rs = 0.86–0.94, $p < 0.05$; Figs. 1a–d). Furthermore, the Borg scale score showed a significant correlation with the leg-muscle O_2Hb and HHb levels during supine CPET (Rs = −0.6, and 0.8, respectively; $p < 0.05$; Figs. 1e, f). The leg-muscle O_2Hb and HHb levels significantly correlated with the work rate (R = −0.62, and 0.8, respectively; $p < 0.05$; Figs. 1g, h).

Table 1 Subject characteristics ($n = 15$)

Characteristics	Mean (SD)
Age, years	20.7 (0.6)
Height, cm	172.1 (5.7)
Body weight, kg	61.7 (6.6)
Cardio-pulmonary exercise testing	
At rest	
Borg scale	0 (0–0)
Work rate (Watts)	0 (0)
HR (beat/minute)	72.1 (11.3)
VO_2 (ml/kg/min)	3.8 (0.7)
VE (L)	6.9 (1.1)
Anaerobic threshold (AT)	
Borg scale	2 (1–5)
Work rate (Watts)	86.7 (22.1)
HR (beat/minute)	120.3 (20.3)
VO_2 (ml/kg/min)	18.8 (4.9)
VE (L)	27.3 (6.5)
O_2Hb (a.u)	−0.09 (0.15)
HHb (a.u)	0.04 (0.12)
End of test (maximum)	
Borg scale	8 (5–10)
Work rate (Watts)	175.3(21.3)
HR (beat/minute)	173.9 (13.5)
VO_2 (ml/kg/min)	35.3 (8.3)
VE (L)	41.5 (12.9)
O_2Hb (a.u)	−0.35 (0.2)
HHb (a.u)	0.46 (0.18)

SD standard deviation, *HR* heart rate, *VO_2* oxygen uptake, *VE* minute ventilation, *O_2Hb* oxygenated haemoglobin, *HHb* deoxygenated haemoglobin concentration

4 Discussion

This study showed that Borg scale score had significant correlations with physiological parameters such as the HR, VO_2, and VE, which gradually increased with the work rate during supine CPET in healthy adults. The Borg scale score also significantly correlated with leg-muscle O_2Hb and HHb levels, as assessed by NIRS, during supine CPET. Additionally, the leg-muscle O_2Hb and HHb levels had significant correlations with the work rate during supine CPET.

Our previous study showed that the rating of perceived exertion significantly correlated with the work rate, HR and VO_2 during upright CPET in healthy adults [9]. The Borg scale score appears to correlate with physiological parameters such as HR, VO_2 and VE during supine

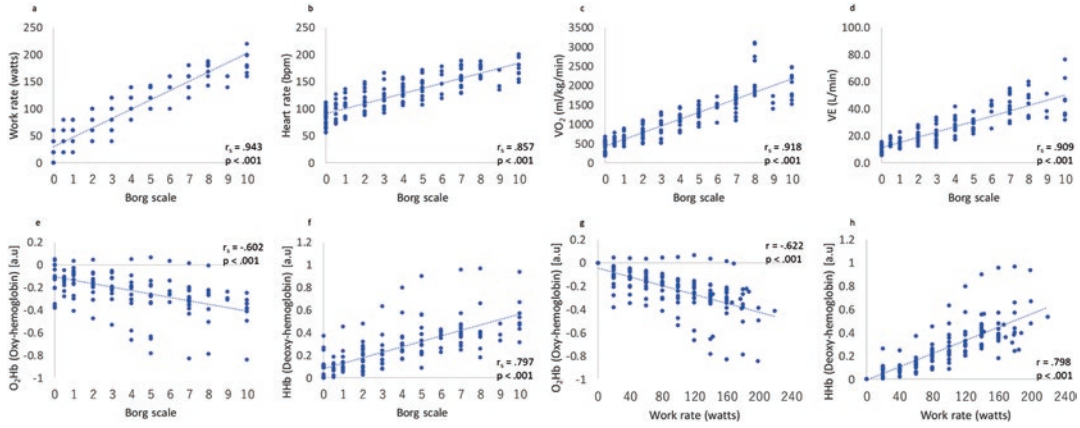

Fig. 1 Relationship between the Borg scale rating of perceived exertion and physiological outcomes and O_2Hb and HHb levels during supine cardiopulmonary exercise testing Scatterplots illustrating the relationships between the Borg scale score and physiological and NIRS parameters every minute during supine cardiopulmonary exercise testing for each subject are shown. (**a**) the Borg scale and work rate; (**b**) the Borg scale and heart rate; (**c**) the Borg scale and VO_2; (**d**) the Borg scale and VE; (**e**) the Borg scale and O_2Hb; (**f**) the Borg scale and HHb; (**g**) O_2Hb and work rate; (**h**) HHb and work rate
VO_2 oxygen uptake, *VE* minute ventilation, *O_2Hb* oxygenated haemoglobin, *HHb* deoxygenated haemoglobin concentration, *NIRS* near infrared spectroscopy

CPET, similar to the values observed in the upright CPET. The Borg scale may be considered valid to determine the rating of perceived exertion in supine exercise, as with upright exercise.

In a previous report, the leg-muscle HHb levels significantly correlated with work rate during upright CPET [10], and another reported that leg-muscle O_2Hb decreased and HHb increased with the increased work rate during upright cycling exercise [11]. Supine CPET and upright tests, therefore, may have similar relationships with leg-muscle O_2Hb and HHb levels and work rates.

In conclusion, the Borg scale score may be used to determine the rating of perceived exertion, whole-body fatigue and local-muscle fatigue during supine exercise. Moreover, leg muscle oxygenation is associated with the work rate in supine exercise, similar to that of upright exercise.

Acknowledgments This study was supported by a Grant-in-Aid for Exploratory Research from the Niigata University of Health and Welfare, Japan.

References

1. Anding K, Bär T, Trojniak-Hennig J et al (2015) A structured exercise programme during haemodialysis for patients with chronic kidney disease: clinical benefit and long-term adherence. BMJ Open 5:e008709
2. Kimawi I, Lamberjack B, Nelliot A et al (2017) Safety and feasibility of a protocolized approach to in-bed cycling exercise in the intensive care unit: quality improvement project. Phys Ther 97:593–602
3. Cornelis N, Buys R (2016) The effects of exercise modality on maximal and submaximal exercise parameters obtained by graded maximal exercise testing. Int J Cardiol 222:538–547
4. Inglis EC, Iannetta D, Murias JM (2017) The plateau in the NIRS-derived [HHb] signal near the end of a ramp incremental test does not indicate the upper limit of O. Am J Physiol Regul Integr Comp Physiol 313:R723–R729
5. Zamunér AR, Moreno MA, Camargo TM et al (2011) Assessment of subjective perceived exertion at the anaerobic threshold with the Borg CR-10 scale. J Sports Sci Med 10:130–136
6. Rupp T, Thomas R, Perrey S, Stephane P (2008) Prefrontal cortex oxygenation and neuromuscular responses to exhaustive exercise. Eur J Appl Physiol 102:153–163

7. Hopker JG, Jobson SA, Pandit JJ (2011) Controversies in the physiological basis of the 'anaerobic threshold' and their implications for clinical cardiopulmonary exercise testing. Anaesthesia 66:111–123
8. Muthalib M, Millet GY, Quaresima V, Nosaka K (2010) Reliability of near-infrared spectroscopy for measuring biceps brachii oxygenation during sustained and repeated isometric contractions. J Biomed Opt 15:017008
9. Morishita S, Tsubaki A, Nashimoto S, Fu JB, Onishi H (2018) Face scale rating of perceived exertion during cardiopulmonary exercise test. BMJ Open Sport Exerc Med 4:e000474
10. Re R, Pirovano I, Contini D, Spinelli L, Torricelli A (2018) Time domain near infrared spectroscopy device for monitoring muscle oxidative metabolism: custom probe and in vivo applications. *Sensors (Basel)* 18:E264
11. Ferreira LF, Koga S, Barstow TJ (2007) Dynamics of noninvasively estimated microvascular O2 extraction during ramp exercise. *J Appl Physiol (1985)* 103:1999–2004

Systemic and Quadriceps Muscle O_2 Dynamics in Subjects Without Attenuation Point of Deoxygenated Haemoglobin Concentration During Ramp Cycling Exercise

Shun Takagi, Ryotaro Kime, Shizuo Sakamoto, and Toshihito Katsumura

Abstract

The aim of this study was to compare systemic and quadriceps muscle O_2 dynamics between aerobic capacity-matched subjects without (NAP; $n = 5$) and with (CON; $n = 13$) attenuation point in deoxygenated haemoglobin concentration (deoxy-Hb) at vastus lateralis ($AP_{deoxy\text{-}Hb@VL}$) during ramp cycling exercise. Muscle O_2 saturation (SmO_2) and deoxy-Hb were monitored at the vastus lateralis (VL), rectus femoris (RF), and vastus medialis (VM) by spatial resolved near infrared spectroscopy during exercise. Cardiac output (CO) and pulmonary O_2 uptake (VO_2) were also continuously measured. During high-intensity exercise, in NAP, steeper slopes of both deoxy-Hb and SmO_2 were found at VM, similar to VL muscle. Additionally, at RF, the slope of deoxy-Hb was steeper in NAP than CON. While the slope of pulmonary VO_2 was similar between groups, the slope of CO was shallower in NAP than CON. During moderate intensity exercise, the slopes of all variables were similar between groups. These results suggest that the slope of muscle deoxygenation was enhanced not only in VL but also other thigh muscles in NAP, compared to CON. Because the slope of CO was associated with the slope of SmO_2 and deoxy-Hb at VL during high-intensity exercise, the differences in subjects with and without $AP_{deoxy\text{-}Hb@VL}$ may be partly explained by systemic O_2 supply, rather than O_2 balance in the other quadriceps muscles.

Keywords

NIRS · Muscle haemoglobin oxygenation · Systemic O_2 supply · Muscle O_2 balance

S. Takagi (✉)
Faculty of Education and Welfare, Biwako-Gakuin University, Shiga, Japan

Faculty of Health and Sports Science, Doshisha University, Kyoto, Japan

Department of Sports Medicine for Health Promotion, Tokyo Medical University, Tokyo, Japan
e-mail: s-takagi@biwakogakuin.ac.jp

R. Kime · T. Katsumura
Department of Sports Medicine for Health Promotion, Tokyo Medical University, Tokyo, Japan

S. Sakamoto
Faculty of Sport Sciences, Waseda University, Tokyo, Japan

Faculty of Sport Science, Surugadai University, Saitama, Japan

F. Scholkmann et al. (eds.), *Oxygen Transport to Tissue XLIII*, Advances in Experimental Medicine and Biology 1395, https://doi.org/10.1007/978-3-031-14190-4_70

1 Introduction

Muscle deoxygenated haemoglobin concentration (deoxy-Hb) evaluated by near infrared spectroscopy (NIRS) reflects the balance of O_2 unloading and blood outflow from the muscle, and deoxy-Hb is generally increased with increasing exercise intensity [1]. However, at vastus lateralis (VL) muscle during high-intensity levels of ramp cycling exercise, the slope of deoxy-Hb is usually attenuated, and the attenuation point in deoxy-Hb at VL ($AP_{deoxy\text{-}Hb@VL}$) is observed near the end of exercise. In contrast, in 10–30% of subjects, no clear attenuation point in muscle deoxygenation is observed, as previous studies have reported [2, 3]. Although the details of the mechanisms causing the difference are still unclear, one possible explanation may be the difference in blood flow distribution and/or muscle activities between other thigh muscles [4]. However, differences in O_2 dynamics between subjects with and without $AP_{deoxy\text{-}Hb@VL}$ have not been fully established. Recent studies have demonstrated that amplitude of muscle deoxygenation was associated with systemic aerobic capacity [1]. Therefore, the aim of this study was to compare systemic and quadriceps muscle O_2 dynamics between aerobic capacity-matched subjects with and without $AP_{deoxy\text{-}Hb@VL}$ during ramp cycling exercise. We hypothesised that the slope of muscle deoxygenation would be attenuated (i.e., shallower slope of deoxy-Hb and/or muscle O_2 saturation) during high-intensity exercise in the other quadriceps muscles in subjects without $AP_{deoxy\text{-}Hb@VL}$ compared to subjects with $AP_{deoxy\text{-}Hb@VL}$.

2 Methods

2.1 Subjects

Twenty-three healthy young men (age 21 ± 1 years; height 175.6 ± 7.9 cm; body weight 75.1 ± 13.1 kg, mean ± SD) participated in this study. None had been involved in any type of endurance training for at least 12 months before enrollment in the study. This study was approved by the institutional ethics committee. All subjects were informed of the purpose of the study and gave written consent.

2.2 Experimental Design

The subjects performed 20 or 30 W/min ramp cycling exercise until exhaustion (Aerobike 75XLII, Combi, Japan). Breath-by-breath pulmonary gas exchanges were monitored continuously throughout the exercise (AE310S, Minato Medical Science, Japan) to determine pulmonary peak O_2 uptake (VO_2) and respiratory compensation point (RCP) [5]. Cardiac output (CO), stroke volume (SV), and heart rate (HR) were also measured continuously using transthoracic impedance cardiography (PhysioFlow, Manatec Biomedical, France). Muscle O_2 saturation (SmO_2) and relative changes from rest in oxygenated haemoglobin concentration (oxy-Hb), deoxygenated haemoglobin concentration (deoxy-Hb), and total haemoglobin concentration (total-Hb) were measured at the vastus lateralis (VL), rectus femoris (RF), and vastus medialis (VM) muscles in the left leg by spatial resolved near infrared spectroscopy (Hb12–4, Astem Co., Japan). Fat layer thickness at the measurement site was measured by using an ultrasound device (EUB-7500, Hitachi Medical Corporation, Japan), and the effects of light scattering in the fat layer on NIRS data was corrected by normalising measurement sensitivity [6]. Arterial O_2 saturation (SpO_2) was measured immediately after peak exercise by pulse oximetry (MD300C22, Fukuda-Denshi, Japan). Fat-free mass (FFM) was evaluated by bio-impedance analysis (InBody 720, InBody Japan, Japan). VO_2, SV, and CO were subsequently normalised by FFM.

$AP_{deoxy\text{-}Hb@VL}$ was determined by piecewise double-linear analysis. The double linear fit was used at the onset of the systematic increase in the deoxy-Hb until the last data point corresponding to the end of the test [4]. In this study, $AP_{deoxy\text{-}Hb@VL}$ was defined as when the slope determined during higher intensity was shallower than the slope during lower intensity. As a result, $AP_{deoxy\text{-}Hb@VL}$ was not detected in 5 subjects. Additionally, 5 subjects with $AP_{deoxy\text{-}Hb@VL}$ were excluded due to

large noise or unstable data. Consequently, variables were compared between subjects without $AP_{deoxy\text{-}Hb@VL}$ (NAP; n = 5) and with $AP_{deoxy\text{-}Hb@VL}$ (CON; n = 13). Body weight, FFM, pulmonary peak VO_2, and peak power output were matched between groups. Because $AP_{deoxy\text{-}Hb@VL}$ ranged from 72% to 84% of peak VO_2 in CON, the slopes of variables were evaluated at moderate (55–70% of peak VO_2) and high (85–100% of peak VO_2) intensity exercise.

2.3 Statistical Analysis

All data are given as means ± standard deviation (SD). The amplitudes of variables during exercise were averaged over the last 10 sec every 5% of peak VO_2. To compare changes in variables during exercise, a 2-way repeated-measures analysis of variance (ANOVA) was used, with group and exercise intensity as factors. Because of a low number of subjects in NAP, ANOVA was limited from 50% to 100% of peak VO_2. Where appropriate, the Bonferroni post hoc test was performed. To detect significance accurately in spite of the low number of subjects, the slopes of physiological variables, RCP, SpO_2 and physical variables were compared between groups by unpaired t-tests. For all statistical analyses, significance was accepted at $p < 0.05$.

3 Results

At RF, there was a significant group × exercise intensity interaction for oxy-Hb ($p < 0.05$) and total-Hb ($p < 0.05$), and these were significantly higher in NAP than CON at 90–100% of peak VO_2. However, neither deoxy-Hb nor SmO_2 at RF were significantly different between groups, and there were no significant interactions or main effects of group of any NIR_{SRS} variables at VL and VM. Similarly, no significant differences in systemic O_2 dynamics were observed at group mean of any variables.

The slopes of the variables are shown in Fig. 1. During high-intensity exercise, at VL, significantly steeper slopes of both deoxy-Hb and SmO_2 were found in NAP than CON. Also at VM, the slope of deoxy-Hb tended to be steeper in NAP compared with CON, while the slope of SmO_2 was significantly steeper in NAP. At RF, the slope of deoxy-Hb tended to be steeper in NAP than CON, even though there were no significant differences in the slope of SmO_2 between groups. While the slopes of pulmonary VO_2 and HR were not significantly different between groups, the slopes of CO and SV were shallower in NAP than CON. The slope of CO was significantly positively related to the slope of SmO_2 at VL during high-intensity exercise ($r = 0.52$, $p < 0.05$), while the slope of CO tended to be negatively correlated with the slope of deoxy-Hb ($r = -0.45$, $p = 0.08$) (Fig. 2). During moderate intensity, the slopes of all variables were similar between groups.

RCP was observed at similar intensity between groups (83.8 ± 3.3 vs. 82.6 ± 4.5% of peak VO_2, $p = 0.62$). Moreover, there were no significant differences in respiratory exchange ratio (RER, 1.17 ± 0.02 vs. 1.18 ± 0.05, $p = 0.75$) and rating of perceived exertion (RPE, 19 ± 1 vs. 19 ± 1, $p = 0.63$) at peak exercise between groups. SpO_2 was not significantly different between groups immediately after exhaustion (96 ± 1% vs 96 ± 1%, $p = 0.34$).

4 Discussion

In NAP during high-intensity exercise, neither a shallower slope of deoxy-Hb nor a shallower slope of SmO_2 was observed at RF and VM. These results indicate that the slope of muscle deoxygenation was enhanced at not only VL, but also the other quadriceps muscles, in contrast to our hypothesis. At RF, SmO_2 was similar between groups while oxy-Hb and total-Hb were significantly higher near end of exercise, based on amplitude and slope analysis (data regarding slopes in oxy-Hb and total-Hb are not shown). Hence, even though the steeper slope of deoxy-Hb at RF may be attributed to reduced blood outflow from RF, our findings lead us to speculate that the differences in subjects with and without $AP_{deoxy\text{-}Hb@VL}$ may not be fully explained by the other quadriceps' O_2 bal-

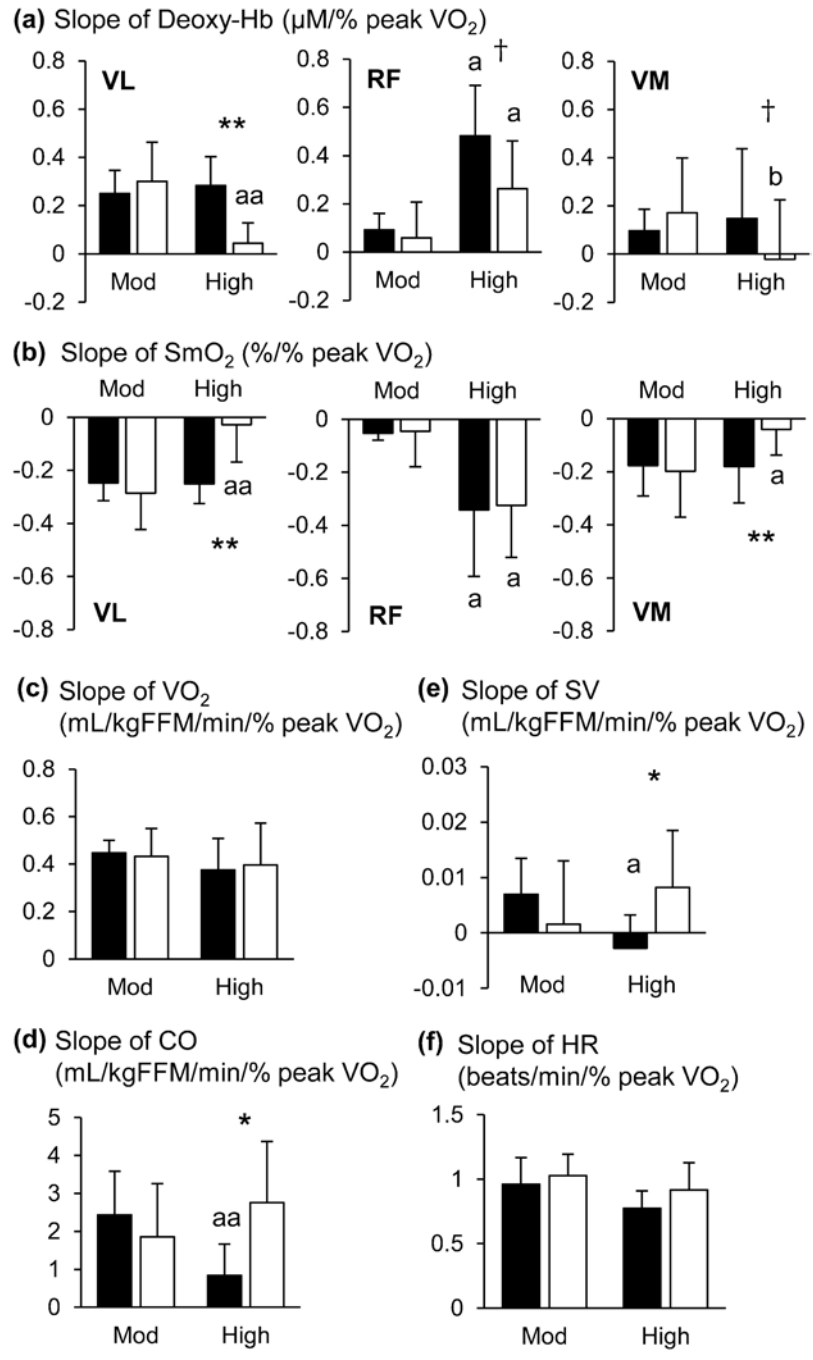

Fig. 1 Slopes of deoxy-Hb (**a**), SmO_2 (**b**), VO_2 (**c**), CO (**d**), SV (**e**), HR (**f**) in NAP (black, $n = 5$) and CON (white, $n = 13$). Significantly different between groups at same exercise intensity (*: $p < 0.05$, **: $p < 0.01$, †: $p < 0.1$). Significantly different between exercise intensity in the same group (a: $p < 0.05$, aa: $p < 0.01$, b: $p < 0.1$). *Deoxy-Hb* deoxygenated haemoglobin concentration, *SmO_2* muscle O_2 saturation, *VO_2* pulmonary O_2 uptake, *CO* cardiac output, *SV* stroke volume, *HR* heart rate, *VL* vastus lateralis, *RF* rectus femoris, *VM* vastus medialis, *FFM* fat-free mass, *NAP* subjects without attenuation point in deoxygenated haemoglobin concentration at vastus lateralis, *CON* subjects with attenuation point in deoxygenated haemoglobin concentration at vastus lateralis, *Mod* moderate intensity exercise (55–70% of peak VO_2), High: high-intensity exercise (85–100% of peak VO_2). Values are mean ± SD

ance, secondary to blood flow distribution between quadriceps muscles and/or compensatory muscle activities in other quadriceps muscles. One possible explanation may be the contribution of other muscle O_2 balance, such as lower leg muscles [7], and therefore, future studies are needed to measure blood flow and activities in several leg muscles, including the lower leg muscles. In addition, our findings should be confirmed in a large group of subjects as the sample size in this study is extremely small.

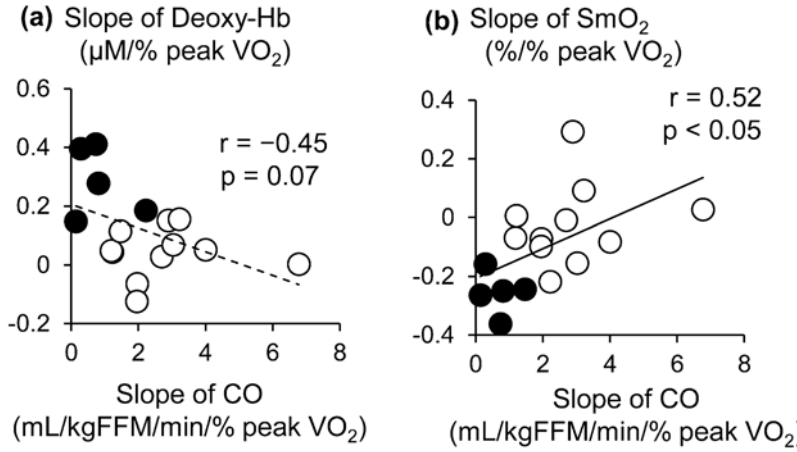

Fig. 2 Relationship between slopes of CO and slope of muscle deoxygenation at VL during high-intensity exercise in NAP (black, $n = 5$) and CON (white, $n = 13$). (**a**) slope of CO and slope of deoxy-Hb. (**b**) slope of CO and slope of SmO_2. *CO* cardiac output, *VL* vastus lateralis, *deoxy-Hb* deoxygenated haemoglobin concentration, SmO_2 muscle O_2 saturation, VO_2 pulmonary O_2 uptake, *FFM* fat-free mass, *NAP* subjects without attenuation point in deoxygenated haemoglobin concentration at vastus lateralis, *CON* subjects with attenuation point in deoxygenated haemoglobin concentration at vastus lateralis

Notably, a shallower slope of CO was observed during high-intensity exercise in NAP. This could be explained by the shallower slope of SV, because the slope of HR was similar. Though details of the mechanisms are unknown, previous studies also reported that there was an inter-individual difference in CO during high-intensity exercise [8]. In this study, pulmonary VO_2 was similar between groups, and this means that the estimated slope of systemic O_2 extraction may be steeper in NAP, based on Fick's principle. We confirmed the relationship between the slope in CO and slope of muscle deoxygenation at VL. Therefore, our findings newly suggested that the steeper slope of muscle deoxygenation in NAP may be partly explained by an increase in systemic O_2 extraction, secondary to a blunted increase in convective O_2 supply.

RCP is related to the ventilatory response to metabolic acidosis, which may coincide with $AP_{deoxy\text{-}Hb@VL}$ [9]. In this study, RCP was not significantly different between groups and values were similar to values reported in previous studies [9]. Because RER and RPE at peak exercise were also not significantly different between groups, degrees of exhaustion were similar between groups. Arterial desaturation potentially accelerated muscle deoxygenation [10]; however, SpO_2 was similar between groups. Therefore, in this study, differences in the slope of muscle deoxygenation between groups cannot be explained by these factors.

In conclusion, during intense exercise, the slope of muscle deoxygenation was enhanced not only in VL but also other quadriceps muscles in NAP compared to CON. The differences in subjects with and without $AP_{deoxy\text{-}Hb@VL}$ may be explained by systemic O_2 supply, rather than O_2 balance in other quadriceps muscles.

Acknowledgments The authors are grateful for revision of this manuscript by Andrea Hope. This work was supported in part by JSPS KAKENHI Grant Number 19 K20092 and the Harris Science Research Institute of Doshisha University to Shun Takagi.

References

1. Takagi S (2016) Skeletal muscle oxygen dynamics and peak aerobic capacity. J Phys Fitness Sports Med 5(5):379–383
2. Belardinelli R, Barstow TJ, Porszasz J et al (1995) Changes in skeletal muscle oxygenation during incremental exercise measured with near infrared

spectroscopy. Eur J Appl Physiol Occup Physiol 70(6):487–492
3. Ferreira LF, Koga S, Barstow TJ (2007) Dynamics of noninvasively estimated microvascular O_2 extraction during ramp exercise. J Appl Physiol (1985) 103(6):1999–2004
4. Iannetta D, Qahtani A, Millet GY et al (2017) Quadriceps muscles O_2 extraction and EMG breakpoints during a ramp incremental test. Front Physiol 8:686
5. Beaver WL, Wasserman K, Whipp BJ (1986) A new method for detecting anaerobic threshold by gas exchange. J Appl Physiol (1985) 60(6):2020–2027
6. Niwayama M, Suzuki H, Yamashita T et al (2012) Error factors in oxygenation measurement using continuous wave and spatially resolved near-infrared spectroscopy. J Jpn Coll Angiol 52:211–215
7. Takagi S, Kime R, Niwayama M et al (2013) Muscle oxygen saturation heterogeneity among leg muscles during ramp exercise. Adv Exp Med Biol 765:273–278
8. Trinity JD, Lee JF, Pahnke MD et al (2012) Attenuated relationship between cardiac output and oxygen uptake during high-intensity exercise. Acta Physiol (Oxf) 204(3):362–370
9. Boone J, Vandekerckhove K, Coomans I et al (2016) An integrated view on the oxygenation responses to incremental exercise at the brain, the locomotor and respiratory muscles. Eur J Appl Physiol 116(11–12):2085–2102
10. Legrand R, Ahmaidi S, Moalla W et al (2005) O_2 arterial desaturation in endurance athletes increases muscle deoxygenation. Med Sci Sports Exerc 37(5):782–788

Jaw-Clenching Intensity Effects on Masseter Oxygen Dynamics and Fatigue: A NIRS Oximetry Study

Arata Tsutsui, Kazunori Nakajima, Takahiro Sakaue, Shinji Togo, Yoshiaki Matsuda, Tomotaka Takeda, and Kenichi Fukuda

Abstract

The purpose of this study was to clarify the effects of jaw-clenching intensity on masseter muscle oxygen dynamics during clenching and recovery and masseter muscle fatigue using the spatially resolved method of near-infrared spectroscopy. Pulse rate, mean power frequency from electromyography in the masseter and visual analogue scale for masseter fatigue were also examined as related items. The 25% and 50% maximum voluntary contractions were determined using electromyography before the experiment and used as visual feedback on the screen. Twenty-three healthy adult male subjects volunteered for this study. Clenching decreased oxygen and oxygenated haemoglobin, and increased deoxygenated haemoglobin in the masseter muscle. The higher the intensity of clenching, the more prominent the effect. The oxygen dynamics tended to return to normal after clenching, but the change was slower with higher clenching intensity. Pulse rate increased with clenching, and the increment was more prominent with higher clenching intensity. Clenching caused a shift of mean power frequency to a lower range, an increase in subjective fatigue, an early appearance of a breakpoint appearance time and a prolongation of a 1/2 recovery time. All of these effects were more evident with increasing clenching intensity. In conclusion, clenching intensity influenced the oxygen dynamics of the masseter muscle and fatigue state during clenching and recovery. The higher the intensity, the greater the impact.

Keywords

Electromyography · Muscle hemoglobin oxygenation · Muscle oxygen supply · Muscle hemodynaamics

1 Introduction

Aerobic metabolism plays an important role in energy supply during muscle activity, except for short periods of intense exercise. Therefore, oxygen supply to muscle tissue via the bloodstream plays a major role in sustained muscle activity. Factors that determine oxygen supply and consumption to muscle tissue include; heart rate and

A. Tsutsui (✉) · K. Nakajima · T. Sakaue · S. Togo · Y. Matsuda · T. Takeda
Department of Oral Health and Clinical Science, Division of Sports Dentistry, Tokyo Dental College, Tokyo, Japan
e-mail: tsutsuiarata@tdc.ac.jp

K. Fukuda
Department of Oral Health and Clinical Science, Division of Special Needs Dentistry and Orofacial Pain, Tokyo Dental College, Tokyo, Japan

F. Scholkmann et al. (eds.), *Oxygen Transport to Tissue XLIII*, Advances in Experimental Medicine and Biology 1395, https://doi.org/10.1007/978-3-031-14190-4_71

cardiac output, haemoglobin concentration in arterial blood, dilation and contraction of local muscle blood vessels, and oxygen availability in mitochondria [1, 2]. This oxygen supply and consumption balance can be determined from the muscle tissue oxygen dynamics during muscle activity. In addition, ischaemia and decreased blood perfusion in muscle tissue due to changes in circulatory dynamics are thought to cause insufficient oxygen supply to muscle tissue and contribute to muscle fatigue and pain [3]. Muscle fatigue (tolerance) can also be assessed from the perspective of oxygen dynamics [4, 5].

Near-infrared spectroscopy (NIRS) has been used to measure active muscle oxygen dynamics. During skeletal muscle activity, oxygenated haemoglobin (Oxy-Hb), deoxygenated haemoglobin (Deoxy-Hb), total haemoglobin (Total-Hb), and tissue oxygen saturation (StO_2) values can be used to observe differences in muscle activity intensity, exercise style, etc. [5]. During the recovery period immediately after exercise, the magnitude of exercise hyperaemia can be considered a crucial indicator for determining whether the blood flow requirement during contraction is adequately maintained or not [3]. Breakpoint appearance time (BAT) and 1/2 recovery time (1/2 RT) calculated from StO_2 are considered indicators of muscle fatigue [4, 6–8]. BAT reflects the oxygen consumption capacity associated with muscle activity [6, 7]. 1/2 RT reflects the time required to meet the oxygen requirements for muscle activity [4, 8, 9].

Studies of masticatory muscle dynamics by NIRS have included studies on haemodynamic changes of masseter and temporalis muscles during isometric contraction in terms of Hb concentration and StO_2 [10, 11], studies on easy fatigability of the masseter muscle and masseter muscle StO_2 [6, 7]. However, no studies have examined the effects of jaw clenching and clenching intensity on masseter muscle oxygen dynamics and masseter muscle fatigue during muscle activity and recovery using multiple parameters of NIRS and other muscle fatigue assessments.

The purpose of this study was to clarify the effects of clenching intensity on masseter muscle oxygen dynamics during recovery and masseter muscle fatigue using the spatially resolved method of near-infrared spectroscopy (SR-NIRS). In addition, pulse rate (PR), which is involved in the regulation of systemic circulatory blood flow, visual analogue scale (VAS) for muscle fatigue, and shifts in mean power frequency (MPF) which are calculated from electromyography (EMG), fast Fourier transform (FFT) frequency analysis, which is widely used as an index of muscle fatigue [7, 12, 13], were also evaluated. An oral appliance (OA) was used during clenching to facilitate clenching, reduce the burden of remaining teeth and decrease the left-right difference in masseter muscle activity during measurement [14].

2 Methods

There were 23 healthy adult male volunteers (mean age: 26.77 ± 4.17 years), all of whom were employees of Tokyo Dental College Suidobashi Hospital or students of Tokyo Dental College. Participants gave their consent after sufficient explanation of the research plan. The inclusion criteria for the volunteers were general health, no subjective abnormalities in the oral cavity, temporomandibular joint or parietal muscles, and no history of cerebral nerve or cardiovascular disease. This study was approved by the Ethics Committee of the Tokyo Dental College (Approval No. 928).

The subjects were instructed to refrain from drinking alcohol on the day before the experiment and to drink water only 2 h before the experiment. The experimental schedule and block design are shown in Fig. 1a.

SR-NIRS (Oxy-Pro (Hb141) tissue oxygen saturation sensor, Astem, Kanagawa, Japan) was used. This device measures oxygen dynamics around 11 ~ 20 mm from the skin surface. Since the distances from the skin surface between the lateral and medial surfaces of the middle portion of the masseter muscle in males have been reported to be 9.4 mm and 24.8 mm [15], the measurement range with this device was reasonable. The gauge was attached at the centre of the masseter muscle on one side, and a shade was

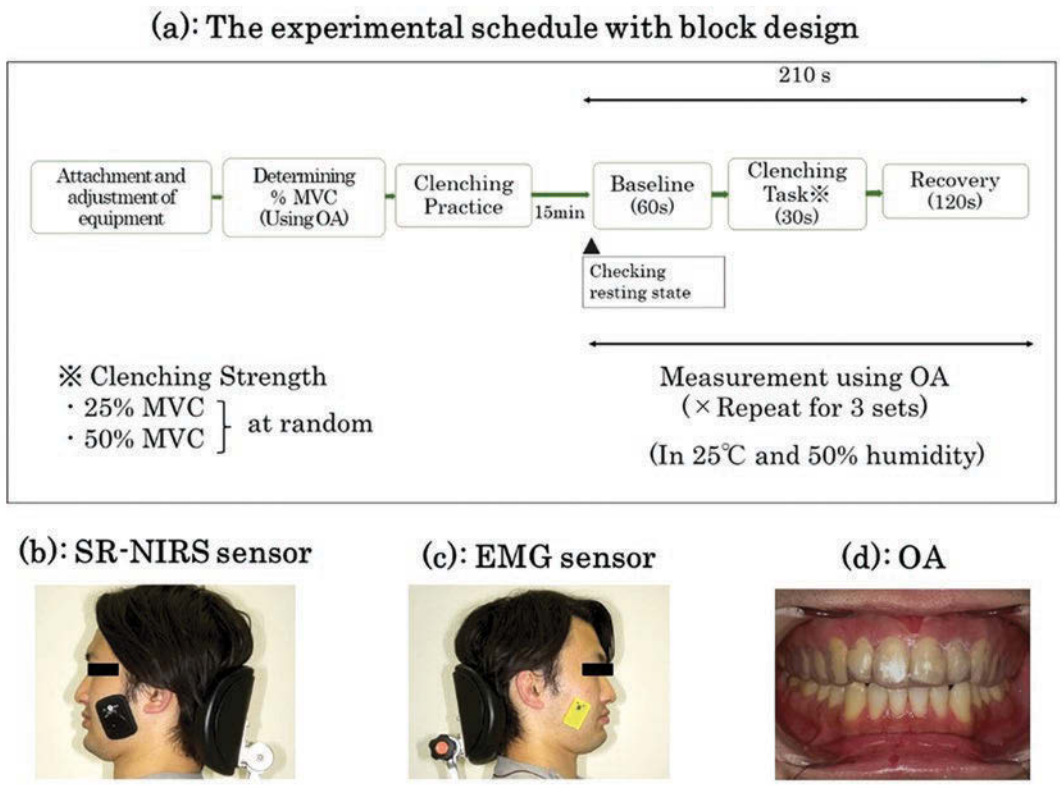

Fig. 1 (**a**) The experimental schedule with block design (**b**) EMG (**c**) SR-NIRS (**d**) OA

attached for shielding light (Fig. 1b). The test muscle was determined randomly, and the sampling frequency was recorded at 5.0 Hz. The thickness of subcutaneous fat, a source of error in muscle oxygen dynamics [16], was measured and corrected according to the manufacturer's instructions. The evaluation items: StO_2, Total-Hb, Oxy-Hb, Deoxy-Hb. BAT and 1/2 RT were calculated from the change in StO_2 as an index of muscle fatigue. BAT was identified as an intersection of the two tangents from clenching on the oxygen saturation curve [6, 7]. The 1/2 RT is the time from the end of muscle activity to when oxygen saturation reaches half of the maximum recovery level [4, 8, 9]. A pulse oximeter (WristOx2 3150 BLE, Nonin, Minnesota, USA) measured PR with 1.0 Hz sampling frequency. A DSP Wireless Electromyography sensor (SS-EMGD-HMAG, Sports sensing, Fukuoka, Japan) measured muscle activity of the masseter muscle with 1000 Hz sampling frequency, and EMG analysis software (EMG Multi ANALYSIS PROGRAM Map1038 Ver.7.9, Nihon santeku, Osaka, Japan) analysed the EMG and calculated MPF. The site of the EMG sensor application was the other side of the NIRS gauge (Fig. 1c). The 25% maximum voluntary contractions (MVC) and 50% MVC were determined before the experiment, and the measurement was performed with visual feedback on the screen. The subjective degree of fatigue of the masseter muscle was marked on the VAS. Zero means no fatigue and as the value increases, so too does the degree of fatigue.

Analysed ranges of oxygen dynamic items and PR were the last 15 s in baseline and task, and the 15 s after 15 s of task completion in recovery. MPF was analysed in all task periods.

OA for maxilla was fabricated using Clear Ethylene Vinyl Acetate Drufosoft® 3 mm blank (Dreve-Dentamid, Unna, Germany) (Fig. 1d).

In the statistical analysis, the Shapiro-Wilk test was used to evaluate the normality of the distribution of the measured values. One-way analy-

sis of variance and Bonferroni's multiple comparisons were used for statistical analysis of masseter muscle oxygen dynamics and PR changes. The paired t-test was used for the analysis of masseter muscle fatigue using the SPSS Statistics 25.0 software package (IBM, Chicago, IL, USA) at $p < 0.01$ for all.

3 Results

The results of oxygen dynamics and pulse rate changes in the masseter muscle during muscle activity due to clenching are shown in Table 1. The results of oxygen dynamics and pulse rate changes in the masseter muscle during recovery are shown in Table 2. The results of masseter muscle fatigue are shown in Table 3.

During the clenching task, 25% MVC and 50% MVC showed a significant decrease in StO_2 and Oxy-Hb and a significant increase in Deoxy-Hb compared to baseline. In addition, 50% MVC showed significantly smaller StO_2 and significantly larger Deoxy-Hb than 25% MVC.

During the recovery period, StO_2 (50% MVC), Total-Hb, Oxy-Hb, and Deoxy-Hb (25% MVC) against baseline during the recovery period after muscle activity. The 50% MVC showed significantly greater StO_2, Total-Hb, and Oxy-Hb and significantly smaller Deoxy-Hb than 25% MVC.

In PR, 50% MVC showed a significant increase compared to baseline. Also, 50% MVC showed a significant increase compared to 25% MVC.

About the masseter muscle fatigue, 50% MVC showed a lower shift in MPF compared to 25% MVC. In VAS, each MVC showed subjective fatigue, and 50% MVC showed an increased VAS value (increased fatigue) compared with 25% MVC.

4 Discussion and Conclusion

In the jaw-closing muscles, type I fibres are significantly larger (40%) than in the supra- and infrahyoid muscles [17]. Therefore, in the masseter muscle, which contains many types I fibers, muscle metabolism using oxygen in mitochondria occurs frequently, and oxygen supply by blood flow is important for stable muscle activity. The balance between vasodilation [18] and intramuscular pressure [19, 20] during clenching is one of the factors that determine regional muscle blood flow. In the present study, the increase in clenching and clenching intensity may have increased muscle metabolism, leading to a decrease in StO_2, Oxy-Hb (50% MVC), and an increase in Deoxy-Hb. And, muscle blood flow was maintained by the balance between extravascular compression by intramuscular pressure and peripheral vasodilation. Therefore, the effects of clenching and increased clenching intensity on Total-Hb were considered small.

An isometric contraction occurs post-exercise hyperkinesia to reduce the accumulated metabolites [11]. Consequently, an elevation in Total-Hb and Oxy-Hb during the recovery period after muscle activity was seen. The fact that Deoxy-Hb at 25% MVC remained unremoved seems to be parallel to a study, for Deoxy-Hb in low-intensity clenching, recovery to baseline levels was not observed even after 3 min.

Regarding the change in heart rate, Bakke et al. [21] reported that, in skeletal muscle, heart rate is thought to increase with sustained isometric effort ≧15% MVC, and the larger the muscle mass involved, the more pronounced the increase. In the present study, isometric contraction at the 50% task in a limited area of the craniofacial system caused an increase in PR. This increase in PR may have provided the oxygen and energy supply necessary for the stronger clenching.

The SR-NIRS results showed that increasing clenching strength shortened BAT and prolonged 1/2 RT. Shortened BAT and prolonged 1/2 RT mean fatigue from the exercise load increases [6, 9, 10].

It is necessary to examine the differences in the masticatory side and the effects of clenching between natural teeth in the future. In this study, measurement under high intensity such as 75% MVC and 100% MVC was not conducted because it was difficult to maintain bite strength under the same conditions. It may be necessary to conduct measurements at high intensity in

Table 1 Masseter muscle oxygen dynamics and pulse rate during clenching

		One-way ANOVA	A	B	C	Bonferroni multiple comparison tests
			Baseline	25% MVC Task	50% MVC Task	
SR-NIRS	StO_2 [%]	F = 36.66	83.84	73.90	68.33	A vs B: $p < 0.01$
		df = [2.0]	(3.26)	(9.14)	(11.27)	A vs C: $p < 0.01$
		p = 0.00				B vs C: $p < 0.01$
	Total Hb [mM]	F = 1.37	0.0839	0.0837	0.0865	
		df = [2.0]	(0.027)	(0.029)	(0.033)	
		p = 0.27				
	Oxy-Hb [mM]	F = 10.31	0.0705	0.0615	0.0592	A vs B: $p < 0.01$
		df = [2.0]	(0.023)	(0.022)	(0.026)	A vs C: $p < 0.01$
		p = 0.00				B vs C: n.s
	Deoxy-Hb [mM]	F = 38.27	0.0134	0.0220	0.0273	A vs B: $p < 0.01$
		df = [2.0]	(0.005)	(0.011)	(0.014)	A vs C: $p < 0.01$
		p = 0.00				B vs C: $p < 0.01$
Pulse rate [bpm]		F = 23.40	73.13	74.38	78.46	A vs B: n.s.
		df = [2.0]	(12.04)	(11.85)	(13.12)	A vs C: $p < 0.01$
		p = 0.00				B vs C: $p < 0.01$
					Mean (S.D.)	n.s.: Not significant

Table 2 Masseter muscle oxygen dynamics and pulse rate during recovery

		One-way ANOVA	A	B	C	Bonferroni multiple comparison tests
			Baseline	25% MVC recovery	50% MVC recovery	
SR-NIRS	StO_2 [%]	F = 18.54	83.84	82.77	86.44	A vs B: n.s.
		df = [2.0]	(3.26)	(3.65)	(3.71)	A vs C: $p < 0.01$
		p = 0.00				B vs C: $p < 0.01$
	Total Hb [mM]	F = 24.56	0.0839	0.0915	0.1043	A vs B: $p < 0.01$
		df = [2.0]	(0.027)	(0.033)	(0.044)	A vs C: $p < 0.01$
		p = 0.00				B vs C: $p < 0.01$
	Oxy-Hb [mM]	F = 22.68	0.0705	0.0769	0.0912	A vs B: $p < 0.01$
		df = [2.0]	(0.023)	(0.029)	(0.040)	A vs C: $p < 0.01$
		p = 0.00				B vs C: $p < 0.01$
	Deoxy-Hb [mM]	F = 10.58	0.0134	0.0158	0.0131	A vs B: $p < 0.01$
		df = [2.0]	(0.005)	(0.006)	(0.004)	A vs C: n.s.
		p = 0.00				B vs C: $p < 0.01$
Pulse rate [bpm]		F = 0.90	73.13	74.52	74.43	
		df = [2.0]	(12.04)	(11.29)	(12.00)	
		p = 0.42				
					Mean (S.D.)	n.s.: Not significant

Table 3 Masseter muscle fatigue

	25% MVC	50% MVC	Paired t-test
Breakpoint appearance time [s]	15.84	12.46	p = 0.000
	(3.83)	(3.75)	
1/2 recovery time [s]	3.18	4.33	p = 0.002
	(1.59)	(1.49)	
MPF [Hz]	160.55	135.63	p = 0.000
	(14.22)	(19.23)	
VAS [cm]	2.13	4.06	p = 0.000
	(1.57)	(1.97)	
		Mean (S.D.)	n.s.: Not significant

future studies. Furthermore, considering that women are thought to have higher muscular endurance than men, we should compare the difference. In the future, it will be necessary to conduct a more detailed study that considers the above factors, and an effect on the autonomic nervous system in detail.

In conclusion, clenching intensity influenced the oxygen dynamics of the masseter muscle and fatigue state of the masseter muscle during clenching and recovery. The higher the intensity, the greater the impact.

Acknowledgments The authors would like to thank all the study participants.

References

1. Levine BD (2008) VO2max: what do we know, and what do we still need to know? J Physiol 586:25–34
2. Saltin B, Strange S (1992) Maximal oxygen uptake: "old" and "new" arguments for a cardiovascular limitation. Med Sci Sports Exerc 24:30–37
3. Larsson S-E, Bodegård L, Henriksson KG et al (1990) Chronic trapezius myalgia: morphology and blood flowlstudied in 17 patients. Acta Orthop Scand 61:394–398
4. Kime R, Hamaoka T, Sako T et al (2003) Delayed reoxygenation after maximal isometric handgrip exercise in high oxidative capacity muscle. Eur J Appl Physiol 89:34–41
5. Perrey S, Ferrari M (2018) Muscle oximetry in sports science: a systematic review. Sports Med 48:597–616
6. Kondo A, Ishikawa H, Iida J (2001) Assessment of fatigue tendency of masseter muscle using near-infrared spectroscopy. Hokkaido J Dent Sci 22:220–230
7. Horikoshi E, Ishikawa H, Yoshida T et al (2013) Oxygen saturation and electromyographic changes in masseter muscle during experimental chewing of gum with harder texture. Acta Odontol Scand 71:1378–1385
8. McCully KK, Halber C, Posner JD (1994) Exercise-induced changes in oxygen saturation in the calf muscles of elderly subjects with peripheral vascular disease. J Gerontol 49:B128–B134
9. Chance B (1992) Recovery from exercise-induced desaturation in the quadriceps muscles of elite competitive rowers. Am J Phys 262:c766–c775
10. Delcanho RE, Kim YJ, Clark GT (1996) Haemodynamic changes induced by submaximal isometric contraction in painful and non-painful human masseter using near-infra-red spectroscopy. Arch Oral Biol 41:585–596
11. Kim YJ (1999) Haemodynamic changes in human masseter and temporalis muscles induced by different levels of isometric contraction. Arch Oral Biol 44:641–650
12. Arendt-Nielsen L, Mills KR, Forster A (1989) Changes in muscle fiber conduction velocity, mean power frequency, and mean EMG voltage during prolonged submaximal contractions. Muscle Nerve 12:493–497
13. Viitasalo JH, Komi PV (1977) Signal characteristics of EMG during fatigue. Eur J Appl Physiol Occup Physiol 37:111–121
14. Naeije M (1988) Muscle physiology relevant in craniomandibular disorders. J Craniomandib Disord Facial Oral Pain 2:153–157
15. Sugisaki M, Misawa A, Ikai A et al (2001) Sex differences in the hemoglobin oxygenation state of the resting healthy human masseter muscle. J Orofac Pain 15:320–328
16. Kek KJ, Kibe R, Niwayama M et al (2008) Optical imaging instrument for muscle oxygenation based on spatially resolved spectroscopy. Opt Express 16:18173–18187
17. Korfage JA, Schueler YT, Brugman P et al (2001) Differences in myosin heavy-chain composition between human jaw-closing muscles and supra- and infrahyoid muscles. Arch Oral Biol 46:821–827
18. Heinonen I (2014) Muscle-specific functional sympatholysis in humans. Exp Physiol 99:344–345
19. Hamaoka T, McCully KK, Quaresima V et al (2007) Near-infrared spectroscopy/imaging for monitoring muscle oxygenation and oxidative metabolism in healthy and diseased humans. J Biomed Opt 12:062105
20. Moller E (1979) Mechanism of ischemic pain in human muscles of mastication: intramuscular pressure, EMG, force and blood flow of the temporal and masseter muscles during biting. Adv Pain Res Ther 3:271–281
21. Bakke M, Thomsen CE, Vilmann A et al (1996) Ultrasonographic assessment of the swelling of the human masseter muscle after static and dynamic activity. Arch Oral Biol 41:133–140

Index

F. Scholkmann et al. (eds.), *Oxygen Transport to Tissue XLIII*, Advances in Experimental Medicine and Biology 1395, https://doi.org/10.1007/978-3-031-14190-4